



I. R. IRAN

ISSN: 1728-1431

e-ISSN: 1735-9244



International Journal of Engineering

Journal Homepage: www.ije.ir



TRANSACTIONS A: BASICS

Volume 36, Number 10, October 2023

Materials and Energy Research Center

INTERNATIONAL JOURNAL OF ENGINEERING

Transactions A: Basics

DIRECTOR-IN-CHARGE

H. Omidvar

EDITOR IN CHIEF

G. D. Najafpour

ASSOCIATE EDITOR

A. Haerian

EDITORIAL BOARD

- | | | | |
|------|--|-------|--|
| S.B. | Adeloju, Charles Sturt University, Wagga, Australia | A. | Mahmoudi, Bu-Ali Sina University, Hamedan, Iran |
| K. | Badie, Iran Telecomm. Research Center, Tehran, Iran | O.P. | Malik, University of Calgary, Alberta, Canada |
| M. | Balaban, Massachusetts Ins. of Technology (MIT), USA | G.D. | Najafpour, Babol Noshirvani Univ. of Tech., Babol, Iran |
| M. | Bodaghi, Nottingham Trent University, Nottingham, UK | F. | Nateghi-A, Int. Ins. Earthquake Eng. Seis., Tehran, Iran |
| E. | Clausen, Univ. of Arkansas, North Carolina, USA | S. E. | Oh, Kangwon National University, Korea |
| W.R. | Daud, University Kebangsaan Malaysia, Selangor, Malaysia | M. | Osanloo, Amirkabir Univ. of Tech., Tehran, Iran |
| M. | Ehsan, Sharif University of Technology, Tehran, Iran | M. | Pazouki, MERC, Karaj, Iran |
| J. | Faiz, Univ. of Tehran, Tehran, Iran | J. | Rashed-Mohassel, Univ. of Tehran, Tehran, Iran |
| H. | Farrahi, Sharif University of Technology, Tehran, Iran | S. K. | Sadmezhad, Sharif Univ. of Tech, Tehran, Iran |
| K. | Firoozbakhsh, Sharif Univ. of Technology, Tehran, Iran | R. | Sahraeian, Shahed University, Tehran, Iran |
| A. | Haerian, Sajad Univ., Mashhad, Iran | A. | Shokuhfar, K. N. Toosi Univ. of Tech., Tehran, Iran |
| H. | Hassanpour, Shahrood Univ. of Tech., Shahrood, Iran | R. | Tavakkoli-Moghaddam, Univ. of Tehran, Tehran, Iran |
| W. | Hogland, Linnaeus Univ, Kalmar Sweden | T. | Teng, Univ. Sains Malaysia, Gelugor, Malaysia |
| A.F. | Ismail, Univ. Tech. Malaysia, Skudai, Malaysia | P. | Tiong, Nanyang Technological University, Singapore |
| M. | Jain, University of Nebraska Medical Center, Omaha, USA | X. | Wang, Deakin University, Geelong VIC 3217, Australia |
| M. | Keyanpour rad, Materials and Energy Research Center, Karaj, Iran | H. | Omidvar, Amirkabir Univ. of Tech., Tehran, Iran |

EDITORIAL ADVISORY BOARD

- | | | | |
|-------|--|-------|---|
| S. T. | Akhavan-Niaki, Sharif Univ. of Tech., Tehran, Iran | A. | Kheyroddin, Semnan Univ., Semnan, Iran |
| M. | Amidpour, K. N. Toosi Univ of Tech., Tehran, Iran | N. | Latifi, Mississippi State Univ., Mississippi State, USA |
| M. | Azadi, Semnan university, Semnan, Iran | H. | Oraee, Sharif Univ. of Tech., Tehran, Iran |
| M. | Azadi, Semnan University, Semnan, Iran | S. M. | Seyed-Hosseini, Iran Univ. of Sc. & Tech., Tehran, Iran |
| F. | Behnamfar, Isfahan University of Technology, Isfahan | M. T. | Shervani-Tabar, Tabriz Univ., Tabriz, Iran |
| R. | Dutta, Sharda University, India | E. | Shirani, Isfahan Univ. of Tech., Isfahan, Iran |
| M. | Eslami, Amirkabir Univ. of Technology, Tehran, Iran | A. | Siadat, Arts et Métiers, France |
| H. | Hamidi, K.N.Toosi Univ. of Technology, Tehran, Iran | C. | Triki, Hamad Bin Khalifa Univ., Doha, Qatar |
| S. | Jafarmadar, Urmia Univ., Urmia, Iran | | |

TECHNICAL STAFF

M. Khavarpour; M. Mohammadi; V. H. Bazzaz, R. Esfandiar; T. Ebadi

DISCLAIMER

The publication of papers in International Journal of Engineering does not imply that the editorial board, reviewers or publisher accept, approve or endorse the data and conclusions of authors.

CONTENTS

Transactions A: Basics

F. Ghaderi, A. Toloei, R. Ghasemi	Quadrotor Control for Tracking Moving Target, and Dynamic Obstacle Avoidance Based on Potential Field Method	1720-1732
R. Kumar, M. A. Chaudhari, P. Chaturvedi, K. S. Raja Sekhar	A Fault Tolerant Operation of 3-Phase, 5-Level CHBMLI under Open Circuit Fault Conditions	1733-1745
S. Jalali, M. Amelsakhi, M. Momeni Roghabadi, S. A. Hosseini, R. Khajavi	Plastic Properties and Collapse Investigation of Fine-grained Soil Rehabilitated with Styrene Butadiene Rubber: A Case Study in Kerman, Iran	1746-1757
B. Zare, M. Mokhtari, R. Porhoseni	Effects of Xanthan Gum and Lime on Physical Properties and Mechanical Behavior of Organic Soil	1758-1772
S. Djemmah, Y. Madi, M. Voué, A. Haddad, D. Allou, S. Ouallam, H. Bouchafaa, A. Rezzoug	Effect of Mg Addition on Morphology, Roughness and Adhesion of Cr Chromized Layer Produced by Pack Cementation	1773-1782
L. Nikolaichuk, K. Ignatiev, I. Filatova, A. Shabalova	Diversification of Portfolio of International Oil and Gas Assets using Cluster Analysis	1783-1792
S. Khaligh Fard, H. Ahmadi, M. H. Alizadeh Elizei	Electricity Supply Model of Conventional Residential Buildings in Tehran with Priority on Renewable Energy Using Adaptive Fuzzy-neural Inference System	1793-1814
S. El Yassari, A. EL Ghoulbzouri	Numerical Simulation of Fiber-reinforced Concrete under Cyclic Loading using Extended Finite Element Method and Concrete Damaged Plasticity	1815-1826
M. Abedini, H. Jazayeriy, J. Kazemitabar	Improved Simultaneous Localization and Mapping Estimation using Crow Search Algorithm Based Particle Filter	1827-1838
M. Jafarzadeh Marandi, V. Ghiasi, K. Badv	Numerical Evaluation of Two-dimensional Multi-layer Cover System to Regulate Acid Mine Drainage of Tailing Dams	1839-1856
R. Khandan, A. Sivandipour, E. Noroozinejad Farsangi	A Parametric Study on Improved Reduced Beam Section Connections with Post-tensioning to Enhance Seismic Resilience	1857-1867
A. Ahangarani Farahani, A. Dideban	Controller Design of Hybrid-Time Delay-Petri Nets Based on Lyapunov Theory by Adding Control Places	1868-1879

M. Abaei, M. R. Rahimpour, M. Farvizi, M. J. Eshraghi	Microstructure and Corrosion Behavior of Al-Cu-Fe Quasi-crystalline Coated Ti-6Al-4V Alloy	1880-1891
M. Mazloom, N. Fallah	A New Approach for Seismic Damage Detection Based on Results of Pushover Analysis and Modal Based Damage Index	1892-1907
M. Zafardoagoo, S. K. Sadrnezhaad, J. Mostaghimi	NiO-Ni-Al ₂ O ₃ (γ) Nanocatalyst by Pulse Electrocodeposition Over Ni Open-cell Foam for Methane Reforming	1908-1918
L. A. A. Al-Hindawi, A. M. Al-Dahawi, A. Sh. J. Al-Zuheriy	Use of Waste Materials for Sustainable Development of Rigid Pavement	1919-1931
R. M. Babaheydari, S. O. Mirabootalebi, G. H. Akbari, H. Salehifar	Prediction of Hardness of Copper-based Nanocomposites Fabricated by Ball-milling using Artificial Neural Network	1932-1941



Quadrotor Control for Tracking Moving Target, and Dynamic Obstacle Avoidance Based on Potential Field Method

F. Ghaderi^a, A. Toloei^{*a}, R. Ghasemi^b

^a Department of New Technologies and Aerospace Engineering, Shahid Beheshti University, Tehran, Iran

^b Department of Engineering, University of Qom, Qom, Iran

P A P E R I N F O

Paper history:

Received 15 January 2023

Received in revised form 08 March 2023

Accepted 11 March 2023

Keywords:

Quadrotor

Sliding Mode

Obstacle Avoidance

Potential Field

A B S T R A C T

The purpose of this paper is obstacle avoidance and moving target tracking for a quadrotor. Solving the obstacle crossing problem for the quadrotor includes two parts. The first part is controlling the attitude and position. The second part is path planning to pass obstacles. In this paper, the attitude and position of the quadrotor are controlled by super-twisting sliding mode control (SMC) and non-singular terminal super-twisting SMC. The simulation results of these two methods were compared. In the non-singular terminal ST-SMC method, the convergence time was approximately 5% less than the super-twisting SMC method. Also, the non-singular terminal ST-SMC method has more ability to remove disturbances. Because of the better results, the non-single terminal ST-SMC was used to control the position and attitude of the quadrotor to cross obstacles and track the target. In the second step, to cross obstacles, the potential field path planning algorithm is used. This method is a combination of attraction towards the target and repulsion from obstacles. The results of the simulation of crossing the obstacles were presented in four missions. In the first mission, the obstacles and the target are static, and in the second mission, the obstacles are static, and the target is moving. In the following, the obstacles and the target are dynamic; in the last mission, a combination of static and dynamic obstacles is considered, and the target is moving. The simulation results of four missions show that the quadrotor does not hit obstacles and reaches the desired goal, till the applied method is successful.

doi: 10.5829/ije.2023.36.10a.01

1. INTRODUCTION

During the last decade, attention to autonomous robots has increased. Instead of predicting appropriate actions for all possible states in the algorithm, robots are programmed in such a way that by having a certain level of intelligence to perform the desired action in a special situation, they can make decisions on their own [1, 2]. An essential aspect of intelligence in designing a robot's path is identifying obstacles and avoiding them in an unknown environment.

Solving the obstacle avoidance problem for flying robots includes two steps. In the first step, the position and attitude are controlled, and in the second step, path planning is applied to pass the obstacles.

Because of the nonlinear dynamics of the quadrotor, nonlinear methods are used to control the position and

attitude of the quadrotor. Due to the ability to overcome dynamic nonlinearities and eliminate disturbances and low sensitivity to system parameter changes and disturbances, and no need for accurate modeling, the sliding mode method is often used for the quadrotor system [3-5]. In the nonlinear approach was used to stabilize the quadrotor, and the controller was verified through simulation and experimental [3]. Karami et al. [5] presented an inner and outer loop control where sliding mode control was applied in both loops. In the SMC method is used to control the UAV [6]. The results showed the success of the applied method, but the chattering phenomenon has not been removed in this work. Matouk et al.[7] presented a second-order SMC controller to control the attitude and position of the quadrotor. The effect of external disturbances has been ignored. Noordin et al. [8] also used SMC to control the

*Corresponding Author Institutional Email: toloei@sbu.ac.ir
(A. Toloei)

position and height of the UAV. In this research, external disturbances were ignored and the sat function was used to remove the chattering phenomenon.

In this paper, to remove chattering, super-twisting SMC controller and super twisting nonsingular terminal SMC are used to control the system. Also, the role of the controller in reducing the effect of disturbances is considered.

Path planning methods for obstacle avoidance are placed in two categories. The first category deals with routing in the presence of static obstacles, and the second method examines passing dynamic obstacles. A* Algorithm, Genetic Algorithm, Differential Evolution, Ant Colony Optimization, and Particle Swarm Optimization are in the first category. Algorithm A* is an important algorithm in dealing with static obstacles. This method considers the heuristic search of the path to pass the obstacles according to the shortest path. The most important advantage of this method is direct search. The problems of this method are the high amount of calculations and the lack of guarantee the optimal solution [9, 10]. Through direct action on the object, the genetic algorithm can obtain search space without determining rules [11, 12]. The most important feature of this method is the strong global search, and defect of this method is poor stability. The advantages and disadvantages of another path planning method to avoid obstacles, Differential Evolution, are similar to the genetic algorithm, but in this method, the probability of mutation is higher [13]. In the ant colony algorithm method, the behavior of an ant is used to show a practical solution to the path optimization problem [14]. This method has high efficiency, but the speed of convergence is slow in the early stages. In the particle swarm optimization method, the search time is fast, but the convergence speed in the next steps is slow [15]. Various path planning methods have been applied to avoid dynamic obstacles, for example, Fuzzy Logic Algorithm, Neural Network, Rapidly-exploring Random Trees, Artificial Potential Field, Neural Network, Deep Reinforcement Learning, and Reinforcement Learning. The problems of the Rapidly-exploring Random Trees method are high space for calculations and poor real-time performance, but it has a high ability to search [16]. In the Fuzzy logic algorithm, the volume of calculations is small, but it relies on highly specialized knowledge [17]. Among the advantages of Neural Network, we can mention strong learning ability and simple learning rules, but this method has disadvantages, such as long training time and difficulty obtaining samples [18]. In deep reinforcement learning, the dimensions are reduced, and the training time is long [19]. Among the methods of avoiding collision with obstacles, the virtual potential field method is more used in the aerospace industry. The advantages of this method are simple structure, good real-time performance, fast path planning speed. The

obstacle crossing for the quadrotor with disturbance was presented by Zhao et al. [20]. In this article the obstacles are assumed to be static. Kondo and Tsuchiya [21] used the potential field method to create sequential paths to pass through dynamic obstacles. In this article, the target is considered static. Yan et al. [22] defined variables such as speed and relative acceleration and discussed crossing obstacles based on the improved potential field. The obstacles in this article are static, and the target is dynamic. In the artificial potential method, a factor was added to the repulsion function to avoid the local minimum problem [23]. This research is limited to two-dimensional environments.

In previous works, it has not been investigated the non-collision of dynamic and static obstacles with moving target tracking simultaneously. In this paper, quadrotor control in an environment with dynamic and static obstacles with moving target tracking is discussed. In the first part, the quadrotor dynamic modeling is given. Attitude and position control is done by the SMC method. In the following, the comparison of super twisting controller and the super twisting nonsingular terminal SMC has been discussed. In the next section, the obstacle avoidance of the quadrotor with static obstacles with a fixed target, and the obstacle avoidance with moving obstacles and target are discussed. At the end, the combination of fixed and moving obstacles with a dynamic target is investigated. Finally, the simulation results are presented.

2. DYNAMIC MODEL OF QUADROTOR

The dynamic model of the quadrotor can be obtained in two ways: Newton-Euler and Euler-Lagrange [24]. Here the six degrees of freedom model is obtained according to the Newton-Euler method. The following equation introduces the total rotors velocity and the rotor velocity vector:

$$\Omega = \omega_4 + \omega_2 - \omega_1 - \omega_3 \quad , \quad \Omega = \begin{bmatrix} \Omega_1 \\ \Omega_2 \\ \Omega_3 \\ \Omega_4 \end{bmatrix} \quad (1)$$

where $(\Omega_1, \Omega_2, \Omega_3, \Omega_4)$ are the speeds of the four rotors. The following equation shows the effect of the motion vector on the quadrotor dynamics.

$$U_B(\Omega) = E_B \Omega^2 = \begin{bmatrix} 0 \\ 0 \\ U_1 \\ U_2 \\ U_3 \\ U_4 \end{bmatrix} = \begin{bmatrix} 0 \\ 0 \\ b(\Omega_1^2 + \Omega_2^2 + \Omega_3^2 + \Omega_4^2) \\ bl(\Omega_4^2 - \Omega_2^2) \\ bl(\Omega_3^2 - \Omega_1^2) \\ c_d(\Omega_2^2 + \Omega_4^2 - \Omega_1^2 - \Omega_3^2) \end{bmatrix} \quad (2)$$

where l is the length from the center of mass to each rotor, c_T is the thrust force coefficient, and c_d is the drag

force coefficient. The matrix E_B , which represents the motion matrix multiplied by the locust velocity square Ω^2 and produces the motion vector $U_B(\Omega)$, is defined as follows.

$$E_B = \begin{bmatrix} 0 & 0 & 0 & 0 \\ 0 & 0 & 0 & 0 \\ c_T & c_T & c_T & c_T \\ 0 & -c_T l & 0 & c_T l \\ -c_T l & 0 & c_T l & 0 \\ -c_d & c_d & -c_d & c_d \end{bmatrix} \quad (7)$$

The quadrotor dynamic equations are as follows:

$$\begin{aligned} \delta_1 &= \dot{\phi} = \ddot{\phi} + \ddot{\theta} \sin \phi \tan \theta + \ddot{\psi} \cos \phi \tan \theta \\ \delta_2 &= \dot{\theta} = \ddot{\theta} \cos \phi - \ddot{\psi} \sin \phi \\ \delta_3 &= \dot{\psi} = \frac{\sin \phi}{\cos \theta} \ddot{\theta} + \frac{\cos \phi}{\cos \theta} \ddot{\psi} \\ \delta_4 &= \dot{x} = \delta_{10} \\ \delta_5 &= \dot{y} = \delta_{11} \\ \delta_6 &= \dot{z} = \delta_{12} \\ \delta_7 &= \dot{P} = \frac{I_{YY} - I_{ZZ}}{I_{XX}} RQ - \frac{J_{Tp}}{I_{XX}} Q \Omega + \frac{U_2}{I_{XX}} \\ \delta_8 &= \dot{Q} = \frac{I_{ZZ} - I_{XX}}{I_{YY}} RP + \frac{J_{Tp}}{I_{YY}} P \Omega + \frac{U_3}{I_{YY}} \\ \delta_9 &= \dot{R} = \frac{I_{XX} - I_{YY}}{I_{ZZ}} PQ + \frac{U_4}{I_{ZZ}} \\ \delta_{10} &= \dot{U} = (-WQ + VR) + g s_\theta \\ \delta_{11} &= \dot{V} = (-UR + WP) - g c_\theta s_\phi \\ \delta_{12} &= \dot{W} = (-UQ + VP) - g c_\theta s_\phi + \frac{U_1}{m} \end{aligned} \quad (8)$$

In these equations, J_{Tp} , the moment of total rotation of inertia about the rotor axis, (U, V, W) the speed vector of the quadrotor, (P, Q, R) roll, pitch, and yaw, and I_{XX} , I_{YY} , and I_{ZZ} are the moments of inertia in the x, y, and z-axis, whose values are given in Table 1.

Also, the rotors speed inputs U_1, U_2, U_3 , and U_4 are obtained from the following equations:

$$\begin{aligned} U_1 &= c_T (\Omega_1^2 + \Omega_2^2 + \Omega_3^2 + \Omega_4^2) \\ U_2 &= l c_T (-\Omega_2^2 + \Omega_4^2) \\ U_3 &= l c_T (-\Omega_1^2 + \Omega_3^2) \\ U_4 &= c_d (-\Omega_1^2 + \Omega_2^2 - \Omega_3^2 + \Omega_4^2) \\ \Omega &= -\Omega_1 + \Omega_2 - \Omega_3 + \Omega_4 \end{aligned} \quad (9)$$

TABLE 1. quadrotor model parameters used in the simulation

Parameter	Value
I_{XX}	$11 \times 10^{-2} \text{ kg m}^2$
I_{YY}	$19 \times 10^{-2} \text{ kg m}^2$
I_{ZZ}	$1.3 \times 10^{-2} \text{ kg m}^2$
J_{Tp}	$6 \times 10^{-5} \text{ kg m}^2$

m	3.23 kg
l	0.23 m
c_d	$7.5 \times 10^{-7} \text{ N m s}^2$
c_T	$3.13 \times 10^{-5} \text{ N s}^2$

3. SLIDING MODE CONTROLLER

The SMC method is recognized as one of the efficient approaches to design controllers for nonlinear dynamic systems. The main advantage of SMC is low sensitivity to changes and disturbances of system parameters, which eliminates the need for detailed modeling. SMC reduces the complexity of feedback design. In the following, the design of two SMC methods has been discussed.

3.1. Super Twisting SMC ST-SMC is designated to decrease the chattering phenomena for a quadrotor with a relative degree of one. The variable dynamics of the sliding surface are [3]:

$$\dot{s} = \Phi(t, x) + Y(t, x) \quad (10)$$

With limited conditions:

$$\begin{aligned} |\Phi(t, x)| &\leq \Phi \\ 0 < \Gamma_m &\leq Y(t, x) \leq \Gamma_M \\ |S| &\leq S_0 \end{aligned}$$

So that Γ_m , Γ_M , and Φ are positive constant values. Control inputs in ST-SMC are designed as follows:

$$u = u_1 + u_2 \quad (11)$$

where:

$$\dot{u}_1 = \begin{cases} -u. & |u| > 1 \\ -W \text{sign}(s). & |u| \leq 1 \end{cases}$$

$$u_2 = \begin{cases} -\lambda |s_0|^\rho \text{sign}(s). & |s| > s_0 \\ -\lambda |s|^\rho \text{sign}(s). & |s| \leq s_0 \end{cases}$$

The convergence conditions are stated in the following equation:

$$W > \frac{\Phi}{\Gamma_m} > 0 \quad (12)$$

$$\lambda^2 \geq \frac{4 \Phi \Gamma_M (W + \Phi)}{\Gamma_m^3 (W - \Phi)} \quad (13)$$

For $\rho = 1$, the algorithm converges exponentially to the origin. For the systems where $s_0 = \infty$ and there is no limitation in control, the algorithm can be simplified as follows:

$$u(t) = -\lambda |s|^\rho \text{sign}(s) + u_1 \quad (14)$$

$$u = -\lambda |s|^\rho \text{sign}(s) + k \int \text{sign}(S)$$

The control inputs consist of two parts [16]: equivalent part and reaching one as:

$$U_n = u_{eq} + u_r \tag{11}$$

where u_{eq} is obtained by setting the sliding surface derivative equal to zero, and u_r satisfies the Lyapunov stability condition of the sliding surface. Finally, the control commands are obtained as follows:

$$\begin{aligned}
 U_1 &= \frac{m}{(\cos \theta \cos \varphi)} (g + \ddot{z}_d - \lambda_z \dot{z} - k_{z1} |S_z|^\rho \operatorname{sign}(S_z) - k_{z2} \int \operatorname{sign}(S_z)) \\
 U_2 &= \frac{I_x}{L} \left(-\frac{(I_y - I_z)}{I_x} \dot{\theta} \dot{\psi} + \frac{J_{TP}}{I_x} \dot{\theta} \Omega + \ddot{\psi}_d - \lambda_\psi \dot{\psi} - k_{\varphi 1} |S_\varphi|^\rho \operatorname{sign}(S_\varphi) - k_{\varphi 2} \int \operatorname{sign}(S_\varphi) \right) \\
 U_3 &= \left(\frac{I_y}{L} \right) \left(-\frac{(I_x - I_z)}{I_y} \dot{\phi} \dot{\psi} - \frac{J_{TP}}{I_y} \dot{\phi} \Omega + \ddot{\theta}_d - \lambda_\theta \dot{\theta} - k_{\theta 1} |S_\theta|^\rho \operatorname{sign}(S_\theta) - k_{\theta 2} \int \operatorname{sign}(S_\theta) \right) \\
 U_4 &= I_z \left(-\frac{(I_x - I_y)}{I_z} \dot{\phi} \dot{\psi} + \ddot{\psi}_d - \lambda_\psi \dot{\psi} - k_{\psi 1} |S_\psi|^\rho \operatorname{sign}(S_\psi) - k_{\psi 2} \int \operatorname{sign}(S_\psi) \right) \\
 U_x &= \left(\frac{m}{U_1} \right) (\ddot{x}_d - \lambda_x \dot{x} - k_{x1} |S_x|^\rho \operatorname{sign}(S_x) - k_{x2} \int \operatorname{sign}(S_x)) \\
 U_y &= \left(\frac{m}{U_1} \right) (\ddot{y}_d - \lambda_y \dot{y} - k_{y1} |S_y|^\rho \operatorname{sign}(S_y) - k_{y2} \int \operatorname{sign}(S_y))
 \end{aligned} \tag{12}$$

Figures 2 and 3 show the sliding surface. Figures 4 and 5 represent quadrotor control commands as depicted in Equation (12), and Figure 6 represents the attitude of the quadrotor using ST-SMC. The control parameters are prearranged in Table 2.

As it is clear from Figures 1 and 2, the sliding surfaces of position and attitude converge to zero in less than 0.8 seconds which is a favorable time.

In Figures 3 and 4, the control commands of the quadrotor are shown, which show that the chattering phenomenon did not occur and there is no strong oscillation. In addition, the convergence to zero happened in about 2 seconds which is a favorable time.

TABLE 2. Control parameter in the design of the ST-SMC

Design parameter	Value	Design parameter	Value
k_x	22.2	λ_x	0.12
k_y	16.1	λ_y	1.17
k_z	21.5	λ_z	1.55
k_φ	11.5	λ_φ	5
k_θ	11.5	λ_θ	5.5
k_ψ	11.5	λ_ψ	0.98
δ	0.17		

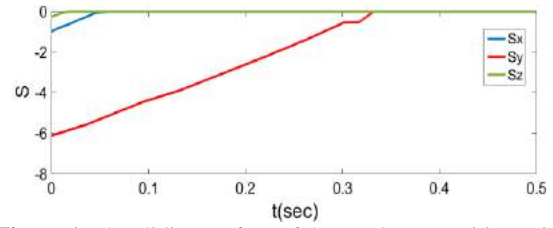


Figure 1. The sliding surface of the quadrotor position using ST-SMC

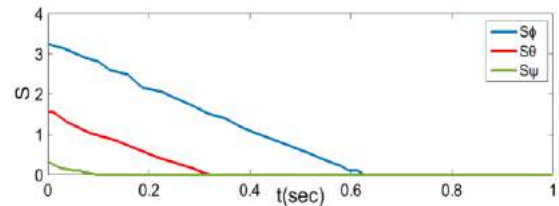


Figure 2. The sliding surface of the quadrotor attitude using ST-SMC

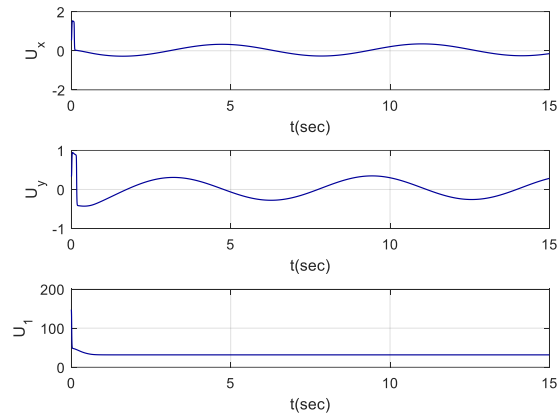


Figure 3. Quadrotor control commands using the ST-SMC

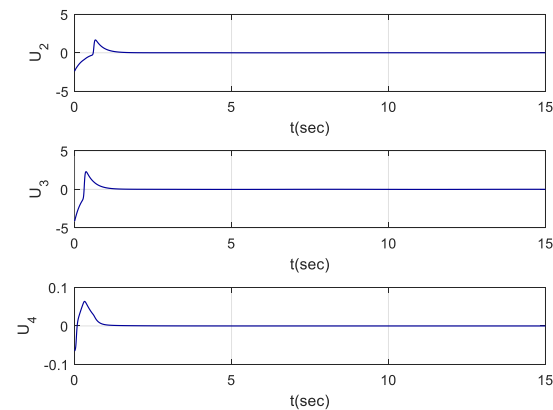


Figure 4. Quadrotor control commands using the ST-SMC

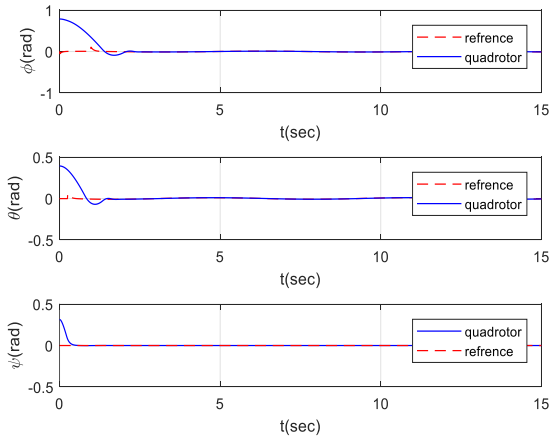


Figure 5. The attitude of the quadrotor using the ST-SMC

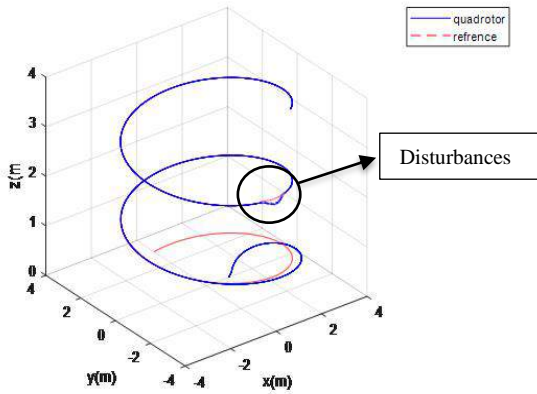


Figure 6. The position of the quadrotor using the ST-SMC in 3D

Figure 5 shows the state of the quadrotor where the angles (ϕ, θ, ψ) have converged in less than 2 seconds, and overshoot and overshoot is less than 5%.

Figure 6 shows the position of the quadrotor in 3D space, which shows that it has tracked the reference path well. In this figure, the reduction of the effect of disturbances using the ST-SMC method is shown.

The simulation results of ST-SMC indicate the success of the applied method. However, in order to obtain better results, the non-singular terminal super-twisting SMC will also be applied in the next section.

3. 2. Nonsingular Terminal Super Twisting Smc

The purpose of the terminal SMC is to reduce the sliding surface convergence time to zero. For this purpose, the sliding surface is considered as follows [25, 26]:

$$S = x_1 + \lambda x_2^{\frac{\alpha}{\beta}} \tag{13}$$

where;

$$\frac{1}{2} < \frac{\alpha}{\beta} < 2 \tag{14}$$

α and β are constant and positive numbers.

Considering the following control:

$$u = -b^{-1}(x) \left(\lambda \frac{\beta}{\alpha} x_2^{2-\frac{\alpha}{\beta}} + \eta s \operatorname{sgn}(s) + f(x) \right) \tag{15}$$

where $\eta > 0$, the surface (13), and the x_1 and x_2 will converge to zero in finite time.

Proof. The nonlinear system is considered as follows:

$$\dot{x}^{(n)}(t) = d(t) + g(x, t)u(t) + f(x, t) \tag{16}$$

where $d(t)$ is the uncertainty or disturbance of the system.

$$d(t) \leq D$$

where D is the maximum disturbance and is a positive number. According to Equation (13) we have:

$$\begin{aligned} \dot{s} &= \dot{x}_1 + \lambda \frac{\alpha}{\beta} x_2^{\frac{\alpha}{\beta}-1} \dot{x}_2 = x_2 + \lambda \frac{\alpha}{\beta} x_2^{\frac{\alpha}{\beta}-1} (f(x) + \\ &g(x) + b(x)u) = \lambda \frac{\alpha}{\beta} x_2^{\frac{\alpha}{\beta}-1} (g(x) - \eta \operatorname{sgn}(s)) \end{aligned} \tag{17}$$

$$s\dot{s} = \lambda \frac{\alpha}{\beta} x_2^{\frac{\alpha}{\beta}-1} (g(x)s - \eta \operatorname{sgn}(s)s) \leq -\lambda \frac{\alpha}{\beta} x_2^{\frac{\alpha}{\beta}-1} \eta |s|$$

where α and β are positive odd integers, and $1 < \frac{\alpha}{\beta} < 2$, there is $x_2^{\frac{\alpha}{\beta}-1} > 0$ for $x_2 \neq 0$. Let $\xi(x_2) = \lambda \frac{\alpha}{\beta} x_2^{\frac{\alpha}{\beta}-1} \eta$. Then;

$$\begin{aligned} s\dot{s} &\leq -\xi(x_2)|s| \quad \text{for } x_2 \neq 0 \\ \xi(x_2) &> 0 \end{aligned} \tag{18}$$

Therefore, for the $x_2 > 0$, stable conditions are in place. Substituting Equation (16) into Equation (12) gives the result;

$$\begin{aligned} \dot{x}_2 &= -\frac{1}{\lambda} \frac{\beta}{\alpha} x_2^{2-\frac{\alpha}{\beta}} + g(x) - \eta \operatorname{sgn}(s) \\ \text{For } x_2 &= 0 \end{aligned} \tag{19}$$

$$\dot{x}_2 = -\frac{1}{\lambda} \frac{\beta}{\alpha} x_2^{2-\frac{\alpha}{\beta}} + g(x) - \eta \operatorname{sgn}(s)$$

For $s > 0$, $\dot{x}_2 \leq \eta$ and for $s < 0$, $\dot{x}_2 \geq \eta$, showing that $x_2 = 0$ is not an attractor and there is a neighborhood of $x_2 = 0$ such that for a $\varepsilon > 0$ as $|x_2| < \varepsilon$, there exist $\dot{x}_2 \leq -\eta$ for $s > 0$ and $\dot{x}_2 \geq \eta$ for $s < 0$. The crossing from $x_2 = \varepsilon$ to $x_2 = -\varepsilon$ for $s > 0$, and from $x_2 = -\varepsilon$ to $x_2 = \varepsilon$ for $s < 0$ happens in a limited time. If $|x_2| > \varepsilon$, from Equation (16) we get switching line $s = 0$ in finite time because $\dot{x}_2 \leq -\eta$ for $s > 0$ and $\dot{x}_2 \geq \eta$ for $s < 0$. As a result, the sliding sliding mode $s = 0$ is obtained from any point of the finite time. Therefore, the sliding surface Equation (13) is obtained

in the finite time, and states will reach zero in the finite time. As a result, the proof is completed.

In this controller, like the ST-SMC controller u_{eq} is obtained by setting the sliding surface derivative equal to

zero, and u_r satisfies the Lyapunov stability condition of the sliding surface. Therefore, the control inputs for the quadrotor were achieved as follows:

$$\begin{aligned}
 U_1 &= \frac{m}{(\cos \theta \cos \varphi - g)} \left[-\dot{z} + \ddot{z}_d \lambda_z \frac{\alpha}{\beta} \dot{z}^{\left(\frac{\alpha}{\beta}-1\right)} \right] / \left[\lambda_z \frac{\alpha}{\beta} \dot{z}^{\left(\frac{\alpha}{\beta}-1\right)} \right] + k_{z1} |S_z|^\rho \operatorname{sign}(S_z) + k_{z2} \int \operatorname{sign}(S_z) \\
 U_2 &= -\frac{I_x}{L} \left[\begin{array}{c} \dot{\phi} + \lambda_\varphi \frac{\alpha}{\beta} \dot{\phi}^{\left(\frac{\alpha}{\beta}-1\right)} \\ \left(\frac{I_y - I_z}{I_x} \dot{\theta} \psi \right) \\ -\frac{J_{TP}}{I_x} \dot{\theta} \Omega - \dot{\phi}_d \end{array} \right] / \left[\lambda_\varphi \frac{\alpha}{\beta} \dot{\phi}^{\left(\frac{\alpha}{\beta}-1\right)} \right] + k_\varphi |S_\varphi|^\rho \operatorname{sign}(S_\varphi) - k_\varphi \int \operatorname{sign}(S_\varphi) \\
 U_3 &= -\left(\frac{I_y}{L}\right) \left[\begin{array}{c} \dot{\theta} + \\ \lambda_\theta \frac{\alpha}{\beta} \dot{\theta}^{\left(\frac{\alpha}{\beta}-1\right)} \\ \left(\frac{I_z - I_x}{I_y} \right) \\ \dot{\phi} \psi + \\ \frac{J_{TP}}{I_y} \dot{\phi} \Omega \\ -\dot{\theta}_d \end{array} \right] / \left[\lambda_\theta \frac{\alpha}{\beta} \dot{\theta}^{\left(\frac{\alpha}{\beta}-1\right)} \right] + k_\theta |S_\theta|^\rho \operatorname{sign}(S_\theta) - k_\theta \int \operatorname{sign}(S_\theta) \\
 U_4 &= -I_z \left[\begin{array}{c} \dot{\psi} + \lambda_\psi \frac{\alpha}{\beta} \dot{\psi}^{\left(\frac{\alpha}{\beta}-1\right)} \\ \left(\frac{I_x - I_y}{I_z} \right) \dot{\phi} \theta - \dot{\psi}_d \end{array} \right] / \left[\lambda_\psi \frac{\alpha}{\beta} \dot{\psi}^{\left(\frac{\alpha}{\beta}-1\right)} \right] + k_\psi |S_\psi|^\rho \operatorname{sign}(S_\psi) - k_\psi \int \operatorname{sign}(S_\psi) \\
 U_x &= -\left(\frac{m}{U_1}\right) \left[\begin{array}{c} \lambda_x \frac{\alpha}{\beta} \dot{x}^{\left(\frac{\alpha}{\beta}-1\right)} (-\ddot{x}_d) \\ + \dot{x} \end{array} \right] / \left[\lambda_x \frac{\alpha}{\beta} \dot{x}^{\left(\frac{\alpha}{\beta}-1\right)} \right] + k_x |S_x|^\rho \operatorname{sign}(S_x) - k_x \int \operatorname{sign}(S_x) \\
 U_y &= -\left(\frac{m}{U_1}\right) \left[\begin{array}{c} \dot{y} + \\ \lambda_y \frac{\alpha}{\beta} \dot{y}^{\left(\frac{\alpha}{\beta}-1\right)} (-\ddot{y}_d) \end{array} \right] / \left[\lambda_y \frac{\alpha}{\beta} \dot{y}^{\left(\frac{\alpha}{\beta}-1\right)} \right] - k_y |S_y|^\rho \operatorname{sign}(S_y) - k_y \int \operatorname{sign}(S_y)
 \end{aligned} \tag{20}$$

The reach time is obtained by setting the derivative of the sliding surface equal to zero:

$$t_s = \frac{-x_i^{\left(\frac{1-\beta}{\alpha}\right)}(t_r)}{\lambda_i^{\frac{\beta}{\alpha}} \left(1 - \frac{\alpha}{\beta}\right)} \tag{21}$$

where t_r is the time that S reaches zero. Table 3 shows the values t_s .

In Figure 7, it is clear that the sliding surfaces of the position reach zero at the desired time. The convergence of (S_x, S_y, S_z) is at 0.09, 0.0145, and 0.02 seconds, respectively.

In Figure 8, the slide surfaces of the attitude are presented. The time to reach zero $(S_\varphi, S_\theta, S_\psi)$ is 0.45,

TABLE 3. Reaching time

$t_s(x)$	$t_s(y)$	$t_s(z)$	$t_s(\varphi)$	$t_s(\theta)$	$t_s(\psi)$
0.4(s)	1(s)	0(s)	1(s)	0.701(s)	2(s)

TABLE 4. Control parameter in the design of the nonsingular terminal ST-SMC

Design parameter	Value	Design parameter	Value
k_x	18.5	λ_x	6.9
k_y	16.1	λ_y	2.8
k_z	25.03	λ_z	2
k_φ	11.5	λ_φ	3
k_θ	11.5	λ_θ	4.19
k_ψ	11.5	λ_ψ	3.17
δ	11.5	$\frac{\alpha}{\beta}$	0.75

0.23 and 0.051, respectively, which is a favorable convergence time.

Figure 9 shows the control commands. As it is known, the chattering phenomenon did not happen in the commands.

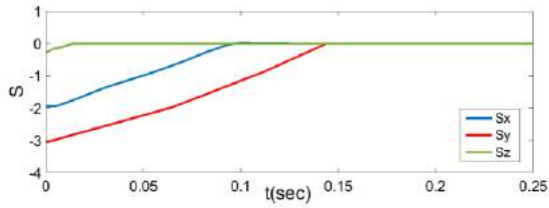


Figure 7. The sliding surface of the quadrotor position using nonsingular terminal ST-SMC

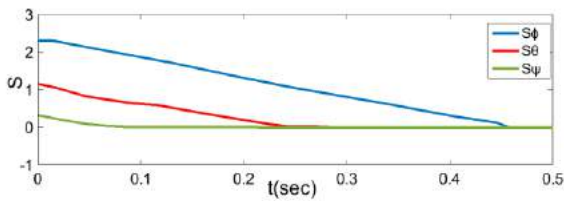


Figure 8. The sliding surface of the quadrotor attitude using nonsingular terminal ST-SMC

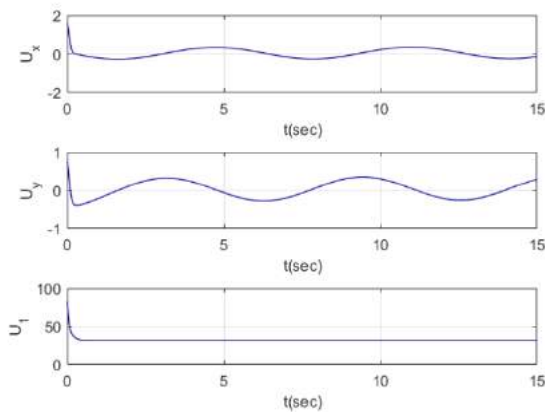


Figure 9. Quadrotor control commands using the nonsingular terminal ST-SMC

Figure 10 shows the control commands. Chattering phenomenon is not observed in these commands and the convergence has happened at the favorable time.

Figure 11 shows the attitude of the quadrotor. In this figure, extreme fluctuation is not observed and the convergence (φ, θ, ψ) happened in 1, 0.7, and 1.5 seconds, which is acceptable.

Figure 12 shows the position of the quadrotor in the spiral path in 3D. (x, y, z) track the reference path well. This figure shows the reduction of the disturbance effect by the applied controller.

The simulation results of both super-twisting SMC and nonsingular terminal super-twisting SMC controllers showed that the two controllers had eliminated the chattering phenomenon. In both controllers, the convergence time of the attitude and position is

favorable, but the convergence time is less in the nonsingular terminal super twisting controller. This controller is more capable of reducing the effects of disturbances. Also, the results of these two controllers

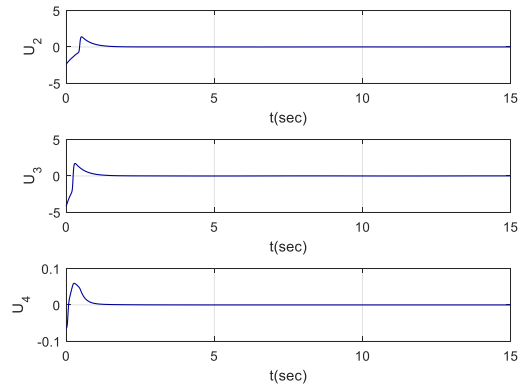


Figure 10. Quadrotor control commands using the nonsingular terminal ST-SMC

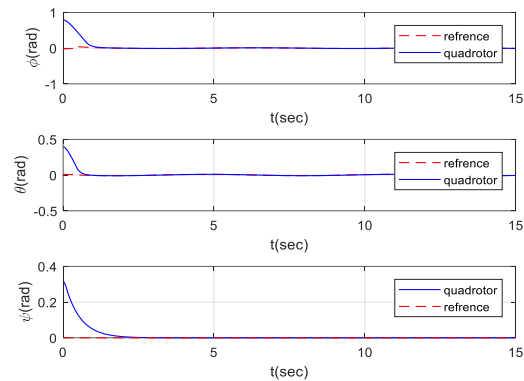


Figure 11. The attitude of the quadrotor using the nonsingular terminal ST-SMC

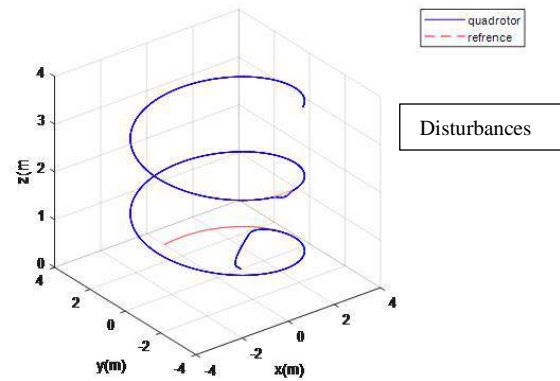


Figure 12. The position of the quadrotor in 3D using the nonsingular terminal ST-SMC

were compared with data reported in literature [27], which showed that the convergence time is higher in the controller discussed by Habibi et al. [27], and chattering also occurred in the control commands. Because of the better results of the nonsingular terminal ST-SMC, this method was applied to control the attitude and position of the quadrotor to cross obstacles. The control parameters are given in Table 4.

4. ARTIFICIAL POTENTIAL FIELD MODEL

Khatib [28] proposed the path planning artificial potential field (AFP). In AFP, the robot is assumed to be a point inside the potential fields. This method combines attraction towards the target and repulsion from obstacles. Figure 13 shows the AFP method, where T shows the target and O shows the obstacles.

The control of the plant by the potential field method is as follows:

$$U_{art}(x) = U_{att}(x) + U_{rep}(x) \quad (22)$$

where, $U_{art}, U_{att}, U_{rep}$, respectively, represent the potential of attraction, the potential of repulsion, and the potential virtual field. Gradient functions are as follows:

$$\begin{aligned} F_{art} &= F_{att} + F_{rep} \\ F_{att} &= -grad[U_{att}(x)] \\ F_{rep} &= -grad[U_{rep}(x)] \end{aligned} \quad (23)$$

where F_{att} is the attraction of the plant and F_{rep} is the force created by $U_{rep}(x)$, that leads to repulsion from the obstacle. F_{rep} is directly related to the distance between the plant and the target. The attraction coefficient k_p is considered, and the attraction potential field $U_{att}(x)$ is as follows:

$$U_{att} = \frac{1}{2} k_p R_{at}^2 \quad (24)$$

In addition, $U_{rep}(x)$ is a positive continuous, and differentiable function, and the effect of this potential is

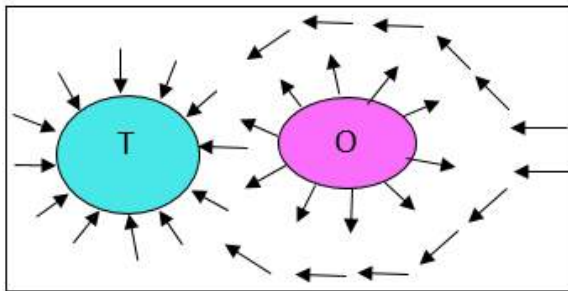


Figure 13. Potential field method

in the limited region around the barrier. As a result, the $U_{rep}(x)$ is:

$$U_{rep}(x) = \begin{cases} 0.5m(\frac{1}{R_{rep}} - \frac{1}{\rho_0})^2 & R_{rep} \leq \rho_0 \\ 0 & R_{rep} > \rho_0 \end{cases} \quad (25)$$

where ρ_0 is the safe distance from the obstacles.

$R_{at} = \|X_d - X\| = \sqrt{(x - x_d)^2 - (z - z_d)^2 - (y - y_d)^2}$ is the distance from the plant to the target, $R_{rep} = \|X_{ob} - X\| = \sqrt{(x - x_{ob})^2 - (y - y_{ob})^2 - (z - z_{ob})^2}$ is the shortest distance from the robot and the obstacles, where $X = (x, y, z)$, $X_{ob} = (x_{obs}, y_{obs}, z_{obs})$, and $X_d = (x_d, y_d, z_d)$ are the position of the plant, the position of obstacles and the position of the target, respectively. According to the kinetic theory, repulsion and attraction functions are given below:

$$F_{att} = -\nabla \left(\frac{1}{2} k_p R_{at}^2 \right) = k_p R_{at} \quad (26)$$

$$U_{rep}(x) = \begin{cases} m(\frac{1}{R_{rep}} - \frac{1}{R_{rep}^2}) \frac{1}{R_{rep}^2} & R_{rep} \leq \rho_0 \\ 0 & R_{rep} > \rho_0 \end{cases} \quad (27)$$

The potential algorithm for crossing obstacles is investigated in three missions. In the first mission, six obstacles were considered; their specifications are listed in Table 5. At this stage, the obstacles are considered static, and the target is fixed.

The simulation of quadrotor crossing obstacles in two dimensions is presented in Figure 14. As it is clear in this

TABLE 5. Obstacles position

Obstacle	X(m)	Y(m)	Z(m)
1	12	30	15
2	35	35	12
3	1	27	12
4	0	10	12
5	0	0	12
6	-20	-8	12

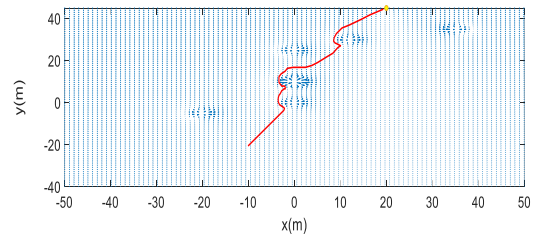


Figure 14. Obstacle avoidance with static obstacles and fixed target

figure, the quadrotor from the starting point (-10, 20) will reach the target at the point (20, 43) after passing the obstacles.

The simulation of quadrotor obstacles avoidance in three dimensions is presented in Figure 15. which shows that the quadrotor has successfully passed through the obstacles and reached the target.

In the second mission, as in the first mission, the obstacles are fixed, but the target is considered dynamic.

Figure 16 shows the passage of the quadrotor through obstacles in two dimensions. In this figure, the quadrotor from the point (-10, -20) reaches the target at the point (10, 43) after passing the obstacles and moves with it to reach the point (5, 43). The target moves from point (25, 43) to point (5,43). These results show the success of the potential method.

Figure 17 shows the crossing of obstacles in three dimensions, which shows the success of the AFP method.

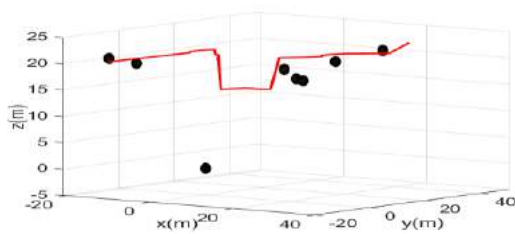


Figure 15. Obstacle avoidance with static obstacles and fixed target in 3D

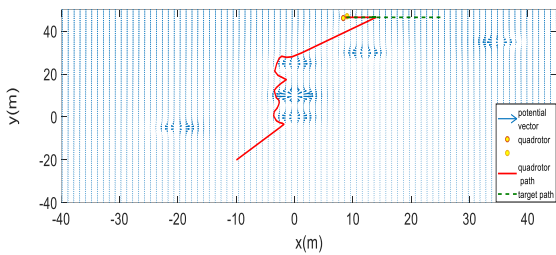


Figure 16. Obstacle avoidance with static obstacles and moving target

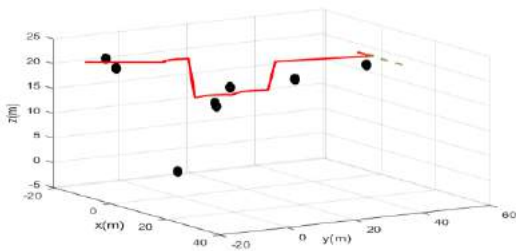


Figure 17. Obstacle avoidance with static obstacles and moving target in 3D

TABLE 6. Obstacles velocity

Obstacle	v_x	v_y	v_z
1	$7t(i)$	$9t(i)$	$3t(i)$
2	0	$-25t(i)$	$2t(i)$
3	$10t(i)$	$-20t(i)$	$5t(i)$
4	$8t(i)$	$-5t(i)$	$4t(i)$
5	$5t(i)$	$-10t(i)$	$2t(i)$
6	$4t(i)$	$10t(i)$	$3t(i)$

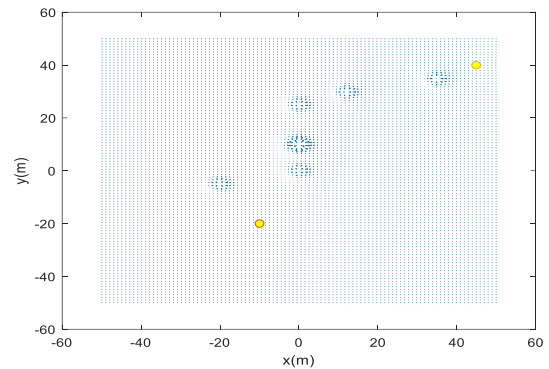


Figure 18. Obstacle avoidance with dynamic obstacles and moving target at the beginning of the mission

In the third mission, obstacles and targets are dynamic. The initial position of the obstacles is shown in Table 3, and the speed of the obstacles is shown in Table 6. Figures 18-23 show the passage of dynamic obstacles during the flight.

Figure 18 shows the initial position of the quadrotor and the target. The initial position of the quadrotor is (-10, -20), and the initial position of the target is (45, 43).

Figure 19 shows the position of the quadrotor after passing the obstacles during the flight. In this figure, the target has moved and reached the point (38, 43).

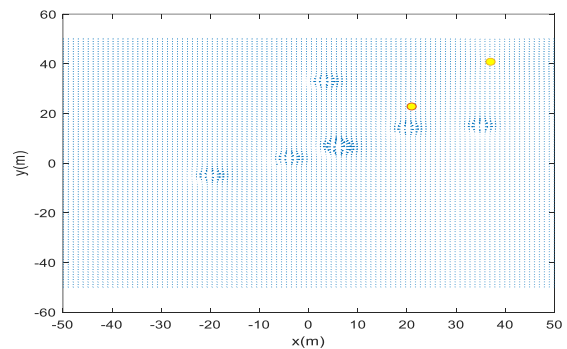


Figure 19. Obstacle avoidance with dynamic obstacles and moving target while crossing obstacles

Figure 20 shows the position of the quadrotor at the moment of reaching the target. The location of the target and the quadrotor is (36, 43).

Figure 21 shows the movement of the quadrotor with the target at the end of the flight. The position of the quadrotor and target is (27, 43).

Figures 18, 19, 21, and 21 show the passage of the quadrotor past each obstacle from the beginning of the flight to reaching the target.

Figure 22 shows the path of the quadrotor passing through moving obstacles and reaching the dynamic target in two dimensions. In this figure, the red line shows the movement path of the quadrotor, and the green dashed line shows the path of the target.

Figure 23 also shows the path of the quadrotor passing moving obstacles and reaching the dynamic target in three dimensions.

In the last mission, the obstacles are a combination of static and dynamic. The target in this mission is moving. The velocities of the obstacles are given in Table 7. The simulation results at different times are shown in Figures 24-28.

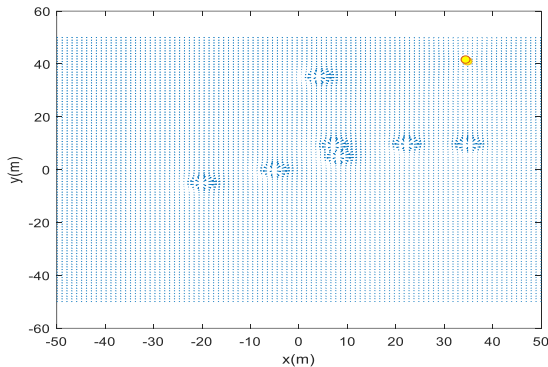


Figure 20. Obstacle avoidance with dynamic obstacles and moving target when the quadrotor reaches the target

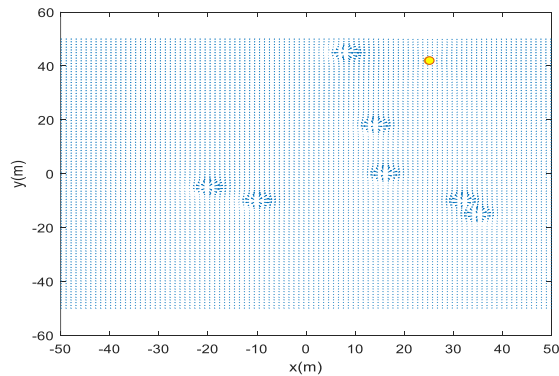


Figure 21. Crossing the obstacles and moving the quadrotor with the target

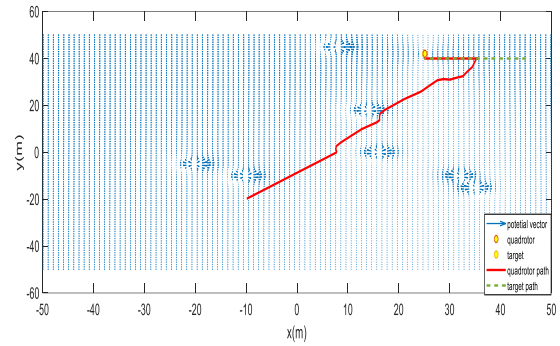


Figure 22. The path of the quadrotor through obstacles in two dimensions

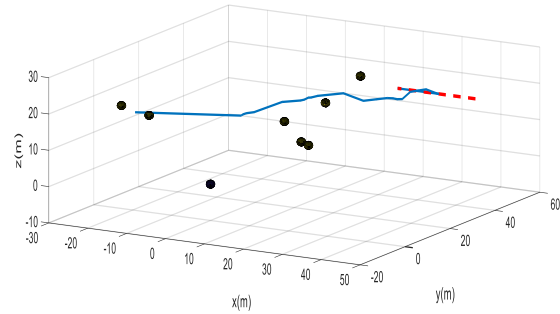


Figure 23. The path of the quadrotor through obstacles in three dimensions

Figures 24 and 25 show the passage of dynamic and static obstacles from the start of the flight until reaching the target. Figure 23 shows the quadrotor crossing obstacles during flight. The position of the quadrotor in this figure is (10, 0) and the target is at the point (40, 43).

Figure 25 shows the moment the quadrotor reaches the target. The position of the quadrotor and target is (35, 43).

Figure 26 shows the crossing of dynamic and static obstacles and the movement of the quadrotor with the target.

TABLE 7. Obstacles velocity

Obstacle	v_x	v_y	v_z
1	0	0	0
2	0	0	0
3	0	0	0
4	$8t(i)$	$-5t(i)$	$4t(i)$
5	$5t(i)$	$-10t(i)$	$2t(i)$
6	$4t(i)$	$10t(i)$	$3t(i)$

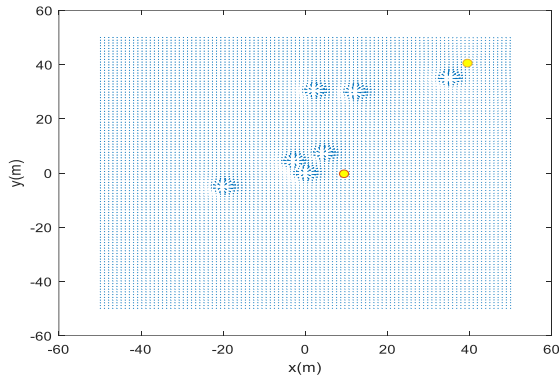


Figure 24. Obstacle avoidance with dynamic and static obstacles and moving target while crossing obstacles

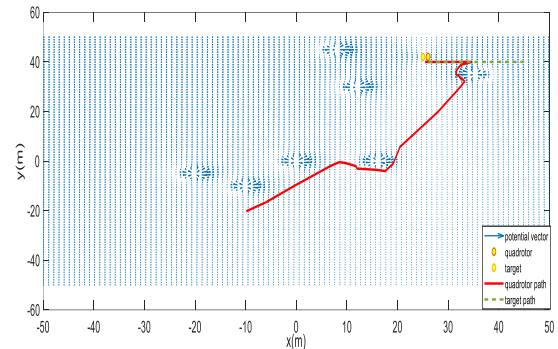


Figure 27. The path of the quadrotor through obstacles in two dimensions

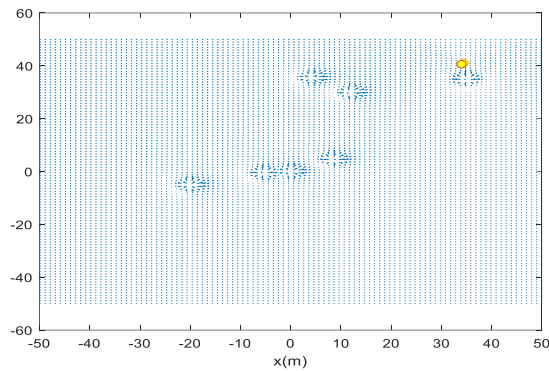


Figure 25. Obstacle avoidance with dynamic obstacles and moving target when the quadrotor reaches the target

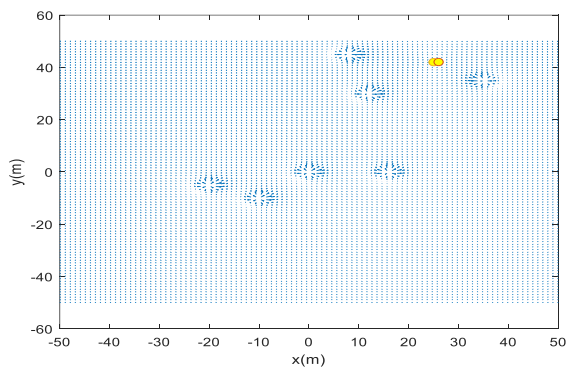


Figure 26. Crossing the obstacles and moving the quadrotor with the target

Figure 27 presents the obstacle crossing and dynamic target quadrotor movement in two dimensions. In this figure, the green dashed line shows the target path and the red line shows the quadrotor path. The red line shows the starting point of the flight (-10, -20) until reaching the

target at the point (30, 43), and the movement along the target to the point (25, 43).

Figure 28 presents dynamic and static obstacle avoidance and quadrotor movement with dynamic purpose in three dimensions.

As it is clear from Figures 14 and 15, the quadrotor has been able to pass through fixed obstacles and fixed targets in two and three dimensions. Figures 14 and 15 also show the path of crossing fixed obstacles in two and three dimensions with a moving target. Figures 18-21 show the successful passage of the quadrotor through the dynamic obstacles at the beginning and the end of the path. Figure 22 also shows the path of the quadrotor from the beginning of the flight to reaching the target and following it. Figure 23 also presents this path in three dimensions. Figures 23-26 also show the success of passing the obstacles during the flight. Figures 27 and 28 show this path in two and three dimensions, respectively. As a result, the simulation results show the success of the AFP method in passing dynamic and static obstacles and tracking the target.

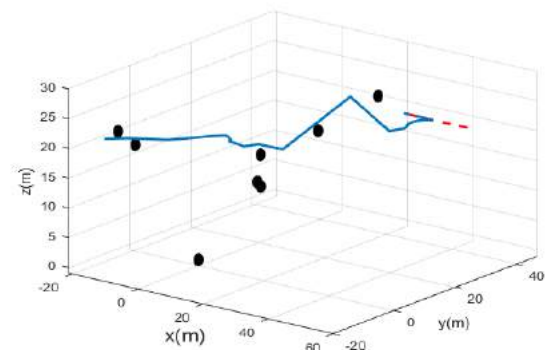


Figure 28. The path of the quadrotor through obstacles in three dimensions

6. CONCLUSION

In this article, the quadrotor crossing dynamic and static obstacles and target tracking in four missions are presented. Solving the problem of crossing obstacles has been done in two parts. The first part deals with controlling the position and attitude, and in the second part, the path planning to pass the obstacles is done using the artificial potential field method. In the first part, super twisting and nonsingular terminal super twisting were compared to control the position and attitude. Convergence time in nonsingular terminal super-twisting controller is less, and the effect of disturbances is reduced more. As a result, the non-singular terminal super-twisting method was used to control the attitude and position in crossing the obstacles. The simulation results of crossing the obstacles using the AFP method also showed that in the first mission, where the obstacles and the target were static, the quadrotor successfully crossed the obstacles and reached the target. In the second mission, where the obstacles were fixed, and the target was moving, the quadrotor crossed the obstacles and reached the target and moved along with target. The success of the applied method is evident in the third mission, which is the obstacles and target were dynamic. In the last mission, where the obstacles were a combination of static and dynamic and the target was moving, the quadrotor successfully crossed the obstacles and reached the target, and moved along with it. As a result, the simulations showed the effectiveness of the applied method.

In future articles, the method implemented in this article can be used in the formation flight of flying robots and maintaining continuity after crossing obstacles.

7. REFERENCES

- Procter, S. and Secco, E.L., "Design of a biomimetic bldc driven robotic arm for teleoperation & biomedical applications", *J Hum Earth Future. ISSN*, (2022), 2785-2997. doi: 10.28991/HEF-2021-02-04-03.
- Andaluz, G.M., Leica, P., Herrera, M., Morales, L. and Camacho, O., "Hybrid controller based on null space and consensus algorithms for mobile robot formation", *Emerging Science Journal*, Vol. 6, No. 3, (2022), 429-447. doi: 10.28991/ESJ-2022-06-03-01.
- Nagaty, A., Saedi, S., Thibault, C., Seto, M. and Li, H., "Control and navigation framework for quadrotor helicopters", *Journal of Intelligent & Robotic Systems*, Vol. 70, (2013), 1-12. doi: 10.1007/s10846-012-9789-z.
- Toloei, A. and Asgari, H., "Quaternion-based finite-time sliding mode controller design for attitude tracking of a rigid spacecraft during high-thrust orbital maneuver in the presence of disturbance torques", *International Journal of Engineering, Transactions C: Aspects*, Vol. 32, No. 3, (2019), 430-437. doi: 10.5829/ije.2019.32.03c.11.
- Karami, H., Ghasemi, R. and Mohammadi, F., "Adaptive neural observer-based nonsingular terminal sliding mode controller design for a class of nonlinear systems", in 2019 6th International Conference on Control, Instrumentation and Automation (ICCIA), IEEE. (2019), 1-5.
- Bensalah, C., M'Sirdi, N.K. and Naamane, A., "Full modelling and sliding mode control for a quadrotor uav in visual servoing task", in IMAACA2019. (2019).
- Matouk, D., Abdessemed, F., Gherouat, O. and Terchi, Y., "Second-order sliding mode for position and attitude tracking control of quadcopter uav: Super-twisting algorithm", *International Journal of Innovative Computing, Information and Control*, Vol. 16, No. 1, (2020), 29-43. doi: 10.24507/ijicic.16.01.29.
- Noordin, A., Basri, M. and Mohamed, Z., "Sliding mode control for altitude and attitude stabilization of quadrotor uav with external disturbance", *Indonesian Journal of Electrical Engineering and Informatics (IJEI)*, Vol. 7, No. 2, (2019), 203-210. doi: 10.52549/ijeie.v7i2.1149.
- Li, M. and Zhang, H., "Auv 3d path planning based on a* algorithm", in 2020 Chinese Automation Congress (CAC), IEEE. (2020), 11-16.
- Wang, L. and Pang, S., "Chemical plume tracing using an auv based on pomdp source mapping and a-star path planning", in OCEANS 2019 MTS/IEEE SEATTLE, IEEE. (2019), 1-7.
- Yan, S. and Pan, F., "Research on route planning of auv based on genetic algorithms", in 2019 IEEE International Conference on Unmanned Systems and Artificial Intelligence (ICUSAI), IEEE. (2019), 184-187.
- Cao, J., Li, Y., Zhao, S. and Bi, X., "Genetic-algorithm-based global path planning for auv", in 2016 9th International Symposium on Computational Intelligence and Design (ISCID), IEEE. Vol. 2, (2016), 79-82.
- MahmoudZadeh, S., Powers, D.M., Yazdani, A.M., Sammut, K. and Atyabi, A., "Efficient auv path planning in time-variant underwater environment using differential evolution algorithm", *Journal of Marine Science and Application*, Vol. 17, (2018), 585-591. doi: 10.1007/s11804-018-0034-4.
- Che, G., Liu, L. and Yu, Z., "An improved ant colony optimization algorithm based on particle swarm optimization algorithm for path planning of autonomous underwater vehicle", *Journal of Ambient Intelligence and Humanized Computing*, Vol. 11, (2020), 3349-3354. doi: 10.1007/s12652-019-01531-8.
- Lim, H.S., Fan, S., Chin, C., Chai, S. and Bose, N., "Particle swarm optimization algorithms with selective differential evolution for auv path planning", (2020). doi: 10.11591/ijra.v9i2.pp94-112.
- Taheri, E., Ferdowsi, M.H. and Danesh, M., "Closed-loop randomized kinodynamic path planning for an autonomous underwater vehicle", *Applied Ocean Research*, Vol. 83, (2019), 48-64. doi: 10.1016/j.apor.2018.12.008.
- Li, X., Wang, W., Song, J. and Liu, D., "Path planning for autonomous underwater vehicle in presence of moving obstacle based on three inputs fuzzy logic", in 2019 4th Asia-Pacific Conference on Intelligent Robot Systems (ACIRS), IEEE. (2019), 265-268.
- Sun, B., Zhu, D., Tian, C. and Luo, C., "Complete coverage autonomous underwater vehicles path planning based on gladius bio-inspired neural network algorithm for discrete and centralized programming", *IEEE Transactions on Cognitive and Developmental Systems*, Vol. 11, No. 1, (2018), 73-84. doi: 10.1109/TCDS.2018.2810235.
- Havenström, S.T., Rasheed, A. and San, O., "Deep reinforcement learning controller for 3d path following and collision avoidance by autonomous underwater vehicles", *Frontiers in Robotics and AI*, Vol. 7, (2021), 211. doi: 10.3389/frobt.2020.566037.
- Zhao, Y., Hao, L.-Y. and Wu, Z.-J., "Obstacle avoidance control of unmanned aerial vehicle with motor loss-of-effectiveness fault

- based on improved artificial potential field", *Sustainability*, Vol. 15, No. 3, (2023), 2368. doi: 10.3390/su15032368.
21. Kondo, K. and Tsuchiya, T., "Predictive artificial potential field for uav obstacle avoidance", in Asia-Pacific International Symposium on Aerospace Technology, Springer. (2021), 493-506.
 22. Yan, S., Pan, F., Xu, J. and Song, L., "Research on uav path planning based on improved artificial potential field method", in 2022 2nd International Conference on Computer, Control and Robotics (ICCCR), IEEE. (2022), 1-5.
 23. Fan, X., Guo, Y., Liu, H., Wei, B. and Lyu, W., "Improved artificial potential field method applied for auv path planning", *Mathematical Problems in Engineering*, Vol. 2020, (2020), 1-21. doi: 10.1155/2020/6523158.
 24. Boudallaa, A., Chennani, M., Belkhat, D. and Rhofir, K., "Vector control of asynchronous motor of drive train using speed controller ∞ ", *Emerging Science Journal*, Vol. 6, No. 4, (2022). doi: 10.28991/ESJ-2022-06-04-012.
 25. Binazadeh, S. and Ghasemi, R., "Distributed fixed time super-twisting sliding mode leader-follower tracking protocol design for nonlinear networked flexible joint robots", *International Journal of Dynamics and Control*, Vol. 8, No. 3, (2020), 908-916. doi: 10.1007/s40435-019-00603-z.
 26. Ebrahim, A., Mohammad-Ali-Nezhad, S. and Ghasemi, R., "Designing observer based fuzzy terminal sliding mode controller for nonlinear dynamical model of vehicles: Fixed time approach", *International Journal of Dynamics and Control*, Vol. 8, (2020), 816-823. doi: 10.1007/s40435-019-00598-7.
 27. Toloei, A., Habibi Totekani, M., Ghasemi, R. and Ghaderi, F., "Formation control of multi-quadrotor using leader-follower method based on sliding mode", *Aerospace Knowledge and Technology Journal*, Vol. 12, No. 1, (2023), 63-77.
 28. Khatib, O., "Real-time obstacle avoidance for manipulators and mobile robots", *The International Journal of Robotics Research*, Vol. 5, No. 1, (1986), 90-98. doi: 10.1177/027836498600500106.

COPYRIGHTS

©2023 The author(s). This is an open access article distributed under the terms of the Creative Commons Attribution (CC BY 4.0), which permits unrestricted use, distribution, and reproduction in any medium, as long as the original authors and source are cited. No permission is required from the authors or the publishers.



Persian Abstract

چکیده

هدف از این مقاله اجتناب از برخورد با موانع و ردیابی هدف متحرک برای یک کوادروتور است. حل مشکل عبور از مانع برای کوادروتور شامل دو بخش است. بخش اول کنترل وضعیت و موقعیت و بخش دوم برنامه ریزی مسیر برای عبور از موانع است. در این مقاله، وضعیت و موقعیت کوادروتور توسط کنترلگر فوق‌پیشگی و کنترلگر فوق‌پیشگی ترمینال غیر منفرد کنترل می‌شود. نتایج شبیه سازی این دو روش مقایسه شد. در روش ST-SMC ترمینال غیر منفرد، زمان همگرایی تقریباً ۵ درصد کمتر از روش SMC فوق‌پیشگی بود. همچنین روش ST-SMC ترمینال غیر منفرد توانایی بیشتری در رفع اختلالات دارد. به دلیل نتایج بهتر، از ترمینال غیر منفرد ST-SMC برای کنترل موقعیت و وضعیت کوادروتور برای عبور از موانع و ردیابی هدف استفاده شد. در مرحله دوم برای عبور از موانع از الگوریتم برنامه ریزی مسیر میدان پتانسیل استفاده شد. این روش ترکیبی از جاذبه به سمت هدف و دافعه از موانع است. نتایج شبیه سازی عبور از موانع در چهار ماموریت ارائه شد. در ماموریت اول موانع و هدف ثابت و در ماموریت دوم موانع ثابت بوده و هدف در حال حرکت است. در ادامه موانع و هدف دینامیک هستند. در آخرین ماموریت ترکیبی از موانع استاتیکی و دینامیک در نظر گرفته شد و هدف در حال حرکت است. نتایج شبیه سازی چهار ماموریت نشان می‌دهد که کوادروتور به موانع برخورد نمی‌کند و به هدف مورد نظر می‌رسد، بنابراین روش اعمال شده موفقیت آمیز است.



A Fault Tolerant Operation of 3-Phase, 5-Level CHBMLI under Open Circuit Fault Conditions

R. Kumar*, M. A. Chaudhari, P. Chaturvedi, K. S. Raja Sekhar

Electrical Engineering Department, Visvesvaraya National Institute of Technology (VNIT), Nagpur, India

PAPER INFO

Paper history:

Received 01 December 2022
Received in revised form 23 May 2023
Accepted 24 May 2023

Keywords:

Cascaded Multi-level Inverter
Level Shift PWM Technique
Fault Detection
Fault Tolerant
Neutral Point Shift Technique

ABSTRACT

Fault detection and its restoration is the major challenge for the smooth functioning of the Multi-Level Inverter (MLI). In this paper, fault detection and its clearance scheme for an Open Circuit (OC) fault on a 3-level 5-level Cascaded H-Bridge Multi-Level Inverter (CHBMLI) has been developed and tested to improve the reliability and suitability of the system. An accurate and fast detection, isolation and bypassing of faulty bridges enhance the reliability, suitability, and acceptability of CHBMLI in any domestic, industrial drive applications. To reschedule the line voltage and current value close to the pre-fault level, a Neutral Point Shift (NPS) technique is presented in this paper. The desired output voltage is governed by Level Shift Pulse Width Modulation (LSPWM) technique. The proposed scheme is developed in MATLAB/Simulink environment and results are validated by using Opal-RT simulator. Simulation results has confirmed the performance and Opal-RT simulator results shows feasibility and applicability of the proposed scheme.

doi: 10.5829/ije.2023.36.10a.02

NOMENCLATURE

A_{cr}	Peak value of triangular carrier signals	V_{AB}, V_{BC}, V_{CA}	Output line voltages
A_m	Peak value of modulating signals	$V_{S_{a14}}$	Instantaneous voltage across switch S_{a14}
f_{cr}	Frequency of carrier signals	i_A	Instantaneous phase-A current
f_m	Frequency of modulating signals	N	Load neutral point
n	Number of bridges	P_n	CHBMLI neutral point
A_1, A_2	Bridges H_1 and H_2 of phase-A	P'_n	Shifted neutral point of CHBMLI
B_1, B_2	Bridges H_1 and H_2 of phase-B	L_1, L_2, L_3	New phase voltages with NPS
C_1, C_2	Bridges H_1 and H_2 of phase-C	a	New line voltage with NPS
V_{dc}	Input DC supply to CHBMLI	θ_{cr}	Phase angle between triangular carrier
v_{H1}, v_{H2}	Instantaneous bridge output ac voltage	α, β, γ	New phase angles with NPS

1. INTRODUCTION

Multilevel Inverters (MLI) are widely accepted in all industrial, domestic, and electric power grid utility systems to improve the sustainability and reliability of the overall system [1]. Due to increasing penetration of renewable energy sources such as wind power and PV solar power, the importance of MLI has increased [2, 3]. The MLI has various advantages such as low voltage stress (dv/dt) across switches, low Total Harmonic Distortion (THD) of output ac voltages, low rating of IGBT switches and providing effective performance by

conventional power electronics inverters [4, 5]. Because of their exclusive merits, the MLI is being used in various applications like v/f control in drive systems, HVDC transmission systems [6, 7]. Many topologies of MLI are available with different switch combinations and source arrangements. Some of the standard multilevel inverter topologies are further subclassified as: Flying Capacitors/Capacitor Clamped MLI (FCMLI), Neutral Point Clamped/Diode Clamped Multi-Level Inverter (NPCMLI), and Cascaded H-bridge MLI (CHBMLI), and their comparison is given in Table 1 [8, 9]. The CHBMLI is one of the most effective and popular

*Corresponding Author Email: rkkumarr68@gmail.com (R. Kumar)

topology. The advantage of CHBMLI is that, if any bridge is faulty, it bypasses the faulty bridge and provides continuous supply from other bridges. Since the CHBMLI requires separate DC sources, hence, it is suitable for several renewable energy sources like wind, PV, and fuel cells as shown in Figure 1. It is also suitable for medium voltage, high power distribution, Battery Energy Storage Systems (BESS), and industrial drives due to a high degree of modularity and high voltage ride-through [10, 11]. In CHBMLI, the number of levels in output voltage increases with an increase in the number of bridges. So, the reliability of the inverter depends on the number of components present in the system.

Due to the large number of semiconductors i.e., IGBT switches in MLI, the chances of failures in components increase which tends to create Open-Circuit (OC) and

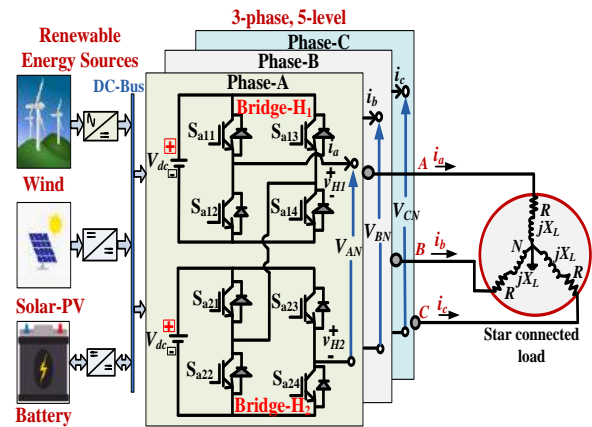


Figure 1. General block diagram of DC micro-grid with 3-phase, 5-level CHBMLI

TABLE 1. Comparative analysis of classical multilevel inverter

Sr. No.	Parameters	NPCMLI	FCMLI	CHBMLI
1	Output phase voltage levels for star connected load	m	m	m
2	Output voltage (line-line) levels	$(2m-1)$	$(2m-1)$	$(2m-1)$
3	Power semiconductor switches ($3-\phi$)	$6(m-1)$	$6(m-1)$	$6(m-1)$
4	Clamping diodes (Independent)	$3(m-1)(m-2)$	0	0
5	DC bus capacitors	$(m-1)$	$(m-1)$	$\frac{3(m-1)}{2}$
6	Balancing capacitors	0	$\frac{3(m-1)(m-2)}{2}$	0
7	Voltage unbalancing problem	Average	High	Very low
8	Modularity	Less	Less	High
9	Asymmetrical input voltage configuration	Not possible	Not possible	Possible
10	Switching states of MLI in state space diagram including multiple states	m^3	m^3	m^3
11	Applications	Motor drive system, STATCOM	Motor drive system, STATCOM	Motor drive system, PV, fuel cells, BESS and grid integrated DG applications

Short-Circuit (SC) faults [12, 13]. The fault in the gate terminal in IGBT switches is considered as an OC fault. The switch fault count is approximately $1/3^{\text{rd}}$ of the total fault in power converters. The OC fault in any switch of CHBMLI bridge leads to unbalanced load, and voltage disturbed. This creates unbalancing in output current and voltage, which increases the chances of other devices failure and may lead to the system collapse. The distribution of faults due to failure of components such as PCB 26%, capacitor 30%, semiconductor devices 21%, solder joint 13%, conductor 3%, and other 7% in power electronics converters is shown in Figure 2 [14]. In this paper, the comparative analysis of the OC fault detection methods, fault detection time, and their parameters are discussed. Sim et al. [15] detected the OC fault of CHBMLI based on output current waveform and

zero voltage switching states, the detection time for identifying the faulty switch takes more than 40 msec. Here, the performance of detection is poor for faulty switch identification. The method presented by Faraz et al. [16] is based on a sliding mode observer to detect the

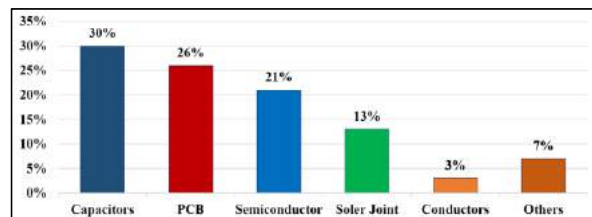


Figure 2. Faults percentages due to failure of devices in converters

OC faulty switch of a modular multilevel converter. The comparison is presented between each leg voltage and the voltage across the capacitor cell. It requires more than 100 msec to check each healthy bridge of the converter. In the fault detection method given by Anand et al. [17], the mean output bridge voltage is taken as detection parameter. The OC fault was detected for CHBMLI by comparing the half-cycle mean value of bridges voltage (HCMV) with normal operating mean output voltage. It can detect faulty switch of CHBMLI within 20 msec with LSPWM. The OC switch fault detection for T-Type MLI is given by He et al. [18]. In this method, the output current of MLI compares with online data which is already trained for OC fault in different conditions. This technique requires a set of data; due to this, it takes more than 20 msec for the execution of data for each healthy bridge. Thanirige et al. [19] presented the fault detection which is based on FFT analysis of phase current signal to detect faulty bridge. The fault is detected in less than 100 msec, this technique detects only faulty cell. This operation takes 60 msec to check the data in each step and this method also requires data training [20]. The accuracy is less under light load conditions. In the method given by Lezana et al. [21], fault detection is done based on output voltage switching frequency analysis for a cascaded multicell converter. The operation of fault detection is implemented by high frequency harmonic analysis. The behavior of fault is predicted under the approximate method. It takes more than 30 msec to implement this technique. A gravitational search algorithm is implemented to detect the OC fault for the cascaded half-bridge MLI [22]. This detection technique takes 20 msec for fault detection operation. It is for the limited number of switches and it does not give clear identification of faulty switches, since it is an approximate method. The generation of balanced three-phase line voltages and currents is described by Deepak and Das [23]. This is achieved by adjusting the three-phase angles with reference signals given to each leg of the inverter. The fault tolerance of MLI is implemented by the neutral point shift (NPS) technique to maximize the available voltage after bypassing the faulty bridge [24]. The fault is tolerated to improve overall system reliability. Research work is carried out in this concern to enhance the performance of the semiconductor switch with reliable operation. The main contributions of this paper are as follows:

- The developed algorithm based on instantaneous parameters for fault detection and inherent isolation of the faulty bridge with minimum fault detection time.
- The neutral point shift (NPS) technique is implemented for fault-tolerant operation under OC faults on the switches to ensure uninterrupted, and reliable supply to the load.

- The proposed algorithm is implemented in MATLAB/Simulation and validated through the real-time simulator Opal-RT.

In section 2, the Cascaded H-bridge (CHB) 5-level inverter and PWM techniques are discussed. The analysis of fault detection and fault-tolerant NPS technique and OC fault detection in 3-phase, 5-level CHBMLI are addressed in section 3. Section 4 deals with the simulation results under different operating conditions. The Opal-RT simulator results are described in section 5. Conclusion of the proposed work is in section 6.

2. CASCADED H-BRIDGE 5-LEVEL INVERTER

The conventional power electronic inverters produce only two voltage levels either $+V_{dc}$ or $-V_{dc}$, but the CHBMLI generates an expected sinusoidal output voltage from several DC input voltage sources. It consists of a series connections of n-bridges. Each bridge gives three output voltage levels as $+V_{dc}$, 0, and $-V_{dc}$ obtained by implementing the different switching patterns [25]. The switching sequence and output voltages under normal operating condition is shown in Table 2. In symmetric cascaded H-bridge multilevel inverter, to get m -number of levels in output voltage, it requires $2^{*(m-1)}$ switches, $(m-1)/2$ number of DC sources or number of H-bridges per phase leg, and switch blocking voltage is $2^{*(m-1)}$ [26]. The sum of all the bridge output voltages gives the phase voltage. In this paper, for obtaining the 5-level, two H-bridges are connected in series in each phase as shown in Figure 1. i.e., ($V_{AN} = V_{H1} + V_{H2}$). The phase output voltages of MLI is given by:

$$\begin{cases} V_{AN} = m_{an} * n * V_{dc} \sin(\omega t) \\ V_{BN} = m_{bn} * n * V_{dc} \sin(\omega t - 120^\circ) \\ V_{CN} = m_{cn} * n * V_{dc} \sin(\omega t + 120^\circ) \end{cases} \quad (1)$$

The phase output magnitude with n-bridges;

$$\begin{cases} V_{ph} = m_{an} * n * V_{dc} \\ V_{line} = \sqrt{3} m_{an} * n * V_{dc} \end{cases} \quad (2)$$

The commonly used PWM techniques are Level Shift PWM (LSPWM) and Phase Shift PWM (PSPWM). These methods are simple and used in various topologies than space vector PWM. In LSPWM, all carrier signals have the same frequency and peak-to-peak amplitude. For an MLI with ' m ' voltage levels, $(m-1)$ triangular carrier signals are required. The carrier signals are disposed over one another. In this paper, the level-shift pulse width modulation (LSPWM) technique is used to control the switching pattern to maintain the desired output voltage. The amplitude (m_a) and frequency (m_f) modulation index are given as,

$$m_a = \frac{A_m}{A_{cr(m-1)}} \text{ and } m_f = \frac{f_{cr}}{f_m}$$

In PSPWM, the carrier signals are phase-shifted from one another, with the same frequency and peak-to-peak amplitude. An MLI with ‘*m*’ output voltage levels, (*m*-1) triangular carrier signals are required, which are shifted by an angle (θ_{cr}). The comparison between PSPWM and LSPWM techniques is shown in Table 3.

$$\theta_{cr} = \frac{360^\circ}{(m-1)}, m_a = \frac{A_m}{A_{cr}}, \text{ and } m_f = \frac{f_{cr}}{f_m}.$$

3. ANALYSIS OF FAULT DETECTION AND FAULT TOLERANT

Internal faults of the CHBMLI, such as the OC and SC faults are major faults. The internal short-circuit (SC) faults occur in IGBT, mainly due to the drastic increase in temperature. The peak current flows through collector

TABLE 2. Switching sequence and output voltage level of 5-levels CHBMLI

Sr. No.	Switching Combination	Output Voltage levels
1	S _{a11} , S _{a14} , S _{a21} , S _{a24}	+2V _{dc}
2	S _{a11} , S _{a14} , S _{a21} , S _{a22}	
3	S _{a11} , S _{a14} , S _{a24} , S _{a23}	
4	S _{a11} , S _{a12} , S _{a21} , S _{a24}	+V _{dc}
5	S _{a14} , S _{a13} , S _{a21} , S _{a24}	
6	S _{a11} , S _{a14} , S _{a23} , S _{a22}	
7	S _{a11} , S _{a12} , S _{a21} , S _{a22}	
8	S _{a11} , S _{a12} , S _{a24} , S _{a23}	
9	S _{a14} , S _{a13} , S _{a21} , S _{a22}	0
10	S _{a14} , S _{a13} , S _{a24} , S _{a23}	
11	S _{a13} , S _{a12} , S _{a21} , S _{a24}	
12	S _{a13} , S _{a12} , S _{a21} , S _{a22}	
13	S _{a13} , S _{a12} , S _{a24} , S _{a23}	
14	S _{a11} , S _{a12} , S _{a23} , S _{a22}	-V _{dc}
15	S _{a14} , S _{a13} , S _{a23} , S _{a22}	
16	S _{a13} , S _{a12} , S _{a23} , S _{a24}	-2V _{dc}

TABLE 3. Comparison between level-shift and phase-shift sinusoidal PWM

Parameters	Phase shift PWM	Level Shift PWM
Switching frequency ($f_{sw} = f_{cr}$)	Same for all switches	Different
Conduction period (<i>T</i>)	Same for all switches	Different
Rotating of switching patterns	Not required	Required
Line-to-line voltage THD	Good	Better

to emitter of IGBT, without gate pulse, due to continuous increase in voltage beyond breakdown. The OC fault occurs due to open gate terminal or improper connection of collector and emitter terminal. In this paper, a fault detection algorithm is developed for 3-phase, 5-level CHBMLI to detect the fault under OC condition.

3. 1. Open-Circuit (OC) Fault Detection The open-circuit fault may occur on any switch, which creates an unbalance in the output voltages and currents. This leads to disturbance in the CHBMLI system. If the disturbance persists, the system will be shutdown. To avoid complete shutdown of the system, the algorithm proposed for fault detection and fault-tolerant techniques are implemented. An accurate and fast fault detection, inherent fault isolation, and bypassing of the faulty bridge ensure the reliability, suitability, and acceptability of CHBMLI in any domestic, industrial drive applications.

During OC fault, in any IGBT switch, the bridge voltage, current, and its magnitude deviates from normal operating condition with constant DC input. The fault detection in bridges is based on the monitoring of instantaneous bridge output voltage (v_{H1} , v_{H2}) and instantaneous output current (i_A). The faulty bridge, the faulty switch is identified by comparing the voltage across diagonal switches of each bridge and the instantaneous output current using fault detection algorithm. The proposed scheme for fault detection in 3-phase 5-level CHBMLI with fault-tolerant NPS technique is shown in Figure 3. For getting the optimality with minimum trade-off, all the possible OC fault conditions have been considered in the proposed

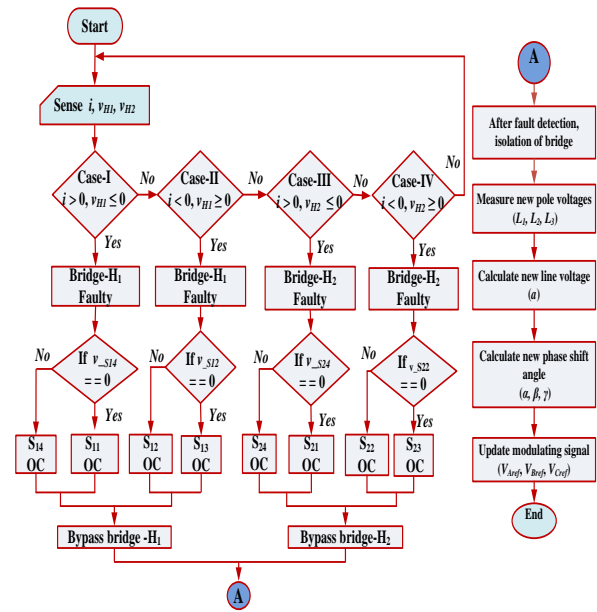


Figure 3. Flow chart for fault detection and fault tolerant with NPS

algorithm. The incorporation of NPS technique with the proposed algorithm shows promising results which are discussed in section 3. The fault detection algorithm provides a control signal to bypass the faulty bridge. Due to bypassing the faulty bridge, the output current and voltages become unbalanced, which is not acceptable for many applications. To make sure the output line currents and voltages are balanced after bypassing the faulty bridge, the NPS fault-tolerant control technique is implemented. To study the fault detection technique on different switches in open circuit fault, different cases are considered by misfiring the gate terminal.

The circuit diagrams, under OC fault conditions, for all the cases show the direction of current (i_A) and voltages (v_{H1} , v_{H2}) are depicted in Figures 4 to 7. The current direction is shown by a solid red line. The operation and switching sequence during OC fault in switch of 5-level CHBMLI is shown in Table 4. For example, if $v_{H1} \leq 0$ and $i_A > 0$ in phase-A, the faulty bridge-H₁ and possible faulty switch is either S_{a11} or S_{a14} . The faulty switch is identified by checking the voltage across the diagonal switches (Here; S_{a11} and S_{a14} are diagonal switches). If $v_{S_{a14}} = 0$ means faulty switch is S_{a12} , otherwise switch S_{a14} .

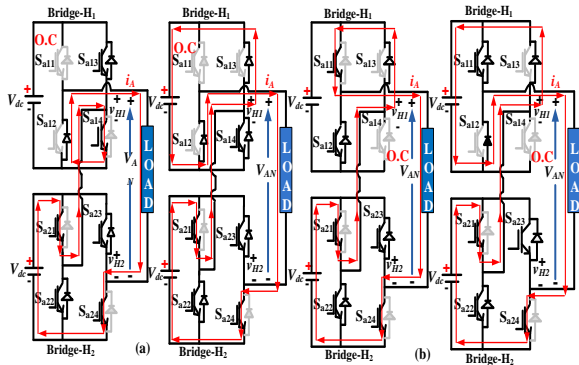


Figure 4. Case I; $i_A > 0$, $v_{H1} \leq 0$ fault on bridge-H₁, faulty switches (a) S_{a11} , and (b) S_{a14} .

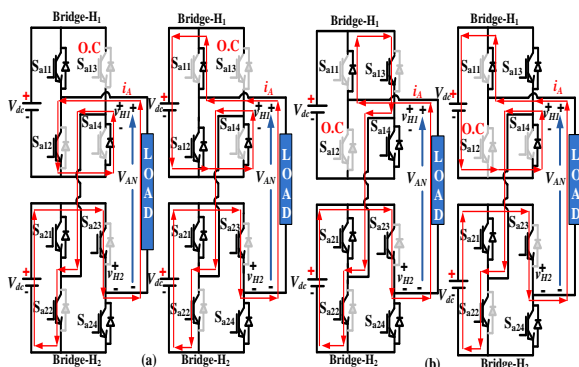


Figure 5. Case II; $i_A < 0$, $v_{H1} \geq 0$ fault on bridge-H₁, faulty switches (a) S_{a13} , and (b) S_{a12} .

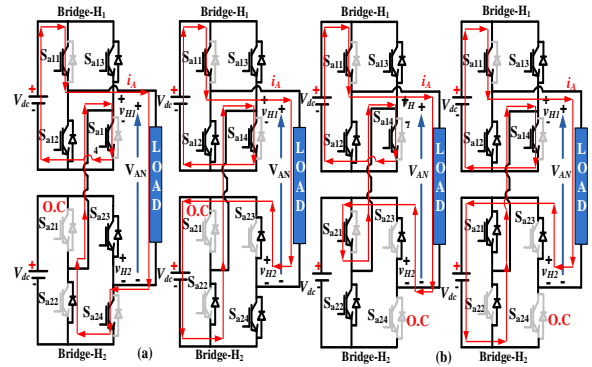


Figure 6. Case III; $i_A > 0$, $v_{H2} \leq 0$ fault on bridge-H₂, faulty switches (a) S_{a21} , and (b) S_{a24}

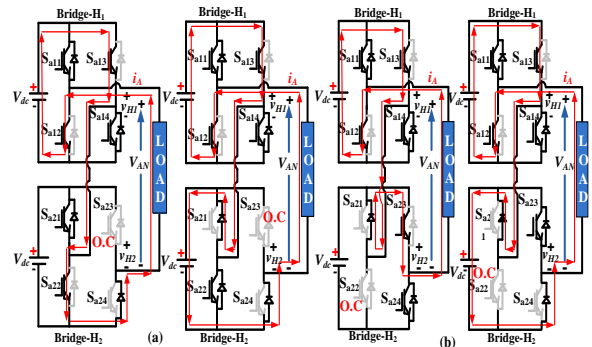


Figure 7. Case IV; $i_A < 0$, $v_{H2} \geq 0$ fault on bridge-H₂, faulty switches (a) S_{a23} , and (b) S_{a22}

TABLE 4. Operation and switching sequence during OC fault in switch of 5-level CHBMLI

Sr. No.	Faulty switch/ Circuit diagram	Switching sequence	i_A	v_{H1}	v_{H2}
1	S_{a11} Fig. 4 (a)	$S_{a21}, S_{a14}, D_{a12}, S_{a24}$	+ve	0	$+V_{dc}$
		$S_{a21}, D_{a13}, D_{a12}, S_{a24}$	+ve	$-V_{dc}$	$+V_{dc}$
2	S_{a13} Fig. 5 (a)	$S_{a23}, S_{a12}, D_{a14}, S_{a22}$	-ve	0	$-V_{dc}$
		$S_{a23}, D_{a11}, D_{a14}, S_{a22}$	-ve	$+V_{dc}$	$-V_{dc}$
3	S_{a14} Fig. 4 (b)	$S_{a21}, D_{a13}, S_{a11}, S_{a24}$	+ve	0	$+V_{dc}$
		$S_{a21}, D_{a13}, D_{a14}, S_{a22}$	+ve	$-V_{dc}$	$+V_{dc}$
4	S_{a12} Fig. 5 (b)	$S_{a23}, D_{a11}, S_{a13}, S_{a22}$	-ve	0	$-V_{dc}$
		$S_{a23}, D_{a11}, D_{a14}, S_{a22}$	-ve	$+V_{dc}$	$-V_{dc}$
5	S_{a21} Fig. 6 (a)	$S_{a11}, S_{a24}, D_{a22}, S_{a14}$	+ve	$+V_{dc}$	0
		$S_{a11}, D_{a23}, D_{a22}, S_{a14}$	+ve	$+V_{dc}$	$-V_{dc}$
6	S_{a23} Fig. 7 (a)	$S_{a13}, S_{a22}, D_{a24}, S_{a12}$	-ve	$-V_{dc}$	0
		$S_{a13}, D_{a21}, D_{a24}, S_{a12}$	-ve	$-V_{dc}$	$+V_{dc}$
7	S_{a24} Fig. 6 (b)	$S_{a11}, D_{a23}, S_{a21}, S_{a14}$	+ve	$+V_{dc}$	0
		$S_{a11}, D_{a23}, D_{a22}, S_{a14}$	+ve	$+V_{dc}$	$-V_{dc}$
8	S_{a22} Fig. 7 (b)	$S_{a13}, D_{a21}, S_{a23}, S_{a12}$	-ve	$-V_{dc}$	0
		$S_{a13}, D_{a21}, D_{a24}, S_{a12}$	-ve	$-V_{dc}$	$+V_{dc}$

3. 2. Faulty Condition For five levels of CHBMLI, each phase consisting two bridges. Under balance condition, there are two isolated neutral points one is the inverter neutral point (P_n) and the other is the load neutral point (N), both of them are at the same potential as shown in Figure 8 (a) and (b). In this figure, all bridges ($A_1, A_2, B_1, B_2, C_1, C_2$) are healthy, hence the line voltages V_{AB}, V_{BC}, V_{CA} are balanced and form an equilateral triangle with 120° phase displacement. When there is a fault at 2nd bridge of phase-A, bridge- A_2 is isolated from the system as shown in Figure 9(a). Hence the line voltages V_{AB}, V_{CA} are disturbed, resulting in unbalance of voltages.

3. 3. Fault Tolerant The simple fault tolerant technique described in literatures are:
 (I) if there is OC fault at bridge- A_2 of phase-A, bypass or deactivate all its counterparts or same number of bridges from the other healthy phases (i.e., from phase-B, bridge- B_2 , and from phase-C, bridge- C_2) to maintain system balanced as shown in Figure 9 (b) [23], so that each phase will have one healthy bridge. However, deactivating the healthy bridge reduce the utilization of the DC-link voltage. This practice is not advisable.

(II) Increase the input DC voltage of healthy bridges i.e., if bridge- A_2 has a fault, then increase the voltage of bridge- A_1 to $2V_{dc}$ to compensate the loss of bridge- A_2 .

But this leads to increase in voltage stress on the switches. So, increasing the input DC voltage to healthy bridge is also one of the drawbacks. The neutral point shift method is used to overcome these drawbacks,

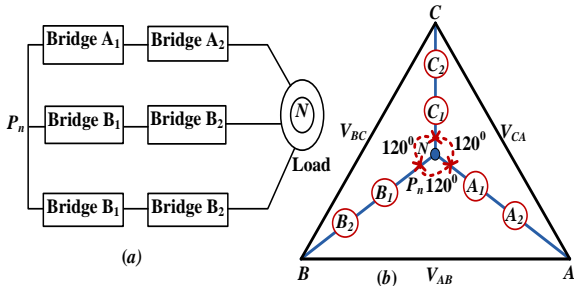


Figure 8. (a) 3-phase, 5-level healthy system (b) line voltages under balanced condition

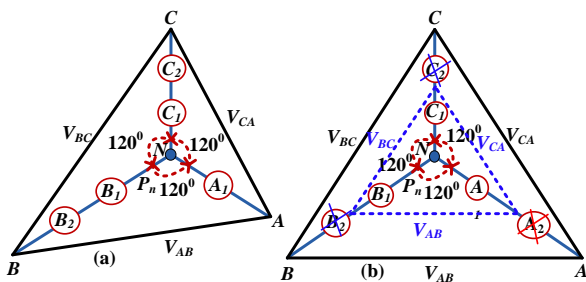


Figure 9. (a) line voltages when OC fault on bridge- A_2 i.e., (1-2-2) (b) Balanced line voltages after bypassing bridges

utilizing all the healthy bridges without an increase in voltage stress.

3. 4. Neutral Point Shift (NPS) Technique The fault-tolerant operation of CHBMLI ensure the continuous operation of the system during and after the fault conditions. The fault-tolerant NPS technique is implemented to balance and maximize the available output line voltages and currents after bypassing the faulty bridge [27]. Normal operating condition, both the neutral points (inverter neutral and load neutral) are at the same potential, and output phase voltages (V_{AN}, V_{BN}, V_{CN}) of CHBMLI are balanced. All phase voltages are displaced by 120° and form an equilateral triangle by joining line voltages (V_{AB}, V_{BC}, V_{CA}). If OC fault occurs on bridge- H_2 of phase-A, only bridge- H_1 of phase-A contributes to the phase voltage (V_{AN}). This reduces the magnitude of phase voltage which results in unbalanced output line voltages. The magnitude of line voltage V_{AB} and V_{CA} are less than V_{BC} . The phase voltages (V_{AN}, V_{BN}, V_{CN}) changes to new phase voltages as L_1, L_2 , and L_3 respectively. To maintain the output line voltages and currents balanced, the neutral point of CHBMLI (P_n) is shifted toward a new neutral point (P'_n) without disturbing other healthy bridges. The shifting of inverter neutral point (P'_n) due to OC fault creates new balanced line voltages 'a'. The new output line voltages form a new equilateral triangle with reduced magnitude than the pre-fault condition. The coordinates (x, y) representation of 3-phase, 5-level CHBMLI with a fault in phase-A of new line voltage 'a' and new phase shift angle (α, β, γ) is shown in Figure 10.

Let (x, y) be the coordinates of new inverter neutral point P'_n ;

$$L_1^2 = x^2 + y^2 \tag{3}$$

$$L_2^2 = (x - a)^2 + y^2 \tag{4}$$

$$L_3^2 = (x - \frac{a}{2})^2 + (y - \frac{\sqrt{3}}{2}a)^2 \tag{5}$$

Putting the Equations (4) and (5) in Equation (3), then the new line voltage 'a' is obtained as:

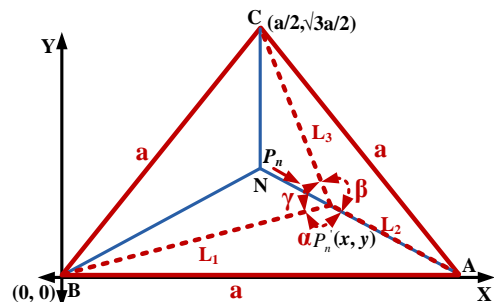


Figure 10. Coordinates representation for parameters calculations

$$a = \sqrt{L_x^2 \pm \sqrt{L_y^2}} \quad (6)$$

Here, $L_x = \frac{1}{2}\{(L_1^2 + L_2^2 + L_3^2)\}$
 and $L_y = (6L_1^2L_2^2 + 6L_2^2L_3^2 + 6L_1^2L_3^2 - 3L_1^4 - 3L_2^4 - 3L_3^4)$

$$L_y \geq 0 \quad (7)$$

To meet the Equations (3)-(7), the following condition must be satisfied:

$$\begin{aligned} L_1 &\leq (L_2 + L_3) \\ L_2 &\leq (L_1 + L_3) \\ L_3 &\leq (L_2 + L_1) \end{aligned} \quad (8)$$

After the calculation of new line voltage 'a', new phase angles are calculated as:

$$\alpha = \cos^{-1}\left(\frac{L_1^2 + L_2^2 - a^2}{2L_1L_2}\right) \quad (9)$$

$$\beta = \cos^{-1}\left(\frac{L_2^2 + L_3^2 - a^2}{2L_2L_3}\right)$$

$$\gamma = (360^\circ - \alpha - \beta)$$

From Equation (6), the value of new voltage 'a' depends on L_x and L_y , + sign gives maximum of 'a' and - sign give minimum value of 'a'. After the detection of a fault, the bridge is bypassed and the modulating signal with all three phase angles given by Equation 9 is generated in a controller, and PWM is implemented. The schematic block diagram of the proposed algorithm for fault detection and fault-tolerant along with LSPWM control for the IGBT switch is shown in Figure 11. It consists of D.C source, 3-phase, 5-level CHBMLI, controller, and load. The controller consists of a fault detection technique to detect the fault, and the NPS technique is implemented to control the modulating signal for fault-tolerant, and reassign the modulating signal (i.e., V_{Aref} , V_{Bref} , V_{Cref}). The generated modulating signals are compared with the multicarrier triangular signal (i.e., LSPWM) and gate pulses are generated to operate MLI.

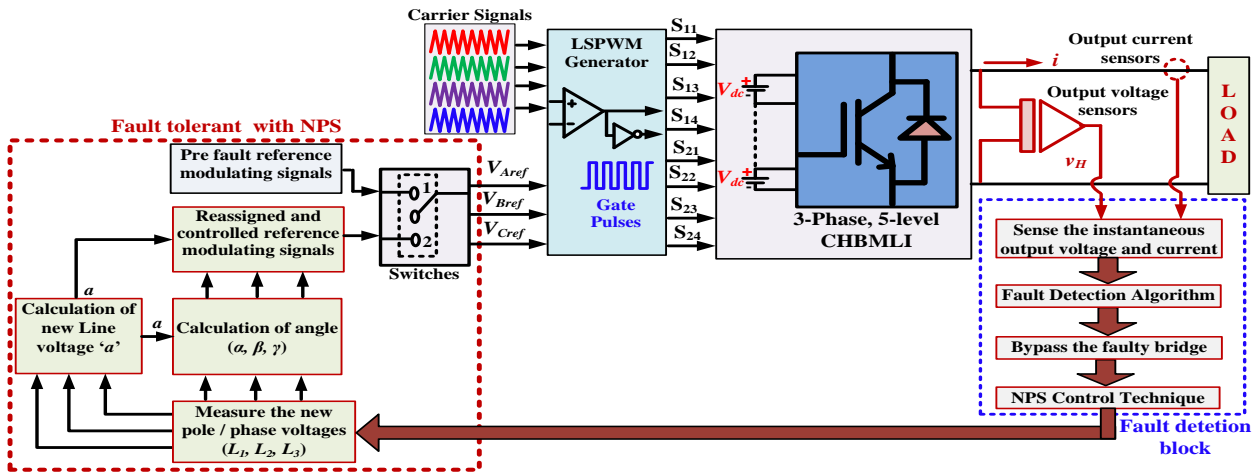


Figure 11. Block diagram of proposed control scheme for 3-phase, 5-level CHBMLI

4. RESULTS AND DISCUSSION

The parameters used for simulation of 3-phase, 5-level CHBMLI with a star-connected RL-load is shown in Table 4. The results are verified with real-time Opal-RT simulator. The LSPWM technique is used for the generation of gate pulses for CHBMLI.

The fault detection algorithm is implemented to detect the OC fault. The operation of the proposed method for fault detection and tolerance is studied for all the cases where as; results for case III and case IV with bridge- H_2 are presented here. In these cases, the fault detection technique senses the instantaneous phase current, instantaneous bridge voltage and instantaneous

TABLE 4. Simulation parameters

Parameters	Ratings
Input DC supply ($V_{dc1}=V_{dc2}=V_{dc}$)	165 V
Load Resistance (R)	10 Ω
Load Inductance (L)	15 mH
Modulation-index (m_a)	1
Modulating signal frequency (f_m)	50 Hz
Carrier signals frequency (f_{cr})	1.5 kHz
PWM technique	LSPWM
Switches	IGBT
Output line voltage	400 V

voltage across switches. Based on the condition corresponding to faulty switch is identified and bypassed for secure and reliable operations. This method detects and tolerates the faulty switch of any phase of the system and, maintains the line voltage and current in balanced condition with the desired magnitude. In case III, an OC fault is created on switch S_{a21} in bridge- H_2 of phase-A, at 0.041s, where the output phase voltage (V_{AN}) and bridge- H_1 output voltage (v_{H1}) are shown in Figure 12 (a) and (b) respectively. The output voltage of bridge- H_2 (v_{H2}) is healthy up to 0.041s which; either becomes 0 or $-V_{dc}$ during fault condition as seen in Figure 12 (c). The change in phase current (i_A) during normal to the faulty condition is observed in Figure 12 (d). The voltage across switch S_{a24} (v_{Sa24}), gate pulse signal for S_{a21} , and the fault detection signal are shown in Figure 12 (e), (f), and (g) respectively.

The fault detection signal goes high at 0.042s thus; the fault which was created at 0.041s is detected at 0.042s. This shows that, in this case the fault detection time is 1 msec. Similarly, in case IV, an OC fault is created on S_{a23} in bridge- H_2 of phase-A at 0.041s, where the output phase voltage (V_{AN}) and bridge- H_1 output voltage (v_{H1}) are plotted in Figure 13 (a) and (b) respectively. Due to fault on S_{a23} , the bridge- H_2 output voltage (v_{H2}) is either 0 or $+V_{dc}$ as shown in Figure 13 (c). The change in current (i_A) during OC fault and voltage across switch (v_{Sa22}) are also shown in Figure 13 (d) and (e) respectively. The gate pulse signal for S_{a23} and the fault detection signal are shown in Figure 13 (f), and (g), respectively.

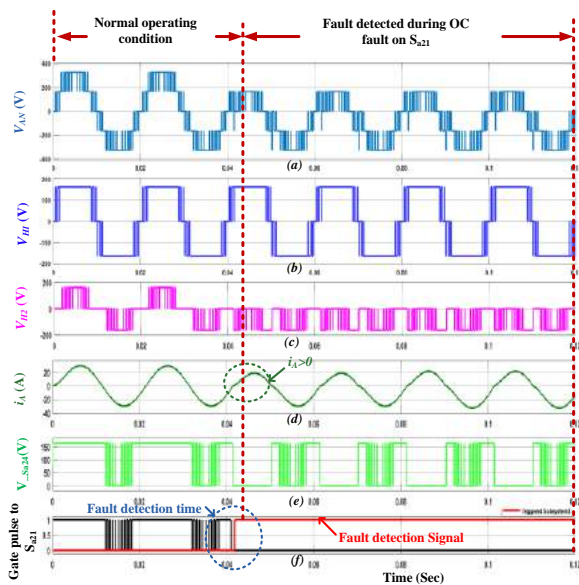


Figure 12. An OC fault on S_{a23} , at $t = 0.041$ sec (a) output voltage (V_{AN}) (b) Bridge- H_1 output voltage (v_{H1}) (c) Bridge- H_2 output voltage (v_{H2}) (d) output current (i_A) (e) v_{Sa22} signal (f) PWM signal for S_{a23} and (g) fault detection signal (red)

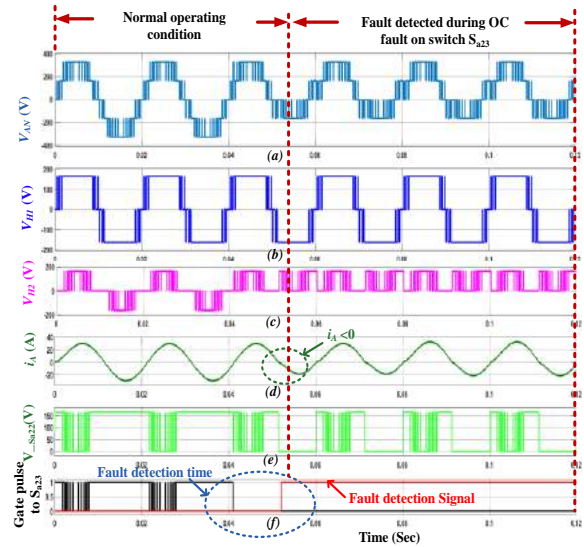


Figure 13. An OC fault on S_{a21} at $t = 0.041$ sec (a) output line voltage (b) output line current (c) phase-A output voltage (d) Bridge- H_2 output voltage (e) phase-A current (f) PWM signal for S_{a23} (black) and fault detection signal (red)

The fault created at 0.041 s is detected at 0.052 s. Hereby; it shows that, in this case the fault detection time is 11 msec. This time is lowest as compare to other fault detection technique. Hence, the proposed algorithm is validated by the results obtained from MATLAB/Simulink.

In Figures 14, and 15 performances of the proposed fault detection inherent fault isolation capability and fault tolerant by NPS technique is presented. Hence; the waveforms under healthy condition, during fault, and after NPS implementation are studied and analyzed. The 3-phase output line voltages and current waveforms during OC fault, on S_{a21} and their post fault conditions are shown in Figure 14. Similarly, the 3-phase output line voltages and current waveforms during OC fault, on S_{a23} and their post fault conditions are shown in Figure 15. The spectrum analysis of line voltage during various condition like; normal operation, during OC fault, and post fault with NPS implementation without for 3-phase, 5-level CHBMLI configuration.

During normal operating condition, the rms value of the line voltages and the THD is 400 V, 17% respectively as shown in Figure 16. But, during OC fault, the observed rms values of voltage and percentage of THD are different. The rms values of line voltage (V_{AB}) is 326 V and THD is 22%, for V_{BC} it is 400 V and THD is 17%, and for V_{CA} it is 326 V and THD is 23%, as shown in Figure 17. During post fault and after implementation of NPS, the line voltages and currents are balanced with rms value of 343 V and THD = 20%, as shown in Figure 18.

Thus, the results obtained from simulation validates performance of proposed technique for fault detection, inherent isolation capability, and fault tolerant operation.

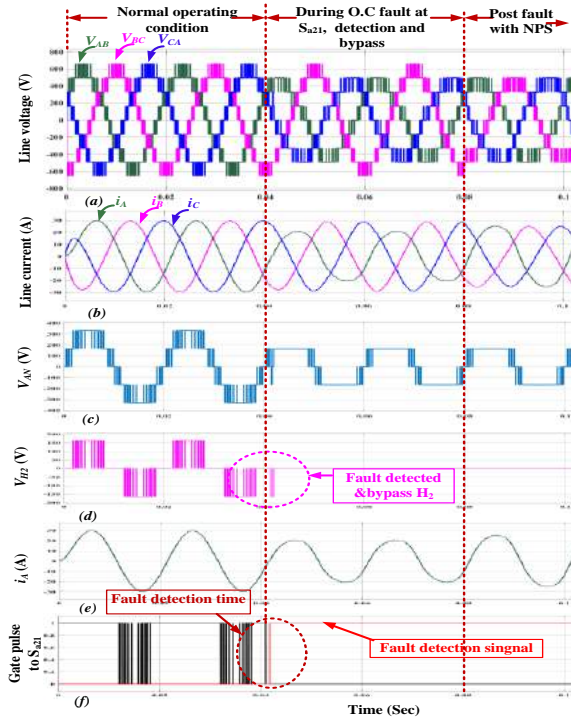


Figure 14. An OC fault on S_{a21} at $t = 0.041$ sec (a) output line voltage (b) output line current (c) phase-A output voltage (d) Bridge- H_2 output voltage (e) phase-A current (f) PWM signal or S_{a21} (black) and fault detection signal (red)

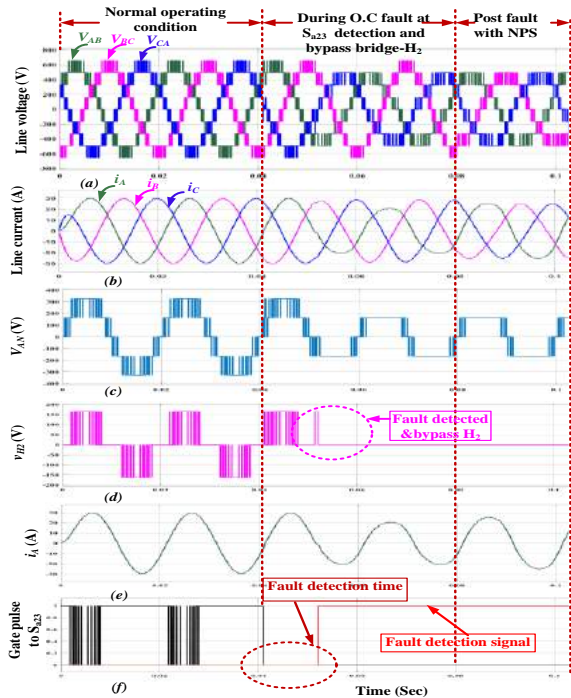


Figure 15. An OC fault on S_{a23} at $t = 0.041$ sec (a) output line voltage (b) output line current (c) phase-A output voltage (d) Bridge- H_2 output voltage (e) phase-A current (f) PWM signal to S_{a23} (black) fault detection signal (red)

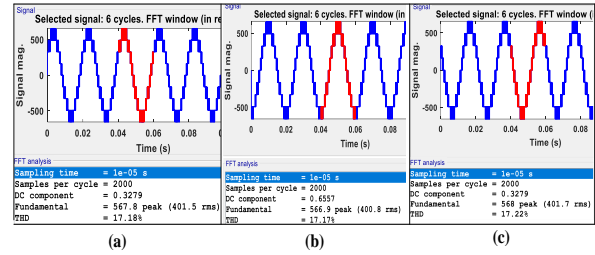


Figure 16. Spectrum analysis of line voltage during Normal operation (a) V_{AB} (b) V_{BC} and (c) V_{CA}

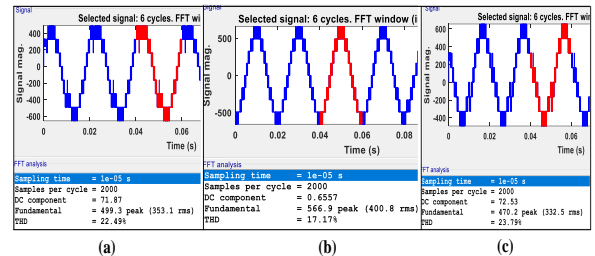


Figure 17. Spectrum analysis of line voltage during OC fault on S_{a23} (a) V_{AB} (b) V_{BC} and (c) V_{CA}

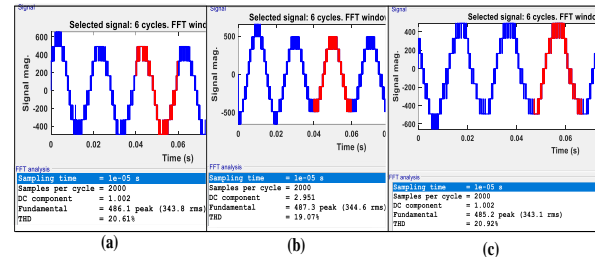


Figure 18. Spectrum analysis of line voltage during post fault with NPS (a) V_{AB} (b) V_{BC} and (c) V_{CA} .

5. OPAL-RT SIMULATOR AND REAL TIME RESULTS

The OP4510 is a family of the latest version of the Opal-RT. It is a firmly united entry-level simulator that consolidates with 128 very fast I/O channels. The OP4510 includes multi-rate FPGA (Kintex-7) with INTEL CPU. The architecture of OP4510 is shown in Figure 19 [28].

An experimental setup of Opal-RT simulator is implemented to examine the proposed algorithm. The proposed algorithm for fault detection, isolation, and fault tolerance is implemented in Simulink and validated in real-time Opal-RT (OP4510) environment. The Opal-RT simulator setup is shown in Figure 20. The simulation is communicated with the Opal-RT real-time simulator via Ethernet cable.

The Opal-RT simulator result of line voltage, line current, phase current (i_A), and phase voltage (V_{AN}) of 3-phase, 5-level CHBMLI under normal operating

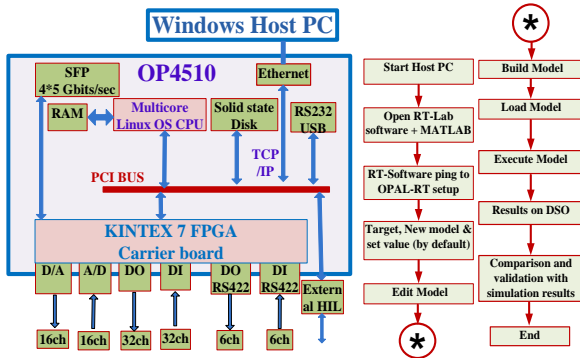


Figure 19. Opal-RT architecture.

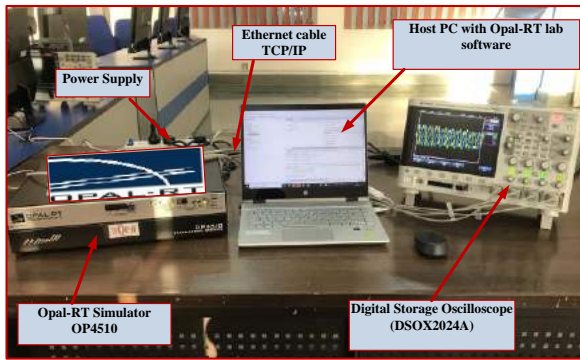


Figure 20. Opal-RT simulator setup

condition can be observed from waveforms shown in Figure 21. In Opal-RT, case III and case IV are studied. In case III, OC fault is created on switch S_{a21} in bridge- H_2 of phase-A. The output voltage of bridge- H_2 (v_{H2}) are $+V_{dc}$, 0, and $-V_{dc}$ which either becomes 0 or $-V_{dc}$ during fault condition, as shown in Figure 22 (a). The v_{-Sa21} and change in phase-A current (i_A) during OC fault are shown in Figure 22 (b) and (c) respectively. The gate pulse for S_{a23} and the fault detection signal are shown in Figure 22 (d). Thus, the performance of the developed algorithm is also verified in Opal-RT.

Similarly, for case IV, the proposed technique; under OC fault condition on switch S_{a23} in bridge- H_2 of phase-A is tested in Opal-RT. Where, the bridge- H_1 output voltage (v_{H1}) is not affected entirely as shown in Figure 23 (a). The output bridge- H_2 voltage (v_{H2}) is either 0 or $+V_{dc}$ during OC fault as shown in Figure 23 (b). The phase current (i_A) is deviated during fault condition as shown in Figure 23 (c). The voltage across switch S_{a22} (i.e., v_{-Sa22}), gate pulse to S_{a23} , and the fault detection signal are shown in Figure 23 (d), (e), and (f), respectively. The results obtained from MATLAB/Simulink are validated by a real-time simulator for case IV, which detected the faulty switch on bridge- H_2 of phase-A. Figure 24, show the real-time Opal-RT simulator results of the line voltage and line current under pre-fault, during OC fault, and post-fault

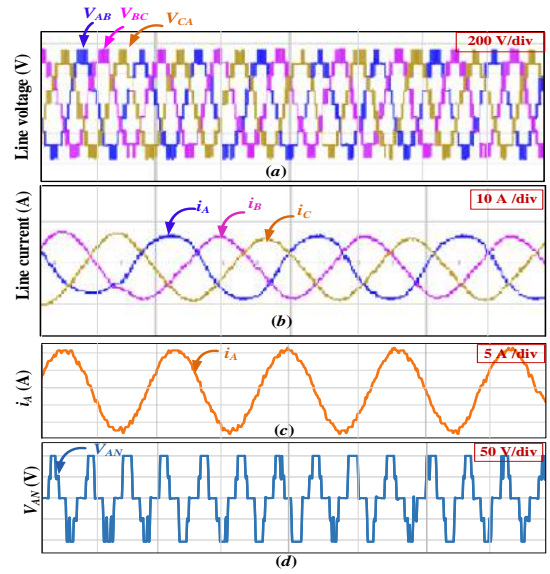


Figure 21. Normal operating condition (a) output line voltage (b) output line current (c) phase current (i_A) (d) phase-A voltage (V_{AN})

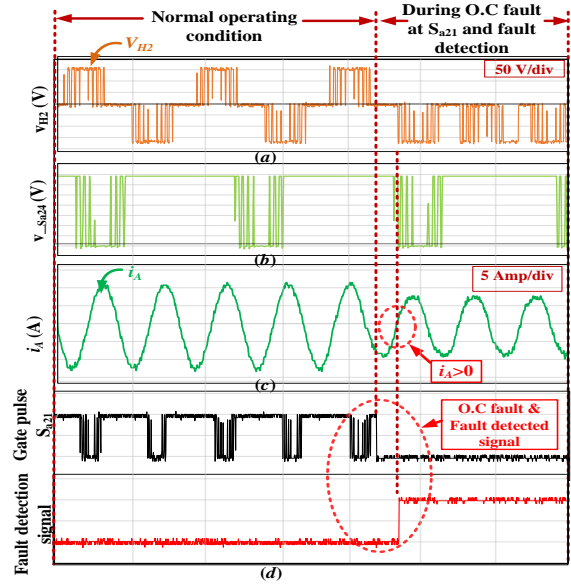


Figure 22. An OC fault on S_{a21} (a) v_{H2} (b) V_{-Sa24} (c) i_A (d) gate pulse to S_{a21} and fault detection signal

with NPS technique. The effectiveness of the proposed fault detection algorithm and NPS technique for tolerance under different conditions are evaluated and validated. The comparison of the proposed algorithm with the various existing techniques based on the different features is shown in Table 6. This comparison shows that the proposed algorithm has least fault detection time and provides fault-tolerant operation also. Thus, this algorithm is useful in supplying uninterrupted power to critical loads.

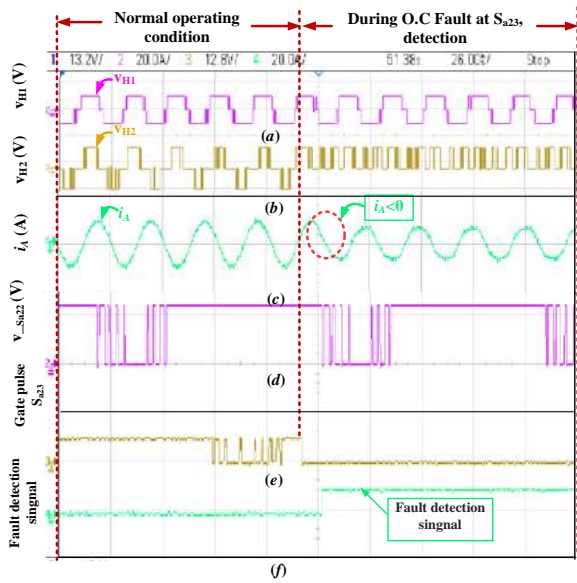


Figure 23. An OC fault on S_{a23} (a) v_{H1} (b) v_{H2} (c) $v_{S_{a22}}$ signal (d) i_A (e) gate pulse to S_{a23} (f) fault detection signal

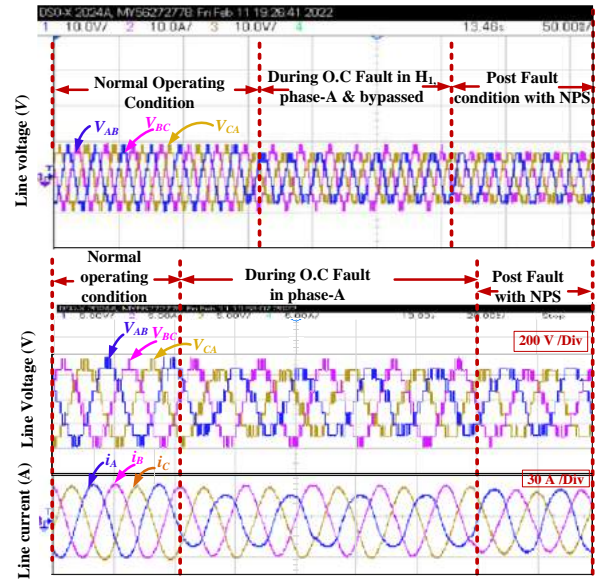


Figure 24. Output line voltage and current under normal operation, during OC fault and post fault with NPS

TABLE 6. Comparison of the proposed technique with the existing technique

Sr. No.	Fault detection methods	Features	Fault detection time	References
1	Based on output current waveform and zero voltage switching states	Fault detection with LSPWM	> 40 msec.	[15]
2	Based on FFT analysis of current signal.	Detect the fault and localize the faulty cells	= 100 msec.	[19]
3	Based on Change in load current during modulating period.	Fault detection and diagnosis	> 60 msec	[20]
4	Based on output voltage and high switching frequency analysis.	<ul style="list-style-type: none"> Fault detection Rejection to normal operation transient 	> 30 msec.	[21]
5	Based on Gravitational search algorithm.	Fault detection and fault isolation.	> 30 msec.	[22]
6	Proposed method with instantaneous voltage, current and voltage across switch.	<ul style="list-style-type: none"> Fault detection and inherent isolation capability NPS to fault tolerance Reliable operation of the system 	< 15 msec.	Proposed algorithm

6. CONCLUSION

In this work, a scheme to improve fault detection in 3-phase 5-level CHBMLI is proposed. Table 6, the incorporation of the NPS technique with the proposed algorithm shows a better performance. The OC fault has been detected within minimum reaction time i.e., 15 millisecond. Another advantage of the proposed scheme accompanied by NPS technique is to reschedule the line voltage and current values close to their preferred level. Despite bypassing the faulty bridge, the output line voltages and currents are balanced due to NPS faulttolerant technique during a post-fault condition. The effectiveness of the proposed technique with different cases is validated in MATLAB/ Simulink as well as Opal-RT (OP4510) simulator. The results obtained by

Opal-RT simulator confirm the fast detection, isolation of faulty bridges, and fault tolerance. Thus, the developed algorithm is useful in supplying uninterrupted power to critical loads.

7. REFERENCES

- Rodríguez, J., Bernet, S., Wu, B., Pontt, J.O. and Kouro, S., "Multilevel voltage-source-converter topologies for industrial medium-voltage drives", *IEEE Transactions on Industrial Electronics*, Vol. 54, No. 6, (2007), 2930-2945. doi: 10.1109/TIE.2007.907044.
- Rahimi Mirazizi, H. and Agha Shafiyi, M., "Evaluating technical requirements to achieve maximum power point in photovoltaic powered z-source inverter", *International Journal of Engineering, Transactions C: Aspects*, Vol. 31, No. 6, (2018), 921-931. doi: 10.5829/IJE.2018.31.06C.09.

3. Alemi-Rostami, M. and Rezazadeh, G., "Selective harmonic elimination of a multilevel voltage source inverter using whale optimization algorithm", *International Journal of Engineering, Transactions B: Applications*, Vol. 34, No. 8, (2021), 1898-1904. doi: 10.5829/IJE.2021.34.08B.11.
4. Saketi, S.K., Chaturvedi, P., Yadeo, D. and Atkar, D., "A reliable and efficient modified t-type fault tolerant five level inverter configuration", *International Transactions on Electrical Energy Systems*, Vol. 31, No. 8, (2021), e12975. doi: 10.1002/2050-7038.12975.
5. Sabyasachi, S., Borghate, V.B., Karasani, R.R., Maddugari, S.K. and Suryawanshi, H.M., "Hybrid control technique-based three-phase cascaded multilevel inverter topology", *IEEE Access*, Vol. 5, (2017), 26912-26921. doi: 10.1109/ACCESS.2017.2727551.
6. Arehpanahi, M. and Paknia, D., "A new single-phase symmetrical cascade multilevel inverter with low number of power switches", *International Journal of Engineering, Transactions B: Applications*, Vol. 31, No. 8, (2018), 1228-1233. doi: 10.5829/ije.2018.31.08b.10.
7. Tousi, B. and Ghanbari, T., "Transformer-based single-source multilevel inverter with reduction in number of transformers", *International Journal of Engineering, Transactions B: Applications*, Vol. 29, No. 5, (2016), 621-629. doi: 10.5829/idosi.ije.2016.29.05b.05.
8. Poorfakhraei, A., Narimani, M. and Emadi, A., "A review of multilevel inverter topologies in electric vehicles: Current status and future trends", *IEEE Open Journal of Power Electronics*, Vol. 2, (2021), 155-170. doi: 10.1109/OJPEL.2021.3063550.
9. Vemuganti, H.P., Sreenivasarao, D., Ganjikunta, S.K., Suryawanshi, H.M. and Abu-Rub, H., "A survey on reduced switch count multilevel inverters", *IEEE Open Journal of the Industrial Electronics Society*, Vol. 2, (2021), 80-111. doi: 10.1109/OJIES.2021.3050214.
10. Maharjan, L., Yamagishi, T., Akagi, H. and Asakura, J., "Fault-tolerant operation of a battery-energy-storage system based on a multilevel cascade pwm converter with star configuration", *IEEE Transactions on Power Electronics*, Vol. 25, No. 9, (2010), 2386-2396. doi: 10.1109/TPEL.2010.2047407.
11. Malinowski, M., Gopakumar, K., Rodriguez, J. and Perez, M.A., "A survey on cascaded multilevel inverters", *IEEE Transactions on Industrial Electronics*, Vol. 57, No. 7, (2009), 2197-2206. doi: 10.1109/TIE.2009.2030767.
12. Valipour, S., Moosavi, S.S., Khaburi, D.A. and Djerdir, A., "An open-circuit fault detection method using wavelet transform for cascaded h-bridge multilevel inverter", in 2017 IEEE Vehicle Power and Propulsion Conference (VPPC), IEEE. (2017), 1-5.
13. Zhang, G. and Yu, J., "Open-circuit fault diagnosis for cascaded h-bridge multilevel inverter based on ls-pwm technique", *CPSS Transactions on Power Electronics and Applications*, Vol. 6, No. 3, (2021), 201-208. doi: 10.24295/CPSSSTPEA.2021.00018.
14. Choi, U.-M., Blaabjerg, F. and Lee, K.-B., "Study and handling methods of power igbt module failures in power electronic converter systems", *IEEE Transactions on Power Electronics*, Vol. 30, No. 5, (2014), 2517-2533. doi: 10.1109/TPEL.2014.2373390.
15. Sim, H.-W., Lee, J.-S. and Lee, K.-B., "A detection method for an open-switch fault in cascaded h-bridge multilevel inverters", in 2014 IEEE Energy Conversion Congress and Exposition (ECCE), IEEE. (2014), 2101-2106.
16. Faraz, G., Majid, A., Khan, B., Saleem, J. and Rehman, N., "An integral sliding mode observer based fault diagnosis approach for modular multilevel converter", in 2019 International Conference on Electrical, Communication, and Computer Engineering (ICECCE), IEEE. (2019), 1-6.
17. Anand, A., Akhil, V.B., Raj, N., Jagadanand, G. and George, S., "An open switch fault detection strategy using mean voltage prediction for cascaded h-bridge multilevel inverters", in 2018 IEEE International Conference on Power Electronics, Drives and Energy Systems (PEDES), IEEE. (2018), 1-5.
18. He, J., Demerdash, N.A., Weise, N. and Katebi, R., "A fast on-line diagnostic method for open-circuit switch faults in sic-mosfet-based t-type multilevel inverters", *IEEE Transactions on Industry Applications*, Vol. 53, No. 3, (2017), 2948-2958. doi: 10.1109/TIA.2016.2647720.
19. Thantirige, K., Rathore, A.K., Panda, S.K., Mukherjee, S., Zagrodnik, M.A. and Gupta, A.K., "An open-switch fault detection method for cascaded h-bridge multilevel inverter fed industrial drives", in IECON 2016-42nd Annual Conference of the IEEE Industrial Electronics Society, IEEE. (2016), 2159-2165.
20. Zhang, J., Empringham, L., De Lillo, L., Dan, H. and Wheeler, P., "Matrix converter open circuit fault diagnosis with asymmetric one zero svm", in 2017 IEEE Energy Conversion Congress and Exposition (ECCE), IEEE. (2017), 3470-3475.
21. Lezana, P., Aguilera, R. and Rodríguez, J., "Fault detection on multicell converter based on output voltage frequency analysis", *IEEE Transactions on Industrial Electronics*, Vol. 56, No. 6, (2009), 2275-2283. doi: 10.1109/IECON.2006.347999.
22. Vyas, U.B., Shah, V.A. and SG, S., "Fault detection technique for modified cascaded half-bridge multi-level inverter with polarity changer in pv grid system", *SN Applied Sciences*, Vol. 3, No. 5, (2021), 589. <https://doi.org/10.1007/s42452-021-04586-5>
23. Deepak, A. and Das, A., "Operation of cascaded h-bridge converter with bypassed cells during fault conditions", in 2016 IEEE International Conference on Industrial Technology (ICIT), IEEE. (2016), 1220-1225.
24. Eaton, D., Rama, J. and Hammond, P., "Neutral shift [five years of continuous operation with adjustable frequency drives]", *IEEE Industry Applications Magazine*, Vol. 9, No. 6, (2003), 40-49. doi: 10.1109/MIA.2003.1245795.
25. Kumar, R., Chaudhari, M.A., Chaturvedi, P. and Sekhar, K.R., "Dynamic operation of ac micro-grid integrated pv-bess using 3-phase 97-level chbmli", in 2022 International Conference on Green Energy, Computing and Sustainable Technology (GECOST), IEEE. (2022), 11-17.
26. Wu, B. and Narimani, M., "High-power converters and ac drives, John Wiley & Sons, (2017).
27. Khaire, N.C., Chaudhari, M.A. and Kumar, R., "Fault-tolerant operation of 3-phase 7-level chbmli with modified neutral point shift method", in 2022 Second International Conference on Power, Control and Computing Technologies (ICPC2T), IEEE. (2022), 1-6.
28. Rajkumar, K., Parthiban, P. and Lokesh, N., "Real-time implementation of transformerless dynamic voltage restorer based on t-type multilevel inverter with reduced switch count", *International Transactions on Electrical Energy Systems*, Vol. 30, No. 4, (2020), e12301. <https://doi.org/10.1002/2050-7038.12301>

COPYRIGHTS

The author(s). This is an open access article distributed under the terms of the Creative Commons 2023© Attribution (CC BY 4.0), which permits unrestricted use, distribution, and reproduction in any medium, as long as the original authors and source are cited. No permission is required from the authors or the publishers



Persian Abstract

چکیده

تشخیص عیب و بازیابی آن چالش اصلی برای عملکرد روان اینورتر چند سطحی (MLI) است. در این مقاله، تشخیص عیب و طرح پاکسازی آن برای یک خطای مدار باز (OC) در یک اینورتر چند سطحی پل H آبشاری ۳ سطحی ۵ سطحی (CHBMLI) توسعه و آزمایش شده است تا قابلیت اطمینان و مناسب بودن را بهبود بخشد. سیستم تشخیص دقیق و سریع، جداسازی و دور زدن پل‌های معیوب، قابلیت اطمینان، تناسب و مقبولیت CHBMLI را در هر کاربرد خانگی و صنعتی درایو افزایش می‌دهد. برای تغییر زمان ولتاژ خط و مقدار جریان نزدیک به سطح پیش از خطا، یک تکنیک تغییر نقطه خنثی (NPS) در این مقاله ارائه شده است. ولتاژ خروجی مورد نظر توسط تکنیک Level Shift Pulse Width Modulation (LSPWM) کنترل می‌شود. طرح پیشنهادی در محیط MATLAB/Simulink توسعه یافته و نتایج با استفاده از شبیه‌ساز Opal-RT تایید می‌شوند. نتایج شبیه‌سازی عملکرد را تأیید کرده است و نتایج شبیه‌ساز Opal-RT امکان‌سنجی و کاربردی بودن طرح پیشنهادی را نشان می‌دهد.



Plastic Properties and Collapse Investigation of Fine-grained Soil Rehabilitated with Styrene Butadiene Rubber: A Case Study in Kerman, Iran

S. Jalali^a, M. Amelsakhi^{*b}, M. Momeni Roghabadi^c, S. A. Hosseini^a, R. Khajavi^a

^a Department of Civil Engineering, Faculty of Engineering, South Tehran Branch, Islamic Azad University, Tehran, Iran

^b Department of Civil Engineering, Faculty of Technical Engineering, Qom University of Technology, Qom, Iran

^c Department of Civil Engineering, Faculty of Engineering, Kerman Branch, Islamic Azad University, Kerman, Iran

PAPER INFO

Paper history:

Received 31 March 2023

Received in revised 13 June 2023

Accepted 14 June 2023

Keywords:

Collapsible Soil Stabilization

Styrene Butadiene Rubber

Intelligent Fuzzy Inference System

Plastic Index

ABSTRACT

Collapsible soils pose significant challenges due to their open structure, which causes settlement when exposed to moisture. Failure to identify these soil types can lead to structural damage when they become saturated or experience changes in moisture content. The presence of such soils in various regions, including Iran, necessitates greater attention and investigation into their behavior and properties. This study examines the impact of butadiene rubber on the stabilization of these soils. Fine-grained soil samples were collected from two different sites in Kerman province (Kerman City). The samples were injected with 2%, 3%, 4%, 5%, 6%, and 7% butadiene rubber for stabilization periods of 4, 7, 14, and 28 days, resulting in a total of 72 tests. The stabilized soils were evaluated using a double consolidation test (ASTM D5333) on intact soil samples. The penetration of butadiene rubber and the resulting rubber columns reduced the degree of collapse. In all cases, the collapse was reduced by more than 88%. The highest reduction was observed with a 7% additive after 28 days of stabilization. Given the increasing use of intelligent systems in predicting the behavior of stabilized collapsible soils, a model was developed to predict the degree of collapse for samples stabilized with butadiene rubber using an adaptive network fuzzy inference system (ANFIS). The accuracy of the model was evaluated, and it successfully predicted the collapse degree. Addition of styrene butadiene rubber additive in the tested soils led to a decrease in the plasticity index of clays with high liquid limits and an increase in the plasticity index of silts with low liquid limits. These changes varied depending on the mineral type. Subsequently, a model was developed to predict the plastic properties of the soil using a fuzzy inference system. The results demonstrate acceptable consistency between the training and prediction data ($R^2=0.93$).

doi: 10.5829/ije.2023.36.10a.03

1. INTRODUCTION

Soils are one of the most important natural materials that have been extensively used by humans in engineering projects for a considerable period. In general, most constructions are either built on or through the soil. However, not all soils possess suitable conditions for construction. Among these, soils sensitive to moisture (according to the definition of ASTM D-5333) are worth mentioning. It is crucial to consider the changes that occur in the properties of these soils, as their structure tends to become unstable upon exposure to moisture.

Collapsible soils are included in this particular group. Naturally, these soils consist of loose deposits with an open structure and are predominantly found in dry and semi-desert regions. The collapse phenomenon can be triggered solely by moisture or in combination with loading. Collapsible soils can originate from transitional soils, particularly alluvial soils, in-situ soils, or inadequately compacted embankments. The issues associated with collapsible soils gained significant attention after the Second World War. Initially, Jennings [1] attributed the collapse of buildings in South Africa to the repositioning of soil particles beneath the structures concerning each other. Traditional stabilizers such as cement, lime, fly ash, etc., have generally been employed to enhance the mechanical properties of collapsible soils.

*Corresponding Author Institutional Email: amelsakhi@qut.ac.ir
(M. Amelsakhi)

Stabilization of collapsible soils has been achieved through injection and mixing techniques. Within the realm of mixed stabilizations, Bell [2], as well as Lutenegeger and Saber [3], introduced a polymer additive to fine-grained soil. Gelsefidi et al. [4] attained favorable outcomes through a study on collapsible soil stability in northern Iran, utilizing nanomaterials. Fauziah et al. [5] utilized a novel type of chemical stabilizer called styrene-butadiene rubber, which reduced the soil's plasticity index. They investigated the resistance properties of the soil after adding butadiene rubber to the fine-grained soil. Meanwhile, this study deals with the behavior of the soil after saturation due to the addition of butadiene rubber. Zhang et al. [6] added biopolymer material to improve soil collapsibility properties and achieved acceptable results. Baghini et al. [7] simultaneously investigated cement and styrene butadiene rubber; they examined the effect of this additive on road construction. Similarly, in this article, butadiene rubber has also been used, but the difference lies in the soil type (coarse-grained soil) and the method of adding the material (mixing). Jalali et al. [8] investigated the improvement of soil properties using styrene butadiene rubber polymer, effectively enhancing soil properties. Zimbaro et al. [9] observed a decrease in the collapsibility properties of sandy soil by using a certain polymer in the collapsible sand. Silveira and Rodrigues [10] compacted the collapsible soil and conducted a double consolidation test; they observed a decrease in the collapsibility index of the soil. For injection stabilization, Ayadat et al. [11] worked to improve the soil of Rambandeh utilizing a stone column. Also, in another article, Ayadat and Hanna [12] investigated different methods of soil improvement. Bahrami and Marandi [13] investigated collapsible soil using an age column in the laboratory. Sarli et al. [14] used recycled materials to improve loess soil. Feitosa et al. [15] improved collapsible soil by mixing sewage sludge. Goodarzi and Salimi [16] discussed the improvement of clay soil using granulated blast furnace slag and basic oxygen furnace slag. Alshaba et al. [17] improved collapsible soil by mixing it with iron powder. Ziani et al. [18] investigated the behavior of soil compaction and improved the properties of the collapsible soil by adding these materials. Gibbs and Bara [19] used clay slurry and injected it into a loess mass. Abbeche et al. [20] focused on collapsible soil injected with salt and examined its geotechnical properties. They observed a significant decrease in the collapsibility index. Fattah et al. [21] conducted a study on soil collapsibility behavior by injecting grout composed of water, cement, and sand. They found that the injected grout improved the properties of the collapsible soil. Ajalloeian et al. [22] investigated the effect of polyvinyl grout on the geotechnical properties of the soil. They injected polymer materials mixed with a certain percentage of water into the collapsible soil, resulting in improved soil resistance and an increased

modulus of elasticity. Ayeldeen et al. [23] examined the mechanical behavior of collapsible soil using two different types of injected biopolymers. Seiphoori and Zamanian [24] utilized nanomaterials to improve collapsible soil. Silveira and Rodrigues [10] investigated collapsible soil behavior and suggested compaction as a means of improvement. Johari et al. [25] explored the use of nanomaterials to improve the properties of collapsible soil. Khodabandeh et al. [26] investigated the properties of rammed soil using nanomaterials, resulting in improved rammed properties. Sabbaqzade et al. [27] examined the mechanical behavior of collapsible soil improved with cement. Valizade and Tabarsa [28] investigated the improvement of mechanical properties of collapsible soil by using plant roots. Nazir et al. [29] conducted research on the improvement of Rambandeh soil properties. Ogila and Eldamarawy [30] improved the geotechnical properties of collapsible soil by using cement kiln dust. El Sawwaf et al. [31] studied several different types of biopolymers for the improvement of collapsible soil. Ziani et al. [18] investigated the behavior of soils improved with pozzolan. Bakir et al. [32] examined the behavior of collapsible soil improved by waste glass fibers. Intelligent systems serve as powerful tools in geotechnical engineering and can apply fuzzy methods to handle uncertainties. Momeni et al. [33] investigated the potential of collapsibility in different central regions of Iran using qualitative assessment and fuzzy set analysis. The study demonstrated a good agreement between the experiments and the fuzzy inference system. Basack et al. [34] improved the compaction, penetration properties, dry density, and CBR of fine-grained soil by incorporating bagasse ash and stone dust.

Due to the presence of a large area of collapsible soils worldwide and the need for new eco-friendly chemical materials to improve the collapsibility properties of these soils, the stabilization of such soil types is receiving significant attention. The application of styrene butadiene rubber (SBR), which is both eco-friendly and produced in significant quantities, is increasingly emphasized for improving soil properties. It is worth mentioning that the use of these stabilizers is beneficial from an economic standpoint, as they are produced domestically, reduce the cost of soil improvement, and mitigate the disastrous environmental effects of projects.

Research results demonstrate that stabilizing with green stabilizers like butadiene rubber provides greater resistance and durability compared to traditional materials such as cement and bitumen. Furthermore, SBR is non-toxic, safe, and non-corrosive, forms a hydrophobic layer that prevents rupturing, and effectively hinders the penetration of water into deeper layers. This study aims to evaluate the reduction in collapsibility by adding different percentages of butadiene rubber (2%, 3%, 4%, 5%, 6%, 7%) over varying periods (4, 7, 14, and 28 days). The collapsibility

index is evaluated using Adaptive Neuro-Fuzzy Inference System (ANFIS), and a calibrated model is developed based on the results of 72 experiments conducted in Kerman City, located in the central region of Iran. Additionally, the plasticity index of the soil at both sites is assessed by adding the additive, and an ANFIS model is developed to predict the soil plasticity index. In this study, butadiene rubber polymer has been used for stabilizing fine-grained soils. Due to the high surface tension of the added material, it is suggested that this polymer be used in coarse-grained soils, or the mixing method be replaced with the injection method. It should be noted that this study solely investigates the effects of SBR on soil plastic index and collapsibility properties, and the corresponding effects on the resistance parameters have not been scrutinized. ANFIS demonstrates acceptable results in modeling the plastic index and collapsibility of fine-grained soils, although the output models cannot be expressed in the form of distinct functions. The paper's first section presents the materials and methods employed in the experiments, followed by an illustration of the sample preparation and injection process. The subsequent section provides a detailed discussion of the experimental results, followed by an analysis of the soil microstructure combined with the added material. Finally, based on the experimental findings, the ANFIS program has been developed, and the outcomes are briefly presented.

The flowchart of how to work is shown in Figure.

2. MATERIALS AND METHODS

According to previous studies indicating the collapsibility of the soil at the tested sites [16], the soil used in this study was collected from two different areas: the western and eastern parts. The samples were obtained from natural ground surfaces following the guidelines of ASTM D1587 and ASTM D4-7015, in intact and lumpy

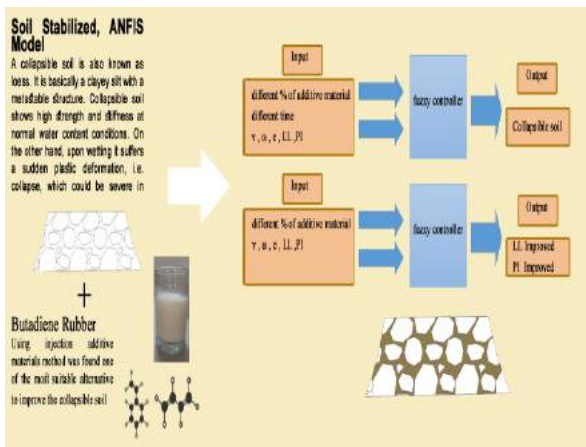


Figure 1. Flowchart of how to conduct the article

form. The tests were conducted following ASTM standards (see Figures 1 and 2). The various parameters mentioned in this article hold the following meanings:

"cp" represents the mean collapsible potential.

"LL" signifies the mean liquid limit.

"Ø" denotes the mean friction angle.

"K" represents the permeability of the soil.

The particle size distribution based on hydrometer analysis is shown in Figure 3. The details of the sampling site are stated in Table 1.

Table 2 presents the results of the initial tests conducted on the soil to determine its initial parameters.

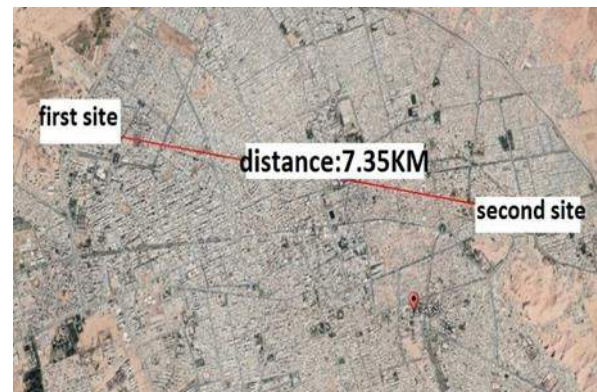


Figure 2. Map showing the sampling location in Kerman City



Figure 3. Particle size distribution (hydrometer analysis)

TABLE 1. Details of the sampling site

Site number	Geographical coordinate	Deep sample(m)	Number of samples
1	30°17'45.7" 57°01'05.4"E	4	72
2	30°17'49.5"N 57°05'41.8"E	5.5	12

TABLE 2. Results of initial tests on the soil

Moisture content (ω)%	CP%	Degree of collapsible based ASTM	Classification	Special Weight (γ kn/m ³)	Moisture content (ω)%	CP%	Degree of collapsible based ASTM	\emptyset	K (m/s)
1	31.2	15	ML	1.46	21.2	11.1	sever	0/404	1/3×10 ⁻⁶
2	59	23	CH	1.4	23.86	13.1	sever	0/39	1/8×10 ⁻⁷

Polymers are abundant in nature, with DNA and RNA being the most prominent natural examples that play a crucial role in life. At its core, a polymer can be defined as a functional chemical substance composed of repeating units. One of the earliest examples of an elastomer or rubber is styrene-butadiene. Approximately seventy percent of polybutadiene production is allocated for the manufacturing of rubber and tires, while an additional 25% to 30% is used as an additive in other tires to enhance their mechanical strength. In 2001, the annual production of this polymer exceeded 2.1 million tons, making it the most widely consumed polymer for tires. The polymerization of styrene butadiene was first achieved in 1910. In subsequent years, extensive research successfully developed a process to produce butadiene from ethanol in 1926, and in 1928, utilized sodium as a catalyst to pioneer the production of styrene-butadiene. Consequently, the Soviet Union became the first nation to achieve industrial-scale production of this polymer in the late 1930s. Germany and the United States also made significant contributions to the research and development of polybutadiene and styrene-butadiene production. Following World War II, major advancements in catalysts, particularly the Ziegler-Natta catalysts, were made in the mid-1950s.

In this study, a brand named X-SBR, manufactured by Paya Rezin Co. in Isfahan, Iran, was utilized as an additive to enhance collapsible soils. Styrene-butadiene rubber, dispersed in water, has been shown in previous research to increase shear resistance properties and decrease the liquid limit of soil when combined. However, the application of these materials to reduce soil volume changes during humidification has not been explored in the literature. Consequently, acquiring this information is necessary to comprehend the stability and effectiveness of soil stabilization when employing this environmentally friendly substance.

The extensive prevalence of collapsible soils worldwide, coupled with the need for eco-friendly chemicals that can improve their collapsibility properties, has underscored the importance of stabilizing such soil types using various polymers. Styrene-butadiene rubber is considered an eco-friendly polymer, and due to its large-scale production, it is also economically viable. Previous studies have employed this substance to improve coarse-grained soils and examine its effects on problematic fine-grained soils. As a result, this study

aims to evaluate the reduction in soil collapsibility by adding different percentages of butadiene rubber (ranging from 2% to 7% of the total weight of the sample) over various periods (4, 7, 14, and 28 days from the time of injection to the commencement of the test). By utilizing Adaptive Neuro-Fuzzy Inference System (ANFIS), the collapsibility index is evaluated, and a calibrated model is developed using data gathered from 72 tests conducted in the central region of Kerman City, Iran.

Fine-grained soils undergo various transformations as the amount of absorbed water increases. As water is added, the grains become coated with a layer of surface water absorption. With further water addition, the thickness of the water layer surrounding the grains increases, facilitating easier sliding of the grains against each other. Therefore, the behavior of soil practically depends on the water content within the complex. Additionally, different fine grains exhibit varying behaviors in terms of surface water absorption. Consequently, the soil's plasticity index will be examined when the additive is introduced at the different percentages mentioned above, and the predicted plasticity index value will be presented in Table 3.

3. RESULTS AND DISCUSSION

3. 1. Investigation of the Possibility of Sterile Butadiene Rubber Penetration into the Tested Soils

In water-based polymer latexes that are sandwiched between fine particles, the water phase is lost through evaporation. This leads to the determination of the effective particle size of the pores (Silveira and Rodrigues, [10]), as explained by the modified Kozeny Carman equation.

$$k = 0.0898 \frac{D^2}{\mu} \times \gamma \omega \times \emptyset^{3.4}$$

TABLE 3. Styrene Butadiene Rubber Additive Properties

Type of polymer	Brand	Color	Viscosity	Particle size	PH
Sterile butadiene rubber	X-SBR	milky	<200	150 nm	10

In the aforementioned equation, K represents the soil's permeability, \emptyset denotes the permeability, and μ signifies the viscosity of water. According to the soil specifications provided in the table, the effective penetration size of soil particles, ML (D1), measures 1.65 micrometers. Similarly, the effective penetration size of soil particles for the second type, CH (D2), is 0.65 micrometers. The particle size of butadiene rubber is 150 nanometers, equivalent to 0.15 micrometers. This indicates that the particles of butadiene rubber, an injection polymer, has successfully infiltrated the desired soils' pores and enhanced their properties.

3.2. Preparation and Stabilization by Injecting the Atterberg Limit Test Sample

In this test, an additive comprising 2%, 3%, 4%, 5%, 6%, and 7% of the soil's weight is introduced to the soil, which has been soaked for 24 hours, less than one hour before the test. All test procedures were conducted in a standardized manner. Two tests were performed for each additive percentage, and the average values were reported (Tables 4 and 5).

In the ML-type soil, which initially had a liquid limit of 38, the addition of a 2% additive led to a 10% decrease in the soil. Subsequently, there was an increasing trend (42%) that continued with a further increase in the additive. On average, the liquid limit increased by 33%.

TABLE 4. Results of Liquid Limit Test on ML Soil

Additive material	Liquid limit soil 1 (LL ₁)	Liquid limit soil 1(LL ₂)	Average liquid limit (LL1)
0	37	39	38
2	37	38	37
3	38	39	38
4	37	40	39
5	45	48	47
6	51	49	49
7	52	52	52

TABLE 5. Results of Liquid Limit Test on CH Soil

Additive material	Liquid limit soil 2 (LL ₁)	Liquid limit soil 2 (LL ₂)	Average liquid limit (LL2)
0	60	58	59
2	61	57	59
3	54	55	54
4	47	49	48
5	45	44	44
6	43	41	42
7	42	40	41

In clay with a high liquid limit, the liquid limit initially increased. However, after adding a 3% additive, it started to decrease, and this downward trend continued. In this soil, the liquid limit decreased by approximately 18%.

The plastic index also increased with the percentage of additives in the first type of soil, which had a low liquid limit. With a 2% additive, the plastic index initially decreased and then exhibited an increasing trend. When the additive percentage exceeded 5%, the plastic index dramatically increased up to 100%. In clay with a high liquid limit, the maximum plastic index was observed with a 2% additive, after which the plastic index decreased. However, this difference decreased at higher percentages, resulting in approximately a 5% reduction (Figure 4).

Naturally, the clay swells due to the absorption of surface water. Water absorption reduces the friction between soil particles, cohesion, resistance, and bearing capacity of the clay mass. Styrene butadiene rubber is composed of two components: a hydrophilic head and a hydrophobic tail. When this polymer is added to the clay, the hydrophilic ions attach themselves to the clay surface, displacing or trapping them within the metal ions. As a result, their absorptive properties diminish, rendering the clay hydrophobic and oily.

The additive in sludge soil exhibited an almost opposite mechanism. The presence of butadiene rubber polymer in the sludge soil increased water absorption by the silt. As the results demonstrate, the addition of butadiene rubber increased the liquid limit. The increase in the specific surface area of the soil, caused by the addition of the polymer to the sludge soil, will raise the moisture required to transition the soil's physical state from solid to plastic and from plastic to liquid.

3.3. Preparation and Stabilization by Injecting the Collapsibility Test Sample

The soil samples obtained were prepared and wax-coated in the laboratory.

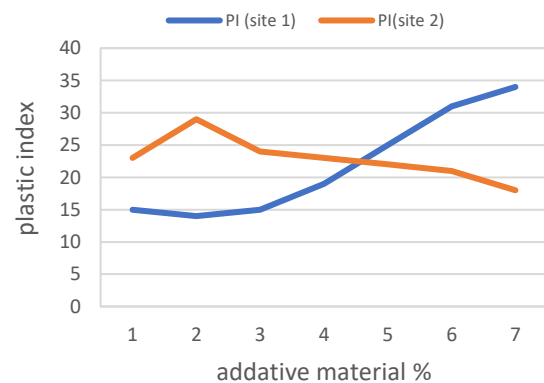


Figure 4. Comparison of the plastic index in type 1 and type 2 soils

The objective was to preserve the natural moisture of the soil and create intact samples with acceptable accuracy following the standard procedure. Firstly, the soil samples were carefully placed inside the ring of the consolidation device (see Figures 5 and 6) using a sharp blade. Then, holes with a diameter of approximately one and a half millimeters ($D=1.5\text{mm}$) and with a distance-to-diameter ratio ($S/D=6.5$) were drilled using a drill. This distance represents the minimum distance between the centers of each hole created on the consolidation sample, ensuring maximum overlap.

Additives in different weight percentages were poured into a container and mixed thoroughly. Subsequently, the injection process was carried out in three steps, with a time interval of 15-20 minutes, using a syringe equipped with a needle that had holes for all-around injection and maximum penetration into the soil (Figures 7 and 8).

3. 4. Storage and Collapsibility Test After the slurry was injected into the soil, the sample was placed in a zippered plastic bag and stored in a moisture can with a lid. It was then placed in a temperature-controlled chamber (Figures 9 and 10).



Figure 5. Sample Drilling

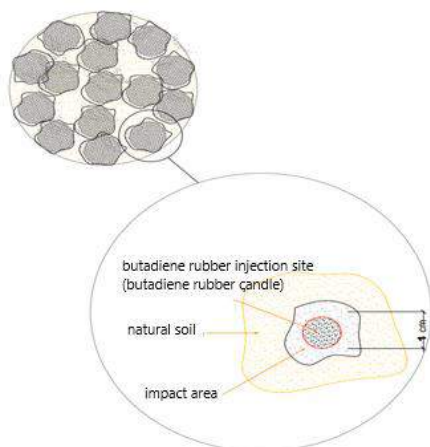


Figure 6. Schematic of Injected Sample



Figure 7. Injection Needle for Sample

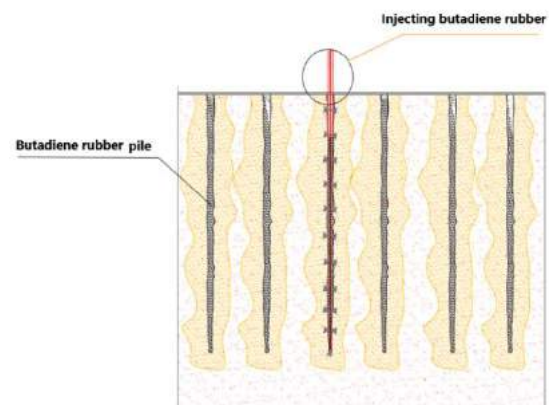


Figure 8. Sample Injection and Drilling Columns of Butadiene Rubber



Figure 9. Sample Storage



Figure 10. Isolating the Samples

To assess the effect of the additive on fine-grained soil, the coefficient of collapsibility index reduction

(Rcp) was calculated using the following formula. RCP directly relates to soil stabilization by butadiene rubber.

$$Rcp = \frac{cp(initial) - cp(secondary)}{cp(inatial)}$$

$$Rcp = CP(initial) - CP(secondary)$$

Where Rcp is the coefficient of collapsibility reduction, CP(initial) is the initial soil collapsibility value, and CP(secondary) is the soil collapsibility value after the additive is introduced (Tables 6 and 7).

TABLE 6. Collapsibility Test Results for Type 1 Soil

Initial character $\gamma=1.76(\text{kn/m}^3)$ $\omega=15.32$ $e=0.68$ $PI=26$ $LL=39$				
Percent of additive material (%)	Time (day)	CP%	average of CP%	RCP%
2	4	1.01	1.26	88.75
2	4	1.1		
2	7	1.8	1.08	90.35
2	7	1.9		
2	14	1.63	1.265	88.7
2	14	0.9		
2	28	1.25	1.242	88.91
2	28	1.23		
3	4	1.1	1.127	89.93
3	4	1.155		
3	7	0.98	1.065	90.49
3	7	1.15		
3	14	1.48	1.055	90.58
3	14	0.63		
3	28	0.39	0.31	93.23
3	28	0.26		
4	4	0.81	0.817	92.7
4	4	0.82		
4	7	0.77	0.69	93.83
4	7	0.61		
4	14	0.96	0.923	94.3
4	14	0.96		
4	28	0.82	0.592	94.71
4	28	0.36		
5	4	0.94	0.766	93.16
5	4	0.585		
5	7	0.713	0.715	93.61
5	7	0.7		
5	14	0.71	0.685	93.88
5	14	0.66		

5	28	0.15	0.252	95.33
5	28	0.16		
6	4	0.46	0.392	93.2
6	4	0.325		
6	7	0.75	0.755	93.25
6	7	0.76		
6	14	0.94	0.720	93.57
6	14	0.5		
6	28	0.53	0.515	95.4
6	28	0.5		
7	4	0.71	0.86	93.32
7	4	1.01		
7	7	0.94	0.82	94.3
7	7	0.92		
7	14	0.61	0.585	94.77
7	14	0.56		
7	28	0.43	0.425	96.2
7	28	0.42		

TABLE 7. Collapsibility Test Results for Type 2 Soil

Percent of additive material (%)	Time (day)	CP%	RCP%
2	4	1.14	91.29
2	7	0.6	95.42
2	14	0.45	96.3
2	28	0.64	95.1
3	4	1.09	91.69
3	7	0.6	95.4
3	14	0.48	96.33
3	28	0.49	
4	4	0.86	93.4
4	7	0.4	96.9
4	14	0.42	97.1
4	28	0.38	97.4
5	4	0.985	92.4
5	7	0.49	96.2
5	14	0.48	96.3
5	28	0.44	96.6
6	4	0.89	93.2
6	7	0.73	94.4
6	14	0.49	96.2
6	28	0.48	96.3
7	4	0.86	93.43
7	7	0.75	94.27
7	14	0.43	96.7
7	28	0.39	97.1

As the processing time increased, there was a further decrease in the collapsibility property due to the reaction between the polymer and soil particles. One of the positive effects of the polymer is coagulation and coagulability. To investigate the impact of processing time and additive percentage on the collapsibility properties of the modified samples, collapsibility reduction diagrams were plotted at different times (Figure 11).

Diagrams illustrating the reduction in collapsibility as a percentage of additive over different periods in site-1 soil reveal that RCP% exceeded 88% in all cases, with the lowest reduction observed at 2% additive. As time progressed, an increase in RCP% was observed. After 7 days, significant increases in RCP% were noted for all additive percentages, with the highest increase occurring at 28 days.

For site-2 soil situated in Shohadaye Darlek Street, the addition of a 2% additive resulted in a reduction in the trend. However, after adding a 5% additive, the trend stabilized (Figure 12).

The collapse phenomenon is a process in which the absorption of water by soil particles leads to the loss of molecular forces between particles through various mechanisms, such as softening, the disruption of capillary forces, the elimination of suction force due to saturation, increased shear stress resistance, and so on.

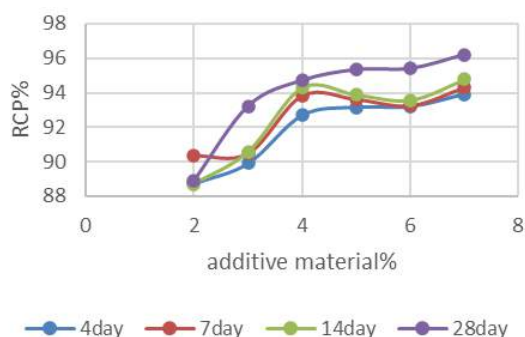


Figure 11. Percentage of Collapsibility Reduction at Different Times and Days

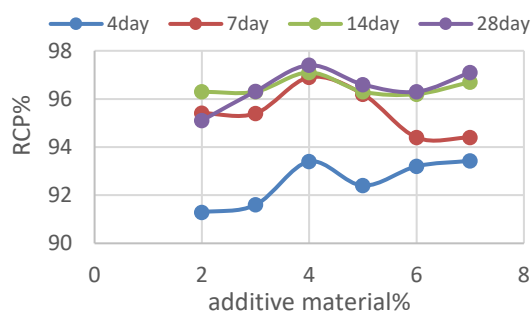


Figure 12. Percentage of collapsibility reduction versus time in site 2

As a consequence, the natural structure of the soil suddenly collapses and is destroyed. These problematic soils, normally dry, stable, and strong, experience numerous deformations, rapid settlement, and a significant decrease in porosity ratio with increasing moisture content and loading. By examining the test results conducted on this soil type, it can be observed that the nature of the polymer breaks a double bond between carbon atoms and replaces it with a single covalent bond. Consequently, the two free ends of this monomer become free radicals. This basic molecule, capable of undergoing reactions, serves as the building block of polymers and is repeated frequently along the polymer molecule chain. Over time, this chain forms and prevents softening between the soil particles when exposed to water. The injection of the additive into the soil fills the soil pores, maintaining the capillary force between the particles unchanged when the collapsible soil is exposed to water, thereby preserving its cohesive structure. The injection of the polymer into the clay with a high fluid limit results in the formation of piles of butadiene rubber in the soil, which act as concrete piles when the soil is saturated and loaded. Consequently, a lower reduction in bearing capacity is observed, and the collapsibility of the soil experiences a significant decrease. In silty soil, the polymer improves the soil around the pile based on the size of soil particles, leading to a reduction in soil collapsibility upon loading and saturation. However, in clay with a high fluid limit, the reduction in collapsibility is more pronounced. Overall, the most substantial decrease in soil collapsibility was observed with a soil additive weight of 7% over 28 days.

3. 5. Microstructural Investigations

To understand the structural changes in the soil samples, SEM photos were taken. Two sets of soil samples were prepared: one without additives and another with additives. Figures 13 and 14 clearly show the effect of styrene butadiene rubber on the formation of new bonds between the soil particles. The introduction of rubber has transformed the soil structure from a discontinuous state to a more continuous form. This enhanced continuity, reduction in existing voids, and increased cohesiveness have improved the collapsibility properties of the soil. The extent of this improvement and void reduction varied based on the percentage of butadiene rubber and the processing time.

Since conducting tests may not always be feasible under certain conditions, a model can be employed to address this issue. In this study, the results obtained from the liquid limit test and plastic index, in conjunction with collapsibility data, were utilized as inputs for MATLAB software and fuzzy logic. The aim was to develop a model capable of determining the plastic index and potential soil collapsibility. To predict the soil's plastic index, 20 data points were used for training, and 8 inputs

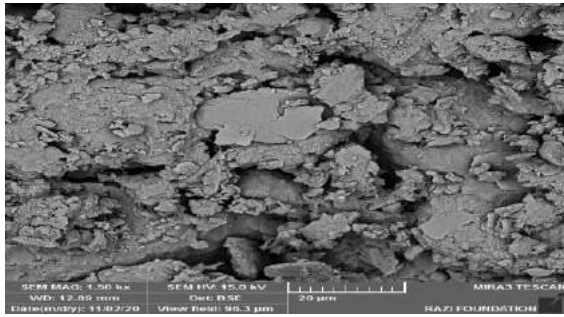


Figure13. SEM Photo of the Soil without Additive

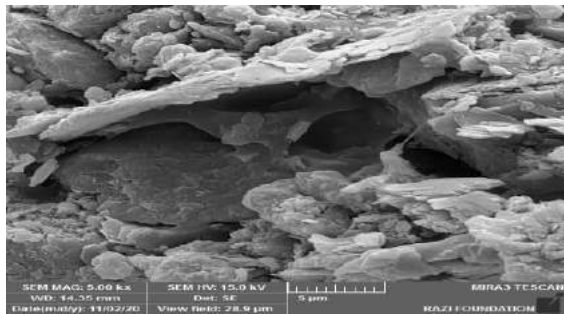


Figure 14. SEM Photo of the Soil with Additive

were utilized for prediction using ANFIS in MATLAB software. For each data point, the following five parameters were taken as inputs: liquid limit of the base soil (LL), plastic index of the base soil (PI), specific weight of the soil (γ), time (t), and percentage of additive. The output was the plastic index of the soil, which was determined for model development. Gaussian membership function was employed as the membership function, and a total of 6 rules were used (Table 8).

The two plastic index functions are in good agreement with the inputs from the laboratory results and the plastic index predicted by ANFIS (Figure 15). The coefficient of determination (R) used to determine the soil plastic index is 0.99, indicating a high correlation between the experimental and predicted values (Figure 16).

To predict the soil collapsibility index, this model utilizes 36 input data for training and 12 data for



Figure 15. ANFIS results versus laboratory values corresponding to prediction data

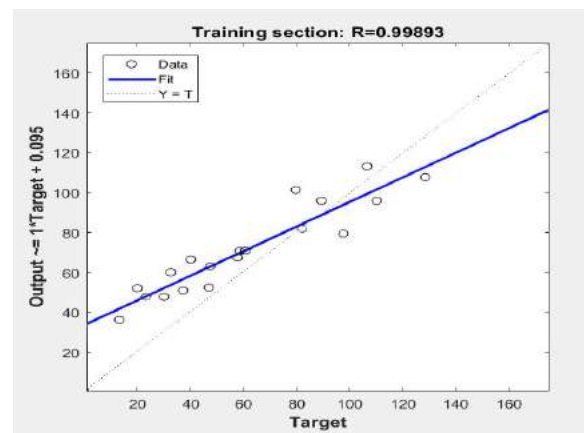


Figure 16. ANFIS results versus laboratory values corresponding to experimental data

prediction from two different sites. The data from Table 9, including moisture percentage (W%), basic soil plastic index (PI), porosity ratio (e), soil specific gravity (γ), time (t), and additive percentage, were considered as input, and collapsibility index (CP%) as output for modeling. The number of input data was 6, and the number of rules used was 8.

In the production model, the parameters used for ANFIS training are listed in Table 9. The membership functions employed are Gaussian. The membership functions (rules) resulted in accurate modeling based on

TABLE 8. Parameters Used in ANFIS for Plastic Index

ANFIS parameter type for PI	ANFIS
MF type	Gaussian
Number of linear parameters	0
Number of nonlinear parameters	3
Number of training data pairs	20
Number of checking data pairs	8
Number of fuzzy rules	6

TABLE 9. Parameters Used in ANFIS for Collapsibility Index

ANFIS parameter type for CP	ANFIS
MF type	Gaussian
Number of linear parameters	6
Number of nonlinear parameters	3
Number of training data pairs	51
Number of checking data pairs	21
Number of fuzzy rules	8

the available data. Choosing a low number of rules would weaken the model while increasing the number of rules would complicate calculations. The created FIS for the soil collapsibility prediction model is shown in Figure 17. The determination coefficient, denoted as R, indicates the explanatory power of the model. It quantifies the percentage of variation in the dependent variable (criterion) explained by the independent variables (predictions). This coefficient serves as one of the model fit indices, reflecting the strength of the dependent variable based on the independent variables. Figure 18 depicts the regression diagram, which is highly effective for analyzing model errors. The diagram illustrates the correlation between actual and estimated values produced by the model. The closer the fitted line to the data (blue line) is to unity, the stronger the correlation between the actual and estimated values. The actual values closely align with the estimated values, demonstrating a reasonable and desirable performance of the model. The coefficient of determination (R) for the soil collapsibility index is 0.87, indicating a high

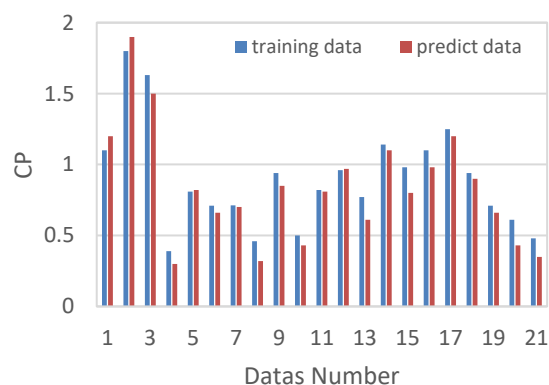


Figure 17. ANFIS results versus laboratory values corresponding to prediction data

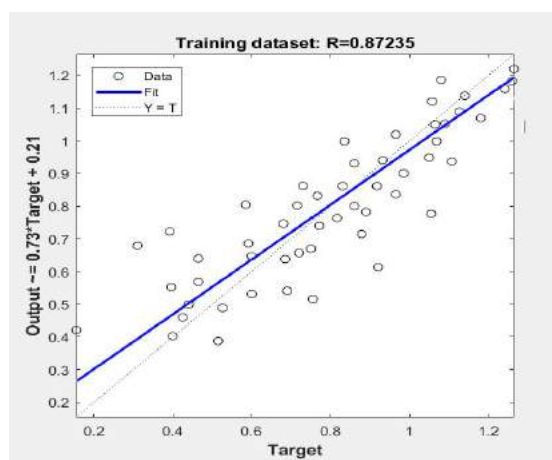


Figure18. ANFIS results versus laboratory values corresponding to experimental data

correlation between the experimental and predicted values and acceptable performance. According to literature, an RMSEA value below 0.1 suggests an excellent fit for the model. A value between 0.1 and 0.5 indicates a good fit, while a value between 0.5 and 0.8 implies an average fit. The obtained RMSEA value is 0.12558, indicating a good fit for the model. Overall, the results obtained from the plastic index test and potential collapsibility, along with their comparison with the models developed in the fuzzy inference system, demonstrate a well-fitted model aligned with the experimental results.

4. CONCLUSIONS

Over time, various additives have been utilized to enhance the collapsibility properties of soil, and their effects have been investigated extensively. This study specifically focuses on the impact of a novel polymer called styrene-butadiene rubber on improving the properties of fine-grained collapsible soil in the central region of Iran, specifically Kerman. After determining the fundamental characteristics of the base soil, such as granularity, moisture percentage, specific gravity, and Atterberg limits, the collapsibility of two types of fine-grained soil (ML, CH) was examined using varying proportions of the aforementioned additive at different time intervals. To evaluate the soil properties, the additive was mixed with soil samples at weights of 7%, 6%, 5%, 4%, 3%, and 2%. Subsequently, collapsibility tests were conducted after different durations (14, 7, 4, and 28 days). A total of 84 tests were performed, and the results were compared.

The theory of fuzzy sets was employed for the proposed modeling. The developed model serves to predict potential soil collapsibility when the additive percentage and initial potential of the soil are known, even in the absence of the necessary conditions for injection and the desired tests. In this model, 80% of the data was used for input, while the remaining 20% was utilized for training purposes. Based on the tests conducted on two different soil samples, ML and CH soils, it was observed that they had moisture contents of 21.2% and 23.86%, and specific gravities of 17.1 g/cm³ and 17 g/cm³, respectively.

Finally, the obtained results can be summarized as follows:

1. The Atterberg limit test results on ML soil indicated that the addition of the additive resulted in an approximately 33% increase in the liquid limit and a 100% increase in the plastic index.
2. Test results on the second type of soil, CH soil, revealed that the additive generally reduced the Atterberg limit and decreased the plastic index by 90%.

3. The most significant reduction in potential soil collapsibility was observed with a 7% additive content over 28 days.
4. A fuzzy inference system was proposed to predict the plastic index using five data inputs and one output. The prediction model demonstrated the highest degree of concurrence with the actual model.
5. The diagram used to determine the soil plastic index yielded an R-value of 0.99 for the trained and predicted data in ANFIS modeling, indicating the model's high accuracy.
6. Based on the test results, it can be concluded that butadiene rubber effectively reduced collapsibility, with a reduction percentage exceeding 90% in most cases.
7. Adding styrene-butadiene rubber to fine-grained collapsible soil at various times and percentages led to the finding that the lowest level of soil collapsibility was attained after a 7-day testing period. Moreover, the optimal percentage of the additive was approximately 4% or higher.
8. The developed ANFIS model was trained using 51 input data points and 21 prediction data points, with the output being the collapsibility index. For the training data, an R2 value of 0.99 and an RMSE value of 20.5% were obtained, confirming the model's accuracy.
9. In comparison to a previous study (Seiphori et al., 2020) that employed clay and cement slurry at varying percentages (1.5%, 2%, 3%, etc.) over similar periods (4, 7, 14, and 28 days) and resulted in a 76% improvement in the collapsibility of fine-grained soil (CL), this study utilizing SBR demonstrates an improvement of 88% and 92% respectively for ML and CH soil types. Both clay slurry and SBR are environmentally safe, but the latter is more affordable and accessible, making it a recommended option for similar research and projects.

5. ACKNOWLEDGEMENTS

We are indebted to Zima Raz Pars Company for their invaluable support and contribution to this project.

6. REFERENCES

1. Jennings, J., "The additional settlement of foundations due to a collapse of structure of sandy subsoils on wetting", in Proc. 4th Int. Conf. on SMFE. Vol. 1, (1957), 316-319.
2. Bell, F., "Engineering treatment of soils, CRC Press, (1993).
3. Lutenegeger, A.J. and Saber, R.T., "Determination of collapse potential of soils", *Geotechnical Testing Journal*, Vol. 11, No. 3, (1988), 173-178. <https://doi.org/10.1520/GTJ10003J>
4. Alireza, S.G.S., Mohammad, M.S. and Hasan, B.M., "Application of nanomaterial to stabilize a weak soil", (2013).
5. Ahmed, F., Atemimi, Y. and Ismail, M., "Evaluation the effects of styrene butadiene rubber addition as a new soil stabilizer on geotechnical properties", *Electronic Journal of Geotechnical Engineering*, Vol. 18, (2013).
6. Zhang, G., Germaine, J., Whittle, A. and Ladd, C., "Index properties of a highly weathered old alluvium", *Geotechnique*, Vol. 54, No. 7, (2004), 441-451. <https://doi.org/10.1680/geot.2004.54.7.441>
7. Baghini, M.S., Ismail, A., Naseralavi, S.S. and Firoozi, A.A., "Performance evaluation of road base stabilized with styrene-butadiene copolymer latex and portland cement", *International Journal of Pavement Research and Technology*, Vol. 9, No. 4, (2016), 321-336. doi: 10.1016/j.ijprt.2016.08.006.
8. Jalali, S., Sakhi, M.A., Roghabadi, M.M., Hosseini, S.A. and Khajavi, R., "Collapsibility prediction of stabilized soil with styrene-butadiene rubber polymer using anfis", *Tehnički Vjesnik*, Vol. 29, No. 5, (2022), 1637-1644. <https://doi.org/10.17559/TV-20210528224934>
9. Zimbaro, M., Ercoli, L., Mistretta, M.C., Scaffaro, R. and Megna, B., "Collapsible intact soil stabilisation using non-aqueous polymeric vehicle", *Engineering Geology*, Vol. 264, (2020), 105334. <https://doi.org/10.1016/j.enggeo.2019.105334>
10. Silveira, I.A. and Rodrigues, R.A., "Collapsible behavior of lateritic soil due to compacting conditions", *International Journal of Civil Engineering*, Vol. 18, No. 10, (2020), 1157-1166. <https://doi.org/10.1007/s40999-020-00523-6>
11. Ayadat, T., Hanna, A. and Etezzad, M., "Failure process of stone columns in collapsible soils", (2008).
12. Ayadat, T. and Hanna, A., "Assesment of soil collapse prediction methods", *International Journal of Engineering, Transactions B: Applications*, Vol. 25, No. 1, (2012), 19-26.
13. Bahrami, M. and Marandi, S., "Large-scale experimental study on collapsible soil improvement using encased stone columns", *International Journal of Engineering, Transactions B: Applications*, Vol. 34, No. 5, (2021), 1145-1155. doi: 10.5829/ije.2021.34.05b.08.
14. Sarli, J.M., Hadadi, F. and Bagheri, R.-A., "Stabilizing geotechnical properties of loess soil by mixing recycled polyester fiber and nano-SiO₂", *Geotechnical and Geological Engineering*, Vol. 38, (2020), 1151-1163. <https://doi.org/10.1007/s10706-019-01078-7>
15. Feitosa, M.C., Ferreira, S.R., Delgado, J.M., Silva, F.A., Oliveira, J.T., Oliveira, P.E. and Azevedo, A.C., "Sewage sludge valorization for collapsible soil improvement", *Buildings*, Vol. 13, No. 2, (2023), 338. <https://doi.org/10.3390/buildings13020338>
16. Goodarzi, A. and Salimi, M., "Stabilization treatment of a dispersive clayey soil using granulated blast furnace slag and basic oxygen furnace slag", *Applied Clay Science*, Vol. 108, (2015), 61-69. <https://doi.org/10.1016/j.clay.2015.02.024>
17. AlShaba, A., Abdelaziz, T. and Ragheb, A., "Treatment of collapsible soils by mixing with iron powder", *Alexandria Engineering Journal*, Vol. 57, No. 4, (2018), 3737-3745. <https://doi.org/10.1016/j.aej.2018.07.019>
18. Ziani, H., Abbèche, K., Messaoudene, I. and Andrade Pais, L., "Treatment of collapsible soils by additions of granulated slag and natural pozzolan", *KSCE Journal of Civil Engineering*, Vol. 23, (2019), 1028-1042. <https://doi.org/10.1007/s12205-019-0051-0>
19. Gibbs, H.J. and Bara, J.P., "Stability problems of collapsing soil", *Journal of the Soil Mechanics and Foundations Division*, Vol. 93, No. 4, (1967), 577-594.
20. Abbeche, K., Bahloul, O., Ayadat, T. and Bahloul, A., Treatment of collapsible soils by salts using the double consolidation

- method, in Experimental and applied modeling of unsaturated soils. 2010.69-78.
21. Fattah, M.Y., Al-Ani, M.M. and Al-Lamy, M.T.A., "Treatment of collapse of gypseous soils by grouting", *Proceedings of the Institution of Civil Engineers-Ground Improvement*, Vol. 166, No. 1, (2013), 32-43. <https://doi.org/10.1680/grim.11.00020>
 22. Ajalloeian, R., Matinmanesh, H., Abtahi, S.M. and Rowshanzamir, M., "Effect of polyvinyl acetate grout injection on geotechnical properties of fine sand", *Geomechanics and Geoengineering*, Vol. 8, No. 2, (2013), 86-96. <https://doi.org/10.1080/17486025.2012.705897>
 23. Ayeldeen, M., Negm, A., El-Sawwaf, M. and Kitazume, M., "Enhancing mechanical behaviors of collapsible soil using two biopolymers", *Journal of Rock Mechanics and Geotechnical Engineering*, Vol. 9, No. 2, (2017), 329-339. <https://doi.org/10.1016/j.jrmge.2016.11.007>
 24. Seiphoori, A. and Zamanian, M., "Improving mechanical behaviour of collapsible soils by grouting active clay nanoparticles", (2020). <https://doi.org/10.13140/RG.2.2.24982.57928>
 25. Johari, A., Golkarfard, H., Davoudi, F. and Fazeli, A., "A predictive model based on the experimental investigation of collapsible soil treatment using nano-clay in the sivand dam region, iran", *Bulletin of Engineering Geology and the Environment*, Vol. 80, (2021), 6725-6748. <https://doi.org/10.1007/s10064-021-02360-w>
 26. Khodabandeh, M.A., Nagy, G. and Török, Á., "Stabilization of collapsible soils with nanomaterials, fibers, polymers, industrial waste, and microbes: Current trends", *Construction and Building Materials*, Vol. 368, (2023), 130463. <https://doi.org/10.1016/j.conbuildmat.2023.130463>
 27. Sabbaqzade, F., Keramati, M., Moradi Moghaddam, H. and Hamidian, P., "Evaluation of the mechanical behaviour of cement-stabilised collapsible soils treated with natural fibres", *Geomechanics and Geoengineering*, Vol. 17, No. 6, (2022), 1735-1750. <https://doi.org/10.1080/17486025.2021.1974579>
 28. Valizade, N. and Tabarsa, A., "Laboratory investigation of plant root reinforcement on the mechanical behaviour and collapse potential of loess soil", *European Journal of Environmental and Civil Engineering*, Vol. 26, No. 4, (2022), 1475-1491. <https://doi.org/10.1080/19648189.2020.1715848>
 29. Nazir, A., El Sawwaf, M., Azzam, W. and Ata, M., "Utilization of marble dust for improving the geotechnical characteristics of collapsible soil", *Journal of Geological Research*, Vol. 2, No. 4, (2020), 36-45. <https://doi.org/10.30564/jgr.v2i4.2352>
 30. Ogila, W.A.M. and Eldamarawy, M.E., "Use of cement kiln dust for improving the geotechnical properties of collapsible soils", *Indian Geotechnical Journal*, (2022), 1-16. <https://doi.org/10.1007/s40098-021-00550-7>
 31. El Sawwaf, M.A., Shahien, M.M., Nasr, A.M. and Habib, M.S., "A comparative study of stabilising collapsible soil using different types of biopolymers", *Proceedings of the Institution of Civil Engineers-Ground Improvement*, (2023), 1-13. <https://doi.org/10.21203/rs.3.rs-1972593/v1>
 32. Abbeche, K., Panczer, G. and Belagraa, L., "Study of the effect of waste glass fibers incorporation on the collapsible soil stability behavior", *KnE Engineering*, (2020), 157-166. <https://doi.org/10.18502/keg.v5i4.6806>
 33. Momeni, M., Shafiee, A., Heidari, M., Jafari, M.K. and MahdaviFar, M.R., "Evaluation of soil collapse potential in regional scale", *Natural Hazards*, Vol. 64, (2012), 459-479. <https://doi.org/10.1007/s11069-012-0252-z>
 34. Basack, S., Goswami, G., Khabbaz, H., Karakouzian, M., Baruah, P. and Kalita, N., "A comparative study on soil stabilization relevant to transport infrastructure using bagasse ash and stone dust and cost effectiveness", *Civil Engineering Journal*, Vol. 7, No. 11, (2021), 1947. <https://doi.org/10.28991/cej-2021-03091771>

COPYRIGHTS

©2023 The author(s). This is an open access article distributed under the terms of the Creative Commons Attribution (CC BY 4.0), which permits unrestricted use, distribution, and reproduction in any medium, as long as the original authors and source are cited. No permission is required from the authors or the publishers.

**Persian Abstract****چکیده**

خاک های رمبنده در طبیعت خاک های مشکل ساز هستند. به دلیل ساختار باز، در صورت قرار گرفتن در معرض رطوبت دچار نشست می شوند. در صورت عدم شناسایی این نوع خاک ها، سازه های ساخته شده بر روی آنها در صورت اشباع و تغییر رطوبت خاک آسیب می بینند. وجود این خاکها در بسیاری از نقاط جهان از جمله ایران نیازمند توجه و بررسی بیشتر رفتار و خواص خاکهای انباشتنی است. این مطالعه به بررسی اثر لاستیک بوتادین بر تثبیت این خاکها پرداخته است. خاکهای ریزدانه مورد آزمایش از دو مکان مختلف واقع در استان کرمان، شهر کرمان، خیابان شهدای دارلک و میدان کوثر نمونه برداری شدند. نمونه ها با لاستیک بوتادین ۲، ۳، ۴، ۵، ۶ و ۷ درصد به مدت ۴، ۷، ۱۴ و ۲۸ روز برای تثبیت (۷۲ آزمایش) تزریق شدند. خاکهای تثبیت شده با آزمون تحکیم مضاعف (ASTM D5333) بر روی نمونه های خاک سالم مورد ارزیابی قرار گرفتند. نفوذ لاستیک بوتادین و همچنین ستون های لاستیکی بوتادین تشکیل شده باعث کاهش سطح ریزش شد. در همه موارد، فروپاشی بیش از ۸۸٪ کاهش یافت. بیشترین میزان کاهش در ۷ ماده افزودنی و به مدت ۲۸ روز رخ داد. با توجه به گسترش سیستم های هوشمند در پیش بینی رفتار خاک های جمع شونده تثبیت شده، مدلی برای پیش بینی درجه ریزش نمونه های تثبیت شده با لاستیک بوتادین با سیستم استنتاج فازی شبکه تطبیقی (ANFIS) ساخته شد و دقت آن مورد ارزیابی قرار گرفت. با افزودن درصد های ذکر شده افزودنی لاستیک استایرن بوتادین به خاک های مورد آزمایش، کاهش شاخص پلاستیک خاک رس با حد مایع بالا و همچنین افزایش شاخص پلاستیک سیلت با حد مایع کم نشان داده شد. این با توجه به نوع ماده معدنی تغییر کرد. سپس این مدل برای پیش بینی خواص پلاستیک خاک با استفاده از سیستم استنتاج فازی توسعه داده شد. نتایج نشان می دهد که داده های آموزش و پیش بینی به طور قابل قبولی سازگار هستند ($R^2=0.93$)



Effects of Xanthan Gum and Lime on Physical Properties and Mechanical Behavior of Organic Soil

B. Zare, M. Mokhtari*, R. Porhoseni

Departament of Civil Engineering, Yazd University, Yazd, Iran

PAPER INFO

Paper history:

Received 05 May 2023

Received in revised form 30 June 2023

Accepted 01 July 2023

Keywords:

Organic Soil

Soil Stabilization

Xanthan Gum Biopolymer

Lime

Shear Strength Parameters

ABSTRACT

A sample of organic soil collected from the Chaharmahal-Bakhtiari Province, Iran, was treated with 0.5, 1, 1.5, 2, 2.5, and 3% of xanthan gum and 1, 3, and 5% of lime. The untreated and the treated specimens were subjected to physical and mechanical tests, including soil classification, pH measurement, compaction test, unconfined compressive strength test, indirect tensile test, and direct shear test. An increase in lime by 3% led to the greatest increase in the compressive strength (5 and 6 times for the 7-day and 21-day samples, respectively) and the tensile strength (3.7 and 4.5 times for the 7-day and 21-day samples, respectively). Xanthan gum also improved the compressive strength (3 and 6 times for the 7-day and 21-day samples, respectively) and the tensile strength (5.9 and 7.5 times for the 7-day and 21-day samples, respectively). Increasing lime up to 3% enhanced the adhesion of the stabilized soil for 3.5 and 7.5 times that of the organic soil for 7 and 21 days of curing, respectively. Also, the friction angle increased by 40% and 68% times with the increase of lime up to 3% during 7 and 21 days of curing, respectively. Stabilization with xanthan gum led to 11.5 and 17.5 times increase adhesion for 7-day and 21-day samples, respectively. Moreover, xanthan gum increased the friction angle by 47% and 75% for 7-day and 21-day samples, respectively. The findings generally suggest that xanthan gum can be a good ecofriendly alternative to lime as a soil stabilizer.

doi: 10.5829/ije.2023.36.10a.04

NOMENCLATURE

A	Mass of the as-received test specimen (g)	T	Tensile strength (KN/m ²)
B	Mass of the oven-dried specimen	P	Maximum compressive force applied by the machine (kN)
C	Weight of ash	L	Length of the specimen (m).
D	Ash content	d	Diameter of the specimen (m).

1. INTRODUCTION

As a substrate for all structures, soil has a special place in civil engineering. However, engineers increasingly face the challenges of construction on poor-quality and problematic soils due to rapid urbanization and the need for infrastructures [1]. Such soils have unfavorable geotechnical characteristics, including their significant settlement and low strength [2], which makes it necessary to stabilize them. Improvement of soil can change and enhance its properties, ultimately leading to the reduction of structure settlement, better soil shear strength, and higher bearing capacity [3,4]. Geotechnical engineering offers various methods to stabilize problematic soils, one

of which is the use of additives [5, 6]. It should be noted that the type of additive and its composition as well as soil characteristics are the main parameters affecting the strength of stabilized soil [7].

Organic soil is a soft layer of soil with a high moisture content, high compressibility, low load-bearing capacity, low shear strength, and low density. It is composed of fine fractioned particles of organic matter and soft clay [8]. Since it is mainly formed as a result of the accumulation and decomposition of plants in wetlands or under water, it sometimes partly contains decayed plant matter. Due to its characteristics, organic soil tends to have very little load resistance even to small loads, and the roads, railways and other structures built on it are exposed to problems such

*Corresponding Author Email: mokhtari@yazd.ac.ir (M. Mokhtari)

as large and extensive cracking, even in the early stages of construction. From the geotechnical engineering perspective, this soil falls in the category of problematic soils [9,10]. Therefore, not only does this soil need treatment, but the treatment method is also an important issue. There are various techniques to improve the engineering properties of problematic soils, such as removing organic soil and replacing it with better alternatives, preloading, and using soil stabilization methods. If none of these are viable options, it might be better to relocate the project [11,12]. A common way of treating weak soils is to stabilize them. However, it may be difficult to choose a stabilization method in a systematic way. It is geotechnical engineers, indeed, that should determine a preferable method with regard to a wide range of technical and economic issues as well as the available labor and equipment based on personal experience and test results. Soil stabilization methods can be divided into physical-mechanical, chemical, and biological types [13,14]. Chemical stabilization has been widely done to improve the engineering properties of problematic soils. A review of the literature shows that organic soils, or the soils containing organic matter, can be successfully stabilized with traditional binders such as lime [15–17], cement [17-19] and fly ash [20, 21]. Meanwhile, for many years, researchers and engineers have used lime for stabilization as a popular soil improvement technique [2].

Although chemical stabilizers are effective, they cannot be considered eco-friendly because they can be toxic, alter soil pH, and contaminate groundwater. In addition, the processes through which these stabilizers are produced are usually large sources of greenhouse gas emissions [6]. In recent years, there has been considerable interest in using certain biopolymers, such as xanthan gum, instead of traditional chemical stabilizers with increasing public pressure to use eco-friendly and sustainable materials [22]. For instance, Chang et al. [23] sought to stabilize sand, clay, natural soil and red-yellow soil with the xanthan gum biopolymer. They achieved an improvement in the compressive strength and elastic modulus of those materials by adding increasing amounts of xanthan gum to them. As the Scanning Electron Microscope (SEM) images taken in this study showed, xanthan gum binds the sand particles that otherwise do not bond together, thereby improving the soil strength. This improvement depends on the strength of xanthan gum fibers. In clay, however, the improvement of strength occurs through the direct reaction of xanthan gum and charged soil particles (e.g., hydrogen bonding). As that study estimated, using 1 to 1.5% of xanthan gum as a stabilizer can be cost-effective. At the end, it was concluded that xanthan gum is a suitable material for soil stabilization as it does not decompose for a long time (750 days) and retains its compressive strength and elastic modulus. Latifi et al. [24] studied the use of xanthan gum

biopolymer in the stabilization of peat soil and evaluated the effect of curing time (3, 7, 28 and 90 days). The optimal amount of xanthan gum to increase compressive and shear strengths was found to be 2%. While using more xanthan gum increases the compressive strength, it is not economical and causes excessive viscosity, which makes its use problematic. The results of study showed that prolonging the curing time improves the behavior of xanthan gum-peat soil mixtures. Ayeldeen et al. [25] used xanthan gum and guar gum to stabilize collapsible soils in dry and wet conditions. They reported that both biopolymers increase the cohesion, decrease the collapse potential, increase the optimum moisture content, and decrease the specific dry weight of the soil. In that study, the soil treated with guar gum showed 20% better results than the one improved with xanthan gum. In a study by Chang et al. [26] on the use of gellan gum biopolymer in sandy soil, it was found that the addition of this substance to the soil increases its unconfined compressive strength, cohesion, and internal friction angle. As also reported, gellan gum has a good reaction with soil and quickly decreases its permeability.

The uniaxial compression, direct shear, and consolidation tests conducted by Latifi et al. [27] on xanthan gum-treated kaolinite and bentonite clay soils showed that xanthan gum increased the hardness, shear strength, and compressive strength of these soils. These effects would be improved with longer curing. Smitha and Sachan [28] studied the behavior of a mixture of Sabarmati river sand (in India) with agar biopolymer by conducting a series of experiments. They showed that the agar biopolymer could increase the shear strength of the sandy soil by binding the sand particles together, covering the surface of the particles, and filling the void space among them. In an attempt, Muguda et al. [29] evaluated the effects of xanthan gum and guar gum biopolymers on the unconfined compressive strength and the tensile strength of a soil specimen containing kaolin, sand and gravel. As the results showed, both biopolymers successfully increased the compressive strength and the tensile strength of the soil specimen. In a study by Hataf et al. [30], chitosan biopolymer was investigated for its effects on the compressive strength and the shear strength of a low-plasticity clay specimen containing fine sand and gravel. The results showed that the biopolymer could improve the properties of the studied soil by increasing the interaction among its particles. As it was observed, in the specimens dried at room temperature (20°C), the biopolymer initiated cementation and crystallization on the external surface while the internal part was still moist. This caused poor crosslinking and, consequently, poor shear strength. Therefore, the best strengthening effect of the biopolymer would occur upon the complete evaporation of water. Chen et al. [31] investigated the effect of drying up on the shear strength of xanthan gum-treated sandy soil. In their study, the treated soil

specimens that were dried in an oven at 40°C had higher shear strength than the untreated ones. However, there was no significant difference of shear strength between the xanthan gum-treated soil specimens dried at room temperature and those dried in the oven.

Dehghan et al. [32] investigated the effect of two biopolymers, xanthan gum and guar gum, on the mechanical properties of collapsible soil. In order to evaluate the engineering characteristics, compaction, permeability, consolidation and unconsolidated-undrained triaxial tests were performed. The researchers reported that biopolymers reduced the maximum dry density and permeability and improved the mechanical properties of the collapsible soil. Singh and Das [33] found that xanthan gum decreases mass loss during repeated freeze–thaw cycles. As observed by Kwon et al. [34], the soil stabilized with xanthan gum polymer was more resistant to hydraulic erosion. According to Sujatha et al. [35], xanthan gum resulted in a link between its molecules and soil surface. This led to a decrease in soil permeability and a rise in the modified soil strength. As the results of this process, the new soil structure had lower maximum dry density and a higher optimal moisture content due to the resistance of the improved soil to compaction.

In addition, Hamza et al. [36] conducted a study to comprehensively examine the efficiency of biopolymer xanthan gum (XG), as a green building material, in stabilizing and improving the characteristics of the weak subsoil of structures. In this regard, a wide range of geotechnical properties was investigated, including compaction, unconfined compressive strength (UCS), elastic modulus (E50), energy absorption capacity (Ev), soaked and unsoaked California bearing ratio (CBR), swelling potential, and consolidation parameters for stabilized and unstabilized soils. The soil was stabilized with different percentages of XG (0, 0.5, 1.0, 1.5, 2.0, and 5.0%) within different curing periods (0, 4, 7, 14, 28, and 60 days). The results of the tests indicated a slight decrease in the maximum dry compaction of the stabilized soil and an increase in the optimum humidity. It was also shown that addition of xanthan gum biopolymer to soil could increase soil strength parameters (UCS, E50, Ev, and CBR). Besides, the compaction and the swelling of the stabilized samples decreased by 83% and 79%, respectively [36].

Bozyigit et al. [37] conducted research under the title of “Performance of eco-friendly polymers for soil stabilization and their resistance to freeze-thaw action”. They used three types of polymers including xanthan gum, guar gum, and anionic polyacrylamide polymer to improve the strength properties of kaolin clay. The soil samples were stabilized with different percentages of the polymers and subjected to 5 and 10 freeze-thaw cycles after curing for 7, 14, and 28 days. Then, a uniaxial strength test was performed on the prepared samples.

According to their results, the polymers increased the strength and resistance of the soil against the freeze-thaw cycles. This suggested the appropriacy of those eco-friendly polymers for areas that are subject to freeze and thaw conditions through seasons. It was also indicated that the curing period affects the strength of stabilized soil, although this effect is insignificant in samples containing anionic polyacrylamide [37].

As the literature suggests, many researchers have investigated the effects of xanthan gum, guar gum, modified starches, agar and glucan, and other such biopolymers on the properties and behavior of sand, silt, clay, and other typical soils [38,39]. Due to the acceptable test results and environmental considerations, biopolymers are considered as acceptable materials to clog pore spaces and increase the binding of soil particles [40-42].

The ability of a biopolymer to improve the properties and behavior of a soil depends on the type of the soil and its composition, the type and quality of the biopolymer, and the curing conditions [43]. The results of the literature review show the successful performance of xanthan gum biopolymer to stabilize clay and sand soil. This biopolymer has caused a significant increase in the strength parameters of the investigated soils. Some studies have used conventional materials, such as lime and cement, in addition to xanthan gum biopolymer in soil stabilization, comparing the results of stabilization with those of conventional materials and xanthan gum. The results obtained from all these studies show better the performance of xanthan gum than conventional materials in many instances. In addition to its successful performance in improving the mechanical behavior of soil compared to other stabilizing materials, xanthan gum can be a suitable alternative to traditional materials for soil stabilization due to its eco-friendly properties. The present research contributions are:

- Unlike previous studies which have examined the functions of the aforementioned biopolymers in clay and sandy soil, the present study deals with the effect of xanthan gum on the engineering performance of organic soil.
- Comparison has been made with organic soil treated by a traditional method.
- Macro scale investigation on the effect of xanthan gum on soil was completed by direct shear, indirect tensile and compressive strength tests and additionally micro scale tests were carried out through Scanning Electron Microscopy (SEM).

2. MATERIALS AND METHODS

2. 1. Organic Soil The soil used in this study was taken from the Choghakhor region in Chaharmahal-Bakhtiari Province, Iran (Figure 1). The organic soil of

this region lies at the depths of 0.5 to 4 meters. An image of this soil is presented in Figure 2(a).

2. 2. Xanthan Gum Biopolymer Xanthan gum is a mass-produced food additive typically used as a thickening agent. This substance is produced by *Xanthomonas campestris* in the process fermentation of glucose or sucrose. The biopolymer is an anionic polysaccharide composed of D-glucuronic acid, D mannose (a sugar obtained from the oxidation of mannitol), pyruvylated mannose, 6-O-acetyl D-mannose, and 1,4-linked glucan, with the chemical structure (C₃₅H₄₉O₂₉) [23]. The gum is shown in Figure 2(b). The characteristics of lime used in this research are also provided in Table 1.

The most important application of xanthan gum is in the creation of artificial plasticity [44]. Under static conditions, adding a small amount of xanthan gum increases the viscosity of a liquid. This biopolymer also has interesting properties such as high resistance to temperature and pH changes, excellent solubility in cold water, ion salt compatibility, and retention capacity [45]. Furthermore, the anionic and hydrophilic surface characteristics of this substance facilitate reactions with cations [46,47]. Xanthan gum has a wide range of applications in various industries as a stabilizer, emulsifier, suspending agent, and thickener. For example, it is used as a thickening agent in the food industry, as drilling mud in the oil industry, and as a viscosity-modifying agent in concrete [23]. It can also serve as a stabilizer to ensure long-term durability and prevent the dispersion of particles. These features combined with wide availability make xanthan gum an interesting choice for soil stabilization. The xanthan gum used in this study was a whitish powder 92% of which could pass through sieve No. 200.

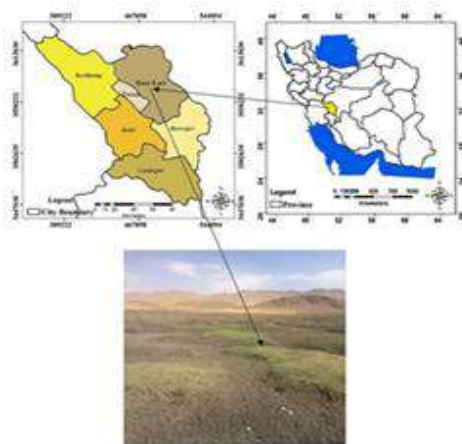


Figure 1. Study area

TABLE 1. The characteristics of the applied xanthan gum

Parameters	Features	Results
Appearance	Whitish or light-yellow powder	Conform
Particle size (mesh)	100% through 80 meshes, not less than 92% through 200 meshes	200
Viscosity (1% KCL, cps)	>1200	1566
Shear ratio	≥6.5	7.64
V1/V2	1.02~1.45	Conform
pH (1% solution)	6.0-8.0	6.96
Loss on Drying (%)	≤15	6.65
Ashes (%)	≤16	10.3
Pb (ppm)	≤2	Conform
Total Nitrogen (%)	≤1.5	Conform
Pyruvic Acid (%)	≥1.5	Conform
Total plate count (CFU/g)	≤2000	300
Moulds/Yeasts (CFU/g)	≤100	<100
Coliform (MPN/g)	≤0.3	Conform
<i>Salmonella</i>	Absent	Conform

2. 3. Lime Lime is one of the materials commonly used in soil stabilization. In this study, quick lime (Figure 2c) was used with the concentrations of 1, 3, and 5% by the weight of dry soil. The chemical characteristics of the lime used in this research are provided in Table 2.

TABLE 2. The characteristics of the lime used

Chemical compounds	Amount (%)
CaO	47.27
SiO ₂	8.71
Al ₂ O ₃	3.17
Fe ₂ O ₃	1.56
MgO	0.987
K ₂ O	0.79
SO ₃	0.678
TiO ₂	0.232
Na ₂ O	0.082
ZnO	0.034
SrO	0.029
MnO	0.026
CuO	0.026
PbO	0.024
Cl	0.023
LOI2	36.15

² Loss on Lgnition

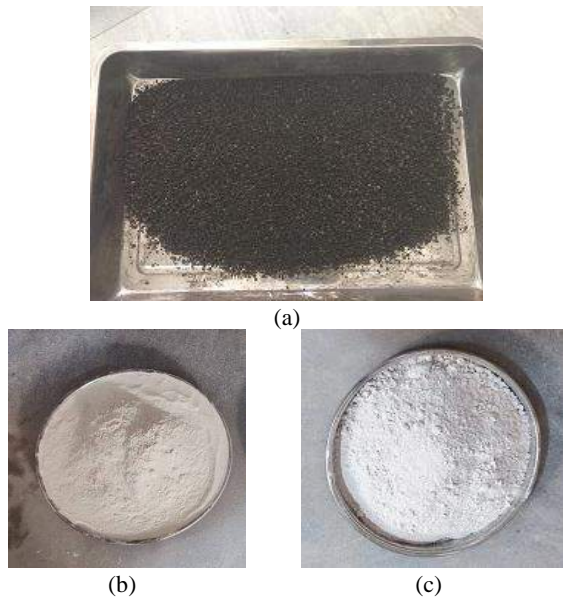


Figure 2. Materials used in this research: a) soil, b) Xanthan gum, c) Lime

2. 4. Classification of the Studied Soil The studied soil was classified according to the widely used Von Post and ASTM organic soil classification systems [48, 49]. Von Post is the best-known system for the classification of organic soils. According to it, soils are of 10 classes of decomposition from H1 to H10 based on such factors as chemical properties, physical properties, rate of degradation, amount and type of plant matter in the soil, and genetic processes [50, 51]. H1 and H10 represent organic soils with the lowest and the highest decomposition rates, respectively. It should be noted that this classification system is qualitative and lacks quantitative boundaries for the exact differentiation of soil classes. In the ASTM system, however, organic soils are classified based on the amount of organic matter, the amount of minerals, and pH [44].

2. 5. Chemical and Physical Properties of Organic Soils Organic soils typically comprise large amounts of organic matter and water and smaller amounts of minerals and air. Given the variability of the ratio of these four components, it may be difficult to describe the physical characteristics of organic soils [50]. To determine the physical and chemical properties of the studied soil, a number of tests were conducted on its moisture content, organic matter content, ash content, pH, and specific gravity. The procedures of these tests are described in the following sections.

2. 5. 1. Soil Moisture Measurement Because of high precipitation and high groundwater level in the areas covered by organic soils as well as the water absorption property of the plant residues in these soils, they tend to

have much higher natural moisture contents than fine-grained soils such as clay. In this study, soil moisture was measured according to ASTM D 2974-87 [52]. To this end, four 50 g specimens were placed as received in an oven for 24 hours. The moisture contents of the specimens were calculated using Equation (1), and then the four resulting values were averaged.

$$\text{Moisture content \%} = \frac{A-B}{B} \times 100 \quad (1)$$

In Equation (1), A is the mass of the as-received test specimen, and B is the mass of the oven-dried specimen both in grams.

2. 5. 2. Measurement of Ash and Organic Matter Contents

The ash content and the organic matter content of the organic soil were determined according to ASTM D 2974-87 [52]. For this purpose, after the measurement of the moisture content, the specimens were placed in an oven, where the temperature was slowly increased to 440°C until there was no more change in the weight of the specimens. The weight of ash was measured by the subtraction of the weight of the oven-dried specimens from the weight of the moisture-containing specimens. Then, the ash content of the organic soil was measured by using the following equation:

$$D\% = \frac{C \times 100}{B} \quad (2)$$

where C is the weight of ash, B is the weight of the oven-dried test specimen, and D is the ash content.

The organic matter content was also measured by the subtraction of the ash content from 100 using the following equation:

$$\text{Organic matter \%} = 100 - D \quad (3)$$

where D is the ash content.

2. 5. 3. pH Measurement Several pH tests were performed on the original organic soil specimens, the mixtures of organic soil with 0.5, 1, 1.5, 2, 2.5, and 3% of xanthan gum, and the mixtures of that soil with 1, 3, and 5% of lime after 21 days of curing. The testing was based on ASTM D2976 - 15 D [53].

2. 5. 4. Specific Gravity Measurement The specific gravity of the soil was measured according to ASTM D 854-14 [54]. This test was conducted on three samples taken from different sections of the soil, and the three measurements were averaged.

2. 6. Proctor Compaction Test The standard proctor compaction test was performed according to ASTM D-698 [55]. For this purpose, mixtures of organic soil with 0.5, 1, 1.5, 2, 2.5, and 3% of xanthan gum and with 1, 3, and 5% of lime were subjected to separate compaction tests.

To prepare the soil-xanthan gum mixtures, first, dry soil was mixed with the desired amount of xanthan gum in a mixer for a few minutes, and then mixing continued by hand with occasional spraying of water until the mixture became almost homogeneous. Next, the compaction tests were performed, and the optimum moisture content and the maximum dry unit weight were determined.

2. 7. Unconfined Compressive Strength Test

Based on ASTM D2166 [56], some unconfined compressive strength tests were conducted on the organic soil, its mixtures with 0.5, 1, 1.5, 2, 2.5, and 3% of xanthan gum and its mixtures with 1, 3, and 5% of lime. All the test specimens were prepared with the optimum moisture contents and the maximum dry unit weights obtained from the compaction tests. Cylindrical test specimens were also created each with a height of 8 cm and a diameter of φ cm using a hydraulic jack (Figure 3). For better curing, the created specimens were placed in plastic bags tightly sealed after the removal of the trapped air, and then they were kept at room temperature. For each mix design (i.e., organic soil, organic soil + xanthan gum, organic soil + lime), two groups of specimens, one for 7 days of curing and the other for 21 days of curing, were prepared.

2. 8. Indirect Tensile Strength Test The indirect tensile test was performed according to ASTM C496 [57]. For this test, the specimens were created in the same number and with the same dimensions and curing times as in the unconfined compressive strength test. As instructed by ASTM C496 [57], which is related to the tensile strength of cylindrical specimens, each prepared specimen was inserted in the machine horizontally, with two metal plates placed at the top and bottom to ensure uniform linear load distribution (Figure 4). Thus, the centerline of the specimen was aligned with the symmetry line of the machine's loading plate. Then, the force was applied until the specimen cracked and fractured. The maximum compressive force applied to the specimen was inserted in



Figure 3. Cylindrical specimen made of organic soil

Equation (4) to obtain its tensile strength.

$$T = \frac{2P}{\pi L d} \quad (4)$$

In the above equation, T is the tensile strength ($\frac{kN}{m^2}$), P is the maximum compressive force applied by the machine (kN), and L and d are the length and the diameter of the specimen (m).

2. 9. Direct Shear Test As instructed by ASTM D3080-04 [58], direct shear tests were conducted on the organic soil, its mixtures with 0.5, 1, 1.5, 2, 2.5, and 3% of xanthan gum and its mixtures with 1, 3, and 5% of lime after 7 and 21 days of curing. These specimens were also prepared with the optimum moisture contents and the maximum dry unit weights obtained from the compaction tests (Figure 5). They were kept at room temperature in sealed bags. For each mix design (i.e., organic soil, organic soil + xanthan gum, organic soil + lime), two groups of specimens, one for 7 days of curing and the other for 21 days of curing, were prepared.

3. RESULTS AND DISCUSSION

In the following, the results obtained in each part of the study are presented and discussed in separate sections.



Figure 4. Preparation and loading of organic soil samples for indirect tensile testing

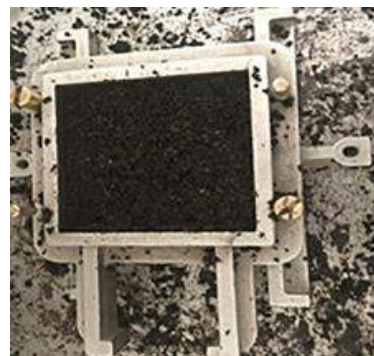


Figure 5. Preparation of a direct shear test specimen

3. 1. Physical and Chemical Properties The results of the measurements conducted to determine the moisture content, ash content, organic matter content, pH, and specific gravity of the studied soil are provided in Table 3.

3. 2. Soil Classification As the testing and examination of the studied soil showed, it can be classified from H3 to H6 on the von Post scale [51]. It also has an increasing rate of decomposition, and its color changes from brown to dark brown with depth.

According to the data provided in Table 3, the organic matter content of the soil ranges from 67% to 69.2%, its ash content is higher than 15%, and its pH is from 5.7 to 7. Thus, based on ASTM, this soil is classified as a regular type of organic soil with a high ash content and low acidity. Also, since it has a high amount of organic matter and plant residues, which burn when exposed to fire, its organic matter content was determined by the test proposed in ASTM D2974-87 [52]. As shown in Table 3, the soil contains a large amount of organic matter averaging around 68.1%.

3. 3. Proctor Compaction Test Based on the results of the proctor compaction test (Figure 6), the optimal moisture content of the organic soil was found to be 38.89%, and its maximum dry unit weight was 11.3 kN/m³.

The results of the compaction test for the mixtures with different percentages of lime and xanthan gum are shown in Figures 6 and 7, respectively. As it can be seen, mixing the soil with lime and xanthan gum changed both the optimum moisture content and the maximum dry unit weight, increasing the former and decreasing the latter. Basically, adding lime to the soil results in an immediate cation exchange reaction, which causes the soil particles to clot together. This process leads to the appearance of more voids among the particles and, therefore, a more porous structure with a lower maximum dry unit weight. Since more water is needed to fill these voids, this process also increases the optimum moisture content of the soil. These effects for the lime-soil mixtures are illustrated in Figure 6.

TABLE 3. Physical and chemical properties of Choghakhor organic soil

Property	Value	Standard
Natural moisture content (%)	262-328	ASTM D 2974-87
Von Post class	H3-H6	-
Specific gravity	2.11	ASTM D 854-14
Organic matter content (%)	67-69.2	ASTM D 2974-87
Ash content (%)	33-30.8	ASTM D 2974-87
pH	6.5	ASTM D2976 - 15

Xanthan gum mixed with organic soil reacts directly with fine soil and water particles. As the amount of the gum increases in the mixture, the excess amount absorbs more water and makes the suspension more viscous, resulting in increased gaps among the particles and less desirable compaction (Figure 7). As other studies have also reported, an increase in the amount of xanthan gum increases the viscosity of the mixture and lowers its workability [23, 59], leading to the separation of the light soil particles and the reduction of the dry unit weight. Increasing the xanthan gum content of stabilized soils also increases their optimum moisture content. These results are consistent with the observations of Ayeldeen et al. [25].

3. 4. Effects of Lime and Xanthan Gum on pH of Treated Soil Specimens

The pH measurements after 21 days of curing showed an increase in the pH value of the treated soil specimens. This increase was due to the alkaline conditions, which caused the hydration reaction to progress. In the lime-treated soil, this was due to the presence of (OH⁻) and (Ca⁺²) ions, which initiated a pozzolanic reaction. As for the xanthan gum-treated soil, the substance bound directly to the electric charges around fine-grained particles through the cationic and hydrogen bonds between carboxyl (COOH⁻) and hydroxyl (OH⁻) groups, causing the pH to rise [23]. The pH values of the treated organic soil specimens are given in Table 4.

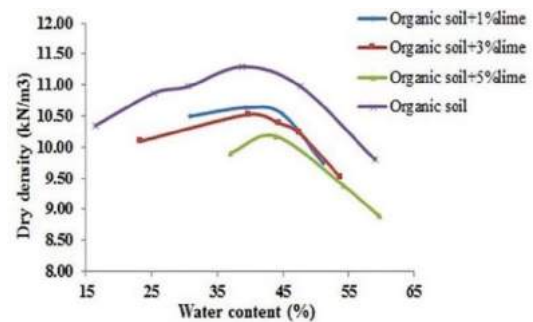


Figure 6. Proctor compaction curve of the lime-treated organic soil specimens

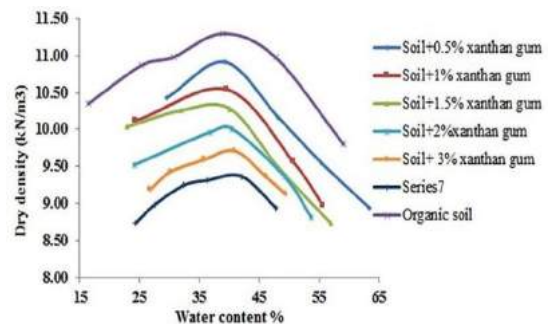


Figure 7. Proctor compaction diagram of the xanthan gum-treated organic soil specimens

TABLE 4. Effects of adding different amounts of stabilization materials on the pH of the organic soil

Specimen	pH
Organic soil (untreated)	6.5
Organic soil + 1% lime	8.19
Organic soil + 3% lime	8.25
Organic soil + 5% lime	8.38
Organic soil + 0.5% xanthan gum	7.04
Organic soil + 1% xanthan gum	7.06
Organic soil + 1.5% xanthan gum	7.15
Organic soil + 2% xanthan gum	7.22
Organic soil + 2.5% xanthan gum	7.29
Organic soil + 3% xanthan gum	7.36

3. 5. Unconfined Compressive Strength This section discusses the effects of lime and xanthan gum on the compressive strength of the studied organic soil.

3. 5. 1. Effect of Lime on Unconfined Compressive Strength of Soil

After curing, the specimens made for unconfined compressive strength tests were subjected to compressive loading until fracture (Figure 8). The unconfined compressive strength of the studied soil was measured on days 7 and 21 after the addition of different amounts of lime to it. The results are presented in Figures 9a and 9b. As it can be seen, adding lime to the soil increased its unconfined compressive strength. However, this effect peaked with 3% w/w of lime; the use of 5% lime, indeed, resulted in less unconfined compressive strength improvement. The 7-day unconfined compressive strength of the soil treated with 3% lime was 402 kPa, which was about five times that of the untreated soil (77.88 kPa). The unconfined compressive strength diagrams of the specimen cured for 21 days showed that prolonging the curing could greatly increase the compressive strength.



Figure 8. Plane failure of the specimens in the unconfined compression test

When lime is mixed with soil in the presence of water, the dissociation of CaO increases the concentration of calcium and hydroxide ions, which raises the pH of the environment. The high pH of the lime-treated soil increases the solubility and reactivity of the particles in the soil. The pozzolanic reactions taking place between the calcium ions and the dissolved silicates in soil result in stable elements such as calcium silicates and calcium aluminates. The resulting hydrate gels serve as natural binders, leading to higher strength and better cementation of the lime-treated soil. As these pozzolanic reactions progress, they slowly improve the strength of the lime-treated soil over a long period of time [15].

3. 5. 2. Effect of Xanthan Gum on Unconfined Compressive Strength of Soil

The test results for the unconfined compressive strength of the organic soil treated with 0.5, 1, 1.5, 2, 2.5, and 3% xanthan gum after 7 and 21 days of curing are presented in Figures 10(a) and 10(b), respectively. As it can be seen in both diagrams, the compressive strength of the soil increased considerably with the addition of xanthan gum. The highest 7-day unconfined compressive strength belonged to the mixture with 3% xanthan gum, which was about three times as much as the unconfined compressive strength of the untreated specimen. After 21 days of curing, this ratio increased to 6. The results also show that adding xanthan gum to soil increases its ductility, which can be attributed

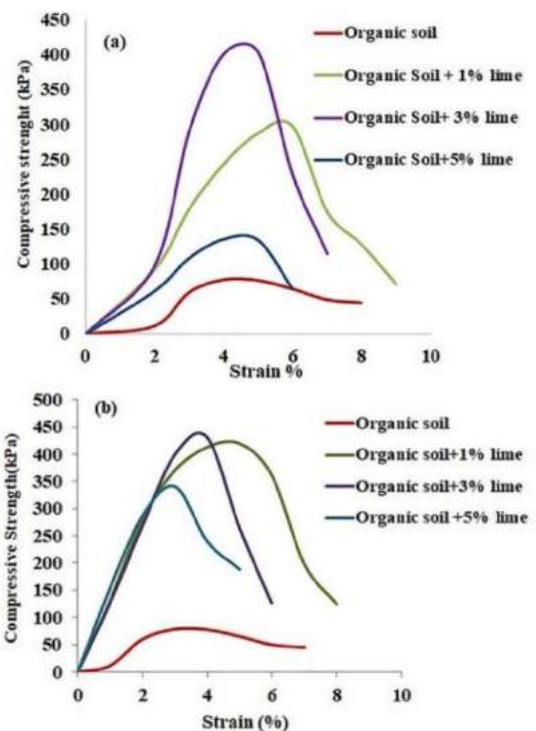


Figure 9. Unconfined compressive strength of the organic soil treated with different amounts of lime after a) 7 days of curing and b) 21 days of curing

to the binding property of this biopolymer. As shown in Figure 10, the specimens containing 1.5% to 3% xanthan gum had their maximum unconfined compressive strength at a 10% vertical strain, which suggests ductile behavior.

Besides, as the curing time increased, the greater reaction of xanthan gum with the soil particles resulted in a nonlinear increase in the compressive strength, but this increase slowed down as the amount of xanthan gum increased. This is because the growth of cementitious products over time causes soil particles to stick together and fill the pores in the xanthan gum-soil matrix [24]. The most effective range of xanthan gum content is from 1.5% to 2%; higher amounts of xanthan gum increase the viscosity of the mixture and decrease its workability. Other studies have also reported a similar pattern of compressive strength improvement in the treatment of other soils with xanthan gum [23, 24, 27].

These results are also consistent with the findings of a study by Arman and Munfakh [15] who explored the effect of xanthan gum on clayey soils. They reported that a higher compressive strength can be achieved with lower amounts of this biopolymer than with higher amounts of lime. The results of the study conducted by Latifi et al. [27] confirmed these findings.

3. 5. 3. Comparison of Effects of Xanthan Gum and Lime on Unconfined Compressive Strength The results of the unconfined compressive strength tests on the mixtures of the organic soil with lime and xanthan

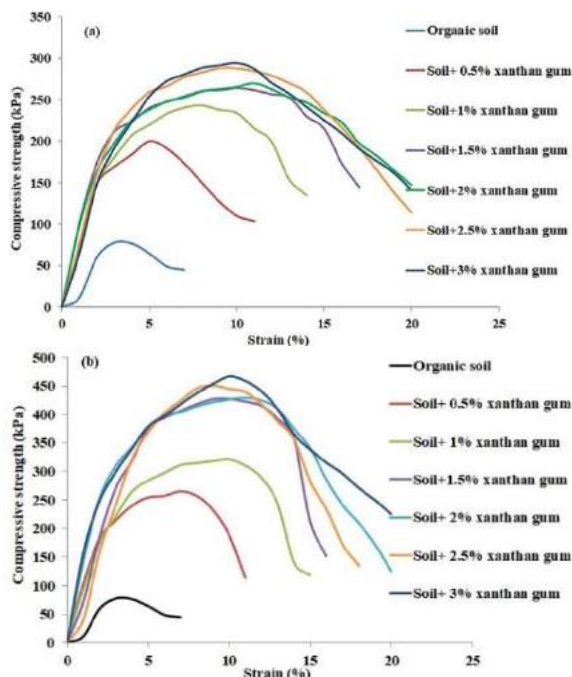


Figure 10. Unconfined compressive strength of the organic soil treated with different amounts of xanthan gum after a) 7 days of curing and b) 21 days of curing

gum can be used to compare the effects of these two treatment agents. As shown in Figure 11, while both lime and xanthan gum improved the unconfined compressive strength of the organic soil, the latter was more effective in this respect.

These findings are interesting because, when it comes to stabilizing organic soils, the non-toxic, edible environment-friendly xanthan gum is a superior alternative to conventional lime treatment.

3. 6. Comparison of Effects of Xanthan Gum and Lime on Tensile Strength Figure 12 presents the results of the indirect tensile tests performed on the organic soil treated with different amounts of xanthan gum and lime after 7 and 21 days of curing. As the results suggest, xanthan gum significantly increased the tensile strength of the specimens. This is because, when combined with water and soil, xanthan gum increases the cohesion of the mixture, which results in increased tensile strength. Up to 3% of this biopolymer caused a significant improvement in the tensile strength, so much so that the 7-day tensile strength of the treated specimens (79 kPa) was 5.9 times higher than that of the untreated specimens (13.3 kPa). The curing time also had a positive effect on the tensile strength. As shown in Figure 12, the tensile strength of the specimens increased by about 24% when the curing time increased from 7 days to 21 days.

Treating the soil with lime also improved its tensile strength. For example, the tensile strength of the specimen treated with 3% lime was almost 3.7 times higher than that of the untreated specimen, as reported in Figure 12. This figure also compares the effects of lime and xanthan gum on the tensile strength of the organic soil. As it can be seen, in all the additive contents, xanthan gum provided a significantly better tensile strength than lime. For example, consider the 3% additive content. While the 7-day tensile strength of the specimen treated with 3% lime was 49 kPa, the 7-day tensile strength of the specimen

treated with 3% xanthan gum was 149 kPa, which is 3.04 times higher than that of the specimen treated with 3% lime. The curing time also had a positive effect on the tensile strength. As shown in Figure 12, the tensile strength of the specimens increased by about 24% when the curing time increased from 7 days to 21 days.

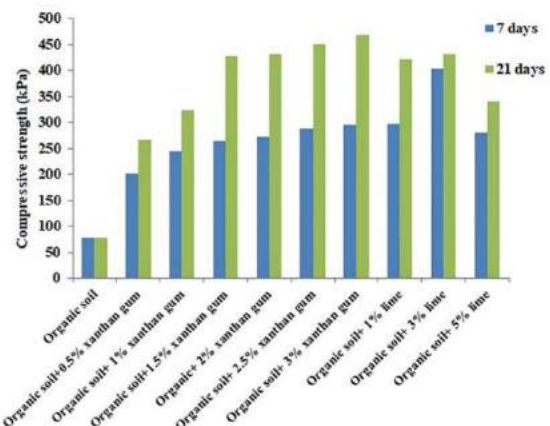


Figure 11. Comparison of the effects of xanthan gum and lime on unconfined compressive strength

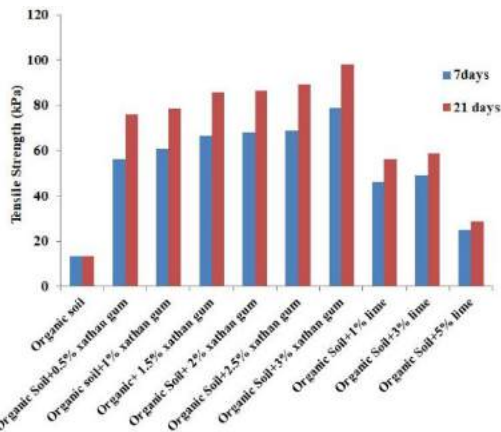


Figure 12. Comparison of the xanthan gum-treated and lime-treated organic soil specimens in terms of tensile strength after 7 and 21 days of curing

treated with 3% xanthan gum was 79 kPa. Thus, xanthan gum improves the tensile strength of soil better than lime, and the difference between the two increases over time. For example, after 21 days of curing, the tensile strength of the specimen treated with 3% lime reached 59 kPa, but that of the specimen treated with 3% xanthan gum went up as high as 98 kPa.

3. 7. Shear Strength Parameters

The shear strength parameters of the soil including friction angle and cohesion were determined by plotting a failure envelope diagrams. The failure envelope of the specimens cured with xanthan gum for 7 and 21 days are also shown in Figures 13(a) and 13(b). As the results showed, adding different amounts of xanthan gum had a significant impact on the shear strength of the soil. When the concentration of xanthan gum was increased in the mixture, the cohesion and friction angle of the specimen were enhanced. It can be seen from Figure 14(a) that, for the specimen treated with 3% xanthan gum, the cohesion was 44.8 kPa after 7 days of curing, which was ten times higher than that of the untreated organic soil (4.3 kPa). Using Figure 14(a), it is possible to examine the effect of curing time on the cohesion. As it can be seen, an increase in the curing time to 21 days significantly increased the cohesion of the specimens. The cohesion of the specimen treated with 3% xanthan gum reached 69.4 kPa after 21 days of curing. The treatment also increased the friction angle of the soil, for example, from 16.7 degrees in the untreated specimen to 25.1 degrees in the specimen treated with 3% xanthan gum and 7 days of curing. The results suggest that curing time has little effect on the friction angle of soil (Figure 14b).

The effect of xanthan gum on shear strength parameters is attributed to the long-chain functional groups like hydroxyl, ester, or amines in the structure of the gum. The characteristic reactions of these functional

groups are facilitated with more reaction sites offered. Another factor that plays a role in this regard is the strength of the chemical bonds that bind the surfaces of soil particles and gel together [25, 38].

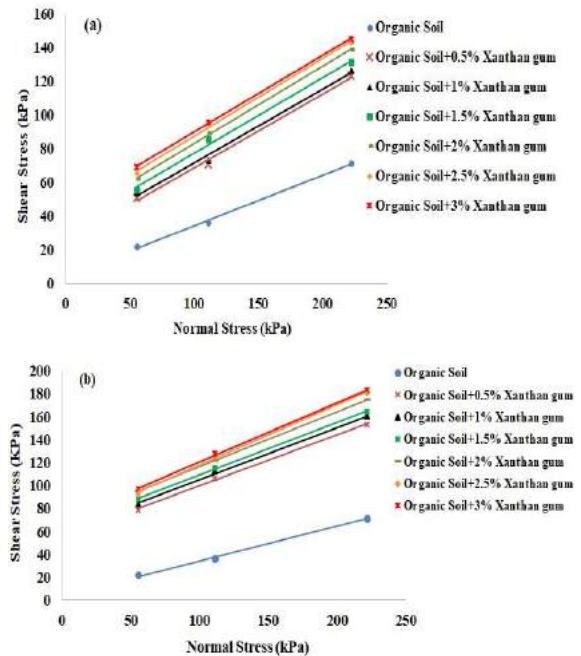


Figure 13. Shear failure envelope of the untreated organic soil and the organic soil treated with different amounts of xanthan gum after a) 7 days and b) 21 days of curing

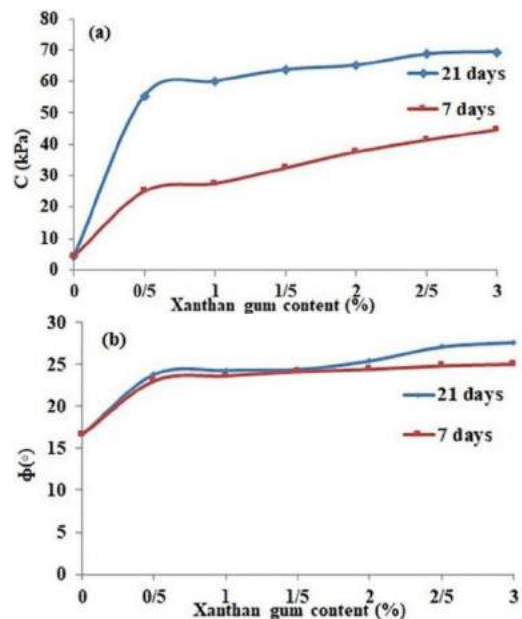


Figure 14. Cohesion and friction angle of the untreated organic soil and the organic soil treated with different amounts of xanthan gum after a) 7 days and b) 21 days of curing

The failure envelope of the specimens after 7 and 21 days of curing with lime are also shown in Figures 15(a) and 15(b). Lime could also improve the shear strength parameters. The effect of lime on the cohesion and friction angle of the organic soils are shown in Figures 16(a) and 16(b). From Figure 16(a), it is understood that, in 7 and 21 days of curing, the increase of lime up to 3% raised the cohesion of the stabilized and processed soil 3.5 and 5.7 times, respectively. The friction angel also increased due to the addition of lime. As lime was increased up to 3% during 7 and 21 days of curing, the friction angle grew 40% and 68%, respectively.

3. 8. Effect of Time on Soil Stabilized with Xanthan Gum Considering that stabilization with xanthan gum materials is more recent than lime, the long-term behavior of a stabilized sample was investigated. The review of the

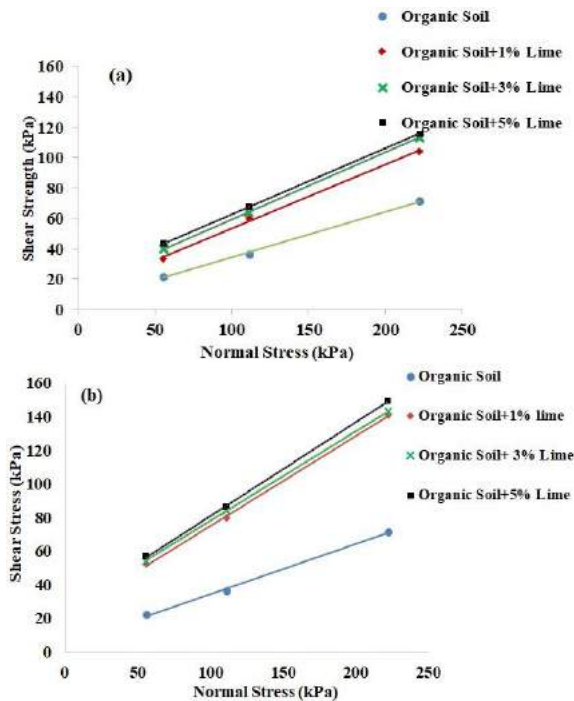


Figure 15. Shear failure envelope of the untreated organic soil and the organic soil treated with different amounts of lime after a) 7 days and b) 21 days of curing

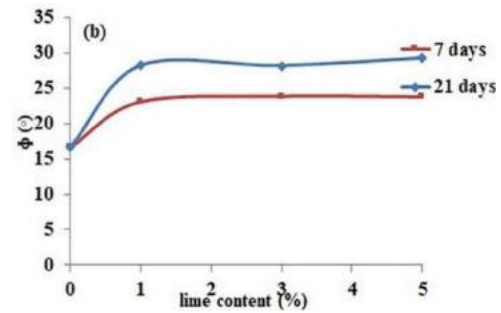
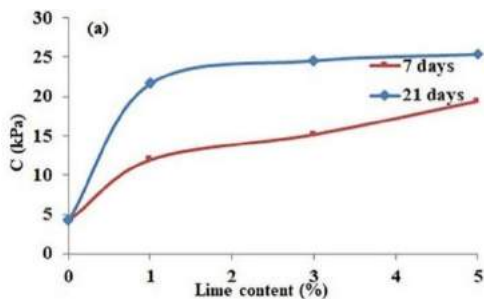


Figure 16. Cohesion and friction angle of the untreated organic soil and the organic soil treated with different amounts of lime after a) 7 days and b) 21 days of curing

technical literature and the results of research on stabilization with lime show that pozzolanic reactions are completed and soil resistance increases in long periods, after which it no longer decreases. The present research mainly focused on the compressive and tensile strengths of the samples stabilized with xanthan gum, the results of which are presented below.

3. 8. 1. Compressive Strength As shown in Figure 17(a), the compressive strength of all the samples stabilized with xanthan gum and cured for 56 days were still on the rise. After this period, the compressive strength of the soil treated with 3% xanthan gum increased for about 10 times compared to the unstabilized soil. The results obtained in this research are consistent with those of the other studies investigating the effects of longer treatments with xanthan gum on soil stabilization. Chang et al. [23] investigated the strength of stabilized sand samples during 750 days of curing and showed no decomposition of xanthan gum or decrease in the strength. Latifi et al. [24] also showed that the strength of the samples stabilized with xanthan gum and cured for 90 days had an increasing trend.

3. 8. 2. Tensile Strength Figure 17(b) presents the tensile strength of the samples cured for 56 days compared to those cured for 7 and 21 days. As it can be seen, increasing the curing time up to 56 days enhanced the tensile strength, After this period, the tensile strength of the soil treated with 3% xanthan gum increased for about 9 times compared to the unstabilized soil.

3. 9. Microscopic Behavior To further elucidate the effects of the treatments performed on the organic soil, the microstructure of the specimens was examined through scanning electron microscopy (SEM). Figure 18(a) presents the SEM image of the untreated organic soil as an example. As it can be seen, the constituting particles of the organic soil are spaced out, indicating high porosity. Each section of this organic soil has a series of internal pores inside its coarse-grained components and a

series of external pores between the grains and the outer space. This explains the high water retention capacity of this soil, as water can easily fill the voids inside and among the soil particles [52].

As shown in Figure 18(b), the lime-treated organic soil, too, has much fewer cavities than the untreated soil, which can be attributed to the cementation process resulting from pozzolanic and hydration reactions. Furthermore, the bond formed between the products of the pozzolanic reactions and the soil constituents has increased the strength of the lime-treated organic soil.

As Figure 18(c) indicates, the xanthan gum in the treated soil covers the outer surface of the particles while filling the void space among them too. Due to the high cohesion of xanthan gum, some fibers are formed in the network of the constituting particles of the soil. The appearance of these fibers and the filling of the void space among the particles lead to reduced water retention capacity. The figures clearly show that the treated soil has a more compact and cohesive structure than the untreated soil. This explains the significantly improved strength parameters of the xanthan gum-treated organic soil compared to the untreated specimen. A similar process has been observed in the SEM examination of xanthan gum-treated clay [42].

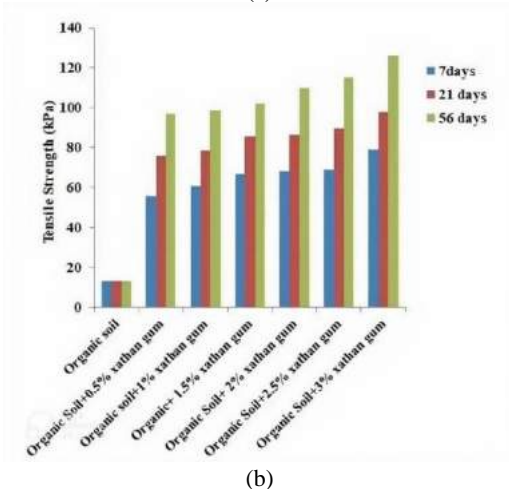
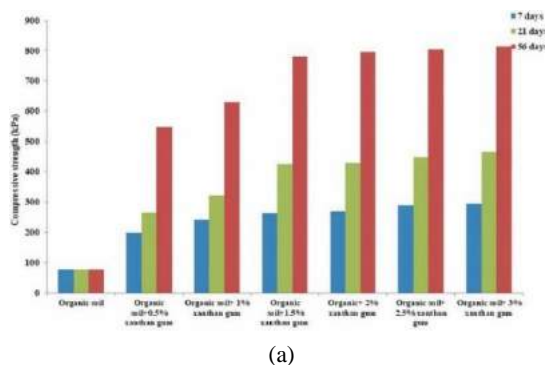


Figure 17. The effect of time on the soil stabilized with xanthan gum: a) Compressive strength, b) Tensile strength

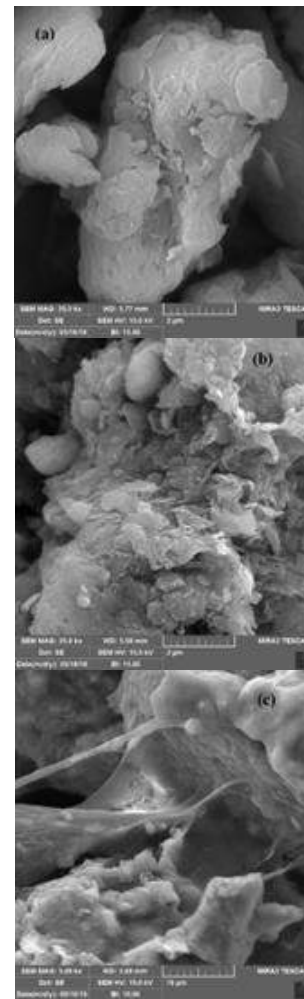


Figure 18. SEM image of the particles in the a) untreated organic soil, b) lime-treated organic soil, and c) xanthan gum-treated organic soil

4. CONCLUSION

Lime is a conventional soil stabilizer with significant positive effects on the mechanical properties of organic soils. However, it has major flaws in terms of environment-friendliness. The results of this study on the treatment of organic soil with xanthan gum as an environment-friendly stabilization agent indicated the ability of this gum to significantly improve the strength properties of the studied soil. The findings of the research are itemized as follows:

- Mixing the organic soil with lime or xanthan gum increased its optimum moisture content but decreased its maximum dry unit weight.
- The addition of lime and xanthan gum increased the pH of the treated organic soil to about 29% and 13%, respectively.
- The unconfined compressive strength of the organic soil treated with 1, 3 and 5% lime was measured

after 7 and 21 days of treatment. In general, the addition of lime increased the compressive strength of the soil; with 3% w/w of lime, the soil strength increased for about 5 times compared to the unstabilized soil, but it decreased with further addition of lime.

- The addition of xanthan gum to the organic soil improved its resistance. In this regard, the 7-day and 21-day compressive strengths of the samples were 3 and 4.7 times that of the unstabilized soil, respectively. Also, xanthan gum was significantly more effective than lime to improve this factor.
- The stress-strain curve of the unconfined compression test showed that the xanthan gum-treated organic soil specimens were more ductile than their lime-treated counterparts, bearing more strain at the same axial stress.
- The treatment of the organic soil with different amounts of lime and xanthan gum improved its tensile strength. In this respect, after 7 days, the tensile strength of the soil sample stabilized with 3% xanthan gum was about 9.5 times and the tensile strength of the soil sample stabilized with 3% lime was about 3.5 times that of the unstabilized soil.
- In the case of lime, the improvement in tensile strength reached its peak when the soil was treated with 3% lime, but it decreased with further increase in the lime content. However, in the case of xanthan gum, the improvement of the tensile strength continued for the entire range studied.
- Prolonging the curing process from 7 days to 21 days increased the tensile strength of all the specimens that were treated with lime or xanthan gum. However, this increase was higher in the xanthan gum-treated specimens than in their lime-treated counterparts.
- Comparing the lime-treated and xanthan gum-treated soil specimens in terms of shear strength parameters after different curing periods showed that xanthan gum is generally more effective in improving the shear strength of organic soil.

5. REFERENCES

1. Mir, B. A., Reddy, S. H., "Mechanical Behaviour of Nano-material (Al_2O_3) Stabilized Soft Soil", *International Journal of Engineering, Transactions C: Aspects*, Vol. 34, No. 3, (2021), 636-643. doi:10.5829/ije.2021.34.03c.07
2. Ghasem Ghanbari, P., Momeni, M., Mousivand, M., and Bayat, M., "Unconfined Compressive Strength Characteristics of Treated Peat Soil with Cement and Basalt Fibre", *International Journal of Engineering, Transactions B: Applications*, Vol. 35, No. 5, (2022), 1089-1095. <https://doi.org/10.5829/ije.2022.35.05b.24>
3. Saidate, I., Berga, A.E., Rikioui, T., "Stabilization of Gypsum Clay Soil by Adding Lime", *Civil Engineering Journal*, Vol. 8, No. 11, (2022), 2511-2520. doi: 10.28991/CEJ-2022-08-11-010
4. Poorebrahim, G. R., Malekpoor, M. R., "Behavior of compacted lime-soil columns", *International Journal of Engineering, Transactions B: Applications*, Vol. 27, No. 2, (2014), 315-324. Doi: 10.5829/idosi.ije.2014.27.02b.15
5. Turkane, S. D., Chouksey, S. K., "Partial replacement of conventional material with stabilized soil in flexible pavement design", *International Journal of Engineering, Transactions B: Applications*, Vol. 35, No. 5, (2022), 908-916. doi: 10.5829/ije.2022.35.05b.07
6. Nguyen, D. T., Phan, V. T. A., "Engineering properties of soil stabilized with cement and fly ash for sustainable road construction", *International Journal of Engineering, Transactions C: Aspects*, Vol. 34, No. 12, (2021), 2665-2671. doi: 10.5829/ije.2021.34.12c.12
7. Javdanian, H., "The effect of geopolymerization on the unconfined compressive strength of stabilized fine-grained soils", *International Journal of Engineering, Transactions B: Applications*, Vol. 30, No. 11, (2017), 1673-1680. doi: 10.5829/ije.2017.30.11b.07
8. Mustapa, N. A., Rashid, A. S., Wan, W. H., Hassan, S. H., Tabatabaei, S. A., Isobe, K., and Ganiyu, A. A., "Gypsum Stabilization of Organic Soil: Strength And Compressibility", *Suranaree Journal of Science & Technology*, Vol. 28, No. 4, (2021).
9. Pokharel, B., Siddiqua, S., "Effect of calcium bentonite clay and fly ash on the stabilization of organic soil from Alberta, Canada", *Engineering Geology*, Vol. 293, (2021), 106291. <https://doi.org/10.1016/j.enggeo.2021.106291>
10. Fahad Hossain, A.S.M., Ali, A. B., Munayem, S. R., Chakma, S., and Rahman, F., "Observation of the behavior of organic soil by adding lime, fly ash and cement", *Journal of Advances in Geotechnical Engineering*, Vol. 2, No. 3, (2019), 1-5. Doi: <http://doi.org/10.5281/zenodo.3460264>
11. Mitchell, J. K., Soga, K., "Fundamentals of soil behavior", New York: John Wiley & Sons, (2005).
12. Nowak, G., and Kanty, P., "Mass Stabilization as reinforcement of organic soils", In E3S Web of Conferences (Vol. 97, p. 4046). <https://doi.org/10.1051/e3sconf/20199704046>
13. Afrin, H., "A review on different types soil stabilization techniques", *International Journal of Transportation Engineering and Technology*, Vol. 3, No. 2, (2017), 19-24. doi:10.11648/j.ijtet.20170302.12
14. Janani, V., Ravichandran, P. T., "Recent Trends in Stabilization of Expansive Soil using Calcined Clay", *International Journal of Engineering, Transactions A: Basics*, Vol. 36, No. 1, (2023), 163-170. doi: 10.5829/ije.2023.36.01a.18
15. Arman, A., Munfakh, G. A., "Lime stabilization of organic soils", *Highway Research Record*, Vol. 381, (1972), 37-45.
16. Sakr, M. A., Shahin, M. A., and Metwally, Y. M., "Utilization of lime for stabilizing soft clay soil of high organic content", *Geotechnical and Geotechnical Engineering*, Vol. 27, No. 1, (2009), 105-113. <https://doi.org/10.1007/s10706-008-9215-2>
17. Saride, S., Puppala, A. J., and Chikyala, S. R., "Swell-shrink and strength behaviors of lime and cement stabilized expansive organic clays", *Applied Clay Science*, Vol. 85, (2013), 39-45. <https://doi.org/https://doi.org/10.1016/j.clay.2013.09.008>
18. Kalantari, B., "Civil engineering significant of peat", *Global Journals of Research in Engineering*, Vol. 13, No. E2, (2013), 25-28.
19. Wong, L. S., "Formulation of an optimal mix design of stabilized peat columns with fly ash as a pozzolan", *Arabian Journal for Science and Engineering*, Vol. 40, No. 4, (2015), 1015-1025. <https://doi.org/10.1007/s13369-015-1576-2>
20. Kolay, P. K., Suraya, N. B. R., "Stabilization of organic soil by different types of stabilizer", In International Conference on Civil

- Engineering in the New Millennium: Opportunities and Challenges, Bengal Engineering and Science University, Shibpur, India, Vol. 3, (2007), 1394-1400.
21. Tastan, E. O., Edil, T. B., Benson, C. H., and Aydilek, A. H., "Stabilization of organic soils with fly ash", *Journal of geotechnical and Geoenvironmental Engineering*, Vol. 137, No. 9, (2011), 819-833. [https://doi.org/https://doi.org/10.1061/\(ASCE\)GT.1943-5606.0000502](https://doi.org/https://doi.org/10.1061/(ASCE)GT.1943-5606.0000502)
 22. Mendonça, A., Morais, P. V., Pires, A. C., Chung, A. P., and Oliveira, P. V., "A review on the importance of microbial biopolymers such as xanthan gum to improve soil properties", *Applied Sciences*, Vol. 11, No. 1, (2020), 170. <https://doi.org/10.3390/app11010170>
 23. Chang, I., Im, J., Prasadhi, A. K., and Cho, G.-C., "Effects of Xanthan gum biopolymer on soil strengthening", *Construction and Building Materials*, Vol. 74, (2015), 65-72. <https://doi.org/10.1016/j.conbuildmat.2014.10.026>
 24. Latifi, N., Horpibulsuk, S., Meehan, C. L., Majid, M. Z. A., and Rashid, A. S. A., "Xanthan gum biopolymer: an eco-friendly additive for stabilization of tropical organic peat", *Environmental Earth Sciences*, Vol. 75, (2016), 1-10. [https://doi.org/https://doi.org/10.1061/\(ASCE\)MT.1943-5533.0001706](https://doi.org/https://doi.org/10.1061/(ASCE)MT.1943-5533.0001706)
 25. Ayeldeen, M., Negm, A., El-Sawwaf, M., and Kitazume, M., "Enhancing mechanical behaviors of collapsible soil using two biopolymers", *Journal of Rock Mechanics and Geotechnical*, Vol. 9, No. 2, (2017), 329-339. <https://doi.org/https://doi.org/10.1016/j.jrmge.2016.11.007>
 26. Chang, I., Im, J., Cho, G.-C., "Geotechnical engineering behaviors of gellan gum biopolymer treated sand", *Canadian Geotechnical Journal*, Vol. 53, No. 10, (2016), 1658-1670.
 27. Latifi, N., Horpibulsuk, S., Meehan, C. L., Abd Majid, M. Z., Tahir, M. M., and Mohamad, E. T., "Improvement of problematic soils with biopolymer—an environmentally friendly soil stabilizer", *Journal of Materials in Civil Engineering*, Vol. 29, No. 2, (2017), 04016204. [https://doi.org/https://doi.org/10.1061/\(ASCE\)MT.1943-5533.0001706](https://doi.org/https://doi.org/10.1061/(ASCE)MT.1943-5533.0001706)
 28. Smitha, S., Sachan, A., "Use of agar biopolymer to improve the shear strength behavior of sabarmati sand", *International Journal of Geotechnical Engineering*, Vol. 10, No. 4, (2016), 387-400. <https://doi.org/10.1080/19386362.2016.1152674>
 29. Muguda, S., Booth, S. J., Hughes, P. N., Augarde, C. E., Perlot, C., Bruno, A. W., and Gallipoli, D., "Mechanical properties of biopolymer-stabilised soil-based construction materials", *Géotechnique Letters*, Vol. 7, No. 4, (2017), 309-314. <https://doi.org/10.1680/jgele.17.00081>
 30. Hataf, N., Ghadir, P., and Ranjbar, N., "Investigation of soil stabilization using chitosan biopolymer", *Journal of Cleaner Production*, Vol. 170, (2018), 1493-1500. <https://doi.org/10.1016/j.jclepro.2017.09.256>
 31. Chen, C., Wu, L., Perdjon, M., Huang, X., and Peng, Y., "The drying effect on xanthan gum biopolymer treated sandy soil shear strength", *Construction and Building Materials*, Vol. 197, (2019), 271-279. <https://doi.org/10.1016/j.conbuildmat.2018.11.120>
 32. Dehghan, H., Tabarsa, A., Latifi, N., and Bagheri, Y., "Use of xanthan and guar gums in soil strengthening", *Clean Technologies and Environmental Policy*, Vol. 21, (2019), 155-165. <https://doi.org/10.1007/s10098-018-1625-0>
 33. Singh, S. P., Das, R., "Geo-engineering properties of expansive soil treated with xanthan gum biopolymer", *Geomechanics and Geoenvironmental Engineering*, Vol. 15, No. 2, (2020), 107-122. <https://doi.org/10.1080/17486025.2019.1632495>
 34. Kwon, Y.-M., Ham, S.-M., Kwon, T.-H., Cho, G.-C., and Chang, I., "Surface-erosion behaviour of biopolymer-treated soils assessed by EFA", *Géotechnique Letters*, Vol. 10, No. 2, (2020), 106-112. <https://doi.org/10.1680/jgele.19.00106>
 35. Sujatha, E. R., Atchaya, S., Sivasaran, A., and Keerdthe, R. S., "Enhancing the geotechnical properties of soil using xanthan gum—An eco-friendly alternative to traditional stabilizers", *Bulletin of Engineering Geology and the Environment*, Vol. 80, (2021), 1157-1167. <https://doi.org/10.1007/s10064-020-02010-7>
 36. Hamza, M., Nie, Z., Aziz, M., Ijaz, N., Ijaz, Z., and Rehman, Z. ur., "Strengthening potential of xanthan gum biopolymer in stabilizing weak subgrade soil", *Clean Technologies and Environmental Policy*, Vol. 24, No. 9, (2022), 2719-2738. <https://doi.org/10.1007/s10098-022-02347-5>
 37. Bozyigit, I., Zingil, H. O., and Altun, S., "Performance of eco-friendly polymers for soil stabilization and their resistance to freeze-thaw action", *Construction and Building Materials*, Vol. 379, (2023), 131133. <https://doi.org/10.1016/j.conbuildmat.2023.131133>
 38. Khatami, H. R., O'Kelly, B. C., "Improving mechanical properties of sand using biopolymers", *Journal of Geotechnical and Geoenvironmental Engineering*, Vol. 139, No. 8, (2013), 1402-1406. [https://doi.org/10.1061/\(ASCE\)GT.1943-5606.00008](https://doi.org/10.1061/(ASCE)GT.1943-5606.00008)
 39. Bagheri, P., Gratchev, I., and Rybachuk, M., "Effects of Xanthan Gum Biopolymer on Soil Mechanical Properties", *Applied Sciences*, Vol. 13, No. 2, (2023), 887. <https://doi.org/10.3390/app13020887>
 40. Zhou, C., So, P. S., and Chen, X. W., "A water retention model considering biopolymer-soil interactions", *Journal of Hydrology*, Vol. 586, (2020), 124874. [Doi:https://doi.org/10.1016/j.jhydrol.2020.124874](https://doi.org/10.1016/j.jhydrol.2020.124874)
 41. Anandha Kumar, S., and Sujatha, E. R., "Compaction and permeability characteristics of biopolymer-treated soil", In *Sustainable Practices and Innovations in Civil Engineering: Select Proceedings of SPICE*, (2019), 107-117. https://doi.org/10.1007/978-981-15-5101-7_11
 42. Kwon, Y. M., Chang, I Lee, M., and Cho, G. C., "Geotechnical engineering behavior of biopolymer-treated soft marine soil", *Geomechanics and Engineering*, Vol. 17, (2019), 453-464. <https://doi.org/10.12989/gae.2019.17.5.453>
 43. Bouazza, A., Gates, W. P., and Ranjith, P. G., "Hydraulic conductivity of biopolymer-treated silty sand", *Géotechnique*, Vol. 59, No. 1, (2009), 71-72. <https://doi.org/10.1680/geot.2007.00137>
 44. Casas, J. A., Santos, V. E., Garcia-Ochoa, F., "anthan gum production under several operational conditions: molecular structure and rheological properties", *Enzyme and Microbial Technology*, Vol. 26, No. 2-4, (2000), 282-291. [https://doi.org/10.1016/S0141-0229\(99\)00160-X](https://doi.org/10.1016/S0141-0229(99)00160-X)
 45. Sun, C., and Gunasekaran, S., "Effects of protein concentration and oil-phase volume fraction on the stability and rheology of menhaden oil-in-water emulsions stabilized by whey protein isolate with xanthan gum", *Food Hydrocolloids*, Vol. 23, No. 1, (2009), 165-174. <https://doi.org/10.1016/j.foodhyd.2007.12.006>
 46. Bergmann, D., Furth, G., and Mayer, C., "Binding of bivalent cations by xanthan in aqueous solution", *International Journal of Biological Macromolecules*, Vol. 43, No. 3, (2008), 245-251. <https://doi.org/10.1016/j.ijbiomac.2008.06.001>
 47. Nolte, H., John, S., Smidsrød, O., and Stokke, B. T., "Gelation of xanthan with trivalent metal ions", *Carbohydrate Polymers*, Vol. 18, No. 4, (1992), 243-251. [https://doi.org/10.1016/0144-8617\(92\)90089-9](https://doi.org/10.1016/0144-8617(92)90089-9)
 48. Gofar, N., "Determination of coefficient of rate of horizontal consolidation of peat soil", Universiti Teknologi Malaysia, (2006).
 49. Landva, A. O., Pheeney, P. E., "Peat fabric and structure", *Canadian Geotechnical Journal*, Vol. 17, No. 3, (1980), 416-435. <https://doi.org/10.1139/t80-048>

50. Andriesse, J. P., "Nature and management of tropical peat soils", Food & Agriculture Org, (1988).
51. Von Post, L., and Granlund, E., "Peat resources in southern Sweden-Sveriges geologiska undersökning", *Yearbook*, Vol. 335, No. 19.2 Series C, (1926), 1-127.
52. ASTM D 2974-87, "Standard test methods for moisture, ash and organic matter of peat and other organic soils", American Society for Testing and materials, (1993).
53. ASTM D2976-15, "Standard Test Method for pH of Peat Materials", American Society for Testing and materials (2015).
54. ASTM D854-14, "Standard Test Methods for Specific Gravity of Soil Solids by Water Pycnometer", American Society for Testing and materials, (2014).
55. ASTM D698-12e2, "Standard Test Methods for Laboratory Compaction Characteristics of Soil Using Standard Effort (600 kN-m/m³)", American Society for Testing and materials, (2012).
56. ASTM D2166 / D2166M-16, "Standard Test Method for Unconfined Compressive Strength of Cohesive Soil, ASTM International", American Society for Testing and materials, (2016).
57. ASTM C496 / C496M-17, "Standard Test Method for Splitting Tensile Strength of Cylindrical Concrete Specimens", American Society for Testing and materials, (2017).
58. ASTM D3080-04, "Standard Test Method for Direct Shear Test of Soils Under Consolidated Drained Conditions, ASTM International", American Society for Testing and materials, (2004).
59. Whitcomb, P. J., and Macosko, C. W., "Rheology of xanthan gum", *Journal of Rheology*, Vol. 22, No. 5, (1978), 493-505. Doi: <https://doi.org/10.1122/1.549485>

COPYRIGHTS

©2023 The author(s). This is an open access article distributed under the terms of the Creative Commons Attribution (CC BY 4.0), which permits unrestricted use, distribution, and reproduction in any medium, as long as the original authors and source are cited. No permission is required from the authors or the publishers.

**Persian Abstract****چکیده**

نمونه‌ای از خاک آلی جمع‌آوری شده از استان چهارمحال بختیاری با ۰.۵، ۱، ۱.۵، ۲، ۲.۵، ۳ درصد صمغ زانتان و ۱، ۳ و ۵ درصد آهک تثبیت شد. نمونه‌های تثبیت نشده و تثبیت شده تحت آزمایش‌های فیزیکی و مکانیکی از جمله طبقه‌بندی خاک، اندازه‌گیری pH، آزمایش تراکم، آزمایش مقاومت فشاری، آزمایش کشش غیرمستقیم و آزمایش برش مستقیم قرار گرفتند. افزایش ۳ درصدی آهک منجر به بیشترین افزایش مقاومت فشاری (به ترتیب ۵ و ۶ برابر برای نمونه‌های ۷ و ۲۱ روزه) و مقاومت کششی (به ترتیب ۳.۷ و ۴.۵ برابر برای نمونه‌های ۷ و ۲۱ روزه) شد. صمغ زانتان همچنین مقاومت فشاری (به ترتیب ۳ و ۶ بار برای نمونه‌های ۷ روزه و ۲۱ روزه) و استحکام کششی (به ترتیب ۵.۹ و ۷.۵ برابر برای نمونه‌های ۷ روزه و ۲۱ روزه) را بهبود بخشید. افزایش آهک تا ۳ درصد، چسبندگی خاک تثبیت شده را به ترتیب ۳.۵ و ۷.۵ برابر خاک آلی برای ۷ و ۲۱ روز عمل‌آوری افزایش داد. همچنین زاویه اصطکاک با افزایش آهک تا ۳ درصد طی ۷ و ۲۱ روز عمل‌آوری به ترتیب ۴۰ درصد و ۶۸ درصد افزایش یافت. تثبیت با صمغ زانتان منجر به افزایش چسبندگی به ترتیب ۱۱.۵ و ۱۷.۵ برابر برای نمونه‌های ۷ و ۲۱ روزه شد. علاوه بر این، صمغ زانتان زاویه اصطکاک را برای نمونه‌های ۷ روزه و ۲۱ روزه به ترتیب ۴۷ و ۷۵ درصد افزایش داد. یافته‌ها به‌طور کلی نشان می‌دهد که صمغ زانتان می‌تواند جایگزین مناسبی برای آهک به‌عنوان تثبیت‌کننده خاک باشد.



Effect of Mg Addition on Morphology, Roughness and Adhesion of Cr Chromized Layer Produced by Pack Cementation

S. Djemmah^{*a,b}, Y. Madi^a, M. Voué^b, A. Haddad^c, D. Allou^c, S. Ouallam^c, H. Bouchafaa^a, A. Rezzoug^c

^a University of Science and Technology Houari Boumediene, Laboratory of Technology of Materials (LTM), Algeria

^b University of Mons, Physics of Materials and Optics Unit (LPMO), Research Institute for Materials Science and Engineering, Belgium

^c Research Center in Industrial Technologies (CRTI), Algeria

PAPER INFO

Paper history:

Received 24 May 2023

Received in revised form 19 June 2023

Accepted 20 June 2023

Keywords:

Magnesium Doping
Chromium Chromizing
Surface Roughness
Strength Adhesion

ABSTRACT

In the present study, the effect of adding Magnesium (Mg) as a doping element on the morphology and surface characteristics of the chromized layer was investigated. To achieve this, chromized layers were coated and doped by a chromizing process in pack-cementation at 1050°C. The thickness of the doped layer was about 26 µm, whilst chromized was approximately 24 µm. The surface morphology and composition of the coatings were analyzed using scanning electron microscopy (SEM) and energy dispersive X-ray spectroscopy (EDX). The results showed that a crystalline structure can be successfully deposited by adding Mg as a doping element to the pack mixture. Therefore, Mg acts as a barrier against Cr₂O₃ formation, resulting in a more rich-chromium-zone and forming protective oxide. Moreover, less carbide is formed in the doped layer. The roughness of the layer is enhanced by adding Magnesium (Mg) and it has a lower average roughness (Ra) 3 times than that of chromized, of about 0.315 µm and 1.039 µm, respectively. In addition, progressive loading scratch was performed at 1N and 20N. The results demonstrated that Mg in the chromized layer increases the ability to with-stand varying levels of mechanical stress with strength adhesion of about 19.21N and can be more protective than Cr chromized.

doi: 10.5829/ije.2023.36.10a.05

NOMENCLATURE

Wt%	weight	SEM	Scanning electron microscope
Ra	Average roughness	EDX	Energy-dispersive X-ray spectroscopy
Rz	Mean height roughness	Er	Elastic recovery ratio
Rd	Residual depth	2D	two-dimensional
Pd	Penetration depth	3D	three-dimensional
Lc	Critical load		

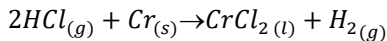
1. INTRODUCTION

In industrial applications, materials must be resistant to environmental attacks such as corrosion, stress, wear and fatigue. Especially when they are applied to applications that requires high temperature applications. However, stainless steels have been used for environments such as petrochemical or electric utility fluidizing particles and any hydrogen halide as the plants [1, 2]. They are a popular choice for their low cost and their physical and mechanical properties [3, 4], despite this they remain of

poor quality in front of many aggressive factors. Among these stainless steels, citing the ferritic steel (AISI 430) which has been found in previous studies to be less resistant to oxidation at high temperatures [5, 6]. To overcome these limitations, surface coatings have been widely employed as an effective means of improving material performance in such environments. One of the surface modification methods frequently employed is diffusion coating through the chromizing process in pack cementation to enrich alloy surfaces with chromium (Cr) [7-9]. However, in chromizing process, the chromium

*Corresponding Author Email: sdjemmah@usthb.dz,
sarah.djemmah@umons.ac.be (S. Djemmah)

(Cr) is used as a master alloy where it contributes to improving in many properties of the coated material due to its excellent hardness, wear resistance, and corrosion resistance [10]. On the other hand, during the high temperature chromizing process the activator usually ammonium chloride (NH_4Cl); presents in the mixture is decomposed into hydrogen chloride (HCl), nitrogen (N_2), and hydrogen gas (H_2). The HCl formed during this process reacts with the chromium present in the pack according to the following reaction [11]:



This reaction is crucial to the formation of the desired chromizing coating. At temperatures around 1000°C , the interaction between chromium and free carbon (C) found in the stainless steel substrate can lead to the formation of chromium carbides such as Cr_7C_3 , $(\text{Cr,Fe})_7\text{C}_3$ and Cr_{23}C_6 on the surface of the metal coated [12-14]. These carbides can enhance wear resistance and give high hardness [15, 16], on the other side they act as a diffusion barrier, restricting the growth of a metallic Cr-rich layer which causes the failure adherence of the layer [17]. Consequently, a decarburized zone can develop below the coating. On the other hand, one of the challenges encountered in the chromizing process is the occurrence of voids, which can arise due to the Kirkendall effect during pack cementation [18, 19]. Additionally, the presence of carbides and intermetallic phases, which occur due to the diffusion reactions, may introduce variations in the topography of the coating and increasing the surface roughness [20, 21]. This undesirable consequence may comprise the functional characteristics of the coated surface [22]. They can also weaken the adhesion of the chromized layer, leading to delamination and durability. The formation of the chromium oxide such as Cr_2O_3 by introduction some oxygen (O) in the pack mixture can enhance the hot oxidation behavior when is exposed to hot damaged environments where they found that retardation in formation of the Cr_2O_3 oxide can lead the increase of the formation of non-protective oxides [23]. Beside this the Cr_2O_3 is known for its relatively low adhesion to the substrate, which can result in poor bonding between the coating and the substrate. This low adhesion can cause delamination to the coated surface, reducing the durability and longevity of the chromizing coating. Additionally, Cr_2O_3 has a relatively high coefficient of thermal expansion compared to the substrate material, which can induce thermal stress and strain within the coating [24]. To address this challenge, turning to the process pack cementation, wherein the addition of dopant elements and substitutions to the mixture cementation pack can alter its properties and improve surface characteristics. The element magnesium (Mg) can be used as a catalyst in the production of chromium hydroxides and oxides at high temperatures, including Mg_xCr_y , oxides which are

considered stable, resistant and auto-protective [25].

Mg element can refine the grain size of chromized layers with coarse grain structure, improving the mechanical properties and potentially reducing roughness. It is thought that magnesium (Mg) dopant may act as a reducing agent, therefore reducing Cr_2O_3 formation and enhancing the Chromium (Cr) diffusion into the substrate, which would then achieve a more uniform and adherent layer and reduce roughness in the chromized layer [26, 27].

Based on our review of the literature, there has been no research on the chromized chromium by pack cementation method, doping with magnesium (Mg) substitution. This study aims to investigate the effect of Magnesium (Mg) addition on the microstructure, morphology and enhancement of surface conditions of the chromized layer on the AISI 430 obtained through chromization process in pack cementation by reducing the formation of intermetallic phases and carbides hence, replaced by protective oxides. Additionally, the study aims to explore the potential of small amounts of magnesium (Mg) for substituting chromium (Cr) oxides and enriching the surface with chromium (Cr). Furthermore, the findings of this study may contribute to the development of advanced chromization technique with enhanced surface properties, contributing a better resistance against delamination, spallation, adhesive and failure and benefitting various industrial applications.

2. MATERIALS METHOD

In this study, Cr-Mg alloy was coated on the surface of AISI 430 Ferritic stainless steel ($10 \times 10 \times 1$) mm^3 using the chromizing process in pack-cementation, by adding a Mg content as a doping element to the Cr pack mixture. The substrates were ground before proceeding coating using mechanical polishing (up to #1000 SiC grit), immersed in acetone solution (for 10 min) and cleaned by an ultrasonic bath. Each sample was placed inside an alumina (Al_2O_3) crucible that could withstand high temperatures (up 1800°C) in two pack mixture (with and without Mg doping element). Thus, they were dipped in a powder mixture containing Cr, NH_4Cl , Al_2O_3 , for the first coating and Cr, NH_4Cl , Al_2O_3 , and Mg for the second coating. The weight ratio of the components of the Cr chromized and Cr (3wt.% Mg) doped coatings is summarized in Table 1.

The crucibles (powder pack and samples) were not passed through a glove box but were placed directly into the furnace to provide a small amount of oxygen (the fast irreversible incorporation). As a safety precaution, the crucible was sealed with lid to not allow the powder spreads in the furnace when injecting Argon (Ar) gas, then placed in the CARBOLITE tubular furnace (Carbolite TZF 12/100/-900, Hope Valley, UK). The crucibles (samples and pack mixture) kept in the furnace at room

temperature ($25^{\circ}\text{C} \pm 1$) under Argon gas injection, keeping the outlet of the furnace open to ensure that most gases were eliminated and escaped from the system then the tube furnace outlets were closed in order to proceed with the coating process (see Figure 1). The treatment was prepared with a heating rate of $6^{\circ}\text{C}/\text{min}$ and kept this heating rate value during all the coating process. The samples were not prepared in a glove box to ensure a small quantity of oxygen that will interact with the powder, knowing that the gases and oxygen escaped will be removed by argon injection.

During the chromizing process, the temperature was reached 50°C at the beginning and held at this value for 1h. This was to avoid thermal shock, which damages the crucible. On the other hand, to provide that the starting temperature is uniform throughout the surface and allows for a controlled and consistent heating process. Afterward, the temperature was increased to 1050°C ($6^{\circ}\text{C}/\text{min}$), and then held for 8 hours in a furnace under Argon (Ar) injection. For cooling down, the samples were kept in the furnace under Argon gas and then they removed.

Investigation of the morphology and composition of the Cr and the Cr-Mg coated alloy was evaluated using a HIROX SH-3000 Desktop scanning electron microscope (SEM) (HIROX, Tokyo, Japan), integrated with energy dispersive X-ray spectroscopy (EDX) BRUKER/AXSI. Thus, the coating surfaces were metalized with conductive layer of gold (Au) before scanning

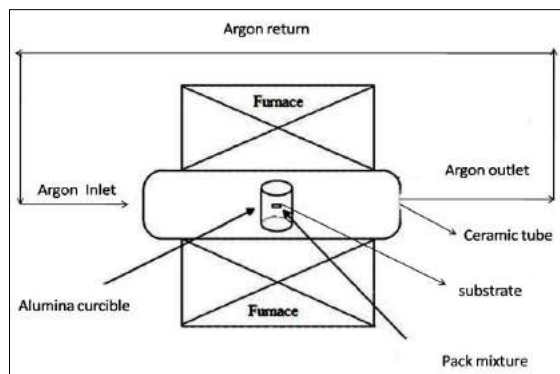


Figure 1. Explanatory schematic of the chromizing process setup

TABLE 1. Composition and content of chromized pack mixtures

Component	Content (wt.%)	
	Cr coated	Cr-Mg Coated
Cr	20	20
Al_2O_3	75	72
NH_4Cl	5	5
Mg	/	3

electron microscopy, which accounted for the appearance of gold (Au) peaks in the EDX spectrum. The metallization was performed with Denton Vacuum Desk V (Denton Vacuum, Philadelphia, USA). A non-contact optical profilometer type WYKO NT1100 (*Sensofar, Terrassa, Spain*) with a magnification objective of $20 \times$ NA 0.15; was utilized to measure the roughness without scratching the coated layers (Cr and Cr-Mg). Adhesion of the coatings was evaluated using a progressive linear scratch test in range of about 1 to 20N. Therefore, tests were performed using a CSM scratch instrument (*CSM Instruments SA, Peseux, Switzerland*). The parameters are shown in Table 2. Moreover, the scratch track was analyzed by optical microscopy type Nikon Eclipse LV100ND (*Nikon instruments, Tokyo, Japan*).

3. RESULTS AND DISCUSSION

3. 1. Microstructure and Phases Investigations

Figure 2 represents SEM micrographs of Cr and Cr-Mg coated surfaces. As can be seen, the chromized surface without Mg adding represents almost uniform darker rough structure, while a small particules were observed in lighter color with a non-uniform distribution along the surface. This particules could be Cr oxides such as Cr_2O_3 and carbides [28]. Thus, the darker region can present the chromium-rich region (Figure 2(a)) distributed across the treated surface. Moreover, no cracks were visible on the surface of the Cr chromized. However, it is known that the deposition of Cr_2O_3 in some parts of the Cr coated may lead to the apparition of cracks. Moreover, some pores have been observed and according to the studies conducted by Fan et al. [29], the kirkendall effect was found to be responsible for pores and voids formation in chromizing coatings.

In order to determine the thickness of chromized coatings, three measurements were taken with optical microscopy for each coating. The thickness was confirmed with a contact profilometer with a diamond stylus that was moved vertically and laterally in contact with the coating to measure the thickness. However, the thickness of the coatings was performed by Cr and Cr doped with 3%.wt Mg coatings had a thickness about of $24.82\mu\text{m}$ and $26.91\mu\text{m}$, respectively.

In Figure 2(b), the structure of Cr doped with 3 wt.% Mg is shown. The SEM image shows crystalline microstructure with a non-uniform distribution of particles size. The aspect appears lighter and smoother than Cr chromized surfaces, where grain can be seen in

TABLE 2. Scratch test parameters under progressive load

Load (N)	Indenter type, R (μm)	sliding speed (mm/min)	Length of the scratch (mm)
[1-20]	Diamond Rockwell C, 200	38	4

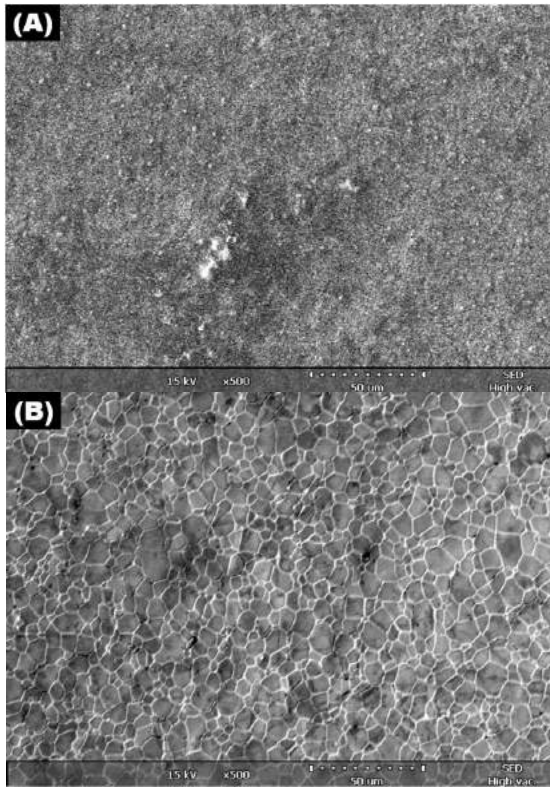


Figure 2. SEM micrographs of coated layer (top surface) deposited by chromizing process in cementation pack under Argon gas at 1050 °C for 8h: (A) Cr chromized; (B) Cr-Mg doped coating

grey with boundaries in lighter color. The growth of this crystalline structure can be explained by the fact that the coating develops crystal structure and new phases as a result of solid-state transformation occurring during the chromizing process at high temperature such as 1050°C. Subsequently, the state solid-state diffusion can exhibit movement, migration and rearrangement of the atoms through the solid-state diffusion due to the concentration gradient and causes the growth of this crystalline structure.

An EDX analysis along the surface of the Cr and Cr-Mg coatings is shown in Figure 3. The EDX spectra in the two coatings show an intense peak of Cr, indicating that Cr is deposited on the surface, resulting in Cr-rich regions that form more easily at higher Cr content [30]. Furthermore, the presence of Mg and O in the Cr-Mg doped was also confirmed by the EDX scanline (Figure 3(b)), where the O peak appears in the Cr chromized is more intense than that of Cr doped due to the formation of Cr₂O₃ in its surface (Figure 3(a)). It suggests that the magnesium (Mg) could potentially react at high temperature with the chromium (Cr) of the master alloy to form a layer containing oxides such as magnesium chromium (MgCr₂O₄) and forming this phase with a small amount in the chromized structure. Thus, it acts as a

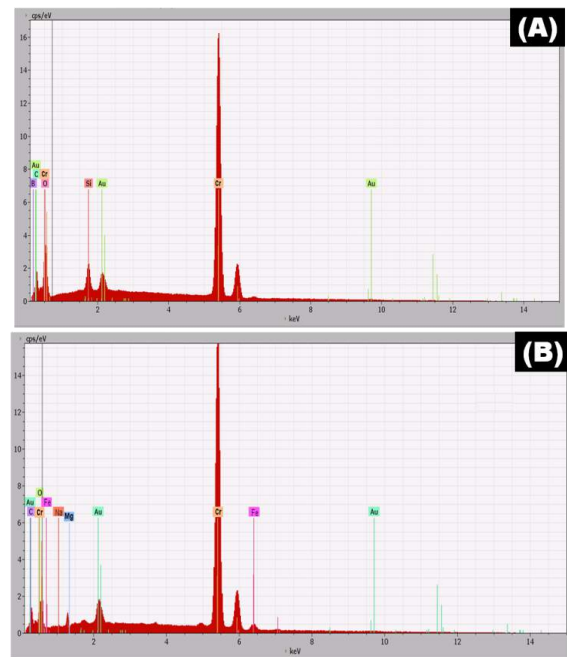
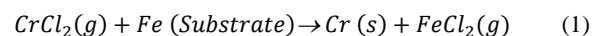


Figure 3. EDX spectrum of the coated layers: (A) Cr chromized surface; (B) Cr doped with 3wt. % Mg

barrier against Cr₂O₃ formation hence enriches the surface of the metallic Cr. Our EDX results are in agreement with the findings of Jafarnejad et al. [31] and Abbasi et al. [32], where they studied the composition of the MgCr₂O₄ oxide by the XRD and EDX analysis. Whereas, a minor amount of iron (Fe) and carbon (C) were observed, it is related to the diffusion of the 430 SS substrate, which reacted during the chromizing process to form probably intermetallic compounds such as (Cr,Fe)₇C₃, Cr₇C₃ and Cr₂₃C₆. They had FCC crystalline structures [33] and they precipitate at the grain boundaries with different amounts in the chromized and doped layer according to the previous studies [34]. These carbides enhance hardness and increase roughness because they are considered as brittle phases [35].

On the other hand, the Cr and Cr-Mg coatings do not contain any chlorine impurities left over from the chemical reactions occurring during the chromizing process at 1050°C. However, the chromized surface is composed only of rich chromium (Cr), chromium carbides and Cr₂O₃ oxide, while Cr-Mg revealed more chromium-rich zones and a small amount of Mg oxide.

In previous studies by Zheng and Rapp [36], they have reported that during the chromizing process and at a temperature about of 880°C, the substrate is subjected to weight loss due to the evaporation of the volatile FeCl₂ which reacts with the substrate by diffusion, resulting in porous coating. The formation of volatile FeCl₂ could be produced by the following chemical reaction [37]:



The results shown in Table 3, represent the weight measure of the substrate before and after the chromizing process. The results demonstrate an increase of the weight gain after chromizing, which may confirm the absence of volatile FeCl_2 in the coated surfaces and that they have not undergone mass consumption [37]. In addition, Cr-Mg chromized showed an increase of 0.0436 g over that of Cr chromized (0.0247 g). This affirms the role of Mg addition in the formation of rich-chromium (Cr) and decrease the formation of carbide in the chromium layer by diffusion process into the substrate.

3. 2. Surface Topography The surface roughness parameters, a direct extension of the line roughness parameters, are commonly used in optical profilometry to describe the topography of chromized coatings. The roughness can be expressed as:

$$R_a = \frac{1}{A} \iint_A |z(x, y) - \bar{z}| dx dy \quad (2)$$

where $z(x, y)$ represents the height, and \bar{z} is the average of height over the surface area (A). The measurement of average roughness (R_a) and mean roughness height (R_z) were recorded using a non-contacter profilometer. Results are shown in Table 4.

Figure 4 represents 2D images of Cr and Cr-Mg chromized coatings. It can be seen from Figure 4-A and B, that the texture of Cr-Mg (3 wt.%) is different to that of Cr chromized (Figure 4(b)). It can be justified by the presence of particles and its non-uniform distribution, they have been observed previously by the SEM analysis (Figure 2(a) and Figure 4(a)). These particles are considered as an intermetallic phase which has a different structure from the Cr. This leads to the increase of the roughness on the surface and causing the clustered morphology within a microscopic regime observation (3D image: Figure 4(c)). Clusedted morp-hology is due to solid-state diffusion and chemical reactions occurring that

TABLE 3. Measurements of weight changes before and after chromizing process

Coating	Weight (g)	
	Before chromizing	After chromizing
Cr	0.9245	0.9164
Cr-Mg (3wt.%)	0.9492	0.960

TABLE 4. Surface roughness parameters for the Cr chrom-ized and Cr doped coatings reported for 20x magnification

Sample	Roughness parametrs (20x NA 0,15)	
	R_a [μm]	R_z [μm]
430-SS	1.918	9.348
Cr coated	1.039	7.834
Cr-Mg coated	0.315	5.803

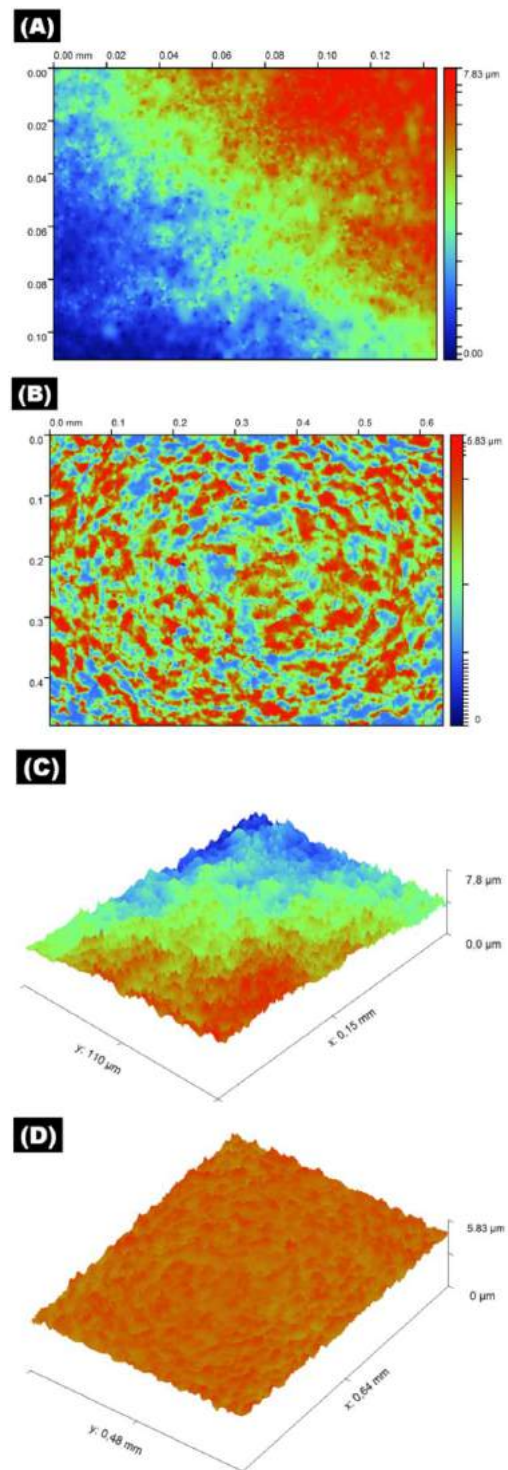


Figure 4. 2D and 3D optical profilometer images: (a), (c) Cr chromized surface; (b), (d) Cr doped with Mg surface

occur during the chromizing process, which can affect the surface characteristics hence its mechanical properties. Deposition of Cr_2O_3 can also increase the roughness of the coated substrate [38].

The distribution of the Cr-Mg surface is more uniform

and it did not show topological defects (Figure 4(d)), such as particles inclusions, asperities, pores and voids which may explain the smoothness of the surface ($R_a = 0.315 \mu\text{m}$) [39], it can be related to the characteristics of the mixture pack used in this chromizing process [20], where the dopant element (Mg) may act as a particulates refiner.

In the absence of Mg dopant, the roughness of the Cr chromized surface increased three times about of $1.039 \mu\text{m}$, compared to the doped Cr-Mg, which showed an average roughness about of $0.315 \mu\text{m}$. The Mg improves the roughness of 430 SS six times compared to its initial state ($R_a = 1.918 \mu\text{m}$). According to Hou and Kang [40], coatings containing Mg oxides could have a rough surface. Whereas, it has been found that doping with Mg decrease the surface roughness [26].

3.3. Adhesion Testing The adhesion of the layers was investigated by a progressi-ve scratch test, gradually increasing the loading force from 1N to 20N applied load. This scratched the coating surface with a loading rate of 38 N/min. Hence, it caused a scratch length of 4mm (Table 2). However, different behavior can be exhibited in the recorded diagram of penetration depths (Rd and Pd) of the Cr (Figure 5(a)) and Cr-Mg (Figure 5(b)) chromized layers. The first critical load (L_{c1}) of the Cr chromized was observed at $L_{c1} = 3.91\text{N}$, at which point cracks occurred during scratch loading. The initial observed critical load of the Cr doped with Mg was about $L_{c1} = 7.32\text{N}$, revealing minor cracks at this stage. It is considered a lower critical load according to the studies of Lee et al [7].

Considering that the recorded critical load (determined by L_c) may be considered as an indicator of strength adhesion and adhesion failure [41]. Accordingly, the Cr chromized at the second and third recorded critical load; $L_{c2} = 7,75\text{N}$ and $L_{c3} = 15.85 \text{N}$, respectively, showed a significant and visible damage corresponding to the occurrence delamination failure and the beginning of the pull-off of the layer from the coated surface. Though the Cr doped resisted until $L_{c2} = 19.21 \text{N}$ and did not show any delamination, it experienced plastic deformation despite that. The adhesion strength is classified as HF1 an excellent quality for the Cr-Mg doped, indicating that Cr doped exhibits no detachment or delamination when subjected to scratch test, while the Cr chromized is classified as HF2.

The trends of the penetration depth (Pd) and residual depth (Rd) were similar until averaged to $20 \mu\text{m}$, then increased and averaged approximately $140 \mu\text{m}$ after the critical load $L_{c3} = 15.85 \text{N}$ (Figure 5(a)). This behavior can be explained by the fact that the Cr chromized experienced a failure mode at this critical load (L_{c3}), which caused the increase in Pd and Rd values. The increase of the penetration depth is caused by the rough surface conditions and by the crack formation after subjecting to the scratch test.

On the other hand, the trends of Pd and Rd profiles

for the Cr-Mg doped remain stable and uniform where its penetration depth (Pd) increased at a maximum depth value of $32 \mu\text{m}$ and Rd practically increased with a very low trend (Figure 5(b)), but still lower than those of the Cr chromized (Figure 5(a)). This result, can be attributed to the uniform and smooth fine matrix and surface of the Cr-Mg doped (Table 4), which could limit the amount of

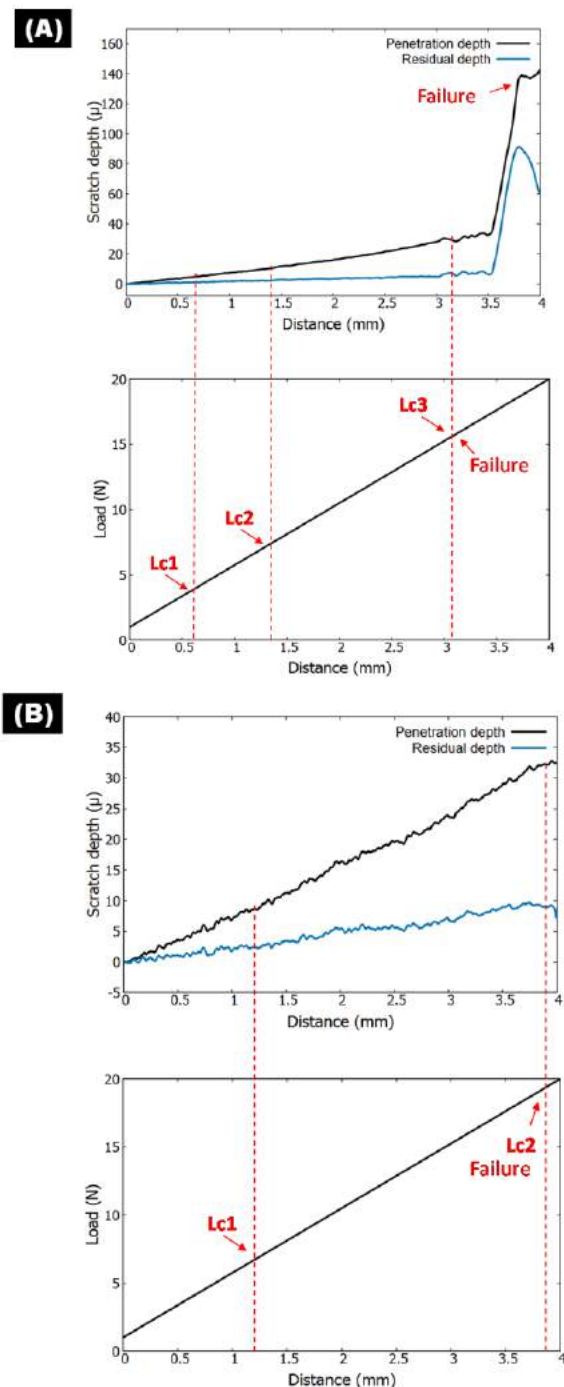


Figure 5. Plot of penetration depths after scratch progressive test under load range of 1 to 20N: A- Cr chromized; B- Cr-Mg doped

penetration and residual deformation that occurs before failure and remain the surface to be more resistant to deformation .

Elastic recovery ratio Er (%) is one of the physical properties describing viscoelastic surfaces. (Er) can be calculated by the following equation:

$$Er \% = \frac{Pd - Rd}{Pd} \times 100 \quad (3)$$

where, Pd is the penetration depth and Rd is the residual depth measured against the applied load.

The results of the elastic recovery ratio (Er) measured for the chromized coating tested are shown in Table 5. The results reveal that the highest elastic recovery ratio (Er) is recorded for the Cr-Mg chromized surface, and it indicates an excellent viscoelastic behavior of the coated surface compared with that of Cr chromized.

Figure 6 show optical microscopic observations of scratch tracks. The surface of the Cr chromized was dark so it was hard to create the proper reflection to the recorded image at high resolutions (high magnifications) hence the image of scratch track showed a lighter area

TABLE 5. Depth penetration measurements after scratch test

Coating	Scratch parametrs		
	Pd [μm]	Rd [μm]	Er [%]
Cr chromized	141	60	57.85
Cr-Mg chromized	32	7.5	76.56

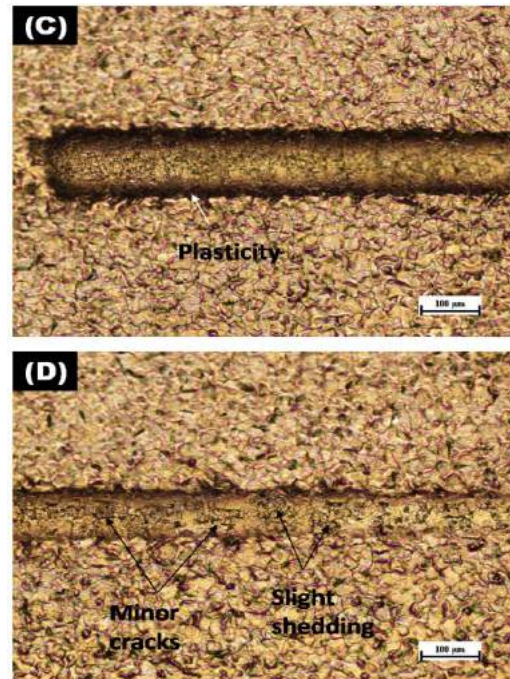
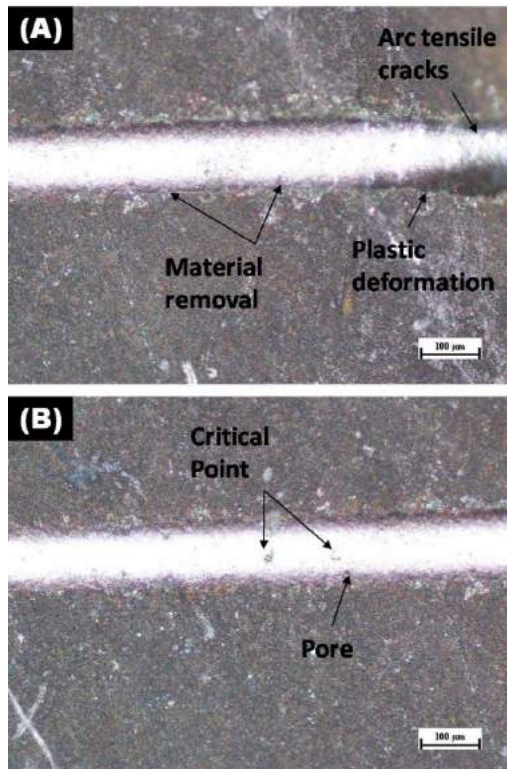


Figure 6. Optical micrographs of scratch tracks after 1-20 N applied progressive load: (A) Cr chromized; (B) Cr-Mg chromized

(Figure 6(a) and (b)). The scratch test trace of the Cr-Mg chromized showed tiny minor cracks at the first critical load $L_{C1} = 7.32$ N (Figure 6(d)), while a plasticity at the edge area and very slightly shedding were observed. It indicates that the Cr-Mg layer in response to the applied progressive load varying from 1N to 20N, deforms plastically without fracture, delamination or material removal (Figure 6(c)). However, the Cr-Mg (3wt.%) doped layer tends to have a high resistance to plastic deformation. This means that the surface can recover its shape easily and its less subject to permanently deformed or damaged by the scratch test. As shown in Table 5, the doped layer exhibited an excellent elastic recovery ratio of about $Er = 76\%$. Despite this, very small areas of shedding caused by the minor cracks, which is considered acceptable and normal for the coatings as described by Vidakis et al. [42]. Moreover, the property indicates that coatings are tough and they are not damaged by deformation. On the other hand, the Cr chromized under the major critical load $L_{C3} = 15.85$ N experienced a plastic deformation followed by arc tensile cracks and beginning of a delimitation failure. Along the track, removal of material was detected (Figure 6(a)).

4. CONSLUSIONS

The results of this present study showed the effect of the addition of Magnesium as a doping element in the pack mixture of the chromized layer conducted at 1050°C . The

addition of Mg caused substantial changes in the microstructure, resulting in a crystalline structure without pores, cracks or rough particles. As a result of the EDX analysis, there is an increased rich-chromium deposition on the surface of the doped layer, which confirms that Mg enhances the diffusion of chromium (Cr) in the surface of the AISI 430. During the chromizing process, Mg reacts as a barrier to the formation of chromium oxides such as Cr₂O₃. It is replaced by a small region of magnesium oxide reacted with Cr, which is believed to be more protective than Cr₂O₃ oxide. Moreover, intermetallic phase formation, including CrC, Cr₇C₃ and Cr₂₃C₆, was less in the doped layer than in the chromized layer. Surface characteristics studies showed a desirable improvement of the Cr-Mg layer. Furthermore, Mg addition resulted in a significant improvement in surface roughness, three times lower than the chromized surface. However, this enhancement in roughness improved resistance against scratch-induced damage, as the doped layer successfully withstood a progressive load ranging from 1N to 20N. Therefore, strength adhesion was 19.21N before failure, which is classified as HF1 quality. However, failure was observed in the form of plastic deformation without fractures, due to its high elastic recovery ratio Er = 76%. In contrast, the chromized layer revealed cracks, plastic deformation, pores, and material removal. It had a strength adhesion of 15.85 N and an elastic recovery ratio of about Er = 57%. In conclusion, adding Mg to the pack mixture of the chromized coating can enhance microstructure, roughness and adhesion characteristics.

5. ACKNOWLEDGMENT

We like to express our gratitude to the Laboratory of Materials Physics and Optics (LPMO), and the Research Institute for Materials Science and Engineering, University of Mons (*Belgique*) for the scientific collaboration. This work was supported by the Corrosion, Protection and Durability of Materials Division of the Research center in Industrial Technologies *CRTI (Algeria)*.

6. REFERENCES

- Pérez, F., Hierro, M., Pedraza, F., Gomez, C. and Carpintero, M., "Aluminizing and chromizing bed treatment by cvd in a fluidized bed reactor on austenitic stainless steels", *Surface and Coatings Technology*, Vol. 120, (1999), 151-157. [https://doi.org/10.1016/S0257-8972\(99\)00355-2](https://doi.org/10.1016/S0257-8972(99)00355-2)
- Lin, N., Guo, J., Xie, F., Zou, J., Tian, W., Yao, X., Zhang, H. and Tang, B., "Comparison of surface fractal dimensions of chromizing coating and p110 steel for corrosion resistance estimation", *Applied Surface Science*, Vol. 311, (2014), 330-338. <https://doi.org/10.1016/j.apsusc.2014.05.062>
- Tsai, L.-C., Sheu, H.-H., Chen, C.-C. and Ger, M.-D., "The preparation of the chromized coatings on aisi 1045 carbon steel plate with the electroplating pretreatment of ni or ni/cr-c film", *International Journal of Electrochemical Science*, Vol. 10, No. 1, (2015), 317-331.
- Santander, J.A., Lopez, E., Tonetto, G.M. and Pedemera, M.N., "Preparation of ninbo/aisi 430 ferritic stainless steel monoliths for catalytic applications", *Industrial & Engineering Chemistry Research*, Vol. 53, No. 28, (2014), 11312-11319. <http://dx.doi.org/10.1021/ie501884g>
- Carvalho, C.E.R.d., Costa, G.M.d., Cota, A.B. and Rossi, E.H., "High temperature oxidation behavior of aisi 304 and aisi 430 stainless steels", *Materials Research*, Vol. 9, (2006), 393-397. <https://doi.org/10.1590/S1516-14392006000400009>
- Sabioni, A.C.S., Huntz, A.M., Salgado, M.F., Pardini, A., Rossi, E.H., Paniago, R.M. and Ji, V., "Atmosphere dependence of oxidation kinetics of unstabilized and nb-stabilized aisi430 ferritic stainless steels in the temperature range 850–950° c", *Materials at High Temperatures*, Vol. 27, No. 2, (2010), 89-96. <https://doi.org/10.3184/096034010X12710805379897>
- Lee, S., Cho, K., Lee, W. and Jang, H., "Improved corrosion resistance and interfacial contact resistance of 316l stainless-steel for proton exchange membrane fuel cell bipolar plates by chromizing surface treatment", *Journal of Power Sources*, Vol. 187, No. 2, (2009), 318-323. <https://doi.org/10.1016/j.jpowsour.2008.11.064>
- Popoola, A., Aigbodion, V.S., Fayomi, O. and Abdulwahab, M., "Experimental study of the effect of siliconizing parameters of thermochemical treatment of low carbon steel", *Silicon*, Vol. 8, (2016), 201-210. <https://doi.org/10.1007/s12633-015-9387-3>
- Dong, Z., Zhou, T., Liu, J., Zhang, X., Shen, B., Hu, W. and Liu, L., "Effects of pack chromizing on the microstructure and anticorrosion properties of 316l stainless steel", *Surface and Coatings Technology*, Vol. 366, (2019), 86-96. <https://doi.org/10.1016/j.surfcoat.2019.03.022>
- Ganji, O., Sajjadi, S.A., Yang, Z.G., Mirjalili, M. and Najari, M.R., "On the formation and properties of chromium carbide and vanadium carbide coatings produced on w1 tool steel through thermal reactive diffusion (trd)", *Ceramics International*, Vol. 46, No. 16, (2020), 25320-25329. <https://doi.org/10.1016/j.ceramint.2020.06.326>
- Leferink, R. and Huijbregts, W., "Chromium diffusion coatings for the protection of low-alloy steel in a sulphidizing atmosphere", *Corrosion Science*, Vol. 35, No. 5-8, (1993), 1235-1242. [https://doi.org/10.1016/0010-938X\(93\)90343-F](https://doi.org/10.1016/0010-938X(93)90343-F)
- Sen, S., "A study on kinetics of crxc-coated high-chromium steel by thermo-reactive diffusion technique", *Vacuum*, Vol. 79, No. 1-2, (2005), 63-70. <https://doi.org/10.1016/j.vacuum.2005.01.009>
- Meng, T., Guo, Q., Xi, W., Ding, W., Liu, X., Lin, N., Yu, S. and Liu, X., "Effect of surface etching on the oxidation behavior of plasma chromizing-treated aisi440b stainless steel", *Applied Surface Science*, Vol. 433, (2018), 855-861. <https://doi.org/10.1016/j.apsusc.2017.10.111>
- Bai, C.-Y., Lee, J.-L., Wen, T.-M., Hou, K.-H., Wu, M.-S. and Ger, M.-D., "The characteristics of chromized 1020 steel with electrical discharge machining and ni electroplating pretreatments", *Applied Surface Science*, Vol. 257, No. 8, (2011), 3529-3537. <https://doi.org/10.1016/j.apsusc.2010.11.070>
- Iorga, S., Ciuca, S., Leuvre, C. and Colis, S., "Influence of the thermo-chemical conditions on the carbo-chromization process of α-fe matrices obtained by powder sintering technique", *Journal of Alloys and Compounds*, Vol. 512, No. 1, (2012), 100-104. <https://doi.org/10.1016/j.jallcom.2011.09.030>
- Hu, J., Zhang, Y., Yang, X., Li, H., Xu, H., Ma, C., Dong, Q., Guo, N. and Yao, Z., "Effect of pack-chromizing temperature on microstructure and performance of aisi 5140 steel with cr-

- coatings", *Surface and Coatings Technology*, Vol. 344, (2018), 656-663. <https://doi.org/10.1016/j.surfcoat.2018.03.099>
17. Murakami, T., Hibi, Y., Mano, H., Matsuzaki, K. and Inui, H., "Friction and wear properties of the siliconized, chromized and borochromized steel substrates", in Materials Science Forum, Trans Tech Publ. Vol. 783, (2014), 1464-1469.
 18. Tarakci, M. and Guruswamy, S., "Influence of surface roughness on the coercivity and magnetic interactions in coCr_x (x= pt, pd, ta, b) thin film media", *Surface Engineering: Science and Technology II*, (2002), 283-292.
 19. Hakami, F., Pramanik, A. and Basak, A., "Duplex surface treatment of steels by nitriding and chromizing", *Australian Journal of Mechanical Engineering*, Vol. 15, No. 1, (2017), 55-72. <https://doi.org/10.1080/14484846.2015.1093256>
 20. Liu, S., Yang, J., Liang, X., Sun, Y., Zhao, X. and Cai, Z., "Investigation of the preparation, corrosion inhibition, and wear resistance of the chromized layer on the surfaces of t9 and spec steels", *Materials*, Vol. 15, No. 22, (2022), 7902. <https://doi.org/10.3390/ma15227902>
 21. Chou, C.-C., Lee, J.-W. and Chen, Y.-I., "Tribological and mechanical properties of hfcvd diamond-coated wc-co substrates with different cr interlayers", *Surface and Coatings Technology*, Vol. 203, No. 5-7, (2008), 704-708. <https://doi.org/10.1016/j.surfcoat.2008.08.055>
 22. Ghorbani, H. and Poladi, A., "Md-simulation of duty cycle and tan interlayer effects on the surface properties of ta coatings deposited by pulsed-dc plasma assisted chemical vapor deposition", *International Journal of Engineering, Transactions B: Applications*, Vol. 33, No. 5, (2020), 861-869. <https://doi.org/10.5829/ije.2020.33.05b.18>
 23. Akbarzadeh, M., Zandrahimi, M. and Moradpour, E., "A study of the tribological properties of sputter-deposited mosx/cr coatings", *International Journal of Engineering, Transactions B: Applications*, Vol. 31, No. 5, (2018), 792-798. <http://dx.doi.org/10.5829/ije.2018.31.05b.14>
 24. Ye, F., Mohammadtaheri, M., Li, Y., Shiri, S., Yang, Q. and Chen, N., "Diamond nucleation and growth on wc-co inserts with Cr₂O₃-Cr interlayer", *Surface and Coatings Technology*, Vol. 340, (2018), 190-198. <https://doi.org/10.1016/j.surfcoat.2018.02.056>
 25. Han, D., Hou, Y., Jiang, B., Geng, B., He, X., Shagdar, E., Lougou, B.G. and Shuai, Y., "Enhanced corrosion resistance of alloy in molten chloride salts by adding nanoparticles for thermal energy storage applications", *Journal of Energy Storage*, Vol. 64, (2023), 107172. <https://doi.org/10.1016/j.est.2023.107172>
 26. Chang, T.-C., Wang, J.-Y., Chia-Ming, O. and Lee, S., "Grain refining of magnesium alloy az31 by rolling", *Journal of Materials Processing Technology*, Vol. 140, No. 1-3, (2003), 588-591. [https://doi.org/10.1016/S0924-0136\(03\)00797-0](https://doi.org/10.1016/S0924-0136(03)00797-0)
 27. Wang, M., Huang, W., Shen, Z., Gao, J., Shi, Y., Lu, T. and Shi, Q., "Phase evolution and formation of λ phase in Ti₃O₅ induced by magnesium doping", *Journal of Alloys and Compounds*, Vol. 774, (2019), 1189-1194. <https://doi.org/10.1016/j.jallcom.2018.09.350>
 28. Yan, G., Yu, W. and Shengping, S., "Oxidation protection of enamel coated ni based superalloys: Microstructure and interfacial reaction", *Corrosion Science*, Vol. 173, (2020), 108760. <https://doi.org/10.1016/j.corsci.2020.108760>
 29. Fan, H.J., Gösele, U. and Zacharias, M., "Formation of nanotubes and hollow nanoparticles based on kirkendall and diffusion processes: A review", *Small*, Vol. 3, No. 10, (2007), 1660-1671. <https://doi.org/10.1002/smll.200700382>
 30. Hasibi, H., Mahmoudian, A. and Khayati, G., "Modified particle swarm optimization-artificial neural network and gene expression programming for predicting high temperature oxidation behavior of Ni-Cr-W-MO alloys", *International Journal of Engineering, Transactions B: Applications*, Vol. 33, No. 11, (2020), 2327-2338. <https://doi.org/10.5829/ije.2020.33.11b.23>
 31. Jafarnejad, E., Khanahmadzadeh, S., Ghanbary, F. and Enhessari, M., "Synthesis, characterization and optical band gap of pirochromite (MgCr₂O₄) nanoparticles by stearic acid sol-gel method", *Current Chemistry Letters*, Vol. 5, No. 4, (2016), 173-180. <http://dx.doi.org/10.5267/j.ccl.2016.7.001>
 32. Abbasi, A., Sajadi, S.M.S., Amiri, O., Hamadian, M., Moayedi, H., Salavati-Niasari, M. and Beigi, M.M., " MgCr₂O₄ and mgcr₂o₄/ag nanostructures: Facile size-controlled synthesis and their photocatalytic performance for destruction of organic contaminants", *Composites Part B: Engineering*, Vol. 175, (2019), 107077. <https://doi.org/10.1016/j.compositesb.2019.107077>
 33. Xia, F., Xu, W., Chen, L., Wu, S. and Sangid, M.D., "Generalized stacking fault energies of Cr₂₃C₆ carbide: A first-principles study", *Computational Materials Science*, Vol. 158, (2019), 20-25. doi. <https://doi.org/10.1016/j.commatsci.2018.11.006>
 34. Almubarak, A., Abuhaimed, W. and Almazrouee, A., "Corrosion behavior of the stressed sensitized austenitic stainless steels of high nitrogen content in seawater", *International Journal of Electrochemistry*, Vol. 2013, (2013). doi. <https://doi.org/10.1155/2013/970835>
 35. Wang, Z., Lu, J. and Lu, K., "Wear and corrosion properties of a low carbon steel processed by means of smat followed by lower temperature chromizing treatment", *Surface and Coatings Technology*, Vol. 201, No. 6, (2006), 2796-2801. doi. <https://doi.org/10.1016/j.surfcoat.2006.05.019>
 36. Zheng, M. and Rapp, R.A., "Simultaneous aluminizing and chromizing of steels to form (Fe, Cr) 3Al coatings", *Oxidation of Metals*, Vol. 49, No. 1-2, (1998), 19-31. doi. <https://doi.org/10.1023/A:1018870105824>
 37. Jyrkas, K., Lajunen, L., Siivari, J. and Patrikainen, T., "Diffusion nickelising and chromising of steel by chloride compounds using chemical vapour deposition in a flow reactor", *Scandinavian Journal of Metallurgy*, Vol. 19, No. 6, (1990), 288-304.
 38. NAEIMI, F. and Tahari, M., "Effect of surface morphologies on the isothermal oxidation behavior of mrcraly coatings fabricated by high-velocity oxyfuel processes", *International Journal of Engineering, Transactions C: Aspects*, Vol. 30, No. 3, (2017), 432-438.
 39. Beltrami, M., Dal Zilio, S., Kapun, G., Ciubotaru, C.D., Rigoni, F., Lazzarino, M. and Sbaizero, O., "Surface roughness control in nanolaminar coatings of chromium and tungsten nitrides", *Micro and Nano Engineering*, Vol. 14, (2022), 100107. <https://doi.org/10.1016/j.mne.2022.100107>
 40. Hou, W. and Kang, Z., "Preparation of duplex film through microarc oxidation coloring and polymer plating on mg-li alloy and its corrosion resistance", *International Journal of Electrochemical Science*, Vol. 8, No. 4, (2013), 5613-5620.
 41. Quan, C. and He, Y., "Properties of nanocrystalline cr coatings prepared by cathode plasma electrolytic deposition from trivalent chromium electrolyte", *Surface and Coatings Technology*, Vol. 269, (2015), 319-323. <https://doi.org/10.1016/j.surfcoat.2015.02.001>
 42. Vidakis, N., Antoniadis, A. and Bilalis, N., "The vdi 3198 indentation test evaluation of a reliable qualitative control for layered compounds", *Journal of Materials Processing Technology*, Vol. 143, (2003), 481-485. [https://doi.org/10.1016/S0924-0136\(03\)00300-5](https://doi.org/10.1016/S0924-0136(03)00300-5)

COPYRIGHTS

©2023 The author(s). This is an open access article distributed under the terms of the Creative Commons Attribution (CC BY 4.0), which permits unrestricted use, distribution, and reproduction in any medium, as long as the original authors and source are cited. No permission is required from the authors or the publishers.

**Persian Abstract****چکیده**

در مطالعه حاضر، اثر افزودن منیزیم (Mg) به عنوان عنصر دوپینگ بر روی مورفولوژی و ویژگی‌های سطحی لایه کرومی شده بررسی شد. برای دستیابی به این هدف، لایه‌های کرومیزه با فرآیند کرومیزاسیون در بسته‌بندی سیمانی در دمای ۱۰۵۰ درجه سانتی‌گراد پوشش داده و دوپ شدند. ضخامت لایه دوپ شده حدود ۲۶ میکرومتر بود، در حالی که کروم شده تقریباً ۲۴ میکرومتر بود. مورفولوژی سطح و ترکیب پوشش‌ها با استفاده از میکروسکوپ الکترونی روبشی (SEM) و طیف‌سنجی اشعه ایکس پراکنده انرژی (EDX) آنالیز شد. نتایج نشان داد که یک ساختار کریستالی را می‌توان با افزودن منیزیم به عنوان یک عنصر دوپینگ به مخلوط بسته با موفقیت رسوب کرد. بنابراین، منیزیم به عنوان یک مانع در برابر تشکیل Cr_2O_3 عمل می‌کند، که منجر به ایجاد یک منطقه کروم غنی تر و تشکیل اکسید محافظ می‌شود. علاوه بر این، کاربرد کمتری در لایه دوپ شده تشکیل می‌شود. زبری لایه با افزودن منیزیم (Mg) افزایش می‌یابد و متوسط زبری (Ra) آن ۳ برابر کمتر از کرومیزه است که به ترتیب حدود ۰.۳۱۵ میکرومتر و ۱.۰۳۹ میکرومتر است. علاوه بر این، خراش بارگذاری پیش‌رونده در N1 و N20 انجام شد. نتایج نشان داد که منیزیم در لایه کرومی شده توانایی مقاومت در برابر سطوح مختلف تنش مکانیکی را با چسبندگی استحکامی در حدود ۱۹.۲۱ نیوتن افزایش می‌دهد و می‌تواند محافظت بیشتری نسبت به کروم کروم داشته باشد.



Diversification of Portfolio of International Oil and Gas Assets using Cluster Analysis

L. Nikolaichuk^{*a}, K. Ignatiev^b, I. Filatova^c, A. Shabalova^c

^a Educational Research Center for Digital Technologies, Saint-Petersburg Mining University, Saint-Petersburg, Russia

^b Investment Efficiency Department, Gazpromneft STC, Saint-Petersburg, Russia

^c Department of Economics, Organization and Management, Saint-Petersburg Mining University, Saint-Petersburg, Russia

PAPER INFO

Paper history:

Received 12 May 2023

Received in revised form 15 June 2023

Accepted 18 June 2023

Keywords:

Oil and Gas Business

Management Decisions

Multicriteria Analysis

Risk Reduction

Investment Projects' Valid Metrics

ABSTRACT

Improving the tools and mathematical methods to diversify the portfolio of oil and gas assets in the face of limited investment, high market volatility, increasing risks and uncertainties at the current level of technology development is a very urgent task. In order to form an effective investment portfolio, the authors proposed asset diversification using cluster analysis, which implies grouping sample objects according to a set of specific features. The method under consideration involves five stages of asset valuation in order to consider those assets in a three-dimensional space, taking into account the specifics of the oil and gas business, including determination of individual asset trajectory, performing spatial approximation, calculating the clustering coefficient, ranking the resulting pairs, and directly solving the portfolio formation optimization problem. This paper provides a reasonable set of metrics for diversification of the investment portfolio based on cluster analysis: main criterion - ΔPV , additional criteria - $\Delta Production$, $\Delta OPEX/toe$, $\Delta CAPEX/toe$, characterized geological, environmental, social and economic aspects. Thus, the proposed methodology provides an opportunity to identify the most attractive investment projects, thereby allowing large oil and gas companies to diversify their business with minimal risk and maximum return on invested capital.

doi: 10.5829/ije.2023.36.10a.06

NOMENCLATURE

R_t	Clustering coefficient	Q	Number of subjects
CRF_t	Common risk factor	t	Time span of the sample
IRF_t	Individual risk factor		

1. INTRODUCTION

Formation of investment portfolios for oil and gas companies is considered as a vital necessity to optimize investment activities and achieve maximum positive effect (MPE). The formation of investment portfolios is possible using various methods depending on the final goals [1-7]. Large consulting companies are increasingly using and offering their clients a variety of robo-advisers and decision support systems in order to form the most suitable asset portfolios for investors [8, 9].

This fact confirms the relevance of the ongoing research aimed at improving the mathematical methods applicable to the formation, rebalancing and diversification of investment portfolios [10-13].

A relevant area for detailed study is the field of data science that considers various intelligent algorithms to solve optimization problems and ranking a large array of input data characterizing the totality of available alternatives [14-18]. With this regards, the described problem can be solved using cluster analysis [19-21].

One of the necessary criteria for the formation of an effective investment portfolio is the observance of the principle of diversification, that is, the inclusion in the portfolio of projects, the chance of success of which depends little or does not depend on each other at all [22]. In the described situation, the approach using cluster analysis is well applicable, which implies the grouping of sample objects according to certain criteria established by the analyst [23, 24].

*Corresponding Author Email: nikolaychuk_la@pers.spmi.ru
(L. Nikolaichuk)

The present study includes cluster analysis as invented by Haddad [25] that proposed an innovative method of cluster analysis based on the use of analytical geometry for calculating a common indicator of a clustering model. One of the main advantage of this method is the ability to measure the level of similarity between assets over time. Moreover, it is capable to clearly distinguish investment alternatives in a consistent manner through selection of relevant metrics that allows determination of the level of similarity between projects through a clear graphical representation.

Within the framework of this study, it seems appropriate to use the designated cluster analysis method for oil and gas projects [26, 27]. In fact, application of Haddad [25] method seems appropriate for oil and gas projects and this study is aimed to describe cluster analysis in diversifying the portfolios of global oil and gas companies. It should be noted that the use of the described methodology and the proposed set of metrics in order to diversify oil and gas projects is carried out for the first time while two new steps of cluster analysis are proposed by this work taking into account the specifics and characteristics of the oil and gas business.

The study is aimed to improve the existing methodology for conducting cluster analysis for making investment decisions in the oil and gas business. The work includes an analysis of key features that reflect the specifics of oil and gas industry projects in four main areas: geological, environmental, social and economic. An analysis is made of the selected most relevant metrics that best reflect the specifics of oil and gas projects, regardless of the national characteristics of states.

2. MATERIALS AND METHODS

Making investment decisions is an important part of a company's development strategy. Making a profit from invested capital is the main purpose of the investment. To eliminate erroneous actions, it is necessary to focus on an investment strategy. There are various investment strategies. This work is focused on a balanced investment strategy and includes asset portfolio diversification and a discounted cash flow model [28-30].

The methods of multivariate analysis include, such as, cluster, factorial, correlation and discriminant analysis where cluster analysis allows division of objects into several sets not by one parameter, but by a set of features [31, 32]. Haddad [25] carried out a practical calculation based on synthetic data, which made it possible to identify two explicit clusters due to the pairwise intersection of the spheres. And the goal of further research of the scientist is to approximate the proposed method based on real data.

According to the proposed methodology, projects are evaluated sequentially in three stages, and the result is

consideration of an asset in the form of a sphere in three-dimensional Euclidean space.

Present study diversifies the portfolio of international oil and gas assets using the described method of cluster analysis, projects of onshore segment were collected according to Wood Mackenzie. First, analysis of assets trajectory over time was carried out based on the data followed with calculation of the change in Individual Risk Factor (IRF) [33]. This stage is characterized with collection of up-to-date information about assets and calculation of relevant metrics for constructing geometric shapes.

Next, total asset risk factor (ARF) was determined through complex geometric correlations. It is necessary to approximate in space the assets represented by the spheres and determine the volume of the lenses, in case they are formed due to the intersection of the spheres.

At the last stage, degree of similarity of assets was assessed dynamically, in case of any intersection between spheres, through calculation of common clustering indicator limited between zero and one and based on calculated volumes of spheres [34].

The study substantiates a set of 4 metrics and their location in space in such a way that the cluster analysis carried out takes into account the specifics of the oil and gas business. They are selected according to the following algorithm, which is described in detail in the results section:

- 1) Substantiation of the resulting indicator chosen among classic indicators of the economic efficiency of an investment project.
- 2) Analysis of specifics of oil and gas projects in geological, environmental, social and economic areas.
- 3) Justification of three variables that form three-dimensional space.
- 4) Checking relevance of proposed metrics and their location by conducting cluster analysis for international oil and gas investment projects.
- 5) Formation of conclusions on proposed metrics and analysis, making adjustments.

3. RESULTS

3. 1. Determination of Individual Assets Trajectory

The calculation of axial variables and the subsequent determination of the relative position based on the indicators of the individual risk factor allows you to determine the spatial trajectory of each asset. Haddad [25] notes the need for a careful choice of variables when using cluster analysis. It is necessary to give preference to those technical and economic indicators, the growth rates of which are comparable. If one of the parameters obviously changes more than the others, the three-dimensional space is stretched, which leads to a reduction in the number of intersections

of the spheres and an artificial decrease in the number of clusters. In other words, the results of the study become inaccurate. Based on this provision, we provide a justification for choosing a set of four indicators, the use of which in the selected methodology of cluster analysis of oil and gas projects allows us to obtain relevant results that adequately reflect the degree of diversification between the assets being evaluated.

The advantages of the Haddad [25] methodology consist of using normalized variables. The metrics applied in the research are shown not in absolute values, but in the form of the rate of change of the indicator over the period of time (the term of the investment project). This condition seems to be the key one, as the dynamic study of clustering patterns over time allows us to investigate in the data set not only at a certain point in time.

To determine the key indicator reflecting the economic efficiency of the project, dynamic methods of evaluation of investment projects are considered, as this assumption is initially included in the conditions of the study. It is also taken into account that the proposed tool will be used by the owners (investors) or management of the company, which, in turn, are interested in profit growth; increase in the value of assets; growth of return on invested capital and ensure the stable operation of the company. This condition justifies the chosen theoretical apparatus, which consists in the consideration of the following indicators of commercial attractiveness of the project. Table 1 summarized the criteria and indicators for the commercial effectiveness of the oil and gas project.

3. 2. Choice of Metrics

Analysis of the commercial effectiveness of projects revealed that present value of the project (i.e. Present Value), deferred on the axes of three-dimensional space, is the most appropriate parameter that sets the volume of sphere and represents the resultant indicator for the parameters.

As a variable reflecting the volume of the figure, the change in the total present value of the projects (ΔPV) was used.

To identify the other three variables (i.e. axis), selected specifications of oil and gas projects including geological, environmental, social and economic aspects in the were taken into account.

Each direction, in turn, can be expressed by metrics presented in Table 2. Taking into account the need to limit to only three explanatory variables, generalized metrics have been proposed.

During the present study, social and environmental metrics were excluded mainly due to incomparability with tax laws, non-comparability of environmental legislation and difficulty in obtaining reasonable data on employment rates.

Thus, the indicator reflecting geological specificity - the change of hydrocarbon production volumes ($\Delta Production$) was taken as the second variable on the X-axis.

The components of the economic direction of the specificity of oil and gas projects were also analyzed, as a result of which the payback period was excluded (see the explanation above).

TABLE 1. Criteria and indicators for the commercial effectiveness of the oil and gas project

Indicator		Meaning of indicator	Criteria values	Possibility of using as a resulting indicator
NPV	Net Present Value	The sum of net discounted cash flows for the entire period of consideration of the project; the integral effect of the project	>0	This metric is viewed as the most appropriate due to the ability to select comparable explanatory variables
IRR	Internal Rate of Return	The discount rate at which the net present value of the project is zero, or the amount of cash proceeds equals the investment; the rate of return inherent in the project	IRR $> r$, the project is accepted; IRR $< r$, the project is rejected	
MIR	Modified Internal Rate of Return	The discount rate at which the terminal value of the project equals the present value of the investment	MIRR $> r$, the project is accepted; MIRR $< r$, the project is rejected	These metrics are considered as possible, however, not a priority due to the difficulty of selecting comparable factors as variables
PI	Profitability Index	The ratio of the sum of reduced cash flows from operating activities to the discounted value of investments	>1	
DP	Discount Payback Period	Minimum time interval from the beginning of the project, beyond which the discounted cash flow, calculated on an accumulative basis, has a positive value	no	

TABLE 2. Specific metrics for oil and gas projects

Specifics	Metrics	Common metric
Geological	Conditions of mineral occurrence; geological properties of reservoirs; permeability, porosity, pressure and density of fractures; physical and chemical properties of hydrocarbons	Possible volume of hydrocarbon production
Environmental	Negative environmental impact: - discharges into water bodies; - emissions into the atmosphere; - waste disposal.	Payment for negative environmental impact
Social	Increase in the inflow of funds in the form of the amount of social contributions - Social. SC; Potential growth of gross regional product - Social. GRP; Potential increase in employment - Social. Employment.	Social result = Social. SC + Social GRP + Social. Employment.
Economic	The long-term nature of investments; Capital intensity; Volatility of oil and gas prices; High risks	Payback period Level of capital expenditures (CAPEX) Level of operating costs (OREX) Discount rate

Taking into account the fact that investment projects of oil and gas enterprises are highly capital-intensive, the Z axis adopted the indicator - change in specific capital expenditures per ton of oil equivalent (Δ CAPEX/toe). And the Y-axis is the change in specific operating costs per ton of oil equivalent (Δ OPEX/toe), since the main share of costs is formed by remoteness from populated areas and the sales market, the level of infrastructure development (availability of roads, power supply, etc.). Relative values were taken intentionally to bring information on different projects located in different states into a comparable form.

Specific risks inherent in the fuel and energy complex, find their quantitative reflection in the value of the discount rate, which is in inverse relation to the value of PV. Traditionally, in view of the above features of oil and gas industry projects, the structure of funding sources is dominated by borrowed sources. In addition, the fact of high riskiness of activities highlights the influence of discount rate in drafting of a project that implies the significance of an indirect reflection of discount within a selected metrics of cluster analysis that is the PV value in this case. As a result, it is deemed that the use of other metrics in the analysis of oil and gas projects will be inappropriate. Additional metrics selection parameters are summarized in Table 3.

3. 3. Hydrocarbon Production Volume Along with changes in hydrocarbon production volume, specific operating or capital costs will inevitably lead to fluctuations in the value of the total cost of the oil and gas project. On the other hand, it is worth noting the directions in which the dependent variables affect the value of the resulting indicator. For instance, an increase in CAPEX/toe, OPEX/toe can lead to a decrease in the final value of the present value of the project while an increase in hydrocarbon production provides an increase

in PV assuming a fixed condition for other parameters. However, at the same time, an increase in output in physical units in the oil and gas sector will naturally increase the level of capital and operating costs. Thus, the variables that form a three-dimensional space in the cluster analysis impose a multidirectional effect on project costs while they also interact with each other.

At the same time, local managers of oil and gas projects seek to ensure a greater growth rate of PV compared to CAPEX and OPEX in the case of incremental hydrocarbon production. Consequently, the rate of sphere volume increase, when using cluster analysis, will usually be greater than the rate of change in the selected variables that form the axes of three-dimensional space.

Thus, the use for cluster analysis of oil and gas projects of the described technical and economic indicators in the proposed combination reduces the probability of distortion of the results, allows to obtain relevant results.

It should be noted that the use of specified variables is not mandatory and other technical and economic indicators are also potential to be used to achieve maximum reflection of the relevant parameters.

Diversification of the project portfolio for a modern company is an important direction of investment policy due to the volatility of world hydrocarbon markets. Therefore, methods are being developed to correctly form a stable portfolio. For approbation of the research the data of international oil and gas corporation were taken. The proposed metrics can be applied in the cluster analysis not only by country, but also by region.

In the presented study, calculations are carried out in MS Excel using the Power Query add-in for analyzing and structuring data. All estimated input parameters are listed in Table 4.

TABLE 3. Choice of Metrics

Criterion	Metrics	Justification
[X]	Δ Production	Reflects the key risk of the industry - mining and geological. Shows the income component of the project.
[Y]	Δ OPEX/toe	Shows the cost part of the project. Prevails in the cost structure.
[Z]	Δ CAPEX/toe	Shows the cost part of the project. Reflects the environmental risks inherent in the industry.
[IRF]	Δ PV	The resulting index for [X], [Y], [Z]. Allows avoiding artificial stretching of the Euclidean space.

TABLE 4. Results of calculation of input parameters

Country	Δ Production, [X]	Δ OPEX/toe, [Y]	Δ CAPEX/toe, [Z]	Δ PV, [IRF]
UAE	0.36	-0.42	0.27	0.20
Kazakhstan	-0.89	-0.87	-0.04	0.14
Russia	-0.53	0.25	0.22	0.69
Libya	-1.00	-0.91	-0.83	0.51
Algeria	-0.58	-0.49	-0.54	0.68
Oman	-0.20	0.38	-0.85	0.70
Italy	0.34	-0.91	-0.51	0.01
Iraq	0.02	-0.89	-0.72	0.10
Yemen	-0.14	-0.12	-0.28	0.56
China	0.03	-0.21	0.25	0.42
Saudi Arabia	-0.96	0.34	0.25	0.14
Germany	-0.49	0.36	-0.29	0.19
Egypt	-0.63	0.12	-0.58	0.79
Turkmenistan	-0.75	-0.36	0.20	0.58
Tunisia	-0.55	0.43	-0.74	0.49
Congo	0.31	0.20	0.22	0.74
Chad	-0.73	0.15	-0.31	0.94
Kuwait	-0.30	-0.92	-0.13	0.42

3.4. Spatial Approximation Total risk factor of assets (the volume of sphere intersection) can be calculated based on individual risk factors wherever spatial intersection of spheres occur. Moreover, having the overall risk factor takes on a value other than zero suggests the similarity of problems for oil and gas projects in the pair under consideration at a given point in time.

3.5. Calculation of Clustering Coefficient Clustering coefficient (R_t) was calculated based on the outcome of previous steps to determine the degree of similarity of the spatial trajectories of a set of assets in a given period of time.

According to Haddad [25], the calculation of the clustering coefficient is carried out according to Equation (1).

$$R_t = \frac{(CRF_{1,2|t}) + (CRF_{2,1|t}) + \dots + (CRF_{Q-1,Q|t}) + (CRF_{Q,Q-1|t})}{IRF_{1|t} + IRF_{2|t} + \dots + IRF_{Q-1|t} + IRF_{Q|t}} \quad (1)$$

It is worth noting here that the value of the clustering coefficient is possible in the range from zero to one. The zero value of the indicator indicates that the analyzed spheres do not intersect, with a value equal to one, the spheres completely coincide.

Spatial visualization of the analyzed data in three-dimensional space is shown in Figure 1 as implemented in Jupyter Notebook software using the Python programming language.

Algorithm for calculating the clustering coefficient is shown in Figure 2.

Based on calculations, we can draw conclusions about the existence of relationships between various oil and gas assets (by country), and, therefore, we can draw

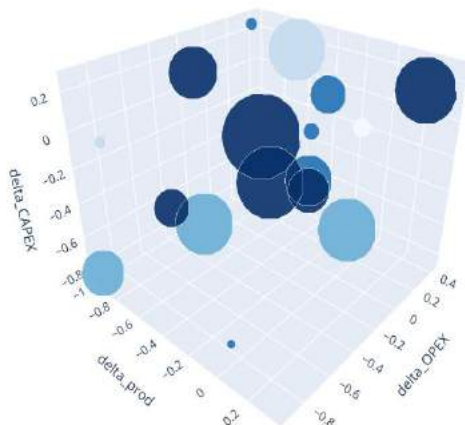


Figure 1. Deposition efficiency on a single square in channel

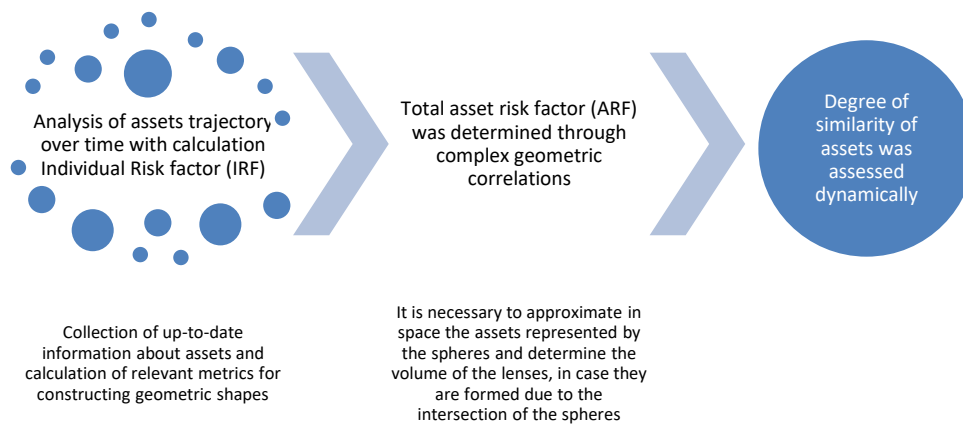


Figure 2. Algorithm for calculating the clustering coefficient

For the selected pairs, the metric required for the final ranking of projects was calculated, which is equal to the ratio of the total current cost of the pair to the total production potential of the pair (PV/Q). After that, a cross matrix of those countries was compiled, the clustering coefficient between which is equal to zero. Appearing semantic gaps in the matrix (intersections of countries that were filtered by a non-zero clustering coefficient) are automatically assigned the value "Null", which is replaced by zeros during further transformations.

The calculated ratios of the total present value attributable to the production potential (thousand rubles/toe) were used as the main characteristic attribute of the pair. The final matrix for portfolio analysis is shown in Table 5. Selection methodology's algorithm of valid metrics for the investment projects' evaluation in the oil and gas industry shown in Figure 3.

The next and final step in the formation of an investment portfolio of international oil and gas assets with the maximum degree of diversification in terms of the estimated indicators is to solve the optimization

conclusions about the advisability of grouping projects when forming a portfolio of oil and gas projects. The degree of diversification can be determined based on the value and time distribution of the clustering coefficient.

Eventually, ranking of the resulting pairs was carried out with the aim of subsequent removal from the sample of alternative assets with a low degree of diversification.

First of all, using the Power Query tool, the crosstab was converted into a bar format with a pairwise comparison of countries in one row by the value of the clustering coefficient, after which the data was ranked from the least to the most diversified. Further, in order to form a portfolio, pairs of countries were selected with a clustering coefficient equal to zero, that is, completely independent of each other in terms of the dynamics of the indicators under consideration.

problem for selecting a portfolio that provides the highest value of the total PV/Q, and at the same time, includes countries that do not have cross-overlapping in zero cells, i.e. not having a pairwise clustering coefficient R other than zero.

4. DISCUSSION

Analyzing Table 2, namely the values of the PV/Q indicator, it can be concluded that the projects of the pairs Libya-Turkmenistan, Libya-Saudi Arabia, as well as Libya-Chad and Libya-Yemen are the most attractive for investment. Investment in oil and gas projects in Kuwait, on the other hand, is undesirable due to a negative present value of projects implemented in this country.

The analysis of the PV/Q ratio shows that the most profitable investments are in the countries Kazakhstan - Saudi Arabia. In their portfolio there is not a single pairwise clustering coefficient other than zero, i.e. none of the pairs in this foursome has zeros in the resulting

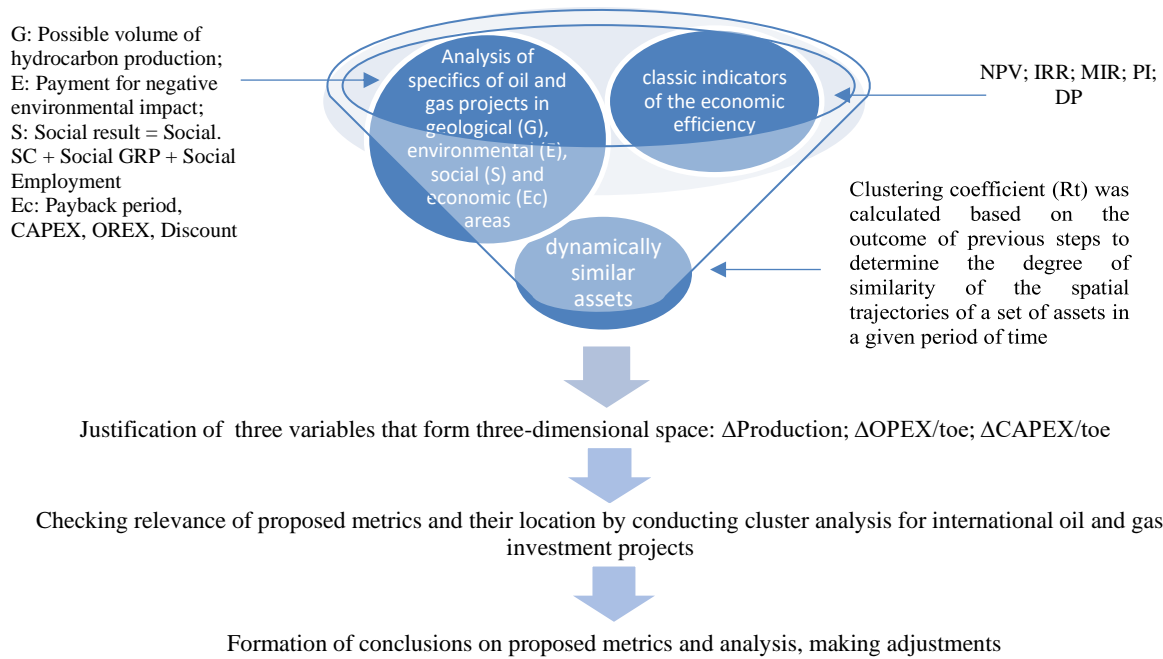


Figure 3. Selection methodology’s algorithm of valid metrics for the investment projects’ evaluation in the oil and gas industry

TABLE 5. Transformed table of calculated values of the PV/Q metric (thousand rubles/toe) for pairs with zero clustering coefficients

Country	Algeria	Chad	China	Congo	Egypt	Germany	Iraq	Italy	Kazakhstan	Kuwait	Libya	Oman	Russia	Saudi Arabia	Tunisia	Turkmenistan	UAE	Yemen
Algeria	0,0	0,0	1,0	0,8	0,0	0,0	0,0	1,4	0,0	0,0	0,0	0,0	0,0	1,1	0,0	0,0	1,1	0,0
Chad	0,0	0,0	0,0	0,0	0,0	0,0	0,1	1,9	13,4	-0,4	42,3	0,0	0,0	0,0	0,0	0,0	1,1	0,0
China	1,0	0,0	0,0	0,0	1,4	1,2	0,1	2,0	11,5	0,0	16,9	0,3	0,0	2,9	1,3	0,0	0,0	0,0
Congo	0,8	0,0	0,0	0,0	0,1	0,4	0,1	1,8	12,6	-0,3	27,7	0,2	0,0	2,0	0,1	0,2	0,0	0,0
Egypt	0,0	0,0	1,4	0,1	0,0	0,0	0,1	1,8	12,3	-0,3	24,1	0,0	0,0	2,0	0,0	0,0	1,1	0,0
Germany	0,0	0,0	1,2	0,4	0,0	0,0	0,1	1,7	9,8	-0,1	10,7	0,0	0,0	1,3	0,0	0,6	1,1	0,0
Iraq	0,0	0,1	0,1	0,1	0,1	0,1	0,0	0,0	0,6	0,0	0,3	0,1	0,2	0,1	0,1	0,1	0,7	0,1
Italy	1,4	1,9	2,0	1,8	1,8	1,7	0,0	0,0	6,2	1,1	4,8	0,6	1,7	2,2	1,8	2,0	1,1	2,2
Kazakhstan	0,0	13,4	11,5	12,6	12,3	9,8	0,6	6,2	0,0	0,0	0,0	2,1	4,4	14,3	11,7	0,0	1,4	13,5
Kuwait	0,0	-0,4	0,0	-0,3	-0,3	-0,1	0,0	1,1	0,0	0,0	4,4	0,1	1,0	0,0	-0,3	0,0	1,0	0,0
Libya	0,0	42,3	16,9	27,7	24,1	10,7	0,3	4,8	0,0	4,4	0,0	1,0	3,1	60,9	19,5	62,3	1,2	34,2
Oman	0,0	0,0	0,3	0,2	0,0	0,0	0,1	0,6	2,1	0,1	1,0	0,0	0,6	0,3	0,0	0,2	0,9	0,0
Russia	0,0	0,0	0,0	0,0	0,0	0,0	0,2	1,7	4,4	1,0	3,1	0,6	0,0	0,0	0,0	0,0	1,1	0,0
Saudi Arabia	1,1	0,0	2,9	2,0	2,0	1,3	0,1	2,2	14,3	0,0	60,9	0,3	0,0	0,0	1,6	0,0	1,1	5,8
Tunisia	0,0	0,0	1,3	0,1	0,0	0,0	0,1	1,8	11,7	-0,3	19,5	0,0	0,0	1,6	0,0	0,3	1,1	0,0
Turkmenistan	0,0	0,0	0,0	0,2	0,0	0,6	0,1	2,0	0,0	0,0	62,3	0,2	0,0	0,0	0,3	0,0	1,1	0,0
UAE	1,1	1,1	0,0	0,0	1,1	1,1	0,7	1,1	1,4	1,0	1,2	0,9	1,1	1,1	1,1	1,1	0,0	0,0
Yemen	0,0	0,0	0,0	0,0	0,0	0,0	0,1	2,2	13,5	0,0	34,2	0,0	0,0	5,8	0,0	0,0	0,0	0,0

matrix when intersecting with each other. At the same time, investments in each pair assume a positive PV/Q, which, together with a high degree of diversification, with a significant degree of confidence, allows you to provide income for the investor company. It is important to understand that the results of the analysis are a demonstration of the work of the proposed method and are not real recommendations for investment, since the forecast values are generated synthetically. The results of the analysis are clearly illustrated in Figure 4.

It is worth noting that portfolio management in the context of high market volatility in the current environment and increasing risks in the global oil and gas business requires the development of new approaches to the formation and diversification of the investment portfolio. In order to further develop the methodology, a

simulation model can be developed. Simulation of the growth rates of the indicators considered in the work will allow us to track the change in the position of clusters in space, the volume of spheres in the dynamics.

Consequently, on the basis of such analysis, it becomes possible to move away from averaging and assess how clusters interact with each other from year to year. The experiments carried out with the simulation model will make it possible to quantitatively assess the stability of a differentiated portfolio in the event that one or more of the projects included in it undergo changes in the indicators used in the cluster analysis. The sets of scenarios developed based on the results of experimentation with the simulation model will reduce the uncertainty in investment decisions.

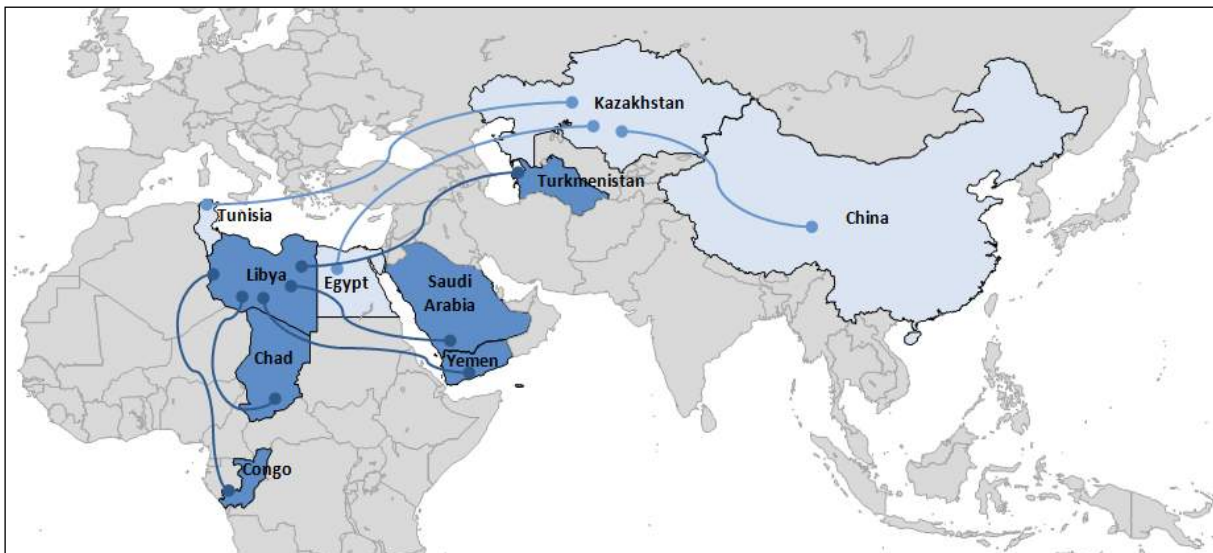


Figure 4. Visualization of the most attractive projects for investment by country pairs

5. CONCLUSION

The expansion of the used methodology through the use of simulation modeling methods will ensure a quick response to changes in external environment and timely adaptation of the portfolio to new conditions. Implementation of multi-criteria sensitivity analysis performed by creating a simulation model improves the quality of portfolio risk management. In this regard, it becomes possible to quantitatively assess the probability of portfolio stability reduction and develop in advance the order of actions in case of risk situation occurrence. The methodology modernized in this way allows increasing the accuracy of economic analysis in conditions of high volatility.

The set of metrics and their location in space, proposed in work, on the one hand, reflects features of oil and gas sector, and on the other hand, allows ranking attractiveness of investment projects implemented in different countries. Article presents the modernization of cluster analysis method, focused specifically on the oil and gas industry. The most adequate results are obtained when using the value of ΔPV as an individual risk factor, since it is the resulting indicator for other metrics and accumulates the most key risks of the project. The general risk factor is determined by using $\Delta OPEX/toe$, $\Delta CAPEX/toe$, $\Delta Production$ as metrics. These metrics prevent unrealistic results from analysis and allow identifying countries whose investments in oil and gas business are highly diversified.

There are limitations in study, since analysis includes three variables, metrics proposed are generalized. The study does not take into account force majeure, natural disasters, market price collapses, occurrence of which will affect the values of selected metrics. Also, political risks, changes in legislation in each individual country are not taken into account, proposed metrics are aimed primarily at comparing attractiveness of investment projects from a financial point of view.

Due to the fact that the management of an oil and gas company is interested in the growth rate of the present value of the project ahead of the growth rate of costs when increasing production volumes, it is considered appropriate to use these variables in the combination discussed in this paper.

The application of the described methodology with the set of indicators justified in the work can be recommended for implementation by large oil and gas companies in order to diversify their business internationally in an effort to maximize profitability at the lowest risk and to provide the highest return on invested capital.

This study is aimed to project managers of oil and gas companies, namely those who make the decision to include a particular project in the investment portfolio.

6. REFERENCES

1. Brinson, G.P., Hood, L.R. and Beebower, G.L., "Determinants of portfolio performance", *Financial Analysts Journal*, Vol. 42, No. 4, (1986), 39-44.
2. Tsay, R.S., "Analysis of financial time series, John Wiley & sons, (2005).
3. Vasilchenko, A., "Analysis of the project selection technique in the process of a portfolio building for oil and gas company (on the example of gpn-development llc)", *Topical Issues of Rational Use of Natural Resources*, Volume 2, (2019), 668.
4. Burca, V., "Portfolio optimization using an alternative approach. Towards data mining techniques way", *Economic Alternatives*, Vol., No. 1, (2021), 113-133. doi: 10.37075/EA.2021.1.07.
5. Antonakakis, N., Cunado, J., Filis, G., Gabauer, D. and De Gracia, F.P., "Oil volatility, oil and gas firms and portfolio diversification", *Energy Economics*, Vol. 70, No., (2018), 499-515. doi: 10.1016/j.eneco.2018.01.023.
6. Mandacı, P.E. and Kırkpınar, A., "Oil assets and portfolio diversification: Firm-level analysis for borsa istanbul", *Borsa Istanbul Review*, Vol. 22, No. 3, (2022), 571-585. <https://www.sciencedirect.com/science/article/pii/S2214845021000788>
7. Kameli, A., Javadian, N. and Daghbandan, A., "Multi-period and multi-objective stock selection optimization model based on fuzzy interval approach", *International Journal of Engineering, Transactions C: Aspects*, Vol. 32, No. 9, (2019), 1306-1311. doi: 10.5829/ije.2019.32.09c.11.
8. Lenkova Olga, V., "The formation of portfolio development strategy in the petroleum refining segment of an oil and gas holding", *Tomsk State University Journal*, No. 169.
9. Chalikova-Uhanova, M. and Samarukha, A., "Development of oil and gas projects based on the cluster approach on the example of the irkutsk oil company", *Baikal Research Journal*, Vol. 11, No. 2, (2020).
10. Erich, A., *Techniques of financial analysis with financial genome passcode card*. 2002, McGraw-Hill/Irwin.
11. Fein, M.L., "Robo-advisors: A closer look", Available at SSRN 2658701, (2015). <https://ssrn.com/abstract=2658701>
12. Fabozzi, F.J., Markowitz, H.M. and Gupta, F., "Portfolio selection", *Handbook of Finance*, Vol. 2, (2008).
13. Marvin, K., "Creating diversified portfolios using cluster analysis", *Princeton University*, (2015). https://www.cs.princeton.edu/sites/default/files/uploads/karina_marvin.pdf
14. Matrokhina, K.V., Trofimets, V.Y., Mazakov, E.B., Makhovikov, A.B. and Khaykin, M.M., "Development of methodology for scenario analysis of investment projects of enterprises of the mineral resource complex", *Зануски Горного унстумуа*, No. 259 (eng), (2023), 112-124.
15. Iakovleva, E., Belova, M., Soares, A. and Rassõlkin, A., "On the issues of spatial modeling of non-standard profiles by the example of electromagnet emission measurement data", *Sustainability*, Vol. 14, No. 1, (2022), 574. <https://doi.org/10.3390/su14010574>
16. Mardashov, D.V., "Development of blocking compositions with a bridging agent for oil well killing in conditions of abnormally low formation pressure and carbonate reservoir rocks", *Зануски Горного унстумуа*, Vol. 251, (2021), 667-677. <https://doi.org/10.31897/PMI.2021.5.6>
17. Tufegđić, M. and Pravdić, P., "Artificial intelligence techniques in business decision making".
18. Tsiglianu, P., Romasheva, N. and Nenko, A., "Conceptual management framework for oil and gas engineering project implementation", *Resources*, Vol. 12, No. 6, (2023), 64.
19. Shabalov, M.Y. and Dmitrieva, D., "Implementation of cluster scenario approach for economic development of the arctic zone of the russian federation", *International Journal of Applied Business and Economic Research*, Vol. 15, No. 4, (2017), 281-289.
20. Pivovarova, I., "Cluster analysis for structuring spatial data", *International Journal of Mechanical Engineering and Technology*, Vol. 10, No. 2, (2019), 1085-1109.
21. Bashiri, M. and Mohammadkhanloo, M., "A clustering based location-allocation problem considering transportation costs and statistical properties (research note)", *International Journal of Engineering, Transactions C: Aspects*, Vol. 26, No. 6, (2013), 597-604. doi: 10.5829/idosi.ije.2013.26.06c.05.
22. Leković, M., "Investment diversification as a strategy for reducing investment risk", *Ekonomski Horizonti*, Vol. 20, No. 2, (2018), 173-187.
23. Ren, Z., "Portfolio construction using clustering methods", Worcester Polytechnic Institute Worcester, (2005),
24. Landau, S. and Ster, I.C., "Cluster analysis: Overview", *Á Á*, Vol. 11, No. x12, (2010), x1p. doi: 10.1016/B978-0-08-044894-7.01315-4.
25. Haddad, M.F.C., "Sphere-sphere intersection for investment portfolio diversification—a new data-driven cluster analysis", *MethodsX*, Vol. 6, (2019), 1261-1278. doi: 10.1016/j.mex.2019.05.025.
26. Yiping, W., Buqing, S., Jianjun, W., Qing, W., Haowu, L., Zhanxiang, L., Ningning, Z. and Qingchao, C., "An improved multi-view collaborative fuzzy c-means clustering algorithm and its application in overseas oil and gas exploration", *Journal of Petroleum Science and Engineering*, Vol. 197, (2021), 108093. doi: 10.1016/j.petrol.2020.108093.
27. Molchanov, K. and Romasheva, N., "Conceptual approaches for building a balanced portfolio of projects in oil and gas companies

- in exploration and production sector", in E3S Web of Conferences, EDP Sciences. Vol. 140, (2019), 03004.
28. Laopodis, N.T., "Understanding investments: Theories and strategies, Routledge, (2020).
 29. Luenberger, D.G., "Investment science", *OUP Catalogue*, (1997).
 30. Guerard Jr, J.B., Saxena, A. and Gültekin, M.N., Investing in assets: Theory of investment decision-making, in Quantitative corporate finance. 2022, Springer.239-290.
 31. Everitt, B.S., Landau, S., Leese, M. and Stahl, D., "Cluster analysis, John Wiley & Sons, (2011).
 32. Giri, S., Al-Obaidi, M., Harmon, C., Clark, D., Ubersax, C., Dai, C., Young-Smith, C., Outlaw, D., Gbolahan, O. and Khushman, M.d., "Patient-reported geriatric assessment-based frailty index among older adults with gastrointestinal malignancies", *Journal of the American Geriatrics Society*, Vol. 71, No. 1, (2023), 136-144. <https://doi.org/10.1111/jgs.18054>
 33. Mousavi, S., "A multi-criteria decision-making approach with interval numbers for evaluating project risk responses", *International Journal of Engineering, Transactions B: Applications*, Vol. 25, No. 2, (2012), 121-130. doi: 10.5829/idosi.ije.2012.25.02b.05.
 34. Ponomarenko, T., Marin, E. and Galevskiy, S., "Economic evaluation of oil and gas projects: Justification of engineering solutions in the implementation of field development projects", *Energies*, Vol. 15, No. 9, (2022), 3103. <https://doi.org/10.3390/en15093103>

COPYRIGHTS

©2023 The author(s). This is an open access article distributed under the terms of the Creative Commons Attribution (CC BY 4.0), which permits unrestricted use, distribution, and reproduction in any medium, as long as the original authors and source are cited. No permission is required from the authors or the publishers.



Persian Abstract

چکیده

بهبود ابزارها و روشهای ریاضی برای متنوع سازی نمونه کارها دارایی های نفت و گاز در مواجهه با سرمایه گذاری محدود ، نوسانات بالای بازار ، افزایش خطرات و عدم قطعیت ها در سطح فعلی توسعه فناوری یک کار بسیار فوری است. به منظور تشکیل یک سبد سرمایه گذاری مؤثر ، نویسندگان با استفاده از تجزیه و تحلیل خوشه ای ، تنوع دارایی را پیشنهاد کردند ، که این امر حاکی از گروه بندی اشیاء نمونه با توجه به مجموعه ای از ویژگی های خاص است. روش مورد نظر شامل پنج مرحله از ارزیابی دارایی به منظور در نظر گرفتن این دارایی ها در یک فضای سه بعدی ، با در نظر گرفتن مشخصات تجارت نفت و گاز ، از جمله تعیین مسیر دارایی های فردی ، انجام تقریب مکانی ، محاسبه ضریب خوشه بندی است. ، رتبه بندی جفت های حاصل و حل مستقیم مشکل بهینه سازی تشکیل نمونه کارها. در این مقاله مجموعه معقول و معقولی برای تنوع بخشیدن به نمونه کارها سرمایه گذاری بر اساس تجزیه و تحلیل خوشه ای ارائه شده است: معیار اصلی - ΔPV ، معیارهای اضافی - تولید ، $\Delta opex$ / انگشتان پا ، $\Delta Capex/TOE$ ، جنبه های زمین شناسی ، محیط زیست ، اجتماعی و اقتصادی را مشخص می کند بشر بنابرین ، روش پیشنهادی فرصتی را برای شناسایی جذاب ترین پروژه های سرمایه گذاری فراهم می کند ، از این طریق به شرکت های بزرگ نفت و گاز اجازه می دهد تا تجارت خود را با حداقل ریسک و حداکثر بازده سرمایه سرمایه گذاری متنوع کنند.



Electricity Supply Model of Conventional Residential Buildings in Tehran with Priority on Renewable Energy Using Adaptive Fuzzy-neural Inference System

S. Khaligh Fard, H. Ahmadi*, M. H. Alizadeh Elizei

Department of Civil Engineering, Roudehen branch, Islamic Azad University, Tehran, Iran

PAPER INFO

Paper history:

Received 10 June 2023
Received in revised 28 June 2023
Accepted 29 June 2023

Keywords:

Adaptive Fuzzy-neural Inference System
Energy Management System
Renewable Energy
Residential Buildings
Solar Energy
Wind Energy

ABSTRACT

Energy consumption in the building sector, especially in residential buildings, due to the development of urbanization, has taken the largest share among all consumption sectors. Therefore, it is very necessary to predict the energy consumption of buildings, which has been presented as a challenge in recent decades. In this research, adaptive fuzzy-neural inference system (ANFIS) and MATLAB software have been used for forecasting to supply electrical energy to residential buildings with random data that collected based on the hourly electricity consumption of conventional residential buildings in Tehran. According to the applied settings for the solar and wind energy production has been done by solar panels and wind turbines. The use of renewable energy is one of the ways that can reduce the consumption of fossil fuels and also reduce environmental pollution. Statistical indicators such as MSE, RMSE, μ , σ , and R were used to evaluate the model performance. The obtained values well show the ability of this model to foresee the generation and utilization of energy in private residential buildings with tall exactness of about 96% and 90%, respectively. Therefore, this model well show the ability of the needed estimates in the mentioned buildings with high accuracy.

doi: 10.5829/ije.2023.36.10a.07

1. INTRODUCTION

Nowadays, energy is one of the basic components in human life and indeed relations between nations. Pollution from fossil fuels and their limited resources have led all countries to add renewable energy to their energy portfolio. One of the biggest energy customers, particularly in created nations, is buildings. Therefore, using renewable energy converters for residential buildings can be vital to reduce fossil fuels, reducing fossil fuel pollution, and reducing energy consumption.

Subsequently, different strategies have been utilized to decrease and optimize energy utilization. Buildings are one of the biggest sources of energy utilization. If excessive energy consumption continues and fuels the energy crisis within the world, it will too worsen natural contamination. For this purpose, one of the best ways is to control and anticipate the generation and

administration of energy utilization within the building utilizing renewable energy.

Therefore, due to the limitation of energy resources and its very important role in the economic development of a country, paying attention to how to reduce energy consumption and optimizing it is a necessity in every country today [1].

Among several methods to present a model for suitable strategy foreseeing and supply of energy in private buildings, the ANFIS is one of the most careful measuring tools for obscure and nonlinear concepts. Adaptive fuzzy-neural inference system (ANFIS), which best coordinating the highlights of fuzzy frameworks and neural systems, is specified by Bektas Ekici and Teoman Aksoy [2]. As a structure, ANFIS incorporates if-else rules and employments fuzzy match input-output information and neural network learning algorithms for preparing. An adaptive fuzzy-neural inference framework simulates complex nonlinear mapping utilizing neural arrangement learning and fuzzy inference strategies. The ANFIS structure comprises of two models, ANN, and fuzzy logic, and can work with vague

*Corresponding Author Institutional Email: hgahmadi@riau.ac.ir
(H. Ahmadi)

clamor and wrong situations. ANFIS is utilized within the neural network preparing handle to alter the participation work and parameters related to the information in question. It has more precise comes about than the normal squares error degree since it can abuse expert decisions. ANFIS learning calculation may be a hybrid learning calculation employing a post-diffusion learning algorithm and the least-squares strategy [2].

Due to the existence of uncertainties in the real world, it is very vital and important to use more efficient methods such as ANFIS. Therefore, this study aim to present a model for the foremost suitable strategy for foreseeing the utilization and supply of energy in private buildings with a sustainable development approach due to uncertainties in the real world using fuzzy-comparative neural inference system (ANFIS) and Using MATLAB software.

2. RESEARCH BACKGROUND

Nowday for dubious and unstable demand as well as the advancement of alternative energy sources, numerous energy firms (Oil, gas and electricity) have been forced by awesome weight to speed up the interest of efficiency in this climate, in this way boosting generation, reducing costs, and optimizing benefits. To assist in this interest, the application of modern techniques in this industry is rapidly advancing at present [3]. Energy is one of the foremost critical components that influence the solidness of any system, and hence, managing with distinctive energy systems is exceptionally critical to attain the most prominent conceivable advantage from energy sources [4]. Energy sources are partitioned into conventional and renewable sources, and both sorts take part in securing the essential vitality to total the prerequisites of the different bulding. Nowday, residential buildings are expected to be designed and built in a way that minimizes the use of materials and energy consumption, and at the same time maximizes the safety and health of their residents. It is very natural that in order to achieve this very important goal, new buildings with energy efficiency should be built and existing buildings should be strengthened and renovated. For this reason, a significant share of research has been focused on the issue of energy performance of buildings (EPB) due to the negative environmental effects and energy loss [5]. The results of an important part of the current research show that one way to diminish the ever-augmenting require for additional energy supply is, in this manner, to supply more energy-efficient building plans with altered energy-saving properties [6].

Recent studies have attempted to model the energy performance of buildings by predicting and using soft computing methods. Basically, it is stated that the cornerstone of energy efficient building design is the

modeling of heating load (HL) and cooling load (CL), because it determines the heating and cooling equipment requirements needed to maintain indoor air conditions. For this purpose, many simulation tools are widely used [7]. Deb et al. [8] used ANN to forecast the diurnal CL for institutional buildings. Yokoyama et al. [9] used ANN coupled with an optimization method in order to estimate the CL demand.

Li et al. [10] For predicting the cooling energy of the whole building utilizing an counterfeit neural network for the presence of an intelligent network in energy utilization. Hameed et al. [11] have examined brilliantly, multi-purpose optimization for energy and consolation administration. Delgarm et al. [12] have presented an efficient method for multi-objective simulation-based optimization using ENERGYPLUS to increase building energy performance in four areas: building direction, window size, wall specifications, and cladding. According to the extraordinary ubiquity of artificial intelligence technique and particularly manufactured neural systems in building energy investigation, there was a got to audit diverse strategies to attain this. The application of an counterfeit neural network in simulating the behavior of building shells in summer conditions with a modern glass framework to assess and make strides energy execution was examined by Buratti et al. [13]. The climatic conditions and warm characteristics of the building shell were expected as input and temperature of the insides space of the building the yield of the arrange. The results showed that ANN can be utilized as a effective apparatus in simulation [13]. The forecast of energy utilization of a private building with the approach of counterfeit neural organize MLP was examined by Biswas et al. [14]. The finest mistake model was come to by selecting the fitting number of covered up layer neurons. The results arrange comes about were factually palatable in comparison to past ponders [14]. Amara et al. [15] proposed an adaptive circle conditional desire Technique (ACCE) based on circle investigation to characterize sub-action plans. As a result, an adaptive linear model (LM) technique is utilized to anticipate the demand for leftover components utilizing the comes about of the ACCE handle in each time window. After that, the anticipated adjust is utilized to comparatively move forward the execution estimate of add up to power request. The precision of the forecast comes about is assessed utilizing the the mean normalized absolute error (NMAE). As a result, the proposed approach to model intermittent remaining demand on the every day skyline leads to a great 23% exactness [16]. Simulate energy consumption in an hourly regime, perform calculations on residential buildings, and analyze and compare regularly between the energy needs of the building reenacted by EnergyPlus, with climatic inputs related to two air terminals in rurals Rome and with Entries. The information displayed by the WRF estimate model for the

center of Rome show a few errors. Ciancio et al. [17] measured these discrepancies. Alobaidi et al. [18] provide a framework using a vital regression component to predict each household's average daily energy consumption. Exact estimation of energy productivity of private buildings based on the calculation of HL heating load and CL cooling stack is an vital assignment. Nilashi et al. [19] displayed an proficient strategy for foreseeing the vitality execution of private buildings utilizing the ANFIS versatile neural-fuzzy deduction framework. The mean absolute error of MAE of HL and CL predictions is 0.16 and 0.52, respectively, which shows the method's effectiveness in HL and CL predictions [19]. Ullah et al. [20] anticipated energy utilization in a private building with the Markov model. The Markov-based calculation predicts energy utilization in Korean private buildings utilizing data collected through smart meters and four cases of multi-story buildings in Seoul. The forecast comes about of the proposed model were compared with three well-known expectation algorithms: SVM back vector machine and ANN counterfeit neural network and regression classification, and the forecast exactness were satisfactory [20].

Mocanu et al. [21] started a study by using two reinforcement learning models to modeling energy consumption in buildings. As a central hypothetical , a Deep Belief Networkze (DBN) is used in each calculation. The Techniques are at that point created within the MATLAB environment and tried on an genuine database recorded over seven years at hourly determination. Exploratory comes about appear that the RMSE energy expectation exactness interims are 91.42%. [21]. Jang et al. [22] made an ANN artificial neural network. A demonstrate predicts when the warming system ought to work to decrease energy utilization in winter mornings. BEMS exploratory information and ANN demonstrate prescient execution were roughly 13.13% superior than CvRMSE and 0.197% superior than MBE. This investigation consider a difference decrease energy utilization in buildings and makes a difference to supply satisfaction [22]. Qiao et al. [23] audit different model and procedures for anticipating building energy utilization based on existing information collections and systematically demonstrate application areas. It also offers a all encompassing see of building energy utilization [23]. Naji et al. [24] utilized the whole energy necessities of the building is influenced by different components such as the environment, climatic conditions, building materials, separator, etc., using the fuzzy-neural network system ANFIS and Energy Plus and soft computational method with Matlab/Simulink. They have examined he energy utilization of the building [24]. Predicting the energy required by the mansions in the early stages of design using the ANFIS adaptive fuzzy-neural inference framework model was examined by Ekici and Aksoy [2] to anticipate the building energy

utilization. Baheri et al. [1] examined the expectation of electricity and gas utilization in a private building complex within the cold region of Iran, the city of Tabriz employing a neural network and genetic algorithm.

The situation and landscape of solar energy in Iran have been studied by Najafi et al. [25]. With current energy policies, investing in hybrid solar power plants, wind power plants are economically viable. Additionally, it requires more than \$ 2800 million in venture amid 2010-2030. By measuring the eleven-year wind speed of the Iranian capital, Tehran, at the height of ten meters above the ground, Keyhani et al. [26] concluded that this area could be suitable for electrical and mechanical applications not connected to the grid, such as wind. Fazelpour et al. [27] examined the utilization of hybrid frameworks to supply energy to a family in Tehran, Iran. They utilized the photovoltaic system, wind turbine, diesel generator, and capacity battery, and made the wind- hydrogen-battery hybrid framework reasonable. They gotten the best economical system [27]. Tahani et al. [28] modeled a system using solar panels and wind and hybrid batteries optimized for a three-story building in Tehran, the capital of Iran, with the method of minimizing costs and obtaining desirable results. Shivam et al. [29] implemented a multi-objective predictive energy management strategy based on machine learning using solar panels, storage batteries, and neural networks. The resulting model provides a more than fifty percent good forecast [29]. Taghavifar and Zomorodian [30] considered installing a micro-hybrid system in grid mode to sell additional electricity and thus save electricity consumption of the building as a source of income. One system of PV and wind and national electricity network and the other system of PV and wind and national network and generator were examined from the technical-economic point of view in different inflation conditions [30]. Asrami et al. [31] inspected three scenarios for finding the leading arrangement for utilizing photovoltaic solar boards for private buildings in urban regions: lattice association with and without battery and total power supply.

Moreover, the genetic algorithm and TOPSIS method are used to determine the optimal response for each scenario. A residential complex in Tehran, Iran, was selected. As a result, the scenario of electricity transmission generated by renewable sources to the national grid and the use of electricity required from the national grid was selected as the optimal design [31]. Ehyaei and Bahadori [32] investigated the use of small gas turbines to supply electricity to residential buildings in Iran. They obtained good results. On the other hand reliable and exact forecast of electricity generation and consumption is subsequently imperative for Utilities Company and government to arrange for future control era and conveyance. Stack estimating can be classified into short-term stack estimating (STLF), medium-term

stack determining (MTLF) and long-term stack determining (LTLF). Therefore, it is very important to use appropriate methods for this issue.

It can be seen from the above studies that various models have been used in this field. However, there are still some advanced computational frameworks including hybrid models and fuzzy logic-based models and their capacities in electricity supply model of conventional residential buildings have not been widely studied. Considering the above gaps in the literature, this study was motivated to develop and applied of ANFIS versatile fuzzy-neural deduction system in electricity supply. This study is a long-term study that has not been used in many other studies.

3. FOUNDATION OF APPLICATION OF ANFIS VERSATILE FUZZY-NEURAL DEDUCTION SYSTEM

Building energy utilization may be a basic variable, not as it were in logical investigation but moreover in taken a toll examination. Subsequently, tall precision in creating the energy utilization is fundamental since belittling vitality utilization can lead to potential blackouts that can be negative to social and financial ways of life. In differentiate, overestimation leads to superfluous unemployment capacity. Besides, as a result, squandered monetary assets. Subsequently, a few considers have been performed to foresee vitality utilization with diverse factual models and approaches precisely. Since ordinary statistical models require a noteworthy sum of collected information and are moderately exact for straight information, neural organize models can calculate nonlinear information. Properties are watched at diverse electrical loads by urban meter readings [14].

Adaptive fuzzy-neural induction system (ANFIS), which best coordinating the highlights of fuzzy frameworks and neural networks, is characterized by Jang et al. [22]. As a structure, ANFIS incorporates if-else rules and employments fuzzy combine input-output information neural organize learning calculations for the preparation (Figure 1). An versatile fuzzy-neural

deduction framework mimics complex nonlinear mapping utilizing neural arrange learning and fuzzy deduction strategies. The ANFIS structure comprises of two models, ANN and fuzzy rationale, and can work with ill defined commotion and wrong situations. ANFIS is utilized within the neural arrange prepare to alter the enrollment work and parameters related to the information in address. It has more exact comes about than the cruel square squared mistake degree since it can misuse master decisions. ANFIS learning calculation may be a crossover learning calculation employing a post-diffusion learning calculation and the least-squares strategy [2].

4. MODELING APPROACH

4. 1. ANFIS Adaptive Neural-fuzzy Inference System

Various structures have been proposed to implement a fuzzy system by neural networks. The difference between a fuzzy-neural network principle and an artificial neural network is that the weights and values of the neural network input and output are defined as fuzzy numbers.

The neural-fuzzy inference system is one of the most accurate measuring tools for ambiguous and nonlinear concepts. In recent years, robust fuzzy inference systems based on the ANFIS adaptive neural network have been used in various sciences. Using the training power of neural networks and the capabilities of fuzzy systems, these types of systems have been able to use the advantages of these two in analyzing robust complex processes and modeling. ANFIS model is very suitable for describing and interpreting nonlinear systems. According to Figure 1, the steps of designing the optimal fuzzy-neural are as follows:

1. Get preparing data.
2. Make a essential fuzzy system.
3. Altering the parameters of the essential fuzzy framework agreeing to the modeling blunder work by the optimization algorithm.
4. Return the fluffy framework with the finest values of the parameters as the ultimate result.

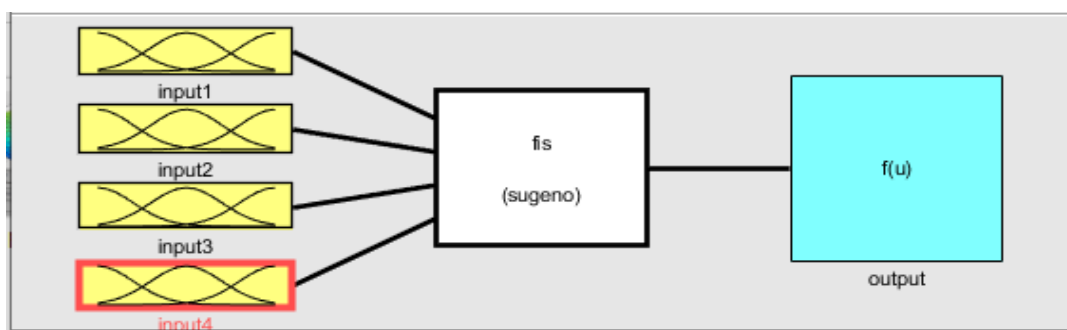


Figure 1. Overview of the fuzzy inference system

5. RESEARCH METHODOLOGY

Concurring to the reason of this investigate, the connected sort (utilizing the demonstrate to foresee energy consumption and generation amid the year for private buildings) and multi-criteria decision-making strategies have been utilized. The optimization segment is displayed utilizing ANFIS adaptive fuzzy-neural deduction framework calculation and MATLAB program.

5. 1. Input Data

5. 1. 1. Energy Load of a Residential Building As an essential parameter, electricity demand must be determined. Electric charge analysis is performed by considering the ordinary utilization of people within the chosen case consider. Family power request for each month is calculated based on its information. In arrange to supply comes about based on reality and, so, as much as conceivable, the foremost common sorts of cooling and warming frameworks within the city that evaporative cooling and water warming advances are considered. Also, the calculation of electric charge is done assuming standard equipment such as TVs, lamps, refrigerators, etc. Figure 2 shows the household electricity consumption index for a year. According to this figure, 3604 kWh of electricity is consumed by households during a year [31].

A parameter has been introduced for electricity consumption in residential houses, which varies depending on the year-day schedule, i.e., $24 * 365$, the year's position. The substance of the database is the sum of energy utilization of a private building amid this period, i.e., 8760 lines (per year).

According to Figures 2 and 3, the average monthly consumption of each household in Tehran is 300 kWh,

the minimum daily consumption is 300 Wh, and the maximum is 1.5 kWh. Using MATLAB software, datarand function are defined, and random amounts of energy consumption per energy consumption of three conventional residential buildings in Tehran are prepared. Conventional buildings refer to buildings up to 7 floors, which include the main urban buildings in Tehran that have access to renewable energy from wind and solar and the city's electricity source. This data is related to three apartment buildings of four, six, and eight units in Tehran and has been prepared for three years. According to Figures 2 and 3, the annual and seasonal electricity consumption of the building in Tehran, in the case of buildings 4, 6, and 8 units, energy consumption is estimated at 12,00, 18,00, and 25,00 kWh, respectively. The available data are presented in three Excel files (for each building), which include the amount of energy consumed by each building. These files have three columns (for each year of data recording) and 8670 rows (for each hour of the day during 365 days of the year) and show the amount of energy consumption of each residential building in Wh. In the above three buildings, renewable wind and solar energies have been used by installing wind turbines and solar panels on their roofs.

5. 1. 2. Solar Radiation Solar radiation information for Tehran have been gotten from the Meteorological Organization. The worldwide solar radiation is flat for Tehran by year, hour, and day, as appeared in Figure 4. The crest of daylight is in June and July, whereas January has the least sum of solar radiation [27].

In this research, one of the foremost common sorts of solar boards accessible within the Iranian advertise, to be specific the sharp of panel, model ND-240QCJ, has an output power of 240 watts and has dimensions of $994 \times 1640 \times 46$ mm. Due to the application of the

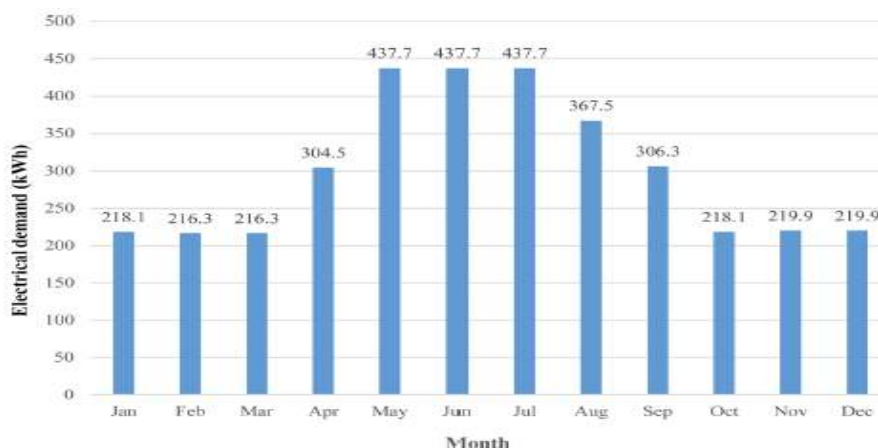


Figure 2. Details of household electricity consumption (energy load) during a year in Tehran [33]

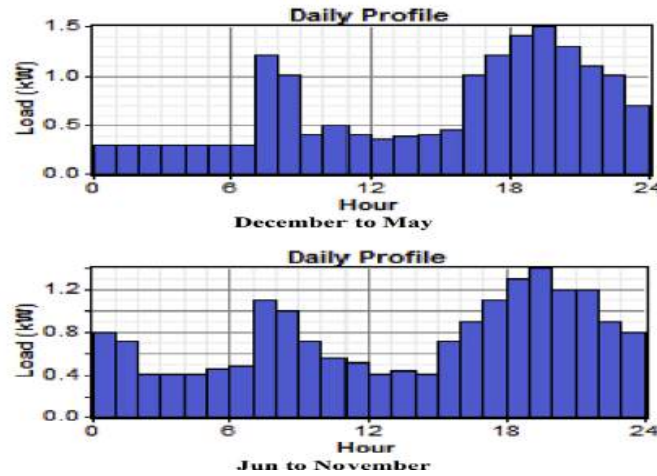


Figure 3. Seasonal household energy consumption in Tehran [27]

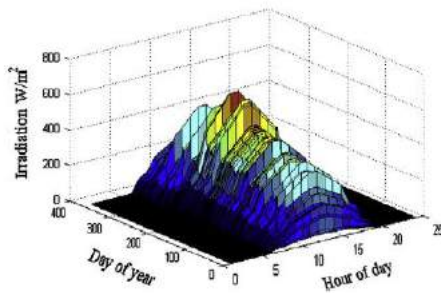


Figure 4. Hourly and daily horizontal solar radiation for Tehran, Iran [29]

manufacturer's output error (about 5%) and the effect of pollution and dust (equivalent to 5%) and the effect of daily temperature (12.5%) and loss coefficient in system cables (5%) and converter efficiency (92%), The output power output of the panel is reduced. In Tehran, the number of hours in which the amount of solar radiation energy is equal to one KWh/m² is equal to 5, which is defined as Peak Sun Hours (PSH). Therefore, the maximum amount of daily energy produced by each panel with the above specifications is calculated as follows:

$$240 \times 0.95 \times 0.95 \times 0.875 \times 0.95 \times 0.92 \times 5 = 0.828 \text{ KWh}$$

On the roofs of 4, 6, and 8 unit buildings, twelve, eighteen, and twenty-four panels with the above specifications and an angle of 30 degrees, which according to Table 1, have the highest efficiency during the year, have been installed respectively. Using MATLAB software, a datarand function is defined, and arbitrary values of solar electricity generation based on generation at distinctive hours of the day and distinctive months of the year (Table 1) in Tehran were prepared. The available data are presented in the form of three

Excel files (for each building) that represent the solar energy production values. These files have three columns (for each year of data recording) and 8670 rows (for each hour of the day during 365 days of the year) and show the energy production values of each residential building in Wh.

5. 1. 3. Wind Speed Tehran's 10-year average wind speed information are gotten based on month to month values given by the Meteorological Organization of Iran and are appeared in Figure 6. Wind information were measured at three-hour interims at an elevation of 10 m. Appropriately, the most noteworthy average month to month wind speed in April is 5 meters per second and the average wind speed in all months of the year is between 3 to 5 meters per second [27].

5. 1. 4. Wind Turbine In this research, a NEW SKY MAX800W home wind turbine has been used to supply wind energy. This turbine is operated with a minimum wind speed of 1.5 meters per second, suitable for Tehran. The roof of the buildings 4, 6, and 8 units, a wind turbine the specifications of Figure 6, is installed in the direction of the prevailing wind in Tehran, from southwest-northeast, which has the highest efficiency of the year. Using MATLAB software, a Datarand function is defined. Random values of wind energy production are based on wind speed at diverse time of the day and diverse months of the year (Figure 5) in Tehran and turbine production capacity and its characteristics (Figure 6). It is provided. The available data are presented in three Excel files (for each building) that represent the values of wind energy production of each building. These files have three columns (for each year of data recording) and 8670 rows (for each hour of the day during 365 days of the year) and show the wind energy production values in Wh.

TABLE 1. Tehran's monthly solar radiation for different slope angles [33]

Season	Month	Monthly solar radiation for $\theta = 0$ (kWh.m ⁻²)	Monthly solar radiation for $\theta = 30$ (kWh.m ⁻²)	Monthly solar radiation for $\theta = 60$ (kWh.m ⁻²)	Monthly solar radiation for $\theta = 90$ (kWh.m ⁻²)
Winter	December	68.49	115.88	132.22	113.13
	January	75.75	123.83	138.73	116.46
	February	100.83	145.95	151.97	117.26
Spring	March	128.58	161.78	151.62	100.84
	April	162.00	180.28	150.26	79.97
	May	189.57	192.97	144.66	57.59
Summer	June	219.39	214.16	151.54	48.32
	July	214.89	212.92	153.89	53.64
	August	200.16	212.28	167.53	77.88
Fall	September	170.16	201.09	178.13	107.45
	October	125.73	169.96	168.64	122.14
	November	87.24	135.28	147.08	119.46

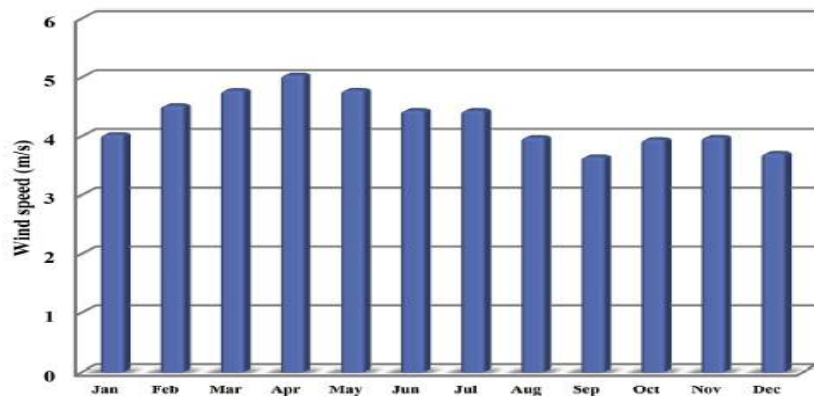


Figure 5. Monthly specifications of daily wind speed data for Tehran, Iran [29]

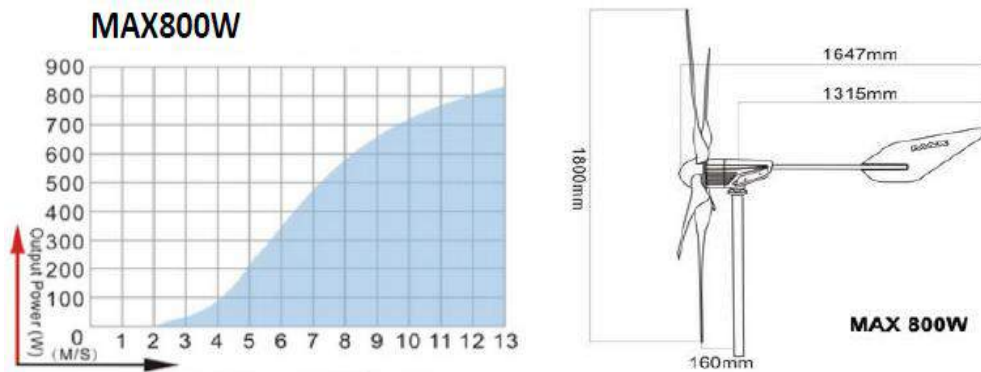


Figure 6. Physical characteristics and power curve of MAX800W turbine

The prepared database contains the consumption and production of wind and solar turbine energies during a period (8760 hours per year) separate for all three buildings.

5. 2. Mackey-Glass Equation The Mackey Glass equation could be a nonlinear time-delay differential condition concurring to Equation (3).

$$\frac{dx}{dt} = \beta \frac{x_\tau}{1+x_\tau^n} - \gamma x, \quad \gamma, \beta, n > 0. \tag{3}$$

That $\beta, \gamma, \tau,$ and n are real numbers, and x_τ indicating the variable x at time $t-\tau$. Depending on the values of the parameters, this condition appears a range of occasional and chaotic elements (Figure 7). From a biological point of view and its mathematical properties, this equation is used to predict time series and some other problems.

The ANFIS adaptive fuzzy-neural inference system is utilized to get ready a time arrangement forecast demonstrate created by the McKee-Glass time-delay differential condition. In time series prediction, known values of time series t are used to predict the value at a future point $t + p$. When predicting, it is assumed that the behavior of this system is constant at different times, and not much change in the behavior of the system should be observed. Furthermore, that is why there is predictability.

Based on the past behavior of the system and using mathematical tools and statistical analysis, the future of the system can be estimated. This system also has Markov properties, and by referring to the little part of the system, it offers a formula for predicting the future. The general concept of this system is given in Figure 8.

$$X(t) = f(x(t-1), x(t-2), \dots, x(t-d))$$

Nonlinear Differential Equation (4)

In the time series prediction structure, using an estimated function $f(.)$ Moreover, using past time data, the future is predicted so that the prediction error is minimized. In this case, it is necessary to use the approximate functions of approximation of functions (regression, ANN, ANFIS, Fuzzy, ...). The artificial neural network ANN and ANFIS have been used in this study.

5. 3. Features and Specifications of the Fuzzy-neural Adaptive Inference System (ANFIS) In this research, the adaptive fuzzy-neural inference system, according to the programs written in MATLAB software, is responsible for predicting (modeling) energy consumption values over time. This system uses 70% of

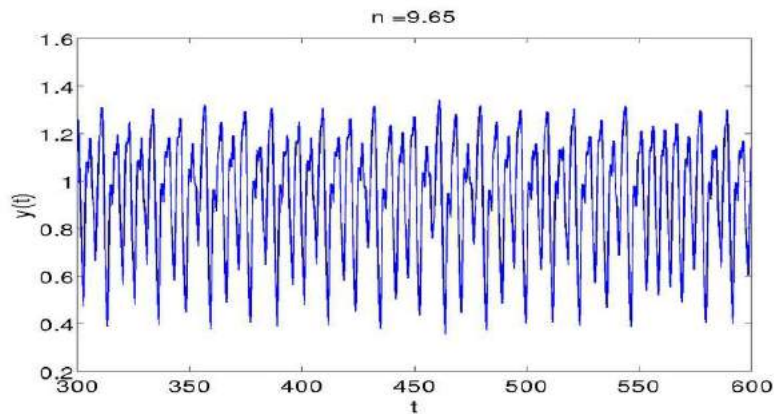


Figure 7. Dynamics in the Mackey-Glass equation, Equation (3), for $\gamma = 1, \beta = 2, \tau = 2,$ and $n = 9.65$

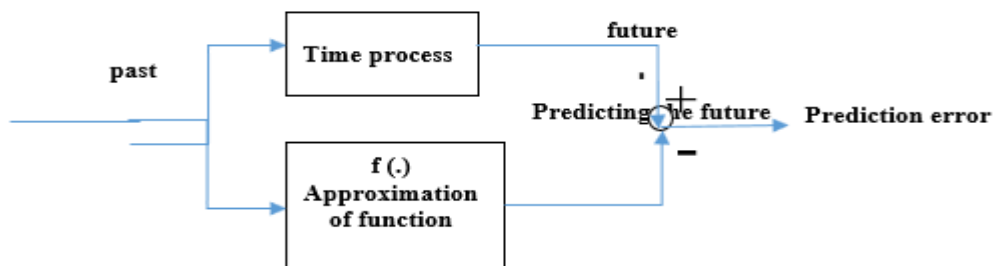


Figure 8. Time series prediction structure and prediction error determination

the input data for network training and 30% for test data. Here, three types of genes are used to design ANFIS, which include:

GENFIS 1 Grid Partition: The data generates a single-output fuzzy inference system of the SUGENO type using a network partition on the data. The type of Gaussian input function is GAUSSMF (Gaussian membership function), and the type of membership function is linear output.

GENFIS 2 (Sub Clustering): A SUGENO FIS structure. It was made utilizing subtraction clustering. Besides, it requires partitioned sets of input and output information as input contentions, which have a infiltration span.

GENFIS 3 (FCM): Utilizing fuzzy c-means clustering, FCM produces a FIS by extricating a set of rules that models information behavior. Given that there's as it were one output, GENFIS 3 has made an starting FIS for ANFIS preparing. The number of clusters is break even with to 10, the number of segments of frameworks is break even with to 2, the greatest number of cycles is rise to to 100, and the least sum of framework advancement is break even with to $1e-5$ (Figure 9).

The number of repetitions of Epochs training here is 100, the target for error rate is zero, the starting step measure is 0.01, the step estimate decrease rate is 0.9, and the step measure increment rate is 1.1. This method usually gives better results than genfis1 and GENFIS2. In this research, this method has been used to predict the amount of energy consumption and production.

5. 3. 1. Output Membership Function Type This method is suitable for multi-input and multi-output

calculations with any level of complexity. The error can be reduced by determining the number of clusters in a targeted way. In the following figure, we can see the relationship between software applications based on the choice of each of the GENFIS methods (Figure 9). (The following is the choice for the FCM method).

5. 4. Steps of Conducting Research

1. Extractable energy values are introduced from solar boards and wind turbines, and the energy utilization of each building gotten by Datarand functions is used as input parameters of the ANFIS fuzzy-neural network. Each file has three columns, each representing the amount of energy produced or consumed for one year in terms of Wh.

2. ANFIS fuzzy-neural network using the data of the first and second columns of the Datarand record in terms of prepared time and predicts the sum of energy generation from renewable sources and energy utilization in each building utilizing the method (FCM) GENFIS3 (CONP, SUNP, WINDP).

3. The values of the third column of each Datarand file are also considered as actual values of solar energy production and wind and energy consumption (RAE). Therefore, maximum renewable energy production (solar and wind) is also available (REM).

4. Predicted amounts of renewable energy from solar panels and wind turbines in each residential building are available separately every year in Wh. (RE).

5. The necessary calculations and outputs have been prepared for each of the buildings of four, six, and eight units separately using MATLAB software.

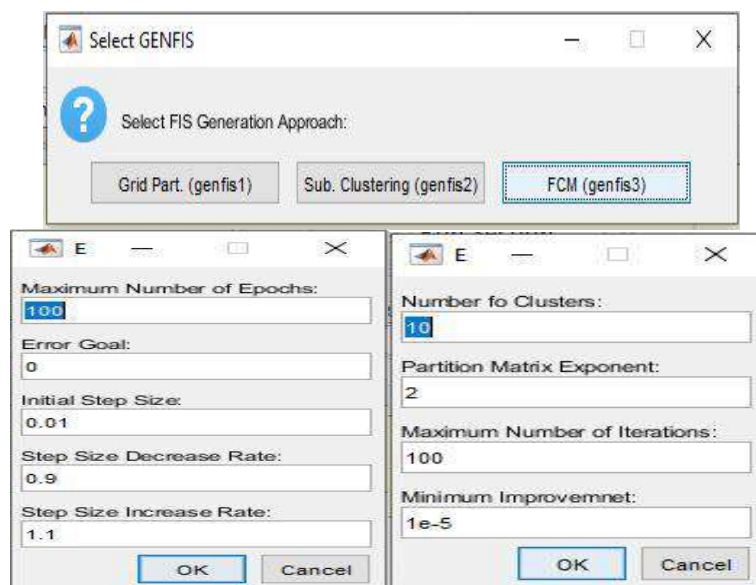


Figure 9. Applied relationship for selecting FCM design method in ANFIS in all three buildings

6. Energy Harvest Management (RAC) algorithm is such that the higher the amount of energy extracted from renewable sources (solar and wind), the lower the amount of harvest from the sources of the municipal electricity network. The ideal model is to supply all the electricity consumption of buildings from renewable energy sources. The worst-case scenario is to supply all the energy consumption of the building from the municipal electricity supply networks. In this study, the sum of energy extracted from renewable sources usually cannot exceed 2200 Wh, while the amount of consumption can be around 12000 Wh, even in an 8-unit building. According to the declared limits of fuzzy logic and ANFIS for the predicted values of production and consumption, in this system, the amount of energy allowed for withdrawal from the city network is determined by subtracting the total energy production from the maximum energy consumption (RAC) and increasing the actual value. The projected consumption values are considered a system error (CE).

7. Considering that the range of energy extractable from wind for all three buildings is between 0 to 200 Wh and sunlight between 0 to 2000 Wh (the existence of a home wind turbine and between 12 to 24 solar panels). The maximum energy extracted from renewable sources for buildings of 4, 6, and 8 units is about 1000, 1500, and 2000 Wh, respectively (REM).

8. The contrast between the entire and genuine generation of renewable energy (solar and wind) (RAE) and the total projected renewable energy production (RE) is considered as the amount of forecast error and the actual renewable energy production, i.e. (GE).

9. Finally, a statistical comparison between the values of CE, RE, RAE, and GE has been made.

6. FINDINGS AND RESEARCH RESULTS

In this investigate, the ANFIS versatile fuzzy-neural induction framework has been utilized to calculate the estimate of energy utilization and generation within the building. One of the foremost vital discoveries of this investigate is to plan a demonstrate for foreseeing vitality generation and utilization in private buildings utilizing the over apparatuses. The comes about appear that the network error is worthy, and their speed and capacity to memorize and effectiveness in assessing the generation and energy utilization of private buildings are exceptionally exact. First, we can examine the results obtained from the energy consumption in 4-unit building and examine its graphs.

The energy utilization of a four-unit building in Figure 10 is exceptionally comparative to the Mackey-Glass chart. Of course, the energy consumption of six- and eight-unit buildings are similar.

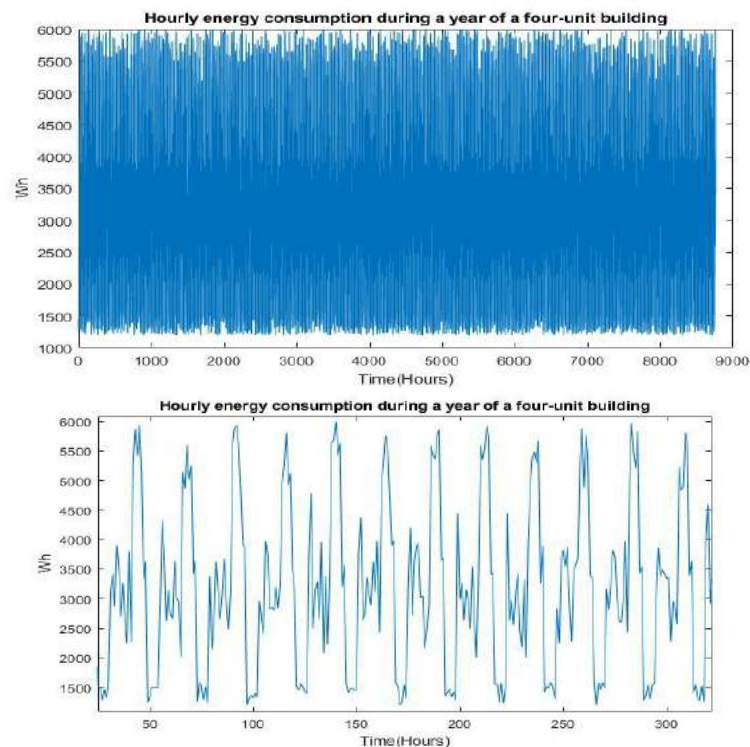


Figure 10. Energy consumption per year and over some time in a 4-unit building

By performing training and testing processes of the ANFIS adaptive fuzzy-neural inference system in all three buildings according to the applied settings (type of learning, number of steps, and error tolerance), the system error rate based on statistical indicators MSE, RMSE, R, mean, std is calculated. These statistical indicators are very suitable. In Figure 11, actual and projected of solar and wind energy production, MSE, RMSE, std and estimated regression equation for 8 unit building are shown in order as can be seen, the calculated

dispersion statistics of MSE=3324.47, RMSE=57.65, Std=57.66 and the value of R^2 is equal to 0.99, which shows a very good fit of this model.

Due to the large number of results obtained, the results obtained from different stages and the outputs of the ANFIS fuzzy-neural inference system related to all three buildings are presented in Table 2. The forecast accuracy in buildings is more than 99%, which is a sign of the proper performance of the designed model.

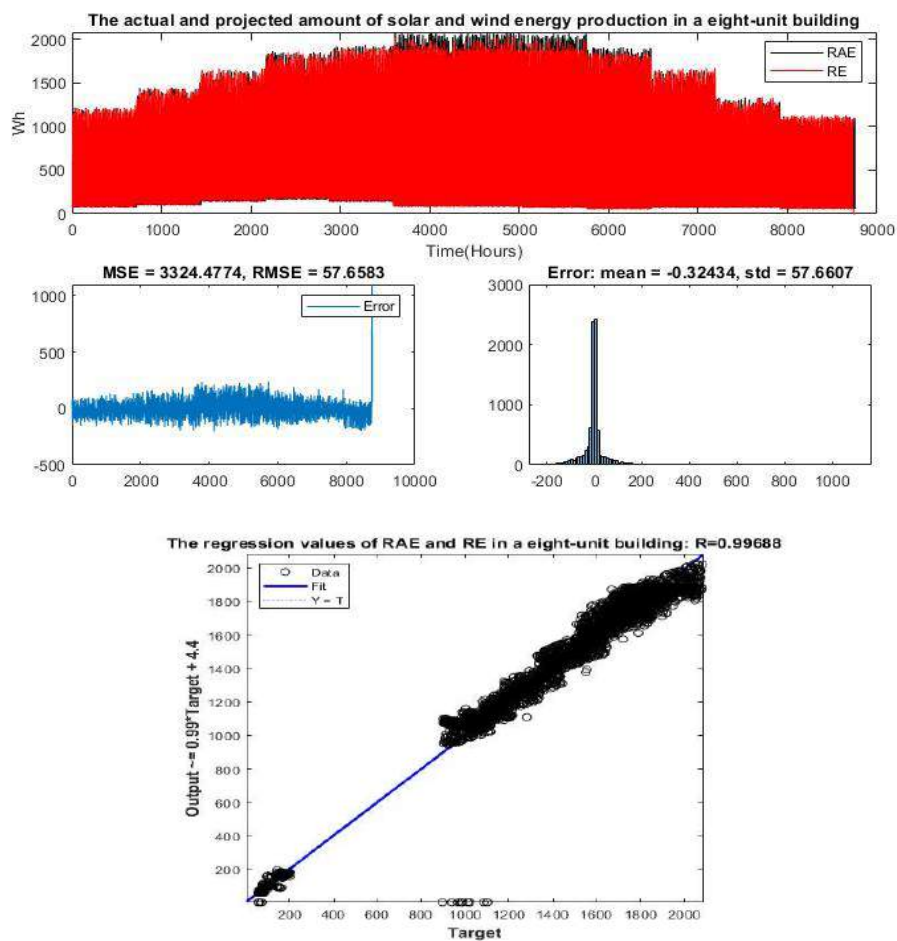


Figure 11. Actual values (RAE) and forecast (RE) of energy production of an 8-unit building using ANFIS

TABLE 2. Statistical indicators of MSE, RMSE, R, MEAN, and STD in ANFIS system in all three residential buildings

Statistical index	4-unit building	6-unit building	8-unit building
MSE	857.37	1864	3324
RMSE	29.28	43.17	57.66
R	0.9968	0.9970	0.9968
μ (mean)	0.67	1.31	0.32
σ (std)	29.28	43.17	57.66

Figures 12, 13, and 14 show the production, forecast, and average absolute error of solar and wind energy. Figures 15, 16, and 17 compare the actual and predicted production of solar and wind energy.

Here we can see the result obtained from the ANIFS system in Table 3. It can be seen that according to Table 3, the average value of energy production forecast error for a four-unit residential building (GE) is about 16 Wh. Also, according to Table 7, the average renewable energy

production is equal to $(3480402/8760) 397$ Wh. It means that the percentage of forecast error is equal to 4%. Therefore, the forecast accuracy is about 96%. The forecast accuracy in buildings of six and eight units is 96.5% and 96.3%, respectively, which is a sign of proper performance of the designed model. Figure 18 shows the absolute average error of energy consumption prediction during one year in an eight-unit building.

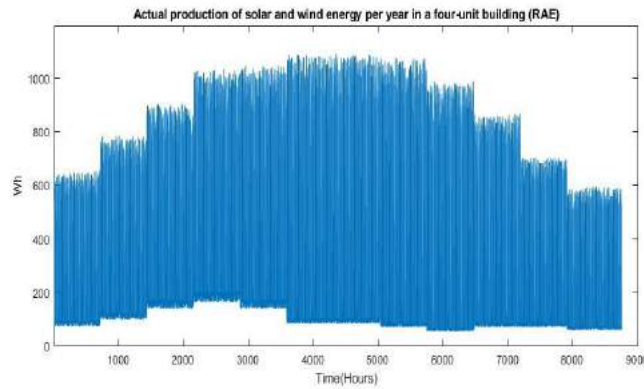


Figure 12. Real solar and wind energy production of a 4-unit building per year

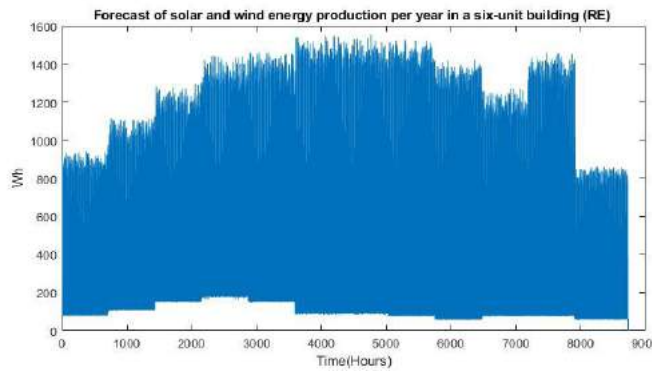


Figure 13. Forecast of solar energy and wind production of a six-unit building per year

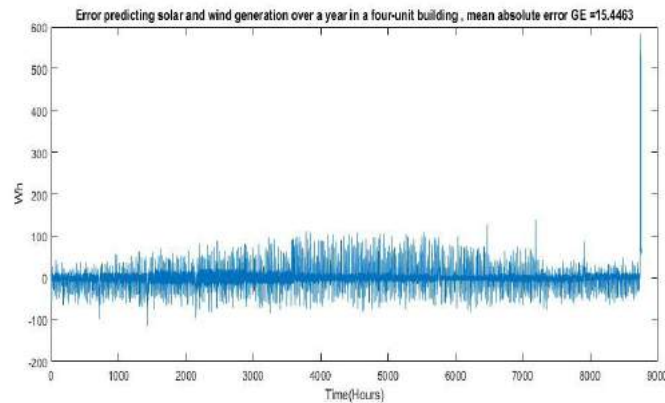


Figure 14. Absolute mean forecast error of solar and wind energy production during a year in a four-unit building

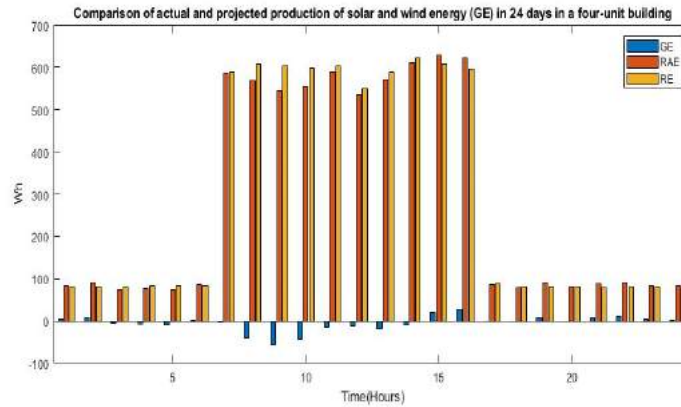


Figure 15. Comparison of actual and projected production of solar and wind energy (GE) in 24 hours in a four-unit building

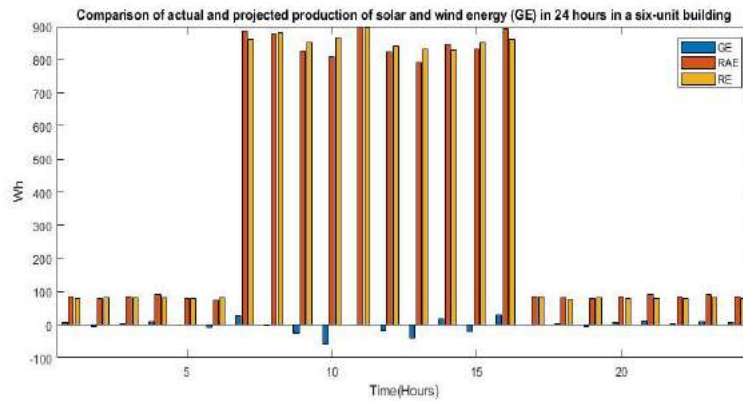


Figure 16. Comparison of actual and projected production of solar and wind energy (GE) in 24 hours in a six-unit building

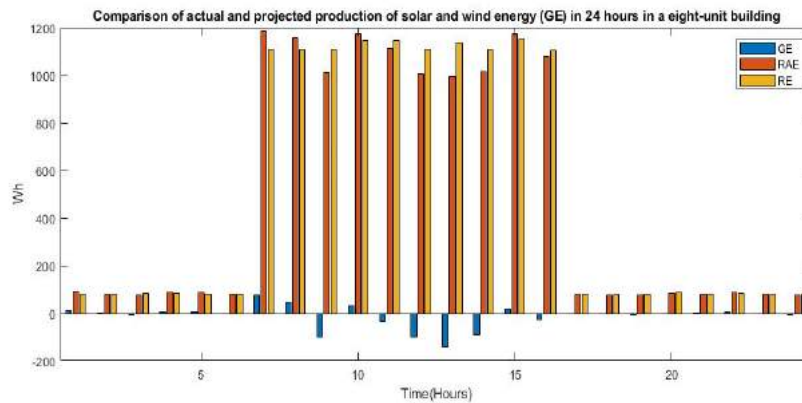


Figure 17. Comparison of actual and projected production of solar and wind energy (GE) in 24 hours in an eight-unit building

TABLE 3. Values of GE, CE, SM, and WM indices in ANFIS system in all three residential buildings

Index	4-unit building (Wh)	6-unit building (Wh)	8-unit building (Wh)
Average energy production forecast error (GE)	15.45	21.72	27.57
Average energy consumption forecast error (CE)	359	510	659
Maximum energy production from the sun (SM)	993	1490	1987
Maximum energy production from the wind (WM)	200	200	200

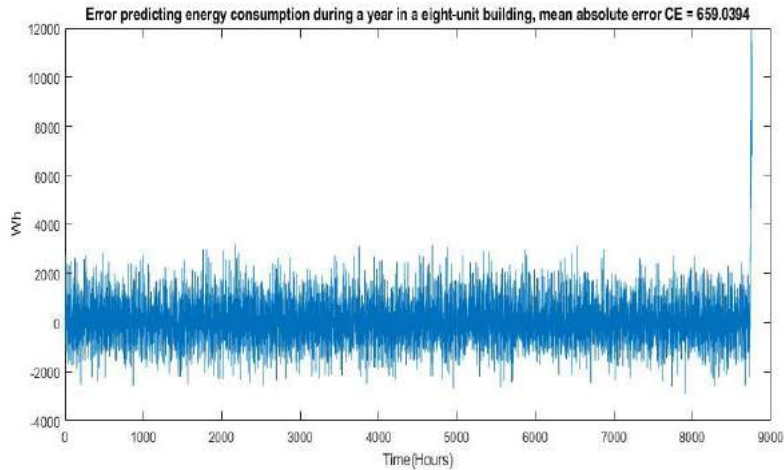


Figure 18. Absolute average of energy consumption forecast error during a year in an eight-unit building

According to Table 3, the average value of energy consumption forecast error for a four-unit residential building (CE) is 359 Wh. Also, according to reported data, the average energy utilization of the building is break even with to $(28237406/8760)$ 3223 Wh. That is means that the percentage of forecast error is equal to 11%. Therefore, the forecast accuracy is about 89%. Prediction accuracy in six- and eight-unit buildings is 89.5% and 90%, respectively, and this is a sign of acceptable performance of the model. Figures 19, 20 and 21 show the results of training, testing, and predicting energy consumption in buildings.

By use the general prediction processes of the ANFIS system and the obtained results, it was observed that the statistical distribution of energy production and consumption in all three buildings is entirely consistent with the normal distribution. The system error rate that calculated based on MSE, RMSE, μ , σ , and R statistical

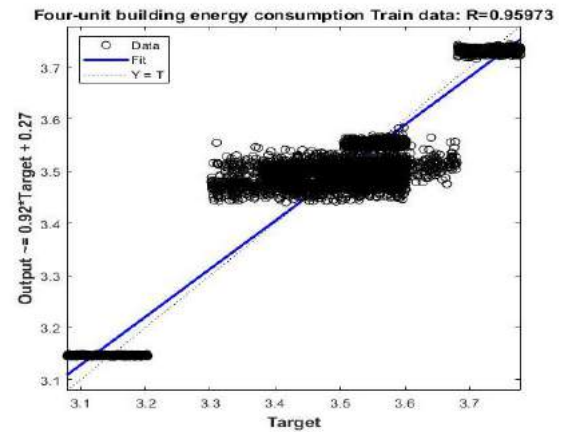
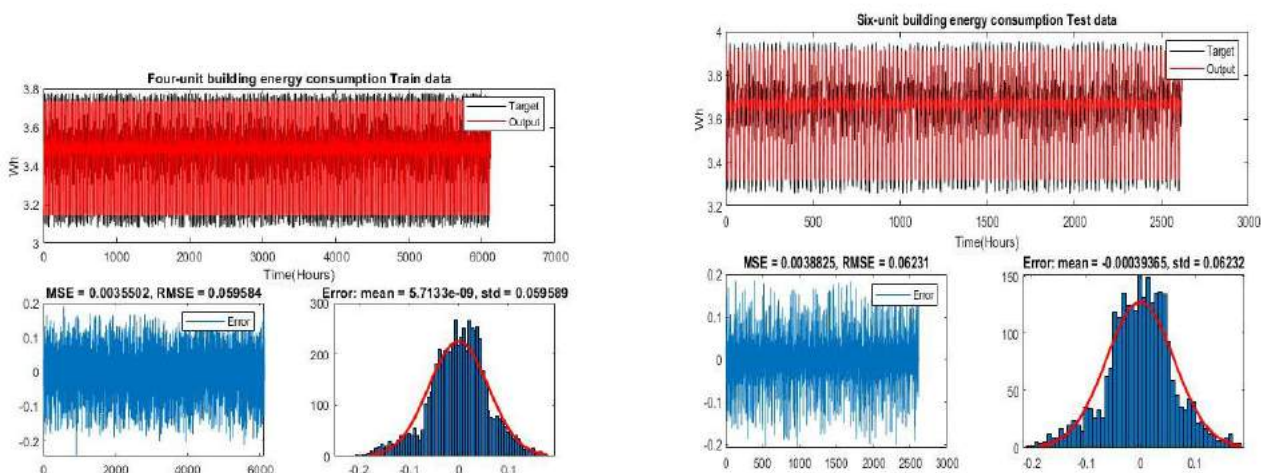


Figure 19. Results of energy consumption training in ANFIS four-unit building



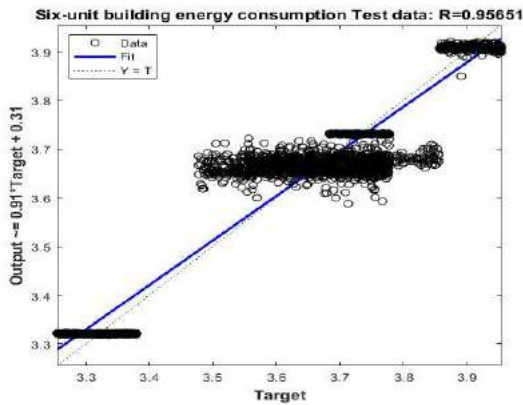


Figure 20. Energy consumption test results in ANFIS six-unit building

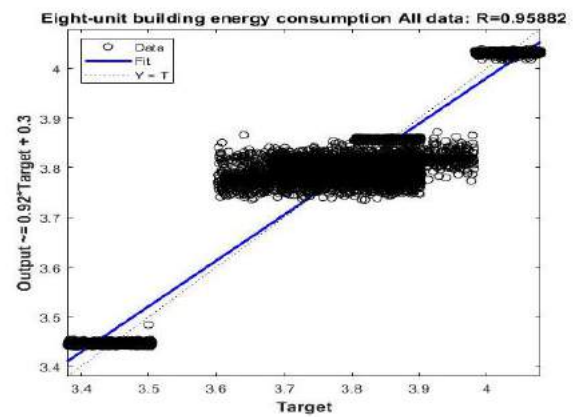
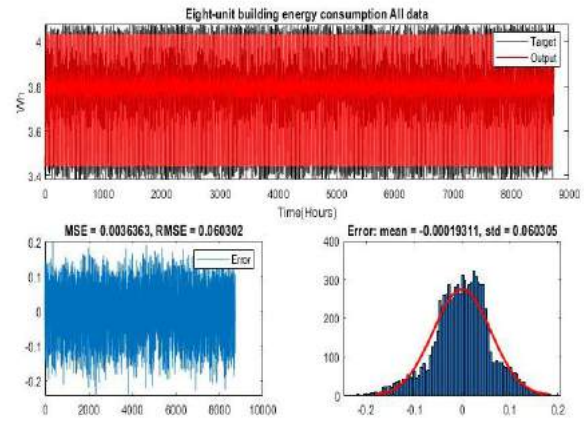


Figure 21. Energy consumption forecast results in ANFIS eight-unit building

indices are very little. The values of R in the outputs for energy consumption and production of solar energy and wind are 95%, 99%, and 97%, respectively, which is a sign of the proper performance of the designed model. Due to the large number of results obtained, the results of different stages of energy consumption forecasting from the output of the ANFIS fuzzy-neural induction framework related to all three buildings are displayed in Table 4. As can be seen, the value of MSE, RMSE, std are very small and are close to zero. therefore the fitted model has very little error, which shows its suitability. R square measure shows how well a regression model matches the data. So we can conclude that the bigger the R² measure, the better the model matches the data under investigation. As can be seen, this criterion is greater than 0.95 for all three building types. It provides a good and high explanation of the model. The std dispersion index also shows the dispersion (changes) of each data value around the average, and as can be seen, it has a small value in all three types of buildings, and shows the appropriateness of the model. Figures 22, 23 and 24 show the results of training, testing and forecasting solar energy production in buildings using a neural network and fuzzy inference system.

Due to the large number of results obtained, the results of different stages of predicting solar energy

production from the outputs of the ANFIS fuzzy-neural inference system for all three buildings are presented in Table 5.

Here also, all three important criteria MSE, RMSE and R² in solar energy production show the appropriateness of the model. As can be seen, the values of MSE and RMSE are very small and close to zero, and the value of R² is greater than 0.99 in all three types of buildings and is almost equal to one, which shows the very accurate fit of our model.

TABLE 4. Results of statistical indicators of energy consumption forecast with ANFIS in all three residential buildings

Statistical index	4-unit building			6-unit building			8-unit building		
	All Data	Train	Test	All Data	Train	Test	All Data	Train	Test
MSE	0.0036	0.0036	0.0037	0.0037	0.0036	0.0038	0.0036	0.0036	0.0036
RMSE	0.06	0.059	0.061	0.061	0.06	0.062	0.06	0.06	0.06
R	0.9589	0.9595	0.9574	0.9581	0.9586	0.9568	0.9587	0.9587	0.9587
μ (mean)	0.0004	0.0006	0.0013	0.0007	0.0006	0.0002	0.0002	0.0006	0.0007
σ (std)	0.06	0.059	0.061	0.061	0.06	0.062	0.06	0.06	0.06

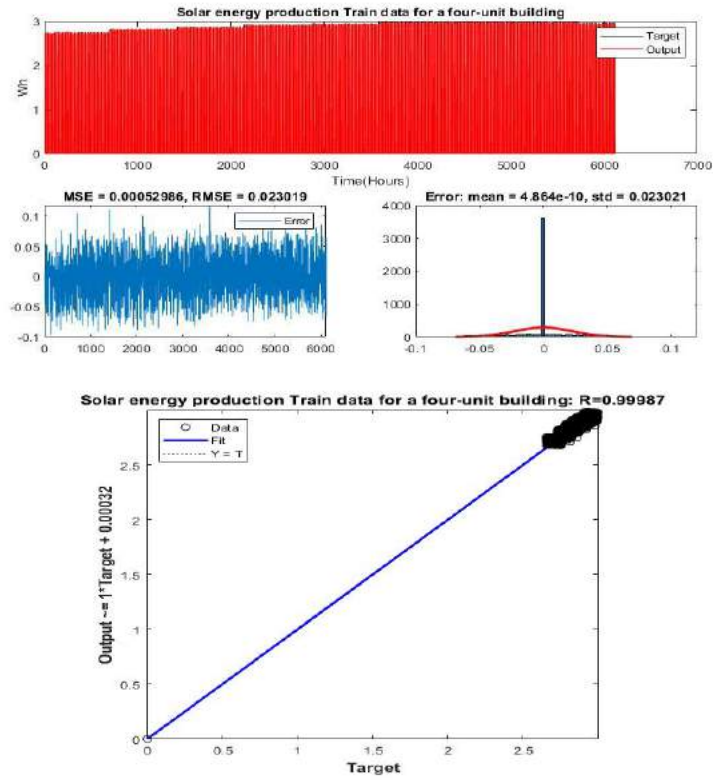


Figure 22. Results of solar energy production training in ANFIS four-unit building

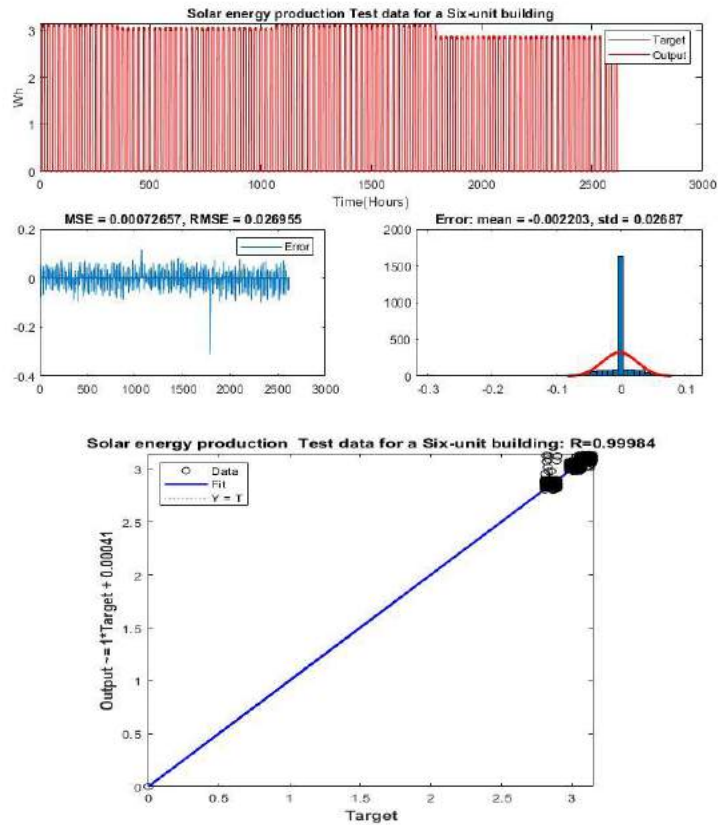


Figure 23. Results of a solar energy production test in ANFIS six-unit building

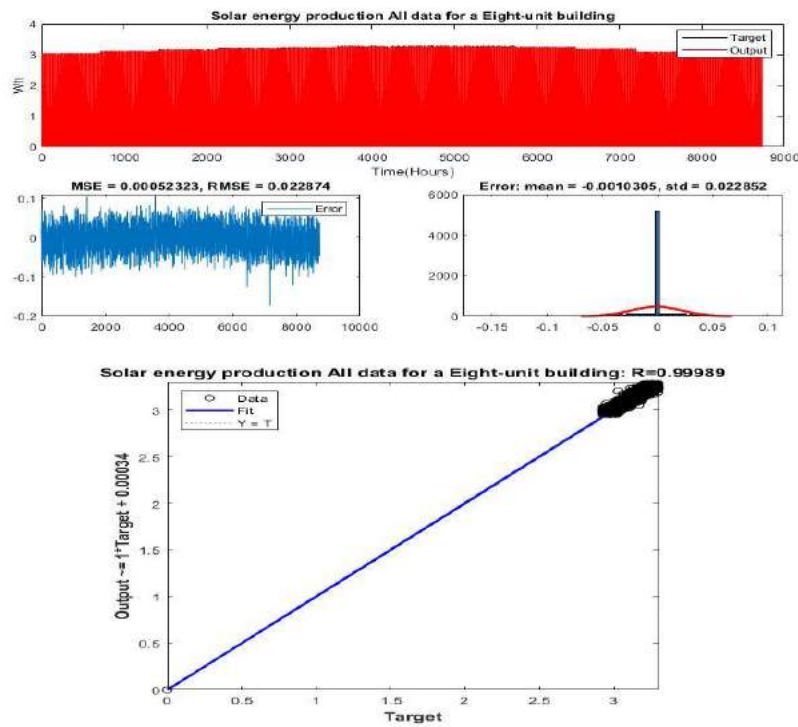


Figure 24. Results of solar energy production forecast in ANFIS eight-unit building

TABLE 5. Results of statistical indicators predicting solar energy production with ANFIS in all three residential buildings

Statistical index	4-unit building			6-unit building			8-unit building		
	All Data	Train	Test	All Data	Train	Test	All Data	Train	Test
MSE	0.0005	0.0005	0.0005	0.0005	0.0005	0.0007	0.0005	0.0005	0.0006
RMSE	0.023	0.023	0.024	0.023	0.022	0.027	0.022	0.022	0.024
R	0.9998	0.9998	0.9998	0.9998	0.9998	0.9998	0.9998	0.9999	0.9998
μ (mean)	0.0011	0.0004	0.0036	0.0011	0.0006	0.0037	0.0014	0.0004	0.0047
σ (std)	0.023	0.023	0.024	0.023	0.022	0.027	0.022	0.022	0.024

Due to the large number of results obtained, the results of different stages of predicting wind energy production from the outputs of the ANFIS fuzzy-neural deduction framework for all three buildings are displayed in Table 6. All three important criteria MSE, RMSE and R^2 in predicting wind energy production show the appropriateness of the model. As can be seen, the values

of MSE, RMSE, Std are very small and close to zero, and the value of R^2 is greater than 0.80 in all three types of buildings, which shows the very accurate fit of our model. Figures 25, 26, and 27 show the results of training, testing, and forecasting wind energy production in buildings using a neural network and fuzzy inference system.

TABLE 6. Results of statistical indicators predicting wind energy production with ANFIS in all three residential buildings

Statistical index	4-unit building			6-unit building			8-unit building		
	All Data	Train	Test	All Data	Train	Test	All Data	Train	Test
MSE	0.0011	0.0010	0.0014	0.0011	0.0010	0.0013	0.0011	0.0010	0.0013
RMSE	0.0338	0.0322	0.0375	0.0332	0.0318	0.0362	0.0336	0.0321	0.0366
R	0.9759	0.9764	0.7986	0.9767	0.9770	0.8073	0.9764	0.9765	0.8077
μ (mean)	0.0018	0.0003	0.0060	0.0013	0.0003	0.0045	0.0001	0.0005	0.0006
σ (std)	0.0338	0.0322	0.0370	0.0332	0.0318	0.0360	0.0336	0.0321	0.0361

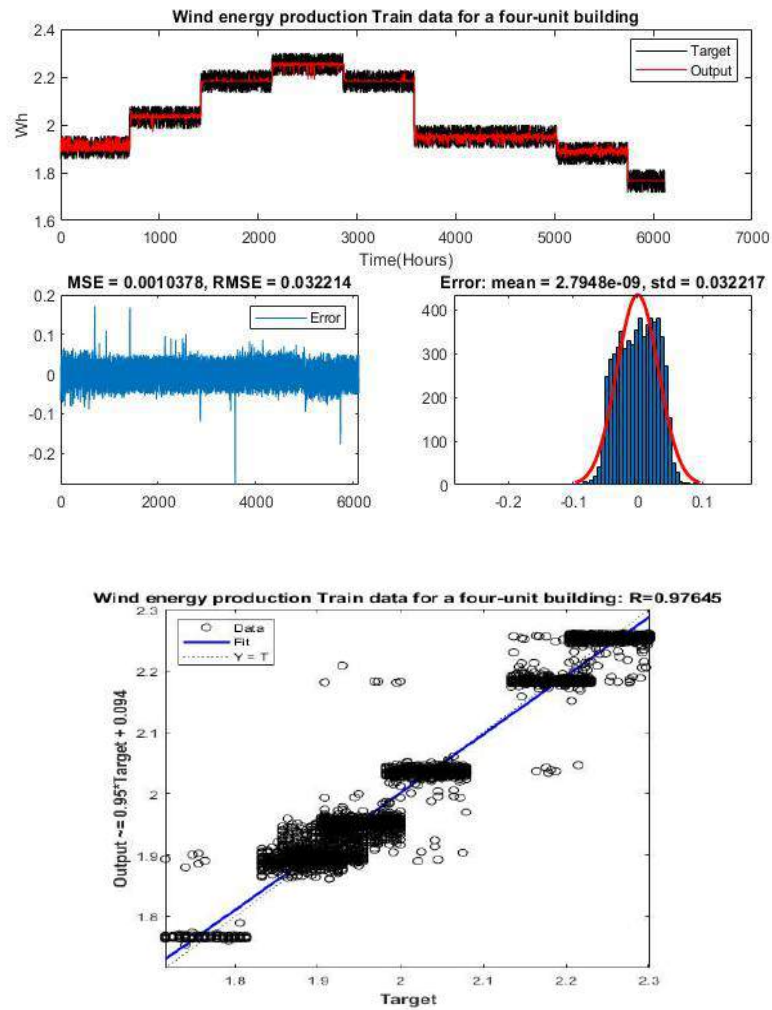
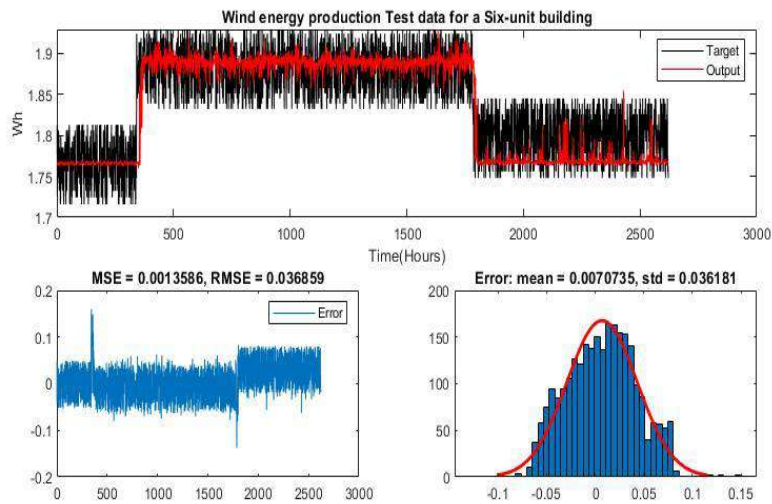


Figure 25. Results of wind energy generation training in ANFIS four-unit building



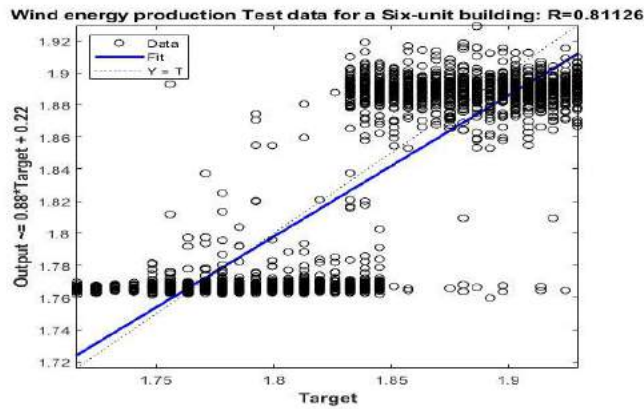


Figure 26. Results of wind energy production test in ANFIS six-unit building

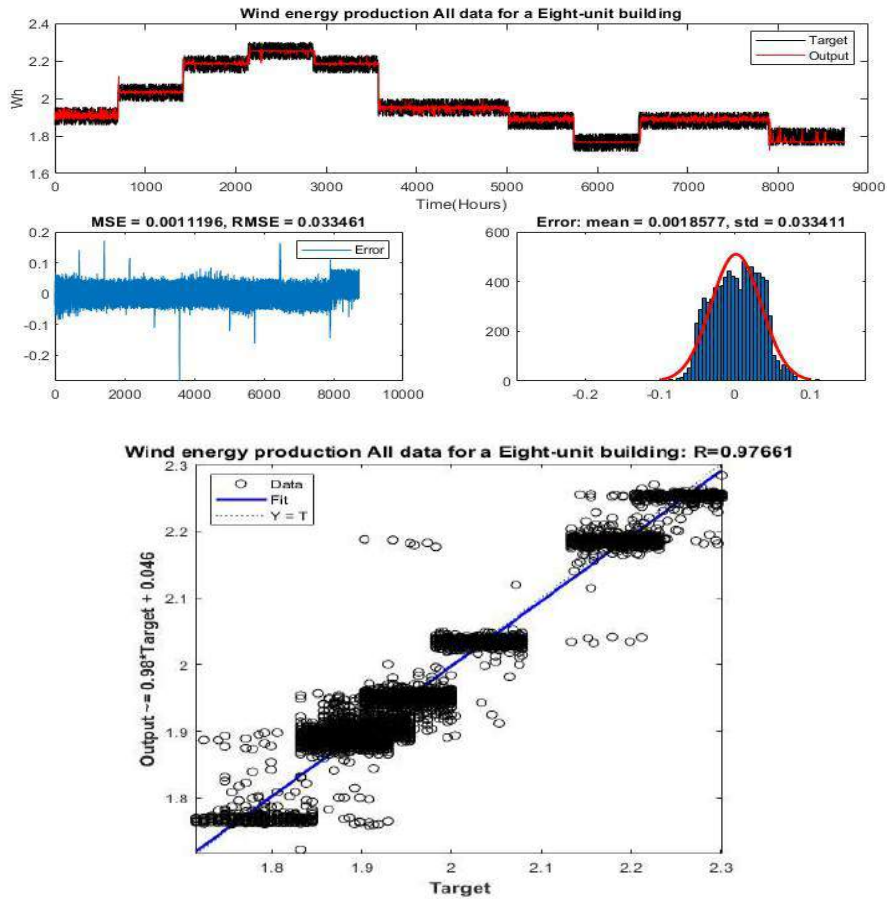


Figure 28. Results of wind energy production forecast in ANFIS eight-unit building

The statistical results presented in Table 7 generally show the performance of the ANFIS fuzzy-neural inference system in this study. In addition to high accuracy in forecasting energy consumption and production, management also determines the energy harvested from the city grid. Day and night, depending on the decisions of building managers. The results of this

research compared to similar studies showed better and clearer results regarding the use of wind or solar energy in residential houses.

One of the most important findings of this research is its primary purpose: to design and present a model for predicting the production and consumption of electricity in conventional residential buildings in Tehran. It has

TABLE 7. Statistical results of actual values and forecast of energy consumption and production with ANFIS in all three residential buildings

Index	4-unit building (Wh)	6-unit building (Wh)	8-unit building (Wh)
Total energy consumption per year (CONR)	28,237,406	42,309,124	56,513,748
Total solar energy production per year (SUNR)	2,603,772	4,025,784	5,191,003
Total wind energy production per year (WINDR)	876,630	876,578	876,375
Total forecast of energy consumption per year (CONP)	27,922,366	41,798,817	55,873,986
Total forecast of solar energy production per year (SUNP)	2,603,916	4,021,003	5,199,955
Total forecast of wind energy production per year (WINDP)	870,600	869,831	870,263
production of solar and wind energy per year (RAE)	3,480,402	4,902,362	6,067,378
Forecast of solar and wind energy production per year (RE)	3,474,516	4,890,835	6,070,219
The maximum energy that can be produced from the sun and wind (REM)	1,193	1,690	2,187
The amount of energy harvested from the national grid per year (RAC)	24,447,849	36,907,981	49,803,767

been prepared using ANFIS adaptive fuzzy-neural inference system with high accuracy and appropriate validity. The output of this research is an intelligent ANFIS system.

7. DISCUSSION AND CONCLUSION

In this paper, the application of an ANFIS for modelling of electricity supply model of conventional residential buildings in Tehran with priority on renewable energy has been demonstrated. By performing training and testing processes of the ANFIS adaptive fuzzy-neural inference system in three buildings according to the applied settings (type of learning, number of steps, and error tolerance), the system error rate based on statistical indicators MSE, RMSE, R, mean, std is calculated. The results of running the models showed that in all the models of actual and projected of solar and wind energy production and consumption. The criteria of dispersion and changes, MSE, RMSE, are very small, close to zero, and the coefficient of determination of the models (R) is also very high and shows the appropriateness of the estimated models. In addition, the values related to the determination of the total production of solar and wind energy per year (SUNR), the amount of energy harvested from the national grid per year (RAC), high accuracy in forecasting energy consumption and production, management also determines the energy harvested from the city grid. Therefore, It is shown that ANFIS with regard to clean and renewable energies, can predict electricity production and consumption pretty well.

8. DECLARATION OF COMPETING INTEREST

The authors declare that they have no known competing financial interests or personal relationships that could

have appeared to influence the work reported in this paper.

9. REFERENCES

- Baheri, A., Najafi, M., Azimi, A. and Aghanajafi, C., "A simplified model to predict and optimize energy consumption of residential buildings in the cold climate regions of Iran", *Energy Sources, Part A: Recovery, Utilization, and Environmental Effects*, (2020), 1-19. <https://doi.org/10.1080/15567036.2020.1859648>
- Ekici, B.B. and Aksoy, U.T., "Prediction of building energy needs in early stage of design by using anfis", *Expert Systems with Applications*, Vol. 38, No. 5, (2011), 5352-5358. <https://doi.org/10.1016/j.eswa.2010.10.021>
- Deif, A. and Vivek, T., "Understanding ai application dynamics in oil and gas supply chain management and development: A location perspective", *HighTech and Innovation Journal*, Vol. 3, (2022), 1-14. doi: 10.28991/HIJ-SP2022-03-01.
- Alrwashdeh, S.S., Ammari, H., Madanat, M.A. and Al-Falahat, A.a.M., "The effect of heat exchanger design on heat transfer rate and temperature distribution", *Emerging Science Journal*, Vol. 6, No. 1, (2022), 128-137. <http://dx.doi.org/10.28991/ESJ-2022-06-01-010>
- Tsanas, A. and Xifara, A., "Accurate quantitative estimation of energy performance of residential buildings using statistical machine learning tools", *Energy and Buildings*, Vol. 49, (2012), 560-567. <https://doi.org/10.1016/j.enbuild.2012.03.003>
- Platt, G., Li, J., Li, R., Poulton, G., James, G. and Wall, J., "Adaptive hvac zone modeling for sustainable buildings", *Energy and Buildings*, Vol. 42, No. 4, (2010), 412-421. <https://doi.org/10.1016/j.enbuild.2009.10.009>
- Seyedzadeh, S., Rahimian, F.P., Rastogi, P. and Glesk, I., "Tuning machine learning models for prediction of building energy loads", *Sustainable Cities and Society*, Vol. 47, (2019), 101484. <https://doi.org/10.1016/j.scs.2019.101484>
- Deb, C., Eang, L.S., Yang, J. and Santamouris, M., "Forecasting diurnal cooling energy load for institutional buildings using artificial neural networks", *Energy and Buildings*, Vol. 121, (2016), 284-297. <https://doi.org/10.1016/j.enbuild.2015.12.050>
- Yokoyama, R., Wakui, T. and Satake, R., "Prediction of energy demands using neural network with model identification by

- global optimization", *Energy Conversion and Management*, Vol. 50, No. 2, (2009), 319-327. <https://doi.org/10.1016/j.enconman.2008.09.017>
10. Li, X., Wen, J. and Bai, E.-W., "Developing a whole building cooling energy forecasting model for on-line operation optimization using proactive system identification", *Applied Energy*, Vol. 164, (2016), 69-88. <https://doi.org/10.1016/j.apenergy.2015.12.002>
 11. Shaikh, P.H., Nor, N.B.M., Nallagownden, P. and Elamvazuthi, I., "Intelligent multi-objective optimization for building energy and comfort management", *Journal of King Saud University-Engineering Sciences*, Vol. 30, No. 2, (2018), 195-204. <https://doi.org/10.1016/j.jksues.2016.03.001>
 12. Delgarm, N., Sajadi, B., Kowsary, F. and Delgarm, S., "Multi-objective optimization of the building energy performance: A simulation-based approach by means of particle swarm optimization (psa)", *Applied Energy*, Vol. 170, (2016), 293-303. <https://doi.org/10.1016/j.apenergy.2016.02.141>
 13. Buratti, C., Lascaro, E., Palladino, D. and Vergoni, M., "Building behavior simulation by means of artificial neural network in summer conditions", *Sustainability*, Vol. 6, No. 8, (2014), 5339-5353. <https://doi.org/10.3390/su6085339>
 14. Biswas, M.R., Robinson, M.D. and Fumo, N., "Prediction of residential building energy consumption: A neural network approach", *Energy*, Vol. 117, (2016), 84-92. <https://doi.org/10.1016/j.energy.2016.10.066>
 15. Amara, F., Agbossou, K., Dubé, Y., Kelouwani, S., Cardenas, A. and Hosseini, S.S., "A residual load modeling approach for household short-term load forecasting application", *Energy and Buildings*, Vol. 187, (2019), 132-143. <https://doi.org/10.1016/j.enbuild.2019.01.009>
 16. Chabaud, A., Eynard, J. and Grieu, S., "A new approach to energy resources management in a grid-connected building equipped with energy production and storage systems: A case study in the south of france", *Energy and Buildings*, Vol. 99, (2015), 9-31. <http://dx.doi.org/10.1016/j.enbuild.2015.04.007>
 17. Ciancio, V., Falasca, S., Golasi, I., Curci, G., Coppi, M. and Salata, F., "Influence of input climatic data on simulations of annual energy needs of a building: Energyplus and wrf modeling for a case study in rome (italy)", *Energies*, Vol. 11, No. 10, (2018), 2835. <https://doi.org/10.3390/en1102835>
 18. Alobaidi, M.H., Chebana, F. and Meguid, M.A., "Robust ensemble learning framework for day-ahead forecasting of household based energy consumption", *Applied Energy*, Vol. 212, (2018), 997-1012. <https://doi.org/10.1016/j.apenergy.2017.12.054>
 19. Nilashi, M., Dalvi-Esfahani, M., Ibrahim, O., Bagherifard, K., Mardani, A. and Zakuan, N., "A soft computing method for the prediction of energy performance of residential buildings", *Measurement*, Vol. 109, (2017), 268-280. <https://doi.org/10.1016/j.measurement.2017.05.048>
 20. Ullah, I., Ahmad, R. and Kim, D., "A prediction mechanism of energy consumption in residential buildings using hidden markov model", *Energies*, Vol. 11, No. 2, (2018), 358. <https://doi.org/10.3390/en11020358>
 21. Mocanu, E., Nguyen, P.H., Kling, W.L. and Gibescu, M., "Unsupervised energy prediction in a smart grid context using reinforcement cross-building transfer learning", *Energy and Buildings*, Vol. 116, (2016), 646-655. <https://doi.org/10.1016/j.enbuild.2016.01.030>
 22. Jang, J., Baek, J. and Leigh, S.-B., "Prediction of optimum heating timing based on artificial neural network by utilizing bems data", *Journal of Building Engineering*, Vol. 22, (2019), 66-74. <https://doi.org/10.1016/j.jobe.2018.11.012>
 23. Qiao, Q., Yunusa-Kaltungo, A. and Edwards, R.E., "Towards developing a systematic knowledge trend for building energy consumption prediction", *Journal of Building Engineering*, Vol. 35, (2021), 101967. <https://doi.org/10.1016/j.jobe.2020.101967>
 24. Naji, S., Shamshirband, S., Bassar, H., Keivani, A., Alengaram, U.J., Jumaat, M.Z. and Petković, D., "Application of adaptive neuro-fuzzy methodology for estimating building energy consumption", *Renewable and Sustainable Energy Reviews*, Vol. 53, (2016), 1520-1528. <https://doi.org/10.1016/j.rser.2015.09.062>
 25. Najafi, G., Ghobadian, B., Mamat, R., Yusaf, T. and Azmi, W., "Solar energy in iran: Current state and outlook", *Renewable and Sustainable Energy Reviews*, Vol. 49, (2015), 931-942. <https://doi.org/10.1016/j.rser.2015.04.056>
 26. Keyhani, A., Ghasemi-Varnamkhandi, M., Khanali, M. and Abbaszadeh, R., "An assessment of wind energy potential as a power generation source in the capital of iran, tehran", *Energy*, Vol. 35, No. 1, (2010), 188-201. <https://doi.org/10.1016/j.energy.2009.09.009>
 27. Fazelpour, F., Soltani, N. and Rosen, M.A., "Economic analysis of standalone hybrid energy systems for application in tehran, iran", *International Journal of Hydrogen Energy*, Vol. 41, No. 19, (2016), 7732-7743. <https://doi.org/10.1016/j.ijhydene.2016.01.113>
 28. Tahani, M., Babayan, N. and Pouyaei, A., "Optimization of pv/wind/battery stand-alone system, using hybrid fpa/sa algorithm and cfd simulation, case study: Tehran", *Energy Conversion and Management*, Vol. 106, (2015), 644-659. <https://doi.org/10.1016/j.enconman.2015.10.011>
 29. Shivam, K., Tzou, J.-C. and Wu, S.-C., "A multi-objective predictive energy management strategy for residential grid-connected pv-battery hybrid systems based on machine learning technique", *Energy Conversion and Management*, Vol. 237, (2021), 114103. <https://doi.org/10.1016/j.enconman.2021.114103>
 30. Taghavifar, H. and Zomorodian, Z.S., "Techno-economic viability of on grid micro-hybrid pv/wind/gen system for an educational building in iran", *Renewable and Sustainable Energy Reviews*, Vol. 143, (2021), 110877. <https://doi.org/10.1016/j.rser.2021.110877>
 31. Asrami, R.F., Sohani, A., Saedpanah, E. and Sayyaadi, H., "Towards achieving the best solution to utilize photovoltaic solar panels for residential buildings in urban areas", *Sustainable Cities and Society*, Vol. 71, (2021), 102968. <https://doi.org/10.1016/j.scs.2021.102968>
 32. Ehyaei, M. and Bahadori, M., "Selection of micro turbines to meet electrical and thermal energy needs of residential buildings in iran", *Energy and Buildings*, Vol. 39, No. 12, (2007), 1227-1234. <https://doi.org/10.1016/j.enbuild.2007.01.006>

COPYRIGHTS

©2023 The author(s). This is an open access article distributed under the terms of the Creative Commons Attribution (CC BY 4.0), which permits unrestricted use, distribution, and reproduction in any medium, as long as the original authors and source are cited. No permission is required from the authors or the publishers.



Persian Abstract

چکیده

موضوع مصرف انرژی خانوارها در بعد ملی، مساله ای اساسی است. استفاده از انرژی های تجدیدپذیر باعث کاهش استفاده از شبکه ملی تامین برق و کاهش مصرف سوخت های فسیلی در نیروگاه ها می شود و در فرآیند توسعه پایدار شهری موثر است. از جمله منابع تولید انرژی تجدیدپذیر در یک ساختمان مسکونی، انرژی خورشیدی و انرژی باد است. مدارهای منبع تغذیه و ولتاژ متغیر تا ولتاژ ثابت در ساختمان ها معمولاً از سیستم های ذخیره انرژی (باتری) استفاده می کنند. ظرفیت این باتری ها نیز محدود است، بنابراین مدیریت تولید، ذخیره سازی و مصرف انرژی بازیافتی نیاز مبرمی به الگوریتم های پیش بینی تولید دارد. در این تحقیق از سیستم استنتاج فازی-عصبی تطبیقی (ANFIS) و نرم افزار MATLAB برای پیش بینی تامین انرژی الکتریکی ساختمان های مسکونی استفاده شده است. همچنین از داده های تصادفی جمع آوری شده بر اساس میزان مصرف برق ساعتی ساختمان های مسکونی متعارف شهر تهران استفاده شده است. تولید انرژی خورشیدی و بادی توسط پنل های خورشیدی و توربین های بادی انجام شده است. برای ارزیابی مدل از شاخص های آماری استفاده شد. مقادیر به دست آمده به خوبی توانایی این مدل را در پیش بینی تولید و مصرف انرژی در ساختمان های مسکونی با دقت بالای حدود ۹۶ درصد و ۹۰ درصد نشان می دهد.



Numerical Simulation of Fiber-reinforced Concrete under Cyclic Loading using Extended Finite Element Method and Concrete Damaged Plasticity

S. El Yassari*, A. EL Ghoulbzouri

MODSGC Unit, National School of Applied Sciences Al Hoceima, University Abdelmalek Essaadi, Tangier, Morocco

PAPER INFO

Paper history:

Received 02 June 2023

Received in revised form 27 June 2023

Accepted 28 June 2023

Keywords:

Fiber Reinforced Concrete

Cyclic Loading

Concrete Damage Plasticity

Steel Fiber

Polypropylene Fiber

Extended Finite Element Method

ABSTRACT

In recent years, the scientific community has shown a growing interest in fiber-reinforced concrete (FRC) for modern structures due to its enhanced ductility compared to traditional reinforced concrete (RC). This paper introduces an analytical model that incorporates a comprehensive fiber reinforcing index (RI) to study various types of FRC. The analysis focuses on the compressive and tensile behaviors, damage evolution under cyclic loading, and crack propagation in the concrete matrix. To effectively simulate crack initiation and propagation in FRC structures, the extended finite element method (XFEM) is employed, leveraging its fracture-solving capabilities. Additionally, the XFEM is combined with the concrete damaged plasticity (CDP) modeling approach to examine the quasi-static and hysteretic performance of FRC columns. Three-dimensional nonlinear finite element models are constructed using the commercial software Abaqus. These models incorporate steel fibers, polypropylene fibers, and a combination of both types of fibers in the FRC structures. Furthermore, the accuracy of the XFEM-CDP-based analysis in predicting hysteretic behavior is validated against results from previous research articles, demonstrating reasonable accuracy. It allows engineers to accurately capture the nonlinear behavior of concrete, including cracking, crushing, and plastic deformation, while also considering the complex crack patterns, providing a better understanding of the seismic performance of FRC structures using numerical simulations.

doi: 10.5829/ije.2023.36.10a.08

1. INTRODUCTION

During earthquakes, bridge columns are often the most vulnerable and deficient components, particularly when in moderate damage states [1]. Transverse stirrups in these columns are prone to deficiencies, leading to multiple damage states, ranging from concrete cracking to cover spalling, and eventually the failure of steel bars at the base of the columns.

The seismic performance of bridge columns can be significantly improved by enhancing their ductility, lateral stiffness, and energy dissipation capacity. Local increases in transverse stirrup density are the conventional method to enhance column ductility, but this approach presents challenges in construction and compromises the quality of concrete pouring [2, 3]. Consequently, fiber-reinforced concrete (FRC) has

emerged as an alternative to reinforced concrete (RC), with studies showing that partial or full substitution of RC with FRC can effectively enhance structural responses and repair damaged infrastructures [4-7]. Full substitution of RC columns with FRC has been proven effective in improving ductility and seismic behavior [2, 4, 8-11].

However, experimental studies on FRC have been abundant. A few efforts have been dedicated to developing constitutive relations and numerical modeling. Experimental approaches suffer from drawbacks such as the difficulty of setting up full-scale models and limited measurement ranges for capturing important parameters like bond-slip behavior, cracking, and plastic strain. Furthermore, experimental methods are time-consuming and costly.

*Corresponding author Email: soufiane.elyassari1@etu.uae.ac.ma
(S. El Yassari)

With the advancements in computer processing power and structural finite element theory, the finite element method has become an effective tool for analyzing the nonlinear and dynamic behavior of RC columns under seismic events. To accurately model the behavior of components such as steel reinforcements and the concrete matrix, precise and effective constitutive relationships are crucial. While constitutive models for steel have matured due to its isotropic nature, concrete presents challenges with its complex mechanical phenomena, including inelastic damage, cracking, hardening, and softening. Consequently, various analytical theories for concrete constitutive laws have been implemented in finite element programs.

The Concrete Damaged Plasticity (CDP) model, integrated with the concept of damaged elasticity, tensile and compressive plasticity, has gained research interest, particularly with the widespread use of the Abaqus software. The CDP model has shown good agreement between numerical predictions and test results for FRC behavior [12, 13]. However, CDP models only accurately predict material behavior prior to fracture initiation. One disadvantage is that these constitutive laws model material degradations and cracks in a smeared manner, failing to account for discontinuities in crack propagation and discrete cracks [14-16].

Several techniques have been proposed to address this issue. One approach is to remove elements when a damage parameter exceeds a critical value. However, this method alters the mass of the model and is sensitive to mesh configurations [15]. Cohesive crack models have also been proposed to simulate crack growth in FRC structures, considering the bridging action of aggregates and fibers. Although these models provide detailed information about concrete and fiber behavior separately, their implementation becomes challenging in complex loading cases and structures, limiting their applicability [13, 17-21].

Researchers have explored meshless methods and adaptive finite elements as alternatives [21, 22]. Cohesive crack models have been used to describe the fracture process zone in ductile and quasi-brittle materials [23, 24]. These models suppress stress and strain singularities at crack tips. Incorporating displacement jumps, XFEM allows for mesh-independent crack path determination [23]. XFEM enables smooth crack growth in finite element meshes without remeshing [23, 25]. Unlike cohesive crack models, XFEM does not require a predefined crack path, making it suitable for studying cracking behavior. However, existing XFEM models have primarily focused on predicting crack growth under monotonic loading, and the simulation of crack growth combined with material fatigue using XFEM remains unexplored.

In this paper, we propose coupling XFEM with the CDP model to simulate cyclic fatigue and cracking behavior in FRC. This combined model enables the

integration of fatigue damage accumulation and crack propagation stages into a comprehensive process. Numerical results obtained using the XFEM-CDP model are validated against independent experimental data with different fiber combinations. The effectiveness and accuracy of the proposed model are demonstrated, showing improved agreement with experimental results compared to classical CDP models.

2. MATERIALS AND METHODS

2. 1. Compressive Behavior Abadel et al. [26] developed an analytical model for predicting compressive stress-strain curves of HyFRC, which quantifies the effect of each type of fiber on compressive strength and stress-strain curves in terms of a comprehensive fibre reinforcing index. The model exhibited a correlation with experimental test results. The compressive behavior σ_c model was as follows:

$$\sigma_c = \left(\frac{\beta \left(\frac{\varepsilon_c}{\varepsilon_0} \right)}{\beta - 1 + \left(\frac{\varepsilon_c}{\varepsilon_0} \right)^\beta} \right) f_{cu} \quad (1)$$

where f_{cu} denotes the ultimate compressive stress, ε_c and ε_0 represents the compressive strain and the strain at peak stress of plain concrete (= 0,002), respectively.

The parameters can be calculated using the following equations:

$$\beta = 1 + 5e^{-1,376RI_v} \quad (2)$$

$$\beta_0 = 0,108f_c - 0,966 \quad (3)$$

$$f_{cfrc} = f_{c0} + 5,222RI_v \quad (4)$$

$$\varepsilon_{frc} = \varepsilon_{c0} + 0,0004RI_v \quad (5)$$

$$RI_v = \sum RI_{vi} \quad (6)$$

$$RI_{vi} = V_i \frac{l_i E_i}{d_i E_s} \quad (7)$$

For the plain concrete, the value of parameter β_0 can be calculated with the help of the Equation 3. RI_v , V_i , l_i , and d_i denote the reinforcing index, fibers' volume fraction, length, and diameter (or their corresponding diameter in non-circular sections), E_i and E_s are the fiber's and steel material's modulus of elasticity, respectively.

2. 2. Tensile Behavior

2. 2. 1. For Plain Concrete The stress-crack opening displacement relationship adopted for plain concrete was proposed to capture the tensile behavior.

$$\frac{\sigma_t}{f_t} = \left(1 + \left(c_1 \frac{w_t}{w_{cr}} \right)^3 \right) e^{(-c_1 \frac{w_t}{w_{cr}})} - \frac{w_t}{w_{cr}} (1 + c_1^3) e^{(-c_1)} \quad (8)$$

$$f_t = 1,4 \left(\frac{f_{cu}-8}{10} \right)^{2/3} \quad (9)$$

$$G_F = (0,0469d_a^2 - 0,5d_a + 26) \left(\frac{f_{cu}}{10} \right)^{0,7} \quad (10)$$

$$w_{cr} = 5,14 \frac{G_F}{f_t} \quad (11)$$

In these equations, the f_t is the tensile strengths of plain concrete, w_t , w_{cr} denotes the crack opening displacement and crack displacement at the complete loss of tensile stress, respectively. d_a and l_{eq} represent the maximum aggregate size of the concrete (20 mm) and the mesh element length, respectively.

2. 2. 1. For FRC Concerning the tensile behavior of FRC, $\sigma_t(w)$, Almusallam et al. [27] proposed an analytical model to describe the tensile softening behavior based on the reinforcing index, RIV. This model was obtained through inverse analysis and provides a good agreement with experimental results.

$$\sigma_t(w_t) = a_1 f_{tfrc} e^{(-a_2 w_t)} \quad (12)$$

$$a_1 = 0,75 \quad (13)$$

$$a_2 = 10e^{-4,3RIV} \quad (14)$$

$$f_{tfrc} = (f_t - 1) + e^{1,23RIV} \quad (15)$$

where f_{tfrc} denotes the tensile strength of FRC.

It was assumed that each element in the numerical simulation had a single crack. This assumption is suitable for optimal simulations. As a result, the strain in terms of crack opening can be determined by summing the elastic strain and the crack opening and dividing it by the element length.

$$\varepsilon_t = \varepsilon_{tm} + w_t/l_{eq} \quad (16)$$

ε_{tm} is the tensile strain corresponding to the tensile strengths.

2. 3. Concrete Damage Plasticity Model In this study, the behavior of steel was simulated using a uniaxial plasticity model, while a more comprehensive CDP model was employed for simulating the behavior of concrete. The CDP model, initially proposed by Lubliner et al. [28] and further developed by Lee and Fenves [29], combines scalar damaged elasticity with non-associated compressive and tensile plasticity to accurately capture the nonlinear deformation and irreversible damage of plain concrete and FRC under various loading conditions.

The CDP model has been refined over time to incorporate the fiber effect, allowing for the analysis of FRC's mechanical behavior with minor modifications. In

this study, the modified CDP model proposed by Chi et al. [12] was utilized.

2. 4. Damage Evolution Law For simplicity, this study used the model proposed by Chi et al. [12]. It can be used for different FRCs, and is easily calibrated with experimental results.

$$d_t = \frac{1}{e^{\frac{1}{m_t}-1}} \left(e^{-\frac{\varepsilon_{t,nom}^{ck}}{m_t}} - 1 \right) \quad (17)$$

$$d_c = \frac{1}{e^{\frac{1}{m_c}-1}} \left(e^{-\frac{\varepsilon_{c,nom}^{in}}{m_c}} - 1 \right) \quad (18)$$

$$\varepsilon_{t,nom}^{ck} = \frac{\varepsilon_t^{ck}}{\varepsilon_{tu}^{ck}} \quad (19)$$

$$\varepsilon_{c,nom}^{in} = \frac{\varepsilon_c^{in}}{\varepsilon_{cu}^{in}} \quad (20)$$

d_c , d_t are the uniaxial compressive and tensile damage variables. m_c , m_t , are the parameters that control damage evolution speed. $\varepsilon_{t,nom}^{ck}$, $\varepsilon_{c,nom}^{in}$ denote the normalized compressive and tensile inelastic strains.

ε_{tu}^{ck} , ε_{cu}^{in} , are the corresponding ultimate strains.

Typically, for plain concrete, Chi et al. [12] suggested the use of $m_t = 0,05$, $m_c = 0,1$, $\varepsilon_{cu}^{in} = 0,033$, $\varepsilon_{tu}^{ck} = 0,0033$.

The fitting of the uniaxial tension and compression simulations with experimental test data yield the exact values of m_t and m_c . For FRC, parameters m_c^{hf} and m_t^{hf} are modified according to the composite material theory as follows:

$$m_c^{hf} = m_c (1 + a_{m1} \lambda_{sf} + b_{m1} \lambda_{pf}) \quad (21)$$

$$m_t^{hf} = m_t (1 + a_{m2} \lambda_{sf} + b_{m2} \lambda_{pf}) \quad (22)$$

where λ_{sf} and λ_{pf} are the characteristic parameters of steel and polypropylene fibers, respectively.

In general, the volume fraction recommended for steel fibers is between 0.5 and 2.0 % to achieve optimal strength improvement and ductility. According to literature, an aspect ratio of 30–80, and a volume fraction of 0.05–0.2% are recommended for polypropylene fibers, to ensure even distribution of fibers [30].

The values $a_{m1} = 0.452$, $b_{m1} = 0.054$, $a_{m2} = 0.628$, and $b_{m2} = 0.156$ were recommended by Chi et al. [12]. The damage evolution law of the FRC specimens are shown in Figure 1.

2. 5. Parameter K_c^{hf} In the case of low hydrostatic stresses, the value $K_c = 2/3$ presents a close estimation of strength. However, for high hydrostatic stresses, a value of $K_c = 0.7$ is considered more appropriate [30].

Observations made by Chi et al. [30] indicate that the main effect on the compressive meridian is influenced by

steel fibers, unlike polypropylene fibers. Steel fibers are more effective in reducing crack propagation compared to polypropylene fibers. As a result, the tensile meridian experiences significant changes compared to the compressive meridian. Therefore, the coefficient K_c is expressed as follows:

$$K_c^{hf} = K_c \cdot \frac{k_t}{k_c} \tag{23}$$

where k_c and k_t are parameters introduced to account for the presence of fibers, as suggested by Rousakis et al. [31].

$$k_t = 1 + 0,080\lambda_{sf} + 0,132\lambda_{pf} \tag{24}$$

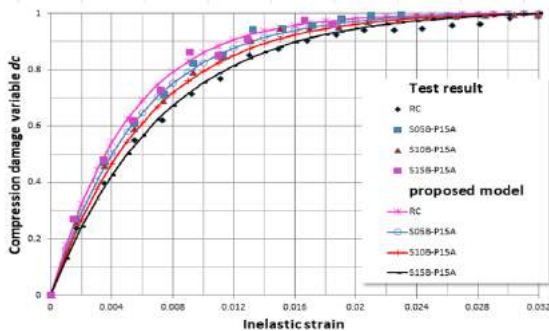
$$k_c = 1 + 0,056\lambda_{sf} \tag{25}$$

$$\lambda_{sf} = V_{sf} \frac{l_{sf}}{d_{sf}} \tag{26}$$

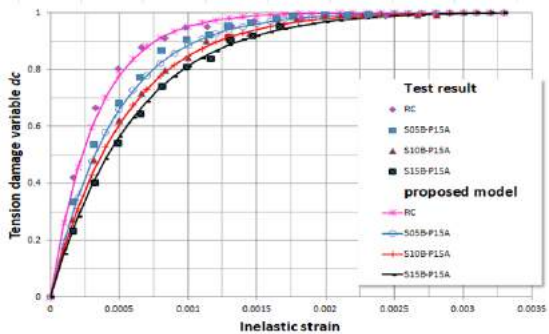
$$\lambda_{pf} = V_{pf} \frac{l_{pf}}{d_{pf}} \tag{27}$$

2. 6. Parameter $\sigma_{b0}^{hf}/\sigma_{c0}^{hf}$ Equation (28) is recommended for low hydrostatic stress, whereas the default value of $\sigma_{b0}^{hf}/\sigma_{c0}^{hf} = 1.16$ can estimate well the strength under high hydrostatic stresses.

$$\frac{\sigma_{b0}^{hf}}{\sigma_{c0}^{hf}} = \frac{k_t^2}{0,132k_c} \left[\left(0,728 - \frac{0,749}{k_t} \right) + \sqrt{\left(0,728 - \frac{0,749}{k_t} \right)^2 + \frac{0,03}{k_t^2}} \right] \tag{28}$$



(a)



(b)

Figure 1. Damage evolution: a) compression b) tension [12]

2. 7. Dilation Angle ψ^{hf} Note that introducing fibers into the concrete matrix helps decrease the volumetric deformation rate (dilation rate), which is attributed to the confinement effect of the fibers. A decrease in the dilation angle reflects this reduction in the volumetric strain rate with increasing fiber characteristics and volume. The following relationship was presented by Chi et al. [12]:

$$\psi^{hf} = \psi_0(1 - a_\psi\lambda_{sf} - b_\psi\lambda_{pf}) \tag{29}$$

In the proposed model, the dilation angle (ψ_0) for plain concrete is determined based on the formulation proposed by Melenk and Babuška [32] and is expressed as follows:

$$\psi_0 = 36 + (\sigma_{c0}/\sigma_{cm0}) \tag{30}$$

In this equation, σ_{c0} is a parameter that ensures the equivalence of units, and σ_{cm0} is recommended to be 10 MPa according to Rousakis et al. [31]. The coefficients a_ψ and b_ψ , which are obtained from literature [12], have values of 0.861 and 0.097, respectively. These coefficients are used to calculate the dilation angle for plain concrete in the proposed model.

2. 8. Concrete Crack Evolution Law The traditional finite element methods (FEM) typically require cracks to follow element edges or predefined paths, such as cohesive zone models. However, the XFEM overcomes this limitation by allowing cracks to form independent of the model mesh, without the need for a predefined crack path. The XFEM incorporates local enrichment functions into the finite element approximation using the partition of unity method, as developed by Melenk and Babuška [32]. Additionally, this study enhances the XFEM by incorporating the generalized Heaviside function [33], simplifying the treatment of arbitrarily curved cracks without complex mapping.

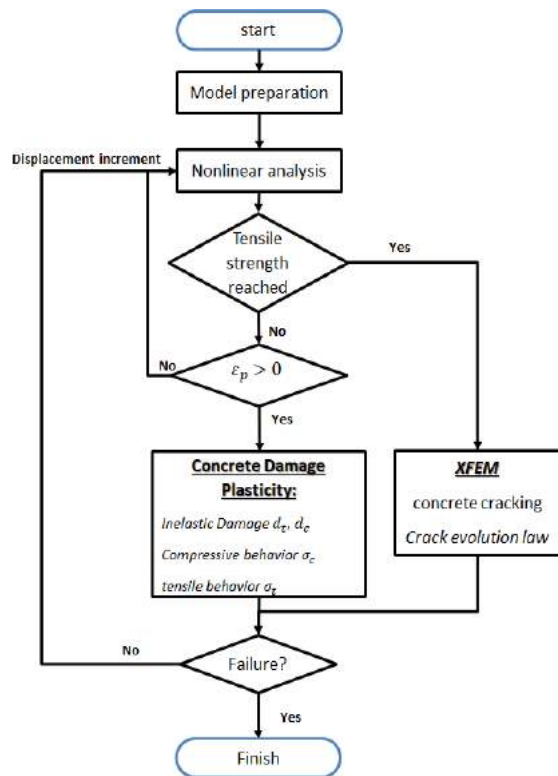
In this study, the evolution of cracks in concrete is determined using the displacement parameter and Equations (8) and (12) as described in this paper. The XFEM is implemented in the Abaqus Implicit software to simulate the process of concrete cracking. The specific parameters used for the XFEM implementation can be found in Table 1.

The proposed approach in this study is a coupled XFEM-CDP model for FRC columns. The flowchart of the implicit simulation scheme used in this study is illustrated in Figure 2.

2. 9. Steel Material Model The reinforcing steel bars in the concrete columns were represented using truss elements (T3D2) in the analysis. These truss elements were assumed to exhibit linear elastic behavior. The material model for the steel bars involved linear hardening until they reached the ultimate stress in tension

TABLE 1. XFEM parameters

	RC	FRC
Crack initiation	ft	a1*ftFRC
Crack evolution law	Exponential	Exponential
Evolution law parameter	c1/wcr	a2
Displacement at failure	wcr	2/a2

**Figure 2.** Flowchart of the coupled XFEM and concrete damage plasticity

(σ_{su}). Subsequently, the strain-softening behavior of the bars was simulated in Abaqus using the damage fracture option.

To calibrate the model with test results, the estimated displacement at failure (w_f) was determined. This calibration process is depicted in Figure 3.

Table 2 provides a summary of the mechanical properties incorporated in the material model for the

reinforcing steel. These properties include parameters such as the yield strength, ultimate strength, elastic modulus, and fracture displacement. These properties are essential for accurately capturing the behavior of the reinforcing steel bars in the numerical simulations.

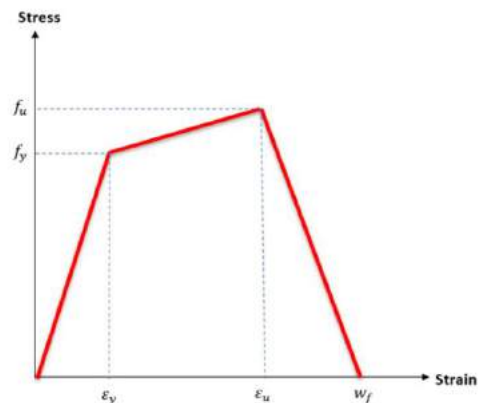
3. RESULTS AND DISCUSSIONS

3. 1. Model Validation with Experimental Results

Simulations were conducted in Abaqus using quasi-static cyclic pushover analysis. Finite element models of columns with various RC and FRC materials were calibrated and validated using experimental data from previous studies [2, 12-14]. Table 3 summarizes the main parameters for the different FRC columns.

Constitutive models of steel bars and concrete matrix components were separately established for numerical modeling. Stirrups were modeled using truss elements (T3D2), and the concrete matrix was assigned a solid three-dimensional eight-node linear brick with full integration (C3D8). Note that the XFEM converges faster with full integration elements C3D8 than with reduced integration elements (C3D8R).

Figures 4-9 depict the hysteretic curves of eight different types of RC, SFRC, PFRC and HyFRC columns, with the solid black line representing experimental results and the dash red line representing numerical simulation results. It can be seen that the cyclic

**Figure 3.** Reinforcing steel model for steel bars**TABLE 2.** Steel parameters for different models

Model	d (mm)	fy (MPa)	fu (MPa)	Es (MPa)	εh	εu
(a) Zhang et al. [2]	10	335	500	2.0*10 ⁵	0.001675	0.06
(b) Zhang, et al. [10]	14	335	500	2.0*10 ⁵	0.001675	0.06
(c) Huang et al. [8]	14	553.9	670.3	2.0*10 ⁵	0.001675	0.06
(d) Liang et al. [9]	16	440	609	1.95*10 ⁵	0.001675	0.08

TABLE 3. Values for CPDM for (a, b, c, d) normal RC, (e, f, g) SFRC, (h) PFRC and (i) HYFRC

Sample	Vsf (%)	Vpf (%)	Ψ (°)	$\sigma_{b0}^{hf}/\sigma_{c0}^{hf}$	K	Mesh size (mm)
(a). RC-Zhang et al. [2]	0.0	0.0	38.70	1.162	0.666	77
(b). RC-Zhang et al. [10]	0.0	0.0	38.70	1.162	0.666	50
(c). RC-Huang et al. [8]	0.0	0.0	38.70	1.162	0.666	40
(d). RC-Liang et al. [9]	0.0	0.0	38.70	1.162	0.666	60
(e). SFRC-Zhang et al. [2]	1.0	0.0	16.775	1.46	0.676	77
(f). SFRC-Zhang et al. [10]	1.0	0.0	16.775	1.46	0.676	50
(g). SFRC-Zhang et al. [10]	1.5	0.0	6.609	1.634	0.681	50
(h). PF-1-1-Huang et al. [8]	0.0	0.15	34.968	1.162	0.718	40
(i). HF-1-1-Huang et al. [8]	1.5	0.15	4.085	1.641	0.731	40

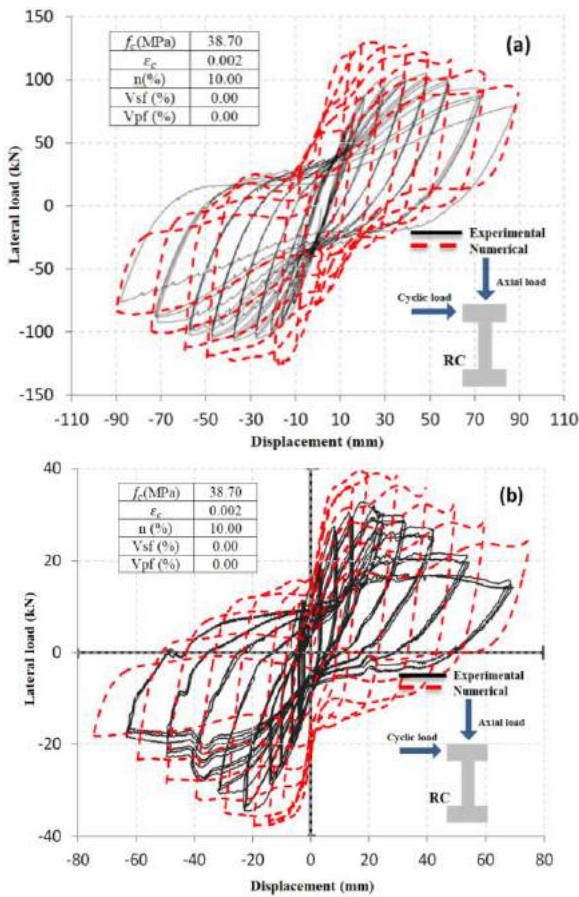


Figure 4. Comparison of the numerical hysteresis curve of RC columns with the experimental hysteresis response curves from: a) [2], b) [10]

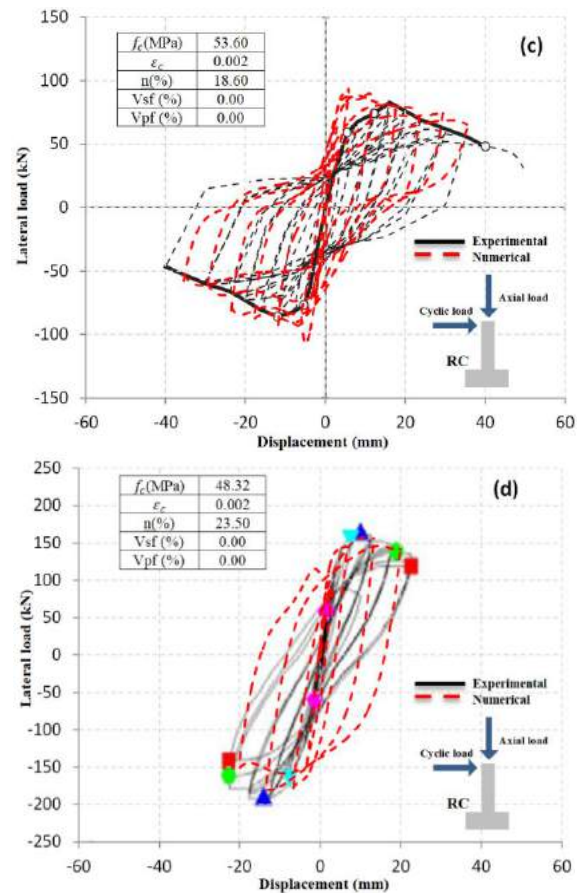


Figure 5. Comparison of the numerical hysteresis curve of RC columns with the experimental hysteresis response curves from: c) [8], d) [9]

deterioration of these columns' performance (i.e., the gradual decrease of stiffness, the loss of strength due to cyclic loading, and the pinched form caused by concrete cracking).

The comparison results in Figures 10-15 show that the dynamic hysteretic model can provide reasonable estimates of the strength capacity of various FRC

columns. Furthermore, the proposed degradation parameters accurately depict the deterioration of strength and stiffness, as well as the pinching effect.

The analytical models SFRC-Zhang and RC-Zhang et al. [2] showed the most significant difference between the test results and the predicted load, 134 and 436 %, respectively. This error was primarily due to the large

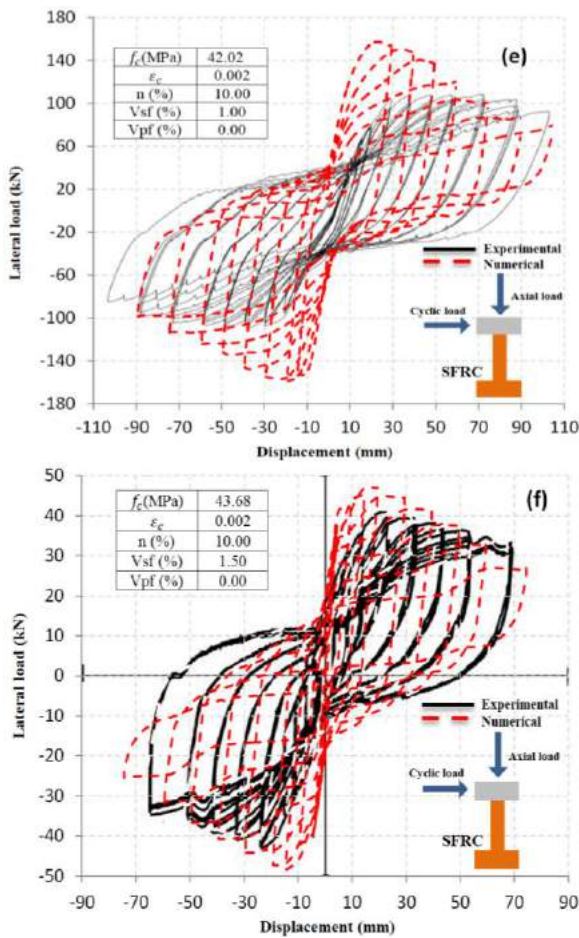


Figure 6. Comparison of the numerical hysteresis curve of SFRC columns with the experimental hysteresis response curves from: a) [2], b) [14]

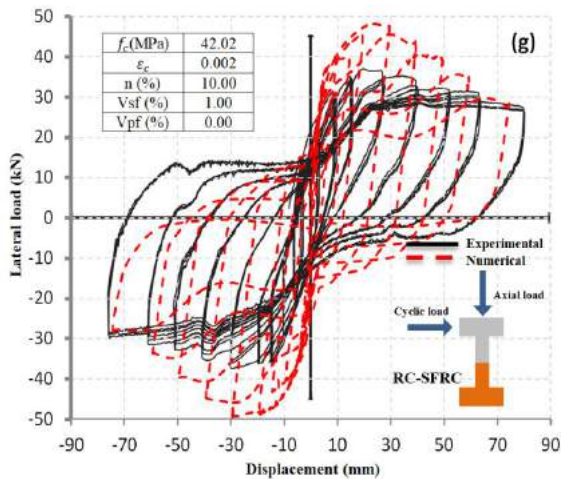


Figure 7. Comparison of the numerical hysteresis curve of RC-SFRC columns with the experimental hysteresis response curves from [10]

mesh size used in these models (which is 77 mm as shown in Table 3). More significant errors in the lateral

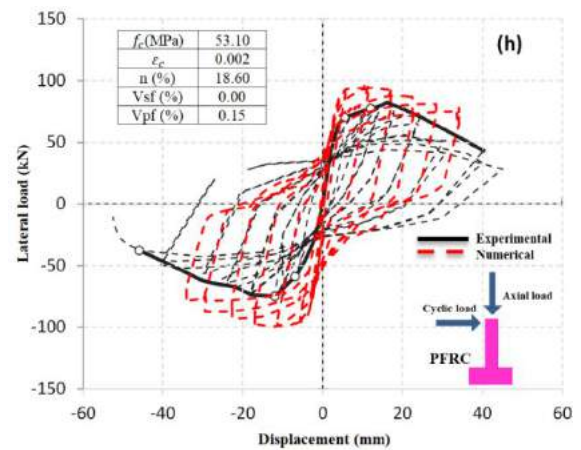


Figure 8. Comparison of the numerical hysteresis curve of PFRC columns with the experimental hysteresis response curves from [8]

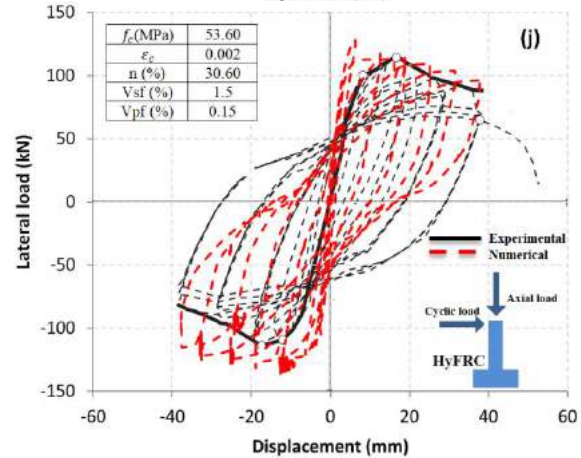
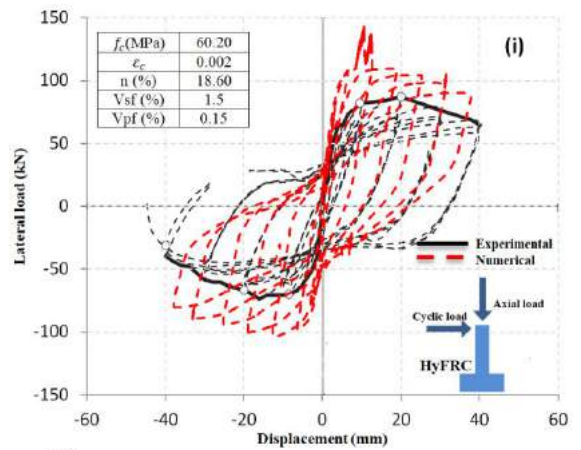


Figure 9. Comparison of the numerical hysteresis curve of HyFRC columns with the experimental hysteresis response curves from [8]

loads occurred at smaller displacements because larger mesh elements require higher fracture energies. This highlights the importance of mesh size sensitivity analysis.

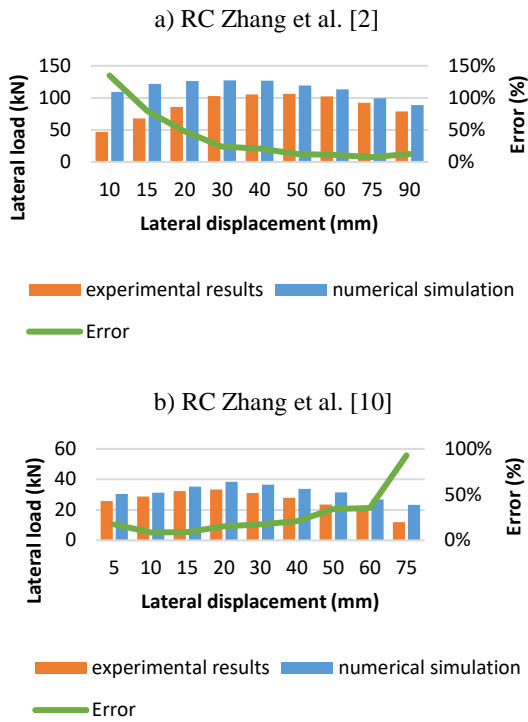


Figure 10. Comparison of numerical results for RC columns with experimental results from: a) [2], b) [14]

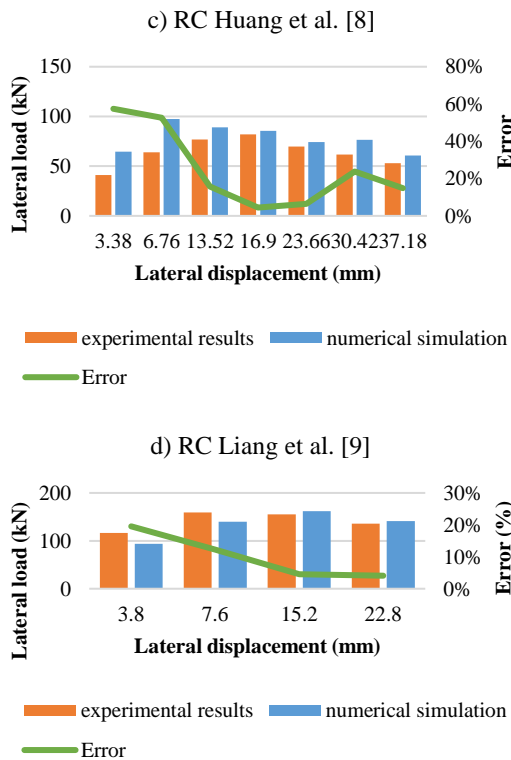


Figure 11. Comparison of numerical results for RC columns with experimental results from: c) [2], d) [14]

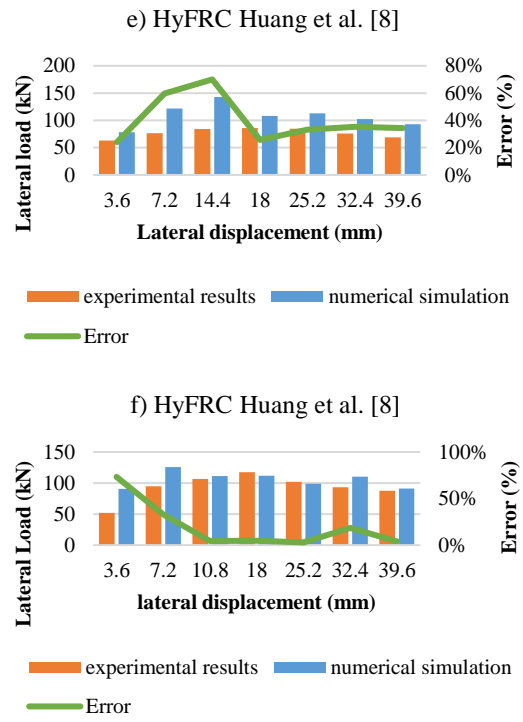


Figure 12. Comparison of numerical results for SFRC columns with experimental results from [2]

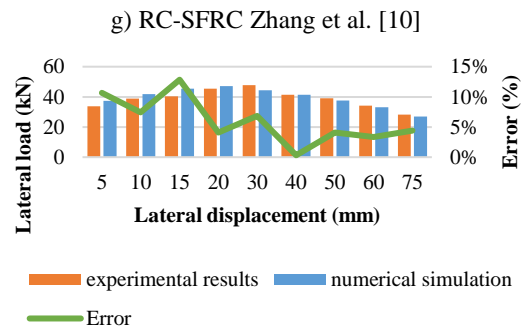


Figure 13. Comparison of numerical results for RC-SFRC columns with experimental from [8]

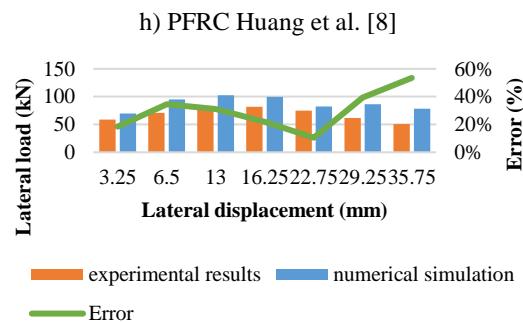


Figure 14. Comparison of numerical results for PFRC columns with experimental from [8]

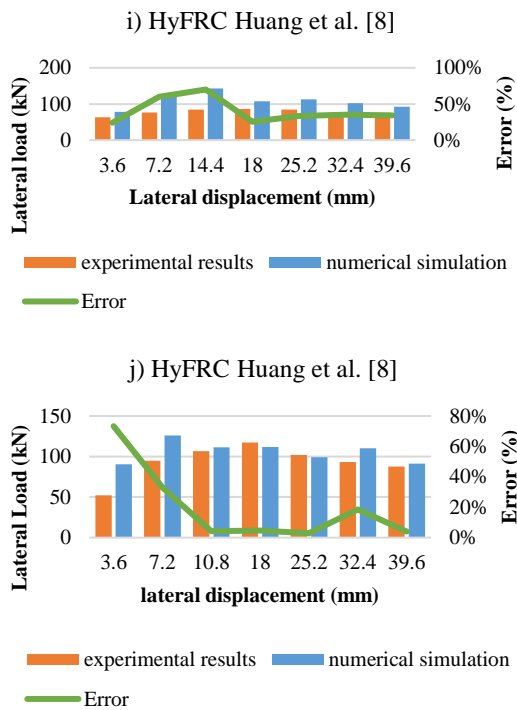


Figure 15. Comparison of numerical results for HyFRC columns with experimental results from [2]

3.2. Mesh Sensitivity Analysis A mesh sensitivity study should be performed before performing a detailed finite element analysis. Three element sizes (25, 40, and 50 mm) were adopted to investigate the effect of the mesh size on the cyclic behavior of the FRC columns, as shown in Figures 16 and 17.

Figure 18 depicts a comparison of different element sizes along with the experimental test results for SFRC column from Broumand and Khoei [14], to investigate the effect of mesh size on accuracy. It can be observed that the load-displacement curve accurately traced the corresponding experimental results. Fine meshes produced results that were very close to the experimental test results for the lateral load.

The precision of the results and computing time of finite element analysis (FEA) are highly dependent on the mesh size. According to the results shown in Table 4, it can be concluded that Fine-mesh FEA models produce more accurate results and better cracking patterns than model with coarse meshes.

On the other hand, models with coarse meshes produce less accurate results, but they save computing time by reducing the model size. These simplified models are typically used to provide rough but rapid analysis estimation.

3.2. Comparison of CDP model And Combined XFEM/CDP

Figure 19 compares the simulation

results and experimental data from previous studies [10]. In addition, a CDP model that excludes the matrix cracking effect was also used for comparison. Both models accurately predict the ultimate lateral force and skeleton curve.

However, when it comes to the unloading stiffness, the CDP model alone fails to reproduce the degradation law observed in the experimental curves. On the other hand, the proposed model, which combines the XFEM with the CDP model, can reasonably reflect the pinch effect observed in the experimental results. This is mainly attributed to the incorporation of cracking and

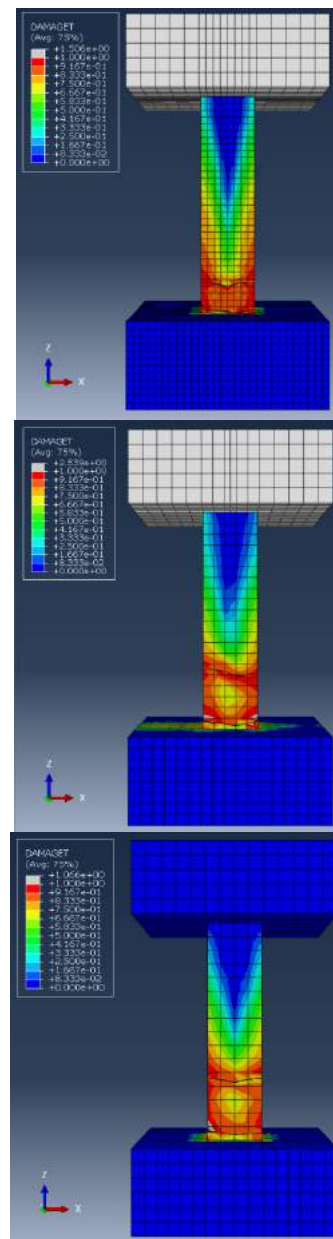


Figure 16. Tensile damage results for different mesh sizes: a) 25 mm, b) 40 mm, c) 50 mm

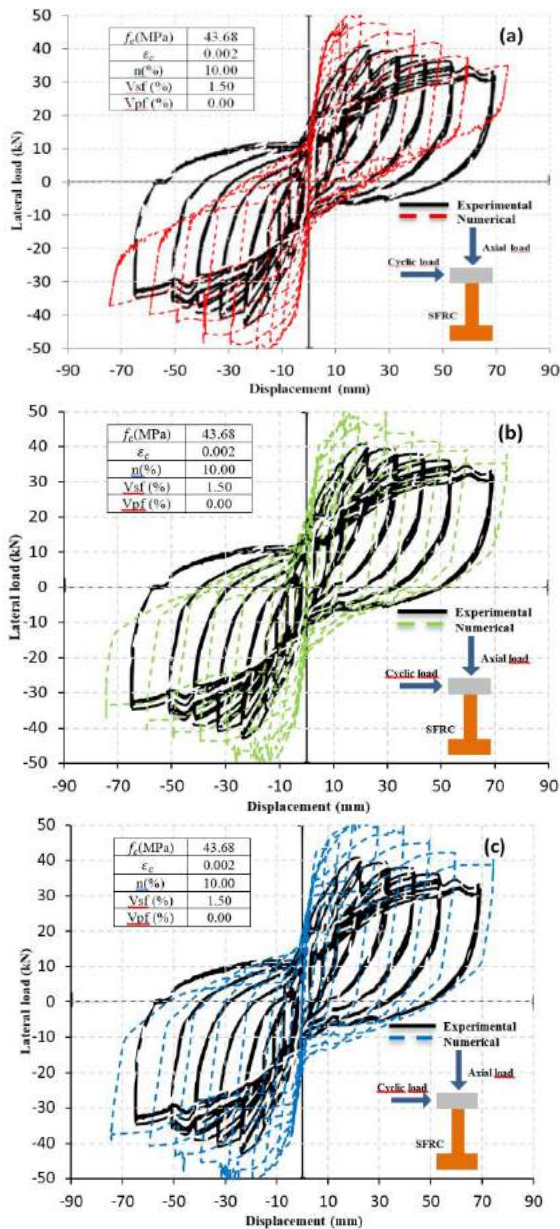


Figure 17. Comparison of Hysteresis curves of SFRC column for different mesh sizes: a) 25 mm, b) 40 mm and c) 50 mm

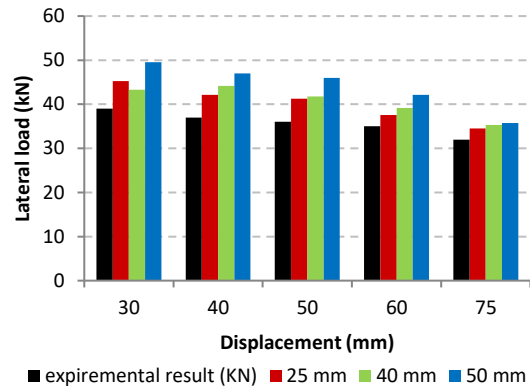


Figure 18. Comparison between the numerical and experimental load values of SFRC column [8] for different mesh sizes: 25 mm, 40 mm and 50 mm

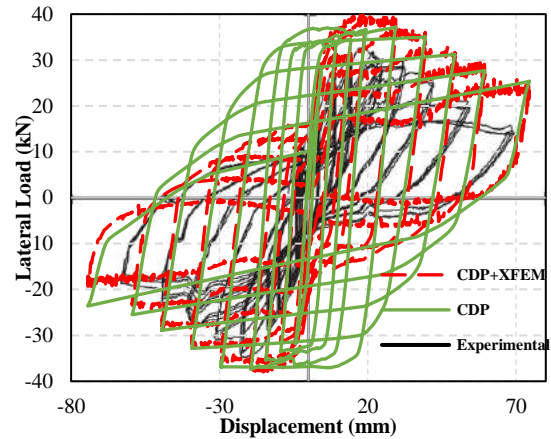


Figure 19. Comparison Comparison of CDP model and combined XFEM-CDP for RC [8]

crack closing behavior during unloading, which leads to the formation of pinched hysteresis loops. In contrast, simulations based solely on the CDP model tend to produce plump hysteresis loops that do not capture the observed behavior accurately.

TABLE 4. Mesh sensitivity analysis results

Lateral displacement (mm)	Experimental result (kN)	Analytical result					
		25 mm		40 mm		50 mm	
		lateral force (kN)	Variation (%)	lateral force (kN)	Variation (%)	lateral force (kN)	Variation (%)
30	39	45.23	24%	43.30	11%	49.55	27%
40	37	42.12	14%	44.17	19%	47.02	27%
50	36	41.26	15%	41.78	16%	45.95	28%
60	35	37.56	7%	39.18	12%	42.10	20%
75	32	34.47	8%	35.32	10%	35.72	12%

4. CONCLUSION

This paper proposes an Abaqus-based method for combining the CDP model with the XFEM for FRC structures, to more realistically reproduce the mechanical responses of FRC. The following conclusions can be presented:

- The proposed coupled (XFEM+CDP) model has been successfully validated using independent experimental results with variations in mesh sizes, material properties, and structural scales. This validation ensures the reliability and applicability of the model.
- The numerical investigation of mesh size sensitivity reveals that the accuracy of the proposed model is dependent on the element size. Proper selection of element size is crucial to achieve accurate results.
- The proposed model demonstrates improved agreement with experimental data compared to classical CDP models. It effectively captures the pinched form of hysteresis loops of concrete under cyclic loadings, providing a more realistic representation of FRC behavior.
- The agreement between the experimental results and numerical predictions provides strong evidence supporting the relevance and effectiveness of the proposed model.

This model can serve as a valuable tool for conducting nonlinear and dynamic numerical simulations of reinforced concrete (RC) and FRC structures using Abaqus software, providing valuable guidelines for practical applications in structural engineering.

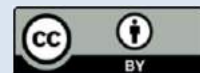
5. REFERENCES

1. Opabola, E. A., and Mangalathu, S. "Seismic fragility assessment of bridges with as-built and retrofitted splice-deficient columns." *Bulletin of Earthquake Engineering*, Vol. 21, No. 1, (2023), 583-603. <https://doi.org/10.1007/s10518-022-01521-w>
2. Zhang, Y. Y., Harries, K. A., and Yuan, W. C. "Experimental and numerical investigation of the seismic performance of hollow rectangular bridge piers constructed with and without steel fiber reinforced concrete." *Engineering Structures*, Vol. 48, (2013), 255-265. <https://doi.org/10.1016/j.engstruct.2012.09.040>
3. Marc-André, D., and Bruno, M. "Tension Lap Splices Strengthened with Ultrahigh-Performance Fiber-Reinforced Concrete." *Journal of Materials in Civil Engineering*, Vol. 27, No. 7, (2015), 4014206. [https://doi.org/10.1061/\(ASCE\)MT.1943-5533.0001169](https://doi.org/10.1061/(ASCE)MT.1943-5533.0001169)
4. Hajsadeghi, M., Jalali, M., Chin, C. S., Zirakian, T., and Bahrebar, M. "Flexural Performance of Fibre Reinforced Concrete with an Optimised Spirally Deformed Steel Fibre." *International Journal of Engineering, Transactions C: Aspects*, Vol. 34, No. 6, (2021), 1390-1397. <https://doi.org/10.5829/ije.2021.34.06c.01>
5. Rahmzadeh, S., and Tariverdilo, S. "Evaluating Applicability of ASTM C 928 Approach in Assessing Adequacy of Patch Repair of Bridge Piers." *International Journal of Engineering Transactions C: Aspects*, Vol. 33, No. 12, (2020), 2455-2463. <https://doi.org/10.5829/ije.2020.33.12c.04>
6. Magbool, H. M., and Zeyad, A. M. "The effect of various steel fibers and volcanic pumice powder on fracture characteristics of Self-Compacting concrete." *Construction and Building Materials*, Vol. 312, (2021), 125444. <https://doi.org/https://doi.org/10.1016/j.conbuildmat.2021.125444>
7. Zhang, P., Wei, S., Wu, J., Zhang, Y., and Zheng, Y. "Investigation of mechanical properties of PVA fiber-reinforced cementitious composites under the coupling effect of wet-thermal and chloride salt environment." *Case Studies in Construction Materials*, (2022).
8. Huang, L., Xu, L., Chi, Y., and Xu, H. "Experimental investigation on the seismic performance of steel-polypropylene hybrid fiber reinforced concrete columns." *Construction and Building Materials*, Vol. 87, (2015), 16-27. <https://doi.org/10.1016/j.conbuildmat.2015.03.073>
9. Liang, X., Xing, P., and Xu, J. "Experimental and numerical investigations of the seismic performance of columns with fiber-reinforced concrete in the plastic hinge region." *Advances in Structural Engineering*, Vol. 19, No. 9, (2016), 1484-1499. <https://doi.org/10.1177/1369433216643896>
10. Zhang, Y., and Dias-da-Costa, D. "Seismic vulnerability of multi-span continuous girder bridges with steel fibre reinforced concrete columns." *Engineering Structures*, Vol. 150, (2017), 451-464. <https://doi.org/10.1016/j.engstruct.2017.07.053>
11. Pang, Y., Cai, L., Ouyang, H., and Zhou, X. "Seismic performance assessment of different fibers reinforced concrete columns using incremental dynamic analysis." *Construction and Building Materials*, Vol. 203, (2019), 241-257. <https://doi.org/10.1016/j.conbuildmat.2019.01.087>
12. Chi, Y., Yu, M., Huang, L., and Xu, L. "Finite element modeling of steel-polypropylene hybrid fiber reinforced concrete using modified concrete damaged plasticity." *Engineering Structures*, Vol. 148, (2017), 23-35. <https://doi.org/10.1016/j.engstruct.2017.06.039>
13. Aljazeera, Z. R., and Al-Jaberi, Z. "Numerical Study on Flexural Behavior of Concrete Beams Strengthened with Fiber Reinforced Cementitious Matrix Considering Different Concrete Compressive Strength and Steel Reinforcement Ratio." *International Journal of Engineering Transactions A: Basics*, Vol. 34, No. 4, (2021), 793-802. <https://doi.org/10.5829/ije.2021.34.04a.05>
14. Broumand, P., and Khoei, A. R. "X-FEM Modeling of Dynamic Ductile Fracture Problems with a Nonlocal Damage-Viscoplasticity Model." *Finite Elements in Analysis and Design*, Vol. 99, No. C, (2015), 49-67. <https://doi.org/10.1016/j.finel.2015.01.002>
15. Sadat Hosseini, A., Hajikarimi, P., Fallah Hosseini, S., Aliakbari, A., and Moghadas Nejad, F. "Semi-circular bending setup for predicting fracture characteristics of high-strength fiber-reinforced concrete." *Theoretical and Applied Fracture Mechanics*, Vol. 123, (2023), 103729. <https://doi.org/https://doi.org/10.1016/j.tafmec.2022.103729>
16. Javanmardi, M. R., and Maheri, M. R. "Extended finite element method and anisotropic damage plasticity for modelling crack propagation in concrete." *Finite Elements in Analysis and Design*, Vol. 165, (2019), 1-20. <https://doi.org/https://doi.org/10.1016/j.finel.2019.07.004>
17. Belletti, B., Cerioni, R., Meda, A., and Plizzari, G. "Design Aspects on Steel Fiber-Reinforced Concrete Pavements." *Journal of Materials in Civil Engineering*, Vol. 20, (2008). [https://doi.org/10.1061/\(ASCE\)0899-1561\(2008\)20:9\(599\)](https://doi.org/10.1061/(ASCE)0899-1561(2008)20:9(599))
18. Prisco, M., Dozio, D., and Belletti, B. "On the fracture behaviour

- of thin-walled SFRC roof elements." *Materials and Structures*, Vol. 46, No. 5, (2013), 803-829. <https://doi.org/10.1617/s11527-012-9935-x>
19. Ren, X., and Li, J. "Multi-scale based fracture and damage analysis of steel fiber reinforced concrete." *Engineering Failure Analysis*, Vol. 35, (2013), 253-261. <https://doi.org/10.1016/j.engfailanal.2013.01.029>
 20. Zhang, H., Huang, Y., Xu, S., Natarajan, S., and Yao, F. "An explicit methodology of random fibre modelling for FRC fracture using non-conforming meshes and cohesive interface elements." *Composite Structures*, Vol. 310, (2023), 116762. <https://doi.org/https://doi.org/10.1016/j.compstruct.2023.116762>
 21. Rabczuk, T., and Belytschko, T. "Cracking particles: a simplified meshfree method for arbitrary evolving cracks." *International Journal for Numerical Methods in Engineering*, Vol. 61, No. 13, (2004), 2316-2343. <https://doi.org/https://doi.org/10.1002/nme.1151>
 22. Moslemi, H., and Khoei, A. R. "3D adaptive finite element modeling of non-planar curved crack growth using the weighted superconvergent patch recovery method." *Engineering Fracture Mechanics*, Vol. 76, No. 11, (2009), 1703-1728. <https://doi.org/https://doi.org/10.1016/j.engfracmech.2009.03.013>
 23. De Maio, U., Greco, F., Leonetti, L., Nevone Blasi, P., and Pranno, A. "A cohesive fracture model for predicting crack spacing and crack width in reinforced concrete structures." *Engineering Failure Analysis*, Vol. 139, (2022), 106452. <https://doi.org/https://doi.org/10.1016/j.engfailanal.2022.106452>
 24. Kurumatani, M., Soma, Y., and Terada, K. "Simulations of cohesive fracture behavior of reinforced concrete by a fracture-mechanics-based damage model." *Engineering Fracture Mechanics*, Vol. 206, (2018). <https://doi.org/10.1016/j.engfracmech.2018.12.006>
 25. Fallah, N. "A development in the finite volume method for the crack growth analysis without global remeshing." *International Journal of Engineering, Transactions A: Basics*, Vol. 29, No. 7, (2016), 898-908. Retrieved from doi: 10.5829/idosi.ije.2016.29.07a.03
 26. Abadel, A., Abbas, H., Almusallam, T., Al-Salloum, Y., and Siddiqui, N. "Mechanical properties of hybrid fibre-reinforced concrete – analytical modelling and experimental behaviour." *Magazine of Concrete Research*, Vol. 68, No. 16, (2016), 823-843. <https://doi.org/10.1680/jmacr.15.00276>
 27. Almusallam, T., Ibrahim, S. M., Al-Salloum, Y., Abadel, A., and Abbas, H. "Analytical and experimental investigations on the fracture behavior of hybrid fiber reinforced concrete." *Cement and Concrete Composites*, Vol. 74, (2016), 201-217. <https://doi.org/10.1016/j.cemconcomp.2016.10.002>
 28. Lubliner, J., Oliver, J., Oller, S., and Oñate, E. "A plastic-damage model for concrete." *International Journal of Solids and Structures*, Vol. 25, No. 3, (1989), 299-326. [https://doi.org/10.1016/0020-7683\(89\)90050-4](https://doi.org/10.1016/0020-7683(89)90050-4)
 29. Lee, J., and Fenves, G. L. "Plastic-Damage Model for Cyclic Loading of Concrete Structures." *Journal of Engineering Mechanics*, Vol. 124, No. 8, (1998), 892-900. [https://doi.org/10.1061/\(asce\)0733-9399\(1998\)124:8\(892\)](https://doi.org/10.1061/(asce)0733-9399(1998)124:8(892))
 30. Chi, Y., Xu, L., and Yu, H. sui. "Constitutive modeling of steel-polypropylene hybrid fiber reinforced concrete using a non-associated plasticity and its numerical implementation." *Composite Structures*, Vol. 111, No. 1, (2014), 497-509. <https://doi.org/10.1016/j.compstruct.2014.01.025>
 31. Rousakis, T. C., Karabinis, A. I., Kioussis, P. D., and Tepfers, R. "Analytical modelling of plastic behaviour of uniformly FRP confined concrete members." *Composites Part B: Engineering*, Vol. 39, No. 7-8, (2008), 1104-1113. <https://doi.org/10.1016/J.COMPOSITESB.2008.05.001>
 32. Melenk, J. M., and Babuška, I. "The partition of unity finite element method: Basic theory and applications." *Computer Methods in Applied Mechanics and Engineering*, Vol. 139, No. 1-4, (1996), 289-314. [https://doi.org/10.1016/S0045-7825\(96\)01087-0](https://doi.org/10.1016/S0045-7825(96)01087-0)
 33. Moes, N., Dolbow, J., and Belytschko, T. "A Finite Element Method for Crack Growth without Remeshing." *International Journal for Numerical Methods in Engineering*, Vol. 46, (1999), 131-150. [https://doi.org/10.1002/\(SICI\)1097-0207\(19990910\)46:13.0.CO;2-J](https://doi.org/10.1002/(SICI)1097-0207(19990910)46:13.0.CO;2-J)

COPYRIGHTS

©2023 The author(s). This is an open access article distributed under the terms of the Creative Commons Attribution (CC BY 4.0), which permits unrestricted use, distribution, and reproduction in any medium, as long as the original authors and source are cited. No permission is required from the authors or the publishers.

**Persian Abstract**

چکیده

در سال‌های اخیر، جامعه علمی علاقه فزاینده‌ای به بتن تقویت‌شده با الیاف (FRC) برای سازه‌های مدرن به دلیل شکل‌پذیری افزایش یافته آن در مقایسه با بتن مسلح سنتی (RC) نشان داده است. این مقاله یک مدل تحلیلی را معرفی می‌کند که شامل یک شاخص تقویت‌کننده فیبر جامع (RI) برای مطالعه انواع مختلف FRC است. تجزیه و تحلیل بر روی رفتارهای فشاری و کششی، تکامل آسیب تحت بارگذاری چرخه‌ای، و انتشار ترک در زمینه بتن متمرکز است. برای شبیه‌سازی موثر شروع و انتشار ترک در سازه‌های FRC، از روش المان محدود توسعه‌یافته (XFEM) استفاده می‌شود که از قابلیت‌های حل شکست آن استفاده می‌کند. علاوه بر این، XFEM با رویکرد مدل‌سازی پلاستیسیته آسیب‌دیده بتن (CDP) ترکیب می‌شود تا عملکرد شبه استاتیکی و هیستریزیک ستون‌های FRC را بررسی کند. مدل‌های المان محدود غیرخطی سه بعدی با استفاده از نرم افزار تجاری Abaqus ساخته شده‌اند. این مدل‌ها از الیاف فولادی، الیاف پلی پروپیلن و ترکیبی از هر دو نوع الیاف در ساختارهای FRC استفاده می‌کنند. علاوه بر این، دقت تجزیه و تحلیل مبتنی بر XFEM-CDP در پیش‌بینی رفتار هیستریزیک در برابر نتایج مقالات تحقیقاتی قبلی تأیید می‌شود و دقت معقولی را نشان می‌دهد. این به مهندسان اجازه می‌دهد تا رفتار غیرخطی بتن، از جمله ترک خوردگی، خرد شدن، و تغییر شکل پلاستیکی را به طور دقیق ثبت کنند، در حالی که الگوهای ترک پیچیده را نیز در نظر می‌گیرند و درک بهتری از عملکرد لرزه‌ای سازه‌های FRC با استفاده از شبیه‌سازی‌های عددی ارائه می‌دهند.



Improved Simultaneous Localization and Mapping Estimation using Crow Search Algorithm Based Particle Filter

M. Abedini, H. Jazayeriy*, J. Kazemitabar

Faculty of Electrical & Computer engineering, Noshirvani University of Technology, Babol, Iran

PAPER INFO

Paper history:

Received 05 June 2023
Received in revised 27 June 2023
Accepted 28 June 2023

Keywords:

Particle Filter
Fast Simultaneous Localization and Mapping
Crow Search Algorithm
Sample Depletion

ABSTRACT

Trajectory tracking and positioning are essential requirements in many areas, including robots and autonomous vehicles. In some cases, such as in areas where GPS signals are weak or not available, trajectory tracking is used as an alternative positioning system. In these cases, simultaneous localization and mapping (SLAM), is of great importance as it does not require prior knowledge and empirical offline fingerprint. SLAM can be combined with signal processing algorithms among which, particle filter stands out. However, challenges exist such as particle weights degradation and particles impoverishment that need to be dealt with. In fact, the loss of particle diversity for estimation has led to the lack of particles. To overcome this problem, one solution is to diversify the selection of particles after resampling. In this paper, we proposed a crow search algorithm (CSA) to overcome these issues and improve position estimation. The simulation results showed that this algorithm greatly improved the performance of fast SLAM.

doi: 10.5829/ije.2023.36.10a.09

NOMENCLATURE

CSA	Crow Search Algorithm	$x^{i,it}$	Position of the crow i in iteration it
x_k	The state of the moving vehicle or mobile robot in the time k	AP	Awareness Probability
z_k	Observation in the time k	fl	Flight length
x_k^i	The state of the particle i in the time k	F	Fitness function
w_k^i	The weight of the particle i in the time k	v_c	Robott velocity
q	Importance density	(x_v, y_v)	2-D Position of the robot
l	Landmark position	(x_l, y_l)	2-D landmark position
$m^{i,it}$	Position of the crow's hide-out i in the iteration it	Greek Symbols	
it	Number of iterations	ϕ	Robot orientation

1. INTRODUCTION

Simultaneous localization and mapping techniques have been around for many years in a variety of areas, such as human positioning, unmanned vehicles, submarines, and robots, including those used inside the human body. When SLAM was proposed nearly two decades ago it was initially viewed as a side idea. Nowadays, however, it is considered as an inexpensive and integral component of robots and automated moving objects technology. The SLAM problem can be categorized according to different factors. The SLAM technique used in robots first

introduced by Smith et al. [1] which was used to construct an unknown environment map, while simultaneously determining its location. In SLAM, unlike fingerprinting methods [2], both path and position are estimated online without the need for any prior knowledge of the environment. Different SLAM methods, despite their core similarities, are distinguished based on the way sensors are used and implemented. Kalman filters are one of the first techniques to solve SLAM. Extended Kalman Filter (EKF) [3] is used to estimate the state and position of environmental signals on a robot. Given controls $u_{0:k} = \{u_0, \dots, u_k\}$ and robot observations $z_{1:k} =$

*Corresponding Author Institutional Email: Jhamid@nit.ac.ir
(H. Jazayeriy)

$\{z_1, \dots, z_k\}$, we look for the landmarks location or map (l) and the pose $x_{0:k} = \{x_0, x_1, \dots, x_k\}$. In other words, Kalman filter provides a solution to the online SLAM problem, $p(x_k, l | u_{0:k}, z_{1:k})$. The EKF estimation has an error because it uses the Taylor series approximation of the nonlinear estimation function. Also, the EKF estimation is not of much help when the model is both non-linear and non-Gaussian. Therefore, solving the SLAM problem using the Monte Carlo method was one of the other methods proposed to overcome these challenges [4]. Instead of calculating the integral at all points in the Bayesian formulation, it does so by sampling at the points that have the greatest contribution to the integral calculation. Points sampling in Monte Carlo is performed using Perfect Monte Carlo, Rejection Sampling (RS), Importance Sampling (IS), and Sequential Importance Sampling (SIS) methods [5]. The idea behind the SIS method, which is a special case of IS, is to re-use the samples generated in the previous steps to sample the posterior distribution function in the new step. The challenge facing the SIS is weight degeneracy, where the variance of weights for the proposed distribution increases with each step. To overcome this, re-sampling can be used to reduce the variance of weights. The so-called resampling in SIS is called sequential importance resampling (SIR) or particle filter [6]. One of the methods of applying a particle filter to solve the SLAM problem is known as Fast SLAM. Fast SLAM breaks down a SLAM problem into a robot positioning problem and a set of landmark estimation problems that are conditional on the robot status estimation [7]. So far, advanced versions of Fast SLAM have been offered by Lei et al. [8], but all of them are based on one basic rule; as reported by Murphy [9], the representation as such is accurate due to the natural conditional independence in the SLAM problem. Fast SLAM uses a modified particle filter to estimate the posterior paths of the robot. Each particle has k Kalman filters that estimate the K positions of the landmark based on the path estimation. The resulting algorithm is an example of a Rao-Blackwellized particle filter [10, 11].

With the rapid development of computer hardware performance, particle filter is applied in SLAM [12]. The problem with the traditional particle filtering algorithm is the contrast between the degradation and the lack of particles. Re-sampling resolves the problem of particle degradation to some extent, but creates another problem known as sample depletion. In addition, high-precision estimation requires the application of large numbers of particles, which results in computational complexity and inconsistency.

There are two conventional ways to overcome this problem. The first is to diversify the choice of particle location and the other is to better allocate weight to the particles. In this paper, we select the first solution to overcome this problem. To accomplish this method,

scholars have conducted a great deal of studies and have reached the important point that particle filtering based on intelligent optimization mechanism of biological group is a new perspective [13, 14]. In fact, in these methods, the particles in the particle filter are considered as individuals in biological clusters, and the particle distribution using the simulated biological cluster motion law is more reasonable.

Huang et al. [15], and Chen et al. [16], cuckoo and bat algorithms were introduced to have better performance of the particle filtering algorithm. Gao et al. [17] used the firefly algorithm transfer formula to recombine the particle sample. However, re-sampling is still required in this method and optimization of the duplicate particles is not performed. Tian et al. [18] optimized the particle filter using the firefly algorithm, which shows that the firefly algorithm can update particle states in a way that prevents particle starvation. Another advantage of this method is that the same computational efficiency can be achieved with fewer particles.

Although these methods and other methods such as the use of genetic algorithms in target tracking and trajectory tracking control have been proposed [19–21], the issue of simultaneous mapping, in addition to localization, plays a very important role in robots and unmanned vehicles. Zhu et al. [12], combined the particle filtering mechanism in SLAM with improved firefly lighting formula. Moreover, they used the dynamic equilibrium algorithm which delivers global and local simultaneously.

Following new research on particle filtering that harnesses optimization mechanisms of intelligent bio-groups [22, 23], these researches used CSA algorithm. Our goal is to merge CSA and particle filtering to improve resampling of particles, optimize particle weights and obtain higher accuracy with smaller number of particles. We term this method CSAPF-SLAM.

In fact, by creating a reasonable variation in the position of the particles using mechanisms of intelligent bio-groups, we save them from getting involved in local extremes, and thus achieve a better estimate. It seems that the use of metaheuristic algorithm is efficient to diversify the selection of particles after resampling and among them we have chosen the crow search algorithm. Crow search algorithm is one of the MA algorithm that attracted much attention from researchers since it was introduced. The evaluation results of CSA show that it is very efficient for optimization problems, especially problems that science and engineering have difficulty to solve [24]. Meanwhile, this algorithm is easy to implement and has only a few parameters [25]. Also, by combining the particle filter and the crow search algorithm, it is possible to propose a fitness function that solves some problems such as entrapment in the local optimum due to the AP parameter. Furthermore, the algorithm uses particle filter to keep the balance between

the local and global search processes. In fact, a novel neighborhood assigning strategy has been introduced to optimize the local search.

Short statement of precise problem addressed in this manuscript:

- A new method for more accurate estimation of simultaneous localization and mapping in robots in non-linear and non-Gaussian condition.
- A new algorithm to overcome the impoverishment problem in particle filter using CSA.
- A new fitness function for SLAM using particle filter.

In section II, we describe particle filter SLAM and CSA algorithm. Section III describes our proposed method and section IV demonstrates experimental valuations based on Sydney University Dataset [26, 27]. Finally, section V concludes the paper.

2. PARTICLE FILTER AND CSA ALGORITHM

Since the proposed method is a combination of particle filter and crow search algorithm, we describe each of these, separately. We will then explain our proposed algorithm, i.e. CSAPF-SLAM.

2.1. Particle Filter SLAM Algorithm As we know, in SLAM, we are dealing with two issues of localization and mapping [28]. The following equation is used for the problem of moving vehicle or mobile robot position in filter based SLAM algorithms:

$$\tilde{x}_k = \int x_k p(x_k | z_{1:k}) dx_k \quad (1)$$

where x_k is the state of the moving vehicle or mobile robot in the time k and z_k is the observation in the time k .

Filter-based localization methods include the following two steps:

A) Prediction step (time update): The Prediction step according to Chapman-Kolmogorov principle can be as follows:

$$p(x_k | u_{0:k}, z_{1:k-1}, x_0) = \int p(x_k | x_{k-1}, u_k) \times p(x_{k-1} | u_{0:k-1}, z_{1:k-1}, x_0) dx_{k-1} \quad (2)$$

B) Correction step (measurement update): In time k , a value of z_k is available and this can be used for the previous update (time update) via the Bayesian rule:

$$p(x_k | u_{0:k}, z_{1:k}, x_0) = \frac{p(z_k | x_k) p(x_k | u_{0:k}, z_{1:k-1}, x_0)}{p(z_k | u_{0:k}, z_{1:k-1})} \quad (3)$$

To overcome the limitation caused by the Gaussian condition of the distributions as well as the linearization error in EKF, the use of a particle filter is suggested by Arulampalam et al. [29]. In this case, the term

$p(x_k | z_{1:k})$ in Equation (1) is transformed into the following:

$$p(x_k | z_{1:k}) \approx \sum_{i=1}^{N_s} w_k^i \cdot \delta(x_k - x_k^i) \quad (4)$$

where x_k^i is the state of the particle i in the time k and w_k^i is the weight of the particle i in the time k , where particle weight is determined by the following equations:

$$w_k^i \propto \frac{p(x_k^i | z_{1:k})}{q(x_k^i | z_{1:k})} \quad (5)$$

where q is the importance density. Since it is common that only the filtered estimate of $p(x_k | z_{1:k})$ is required at each time step, we have the following relation by performing a series of algebraic operations:

$$w_k^i \propto w_{k-1}^i \cdot \frac{p(z_k | x_k^i) p(x_k^i | x_{k-1}^i)}{q(x_k^i | x_{k-1}^i, z_k)} \quad (6)$$

Considering the sequential importance resampling (SIR), which includes selecting the previous density $p(x_k | x_{k-1})$ as the importance density $q(x_k | x_{1:k-1}, z_k)$, we will have the following recursive equation:

$$w_k^i \propto w_{k-1}^i \cdot p(z_k | x_k^i) \quad (7)$$

Finally, given the location and weight of each particle, the position of the robot or vehicle can be estimated according to the following equation:

$$\tilde{x}_k = \sum_{j=1}^{N_s} w_k^j \cdot x_k^j \quad (8)$$

```

1: for i = 1: Ns
2:   Randomly choose initial state x0i in the search space
3:   w0i = 1/Ns
4: end for
5: k=1
6: while (k <> 0)
7:   // New pose selection and update weights with new observations
8:   for i = 1: Ns
9:     sample a new pose xki ~ p(xk | xk-1i, uk)
10:    wki = wk-1i · p(zk | xki)
11:  end for
12: Apply the selected resampling method for the set of particles and their weights to get a new set of particles and weights
13: // Calculate the estimate (Same as probability integral from probability density function)
14: for j = 1: Ns
15:   x̃k = wkj · xkj
16:   xk += x̃k
17: end for
18: k = k + 1
19: if fitness function condition is realized
20:   k = 0
21: end if
22: end while

```

Figure 1. Pseudo code for particle filter algorithm

In general, Figure 1 shows the pseudo code for particle filter algorithm for estimating the state. It should be noted that the fitness function is calculated based on the importance weight.

So far, we have only discussed positioning in the SLAM algorithm, but mapping should also be performed in SLAM. In other words, we are dealing with the posterior probability density $p(x_k, l | u_{0:k}, z_{1:k}, x_0)$. For our proposed algorithm, we will use one of the most efficient methods using a particle filter called Fast SLAM. As mentioned in the introduction, Fast SLAM uses only the particle filter according to the above equations to determine the position and uses a number of EKF for mapping. Therefore here, according to the posterior factorization provided by Murphy [9], the SLAM posterior will be as follows:

$$p(x_{1:k}, l_{1:m} | z_{1:k}, u_{0:k-1}) = p(x_{1:k} | z_{1:k}, u_{0:k-1}) \cdot p(l_{1:m} | x_{1:k}, z_{1:k}) \tag{9}$$

where $p(x_{1:k} | z_{1:k}, u_{0:k-1})$ is the posterior density of the robot state and $p(l_{1:m} | x_{1:k}, z_{1:k})$ is the position of the landmarks, which we have due to the conditional independence in the position of landmarks:

$$p(x_{1:k}, l_{1:m} | z_{1:k}, u_{0:k-1}) = p(x_{1:k} | z_{1:k}, u_{0:k-1}) \cdot \prod_{i=1}^M p(l_i | x_{1:k}, z_{1:k}) \tag{10}$$

The first term on the right side of the above equation is obtained by using the particle filter in accordance with Equation (3). In other words, for each particle in each step, after determining the position, the position of the landmarks must also be estimated. That is, each particle has a memory of $2m + 3$, in which m is the number of landmarks. Figure 2 will help us understand this concept. In this figure, μ_k^i and Σ_k^i represent mean and covariance of particle i at time k , respectively. Figure 3 displays the pseudo code for Fast SLAM.

2. 2. Crow Search Optimization Algorithm (CSA)

Crow search meta-heuristic is a relatively new algorithm introduced in 2016 inspired by Crows' social and intelligent behaviour by Askarzadeh [30]. Crows

(family or species of crows) are recognized as one of the cleverest birds in nature. It can be said that after humans, crows have proportionally the largest brain among living beings, and this is the reason for the intelligent behaviour of these birds [30]. In fact, this is proven by the brain to body ratio. Reasons to consider crows as smart birds are summarized as follows: Ability to remember human faces, conspiracy capability, powerful memory, ability to solve problems and planning. Crows can remember faces and are able to alert an anonymous face to one another. They also have self-awareness in the mirror and are also able to make and use of tools, as well as communicate in sophisticated ways, or remember to hide their food for several months. Unknown communication systems exist among crows. One of them is the complex language between crows. Crows also stock their surplus food. It has been widely seen that other crows have found their food supply in pursuit of another. Because crows are cautious and masterful in hiding, researchers believe that crows cannot rob another food crop without planning. They are also highly capable of hiding and storing food. In fact, crows can predict the behaviour of thieves using their experience of theft and can determine the safest path to protect their warehouses from theft [30].

The CSA algorithm is such that, like all community-based algorithms, it assumes N as the number of crows in the d -dimensional search space. Each crow i is defined by the vector in this search space as follows:

$$x^{i,it} = [x_1^{i,it}, x_2^{i,it}, \dots, x_d^{i,it}] \tag{11}$$

where $i = 1, 2, \dots, N$, $it = 1, 2, \dots, it_{max}$ and it_{max} is the largest number of iterations. Each crow also has a memory that remembers the best experience of the hide-out location. In each iteration the position of the crow's hide-out i is indicated by $m^{i,it}$. This is the best location Crow i has ever seen and is described as a vector:

$$m^{i,it} = [m_1^{i,it}, m_2^{i,it}, \dots, m_d^{i,it}] \tag{12}$$

Figure 2. Memory diagram of each particle

Particle (i)	Vehicle or robot path at time k	Mean and covariance of feature 1	Mean and covariance of feature 2	...	Mean and covariance of feature m
1	$x_{1:k}^1 = \{(x \ y \ \theta)^T\}_{1:k}^1$	$\mu_1^1 \ \Sigma_1^1$	$\mu_2^1 \ \Sigma_2^1$...	$\mu_m^1 \ \Sigma_m^1$
2	$x_{1:k}^2 = \{(x \ y \ \theta)^T\}_{1:k}^2$	$\mu_1^2 \ \Sigma_1^2$	$\mu_2^2 \ \Sigma_2^2$...	$\mu_m^2 \ \Sigma_m^2$
.
.
.
N_s	$x_{1:k}^{N_s} = \{(x \ y \ \theta)^T\}_{1:k}^{N_s}$	$\mu_1^{N_s} \ \Sigma_1^{N_s}$	$\mu_2^{N_s} \ \Sigma_2^{N_s}$...	$\mu_m^{N_s} \ \Sigma_m^{N_s}$

```

1: for i = 1: Ns
2:   Randomly choose initial state x0i in the search space
3:   w0i = 1/Ns
4: end for
5: k=1
6: while (k <> 0)
7: // New pose selection and update weights with new
   observations
8:   for i = 1: Ns
9:     sample a new pose xki ~ p(xki | xk-1i, uk)
10:    wki = wk-1i · p(zk | xki)
11: // Incorporate the measurement zki into the corresponding
    EKF for mapping
12:   for j = 1: m
13:     update mean μj,ki
14:     update covariance Σj,ki
15:   end for
16: end for
17: Apply the selected resampling method for the set of
    particles and their weights to get a new set of particles and
    weights
18: // Calculate the estimate (Same as probability integral from
    probability density function)
19:   for j = 1: Ns
20:     x̄kj = wkj · xkj
21:     xk+ += x̄kj
22:   Estimate map using μkj and Σkj
23: end for
24: k = k + 1
25: if fitness function condition is realized
26:   k = 0
27: end if
28: end while
    
```

Figure 3. Pseudo code for Fast SLAM

Crows move around in search of better food sources or hide-outs. The steps for updating the crow's position are as follows:

Step One: A crow, for example *j*, is randomly selected from the population. The crow *i* tries to follow the crow *j* to find his hideout (*m_j*). In this case, two modes can be created based on the crow *j*'s knowledge of the chase by *i*. A random number is generated with a uniform distribution between 0 and 1. If this random value is greater than a pre-defined parameter named as Awareness Probability (AP) we go to step 2, otherwise we go step 3.

Step Two: In this step the crow *j* does not know that crow *i* is chasing him. Thus, crow *i*, according to the following relationship, reaches the crow's hide-out *j*:

$$x^{i,it+1} = x^{i,it} + r_i \times fl \times (m^{i,it} - x^{i,it}) \quad (13)$$

where $x^{i,it+1}$ is the location of crow *i* in iteration *t* + 1 and $x^{i,it}$ is the position of the crow *i* in iteration *t* and $m^{i,it}$ is the position of the crow *j* in iteration *t* and r_i is the random number described earlier and *fl* is called flight length. Figure 4 schematically illustrates this case and shows the effect of *fl* on the search ability. Large

values are the result of global search (far) and small values of *fl* are the result of local (neighbourhood) search. As shown in Figure 4, the next position of the crow *i* is on the line between $x^{i,it}$ and $m^{i,it}$. If *fl* is less than 1, the next position of the crow *i* is on a line that may exceed $m^{i,it}$ if *fl* is greater than 1.

Step Three: Crow *j* knows that crow *i* is chasing him. Therefore, to protect his stockpile from theft, crow *j* moves randomly to another location (search space) and the crow *i* will be fooled. This can be summarized in what follows:

$$x^{i,it+1} = \begin{cases} x^{i,it} + r_i \times fl \times (m^{i,it} - x^{i,it}) & \text{if } r_i \geq AP \\ \text{a random position,} & \text{otherwise} \end{cases} \quad (14)$$

Step Four: After updating the crow's position *i* its memory will also be updated as follows:

$$m^{i,it+1} = \begin{cases} x^{i,it+1}, & \text{if } F(x^{i,it+1}) < F(m^{i,it}) \\ m^{i,it}, & \text{otherwise} \end{cases} \quad (15)$$

where *F*(.) represents the value of the objective function.

In CSA, all crows generate new positions and update their memory. These steps continue until the maximum number of iterations. Finally, the best memory response is selected as the CSA optimized response.

In CSA, abundance and diversity are mainly controlled by the awareness probability parameter (AP). By reduction of awareness probability value, CSA is tendentious to encourage search on a local area

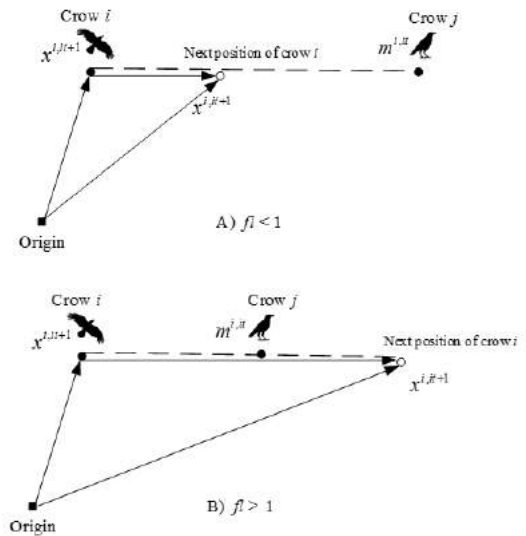


Figure 4. Schematic of the CSA mode for $fl < 1$ and $fl > 1$. Crow *i* can move along the line in different positions [30]

which is found by an appropriate response there. Thus, use of small values of AP, increases abundance. Furthermore, by increasing the AP value, the probability of searching for an area that is adjacent to the current appropriate response is less likely and CSA tends to have a global search space (randomly). Therefore, use of large values of AP increases abundance. Figure 5 displays the pseudo code for crow search algorithm [30].

3. CSAPF-SLAM ALGORITHM

As mentioned in the introduction, the SIR method for particle sampling is used in response to particle degradation problems. However, the SLAM problem still involves other issues such as sample depletion and high precision estimation with fewer particles. In response to these problems, modern particle filtering based on intelligent optimization mechanism of the biological group is a new development direction. The particles in the particle filter are considered as individual's in biological clusters and the distribution of particles is simulated using the motion laws of biological clusters. In other words, copying particles with higher weights and removing samples with lower weights and having the same history for the samples in the resampling process creates a challenge in resampling called particle impoverishment. In fact, the loss of particle diversity for estimation has led to the lack of particles. To overcome this problem, one solution is to diversify the selection of particles after resampling. That's why we go to biological group. In this article, the group of crows is considered as particles.

The following notes are considered in order to adapt the Crow Search Algorithm to the SLAM:

```

1: Randomly initialize the position of a flock of N crows in the
   search space
2: Evaluate the position of the crows
3: Initialize the memory of each crow
4: while iter < itermax
5:   for i = 1: N (all N crows of the flock)
6:     Randomly choose one of the crows to follow (for
       example j)
7:     Define an awareness probability
8:     if rj ≥ APj,iter
9:       xi,iter+1 = xi,iter + ri × fli,iter × (mj,iter - xi,iter)
10:    else
11:      xi,iter+1 = a random position of search space
12:    end if
13:  end for
14:  Check the feasibility of new positions
15:  Evaluate the new position of the crows
16:  Update the memory of crows
17: end while

```

Figure 5. pseudo code for crow search algorithm

1. Initial Population Creation: Initial population is assumed to be equal to FastSLAM particles and their relationships are as follows:

$$x_i = p_i + \text{unifrnd}(-\varepsilon, \varepsilon, \text{size}(p)) \quad (16)$$

where x and p are crow and particle position, respectively. ε is a small number, $\text{size}(p)$ represents particle dimension and $\text{unifrnd}(\cdot)$ is a random uniform distribution. In fact, crows are produced using this method based on the particles and with a slight difference from particles to maintain Fast SLAM correlation.

2. Determine the fitness function of each crow: To have a criterion for updating a crow's memory, after updating its location, the appropriate fit function must also be selected.
3. Crow position updating: The following relation can be used to update the state of a crow:

$$x_k^i = \begin{cases} x_{k-1}^i + r_i \times fl_{k-1}^i \times (m_{k-1}^j - x_{k-1}^i) & \text{rand} \geq AP \\ p_k^i + \text{unifrnd}(-\varepsilon, \varepsilon, \text{size}(p)) & \text{rand} < AP \end{cases} \quad (17)$$

where m_j is the best crow position that crow i chases and rand is an arbitrary random number.

Fast SLAM based on the crow search algorithm is obtained by substituting the position obtained from the crow search algorithm, i.e. Equation (17), in the observed position in Equation (8). Therefore, we will have the following for the mean value:

$$\tilde{x}_k = \sum_{i=1}^{N_s} w_k^i \cdot x_{k,Crow}^i \quad (18)$$

where $x_{k,Crow}^i$ is obtained by the following recursive algorithm:

$$x_{k+1,Crow}^i = \begin{cases} x_{k,Crow}^i + r_i \times fl_k^i \times (m_k^j - x_k^i) & \text{if } r_j \geq AP_k^j \\ \text{a random position} & \text{o.w} \end{cases} \quad (19)$$

Figures 6 and 7 show the flow and pseudocode of proposed algorithm, respectively, that help us in implementation and simulation.

The fitness function in the proposed method is calculated based on an innovation. In fact, the calculated variance between distance of each particle from the average distance between each particle and position estimate at that moment is considered as a function of fitness. In other words:

$$F(\tilde{x}) = \sum_{i=1}^N \frac{x_i - x_{avg}}{x_N} \quad (20)$$

where F is the fitness function and \tilde{x} is the estimated position using the proposed algorithm. The normalization factor (x_N) [8], and x_{avg} are calculated as follows:

$$x_N = \begin{cases} \max |x_i - x_{avg}|_{1 \leq i \leq m}, \max |x_i - x_{avg}|_{1 \leq i \leq m} > 1 \\ 1, & \text{others} \end{cases} \quad (21)$$

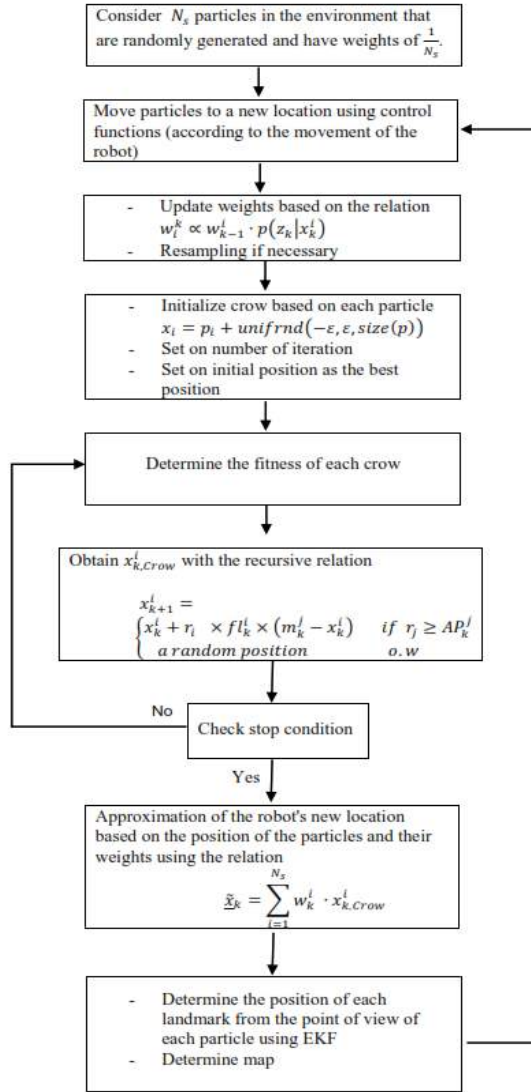


Figure 6. Flow of the proposed algorithm

```

1: for  $i = 1:N_s$ 
2:   randomly choose initial state  $x_0^i$  in the search space
3:    $w_0^i = 1/N_s$ 
4: end for
5:  $k=1$ 
6: while ( $k <> 0$ )
7: // New pose selection and update weights with new observations
8:   for  $i = 1:N_s$ 
9:     sample a new pose  $x_k^i \sim p(x_k | x_{k-1}^i, u_k)$ 
10:     $w_k^i = w_{k-1}^i \cdot p(z_k | x_k^i)$ 
11:    // Incorporate the measurement  $z_k^i$  into the corresponding EKF for mapping
12:    for  $j = 1:m$ 
13:      update mean  $\mu_{j,k}^i$ 
14:      update covariance  $\Sigma_{j,k}^i$ 
15:    end for
16:  end for
17: Apply the selected resampling method for the set of particles and their weights to get a new set of particles and weights
18: // Initialize crow based on each particle
  
```

```

19: for  $j = 1:N_s$ 
20:    $x_i = p_i + \text{unifrnd}(-\epsilon, \epsilon, \text{size}(p))$ 
21: end for
22: Initialize the memory of each crow
23: Set on number of iteration as  $iter_{max}$ 
24: while  $iter < iter_{max}$ 
25:   for  $i = 1:N_s$  (all  $N$  crows of the flock)
26:     Randomly choose one of the crows to follow (for example  $j$ )
27:     Define an awareness probability
28:     if  $r_j = AP^{j,iter}$ 
29:        $x^{i,iter+1} = x^{i,iter} + r_i \times fl^{i,iter} \times (m^{j,iter} - x^{i,iter})$ 
30:     else
31:        $x^{i,iter+1} =$ 
           a randomposition of search space
32:     end if
33:   end for
34: Check the feasibility of new positions
35: Evaluate the new position of the crows
36: Update the memory of crows
37: Determine the fitness function of each crow
38: end while
39: // Calculate the estimate (Same as probability integral from probability density function)
40: for  $j = 1:N_c$ 
41:    $\tilde{x}_k = w_k^j \cdot x_k^j$ 
42:    $x_k += \tilde{x}_k$ 
43:   Estimate map using  $\mu_k^j$  and  $\Sigma_k^j$ 
44: end for
45:  $k = k + 1$ 
46: if fitness function condition is realized
47:    $k = 0$ 
48: end if
49: end while
  
```

Figure 7. Pseudo code for proposed algorithm

$$x_{avg} = \frac{1}{N} \sum_{i=1}^N |\tilde{x} - x_i| \quad (22)$$

4. EXPERIMENTAL EVALUATION

To evaluate the proposed method and compare it with the existing Fast SLAM method, we first deal with the problem solving scenario. In the scenario, we look at the problem-solving steps and the relationships between the sensor observations and the control functions to localization and estimate the position of the landmarks.

4. 1. Scenario

In general, our problem-solving

scenario is as follows:

1. The robot starts moving from a point and spatial variations relative to that point are measured. At the starting point of motion, we take space containing N_s particles that are randomly generated and have weights of $1/N_s$.
2. The robot spends a moment along the way. In this case, we are faced with two issues:

A) Robot pose localization

It is clear that the particles must also be moved to new

$$\begin{bmatrix} x(k) \\ y(k) \\ \phi(k) \end{bmatrix} = f(x, u) = \begin{bmatrix} x(k-1) + \Delta T \left(v_c \cos(\phi) - \frac{v_c}{L} \tan(\phi) (a \sin(\phi) + b \cos(\phi)) \right) \\ y(k-1) + \Delta T \left(v_c \sin(\phi) + \frac{v_c}{L} \tan(\phi) (a \cos(\phi) - b \sin(\phi)) \right) \\ \phi(k-1) + \Delta T \frac{v_c}{L} \tan(\alpha) \end{bmatrix} \quad (23)$$

where v_c , L , a and b are robot velocity, the distance between the front and rear wheels, the distance between the laser and the center of the rear axle and the distance between the laser and the center of the front axle, respectively. In this way we moved the particles to a new position. Now we need to update the weights as well, which is based on the relation $w_i^k \propto w_{i,k-1}^i \cdot p(z_k | x_k^i)$. Obviously, sampling will also take place if necessary. After this step, particle impoverishment correction algorithms are performed by affecting location and weight. From the new position of the particles and their weights, the new location of the robot is approximated by Equation (8). If we use the CSAPF method, we conclude Equation (18) where $x_{k,Crow}^i$ is obtained by Equation (19).

B) Determining the location of landmarks

Based on the inverse of the observation model, which is the $l_{j,k}^i = h^{-1}(z_k, x_k^i)$, the position of each landmark is obtained from the point of view of each particle using EKF. In the following equation, $l_{j,k}^i$ represents the position of Landmark j from the perspective of particle i at time k , z_k is observation at time k , and x_k^i is the position of particle i at time k , which is obtained in section A. The function h , which is the observation model, has the following relations for the measurements of distance and angle sensors:

$$\begin{bmatrix} z_r \\ z_\theta \end{bmatrix} = h(x) = \begin{bmatrix} \sqrt{(x_1 - x_v)^2 + (y_1 - y_v)^2} \\ \text{atan}\left(\frac{y_1 - y_v}{x_1 - x_v}\right) - \phi + \frac{\pi}{2} \end{bmatrix} \quad (24)$$

The above equation shows that if the position of the robot is known in two-dimensional coordinates (x_v, y_v) and its orientation is ϕ and the landmark position is (x_1, y_1) , h indicates the measurements received by the sensors. Obviously, by inverting this function, the location of the landmarks can be approximated based on the position of the robot and observation measurements.

3. The robot spends a moment on the path again. At this time, determining the position of the robot is like the second step. But landmark localization is divided into two categories:

A) Facing new landmarks: The position of the new landmarks that the robot encounters are determined as in step two.

B) Facing previous landmarks: If the robot sees the previous landmarks again, then the previous position is

points. This particle transfer is applied to each particle by control functions (steering angle, speed, and noise).

updated with new information. This happens with Kalman's gain. This way, using the h function, a prediction about the measurements is made from the previous position of the landmark and the current position of the robot. In other words $\hat{z} = h(l_{j,k-1}^i, x_k^i)$. Then, we get the updated position of this landmark using the $l_{j,k}^i = l_{j,k-1}^i + K(z_k, \hat{z})$ where K is Kalman gain. It should be noted that at any moment, we have assumed that the corresponding variables are known. This is one of the assumptions of using Fast SLAM.

After stating the scenario, to prove the claim, the simulation must be performed using valid datasets. In the next section, we have dealt with the issue.

4. 2. Simulation

In order to test the proposed algorithm, we use simulator and presented dataset in Sydney University [26]. In this simulator, the robot is equipped with steering wheel angle sensors, laser and encoder. We used MATLAB code to simulate a particle filter with 150 particles. In this paper, we apply crow search algorithm to particle filter based SLAM. This paper compares localization accuracy of particle filter SLAM and CSAPF-SLAM.

1. System model

The schematic diagram of robot motion and robot observation is selected in accordance with what is shown in literature [12]

2. Performance analysis

In MATLAB platform, in a $100m \times 100m$ area, original PF-SLAM and CSAPF-SLAM are simulated. Robot motion velocity, sensor observation range and AP factor are considered 0.5 m/s, 15m and 0.3, respectively [12]. System Noise and observation noise are considered 0.1. In this paper, the position of the landmarks is considered constant in all run. In fact, in order to be a good reference for comparison, the data received by the sensors on robot and consequently the position of the landmarks is considered constant. However, this does not mean that the robot or vehicle is aware of landmarks position and this does not diminish the universality of the method. Figures 8 and 9 demonstrate simulation results using Fast SLAM and the proposed CSAPF-SLAM algorithms respectively. Blue and red solid lines represent GPS information and estimated path of robot respectively. Green stars correspond to landmarks and red stars are their estimated position. Horizontal and vertical axis in both

figures are in meters. From Figures 8 and 9 it is found that CSAPF-SLAM algorithm has a better performance and is closer to the original path (GPS information) than PF-SLAM and estimated position of landmarks are more accurate. The mean square error (MSE) criterion has been used to confirm performance improvement. Figures 10 and 11 show the considerable improvement of the path and landmarks' position, respectively. The graphs show the effect of increasing the number of particles on the landmarks position estimation error and the path estimation error. As can be seen, the error rate in the proposed method has improved significantly compared to the Fast SLAM method, and in both methods the error rate has decreased with increasing number of particles. Vertical axis in both figures are in meters.

It should be noted that the MSE obtained for each particle is the result of the average number of times the program runs for that particle. In other words, due to the random nature of particle selection and the use of random distributions in parts of the crow search

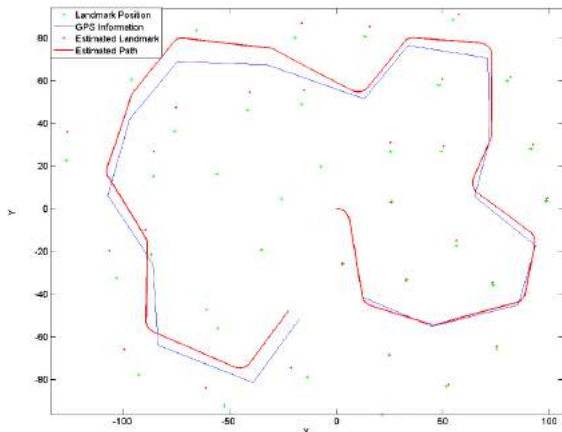


Figure 8. Bailey Simulator results for FastSLAM

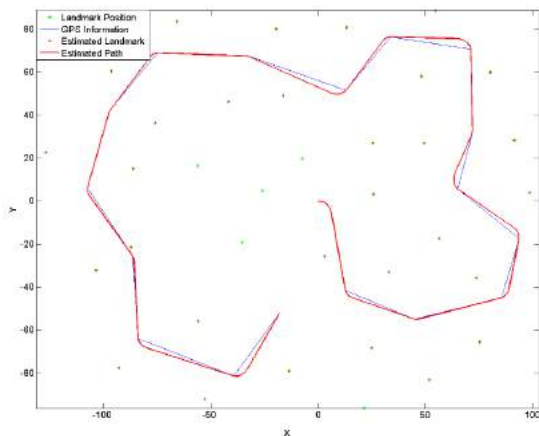


Figure 9. Bailey Simulator results for CSAPF-SLAM

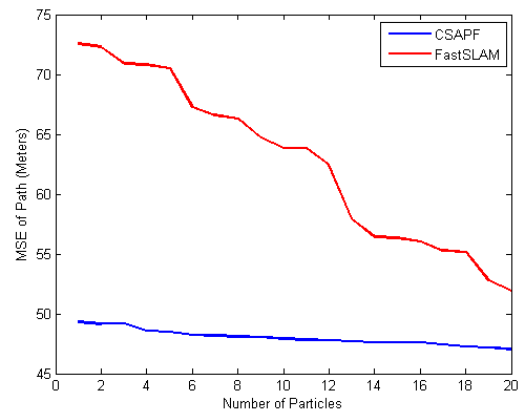


Figure 10. Mean Square Error between true and estimated path for Bailey Simulator

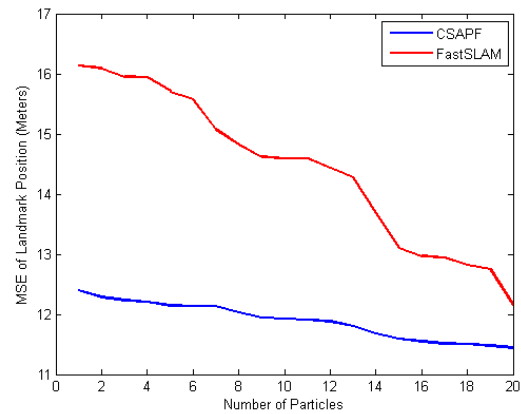


Figure 11. Mean Square Error between true and estimated landmarks position for Bailey Simulator

algorithm, similar to other meta-heuristic methods, with one run of simulation, proposed method performance improvement may not always be observed with increasing particle number. However, more program runs lead to the conclusion that the MSE mean decreases with increasing number of particles. The number of runs in our simulations was equal to 5.

3. Verification using real-world dataset

To confirm the test in real conditions, a vehicle with the sensors mentioned in the previous section will travel outdoors for 30 minutes in the presence of trees for a distance of 4 km. So here, unlike the methods in which landmarks are moving [31], we consider them fixed. This data set is known as Victoria Park Dataset and we have used it in our work.

Figures 12 and 13 show the results of Fast SLAM and CSAPF-SLAM simulations for Victoria Park Dataset, respectively. The horizontal and vertical axes are in meters. In both figures, the continuous blue dots represent the GPS information and the red line

represents the simulations from the two algorithms, and the stars represent the landmark position estimates.

As can be seen from the comparison of the two figures, the proposed CSAPF-SLAM algorithm is more consistent with the information obtained from GPS. Here too, the MSE criterion is used for comparison. Figure 14 shows the MSE for estimating the path in terms of the number of particles. In this figure, it is clear that the proposed CSAPF-SLAM algorithm achieves a significant improvement compared to Fast SLAM.

Another factor that is important to consider is the program running time. Although Figure 15 shows the longer time required to execute the proposed CSAPF method than Fast SLAM, but this amount of time increase versus increased accuracy seems negligible.

It can be seen that in the simulations, if we increase the number of particles, N_s in Figure 7, we get a higher accuracy estimate. Although by this we have lost more time for processing. Also, if we increase the velocity of the robot or vehicle, v_c in Equation (23), the

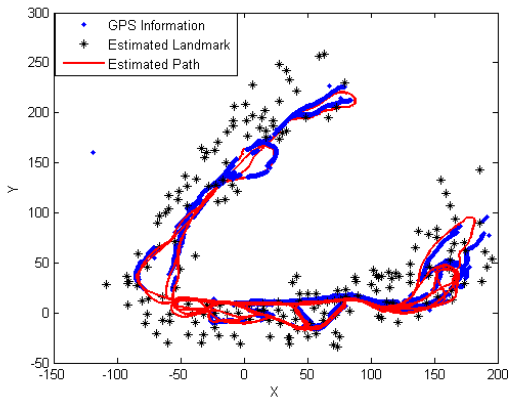


Figure 12. Fast SLAM simulation results using Victoria Park Dataset

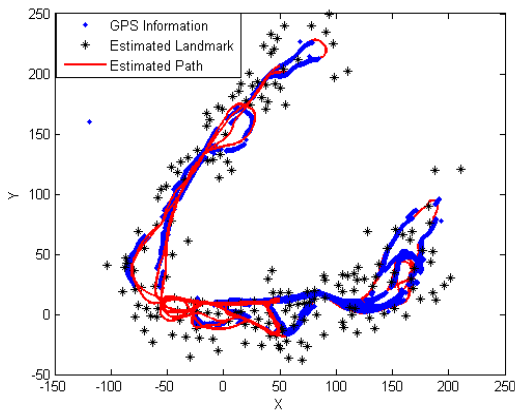


Figure 13. CSAPF-SLAM simulation results using Victoria Park Dataset

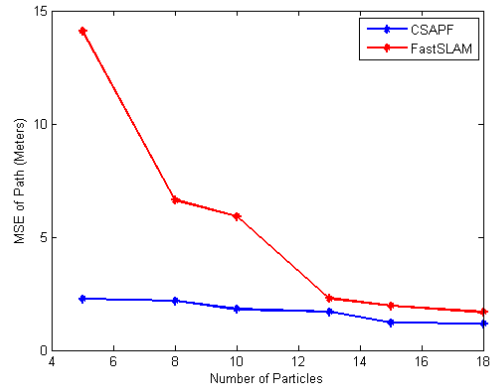


Figure 14. Mean Square Error between true and estimated path for Victoria Park Dataset

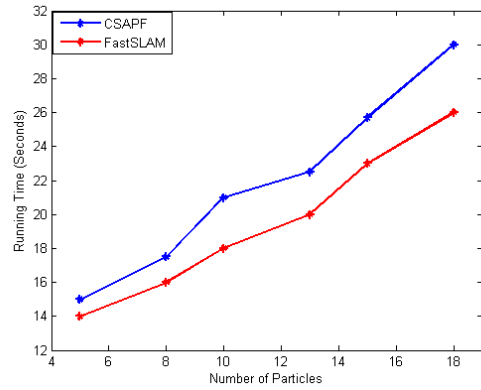


Figure 15. Running time of FastSLAM and CSAPF-SLAM for Victoria Park Dataset

observations and as a result the estimation will be less accurate. The next factor that can lead to a more accurate estimate is the use of a higher quality laser.

5. CONCLUSION

In all particle filter-based algorithms, using resampling to overcome particle degeneracy leads to particle impoverishment. This problem is also present in particle filter-based SLAM methods. Although the effect of particle impoverishment improvement is not directly observable, a reduction in particle impoverishment can be seen in improving the estimate. Therefore, our criterion for examining the reduction of particle impoverishment is the rate of improvement of the estimate.

There are two conventional ways to overcome this problem. The first is to diversify the choice of particle location and the other is to better allocate weight to the particles. In this paper, we select the first solution to

overcome this problem and we present a new method called CSAPF-SLAM.

The proposed method was investigated using the Car Park Dataset and Victoria Park Dataset and the simulation results show that although more run time was spent, the estimation error was significantly reduced.

In the future, situations could be considered in which the environment would include moving objects in addition to stationary objects, or the problem of cooperative SLAM for multiple robots could be considered in which multiple robots and their paths could be identified.

Statements and Declarations

Funding

The authors declare that no funds, grants, or other assistance were received during the preparation of this manuscript.

Competing Interests

The authors have no relevant financial or non-financial interests to disclose.

Author Contributions

All authors contributed to the conception and design of the study. Material preparation, data collection and analysis were performed by Hamid Jazayeriy, Javad Kazemitabar and Mohsen Abedini. The first draft of the manuscript was written by Mohsen Abedini, and all authors have commented on previous versions of the manuscript. All authors read and approved the final manuscript.

Ethics Approval

This study uses the Victoria Park dataset. This dataset does not relate to humans or animals. Therefore, ethical approval is not applicable.

Consent to Participate

This paper does not include human participants who need to obtain consent.

Consent to Publish

This paper does not include human participants who need to obtain consent. The authors consent to the publication of this paper.

Data Availability

The data that support the findings of this study are openly available in Australian Centre for Field Robotics (ACFR) known as "Victoria Park Dataset" at http://www-personal.acfr.usyd.edu.au/nebot/victoria_park.htm, [27].

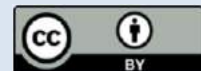
6. REFERENCES

- Smith, R., Self, M., and Cheeseman, P. "Estimating Uncertain Spatial Relationships in Robotics." In I. J. Cox & G. T. Wilfong (Eds.), *Autonomous Robot Vehicles*, New York, NY: Springer New York, (1990), 167-193. https://doi.org/10.1007/978-1-4613-8997-2_14
- Alitaleshi, A., Jazayeriy, H., and Kazemitabar, S. J. "WiFi Fingerprinting based Floor Detection with Hierarchical Extreme Learning Machine." In 2020 10th International Conference on Computer and Knowledge Engineering (ICCKE), 113-117. <https://doi.org/10.1109/ICCKE50421.2020.9303624>
- Hooshmand, M., Yaghobi, H., and Jazaeri, M. "Irradiation and Temperature Estimation with a New Extended Kalman Particle Filter for Maximum Power Point Tracking in Photovoltaic Systems." *International Journal of Engineering Transactions C: Aspects*, Vol. 36, No. 6, (2023), 1099-1113. <https://doi.org/10.5829/ije.2023.36.06c.08>
- Yuen, D. C. K., and MacDonald, B. A. "An evaluation of the sequential Monte Carlo technique for simultaneous localisation and map-building." In Proceedings of the 2003 IEEE International Conference on Robotics and Automation, Vol. 2, 1564-1569. <https://doi.org/10.1109/robot.2003.1241817>
- Doucet, A., Godsill, S., and Andrieu, C. "On sequential Monte Carlo sampling methods for Bayesian filtering." *Statistics and Computing*, (2000), 197-208. <https://doi.org/10.1023/A:1008935410038>
- Talebi, Z., and Timarchi, S. "Improved distributed particle filter architecture with novel resampling algorithm for signal tracking." *International Journal of Engineering Transactions C: Aspects*, Vol. 33, No. 12, (2020), 2482-2488. <https://doi.org/10.5829/ije.2020.33.12c.07>
- Montemerlo, M., Thrun, S., Koller, D., and Wegbreit, B. "FastSLAM: A Factored Solution to the Simultaneous Localization and Mapping Problem." In *Proceedings of the 2002 AAAI National Conference on Artificial Intelligence*, 593-598. <https://doi.org/10.1.1.16.2153>
- Lei, X., Feng, B., Wang, G., Liu, W., and Yang, Y. "A novel fastSLAM framework based on 2D lidar for autonomous mobile robot." *Electronics (Switzerland)*, Vol. 9, No. 4, (2020), 1-25. <https://doi.org/10.3390/electronics9040695>
- Murphy, K. P. "Bayesian map learning in dynamic environments." *MIT Press*, (2000), 1015-1021. <https://doi.org/10.1.1.21.3240>
- Doucet, A., Freitas, N. de, Murphy, K. P., and Russell, S. J. "Rao-Blackwellised Particle Filtering for Dynamic Bayesian Networks." In Proceedings of the 2000 16th Conference on Uncertainty in Artificial Intelligence, 176-183. San Francisco, CA, USA: Morgan Kaufmann Publishers Inc.
- Murphy, K., and Russell, S. "Rao-Blackwellised Particle Filtering for Dynamic Bayesian Networks." In *Sequential Monte Carlo Methods in Practice*, New York, NY: Springer New York, (2001), 499-515. https://doi.org/10.1007/978-1-4757-3437-9_24
- Zhu, D., Sun, X., Wang, L., Liu, B., and Ji, K. "Mobile robot SLAM algorithm based on improved firefly particle filter." Proceedings - 2019 International Conference on Robots and Intelligent System, ICRIS 2019, (2019), 35-38. <https://doi.org/10.1109/ICRIS.2019.00018>
- Sadati Tilehboni, S. A., Jazayeriy, H., and Valinataj, M. "Genetic Algorithm with Intelligence Chaotic Algorithm and Heuristic Multi-Point Crossover for Graph Coloring Problem." *Signal and Data Processing*, Vol. 14, No. 2, (2017), 75-95.
- Sangdani, M. H., and Tavakolpour-Saleh, A. R. "Particle swarm optimization based parameter identification applied to a target tracker robot with flexible joint." *International Journal of*

- Engineering Transactions C: Aspects*, Vol. 33, No. 9, (2020), 1797-1802. <https://doi.org/10.5829/ije.2020.33.09c.14>
15. Huang, C., Fei, J., Wang, L., and Liu, X. "Particle Filter Method Based on Multi-strategy Difference Cuckoo Search Algorithm." *Nongye Jixie Xuebao/Transactions of the Chinese Society for Agricultural Machinery*, Vol. 49, (2018), 265-272. <https://doi.org/10.6041/j.issn.1000-1298.2018.04.030>
 16. Chen, Z., Bo, Y., Tian, M., Wu, P., and Ling, X. "Dynamic Perceptive Bat Algorithm Used to Optimize Particle Filter for Tracking Multiple Targets." *Journal of Aerospace Engineering*, Vol. 31, No. 3, (2018), 1-17. [https://doi.org/10.1061/\(ASCE\)AS.1943-5525.0000834](https://doi.org/10.1061/(ASCE)AS.1943-5525.0000834)
 17. Gao, M. L., Li, L. L., Sun, X. M., Yin, L. J., Li, H. T., and Luo, D. S. "Firefly algorithm (FA) based particle filter method for visual tracking." *Optik*, Vol. 126, No. 18, (2015), 1705-1711. <https://doi.org/10.1016/j.jlleo.2015.05.028>
 18. Tian, M. C., Bo, Y. M., Chen, Z. M., Wu, P. L., and Zhao, G. P. "Firefly algorithm intelligence optimized particle filter." *Zidonghua Xuebao/Acta Automatica Sinica*, Vol. 42, No. 1, (2016), 89-97. <https://doi.org/10.16383/j.aas.2016.c150221>
 19. Havangi, R. "A new modified particle filter with application in target tracking." *Iranian Journal of Electrical and Electronic Engineering*, Vol. 16, No. 4, (2020), 449-460. <https://doi.org/10.22068/IJEEE.16.4.449>
 20. Iswanto, Ma'arif, A., Raharja, N. M., Supangkat, G., Arofiati, F., Sekhar, R., and Rijalusalam, D. U. "Pid-based with odometry for trajectory tracking control on four-wheel omnidirectional COVID-19 aromatherapy robot." *Emerging Science Journal*, Vol. 5, (2021), 157-181. <https://doi.org/10.28991/ESJ-2021-SPER-13>
 21. Moghaddasi, S. S., and Faraji, N. "A hybrid algorithm based on particle filter and genetic algorithm for target tracking." *Expert Systems with Applications*, Vol. 147, No. 7, (2020), 915-923. <https://doi.org/10.1016/j.eswa.2020.113188>
 22. Shijing, D., Hongru, C., Xudong, W., Deshi, W., and Yongyong, Z. "Modal Optimization Design of Supporting Structure Based on the Improved Particle Swarm Algorithm." *International Journal of Engineering, Transactions A: Basics*, Vol. 35, No. 4, (2022), 740-749. <https://doi.org/10.5829/IJE.2022.35.04A.14>
 23. Rashno, A., and Fadaei, S. "Image Restoration by Projection onto Convex Sets with Particle Swarm Parameter Optimization." *International Journal of Engineering Transactions C: Aspects*, Vol. 36, No. 2, (2023), 398-407. <https://doi.org/10.5829/IJE.2023.36.02B.18>
 24. Samieyan, B., MohammadiNasab, P., Mollaei, M. A., Hajizadeh, F., and Kangavari, M. "Novel optimized crow search algorithm for feature selection." *Expert Systems with Applications*, Vol. 204, (2022), 117486. <https://doi.org/https://doi.org/10.1016/j.eswa.2022.117486>
 25. Hussien, A. G., Amin, M., Wang, M., Liang, G., Alsanad, A., Gumaei, A., and Chen, H. "Crow search algorithm: Theory, recent advances, and applications." *IEEE Access*, Vol. 8, (2020), 173548-173565. <https://doi.org/10.1109/ACCESS.2020.3024108>
 26. "Tim Bailey Simulator." Retrieved from <http://www-personal.acfr.usyd.edu.au>
 27. Guivant, J. "Victoria Park Dataset." Retrieved from http://www-personal.acfr.usyd.edu.au/nebot/victoria_park.htm
 28. Hadian Jazi, S., Farahani, S., and Karimpour, H. "Map-merging in multi-robot simultaneous localization and mapping process using two heterogeneous ground robots." *International Journal of Engineering, Transactions A: Basics*, Vol. 32, No. 4, (2019), 608-616. <https://doi.org/10.5829/ije.2019.32.04a.20>
 29. Sanjeev Arulampalam, M., Maskell, S., Gordon, N., and Clapp, T. "A Tutorial on Particle Filters for Online Nonlinear/Non-Gaussian Bayesian Tracking." *IEEE Transactions on Signal Processing*, Vol. 50, No. 2, (2002), 174-188. <https://doi.org/10.1109/78.978374>
 30. Askarzadeh, A. "A novel metaheuristic method for solving constrained engineering optimization problems: Crow search algorithm." *Computers and Structures*, Vol. 169, (2016), 1-12. <https://doi.org/10.1016/j.compstruc.2016.03.001>
 31. Badalkhani, S., and Havangi, R. "Effects of moving landmark's speed on multi-robot simultaneous localization and mapping in dynamic environments." *Iranian Journal of Electrical and Electronic Engineering*, Vol. 17, No. 1, (2020), 1-10. <https://doi.org/10.22068/IJEEE.17.1.1740>

COPYRIGHTS

©2023 The author(s). This is an open access article distributed under the terms of the Creative Commons Attribution (CC BY 4.0), which permits unrestricted use, distribution, and reproduction in any medium, as long as the original authors and source are cited. No permission is required from the authors or the publishers.

**Persian Abstract**

چکیده

ردیابی مسیر و موقعیت یابی در بسیاری از زمینه ها، از جمله ربات ها و وسایل نقلیه خودران ضروری است. در برخی موارد، مانند مناطقی که سیگنال های GPS ضعیف هستند یا در دسترس نیستند، ردیابی مسیر به عنوان یک سیستم موقعیت یابی جایگزین استفاده می شود. در این موارد، مکان یابی و نقشه برداری همزمان (SLAM) از اهمیت بالایی برخوردار است، زیرا نیازی به دانش قبلی و اثر انگشت آفلاین تجربی ندارد. SLAM را می توان با الگوریتم های پردازش سیگنال ترکیب کرد که در میان آنها فیلتر ذرات برجسته است. با این حال، چالش هایی مانند تباهی وزن ذرات و فقدان ذرات وجود دارد که باید با آنها مقابله کرد. در واقع، از دست رفتن تنوع ذرات برای تخمین منجر به فقدان ذرات می شود. برای غلبه بر این مشکل، یک راه حل، تنوع بخشیدن به انتخاب ذرات پس از نمونه برداری مجدد است. در این مقاله، ما یک الگوریتم جستجوی کلاغ (CSA) برای غلبه بر این مسائل و بهبود تخمین موقعیت پیشنهاد می کنیم. نتایج شبیه سازی نشان می دهد که این الگوریتم عملکرد FastSLAM را تا حد زیادی بهبود می بخشد.



Numerical Evaluation of Two-dimensional Multi-layer Cover System to Regulate Acid Mine Drainage of Tailing Dams

M. Jafarzadeh Marandi^a, V. Ghiasi^{*b}, K. Badv^a

^a Department of Civil Engineering, Faculty of Engineering, Urmia University, Urmia, Iran

^b Department of Civil Engineering, Faculty of Civil and Architecture Engineering, Malayer University, Malayer, Iran

PAPER INFO

Paper history:

Received 16 April 2023

Received in revised form 03 July 2023

Accepted 04 July 2023

Keywords:

Tailing Dam

Acid Mine Drainage

Cover Systems

Oxygen Diffusion

Numerical Modeling

ABSTRACT

In the mining industry, cover systems for tailings are an effective means of reducing acid mine drainage. An example of this type of system is the multi-layer cover system that is used in arid climates where the annual evaporation rate is greater than the annual rainfall. For users and designers of mine tailings dams, the current research is aimed at identifying the optimal cover system and engineering of the mine waste disposal site, as well as investigating effective geotechnical parameters in controlling the oxygen gas entering the mine waste disposal site. In this research, after careful examination of scientific literature and data collection, it is first validated using numerical modeling, Finite Element Method (FEM) based on the VADOSE/W software, and then modeling is done based on the collected data. One-dimensional modeling has often been used in studies on the evaluation of cover systems, but in this research, two-dimensional modeling has been used to analyze the behavior of coating systems. The key to the successful operation of cover systems is maintaining the storage layer at a saturation level of about 85% throughout the year. The two cover systems, "storage and release", "optimized storage and release," are ineffective in maintaining the storage layer at about 85% saturation. However, the capillary barrier cover system has worked successfully and maintained the degree of saturation of the storage layer at about 80%. Due to the use of low-sulfide waste material as an oxygen-consuming layer, the performance of all three cover systems was acceptable. However, it is worth noting that the capillary barrier cover system was able to immediately cut off the diffusion of oxygen due to the high degree of saturation of the storage layer, while in the other two cover systems, this decrease in diffusion and oxygen concentration was gradual. Therefore, the capillary barrier cover system is suggested as the most optimal system according to the weather conditions and the type of waste materials.

doi: 10.5829/ije.2023.36.10a.10

Graphical Abstract

Management and control of acid mine drainage from mining activities



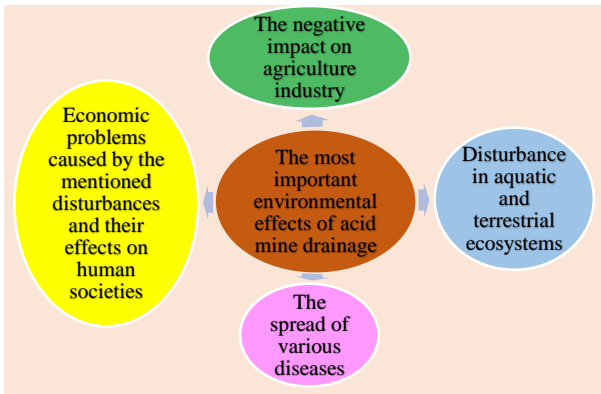
Relations of the production process of acid mine drainage

*Corresponding Author Institutional Email: V.ghiasi@malayeru.ac.ir (V. Ghiasi)

Please cite this article as: M. Jafarzadeh Marandi, V. Ghiasi, K. Badv, Numerical Evaluation of Two-dimensional Multi-layer Cover System to Regulate Acid Mine Drainage of Tailing Dams, *International Journal of Engineering, Transactions A: Basics*, Vol. 36, No. 10, (2023), 1839-1856

In the method of separation and concentration of copper deposits by flotation method, low-grade minerals are separated, which is the main factor in the production of acidic mine drainage, and the lack of efficient management will bring irreparable environmental consequences.

The resulting low-grade minerals should be collected in tailings dams, and in order to prevent the production of acidic mine drainage, a suitable covering system should be used according to the climatic and economic conditions of the region.

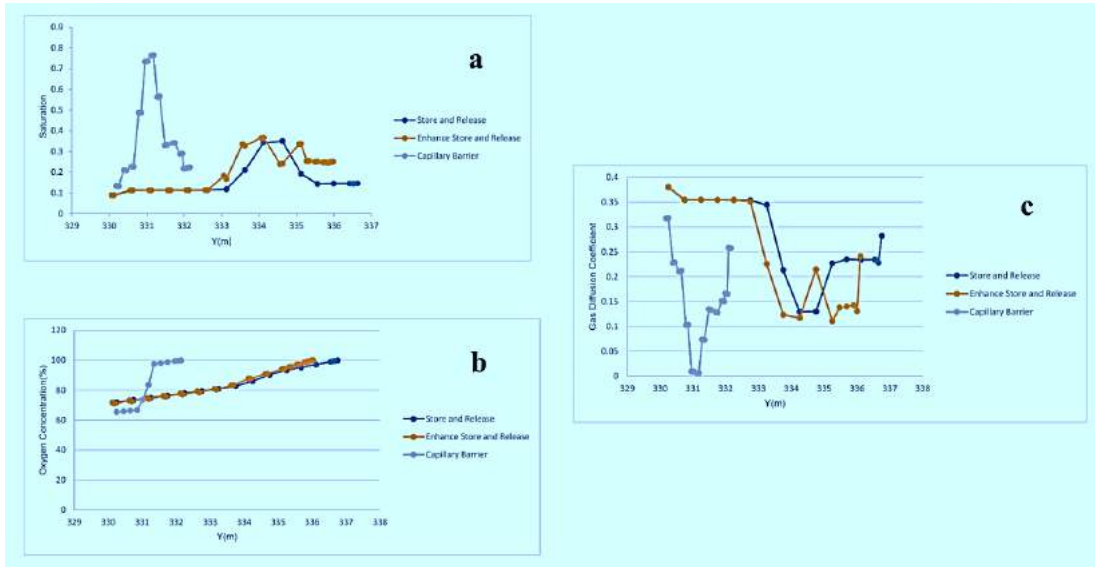


The details of the coating systems evaluated for the climatic conditions of the region studied in this research as a solution for the management of acidic mine drainage

The key point in the successful performance of multilayer coating systems

Keeping the storage layer in the cover system at about 85% saturation throughout the year by using capillary, capillary break, suction, and seepage properties

By comparing the performance of the storage layer and examining the results of the modeling done by the software, we find that the performance of the storage layer itself is a function of the performance and relationship of the other layers of the evaluated coating systems, and therefore, the capillary barrier coating system show the best performance and it is the most suitable suggestion for the study area.



1. INTRODUCTION

Every mining activity change and disturbs, more or less, the condition of the natural environment by mainly energy consumption, deformations of the earth, various changes in water relations, emission of gas, dust, and noise, and others [1, 2]. The effects of mining activities, uncontrolled mining, and tailings produced can adversely affect the environment, resulting in water, air, and soil pollution. Mining can also adversely affect human health because the pollutants may directly or indirectly enter into human body [3].

The tailings dams must be designed according to the volume of mining activities; some large-scale orebodies extend from the surface to the extreme depths of the ground. Such orebodies should be extracted by combining surface and underground mining methods; therefore, many waste materials will be produced [4]. The stability of tailings dams is another important issue that must be considered because the leakage or destruction of tailings dams will lead to environmental disaster; therefore, the geological information is beneficial for determining the geotechnical domain. It can be used for guidance on developing pit slope design parameters in open pit mining or the design of tailing dams and other geotechnical purpose such as defining the probability of failure, slope movement guidance, and risk assessment [5]. Using engineering cover systems on mineral tailings is practiced for several reasons. These include preventing tailings erosion and dust generation, controlling the entry of oxygen and water into tailings (to prevent acid drainage production), preventing the spread of contaminants to the environment by controlling seepage, and providing conditions for establishing a sustainable vegetation system. Regulating water penetration into hazardous industrial, urban, mineral, and radioactive waste disposal areas is one of the most significant reasons for implementing cover systems [6-9]. In the course of mining and afterward, sulfuric acid and metal ions are produced as a result of the oxidation of pyritic materials. A range of water chemistries are created by the reaction between these products and the host rock, surface water, and groundwater [10, 11]. Acid Mine Drainage (AMD) is acidic runoff containing heavy metals and sulfates. Mine drainage is referred to as AMD [12]. It is obtained from the oxidation of sulfide minerals, mainly pyrite, in the tailings of sulfide processing plants and low tailings dumps of sulfide and coal mines. Sulfide is one of the most critical environmental problems in the mining industry [13-15]. Sulfur-oxidizing bacteria (SOB) can also increase AMD production resulting in environmental problems [16-18]. The control of such disease, once it has developed at a mine, can be difficult and expensive. AMD must be collected and treated if it cannot be prevented. As a general rule, the treatment of AMD is more expensive than the control of AMD, which

is often carried out early on in the mining process and may remain necessary for many years after the mining activity has ended. There is a difference between tailings and waste rock in terms of particle size, porosity, the surface area of sulfide minerals, and the homogeneous distribution of sulfide and alkaline minerals. These differences affect the rate of potential oxidation and neutralization processes and the quality of AMD. Waste material characterization and quantification is the first step for designing and implementing AMD control measures [19].

Sulfide minerals are oxidized by oxygen and water, producing sulfuric acid. AMD contamination in mining areas is associated with problems related to surface, groundwater, and soil pollution. In areas where surface and groundwater are contaminated by AMD, purification of water resources for drinking and industrial use is very laborious and costly; Therefore, reducing and avoiding AMD production over the past few decades has been challenging for researchers. It requires the prevention of oxidation by limiting the penetration of oxygen and water into reactive wastes, which can be controlled by implementing a suitable cover system on tailings [20]. Before the development of AMD control measures, possible options such as dry cover, water cover, AMD collection, and treatment are evaluated for technical and economic feasibility. The decision is made primarily based on the total cost of the option and the effect of the option on the generation of AMD and its life span. In the case where AMD has already developed, the treatment may be the most feasible method. The water treatment process will depend on the plant water chemistry and the discharge permit but will typically include pH adjustment, removal of dissolved metals, and removal of suspended solids. An appropriate passive system is selected based on water chemistry, flow rate, local topography, and site characteristics [21].

There are two types of passive treatment technologies: biological and geochemical. As part of biological passive treatment technologies, bacterial activity is generally stimulated, and organic matter is used to adsorb contaminants and stimulate microbial sulfate reduction. Prior to selecting an appropriate treatment technology, AMD conditions and chemistry must be characterized. Passive treatment is often considered when AMD severity and available resources do not warrant active treatment. As a means of neutralizing acidity, alkaline chemicals are continuously added, including lime, slaked or hydrated lime, anhydrous ammonia, or sodium hydroxide [22, 23]. However, since air and water are considered key ingredients of AMD, control methods usually aim to reduce the flux of air or water by isolating the waste material. Oxygen diffusion cover systems that various researchers have studied to reduce AMD production include:

- Single-layer sand cover system
- Sulfide-containing monolayer cover system with raised water leveling mechanism (using desulfurized tailings as cover)
- Multi-layer cover system with store and release mechanism
- Multi-layer cover system with capillary barrier mechanism

The effectiveness of a dry "soil" cover system relies on the presence of low hydraulic conductivity and high moisture retaining layer; a low-permeability soil cover containing a layer of compacted clay can be constructed as a single-layer or multi-layered system over either tailings or waste rock dumps [24]. In single-layer sand cover systems with a water leveling mechanism, the material of the cover system is selected so that water penetrates the mineral tailings in wet seasons. A cover on the tailings limits evaporation and increases the static level of water inside the tailings. As a general rule, according to Figure 1a, the position of the water level should be controlled so that the height of the part of the tailings that is above the static level of water is less than the AEV value of the tailings. Controlling the water level causes capillary saturation to increase the degree of saturation of tailings located above the static surface and prevents oxygen penetration to the waste (below the static level of water). In such a manner, the oxygen diffusion coefficient to the mineral tailings is significantly reduced, and the production of AMD decreases [25-27]. Dagenais et al. [28] numerically studied the behavior of a sand monolayer cover system (with rising water level) and the effect of various parameters such as cover properties and thickness, water level depth, and hydraulic properties of tailings by numerical modeling applying Soil Cover software. The importance of the effect of sand layer thickness on tailings water content profiles was also investigated. Based on their finding, if the sand layer is used as a cover system, the degree of saturation of the surface area of the tailings rises to more than 95%, and oxygen diffusion to the tailings materials decreases. However, if the sand layer is not used, the degree of saturation in the range of the tailings surface remains 70 to 74%, and oxygen diffusion to the tailings materials increases. The results of this study revealed that if a 30 cm layer of sand is used on the tailings, and if the depth of water level from the surface of the tailings (d) is less than half of AEV of materials (according to Figure 1a), the surface area of the tailings keep conditions near saturation for 60 days and penetration of oxygen into the tailings is limited.

As such reducing the oxidation rate of sulfide minerals, AMD production is also controlled. In this study, instead of using the sand layer, which the idea was taken from the work of Dagenais et al. [28] a suitable layer for the growth of vegetation was used so that the

capabilities of the vegetation system were used to control evaporation and transpiration, and the results of the analyzes show proper efficiency and matches with the results of the work of Dagenais et al. [28]. Ouangrawa et al. [29] investigated the effect of the rising static level of water (change of parameter d as shown in Figure 1(a)) on the reduction of AMD production by performing column experiments and analyzing various parameters. This study investigated the effect of changing the height of static water levels by measuring pH and the concentration of major ions, including sulfate, iron, zinc, copper, and lead. The results uncovered that if the depth of the static water level (d) is about half the AEV of the waste material, there will be a significant reduction in AMD production. Also, if the tailings have lower hydraulic conductivity and higher AEV due to reduced drainage capability. The performance of the cover system (with a rising water level) will be improved, and AMD production will be reduced.

Another type of cover system is the sulfide-containing monolayer cover system (Figure 1(a)). As discussed, the main role of the oxygen diffusion cover system with a raised water leveling mechanism is to help create near-saturation conditions in the surface area of the tailings, which leads to a reduction of oxygen diffusion into the tailings. However, some oxygen seeps into the tailings through the cover system. If a compound such as a sulfide in the cover system material initiates a chemical reaction with some of the penetrating oxygen and precipitates in the cover system, the oxygen penetration into the tailings will be further reduced, and AMD will be more controlled. In a similar vein, Demers et al. [30] investigated the behavior of a monolayer cover of desulfurized tailings on mineral tailings and used an instrumentalized column to evaluate the oxygen flow. The results of the present study showed that placing low-sulfide tailings as an oxygen-consuming layer significantly reduces the production of AMD, which is consistent with the results of the work done by Demers et al. [30].

Using a multi-layer oxygen diffusion covering system with a capillary barrier mechanism and a storage-diffusion mechanism (in both integrated and incremental types) is another method applied by researchers to regulate AMD (Figure 1(b)). Two or more layers can be used in a design, including from top to bottom: a revegetated soil layer to retain moisture; a coarse layer to provide lateral drainage of infiltration; a compacted clay layer to prevent oxygen penetration; and a compacted alkaline layer to facilitate cap construction and minimize the reaction of water in the waste with the clay layer. In some cases, instead of revegetation, a layer of coarse material is placed for erosion control. To be effective, clay or other low-permeability soil must be saturated with water to limit oxygen. Using an organic layer at the

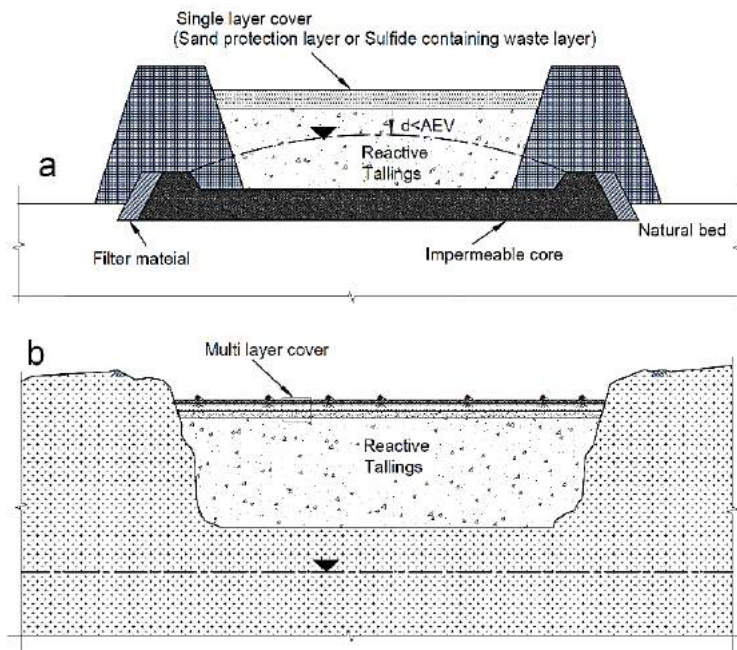


Figure 1. Raised water level cover system (monolayer of sand or monolayer of sulfide-containing tailings) (a) [29], multi-layer cover system (b) (these shapes are not scales and the height of the cover is much lower than the height of the tailings)

tailings/water interface effectively improves the effectiveness of water covers [31, 32]. The erosion of dams due to wind and rain can affect stability and produce environmental problems. Many methods are used to combat this, such as vegetation of the dam banks and chemical stabilization to form an air and water-resistant crust. An ideal soil cover consists of a sufficiently thick soil layer and appropriately regraded slopes that can induce runoff, resist erosion and retain water. The top layer can be vegetated to maximize the evapotranspiration of water to decrease infiltration and resistance to erosion. Furthermore, the presence of plants in the tailings impoundment, especially emergent plants growing at the edges, improves the physical stability of the tailings through their roots. The efficiency of a revegetated soil cover can be further increased by placing a layer of coarse rock beneath the cover to form a capillary break and decrease percolation.

A general rule in the design of multi-layer covering systems with storage-diffusion mechanisms is that the storage layer (moisture retention layer) can store water in wet seasons and release water in dry seasons through evaporation and perspiration to prevent oxygen diffusion and accordingly control AMD production [33]. One of the advantages of this type of cover system is that it can be more successful in dry climates than other cover systems. The basis of multi-layer covering systems is to keep the storage layer near high saturation, in which the oxygen diffusion coefficient is low, consequently reducing the oxidation rate of sulfide minerals and AMD production to a minimum [34].

In another study, Bosse et al. [35] examined the storage and diffusion covering systems made of phosphate limestone tailings in a semiarid climate to control AMD and tested the performance of the covering system at two different states, i.e., thicknesses and critical. According to the results, it was found that the designed cover system has succeeded in storing rainwater in wet seasons and releasing it in dry seasons. It was also found that the geometry of the designed cover is another important factor that should be considered in their design.

One-dimensional modeling has been used to evaluate covering systems so far, and the effect of the oxygen infiltration process and thickness change of the storage layer of a multi-layer covering system in controlling AMD has not been scrutinized to the best of researchers' knowledge.

Therefore, in the current paper, various coating systems suitable for semiarid climates have been examined. Among the available scenarios, using software analysis, the most optimal and most suitable coating system has been selected according to the climatic conditions of the region and the type of tailings from Songun copper mine; in addition, the sensitivity analysis of covering systems to changes in the thickness of the storage layer and the effect of oxygen infiltration on AMD control (Songun copper mine tailings) was evaluated using two-dimensional modeling in several different scenarios. Furthermore, the effect of the arrangement of low and high sulfide materials in the upper and lower parts of the covering system to increase oxygen consumption and improve the system's efficiency

has been challenged for the first time. Also, for the first time, a multi-layer capillary barrier covering system containing a fine-grained layer between two coarse-grained layers to control AMD (Songun 2copper mine tailings) was proposed and evaluated. The most important parameter to control the efficiency of coating systems is its ability in terms of the connection of different layers to maintain the storage layer in near-saturation conditions, which controls the diffusion of oxygen and also limits the reach of water to the waste materials and thus minimizes the production of acidic drainage.

Applying numerical modeling, the behavior of these covers in regulating the oxygen-percolating copper tailings was evaluated. Different scenarios were elucidated for modeling, which includes three types of multi-layer cover systems in the order of the layers, and the material of the layers is very important. The comparison of the oxygen diffusion coefficient in the proposed coating systems has been discussed, and according to the graph presented, the oxygen diffusion coefficient in the engineering layer of the capillarity barrier coating system and especially in the storage layer, is much lower than the other two coating systems, which is in good agreement with the other two diagrams.

2. MATERIALS AND METHODS

This research aims to design an optimal coating system to control and reduce acid drainage from mineral waste materials, which is one of the problems of human societies, especially in Iran. Due to the arid and semiarid conditions of the country, where the annual evaporation rate is higher than the annual rainfall in most months of the year, and we are always facing problems in providing

a sustainable water source, we must use multi-layer soil cover systems. The main condition for the production of acidic sewage, which causes soil and water pollution downstream and many problems caused by it, is the access of oxygen or water to the waste materials, which during chemical reaction with the waste materials of Boise containing sulfide materials such as pyrite causes the production of acidic sewage, so to control the production of acidic sewage should be prevented from penetration and reaction of these two with waste materials. The key point in the design of these covering systems is to create conditions with the design of different layers so that the water from rainfall in wet seasons is stored in the layers of the covering system, and in hot and rainless seasons, it can keep the storage layer saturated as well as the underlying layer. The storage layer must create a vacuum and negative suction conditions to prevent water seepage from the storage layer so that both the storage layer remains saturated and prevents water from reaching the waste materials. The saturation of the storage layer around 85 % is the condition of preventing oxygen from reaching the waste materials through the diffusion process. The research flowchart for the current study is illustrated in Figure 2. Geomaterial parameters used in modeling are presented in Table 1.

2. 1. Site Description

Northwest Iran has a cold semiarid climate [36]. Songun copper mine is in northwestern Iran in East Azarbaijan, Varzeqan City. It is located in a mountainous area with cold, icy winters and mild summers. The average maximum temperature was recorded at 33 °C in summer and 4 °C below zero in winter. The average annual rainfall is 250 mm, and relative humidity per year ranges from 52 to 82%. The prevailing wind direction is south to west. It is foggy

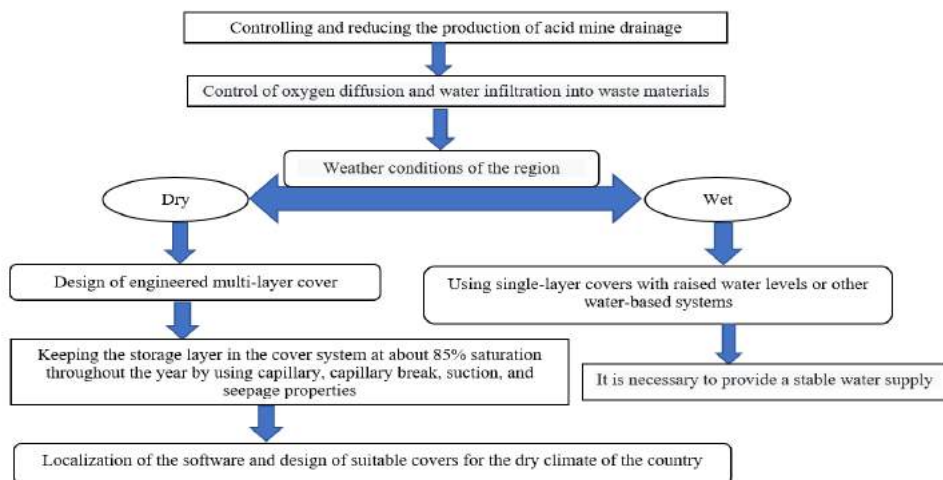


Figure 2. Research flowchart for the current study

TABLE 1. Geomaterial Parameters Used in Modeling

Angel of internal friction(ϕ°)	
Bed Rock	30°
Waste Material with high sulfide	35°
Waste Material with low sulfide	34°
Coarse-Grained Layer	35°
Fine-Grained Layer	37°
Growth Layer	31°
Silty Sand (Storage Layer)	29°
Compacted Layer	43°
Unit weight(γ)(KN/m³)	
Bed Rock	26.5
Waste Material with high sulfide	19.5
Waste Material with low sulfide	19.5
Coarse-Grained Layer	19
Fine-Grained Layer	16
Growth Layer	18
Silty Sand (Storage Layer)	17
Compacted Layer	21
Porosity(e) (%)	
Bed Rock	1
Waste Material with high sulfide	40
Waste Material with low sulfide	30
Coarse-Grained Layer	38
Fine-Grained Layer	32
Growth Layer	42
Silty Sand (Storage Layer)	25
Compacted Layer	12
Poisson's ratio(ν)	
Bed Rock	0.1
Waste Material with high sulfide	0.33
Waste Material with low sulfide	0.27
Coarse-Grained Layer	0.22
Fine-Grained Layer	0.17
Growth Layer	0.38
Silty Sand (Storage Layer)	0.25
Compacted Layer	0.19
Young's Modulus (E)(Mpa)	
Bed Rock	65
Waste Material with high sulfide	85
Waste Material with low sulfide	105
Coarse-Grained Layer	45

Fine-Grained Layer	15
Growth Layer	12
Silty Sand (Storage Layer)	22
Compacted Layer	59

around the mine on most days of spring and summer. The highest temperature occurs between July and August, and the lowest is between January and February. According to the statistics related to precipitation and evaporation published by the Meteorological Department of Varzeqan City, the evaporation rate in most months of the year is more than precipitation, so the climate of the mining area is dry. Due to the region's arid climate, the use of monolayer covering to control AMD tailings is not recommended, and the design of multi-layer covering systems is preferred. Due to the sulfide nature of Songun copper mine tailings (presence of pyrite and chalcopyrite at the rate of 1 to 10%) and also the presence of high seasonal rainfall in the area, AMD production is one of the environmental problems of the region. Unfortunately, AMD from the tailings dam of Songun copper mine is discharged into the river, and the negative environmental effects on Arasbaran forests are obvious [37]. pH parameters and sulfate, copper, and manganese amounts are excessive [38]. Hence, to prevent environmental pollution, in addition to installing an acid wastewater treatment system at the output of Songun copper mine, it is essential to use a suitable covering system on tailings to reduce AMD production.

2. 2. Modeling Scenarios

According to Figure 3, an uncovered scenario as the baseline scenario (case a) and three scenarios (cases b, c & d) for covering Songun copper mine tailings dam was evaluated so that the thickness of the systems varies depending on the type of system. The storage and diffusion cover system, the upgraded storage and diffusion covering system, and the capillary barrier system are referred to as the first, second, and third scenarios, respectively. In the baseline scenario, the basis of all tailings is high-sulfide. However, in other scenarios, it has been proposed innovatively that the sulfide materials are first accumulated, and then the low sulfide tailings are applied to it. In these scenarios, firstly, the vegetation layer used in the upper part of all cover systems (0.20 m thick) must survive the dry season to maintain its performance with the least delay after the start of the wet season. Secondly, the storage layer below the vegetation layer should be able to store all the annual rainfall that may occur in a relatively short time (wet season).

- Baseline scenario (a), Uncovered condition (to evaluate the performance of tailings in uncovered condition)

- Scenario 1 (b), store and release cover system
- Scenario 2 (c), optimized store and release cover system
- Scenario 3 (d), capillary barrier cover system

Baseline scenario: In this scenario, the cover system is not used, and the natural bed in the area is under the tailings. To assess the most critical situation regarding AMD production, the groundwater level is considered the lowest annual level. Tailings from the mining activities of Songun copper mine are transferred to the tailings dam on the bed layer through pumping pipes. The base state cross section and the specifications of their materials are presented in Figure 3(a).

As shown in Figure 3(b), a section of the storage and diffusion cover system is shown as the first proposed scenario. The key concept of this system is to store water in the storage layer in wet seasons and to release water stored by evapotranspiration in dry seasons. This cover system consists of three layers placed on low-sulfide tailings materials with a thickness of 70 meters (low-sulfide tailings are located on 210 meters of high-sulfide tailings materials). For the lower layer of the cover system, coarse-grained materials with a thickness of 5 m are proposed. For the middle layer, referred to as the store layer, 1.3 m thick layered sand is proposed, designed to break the capillary. The top layer is 0.2 m thick vegetation designed to prevent erosion and dust.

According to Figure 3(c), the second proposed scenario for the cover system was called the "optimized store and release cover system", similar to the first scenario with three layers. Due to the high cost of building the storage layer (middle layer) and also to control the sensitivity, the covering system against changes in the thickness of the storage layer is proposed. In the second proposed scenario, the thickness of the storage layer was reduced from 1.3 m to 0.65 m to investigate and analyze the effect of reducing the thickness of the storage layer on improving the performance and efficiency of the covering system.

As shown in Figure 3(d), the capillary barrier cover system is the third proposed scenario for Songun copper mine tailings with four layers. Songun copper mine has a cold and humid climate in one part of the year and a hot and dry climate in the other part of the year. Therefore, this scenario is designed and proposed exclusively suitable for the weather conditions of this region. This cover system has effectively maintained the storage layer at a saturation level of nearly 85% throughout the year to prevent the AMD production process. The upper (vegetation) layer is similar to the previous two systems. The third layer of fine-grained material is 0.5 m thick and between two coarse grains layers. The second and fourth layers are composed of coarse-grained materials with a thickness of 0.6 m. The second layer acts as a drainage layer, limiting water reduction in the third layer (moisture retention) through evaporation. The fourth layer, the

capillary bier layer, restricts the downward movement of water and prevents desaturation.

In all the proposed scenarios, the groundwater level from the natural bed floor as the base level is considered to be 50 meters, which is the lowest level during the year. If the cover system effectively controls acid drainage for the lowest groundwater level selected (as the most critical condition) in other seasons of the year, it will show successful performance when the groundwater level is higher.

2. 3. Numerical Modeling

This study used VADOSE/ W computer code for numerical analysis. This software is a two-dimensional finite element software from the Geo-Studio software package. The software formulation includes the analysis of simple and complex problems, from the simple analysis of precipitation to complex problems, including snow, plant transpiration, surface evaporation, runoff, and gas diffusion (radon and oxygen) [39] [39] [39]. The finite element grid used has a uniform rectangular mesh. Model geometry was selected in different identical scenarios with different layering. In Figure 4, The geometry covered the storage and release system, and boundary conditions were illustrated. In the VADOSE/W software, four types of boundary conditions are defined, which include the weather boundary conditions obtained from the study area, a zero percent oxygen, seepage, groundwater flow, and climate boundary condition has been applied.

2. 3. 1. Applied Equations

The VADOSE / W computer program has coupled heat and water transfer to simulate the flow of water, heat, and steam through saturated and unsaturated soils. Oxygen transfer depends on the degree of saturation in the storage layer; However, it does not calculate the flow of water and heat; thus, the oxygen flow is simulated separately. The characteristics of the equations applied for water flow and heat transfer are expressed using Equations (1) and (2) [40, 41].

$$\frac{1}{\rho} \frac{\partial}{\partial x} \left[D_v \frac{\partial P_v}{\partial x} \right] + \frac{1}{\rho} \frac{\partial}{\partial y} \left[D_v \frac{\partial P_v}{\partial y} \right] + \frac{\partial}{\partial x} \left[k_x \frac{\partial \left[\frac{P}{\rho g} + y \right]}{\partial x} \right] + \frac{\partial}{\partial y} \left[k_y \frac{\partial \left[\frac{P}{\rho g} + y \right]}{\partial y} \right] + Q = \lambda \frac{\partial P}{\partial t} \quad (1)$$

$$L_v \frac{\partial}{\partial x} \left[D_v \frac{\partial P_v}{\partial x} \right] + L_v \frac{\partial}{\partial y} \left[D_v \frac{\partial P_v}{\partial y} \right] + \frac{\partial}{\partial x} \left[K_{tx} \frac{\partial T}{\partial x} \right] + \frac{\partial}{\partial y} \left[K_{ty} \frac{\partial T}{\partial y} \right] + Q_t + c_p v_x \frac{\partial T}{\partial x} + c_p v_y \frac{\partial T}{\partial y} = \lambda_t \frac{\partial T}{\partial t} \quad (2)$$

where P pressure, P_v soil moisture vapor pressure, m_v slope function of volumetric water content, k_x and k_y applied hydraulic conductivity in x and y directions, Q applied boundary flow, D_v vapor diffusion coefficient, y elevation head, ρ specific mass of water, g gravity, t time, L_v latent heat of vaporization, K_{tx} and K_{ty} values of thermal conductivity in x and y direction, T temperature,

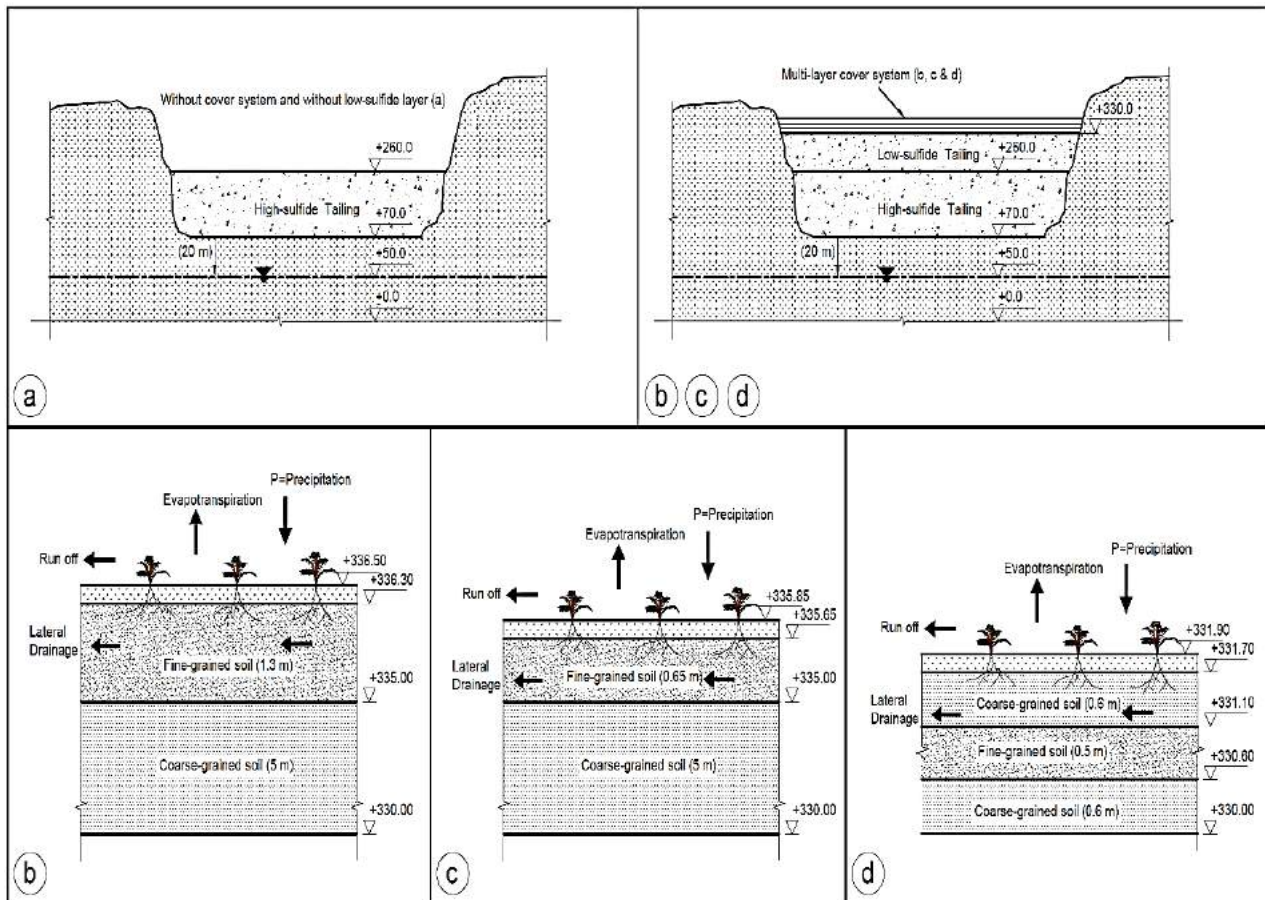


Figure 3. Baseline or exposed Scenario (a), depository and diffusion top scheme (b), upgraded depository and spread cover system (c) blood flow pathway bar, rear top structure (d)

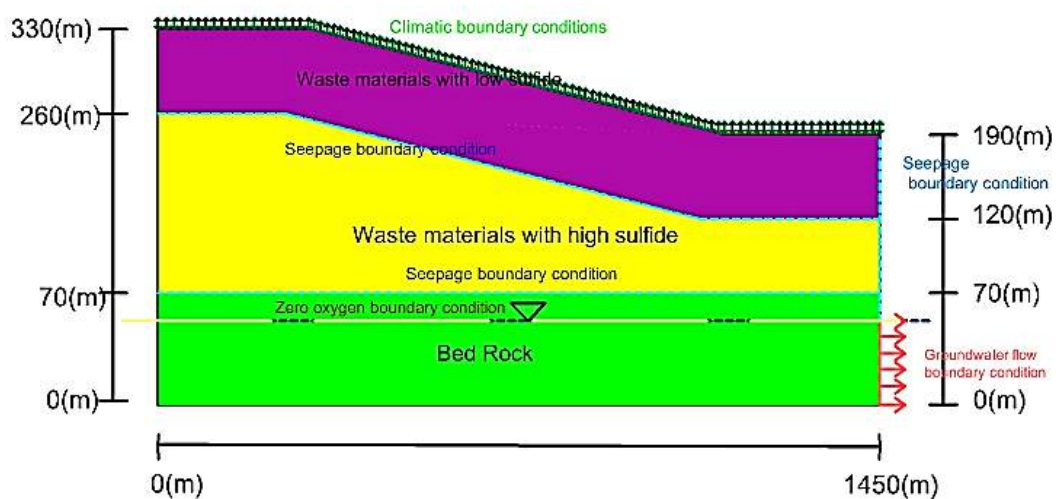


Figure 4. The geometry Covered the storage and release system and Boundary conditions

Q_t boundary flow of temperature applied, C_p specific volumetric heat, λ , apparent volumetric heat capacity of soil and v_x and v_y are the Darcy velocities in the x and y directions. The vapor pressure is obtained from Equation (3):

$$P_v = P_{vs} \left(e^{\frac{-P_w}{\rho R T}} \right) = P_{vs} h_{r,air} \quad (3)$$

P_{vs} is the pressure of saturated vapor for pure free water, w is the molecular mass of water vapor, R is the universal constant coefficient of gases, T is the temperature in Kelvin, and $h_{r,air}$ is the relative humidity of the air. Actual evaporation is calculated using the Batman-Wilson method (Equation (4)) in which E is the actual evaporation (mm/day), Γ is the slope of the vapor pressure saturation temperature curve at average air temperature (kPa / oC), Q is the net radiant energy at the surface (mm/day), ν is a constant psychrometric coefficient, $Ea = f(u) Pa (B-A)$, $f(u) = 0.35 (1 + 0.15Ua)$, Ua wind speed (km/h), Pa steam pressure in the air the evaporation level (kPa), B is the inverse of the relative humidity of the air, and A is the inverse of the relative humidity of the soil surface [42, 43].

$$AE = \frac{\Gamma Q + \nu Ea}{\nu A + \Gamma} \quad (4)$$

In the software, Equations (1) to (4) are solved simultaneously by the finite element method to obtain the actual evaporation rate (E), vapor pressure (P_v), water pressure (P), and temperature (T). The primary method of gas transfer in a porous environment is molecular diffusion or advection through the cavity space. In a porous environment, oxygen is transported through small air-filled cavities at lower saturation levels due to the low diffusion coefficient of oxygen in the water. According to research, oxygen is transported in a porous environment primarily through diffusion, as saturation increases through both the aqueous and gaseous phases [44-53].

For one-dimensional molecular diffusion in an unsaturated porous environment that consumes oxygen at a first-order rate, the instantaneous oxygen flow and oxygen concentration at location z and time t are determined using Fick's first and second laws (Equations (5) and (6)) [46].

$$F(z, t) = -D_e \frac{\partial(z, t)}{\partial z} \quad (5)$$

$$\frac{\partial(\theta_{eff} C)}{\partial t} = \frac{\partial}{\partial y} \left(D_{eff} \frac{\partial C}{\partial y} \right) - k_v C \quad (6)$$

In these equations, C is the concentration of oxygen in the pore air (in terms of mass per unit volume), θ_{eff} is the equivalent porosity for diffusion defined as $\theta_a + H\theta_w$, θ_a is the volumetric content of air, θ_w is the volumetric content of water, H is the Henry equilibrium constant, D_{eff}

is the effective diffusion coefficient (m^2/s), and kr are effective reaction rate coefficient (1/year).

2. 3. 2. Initial and Boundary Conditions

To describe the scenarios in VADOSE/W software, five types of boundary conditions have been used, including the boundary condition of meteorological data type, the boundary condition of oxygen concentration 280 g/m^3 (normal concentration of oxygen in the air) on top of the cover system, the boundary condition of water level and zero oxygen concentration at the bottom of the covering system and the boundary condition of seepage from the side of the waste material. Prerequisites for nodes include pressure, temperature, and initial concentration of oxygen gas. For the initial pressure conditions, temperature, and oxygen gas concentration, the water level, the temperature of the first day, and the initial concentration of zero were used, respectively.

2. 3. 3. Data Input to the Software

To run the VADOSE/W program, meteorological and vegetation data, soil characteristics, including soil moisture characteristic curve, unsaturated hydraulic conduction function, and thermal conductivity, were entered into the software. Thermal specifications for materials are presented in Table 2. The decay coefficient was also required for the materials modeled in the simulation of oxygen gas flow. In the current study, according to Table 3, part of the measured meteorological data of Songun mine is presented, and the whole data was entered into the software (in Table 3, the first day of the solar calendar corresponds to March 21 in the Gregorian calendar). Vegetation of grass enjoying excellent quality was used. Vegetation data required to enter the software include leaf area index (LAI), plant moisture limit function (PML), root depth, and length of the growth period. Diagrams of unsaturated hydraulic conductivity curves and moisture characteristics are presented in Figure 5.

Given that the "optimized store and release cover system" is a particular condition of the "store and release cover system"; Therefore, the material is the same, and as a result, the unsaturated hydraulic conductivity curves and the moisture characteristic are the same for both cover systems.

Specific heat capacity parameters, including mass and soil thermal conductivity (parameters describing heat

TABLE 2. Thermal specifications for materials (Geo-Studio, 2012)

Thermal conductivity (KJ/days/m°C)	Volumetric heat capacity (KJ/m³°C)
150	2500
125	2300

TABLE 3. Meteorological data used in the Vados/W software

Day	Temp (°C)		RH (%)		Wind (m/s)	Precip (mm)	Evpo (mm)
	Max	Min	Max	Min			
1	4.8	-3	98	43	31	0.00	0.0
2	6	-5.3	92	43	32	0.00	0.0
3	1.9	-1	98	84	25	0.00	0.0
⋮	⋮	⋮	⋮	⋮	⋮	⋮	⋮
153	27.2	9.6	87	33	24	8.30	6.9
154	29.1	12.3	89	32	26	6.40	9.0
⋮	⋮	⋮	⋮	⋮	⋮	⋮	⋮
270	6.2	-9.9	72	42	31	6.60	0.0
271	9.6	-2.7	86	34	34	11.80	0.0
⋮	⋮	⋮	⋮	⋮	⋮	⋮	⋮
364	2.4	-1.6	98	73	31	0.00	0.0
365	10.3	-7.1	96	18	24	0.00	0.0

transfer in soil) used in the software, are presented in Table 1. Water content and soil thermal behavior can affect each other because unsaturated soils contain air, water, and solid particles, whereas air and water have different thermal behavior. The material of cover depends on the type of cover system and is selected according to local conditions, including the availability of materials and weather conditions. Also, based on Figure 6, the average percentage of air humidity (a), evaporation (b), rainfall (c), and temperature (d) for each of the 12 months in the period 2009 to 2017 and the average annual rainfall (e) as input information to the software is provided.

3. SIMULATION RESULTS AND DISCUSSION

This section presents the results of two-dimensional numerical modeling, including saturation degree diagrams, oxygen concentration diagrams, and diffusion

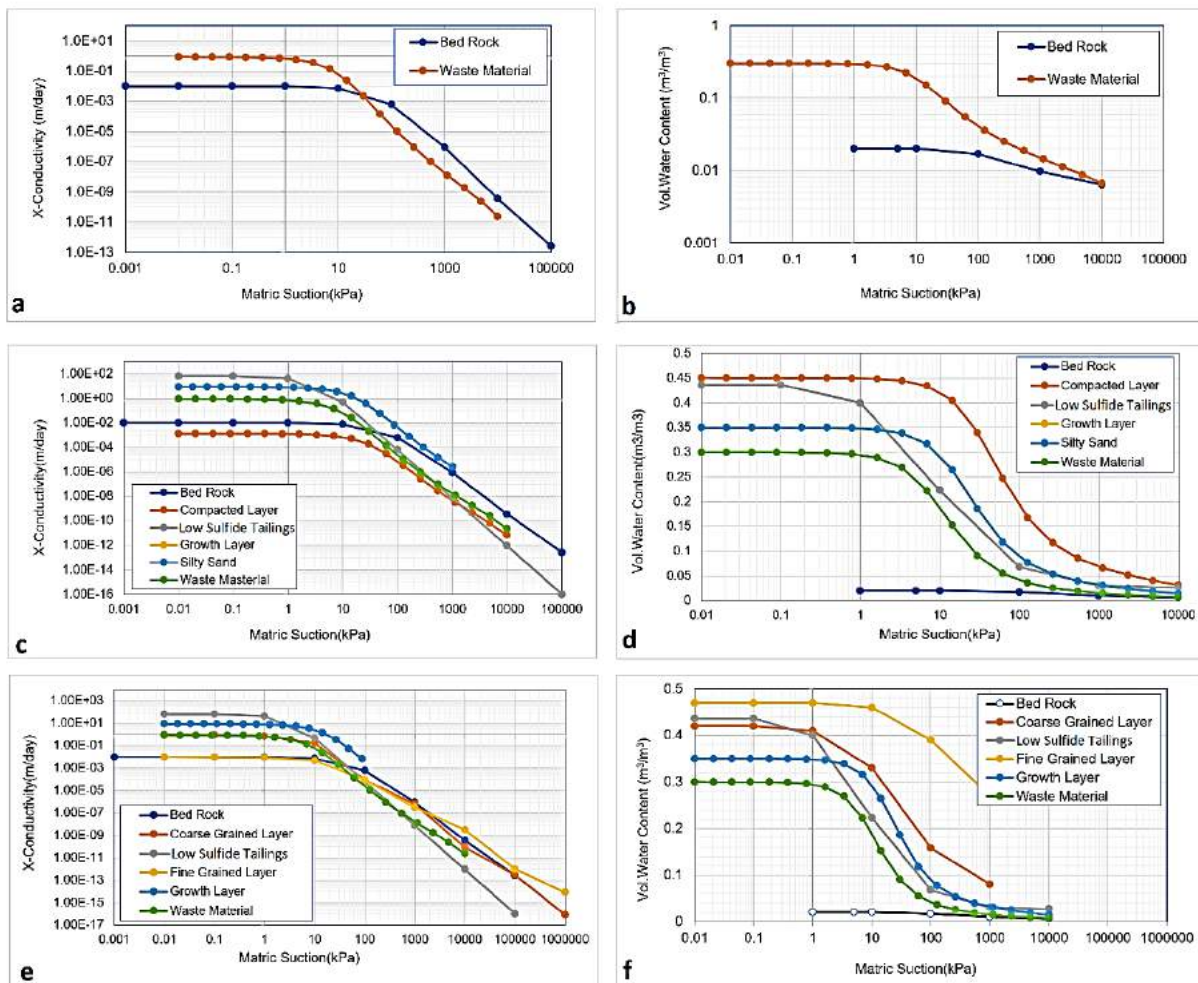


Figure 5. Unsaturated hydraulic conductivity curve and characteristic moisture curve for tailings (a, b for uncovered condition), (c, d for store and release cover system as well as optimized store and release cover system), and (e, f for barrier Capillary cover system)

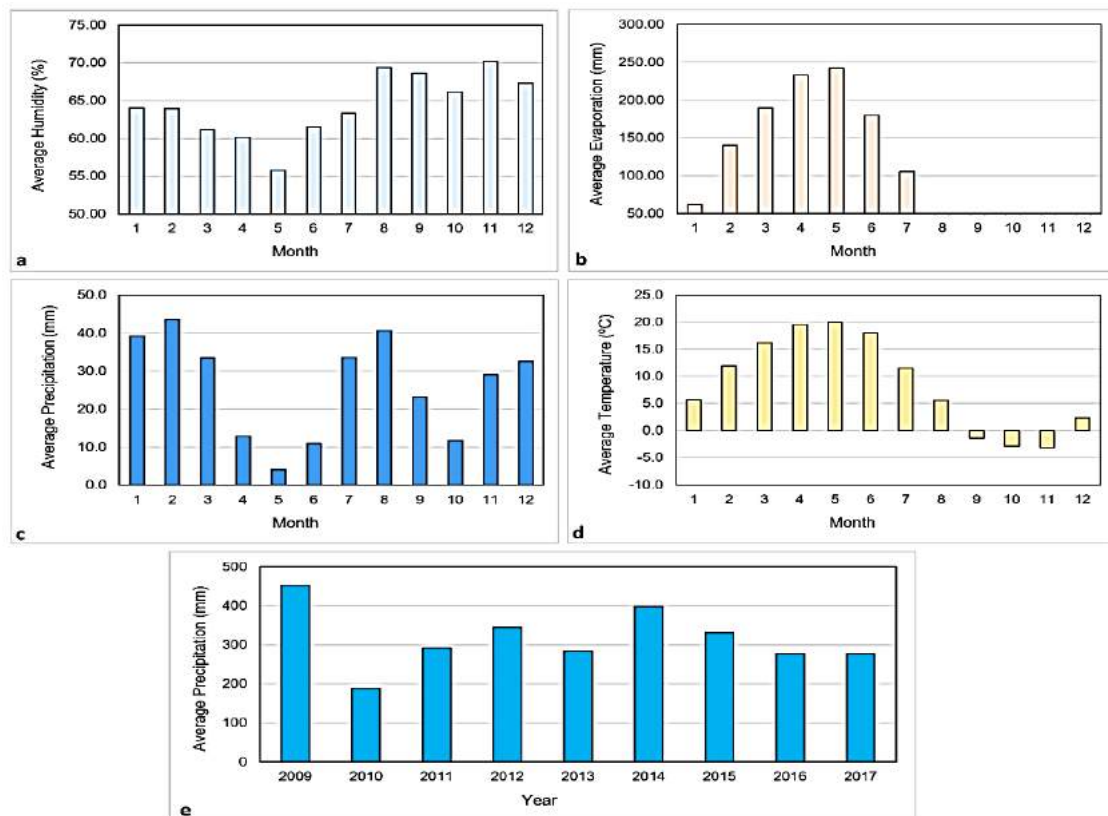


Figure 6. The average percentage of humidity (a), evaporation (b), precipitation (c), and temperature (d) for each of the 12 months from 2009 to 2017 and average annual rainfall (e)

coefficient diagrams for different scenarios. Also, in the second scenario, the effect of lowering the thickness of the store layer of the sulfide-containing multi-layer cover system on the oxygen permeation process and the control of AMD of tailings dams is discussed. Graphs of saturation degree, oxygen concentration, and oxygen diffusion coefficient are presented for the base scenario (without cover) and the three scenarios (first to third) according to Figures 7, 8, and 9, respectively. In the analysis of the following graphs, especially concentration graphs, analysis of changes at the reference level was performed. The reference surface is the same as the upper level of the accumulated tailings with high sulfide content, which is 260 meters high, and the reduction of oxygen concentration at this level is very important, and the base surface is the lower surface of the bedrock. In this study, it has also been suggested that in all cover systems, materials with higher sulfide content can initially be accumulated. Then materials with lower sulfide content be placed on high-sulfide materials to create a naturally oxygen-consuming cover system. In this case, some oxygen penetrates this layer, so AMD production is lessened. However, if multi-layered engineering cover systems are not used and single-layer cover systems are preferred, the performance will not be

successful since these systems are effective in a humid environment. Considering the climatic conditions of Songun copper mine, which is hot and dry for most of the year, multi-layered engineering cover systems should be used instead.

3. 1. Baseline Scenario (No Cover Mode) Based on the results of software analysis according to the diagram in Figure 7(a), in the baseline scenario, the saturation degree was about 20%, and only in the part of the year where the rainfall is high the saturation degree goes to about 40%, which is much less than the permitted limit (about 85%). Based on the saturation degree diagram, we realize that the uncovered tailings cannot retain moisture throughout the year, and the need to design an efficient cover system stands out. Based on the obtained results, according to the diagram of Figure 8(a), the oxygen concentration at the reference level was estimated to be about 91%. Therefore, this scenario has a high potential for the production of acid drainage due to the high penetration of oxygen. Also, according to the diagram in Figure 9(a), the oxygen diffusion coefficient is about 0.23, and only at the end of the year, due to the consumption of oxygen by tailings during the year, the amount of oxygen diffusion coefficient has decreased

slightly that is practically ineffective since abundant oxygen is provided to the tailings throughout the year. At a depth of 50 meters from the base surface (equal to the groundwater level), the oxygen diffusion coefficient reached zero due to the presence of water and its effect on oxygen penetration. According to the above results, the performance of the baseline scenario in terms of control of diffusion and saturation factors and oxygen concentration was unsuccessful, so using a cover system to control the production of AMD is necessary.

3. 2. Scenario 1 (Store and Release Cover System)

According to the diagram in Figure 7(b) in the first scenario, the degree of saturation in the store layer (335 m depth range) was less than 85%, indicating that using this system to keep the store layer close to saturation is unsuccessful. According to the diagram in Figure 8b, the oxygen concentration at the reference surface was about zero, indicating the proposed design's success in placing low-sulfide tailings on high-sulfide tailings. The diagrams also depicted that the layer containing low-sulfide tailings is crucial in reducing oxygen concentration at the reference level. The performance of the designed cover system depends on the performance of the store layer, but the performance of the designed cover system should be evaluated by examining the oxygen diffusion coefficient for the store layer throughout the year. According to the diagram in Figure 9b, the oxygen diffusion coefficient in the cover system varies between 0.08 to 0.40 (m^2/day), which is insufficient to control oxygen diffusion and AMD production.

3. 3. Scenario 2 (Optimized Store and Release Cover System)

This scenario was designed to analyze the performance sensitivity of the cover system to modification of the thickness of the storage layer and to notice how the efficiency of the cover system changes with this modification.

Here, according to the diagram in Figure 7(c), the degree of saturation in the store layer (depth range 335 meters) was much less than 85%, and therefore, this cover system could not keep the store layer saturated and reduce layer thickness. Reduction of the store layer has slightly reduced the saturation degree of this layer, but it was found that the thickness of the storage layer is not the main factor in controlling the saturation degree of this layer, and the efficiency did not improve; therefore, we must design a system that is both economical and efficient. In the second scenario, the amount of evapotranspiration is also lower due to the lower water store (less thickness of the store layer). The evapotranspiration rate in a cover system depends on the plant root depth, root distribution, and negative pore water pressure (suction). The root depth and distribution are the same for both proposed scenarios, but the amount

of suction varies depending on the amount of water in the storage layer. According to Figure 8(c), the oxygen concentration at the reference level is about zero, similar to the previous case. As a result, the performance of this cover system is desirable because our goal is to consume oxygen in low-sulfide materials to reduce and control the production of AMD. According to Figure 9(c), the diffusion coefficient for the cover system varies between 0.08 and 0.43 (m^2/day). Despite the reduction of the thickness of the storage layer in this scenario, the oxygen diffusion coefficient does not change much compared to the previous scenario, which is completely consistent with the results of the previous diagrams.

3. 4. Scenario 3 (Capillary Barrier Cover System)

In this scenario, according to the diagram in Figure 7(d), the degree of saturation for the store layer (depth range of 330 meters) is about 80% (around 85% is desirable). Due to the region's arid climate in most seasons, the cover system of this scenario has been more successful than previous scenarios in keeping the store layer saturated. Here, due to the high degree of saturation of the store layer, almost no oxidation takes place, so AMD production is minimized. According to the diagram in Figure 8(d), oxygen concentration at the reference level is similar to previous cover systems at about zero, indicating that the factor controlling the oxygen concentration of tailings is low-sulfide. As shown in Figure 9(d), the value of the oxygen diffusion coefficient in the capillary barrier cover system varies between 0 and 0.39 (m^2/day). This cover system has reduced the oxygen diffusion coefficient from 0.39 to zero stepwise. The system's efficiency in regulation and reduction of oxygen coefficient will be well shown in the following diagrams. In addition, the success of this system in regulating all three parameters and comparing its performance with other systems indicates the significance of layering and type of cover systems.

3. 5. Comparison of Cover Systems at Store Layer

As depicted in Figure 10, graphs of saturation degree, oxygen concentration, and oxygen diffusion coefficient in the store layer are presented for comparison with the three proposed scenarios (cover systems). According to Figure 10a, the optimal performance of the capillary barrier cover system in maintaining the store layer in the near-saturation state is quite evident. As shown in Figure 10b, the use of the store layer in all scenarios has decreased oxygen concentration infiltration, but the capillary barrier cover system prevents this reduction in steps. The gradual reduction in this system is due to the high degree of saturation in the store layer, which causes the connection of oxygen with the materials under the store layer to be largely cut off and, in turn, leads to better performance in regulating oxygen penetration. However, as explicated in the diagrams, low-sulfide tailings are the

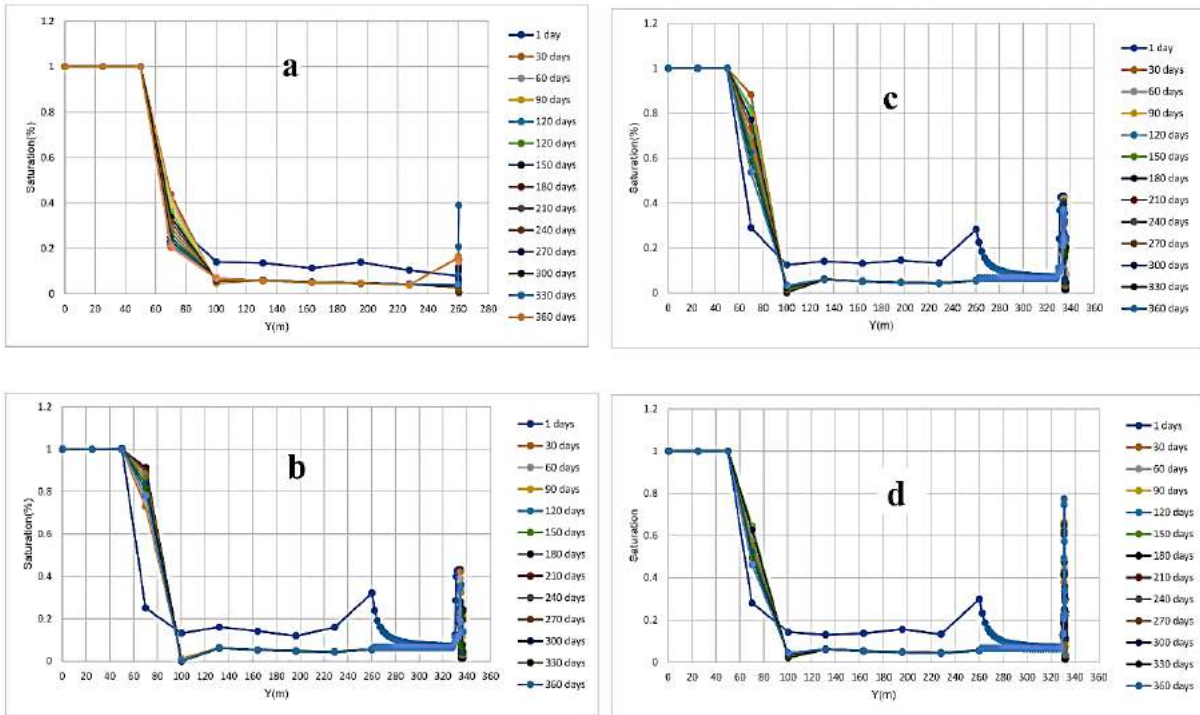


Figure 7. Saturation degree diagrams for the uncovered (a), store and release cover system (b), optimized store and release cover system (c), and capillary barrier cover system (d)

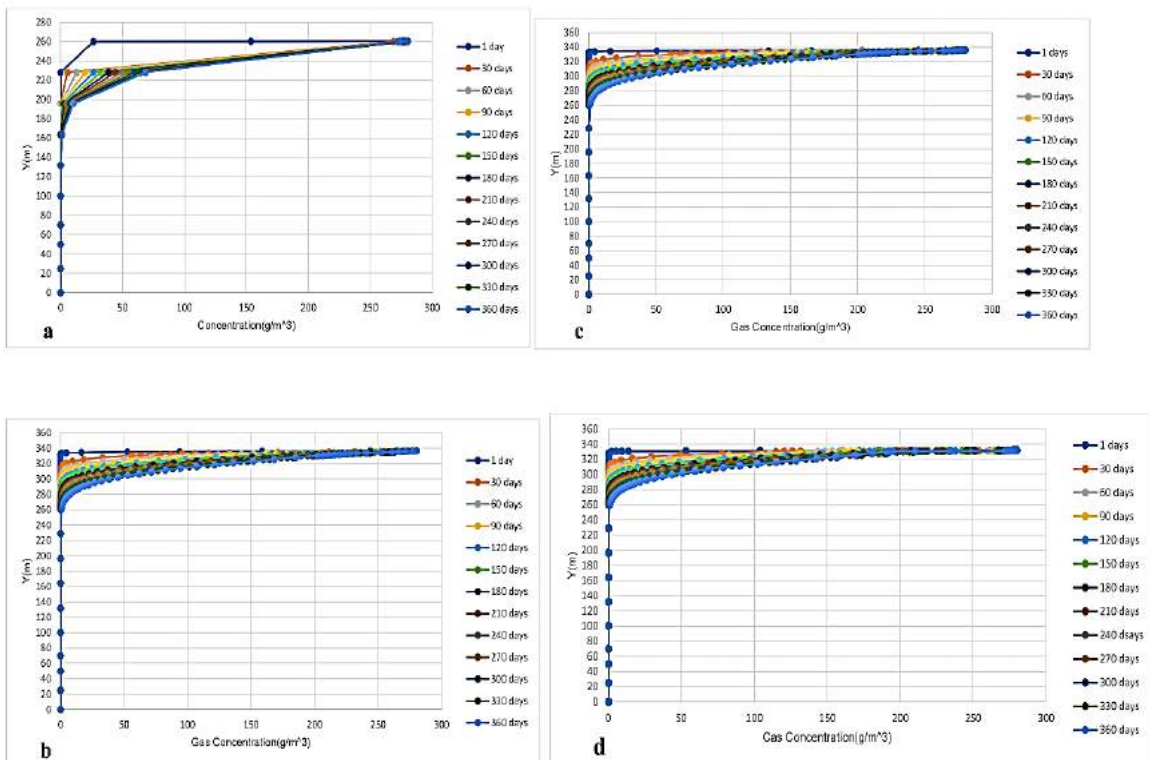


Figure 8. Oxygen concentration diagrams for the uncovered position (a), store and release cover system (b), optimized store and release cover system (c), and capillary barrier cover system (d)

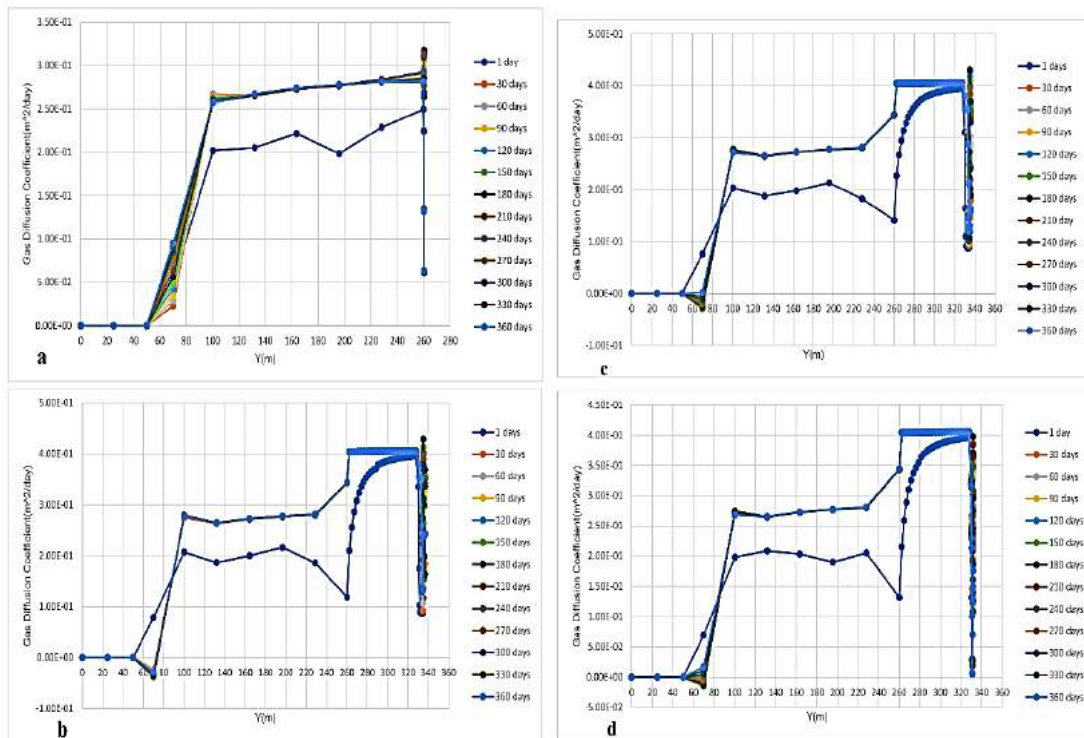


Figure 9. Oxygen diffusion coefficient diagrams for uncovered (a), store and release cover system (b), optimized store and release cover system (c), and capillary barrier cover system (d)

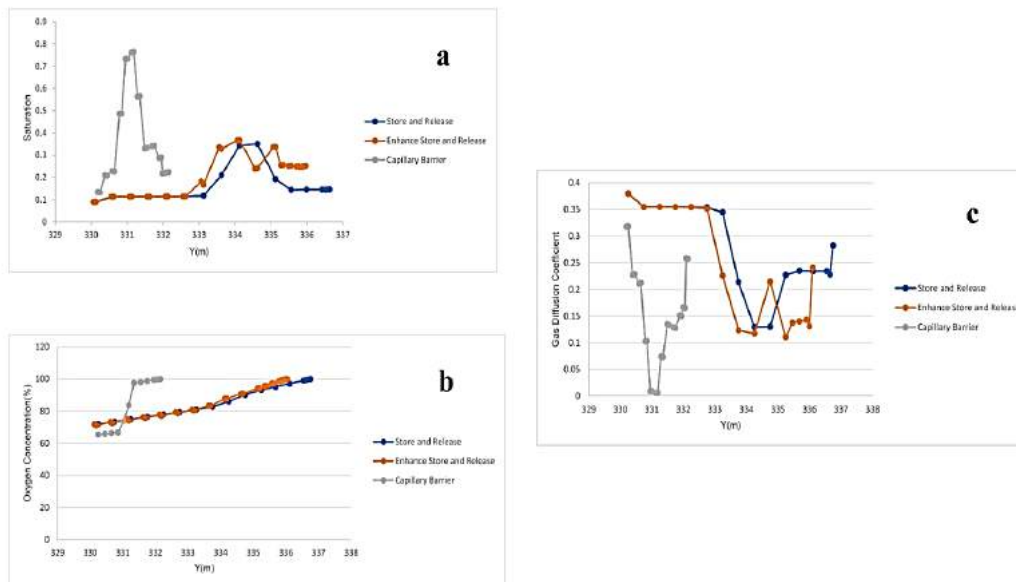


Figure 10. Graphs of saturation degree (a), oxygen concentration (b), and oxygen diffusion coefficient (c) of the store layer in three different cover systems

most important factor in regulating oxygen concentration. According to the diagram in Figure 10c, the oxygen diffusion coefficient for the capillary barrier system is close to zero due to the high degree of

saturation of the storage layer and the complementary performance of the different layers in this system. In comparison with other scenarios, the oxygen diffusion coefficient in the store layer is about (m²/day) 0.12,

reflecting the superiority of the capillary barrier cover system.

4. CONCLUSION

In the current study, using VADOSE / W software, the behavior of the multi-layer cover system in regulating the penetration of oxygen gas was evaluated. Four scenarios were defined for modeling: store and release, optimized store and release, capillary barrier, and uncovered cover systems. The most significant results obtained are as follows:

1. Saturation graphs were used to predict the potentiality of oxygen diffusion into the tailings. In-store and release cover systems and optimized ones, the expected saturation in the storage layer is not achieved, while the capillary barrier has a high ability to keep the store layer close to saturation.

2. In this study, the lowest possible water level during the year is considered the most critical condition to evaluate the performance of each of the proposed cover systems in preventing the oxidation process (in the most critical conditions).

3. In the designed cover systems, the main factor controlling oxygen penetration into the tailings is the granulation of the cover system materials, the high degree of saturation in the storage layer, and the cover system layering.

4. In all cover systems, it is recommended that tailings with lower sulfide content be stored on tailings with higher sulfide content. This creates a situation in which low-sulfide materials act as an oxygen-consuming system, reducing oxygen infiltration into the higher-sulfide materials and thus limiting AMD production.

5. The capillary barrier cover system was particularly designed and evaluated for the arid climate of Songun mine area (and applicable to similar conditions). According to the results, this cover system can maintain the store layer in a state close to saturation of 85%, so the diffusion coefficient of near zero was obtained in the storage layer.

6. In the proposed cover systems, by considering different layers, an attempt was made to keep the store layer close to the saturation level above 85%. The modeling results revealed that with increasing degree of saturation, oxygen penetration depth, and oxygen diffusion in the engineered cover system drop.

7. Only capillary barrier cover system with suitable performance for use on the tailings dam of Songun copper mine limits the production of AMD and its environmental consequences and, in the long run, significantly reduces AMD production. In addition, considering that the cover system is implemented after completing the capacity of tailings dams, it is necessary to take measures to improve the performance despite the

proper functioning of the capillary barrier system. AMD may be prevented from infiltrating into waste rock and groundwater by employing impermeable layers such as geosynthetics in the subsoil of tailings. Additionally, AMD produced can be collected and treated in isolated pools by implementing drains. This will minimize the possibility of environmental damage.

5. REFERENCES

- Dubiński, J., "Sustainable development of mining mineral resources", *Journal of Sustainable Mining*, Vol. 12, No. 1, (2013), 1-6. doi: 10.7424/jsm130102.5.
- Farjana, S.H., Huda, N., Mahmud, M.P. and Saidur, R., "A review on the impact of mining and mineral processing industries through life cycle assessment", *Journal of Cleaner Production*, Vol. 231, (2019), 1200-1217. doi: 10.1016/j.jclepro.2019.05.264.
- Sumalatha, J., Kumar CL, M., KG, S., Sunagar, P. and Norooznejad Farsangi, E., "Studies on contaminated mine soil and its remediation using soil washing technique-a case study on soil at kolar gold fields", *International Journal of Engineering, Transactions A: Basics*, Vol. 35, No. 1, (2022), 201-212. doi: 10.5829/IJE.2022.35.01A.19.
- Soltani Khaboushan, A. and Osanloo, M., "An uncertainty-based transition from open pit to underground mining", *International Journal of Engineering, Transactions B: Applications*, Vol. 32, No. 8, (2019), 1218-1224. doi: 10.5829/ije.2019.32.08b.19.
- Adriansyah, Y., Zakaria, Z., Muslim, D. and Hirnawan, F., "Determining of geotechnical domain based on joint density and fault orientation at batu hijau mine, west sumbawa-indonesia", *International Journal of Engineering*, Vol. 31, No. 4, (2018), 679-683. doi: 10.5829/IJE.2018.31.04A.21.
- Brest, K.K., Henock, M.M., Guellord, N., Kimpiab, M. and Kapiamba, K.F., "Statistical investigation of flotation parameters for copper recovery from sulfide flotation tailings", *Results in Engineering*, Vol. 9, (2021), 100207. doi: 10.1016/j.rineng.2021.100207.
- Agboola, O., Babatunde, D.E., Fayomi, O.S.I., Sadiku, E.R., Popoola, P., Moropeng, L., Yahaya, A. and Mamudu, O.A., "A review on the impact of mining operation: Monitoring, assessment and management", *Results in Engineering*, Vol. 8, (2020), 100181. doi: 10.1016/j.rineng.2020.100181.
- Albright, W.H., Benson, C.H. and Waugh, W.J., "Water balance covers for waste containment: Principles and practice, American Society of Civil Engineers. (2010).
- Daniel, D.E. and Koerner, R.M., "Waste containment facilities: Guidance for construction quality assurance and construction quality control of liner and cover systems, American Society of Civil Engineers, (2007).
- Nordstrom, D., "Mine waters: Acidic to circumneutral", *Elements* Vol. 7, (2011), 393-398. doi: 10.2113/gselements.7.6.393.
- Seal, R.R. and Shanks, W.C., "Sulfide oxidation: Insights from experimental, theoretical, stable isotope, and predictive studies in the field and laboratory", *Applied Geochemistry*, Vol. 23, No. 2, (2008). doi: 10.1016/j.apgeochem.2007.10.006.
- Aaron, G.L., Griffith, E.M. and Hacker, D.B., "Geochemical and hydrologic assessment of drainage from cherry valley coal mine, ohio", *Environmental & Engineering Geoscience*, Vol. 20, No. 3, (2014), 257-272. doi: 10.2113/gseegeosci.20.3.257.
- Lang, H.R. and Baloga, S.M., "Validation airborne visible-infrared imaging spectrometer data at ray mine, arizona", *Environmental & Engineering Geoscience*, Vol. 6, No. 3, (2000), 187-200. doi: 10.2113/gseegeosci.20.3.257.

14. Spindler, K.M. and Olyphant, G.A., "Geophysical investigations at an abandoned mine site subjected to reclamation using a fixated scrubber sludge cap", *Environmental & Engineering Geoscience*, Vol. 10, No. 3, (2004), 243-251. doi: 10.2113/10.3.243.
15. Wheeland, K. and Feasby, G., "Innovative decommission technologies via canada's mend program", in Proc. of the 12th Nat. Conf., Hazardous Mater. Control/Superfund. Vol. 91, (1991), 23-28.
16. Dev, S., Galey, M., Chun, C.L., Novotny, C., Ghosh, T. and Aggarwal, S., "Enrichment of psychrophilic and acidophilic sulfate-reducing bacterial consortia—a solution toward acid mine drainage treatment in cold regions", *Environmental Science: Processes & Impacts*, Vol. 23, No. 12, (2021), 2007-2020. doi: 10.1039/D1EM00256B.
17. Pandey, S., Fosso-Kankeu, E., Redelinguys, J., Kim, J. and Kang, M., "Implication of biofilms in the sustainability of acid mine drainage and metal dispersion near coal tailings", *Science of the Total Environment*, Vol. 788, (2021), 147851. doi: 10.1016/j.scitotenv.2021.147851.
18. Tong, L., Fan, R., Yang, S. and Li, C., "Development and status of the treatment technology for acid mine drainage", *Mining, Metallurgy & Exploration*, Vol. 38, (2021), 315-327. doi: 10.1007/s42461-020-00298-3.
19. Kuyucak, N., "Acid mine drainage prevention and control options", *CIM Bulletin*, (2002), 96-102.
20. Dobchuk, B., "Evaluations of the effectiveness of desulphurized tailings cover at detour lake mine, University of Saskatchewan, Saskatoon, (2002).
21. Hedin, R.S., Watzlaf, G.R. and Nairn, R.W., *Passive treatment of acid mine drainage with limestone*. 1994, Wiley Online Library.
22. Johnson, D.B. and Hallberg, K.B., "Acid mine drainage remediation options: A review", *Science of the Total Environment*, Vol. 338, No. 1-2, (2005), 3-14. doi: 10.1016/j.scitotenv.2004.09.002.
23. Skousen, J., Rose, A., Geidel, G., Foreman, J., Evans, R. and Hellier, W., "Handbook of technologies for avoidance and remediation of acid mine drainage", *National Mine Land Reclamation Center, Morgantown*, Vol. 131, (1998).
24. Yanful, E. and Nicholson, R., "Engineered soil covers for reactive tailings management: Theoretical concepts and laboratory development", in Proceedings Second International Conference on the Abatement of Acidic Drainage. (1991), 461-485.
25. Aachib, M., Mbonimpa, M. and Aubertin, M., "Measurement and prediction of the oxygen diffusion coefficient in unsaturated media, with applications to soil covers", *Water, air, and Soil Pollution*, Vol. 156, (2004), 163-193. doi: 10.1023/B:WATE.0000036803.84061.e5.
26. Aubertin, M., Aachib, M. and Authier, K., "Evaluation of diffusive gas flux through covers with a gcl", *Geotextiles and Geomembranes*, Vol. 18, No. 2-4, (2000), 215-233. doi: 10.1016/S0266-1144(99)00028-X.
27. O'Kane, M., Wilson, G., Barbour, S. and Swanson, D., "Aspects on the performance of the till cover system at equity silver mines ltd", in Proceedings Sudbury'95, conference on mining and the environment (CANMET: Ottawa). (1995).
28. Dagenais, A.-M., Aubertin, M. and Bussière, B., "Parametric study on the water content profiles and oxidation rates in nearly saturated tailings above the water table", in Proceedings of the 7th International Conference on Acid Rock Drainage (ICARD). Vol. 2630, (2006), 405420.
29. Ouangrawa, M., Aubertin, M., Molson, J.W., Bussière, B. and Zagury, G.J., "Preventing acid mine drainage with an elevated water table: Long-term column experiments and parameter analysis", *Water, Air, & Soil Pollution*, Vol. 213, (2010), 437-458. doi: 10.1007/s11270-010-0397-x.
30. Demers, I., Bussiere, B., Mbonimpa, M. and Benzaazoua, M., "Oxygen diffusion and consumption in low-sulphide tailings covers", *Canadian Geotechnical Journal*, Vol. 46, No. 4, (2009), 454-469. doi: 10.1139/T08-132.
31. St-Germain, P. and Kuyucak, N., "Biological water covers—a preliminary assessment", *Mineral Processing and Extractive Metallurgy Review*, Vol. 19, No. 1, (1998), 39-45.
32. St-Germain, P., Larratt, H. and Prairie, R., "Field studies of biologically supported water covers at two noranda tailings ponds", in Proceedings of the Fourth International Conference on Acid Rock Drainage. Vol. 1, No. Issue, (1997), 131-147.
33. O'Kane, M. and Wels, C., "Mine waste cover system design—linking predicted performance to groundwater and surface water impacts", in 6th International Conference on Acid Rock Drainage (ICARD), Cairns. (2003).
34. Feasby, G., Blanchette, M., Tremblay, G. and Sirois, L., "The mine environment neutral drainage (mend) program", in Annual Conference of Metallurgists-Metallurgical Society of the Canadian Institute of Mining And Metallurgy, Pergamon Press. (1993), 219-219.
35. Bossé, B., Bussiere, B., Hakkou, R., Maqsoud, A. and Benzaazoua, M., "Assessment of phosphate limestone wastes as a component of a store-and-release cover in a semiarid climate", *Mine Water and the Environment*, Vol. 32, No. 2, (2013), 152. doi: 10.1007/s10230-013-0225-9.
36. Bajgirani, P.R., Darvishsefat, A.A., Khalili, A. and Makhdoum, M.F., "Using avhrr-based vegetation indices for drought monitoring in the northwest of iran", *Journal of Arid Environments*, Vol. 72, No. 6, (2008), 1086-1096. doi: 10.1016/j.jaridenv.(2007).12.004.
37. Abdollahi Sharif, J., Jafarpour, A. and Yousefi, S., "Determination of the efficient locations to discharge industrial wastewater of the sungun copper mine concentration plant using multi-objective approach based on interval data envelopment analysis", *Journal of Analytical and Numerical Methods in Mining Engineering*, Vol. 5, No. 10, (2015), 93-109. doi: 10.1016/j.janm.2015.10.004.
38. Afshoon, M.R. and Mehrdadi, N., "Quantitative and qualitative study of acid mine drainage (AMD) in sungun copper mine tailings dump with emphasis on its refineability", *Environmental Sciences*, Vol. 19, No. 3, (2021), 143-160. doi: 10.52547/envs.(2021).36082.
39. *Geo-slope international ltd. , "vadose zone modeling with vadose/w2007", 2008, calgary, alberta, canada.*
40. Darcy, H., "Les fontaines publiques de la ville de dijon exposition et application... Par henry darcy, Victor Dalmont, (1856).
41. Edlefsen, N. and Anderson, A., "Thermodynamics of soil moisture", *Hilgardia*, Vol. 15, No. 2, (1943), 31-298.
42. Penman, H., "Naturalevapotranspirationfromopenwater, baresoilandgrass", *Proceedings of the Royal Society of London, A*, (1948), 193,120-145.
43. Wilson, G.W., "Soil evaporative fluxes for geotechnical engineering problems", (1990).
44. Nicholson, R.V., Gillham, R.W., Cherry, J.A. and Reardon, E.J., "Reduction of acid generation in mine tailings through the use of moisture-retaining cover layers as oxygen barriers", *Canadian Geotechnical Journal*, Vol. 26, No. 1, (1989), 1-8. doi: 10.1139/t89-001.
45. Yanful, E.K., "Oxygen diffusion through soil covers on sulphidic mine tailings", *Journal of Geotechnical Engineering*, Vol. 119, No. 8, (1993), 1207-1228.
46. Mbonimpa, M., Aubertin, M., Aachib, M. and Bussière, B., "Diffusion and consumption of oxygen in unsaturated cover

- materials", *Canadian Geotechnical Journal*, Vol. 40, No. 5, (2003), 916-932. <https://doi.org/10.1139/t03-040>
47. Potgieter, G., Cason, E.D., DeFlaun, M.F., Jacobs, K. and van Heerden, E., "Management and stimulation of high metabolic rates of biomes to effectively remediate mine drainage", *Journal of Human, Earth, and Future*, Vol. 3, No. 2, (2022), 204-212. doi: 10.28991/HEF-2022-03-02-06.
48. Nworie, F.S., Mgbemena, N., Ike-Amadi, A. and Eburnoha, J., "Functionalized biochars for enhanced removal of heavy metals from aqueous solutions: Mechanism and future industrial prospects", *Journal of Human, Earth, and Future*, Vol. 3, No. 3, (2022), 377-395. doi: 10.28991/HEF-2022-03-03-09.
49. Kadhim, M., Alfatlawi, T. and Hussein, M., "Experimental and nonlinear analysis of cracking in concrete arch dams due to seismic uplift pressure variations", *International Journal of Engineering, Transactions B: Applications*, Vol. 34, No. 5, (2021), 1156-1166. doi: 10.5829/ije.2021.34.05b.09.
50. Ghiasi, V. and Farzan, A., "Numerical study of the effects of bed resistance and groundwater conditions on the behavior of geosynthetic reinforced soil walls", *Arabian Journal of Geosciences*, Vol. 12, No. 23, (2019), 729. doi: 10.1007/s12517-019-4947-2.
51. Ghiasi, V., Heydari, F. and Behzadinezhad, H., "Numerical analysis and back calculation for embankment dam based on monitoring results (case study: Iran-lurestan rudbar)", *Scientia Iranica*, Vol. 28, No. 5, (2021), 2519-2533. doi: 10.24200/sci.2021.56159.4579.
52. Ghiasi, V. and Koushki, M., "Numerical and artificial neural network analyses of ground surface settlement of tunnel in saturated soil", *SN Applied Sciences*, Vol. 2, No. 5, (2020), 939. doi: 10.1007/s42452-020-2742-z.
53. Ghiasi, V. and Mozafari, V., "Seismic response of buried pipes to microtunnelling method under earthquake loads", *Soil Dynamics and Earthquake Engineering*, Vol. 113, (2018), 193-201. doi: 10.1016/j.soildyn.2018.05.020.

COPYRIGHTS

©2023 The author(s). This is an open access article distributed under the terms of the Creative Commons Attribution (CC BY 4.0), which permits unrestricted use, distribution, and reproduction in any medium, as long as the original authors and source are cited. No permission is required from the authors or the publishers.



Persian Abstract

چکیده

در صنعت معدن، سیستم های پوششی برای باطله ها وسیله ای موثر برای کاهش زهکشی اسید معدن است. سیستم های پوششی چند لایه در آب و هوای خشک که میزان تبخیر سالانه بیشتر از بارندگی سالانه است کارآمد هستند. تحقیق حاضر مناسب برای کاربران و طراحان سدهای باطله معدن میباشد که با هدف شناسایی سیستم پوششی بهینه برای سدهای باطله معدنی و همچنین بررسی پارامترهای ژئوتکنیکی موثر در کنترل گاز اکسیژن ورودی به محل دفع باطله های معدنی جهت کاهش و مدیریت تولید زهاب اسیدی انجام شده است. در این تحقیق پس از بررسی دقیق متون علمی و گردآوری داده ها، ابتدا کارایی و صحت نتایج نرم افزار با استفاده از مدلسازی عددی به روش المان محدود (FEM) در نرم افزار VADOSE/W اعتبارسنجی شده و سپس بر اساس داده های جمع آوری شده مدلسازی صورت می گیرد. در مطالعات پیشین در ارزیابی سیستم های پوششی اغلب از مدل سازی یک بعدی استفاده شده است، اما در این تحقیق کارایی سیستم های پوششی با استفاده از مدلسازی دو بعدی مورد ارزیابی قرار گرفته شده است. نکته کلیدی جهت عملکرد موفقیت آمیز سیستم های پوششی، حفظ لایه ذخیره سازی در سطح اشباع حدود ۸۵ درصد در طول سال است. دو سیستم پوششی «ذخیره و رهاسازی» و «ذخیره سازی و رهاسازی بهینه» در حفظ لایه ذخیره سازی در حدود ۸۵ درصد اشباع ناموفق عمل کرده اند، در حالیکه، سیستم پوششی مانع موبینگی عملکرد موفقیت آمیزی داشته و قادر بوده است که لایه ذخیره را در تمام طول سال در درجه اشباعی در حدود ۸۰٪ نگه دارد. با توجه به استفاده از مواد ضایعات کم سولفید به عنوان یک لایه مصرف کننده اکسیژن، عملکرد هر سه سیستم پوششی در کنترل دسترسی و نفوذ اکسیژن به باطله های پرسولفید قابل قبول بوده نشاندهنده کارایی این ایده منحصربفرد میباشد، البته شایان ذکر است که سیستم پوشش مانع موبینگی به دلیل اشباع بالای لایه ذخیره سازی توانسته است بلافاصله دیفیوژن اکسیژن را بصورت پلکانی کاهش دهد، در حالی که در دو سیستم پوششی دیگر این کاهش در دیفیوژن و غلظت اکسیژن را بصورت تدریجی ایجاد کرده اند، بنابراین سیستم پوشش سد مورگی با توجه به شرایط آب و هوایی و نوع مواد زائد به عنوان بهینه ترین سیستم پوششی در منطقه مورد مطالعه پیشنهاد می شود.



A Parametric Study on Improved Reduced Beam Section Connections with Post-tensioning to Enhance Seismic Resilience

R. Khandan, A. Sivandipour, E. Noroozinejad Farsangi*

Faculty of Civil and Surveying Engineering, Graduate University of Advanced Technology, Kerman, Iran

PAPER INFO

Paper history:

Received 28 April 2023

Received in revised form 10 June 2023

Accepted 09 July 2023

Keywords:

Post-tensioned Connections

Self-centering Connections

Reduced Section Beam Connections

Seismic Resilience

Finite Element Method

ABSTRACT

This study presents novel research on the seismic behavior of self-centering reduced beam section (RBS) connections in steel structures. Unlike traditional moment steel frames that concentrate non-elastic deformations in energy dissipation devices, the innovative self-centering RBS connections utilize post-tensioning techniques to restore the structure to its pre-earthquake condition. By significantly reducing residual deformations, these connections offer a promising alternative for improving seismic resilience. To validate the effectiveness of the post-tensioned (PT) and RBS connections, advanced nonlinear numerical modeling using the Finite Element Method (FEM) in ABAQUS software is employed. This approach allows for a comprehensive investigation, comparing the numerical results with laboratory data. Furthermore, the study goes beyond existing research by incorporating additional high-strength cables into the RBS connections. This novel configuration aims to assess the impact of post-tensioned cables on seismic behavior, adding a new dimension to the understanding of these connections. Through a rigorous parametric study, the research uncovers crucial insights into the seismic performance of the self-centering RBS connections. Notably, the study reveals the significant influence of the initial post-tensioning force on various aspects, including stiffness, maximum moment capacity, and gap-opening behavior of PT connections. The findings demonstrate the potential of increasing the initial post-tensioning force to enhance the energy dissipation capacity and overall performance of the PT connections. Overall, this study presents pioneering research that advances the understanding of self-centering RBS connections and their potential application in steel structures. By emphasizing the novel aspects of the research, it contributes to the body of knowledge in the field and provides valuable insights for improving the seismic resilience of structures.

doi: 10.5829/ije.2023.36.10a.11

1. INTRODUCTION

The rupture of the connection zone in steel structures' design is preferred to happen as the last step of the structure's failure after beams and columns' failure. Following the inappropriate behaviour of welded moment connections in the Northridge earthquake, there have been various details for moment connections in order to achieve a ductile response under seismic loading conditions. The goal of these connection details is to prevent weld rupture and to provide non-elastic deflections in beams and in an area out of the connection zone. Reduced Beam Section (RBS) is one of these

connection types. Weakening a part of the beam at a certain distance from the connection acts as a kind of safety switch that prevents connection problems. The performance of common systems resistant to lateral loads is dependent on the non-elastic behaviour of main structural elements. Hence these systems are inherently incapable of limiting the destruction or the residual drift. The new structures should provide desired behaviour in limiting the destruction and the incapacitated time. The post-tensioned connections have been suggested as a replacement to welded moment connections. This connection consists of high-strength steel cables that are laid along the beam's web, crossing the middle of column

* Corresponding Author Email: noroozinejad@kgut.ac.ir
(E. Noroozinejad Farsangi)

and face the column's web. The steel cables press the beam to the column resulting in sufficient moment resistance and returning force to bring the connection back to its initial position. Under the seismic loading, the connection opens, and a distance (crack) appears between the beam tensile wing and column. In this condition, the angles yield and play the role of energy dissipator. When the moment goes back to zero, the crack is closed, and the connection goes back to its initial condition, a process by which the residual deflections in beam and column is eliminated, and since the energy dissipation devices can easily be replaced, the cost of replacing these devices in post-tensioned connections will be less compared to the buckled beams in conventional moment frames [1-3]. This new type of steel connection was introduced by several researchers [4, 5]. The laboratory sample was utilized to acquire the cyclic response of the connection under investigation. In recent decades, there has been a growing interest in self-centering structures that can effectively return to their original positions. Previous research has explored various post-tensioned (PT) beam-column connections, considering different energy dissipative mechanisms. Previous studies utilizing ANSYS have demonstrated the reliability of employing monotonic analysis to assess the force-drift response of PT connections. These findings are further corroborated in the present paper through verification studies conducted with ABAQUS.

In contrast to previous models, which were limited in scope, comprehensive models were developed in this study to capture out-of-plane movement and beam local buckling behavior in PT connections. Although the viability of incorporating PT elements in steel frames has been confirmed in previous studies, current seismic design guidelines do not encompass regulations specifically addressing this application. Therefore, further research is necessary to thoroughly examine the seismic performance of PT connections and facilitate their widespread implementation in steel buildings. Finite-element (FE) analysis proves to be a valuable approach in investigating the seismic behavior of steel PT connections. FE models are cost-effective and allow for in-depth explorations of structural behavior, offering detailed insights into component behavior that may not be easily observable in experiments.

This paper also proposed the utilization of a reduced beam section to ensure the formation of a stable plastic hinge, effectively acting as a safety mechanism to mitigate connection issues. Additionally, it recommends incorporating additional reinforcement detailing in the contact region to delay yielding and buckling in the beam. In this study, the cyclic response of PT connections was evaluated by comparing it with experimental results conducted by Ricles et al. [6]. The assessment encompassed stiffness, moment capacity, energy dissipation, gap opening, local behavior, as well as stress

and strain distributions. Furthermore, parametric studies through simulations were conducted to explore the influence of initial post-tension forces on the cyclic response of PT connections.

Li et al. [7] presented post-tensioned connections with top and bottom angles. In this connection, the angles screwed to the beams flange play the energy dissipator. A Finite Element Method (FEM) was built of this connection, and they studied the effects of the details presented on the behaviour of the internal connection. To verify the model, 5 samples of the cruciform beam-to-column connection were tested. Furthermore, the time history analysis of six-storey steel frame with a post-tensioned connection was done. Then the results were compared to conventional welded connections, eventually depicting less residual displacement for frames with post-tensioned connections.

Fang et al. [8] studied the effects of factors such as dimension, the characteristics of top and bottom angles, the post-tensioning force amount in steel cables, and the presence of beam flange stiffening plates on the seismic response of beam-to-column connections. The results showed the flexural capacity and the energy dissipation levels are increased by using thicker angles. Also, it has shown that post-tensioned steel connections are a good replacement for conventional weld connections.

In order to study the behaviour of angles in bolted beam/column connections, Garlock et al. [9] tested 7 samples of these connections. In which, the effects of angle dimensions on connection's stiffness, strength and energy dissipation levels were defined. The goal of this study was to define the appropriate angle for post-tensioned connections. Ultimately the suggested angles had a good thickness, dimension, and material. Gerami [10] has investigated the steel moment frames using novel post-tensioned connections. Hosseinnejad et al. [11] investigated the use of smart materials (e.g., SMA) in post-tensioned connections.

Vasdravellis et al. [12] presented a new post-tensioned connection in which there were hourglass-shaped joints used beside the high-strength cables, that was responsible for energy dissipation. The connection was successful in eliminating residual deflection and avoiding damage to the main beams up to 6% drift. By iterating the tests, it was proven that the energy dissipation devices were easily replaced. Maghsoudi and Askari [13] have investigated the post-tensioned I-beams strengthened with CFRP.

Doostdar et al. [14] investigated post-tensioned external bars' effectiveness in strengthening reinforced concrete beams. ANSYS software and experiments confirm increased flexural capacity, decreased ductility. Higher impact observed with lower internal tension reinforcement percentages.

Moradi and Alam [15], presented a study on optimizing the lateral load-displacement of steel

connections in which they used RMS to predict and optimize the lateral response of beam-column connections with PT connection and top and bottom angles. The characteristics of lateral response that was studied in this paper include initial stiffness, load capacity, and the final displacement of PT connections. Based on FEM simulation, six parameters were considered as input variables in this study, namely, the post-tensioned force of the cable, beam depth, width and thickness of beam wing, span, and the height of the column. The goal of the optimization study is to maximize the initial stiffness, load capacity and ultimate drift of PT connections, and or minimize the amount of steel in the beam section which will result in reducing the final cost of structures. In the results, it's shown the more the depth of the beam and the higher the post-tensioned force in cables, the sooner the failure happens.

Some other researchers [2, 16-18] have been using open source platforms like OpenSees to investigate the damage index and seismic performance of building structures.

Sarvestani, [19] spent their time studying self-centering moment frames under near and far field earthquakes. In such a manner that the structural performance and seismic response of steel frames with self-centering moment frames with three various energy dissipation devices; namely top and bottom angles, friction devices of lower wing of the beam, and nut and bolt devices of the web; was studied. Then they were compared from the construction cost, energy dissipation and beam and column section dimensions.

Huang et al. [20] spent researching the initial stiffness of self-centering systems and its use in self-centering moment frame. The results of the tests on self-centering systems often showed a less initial stiffness to the predicted theoretical stiffness. Since the initial stiffness could have a special importance for controlled-deflection moment frames, in this study, they studied the definition of initial stiffness and the reasons for the difference between theoretical and experimental stiffness for some self-centering connection that were tested beforehand. Resulting in some suggestions to increase stiffness in these connections by reviewing the effective factors.

In another research, steel moment frames were exposed to 30 narrow band motions in various levels of earth motion intensity under spectrum acceleration in the first mode of vibration $S_a(T1)$, in order to conduct incremental dynamic analysis. The results are used to calculate the reliability of steel frame structures by using risk curves for residual displacements peak. It's been observed that the peak residual displacements that go past the 0.5% threshold are perceptible by residents and, based on recent studies can result in human discomfort. This is why using PTCs in steel frames is suggested to improve the reliability of the structure. The results showed the annual rate of surpassing the peak residual

storey drift is reduced by using PTC. Hence the reliability of steel frames with PTC is higher compared to normal moment frames [21].

Sofias and Pachoumis [22] tested two RBS connection models under cyclic loading and compared the results of lab model to the analytic model. All the characteristics of these two models, such as steel type, model's geometry, and beam/column dimensions were the same and the only difference was in the geometry of the RBS cut [22-25]. The geometry properties of the RBS are in Table 1.

Based on the results, both samples show similar failure, stiffness, and load-bearing capacity. Despite the different shapes of the RBS cut, the plastic zone was formed the same in both samples.

Bavandi et al. [24], with analyzing dispersion index focused on introducing an efficiency index for post-tensioned steel moment connections, with carrying out time history analysis and parametric studies on 3 models of steel buildings with post-tensioned connection (with various numbers of storeys) chose a model to evaluate and determining the efficiency index; then, a comparison and optimization was performed amongst the seven dispersion indexes that were introduced in the paper. Studies show that the efficiency index of PT connection, which is determined based on the change coefficient index, helps improve the speed and accuracy of the analyses.

In light of the deterioration of infrastructure and the increasing demand to reinforce structures to meet stringent design requirements, there has been a significant focus on the repair and strengthening of structures worldwide. Furthermore, seismic improvement of structures, particularly in regions prone to earthquakes, carries utmost importance. This study aims to explore the rehabilitation and strengthening of steel structures using reduced beam section (RBS) connections supplemented with post-tensioned cables integrated into the beams of the structure. Regrettably, no previous investigations have addressed the rehabilitation of steel structures through the incorporation of high-strength cables.

The primary objective of this paper is to comprehensively examine and evaluate the energy dissipation capacity, ductility, residual displacement, and seismic resilience of structures when employing these cables within steel frameworks. Through a thorough investigation, this study aims to shed light on the

TABLE 1. Geometric properties of RBS beam for RBS1 and RBS2 [22]

Specimen	(a) (mm)	(b) (mm)	(c) (mm)
RBS1 HEA180/60/75/25	108	128	45
RBS2 HEA180/45/75/20	81	128	36

potential benefits and performance implications of utilizing post-tensioned cables as a means of strengthening and rehabilitating steel structures.

2. MODELLING VERIFICATION

Since the topic is post-tensioned steel connections with reduced beam section, we have built a numerical model of one of the steel moment connections with top and bottom angles, and also a laboratory specimen of a beam connection with a reduced section in ABAQUS software. The results and characteristics from Ricles et al. [6] have been used to define the characteristics of the created post-tensioned numerical model and verification of the numerical model procedure. Hence we first introduced the laboratory specimen.

Ricles et al. [6] studied a few laboratories specimen under cyclic displacement loading. Figure 1 shows a schematic of these connections, between two beams and a column. In order to start the numerical model and verification of the results, the results from specimen pc4 that was post-tensioned by 4 steel cables on each side of the beam with an initial restricting force of 88.74 kN.

2.1. Configuring the Model

According to Figure 2, the model under study includes members with below sections:

- 1- Column: the column section is W14×311 profile, and the loading applied to the connection is applied by a hydraulic jack to the free end of the column and at 3658mm away from the joint connection at the base of the column.
- 2- Beam: the beam section is W24×163, and 28830.5mm long.
- 3- Top and bottom angles: for this application, an equal wings angle of 203mm and 15.9mm thickness is used.
- 4- To strengthen the beam wings, we have used sheets with 254×57×12.7mm dimensions.

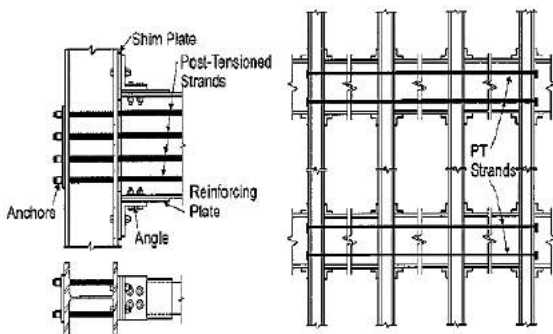


Figure 1. A- steel frame with post-tensioned connection with top and bottom angles B- the details of external connection of post-tensioned beam to column with steel cables [6]

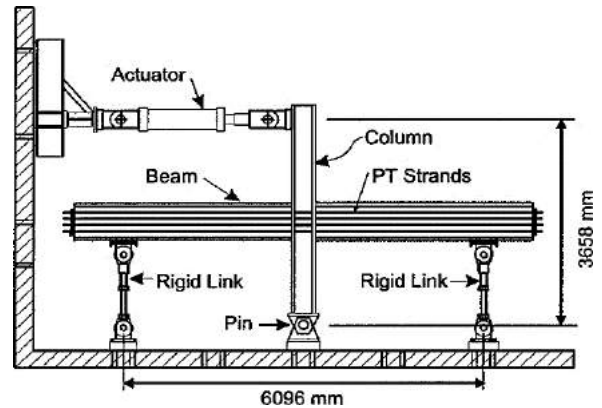


Figure 2. Schematic figure of lab model used in Ricles et al. [6]

- 5- Post-tensioned cables: section area of each cable is 140mm² and passes through a hole of 25mm made in the column’s wings.
- 6- To connect the top and bottom angles to column wings one bolt is used, and to the beam wings a 25.4 mm bolt is used.

The schematic depiction of the laboratory model used in Ricles et al. [6] research is given in Figure 2.

3. MATERIAL PROPERTIES

The yielding and ultimate stresses of the steel used in various configuring components are listed in Table 2.

The finite-element simulations in this study utilized the material properties reported in the reference experimental studies conducted by Ricles et al. [6]. A bilinear elasto-plastic stress-strain relationship was adopted for steel in all components, except for the bolts. High-strength bolts were modeled using a trilinear stress-strain relationship. The material models employed are illustrated in Figure 3.

TABLE 2. Properties of steel used in various parts of the lab specimen [6]

Piece	Yielding stress (MPa)	Plastic strain	Ultimate stress (Mpa)	Plastic strain
Post-tensioned cables	1305	0.00656	1864	0.0627
Stiffener plates	843	0.00421	895	0.0302
Shim plates	843	0.00421	895	0.0302
Angles	263	0.00131	465	0.0518
Beam web	266	0.00133	450	0.0933
Beam wing	230	0.00115	421	0.0967
Bolt	660	0.00330	830	0.074

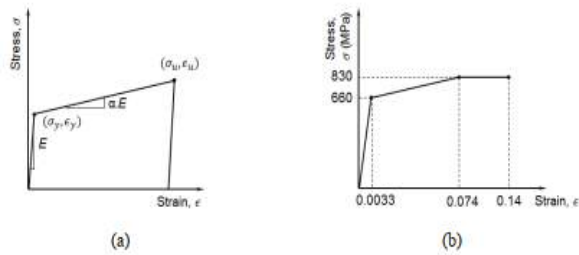


Figure 3. Idealized material behavior used in the finite element analysis: (a) bilinear kinematic hardening; (b) trilinear stress-strain steel model for bolts

In the material modeling, a strain hardening value of 0.05 was assigned for steel in post-tensioned (PT) strands, while a value of 0.02 was selected for steel in angles. For other components, a strain hardening ratio of 0.01 was assumed. Notably, a strain hardening ratio of 0.02 was chosen for angles to achieve improved predictions of the cyclic response after yielding occurred. Furthermore, a strain hardening ratio of 0.05 was considered for PT strands, based on a bilinear stress-strain relationship with a Young's modulus of 199 GPa, yield stress of 1,305 MPa, ultimate stress of 1,864 MPa, and an ultimate strain of 6%, as reported in the study by Ricles et al. [6]. The modulus of elasticity and Poisson's ratio for steel in other components were set at 200 GPa and 0.3, respectively.

4. BOUNDARY CONDITIONS AND LOADING

The support conditions for the beam were implemented in accordance with Figure 4. Specifically, roller support conditions were applied at a distance of 2,830.5 mm from the beam's length, resulting in a vertical displacement of zero. Additionally, the nodes located at the bottom of the column's centerline were constrained to have zero displacement, representing pin support conditions.

To subject the structure to loading, displacement was applied to the column flange. The loading protocol consisted of symmetric cyclic story drifts with amplitudes ranging from 0.1% to 3.5%. These story drifts were defined as the displacement applied to the column flange divided by 3,658 mm, following the approach by Ricles et al. [6].

Prior to conducting the analyses, preloads were applied to the bolts and post-tensioned (PT) bars. Subsequently, multiple load steps were defined to impose displacement drift cycles on the column. Nonlinear static analyses were performed to investigate the cyclic behavior of PT beam-column connections. The analyses accounted for large-deformation effects, incorporating geometric nonlinearity, material nonlinearity, and contact, which are recognized as contributing factors to

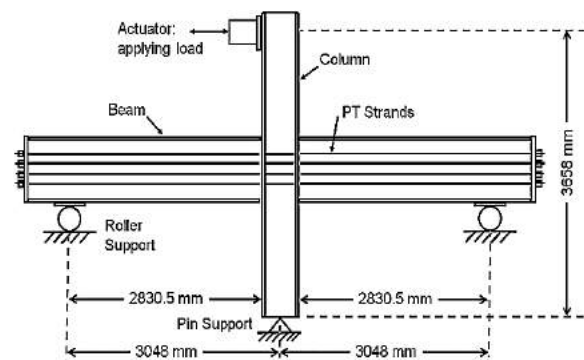


Figure 4. Support conditions of the lab specimen and numerical model of Ricles et al. [6]

nonlinear behavior. Notably, the models did not incorporate any initial geometric imperfections, focusing on capturing the buckling behavior of the structural components.

The applied force was a displacement cyclic loading, and the number of cycles and displacement amounts associated with each cycle are defined based on the protocol in SAC-97 for steel structures. Figure 5 depicts the relevant cycle for loading.

Later in the paper, the analytic model that is exactly the same as the laboratory model is modelled by Abaqus software. All parts of the model, except the post-tensioned cable, are made by solid elements, and in the post-tensioned cables, wire elements are used.

As shown in Figure 6, the various parts of the model are situated in appropriate places, geometrically. 8 high strength steel cables (4 on each side of the beam web) are located along the web's height.

5. MESHING

It is a prerequisite to numerical analysis to go through the meshing, and the elements of the model are divided to smaller elements. The configuring elements for all parts

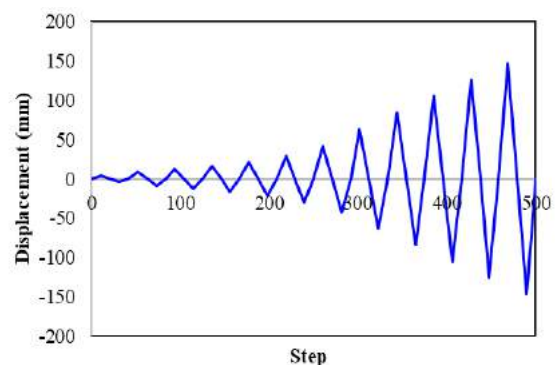


Figure 5. Loading protocol cycle used for this research [6]

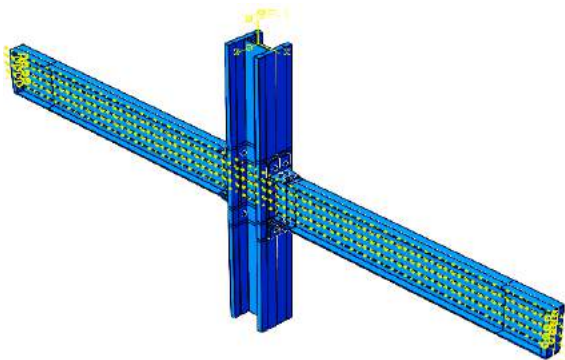


Figure 6. The assembly of consisting parts of the model, in their appropriate place, finalizing the model's geometry

are hexagonal 8-node elements (C3D8R) except the post-tensioned cables that were meshed using 2-node beam elements. The meshing is shown in Figure 7.

After appropriate meshing and getting geometric and appearance of the mesh in order, we can start solving the problem. To achieve the desired number of elements, first step we consider a main parameter that was the goal of the analysis (here it is the displacement of the point in column where the load applies), next step we increase the number of elements (resulting in reducing size of the elements) and repeat solving it in order to evaluate the effects of refining the mesh on the parameter at hand, to the point that there is an agreement between time and the number of the elements, in other words to the point where there is no particular change in the answer by the increase in the elements, or in fact the cost of the calculations outweighs the answers' changes. At this juncture, the model is deemed to be approaching convergence, thereby rendering superfluous the incorporation of additional constituents. Moreover, augmenting the number of elements would not significantly enhance the precision of the solution, but rather would solely result in the elongation of the solution time.

As shown in Figure 8, the size of the mesh and vertical axis in a calculation time curve and in another curve the displacement at load application point in 10 analysis, in the first curve first, the meshing is controlled against the calculation time. With refining the mesh size to 0.06 the calculation time shows no noticeable changes, but from 0.06 onward, the calculation time increases considerably. Another time the meshing is controlled from an accuracy point of view. As seen in the figure, the high displacement changes happen with mesh size changes at first, and curve's slope is high, as the mesh size reduces, the changes reduce too, and so does the curve's slope, to the point that it is almost zero slope.

6. CONTACT SURFACES

The model employed in this study encompassed various components, including columns, beams, angles,

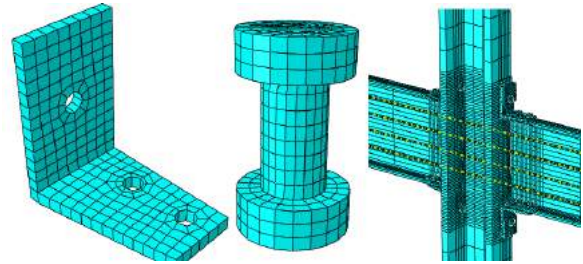


Figure 7. The model B meshing details (A) angles (B) Bolt (C) connection

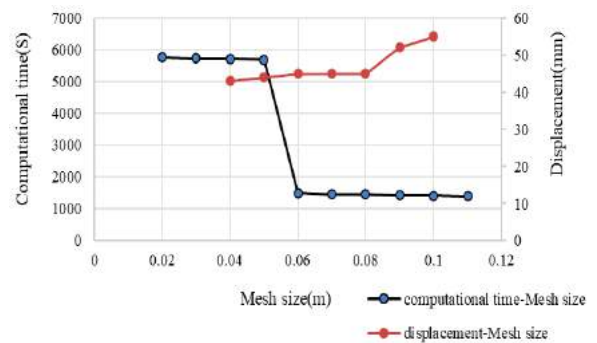


Figure 8. The mesh size curve to (A) analysis time (B) displacement

reinforcing plates, shim plates, bolts, steel post-tensioned (PT) strands, and anchorage plates located at the end of the beams. To ensure computational efficiency and manageable model sizes for finite element simulations of large-scale structural components, certain assumptions were made. Symmetry conditions were applied, resulting in the modeling of only half of the connection assembly. Furthermore, welding elements were not included in the models. However, the influence of welding was considered by imposing appropriate constraints on all degrees of freedom for relevant volumes, such as the beam flange and the beam reinforcing plate. This was accomplished through the application of Tie constraints to account for the welding effect.

To simulate the interaction between different components, contact elements were defined in both the vertical and tangential directions. Vertical interaction was modeled as hard contact, preventing penetration between contact element surfaces. A coefficient of friction of 0.4 was assigned to all contact elements. The following structural component interactions were considered: (a) angle leg and shim plate, (b) angle leg and beam flange, (c) beam web/flanges and shim plate, and (d) PT bars and holes in the column flanges.

In the ABAQUS software, specific options were utilized for the contact elements. The Gauss point detection option was employed to accurately determine the location of contact detection points. The penalty function was chosen as the contact algorithm.

Geometrical penetration or gap and offset were excluded in the analysis. Additionally, certain settings were adjusted to enhance convergence, particularly for the contact between PT bars and holes on the column flanges, which was identified as a potential source of non-convergence. Modifying the normal penalty stiffness factor for the contact element was one technique employed to avoid excessive contact stiffness that could lead to divergence. In Figure 9, the force-displacement hysteresis curve, which is derived from the numerical model in this study that, is compared to the results from Ricles et al. [6].

The results from the numerical model correspond to laboratory results. Also, by studying the two curves together, we can see that the maximum lateral force belongs to the laboratory model whereas the maximum force resulting from the numerical model is equal to 277.9 unit, which shows an error of 3%. Considering the low error between the maximum amounts of these graphs, for two numerical and analytic modes of analysis and also the similarity of behavior pattern and deformation of constituting elements of the connection in the numerical model made in ABAQUS software and laboratory sample used in Racheal et al. [6] study, we find out that the numerical model is made correctly. Now we can claim the derived results are reliable.

7. NUMERICAL MODELS

Two general models are considered in this study. The first group is denoted by RBS sign, in which the connection is the reduced section beam that are connected to the column by top and bottom angles. The second group is denoted by RBS+PT, which are similar to the first group in detail with the exception of having the post-tensioned cables along with the top and bottom angles.

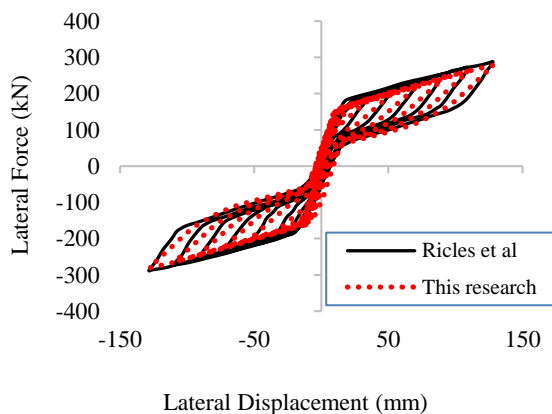


Figure 9. Comparing the results from numerical and laboratory model

7. 1. Steel Connections with Reduced Section (RBS)

In this model, the same details and beam and column dimensions of the verification model is used with the difference that the reduced section with geometric characteristics in Table 3 is used to move the plastic hinge from the critical zone, and also, the post-tensioned cables are deleted. In this connection, the beam and column are connected to each other by means of top and bottom angles.

7. 2. The Connection with Reduced Beam Accompanied by Steel Post-tensioned Cables

In this model same details of RBS model are used, the only difference is that there are 8 steel cables on both sides of the beam parallel to the beam’s web, each one of which are post-tensioned by an initial force of 73.5kN. section area of each cable is 140mm² and crosses the 25mm holes that we created in the column’s web. In this connection the beam and column are connected to each other by the means of top and bottom angles. (Figure 10) this model is identified by PT+RBS.

8. RESULTS AND DISCUSSION

The numerical RBS model results (RBS connections with angles and without steel cables) are listed in Table 4.

In this category of connections, the critical point of tension in the beam resides in the reduced section of the beam. In such way that the tension in beam web and near the reduced section of the beam or at the beam to column connection point. Based on RBS+PT model, the max tension in beam is 245MPa and located at the beam’s web. The numerical RBS+PT model results (RBS connections with post-tensioned cables) are listed in Table 5.

The force-displacement hysteresis curve and push curve of RBS and RBS+PT models are shown in Figure 11.

TABLE 3. the geometric characteristics of reduced beam

Parameter	(a) (mm)	(b) (mm)	(c) (mm)
Value	134	391	30

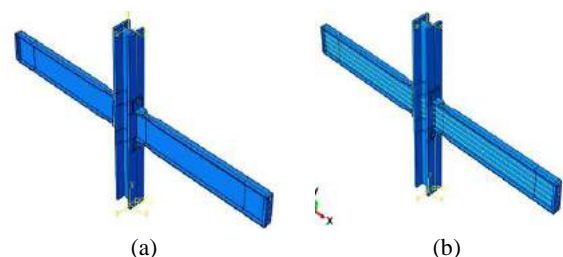


Figure 10. Connection with reduced beam section A- without PT cable, B- with PT cabl

TABLE 4. Results summary for RBS model analysis

Max plastic tension in angle	Max plastic tension in column	Max plastic tension in beam	Max tension in angle (MPa)	Max tension in column (MPa)	Max tension in Beam (MPa)
3.72E-3	0	4.078E-4	218	18.41	24.45

TABLE 5. Results summary for RBS+PT model analysis

Max plastic tension in angle	Max plastic tension in column	Max plastic tension in beam	Max tension in angle (MPa)	Max tension in column (MPa)	Max tension in Beam (MPa)
2.227E-2	1.774E-2	4.127E-2	186	107	245

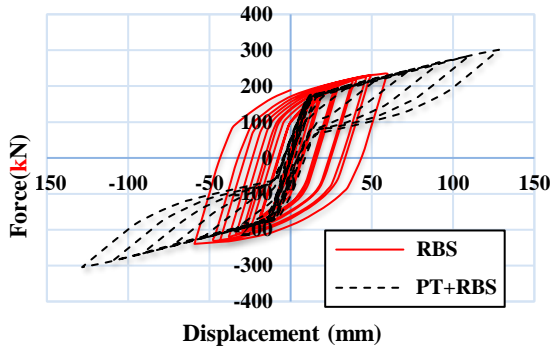


Figure 11. Comparison of RBS and RBS+PT hysteresis curves

Figure 12 shows the energy dissipation amounts along the analyzing time, resulting from plastic displacements which is summarized for RBS and RBS+PT models.

8. 1. Parametric Studies Parametric studies are used to study various parameters’ effects on the cyclic response of post-tensioned connections. The post-tensioning amount, the number of cables, the compound effect of force, and cable increase are the factors that are studied here.

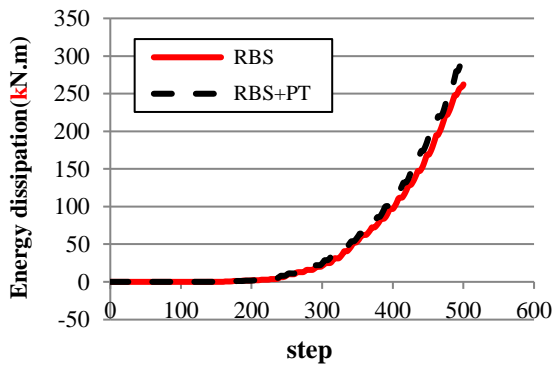


Figure 12. Energy dissipation of RBS and RBS+PT models due to plastic displacement

8. 2. Post-tension Force Effect The self-centering behavior of post-tensioned connections is highly dependent on the post-tensioning force in cables. RBS+PT sample was modeled to study the initial post tensioning force by considering three different levels of that. (RBS+PT0.45, RBS+PT0.5, RBS+PT0.6). In naming these models of these category, PT represents Post-tensioned, and the digits following that is the ratio of initial post-tensioning force to the cables ultimate tension (Ti/Tu). The ultimate force of post-tensioned cables is 261kN. The following introduces the types of models studied for these groups of connections.

8. 3. RBS+PT0.35 Model In this model the 8 cables are post-tensioned with a force equal to 91.87kN in each one of them (25% increase compared to RBS+PT model). the model is under cyclic loading. The force-displacement hysteresis curve compared to that of RBS+PT model is presented in Figure 13.

8. 4. RBS+PT0.45 Model In this model, the 8 cables are post-tensioned with force equal to 117.45kN in each one of them (60% increase compared to RBS+PT model). The model is under cyclic loading. The force-displacement hysteresis curve compared to that of RBS+PT model is presented in Figure 14.

8. 5. RBS+PT0.55 Model In this model, the 8 cables are post-tensioned with a force equal to 143.55kN

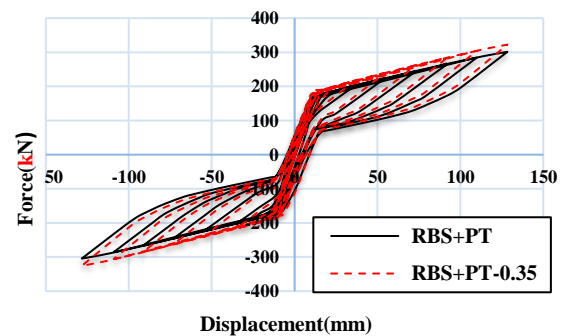


Figure 13. RBS+PT0.35 hysteresis curve compared to RBS+PT

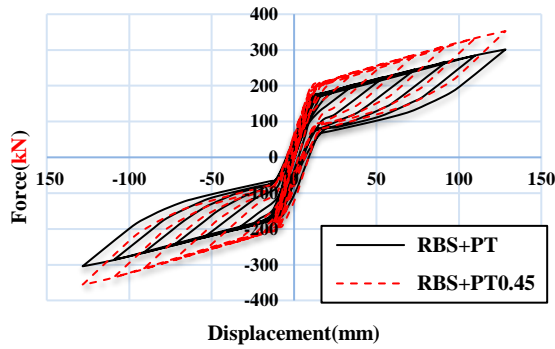


Figure 14. RBS+PT0.45 hysteresis curve compared to RBS+PT

in each one of them (95% increase compared to RBS+PT model). The model is under cyclic loading. The force-displacement hysteresis curve compared to that of RBS+PT model is presented in Figure 15.

The results show that the initial post-tensioning force will affect the stiffness and maximum flexural capacity of the post-tensioned connection.

All models and their responses are listed in Table 6. In this table, θ_r is the relative rotation angle between beam and the column. Other parameters in Table 6, T_i , F_{max} , M_{max} , Δ_{max} , K_i , K_P , and E_d respectively, show the initial post-tensioning force, maximum force, maximum moment, maximum displacement, initial stiffness, and energy dissipation. T_u is the ultimate force in each cable which here is considered to be 261kN. In this part also, the distribution of tensions and stains caused by the main connection elements is presented.

According to Table 6, the unloading happens sooner for connection with less initial post-tensioning (T_i), which is resulted in a bigger gap between beam and column. When the post-tensioning force is increased to 143.5 from 73.5 (almost a 95% increase), the maximum gap angle is reduced 7.32 percent. Also, the connection with higher T_i shows a 26.65% increase in flexural capacity (moment resistance) and a 26.95% increase in initial stiffness. It's worth noting, with increasing the T_i ,

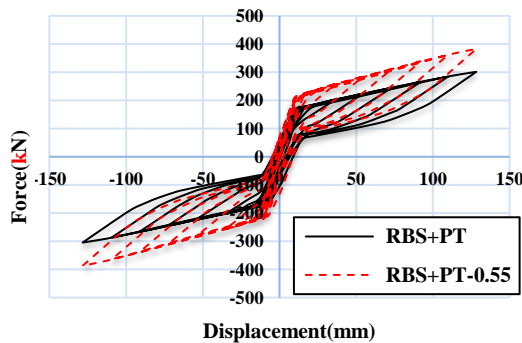


Figure 15. RBS+PT0.55 hysteresis curve compared to RBS+PT

TABLE 6. Responses under cyclic loading

Model	Ti/Tu	Ti (kN)	Mmax (kN.m)	θ_r (rad)	Ki (kN/m)	Ed (kN.m)
RBS+PT(0.28)	0.28	73.5	469	0.028	13302	290
RBS+PT0.35	0.35	91.8	503	0.027	14232	311
RBS+PT0.45	0.45	117.4	550	0.026	15556	469
RBS+PT0.55	0.55	143.5	597	0.025	16893	576
12Ca-RBS+PT0.42	0.28	110.2	634	0.025	13302	666

the energy dissipation of RBS+PT connections is increased by almost 99% as the loading capacity of the PT sections is increasing.

Furthermore, the yielding spread and plasticizing the beams in connection with higher T_i is more intense. The beams in RBS+PT0.55 that has the highest post-tensioning force, and show a 75% bigger plastic strain (PEEQ) .

The simultaneous increase in the number of cables and the initial tensioning force. The cables are the main elements of PT connections, as the shear and moment are transferred from beam to column by means of the cables. Before the gap between the beam and column shows up, the behavior of these connections is under the effect of initial post-tensioning force, whereas the cables stiffness will be the most effective parameter in these connection's behavior. In this part, we keep the length and section area of the cables constant and change the number of those instead. In this way the cables' stiffness is proportionate to their number. In order to increase energy dissipation and improving the system's behavior, we studied the compound effect of increasing the number of cables and their post-tensioning force in the connection, 12Ca=RBS+PT0.42 model with 12 post-tensioned cables, with details similar to RBS+PT model, and with post-tensioning force equal to 110.25kN (1.5 times of RBS+PT model's PT force) is modeled.

The force-displacement hysteresis curve of this connection is shown in Figure 16, based on these outcomes, with the increase in the number of cables, there

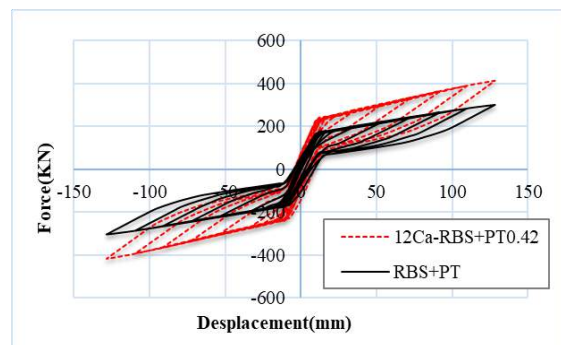


Figure 16. 12Ca-RBS+PT0.42 hysteresis model compared to RBS+PT

is an increase in flexural capacity as well as ductility. The connection with more cables, shows a more self-centering and restoring behavior.

9. SUMMARY AND CONCLUSION

While previous finite element (FE) studies have addressed certain types of post-tensioned (PT) connections, the modeling techniques required for different connections with distinct energy dissipative mechanisms may vary. Moreover, a comprehensive investigation focusing on the FE modeling of steel PT connections with top and seat angles and reduced beam connections (RBS) has not been previously presented. This study aims to address this gap by developing three-dimensional FE models to simulate the cyclic behavior of interior steel PT reduced beam-column connections with top and seat angles. The primary objective is to demonstrate the development of more detailed FE models using advanced features of the Abaqus software, showcasing the capabilities of numerical models in capturing the complex behavior of structural components. Notable features in Abaqus are utilized, such as the utilization of automated pretension elements and providing detailed explanations on modeling steps and options to mitigate convergence issues. Solid elements are employed to model connections to ensure comprehensive representation of local events. The analysis incorporates pretensioned bolts, material and geometric nonlinearity, and contact elements to simulate the behavior of steel PT connections.

This investigation encompasses a parametric analysis of three crucial factors influencing the cyclic behavior of PT connections: the number of post-tensioned cables, the magnitude of the initial post-tensioning force, and the incorporation of a beam web stiffener plate. PT steel connections offer an alternative to conventional rigid connections, overcoming associated limitations. The distinctive characteristic of this connection is the cyclic opening and closing of the gap between the beam and column intersection, facilitated by relative displacement and the restoring force of the cable. The top and bottom angles act as energy dissipators, ensuring effective energy dissipation. The study's findings can be summarized as follows:

- The proposed configuration demonstrates significant innovation, leading to improved seismic performance of the connection.
- Numerical analysis results exhibit strong agreement with laboratory findings, validating the reliability and accuracy of the models.
- All PT models exhibit minimal residual displacements, with cyclic behavior being influenced by factors such as PT cable yielding, local beam buckling, and angle rupture.

- Increasing the post-tensioning force in PT cables by 95% yields a 26.95% increase in stiffness, a 26.65% enhancement in flexural capacity, and an almost 99% escalation in energy dissipation, as indicated by the conducted parametric study.

10. REFERENCES

1. Horton, T.A., Hajirasouliha, I., Davison, B. and Ozdemir, Z., "Accurate prediction of cyclic hysteresis behaviour of rbs connections using deep learning neural networks", *Engineering Structures*, Vol. 247, (2021), 113156. doi: 10.1016/j.engstruct.2021.113156.
2. Guan, X., Burton, H. and Moradi, S., "Seismic performance of a self-centering steel moment frame building: From component-level modeling to economic loss assessment", *Journal of Constructional Steel Research*, Vol. 150, (2018), 129-140. doi: 10.1016/j.jcsr.2018.07.026.
3. Qian, K., Lan, X., Li, Z., Li, Y. and Fu, F., "Progressive collapse resistance of two-storey seismic configured steel sub-frames using welded connections", *Journal of Constructional Steel Research*, Vol. 170, (2020), 106117. doi: 10.1016/j.jcsr.2020.106117.
4. Hu, S., Wang, W., Alam, M.S. and Ke, K., "Life-cycle benefits estimation of self-centering building structures", *Engineering Structures*, Vol. 284, (2023), 115982. doi: 10.1016/j.engstruct.2023.115982.
5. Fang, C., Wang, W., Qiu, C., Hu, S., MacRae, G.A. and Eatherton, M.R., "Seismic resilient steel structures: A review of research, practice, challenges and opportunities", *Journal of Constructional Steel Research*, Vol. 191, (2022), 107172. doi: 10.1016/j.jcsr.2022.107172.
6. Ricles, J.M., Sause, R., Garlock, M.M. and Zhao, C., "Posttensioned seismic-resistant connections for steel frames", *Journal of Structural Engineering*, Vol. 127, No. 2, (2001), 113-121. [https://doi.org/10.1061/\(ASCE\)0733-9445\(2001\)127:2\(113\)](https://doi.org/10.1061/(ASCE)0733-9445(2001)127:2(113))
7. Li, S., Zhao, T., Alam, M.S., Cheng, Z. and Wang, J.-q., "Probabilistic seismic vulnerability and loss assessment of a seismic resistance bridge system with post-tensioning precast segmental ultra-high performance concrete bridge columns", *Engineering Structures*, Vol. 225, (2020), 111321. doi: 10.1016/j.engstruct.2020.111321.
8. Fang, C., Qiu, C., Wang, W. and Alam, M.S., "Self-centering structures against earthquakes: A critical review", *Journal of Earthquake Engineering*, (2023), 1-36. doi: 10.1080/13632469.2023.2166163.
9. Garlock, M.E.M., "Design, analysis, and experimental behavior of seismic resistant post-tensioned steel moment resisting frames, Lehigh University, (2003).
10. Gerami, M., "Multi-stage performance upgrade of steel moment frames by post-tension connections", *International Journal of Engineering, Transactions B: Applications*, Vol. 34, No. 5, (2021), 1132-1144. doi: 10.5829/ije.2021.34.05b.07.
11. Hosseinnejad, H., Lotfollahi-Yaghin, M., Hosseinzadeh, Y. and Maleki, A., "Numerical investigation of response of the post-tensioned tapered steel beams with shape memory alloy tendons", *International Journal of Engineering, Transactions A: Basics*, Vol. 34, No. 4, (2021), 782-792. doi: 10.5829/ije.2021.34.04a.04
12. Vasdravellis, G., Karavasilis, T.L. and Uy, B., "Large-scale experimental validation of steel posttensioned connections with web hourglass pins", *Journal of Structural Engineering*, Vol.

- 139, No. 6, (2013), 1033-1042. doi: 10.1061/(ASCE)ST.1943-541X.0000696.
13. Maghsoudi, A. and Askari D, Y., "Ultimate unbonded tendon stress in CFRP strengthened post-tensioned indeterminate I-beams cast with HSCs", *International Journal of Engineering, Transactions C: Aspects*, Vol. 28, No. 3, (2015), 350-359. doi: 10.5829/idosi.ije.2015.28.03c.03.
 14. Doostdar, H., Nemati, M. and Naghi Pour, M., "Experimental study and modeling of reinforced concrete beams strengthened by post-tensioned external reinforcing bars", *International Journal of Engineering, Transactions A: Basics*, Vol. 23, No. 2, (2010), 127-144.
 15. Moradi, S. and Alam, M.S., "Lateral load-drift response and limit states of posttensioned steel beam-column connections: Parametric study", *Journal of Structural Engineering*, Vol. 143, No. 7, (2017), 04017044. doi: 10.1061/(ASCE)ST.1943-541X.0001772.
 16. Al Kajbaf, A., Fanaie, N. and Najarkolaie, K.F., "Numerical simulation of failure in steel posttensioned connections under cyclic loading", *Engineering Failure Analysis*, Vol. 91, (2018), 35-57. doi: 10.1016/j.engfailanal.2018.04.024.
 17. Mazzoni, S., McKenna, F., Scott, M.H. and Fenves, G.L., "The open system for earthquake engineering simulation (OpenSees) user command-language manual", *University of California, Berkeley: Pacific Earthquake Engineering Research Center*, Vol. 2006, (2006).
 18. Mazloom, M. and Fallah, N., "Seismic vulnerability assessment of existing RC moment frames using a new stiffness based damage index", *International Journal of Engineering, Transactions B: Applications*, Vol. 36, No. 5, (2023), 1000-1011. doi: 10.5829/ije.2023.36.05b.16.
 19. Sarvestani, H.A., "Structural evaluation of steel self-centering moment-resisting frames under far-field and near-field earthquakes", *Journal of Constructional Steel Research*, Vol. 151, (2018), 83-93. doi: 10.1016/j.jcsr.2018.09.013.
 20. Huang, X., Eatherton, M.R. and Zhou, Z., "Initial stiffness of self-centering systems and application to self-centering-beam moment-frames", *Engineering Structures*, Vol. 203, (2020), 109890. doi: 10.1016/j.engstruct.2019.109890.
 21. Bojorquez, E., Lopez-Barraza, A., Reyes-Salazar, A., Ruiz, S.E., Ruiz-García, J., Formisano, A., Lopez-Almansa, F., Carrillo, J. and Bojorquez, J., "Improving the structural reliability of steel frames using posttensioned connections", *Advances in Civil Engineering*, Vol. 2019, (2019). doi: 10.1155/2019/8912390.
 22. Sofias, C. and Pachoumis, D., "Assessment of reduced beam section (RBS) moment connections subjected to cyclic loading", *Journal of Constructional Steel Research*, Vol. 171, (2020), 106151. doi: 10.1016/j.jcsr.2020.106151.
 23. Shen, P.-W., Yang, P., Hong, J.-H., Yang, Y.-M. and Tuo, X.-Y., "Seismic performance of steel frame with a self-centering beam", *Journal of Constructional Steel Research*, Vol. 175, (2020), 106349. doi: 10.1016/j.jcsr.2020.106349.
 24. Bavandi, M., Moghadam, A.S., Mansoori, M.R. and Aziminejad, A., "Introducing a new seismic efficiency index of post-tensioned self-centering steel moment connections", in *Structures*, Elsevier, Vol. 33, (2021), 463-483.
 25. Horton, T.A., Hajirasouliha, I., Davison, B., Ozdemir, Z. and Abuzayed, I., "Development of more accurate cyclic hysteretic models to represent RBS connections", *Engineering Structures*, Vol. 245, (2021), 112899. doi: 10.1016/j.engstruct.2021.112899.

COPYRIGHTS

©2023 The author(s). This is an open access article distributed under the terms of the Creative Commons Attribution (CC BY 4.0), which permits unrestricted use, distribution, and reproduction in any medium, as long as the original authors and source are cited. No permission is required from the authors or the publishers.

**Persian Abstract****چکیده**

با توجه به استفاده گسترده از فولاد در ساختمان سازی و اهمیت زیاد اتصالات فولادی در این ساختمان‌ها، این پژوهش عملکرد لرزه‌ای اتصالات RBS بهبود یافته با سیستم مرکزگرا را برای سازه‌های فولادی مورد بررسی قرار می‌دهد. اتصالات پس‌کشیده مرکزگرا به عنوان جایگزینی برای اتصالات قاب خمشی فولادی مرسوم، با تمرکز تغییرشکل‌های غیرالاستیک در وسایل اتلاف انرژی و بازگرداندن سازه به حالت اولیه قبل از وقوع زلزله، دارای عملکرد مناسبی تحت بار زلزله می‌باشند و این رفتار خودمرکزیت اتصالات با کاهش تغییرشکل‌های پسماند، وجه تمایز اینگونه اتصالات پس‌کشیده با سایر اتصالات خمشی متداول می‌باشد. در این پژوهش، با استفاده از مدلسازی عددی در نرم افزار ABAQUS به روش اجزا محدود، به مدلسازی ترکیبی اتصالات پس‌کشیده PT و RBS و صحت‌سنجی نتایج آنها در مقایسه با نتایج آزمایشگاهی پرداخته شده است، سپس دو مدل RBS جزئیات یکسان مدلسازی گردیده و جهت بررسی اثر کابل‌های پس‌کشیده، یکی از مدل‌ها بوسیله ۸ عدد کابل پرمقاومت، پس‌کشیده شده است و نتایج دو مدل با یکدیگر مقایسه شده است. در ادامه با انجام مطالعات پارامتریک تأثیر سه پارامتر بر عملکرد لرزه‌ای این اتصالات مورد ارزیابی قرار گرفته است. پارامترهای مورد بررسی در این تحقیق شامل مقدار نیروی پس‌کشیدگی اولیه و افزایش تعداد کابل می‌باشند. نتایج به دست آمده نشان می‌دهند که اتصالات دارای کابل پس‌کشیده، شکل‌پذیری خوب، اتلاف انرژی قابل قبول و قابلیت برگشت‌پذیری مناسبی دارند.



Controller Design of Hybrid-Time Delay-Petri Nets Based on Lyapunov Theory by Adding Control Places

A. Ahangarani Farahani, A. Dideban*

Department of Electrical and Computer Engineering Semnan University, Semnan, Iran

PAPER INFO

Paper history:

Received 13 May 2023
Received in revised form 02 July 2023
Accepted 09 July 2023

Keywords:

Control Place
Hybrid-Time Delay-Petri Nets
Stability
Lyapunov Theory

ABSTRACT

The aim of this paper is to propose a new method for controller design using control places in special hybrid Petri Nets called Hybrid-Time Delay-Petri Nets (HTDPN). Most control approaches use the control place of the supervisory control for discrete Petri Nets. However, the new approach uses the place to control the linear dynamical systems which are modeled by the HTDPN tool. This controller consists of control places, transitions, arcs connected to the control place, and weights of the arcs, which are added to the HTDPN model of the system. In this paper, there are three main steps for the controller design. In the first step, the plant is modeled using the HTDPN tool, and in the second step, a controller is designed using the novel method presented. Finally, the weights of arcs connected to the control place are computed using the Lyapunov function theory, which guarantees closed-loop stability. The main advantage of this method is the possibility of using continuous and discrete places simultaneously in nonlinear systems. Unlike most previous approaches, in the proposed method, an expert designer can create a favorite controller in the graphical environment, and then apply changes to the mathematical environment of the HTDPN model. The performance of the proposed controller is evaluated by a comparative study. The comparison criteria in this article are: error criteria (IEA), energy consumption, rise time, settling time and simulation run time. The simulation results showed that the proposed method was 45% and 600% better conditions than the Model Predictive Control (MPC) and optimal control methods, respectively.

doi: 10.5829/ije.2023.36.10a.12

1. INTRODUCTION

In new systems such as traffic systems, biological systems, etc., they are described by differential equations, therefore, they are motivated to develop new methods for analysis, modeling, evaluation and control of systems [1-3]. One of the most successful modeling approaches is Petri Nets [4].

The control of dynamic systems which are modeled by the HTDPN tool has been a matter of great interest. In the last decade, several researchers have been working on the control based on discrete Petri Nets [5, 6]. Supervisory control is one of the essential methods for controller design in Discrete Event Systems (DES) using Petri Nets tool [7]. In supervisory control, the behavior of the system is controlled by adding places and transitions [8]. Demongodin and Koussoulas [9, 10] modeled a controller which was designed based on supervisory control for the industrial system by

differential Petri Nets. In the articles mentioned, differential equation modeling was carried out by Petri Nets, which requires the use of new definitions such as discrete implicit differential transition. Saleh et al. [11], a hybrid adaptive Petri Nets is introduced, in which transition commutes between discrete and continuous behavior depending on a threshold. Ruan and Li [12], for the control of traffic, first, a macroscopic model based on continuous Petri Nets is proposed, and then predictive control laws that improve the behavior of traffic systems are designed. Taleb et al. [13] designed a model predictive control for timed continuous Petri Nets systems. In the methods mentioned, controllers are designed based on the system variables that are generally flow. Continuous systems theory is often described by continuous-time differential or discrete-time differential equations. Therefore, this tool could not be practical to apply to all dynamic systems [14, 15].

*Corresponding Author Email: adideban@semnan.ac.ir (A. Dideban)

Previous attempts have been made to model and control continuous linear dynamic systems, which are modeled by differential equations using Petri Nets. Dideban and Ahangarani Farahani [16] also designed an output feedback controller based on modified Petri Nets. Modified Petri Nets was introduced by Dideban et al. [17], where a discrete transfer function is modeled by Petri Nets. A PID controller based Petri Nets was also proposed by Dideban et al. [18] and Ahangarani Farahani [19]. In these works, some new concepts were added to the conventional Petri Nets, making them rather difficult to be analyzed. The state feedback controller by the Continuous-Time Delay-Petri Nets tool without adding new elements to Petri Nets has been presented by Ahangarani Farahani and Dideban [20]. In the following, the Hybrid Time Delay Petri Net is introduced as a tool for modeling systems with the current sample time signals, including various subsystems, and multi-mode systems [21]. Then a PID controller is designed in which the gains are tuned by the intelligent method. In all the introduced tools, none of the methods provide a controller design based on the graphical and mathematical capabilities of the continuous Petri Nets tool for dynamical systems.

The control place approach is an important method in the control of discrete event systems modeled by Petri Nets. Ma et al. [22] developed an algorithm an optimal control sequence in Petri Nets for designing, which drives a plant net from a source marking to a set of target markings without passing any pre-given forbidden markings. A shunt active power filter (SAPF) based on a three-phase serial flying capacitor multilevel inverter (FCMI) controlled using a Petri net tool is presented by Othman et al. [23]. This controller design is based on the structure of the investigated system and according to the capabilities of the Petri net for the control of discrete event systems. Bashir et al. [24] attempted to prevent deadlock in a manufacturing system, the design of supervisory control which was done based on the Petri Net tool and using the combination of place and transition control. Here, the combination of place and transition has been given flexibility to the designer. Chen and Hu [25] used the developed place-invariant control in automated manufacturing systems based on the Petri Nets tool. In this article, the extended place-invariant control principle is initially proposed. Second, three types of place-invariant, from the special to general, are developed. Finally, the use of this principle is presented to simplify the design of supervisory control. In these articles, all methods and controllers based on Petri Nets are designed for discrete event systems and to prevent the system from entering unsafe conditions. Therefore, these methods cannot be used for dynamic systems that are described by differential equations and discrete events, such as HTDPN.

The principal contribution of this article is to use the idea of control place to design controllers in linear dynamic systems which are modeled by the HTDPN tool. In the proposed approach, the use of control places technique, which is used for the supervisory control of conventional Petri Nets, is extended to HTDPN. Unlike classic control methods for dynamic systems, an important feature of this novel controller is the use of Petri Nets graphics capabilities. In this method, the user can design the controller by adding control places to the HTDPN model in the graphical environment. The designed controller is easily applied to the mathematical part by the incidence matrix. Therefore, controller design is done in the graphical environment instead of the mathematical environment. In other words, here, the controller design methods for discrete event systems are used to design the controller of the dynamic system modeled with a HTDPN. In this paper, the relationship between the control places and other components are determined using the GA (Genetic Algorithm) method. Another innovation in this article is to present the use of Lyapunov's theory to prove stability in Petri Nets based on the incidence matrix. Here, by applying the Lyapunov stability theory on the incidence matrix, the weights of the arcs connected to control place or the control coefficients are obtained. The ability to use continuous and discrete places simultaneously enables us to design a suitable controller in some nonlinear systems. Another innovation of this paper is the use of Lyapunov stability concepts for the mathematical part of the Petri Nets and its use for controller design. The simulation results show that the implementation of this control method using Petri Nets capabilities has better accuracy and less energy consumption than optimal control and MPC Method.

The paper is structured as follows. In section 2, the main concepts, definitions, and mathematics of the Continuous and Hybrid-Time Delay-Petri Nets are proposed. Controller design and stability proof based on Lyapunov theory in the HTDPN is presented in section 3. The dynamic model of the capsubot robot and the implementation of the control method on the system are presented in section 4. Section 5 is dedicated to simulation results, and finally, the conclusion is given in section 6.

2. CONTINUOUS AND HYBRID-TIME DELAY-PETRI NETS

In this section, the CTDPN and HTDPN tool, definitions, and properties are provided. In addition, the mathematical equation has been developed for the HTDPN tool.

A CTDPN is a mathematical and graphical modeling tool for dynamical systems, which are described by

difference equations. The CTDPN tool is defined as follows [20]:

Definition 1: A Continuous -Time Delay-Petri Nets (CTDPN) is a 6-tuple $PN_C = \{P, T, W^-(Pre), W^+(Post), M_0, T_s\}$ such that: $P = \{p_1, p_2, \dots, p_n\}$ and $T = \{t_1, t_2, \dots, t_m\}$ are finite sets of continuous places and transitions, respectively.

Pre and *Post* are the incidence functions that specify the multiplicity of arcs between places and transitions. $M_0 \in \mathbb{R}$ is the initial marking vector, and T_s is the time interval between each run cycle. To model the continuous dynamic system using the CTDPN, the following assumptions and rules should be considered:

Continuous transitions are corresponding to time delays.

In the CTDPN, $M \in \mathbb{R}^n$.

The enabling degree of a transition t_j at a marking $M(p_i)$ is defined as:

$$q(t_j, m) = \min_{i: p_i \in {}^{\circ}t_j} \left(\frac{M(p_i)}{Pre(p_i, t_j)} \right) \tag{1}$$

A continuous transition $t_j \in T$ is enabled, i.e., it can fire, if

$$|M(p_i)| > 0 \forall p_i \in {}^{\circ}t_j$$

where ${}^{\circ}t_j = \{p_i \in P | Pre(p_i, t_j) > 0\}$ is the input place. In the CTDPN tool the weights of the arcs can be negative or non-negative real numbers.

Property 1: The continuous transitions speed in the CTDPN used in the linear system are determined by the input place tokens ($M(p_i)$) divided by the sampling time (T_s).

$$v_j = \frac{M(p_i)}{T_s} \tag{2}$$

Proof: Proof is given in appendix.

Property 2: The fundamental state equation of the CTDPN can be written as follows:

$$m(n) = m(n - 1) + Wm(n - 1) \tag{3}$$

Proof: Proof is given in appendix.

Property 3: The eigenvalues of the dynamical system are equal to the eigenvalues of the W^+ matrix by removing the value of zero.

Proof: Proof is given by Ahangarani Farahani and Dideban [20].

A HTDPN is a modeling tool to model dynamic systems such as systems with current sample time signals, system including various subsystems and multi-mode systems.

Definition 2: A HTDPN is defined as $PN_H = \{P, T, W^-(Pre), W^+(Post), M_0, h, T_s\}$, where $P = \{p_1, p_2, \dots, p_n\}$ and $T = \{t_1, t_2, \dots, t_m\}$ are a finite, not empty, set of continuous and discrete places and transitions, respectively. *Pre* and *Post* are the backward and forward incidence mappings. M_0 and T_s were introduced in definition 1. $h: P \cup T \rightarrow \{C, D\}$ is a hybrid function which indicates whether each node is a discrete

node or a continuous node. In HTDPN, discrete transitions are initially executed [20].

To illustrate this tool, consider the net in Figure 1. All concepts that can be modeled to HTDPN are shown in this figure. Places p_1 and p_2 and transitions t_1 and t_2 are continuous places and transitions, respectively. Places p_3 and p_4 and transitions t_3 and t_4 are discrete places and transitions, respectively.

Here, transition t_1 is enabled only if there is at least one token in p_3 and $M(p_1) > 0$. Therefore the speed of transitions t_1 and t_2 can be written as follows:

$$v_1 = \frac{M(p_1)}{T_s}, \quad v_2 = \frac{M(p_2)}{T_s} \tag{4}$$

However, the following assumptions and rules should be considered:

Continuous transitions are corresponding to time delays. In the HTDPN, continuous places contain real values, while discrete places contain non-negative integer values.

A continuous transition $t_j \in T$ is enabled, if each of the continuous and discrete input places to transition t_j have the following condition at the same time:

$$\begin{aligned} |M(p_i)| > Pre(p_i, t_j) & \quad \text{If } p_i \text{ D-Place} \\ |M(p_i)| > 0 & \quad \text{If } p_i \text{ C-Place} \end{aligned} \quad \forall p_i \in {}^{\circ}t_j$$

The firing speed of the continuous $t_j \in T$ is:

$$v_j = \frac{M(p_i)}{T_s} \quad \text{If } p_i \text{ C-Place} \tag{5}$$

A discrete transition t_l is enabled at discrete $M(p_i)$, if $M(p_i) \geq Pre(p_i, t_l)$

In the first step, the discrete transitions must be evaluated and fired (if enabled) before continuous transitions. Therefore, the fundamental equation for the discrete part of the HTDPN is:

$$\begin{bmatrix} m_c(n) \\ m_d(n) \end{bmatrix} = \begin{bmatrix} m_c(n - 1) \\ m_d(n - 1) \end{bmatrix} + W \begin{bmatrix} 0 \\ X(n) \end{bmatrix} \tag{6}$$

where $X(n)$ is the firing vector of discrete transitions.

The fundamental equation for the continuous part can be written as follows:

$$\begin{bmatrix} m_c(n) \\ m_d(n) \end{bmatrix} = \begin{bmatrix} m_c(n - 1) \\ m_d(n - 1) \end{bmatrix} + W \begin{bmatrix} VT_s \\ 0 \end{bmatrix} \tag{7}$$

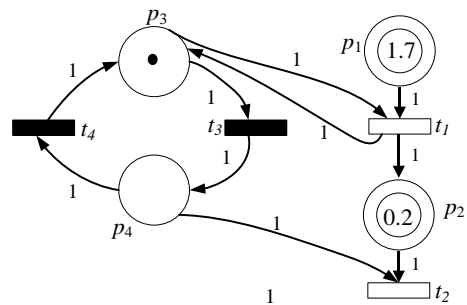


Figure 1. A hybrid Petri Nets model

where the incidence matrix is written as:

$$W = \begin{bmatrix} -1 & 0 & 0 & 0 \\ 1 & -1 & 0 & 0 \\ 0 & 0 & -1 & 1 \\ 0 & 0 & 1 & -1 \end{bmatrix} = \begin{bmatrix} W^C & W^{DC} \\ W^{CD} & W^D \end{bmatrix} \quad (15)$$

where W^C and W^D correspond to arcs among continuous and discrete nodes, respectively. W^{DC} corresponds to arcs among discrete transitions and continuous places. Arcs among continuous transitions and discrete places (W^{CD}) are zero and their effects are given in the V vector.

In this paper, the discrete transitions between continuous places were not used.

$$V(n) = \begin{bmatrix} \frac{M(p_1(n-1))}{T_s} \\ \frac{M(p_2(n-1))}{T_s} \\ 0 \\ 0 \end{bmatrix} \quad (8)$$

For the $X(n)$ vector, if $M(p_i) \geq Pre(p_i, t_i)$, the transition can be fired. In this example, t_3 can be fired and then $X_{t_3}(n) = 1$ and for the transition t_4 , $X_{t_4}(n) = 0$. The simple hybrid system mentioned above has two modes. Therefore, this system can be converted into two continuous systems, in the first mode, the place p_3 has a token and in the second, p_4 has a token. To examine the stability property, it is necessary to construct the matrix J^{c+} . This matrix is defined in definition 3.

Definition 3: In each mode, the augmented continuous incidence matrix J^{c+} is extracted from the system incidence matrix W^+ as follows:

$$J^{c+} = [W^{c+} \quad ; \quad W^{DC+} \cdot m_d(k)] \quad (9)$$

Where m_d can be obtained as:

$$m_d(k) = m_d(k-1) + W^D \cdot X \quad (10)$$

And X is the firing vector of discrete transitions.

3. CONTROLLER DESIGN BASED ON CONTROL PLACE IN THE HTDPN TOOL

A detailed description of the controller design algorithm based on the HTDPN tool is presented in five steps as follows:

Algorithm 1:

Step 1. Calculate the open-loop poles of the system in each discrete mode using the augmented continuous incidence matrix J^{c+} based on property 1 [26].

$$\det(zI - J^{c+}) = 0 \quad (11)$$

$$\begin{cases} \dot{x}_1(t) = x_2(t) \\ \dot{x}_2(t) = -\frac{\mu_{1k}}{M}(M+m)g \cdot \text{sign}(x_2) + \frac{\mu_{2k}}{M}mg \cdot \text{sign}(x_4 - x_2) + \frac{1}{M}u \\ \dot{x}_3(t) = x_4(t) \\ \dot{x}_4(t) = -\mu_{2k}g \cdot \text{sign}(x_4 - x_2) - \frac{1}{m}u \end{cases} \Rightarrow \dot{X}(t) = A_c X(t) + B_c u(t) + f_c(t) \quad (18)$$

If the system in each mode is stable, there is no need to design a controller; otherwise, go to step 2.

Step 2. Add a control place to the HTDPN model of the system.

Step 3. Construct the J_{new}^{c+} in each mode. The dimensions of J_{new}^{c+} are $(n+2) \times (n+2)$.

Step 4. Obtain the fundamental equation of the system in each mode.

$$m_c(n) = m_c(n-1) + J^c v T_s \quad (12)$$

where

$$v = \frac{m(n-1)}{T_s} \quad (13)$$

So equation Equation (12) can be rearranged to Equation (14):

$$m_c(n) = J^{c+} m_c(n-1) \quad (14)$$

Step 5. Calculate k_i as the system is stabilized. Here, the Lyapunov method can be used.

A Lyapunov function can be exploited for the synthesis of nonlinear control systems. First, a Lyapunov function V must be found for the closed-loop system and then a control law is designed, which makes the ΔV negative for the required region of attraction [27]. For this purpose, the following Lyapunov's function candidate is defined:

$$V(n) = m_c^T P m_c > 0 \quad (15)$$

and

$$\Delta V = V(n) - V(n-1) < 0 \quad (16)$$

where

$$\Delta V = m_c^T(n-1) J^{c+T} P J^{c+} m_c(n-1) - m_c^T(n-1) P m_c(n-1) < 0 \Rightarrow \Delta V = m_c^T(n-1) (J^{c+T} P J^{c+} - P) m_c(n-1) < 0 \Rightarrow \Delta V = m_c^T(n-1) (-Q) m_c(n-1)$$

where

$$Q = -(J^{c+T} P J^{c+} - P) \quad (17)$$

In Lyapunov's method for stability, Q must be a positive definite constant matrix.

The flowchart of this algorithm is shown in Figure 2.

4. CONTROLLER DESIGN FOR CAPSUBOT ROBOT

4. 1. Capsubot Dynamic Model The capsbot is selected as the system, that is to be controlled by adding a control place. The simplified schematic model of the legless piezo capsule robot is depicted in Figure 3.

A mathematical model of the capsbot system is derived below [28].

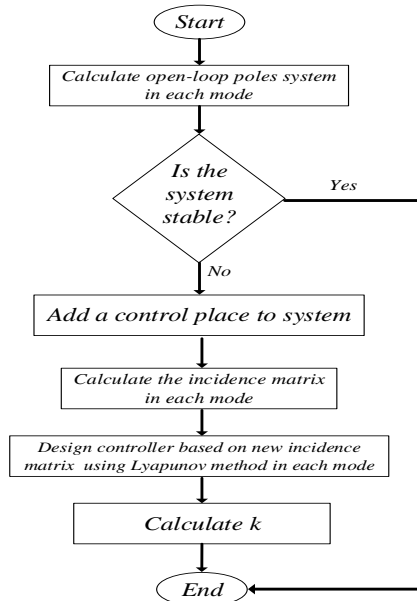


Figure 2. Flowchart algorithm to design a control place based on the HTDPN model

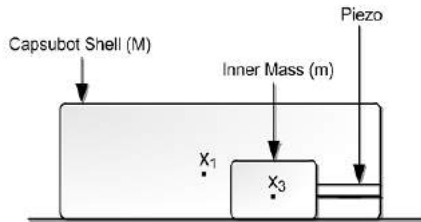


Figure 3. The schematic of the legless piezo capsule robot

where

$$X(t) = [x_1(t) \ x_2(t) \ x_3(t) \ x_4(t)]^T$$

and

$$\begin{cases} \dot{x}_1(t) = x_2(t) \\ \dot{x}_2(t) = -1.3571 \cdot \text{sign}(x_2) + 0.0523 \cdot \text{sign}(x_4 - x_2) + 1.111u \\ \dot{x}_3(t) = x_4(t) \\ \dot{x}_4(t) = -0.0785 \cdot \text{sign}(x_4 - x_2) - 1.6667u \end{cases} \quad (19)$$

After converting the dynamic system from continuous-time system to discrete-time system with the sample time $T_s = 0.01(s)$, the resulting state space is:

$$\begin{aligned} x_1(k) &= x_1(k-1) + 0.01x_2(k-1) - 1.3571 \times 10^{-4} \cdot \text{sign}(x_2(k-1)) \\ x_2(k) &= x_2(k-1) - 1.3571 \times 10^{-2} \cdot \text{sign}(x_2(k-1)) + 0.0111u(k-1) \\ x_3(k) &= x_3(k-1) + 0.01x_4(k-1) \\ x_4(k) &= x_4(k-1) - 0.0785 \times 10^{-2} \cdot \text{sign}(x_4(k-1) - x_2(k-1)) \\ &\quad - 0.0167u(k-1) \end{aligned} \quad (20)$$

$$A_c = \begin{bmatrix} 0 & 1 & 0 & 0 \\ 0 & 0 & 0 & 0 \\ 0 & 0 & 0 & 1 \\ 0 & 0 & 0 & 0 \end{bmatrix}, B_c = \begin{bmatrix} 0 \\ \frac{1}{M} \\ 0 \\ -\frac{1}{m} \end{bmatrix}$$

$$f_c(t) = \begin{bmatrix} 0 \\ -\frac{\mu_{1k}}{M}(M+m)g \cdot \text{sign}(x_2) + \frac{\mu_{2k}}{M}mg \cdot \text{sign}(x_4 - x_2) \\ 0 \\ -\mu_{2k}g \cdot \text{sign}(x_4 - x_2) \end{bmatrix}$$

The parameters of the capsbot robot used are given in Table 1.

A mathematical model of the capsbot microrobot is described as follows:

Finally, the HTDPN with step input for this model is demonstrated in Figure 4.

Here 0^+ is the smallest measurable value in a digital system. The incidence matrix is depicted in Figure 5.

The HTDPN tool models multi-mode systems very well and provides a clear graphical model for analyzing and designing the controller. This system operates in four modes.

The augmented continuous incidence matrix for each mode is given in Table 2.

4. 2. Control Design Based on Place

The dynamic model of the aforementioned capsule robot is a combined nonlinear model that consists of a discrete event part and a linear dynamic part. Therefore, the proposed technique is very difficult to control. In the following, the control method is presented in 5-steps.

Step 1. The open-loop poles of the system in each mode are calculated as:

TABLE 1. Parameters of the capsbot

$M_1(kg)$	$m_2(kg)$	$\mu_{1k}(N/M/s)$	$\mu_{2k}(N/M/s)$	$g(m/s^2)$
0.9	0.6	0.083	0.008	9.81

$$\begin{cases} z_1 = 1 \\ z_2 = 1 \\ z_3 = 1 \\ z_4 = 1 \\ z_5 = -0.0001 + 0.0105i \\ z_6 = -0.0001 - 0.0105i \end{cases}$$

The system is unstable, so it requires a controller.

Step 2. Add a control place to the HTDPN model of the system. The HTDPN model of the system is shown in Figure 4.

The HTDPN model of Equation (19) with the controller is depicted in Figure 6.

In Figure 6, transitions t_{16}, t_{17}, t_{18} and t_{19} act as a switch, and by placing the robot in any mode, these transitions determine which control coefficient to use.

Step 3. The augmented continuous incidence matrix J_{new}^{c+} is structured in Table 3.

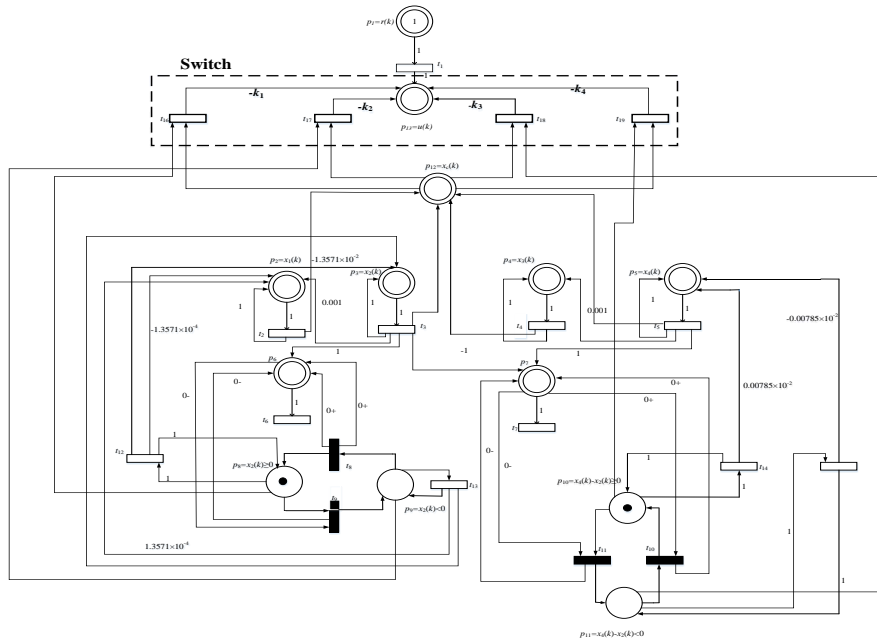


Figure 6. The HTDPN model of the system with Equation (27)

TABLE 3. The incidence matrix for capsule robot with control place in four modes

Mode	Condition	The augmented continuous incidence matrix
1	$x_2(k-1) > 0$ & $x_4(k-1) - x_2(k-1) > 0$	$J_{new}^{c+} = \begin{bmatrix} 0 & 0 & 0 & 0 & 0 & 0 & 0 \\ 0 & 1 & 0.01 & 0 & 0 & -1.3571 \times 10^{-4} & 0 \\ 0 & 0 & 1 & 0 & 0 & -1.3571 \times 10^{-2} & 0.0111K_1 \\ 0 & 0 & 0 & 1 & 0.01 & 0 & 0 \\ 0 & 0 & 0 & 0 & 1 & -0.0785 \times 10^{-2} & 0 \\ 0 & 0 & 0 & 0 & 0 & 1 & -0.0167K_1 \\ 1 & 0 & 0 & 0 & 1 & 0 & 0 \end{bmatrix}$
2	$x_2(k-1) > 0$ & $x_4(k-1) - x_2(k-1) < 0$	$J_{new}^{c+} = \begin{bmatrix} 0 & 0 & 0 & 0 & 0 & 0 & 0 \\ 0 & 1 & 0.01 & 0 & 0 & -1.3571 \times 10^{-4} & 0 \\ 0 & 0 & 1 & 0 & 0 & -1.3571 \times 10^{-2} & 0.0111K_2 \\ 0 & 0 & 0 & 1 & 0.01 & 0 & 0 \\ 0 & 0 & 0 & 0 & 1 & 0.0785 \times 10^{-2} & 0 \\ 0 & 0 & 0 & 0 & 0 & 1 & -0.0167K_2 \\ 1 & 0 & 0 & 0 & 1 & 0 & 0 \end{bmatrix}$
3	$x_2(k-1) < 0$ & $x_4(k-1) - x_2(k-1) > 0$	$J_{new}^{c+} = \begin{bmatrix} 0 & 0 & 0 & 0 & 0 & 0 & 0 \\ 0 & 1 & 0.01 & 0 & 0 & 1.3571 \times 10^{-4} & 0 \\ 0 & 0 & 1 & 0 & 0 & 1.3571 \times 10^{-2} & 0.0111K_3 \\ 0 & 0 & 0 & 1 & 0.01 & 0 & 0 \\ 0 & 0 & 0 & 0 & 1 & -0.0785 \times 10^{-2} & 0 \\ 0 & 0 & 0 & 0 & 0 & 1 & -0.0167K_3 \\ 1 & 0 & 0 & 0 & 1 & 0 & 0 \end{bmatrix}$

$$4 \quad \begin{aligned} &x_2(k-1) < 0 \text{ \& } \\ &x_4(k-1) - x_2(k-1) < 0 \end{aligned}$$

$$J_{new}^{c+} = \begin{bmatrix} 0 & 0 & 0 & 0 & 0 & 0 & 0 \\ 0 & 1 & 0.01 & 0 & 0 & 1.3571 \times 10^{-4} & 0 \\ 0 & 0 & 1 & 0 & 0 & 1.3571 \times 10^{-2} & 0.0111K_4 \\ 0 & 0 & 0 & 1 & 0.01 & 0 & 0 \\ 0 & 0 & 0 & 0 & 1 & 0.0785 \times 10^{-2} & 0 \\ 0 & 0 & 0 & 0 & 0 & 1 & -0.0167K_4 \\ 1 & 0 & 0 & 0 & 1 & 0 & 0 \end{bmatrix}$$

Step 4. Obtain the fundamental equation of the system.

$$m_c(n) = m_c(n-1) + J^c v$$

Step 5. Calculate K_i as the system is stabilized with the Lyapunov method.

$$V = m_c^T(n) P m_c(n) > 0$$

$$\Delta V = m_c^T(n-1)(J^{c+T} P J^{c+} - P)m_c(n-1) < 0 \Rightarrow \Delta V = m_c^T(n-1)(-Q)m_c(n-1)$$

Here, the genetic algorithm method is used to calculate the control coefficients. The genetic algorithm must satisfy Equation (3) and also minimize the following fitness function:

$$F_{obj} = (x_4(t) - x_{4d}(t))^2 \tag{21}$$

The parameters of the genetic algorithm for the system are shown in Table 4.

The convergence trends in the GA for the controller are shown in Figure 7.

Consequently, the K_i for each of the modes are given in Table 5.

5. SIMULATION RESULTS

In this section, the performance of the controller design algorithm will be presented using a control place based on the HTDPN model. In this paper, to investigate the performance of the introduced method, this method is

TABLE 4. The Parameters of the GA.

Generations	Elite Count	Crossover Fraction
50	3	0.7

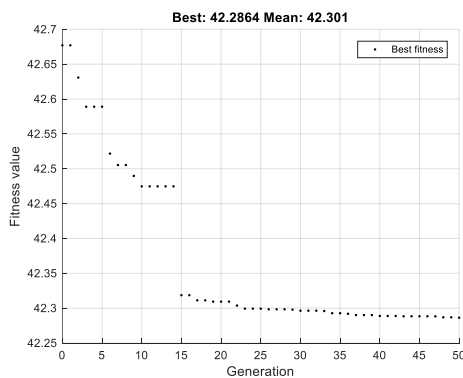


Figure 7. The GA convergence trend in the controller

TABLE 5. Control coefficients of the capsule using Lyapunov theorem.

Mode	Condition	Gain
1	$x_2(k-1) > 0 \text{ \& } x_4(k-1) - x_2(k-1) > 0$	$K_1 = -8.78$
2	$x_2(k-1) > 0 \text{ \& } x_4(k-1) - x_2(k-1) < 0$	$K_2 = -17.436$
3	$x_2(k-1) < 0 \text{ \& } x_4(k-1) - x_2(k-1) > 0$	$K_3 = -16.121$
4	$x_2(k-1) < 0 \text{ \& } x_4(k-1) - x_2(k-1) < 0$	$K_4 = -16.508$

compared with the MPC. Figure 8 shows the capsulot step response in the proposed approach and MPC.

A comparison of the results in Figure 8 shows that the HTDPN response is stable and the proposed control method converges faster than MPC.

Figure 9 and Figure 10 depict capsulot velocity and inner mass velocity, respectively.

These figures show that the inner mass velocity and robot velocity of the proposed method has less oscillation and is smoother than the predictive control method; therefore, the result can be easily implemented.

The input signal in the proposed approach and MPC method is shown in Figure 10.

Figure 11 shows that the input signal in the proposed approach is smoother than the predictive control method. This is while the input signal peak is higher in the presented method. Energy consumption can also be calculated as follows:

$$W = \sum_{i=1}^n U(i) \cdot \Delta\theta(i) \tag{22}$$

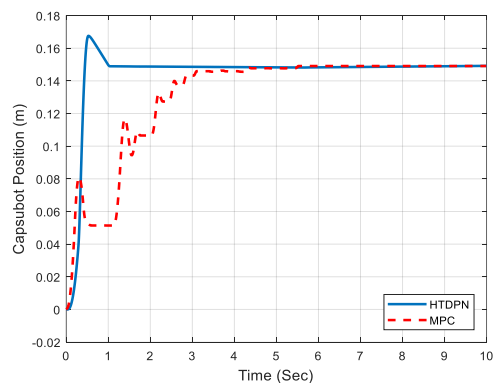


Figure 8. The output of the proposed approach and MPC

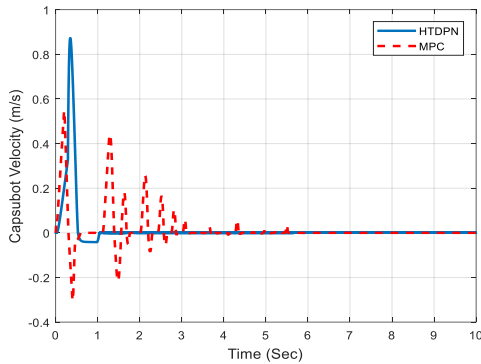


Figure 9. The capsbot velocity

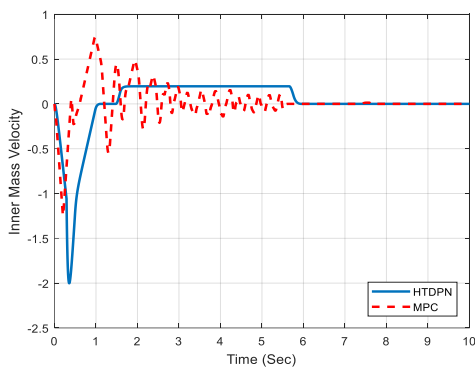


Figure 10. The inner mass velocity

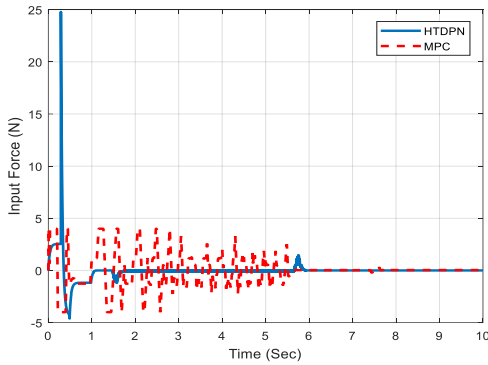


Figure 11. The input signal of the proposed approach and MPC method

The integral absolute error (IAE) is commonly used in the design and evaluation of practical control systems' performance. The IAE is calculated as follows:

$$IAE = \sum_{i=1}^n |e(i)| \tag{23}$$

Table 6 shows a comparison of different criteria for the four simulated methods.

Here, for a more accurate comparison of these methods in Table 5, these parameters are normalized as below:

$$S = \frac{\text{Design parameter value}}{\text{Desired value}} \tag{24}$$

The total of numbers is a criterion for comparing these methods. Table 7 illustrates these normalized criteria.

As Table 7 clearly shows, according to the design criteria, the control place scheme for dynamic systems has proper performance in comparison to the MPC. This controller is designed according to the capacity of the HTDPN tool. Therefore, the designer can perform the desired controller in the graphical environment of the HTDPN tool. Finally, the design result is applied in the incidence matrix for use in the simulation. In addition, the simulation of the system mentioned above by our novel algorithm and the conventional one via the same hardware configuration relays a significant advantage of the new method, which is time efficiency. For future works, it is suggested that other control design algorithms such as fuzzy and optimization methods be implemented

TABLE 6. Comparison of the controller design criteria for the different methods.

Method	Proposed method	MPC	Optimal Control	CLC
Energy Consumption (J)	0.1617	0.352	0.1372	0.3932
IAE (m)	5.572	19.075	581.8096	56.087
Rise Time (S)	0.2119	2.406	6.8857	6.8
Settling Time (S)	0.4651	4.319	8.4218	8.24
Force Peak (N)	25	4	1.518	4.4158
Run Time (S)	0.7336	0.951	0.9689	0.8974

TABLE 7. Comparing the normalized parameters for the different methods

Normalized Values	Proposed method	MPC	Optimal Control	CLC
Energy Consumption	1.1794	2.5675	1	2.865
IAE	1	3.4234	104.4167	10.0658
Rise Time	1	20.366	32.4675	32.091
Settling Time	1	9.2851	18.1159	17.7166
Force Peak	16.4745	2.635	1	2.91
Run Time	1	1.2963	1.3208	1.223
Sum of NV	21.6539	39.5733	158.3209	66.871

with the HTDPN tool and the results be compared with the proposed method.

6. CONCLUSION

In this paper, a novel method for controller design was presented in the environment of the HTDPN tool. In this approach, the desired controller was designed by adding control places in the graphical environment of the HTDPN model system. Using the properties of the HTDPN tool, the controller designed in the graphical environment was transferred to the mathematical environment. Here, the control place technique used in the design of supervisory control in conventional Petri Nets was extended to a HTDPN. Then, by applying Lyapunov's theory to the incidence matrix, the coefficients of the controller were extracted. This controller guarantees that the system was stable. In addition, the control place inputs were determined by the GA method. To prove the performance of the controller, this method was implemented in the capsbot model. It was obvious that this method simplified system analysis and controller design. In addition, due to the use of environment matrices for changes of system states and algebraic operations instead of solving equations, the proposed approach provides a faster mathematical algorithm that can reduce simulation time and complexity for complex systems. Additionally, the results clearly showed that this approach could improve the performance of the controller design.

For future work, it is suggested that the analysis of some system properties, such as controllability and visibility, which are extracted using the state space, should also be investigated and analyzed in modeling using the HTDPN tool.

7. REFERENCES

1. Yin, L., Fang, H. and Shao, H., "Design and implementation of petri net for brain-computer interface system", in 2019 Chinese Automation Congress (CAC), IEEE. (2019), 5810-5814.
2. Du, N., Hu, H. and Zhou, M., "Robust deadlock avoidance and control of automated manufacturing systems with assembly operations using petri nets", *IEEE Transactions on Automation Science and Engineering*, Vol. 17, No. 4, (2020), 1961-1975. doi: 10.1109/TASE.2020.2983672.
3. YadollahzadehTabari, M. and Mohammadizad, P., "Modeling and performance evaluation of energy consumption in s-mac protocol using generalized stochastic petri nets", *International Journal of Engineering, Transactions C: Aspects*, Vol. 33, No. 6, (2020), 1114-1121. doi: 10.5829/IJE.2020.33.06C.08.
4. Liu, F., Chen, S., Heiner, M. and Song, H., "Modeling biological systems with uncertain kinetic data using fuzzy continuous petri nets", *BMC Systems Biology*, Vol. 12, (2018), 63-74. doi: 10.1186/s12918.018.0568.8.
5. Feng, Y., Xing, K., Zhou, M., Wang, X. and Liu, H., "Robust deadlock prevention for automated manufacturing systems with unreliable resources by using general petri nets", *IEEE Transactions on Systems, Man, and Cybernetics: Systems*, Vol. 50, No. 10, (2018), 3515-3527. doi: 10.1109/TSMC.2018.2884316.
6. Li, J., Yu, X. and Zhou, M., "Analysis of unbounded petri net with lean reachability trees", *IEEE Transactions on Systems, Man, and Cybernetics: Systems*, Vol. 50, No. 6, (2018), 2007-2016. doi: 10.1109/TSMC.2018.2791527.
7. Gao, X. and Hu, X., "A petri net neural network robust control for new paste backfill process model", *IEEE Access*, Vol. 8, No., (2020), 18420-18425. doi: 10.1109/ACCESS.2020.2968510.
8. Demongodin, I. and Koussoulas, N.T., "Differential petri net models for industrial automation and supervisory control", *IEEE Transactions on Systems, Man, and Cybernetics, Part C (Applications and Reviews)*, Vol. 36, No. 4, (2006), 543-553. doi: 10.1109/TSMCC.2005.848154.
9. Demongodin, I. and Koussoulas, N.T., "Differential petri nets: Representing continuous systems in a discrete-event world", *IEEE transactions on Automatic Control*, Vol. 43, No. 4, (1998), 573-579. doi: 10.1109/9.665073.
10. Demongodin, I. and Koussoulas, N.T., "Modeling of mixed continuous/discrete-event systems via differential petri nets", in Proceedings of Third International Conference on Electronics, Circuits, and Systems, IEEE. Vol. 1, (1996), 475-478.
11. Saleh, A., Chiachío, M., Salas, J.F. and Kolios, A., "Self-adaptive optimized maintenance of offshore wind turbines by intelligent petri nets", *Reliability Engineering & System Safety*, Vol. 231, (2023), 109013. doi: 10.1016/j.res.2022.109013.
12. Ruan, K. and Li, L., "Traffic network modeling and volume control using labeled petri nets", in 2021 IEEE International Intelligent Transportation Systems Conference (ITSC), IEEE. (2021), 3578-3583.
13. Taleb, M., Leclercq, E. and Lefebvre, D., "Model predictive control for discrete and continuous timed petri nets", *International Journal of Automation and Computing*, Vol. 15, (2018), 25-38. doi: 10.1007/s11633-016-1046-7.
14. Caligola, S., Carlucci, T., Fummi, F., Laudanna, C., Constantin, G., Bombieri, N. and Giugno, R., "Efficient simulation and parametrization of stochastic petri nets in systemc: A case study from systems biology", in 2019 Forum for Specification and Design Languages (FDL), IEEE. (2019), 1-7.
15. Ding, Z., Xiao, L. and Hu, J., "Performance analysis of service composition using ordinary differential equations", in 2008 12th IEEE International Workshop on Future Trends of Distributed Computing Systems, IEEE. (2008), 30-36.
16. Dideban, A. and Ahangarani Farahani, A., "A new adaptive controller for the three axis satellite simulator based on continuous time delay petri nets tool", *Space Science and Technology*, (2022). doi: 10.22034/jsst.2022.314634.1376.
17. Dideban, A., Farahani, A.A. and Razavi, M., "Modeling continuous systems using modified petri nets model", *Modeling and Simulation in Electrical and Electronics Engineering (MSEEE), Semnan, Iran*, Vol. 1, No. 2, (2015), 75-79. doi: 10.22075/MSEEE.2015.247.
18. Dideban, A. and Sabouri Rad, M., "Electrical circuit modelling with petri net by using of control arcs", *Journal of Modeling in Engineering*, Vol. 11, No. 35, (2014), 39-47. doi: 10.22075/JME.2017.1657.
19. Farahani, A.A., Dideban, A. and Najafgholi, E., "Modeling continuous systems by petri nets using speed control arcs", in 2016 4th International Conference on Control, Instrumentation, and Automation (ICCIA), IEEE. (2016), 75-80.

20. Ahangarani, A. and Dideban, A., "Continuous-time delay-petri nets as a new tool to design state space controller", *Information Technology and Control*, Vol. 45, No. 4, (2016), 401-411. doi: 10.5755/j01.itc.45.4.13665.
21. Ahangarani Farahani, A. and Dideban, A., "Hybrid time delay petri nets as a mathematical novel tool to model dynamic system with current sample time", *Control and Optimization in Applied Mathematics*, Vol. 3, No. 1, (2018), 45-64. doi: 10.30473/coam.2019.41925.1090.
22. Ma, Z., Zou, M., Zhang, J. and Li, Z., "Design of optimal control sequences in petri nets using basis marking analysis", *IEEE transactions on Automatic Control*, Vol. 67, No. 7, (2021), 3685-3692. doi: 10.1109/TAC.2021.3106883.
23. Othman, S., Alali, M.A., Sbita, L., Barbot, J.-P. and Ghanes, M., "Modeling and control design based on petri nets tool for a serial three-phase five-level multicellular inverter used as a shunt active power filter", *Energies*, Vol. 14, No. 17, (2021), 5335. doi: 10.3390/en14175335.
24. Bashir, M., Zhou, J. and Muhammad, B.B., "Optimal supervisory control for flexible manufacturing systems model with petri nets: A place-transition control", *IEEE Access*, Vol. 9, (2021), 58566-58578. doi: 10.1109/ACCESS.2021.3072892.
25. Chen, C. and Hu, H., "Extended place-invariant control in automated manufacturing systems using petri nets", *IEEE Transactions on Systems, Man, and Cybernetics: Systems*, Vol. 52, No. 3, (2020), 1807-1822. doi: 10.1109/TSMC.2020.3035668.
26. Baniardalani, S., "Fault diagnosis of discrete-time linear systems using continuous time delay petri nets", *International Journal of Industrial Electronics Control and Optimization*, Vol. 3, No. 1, (2020), 81-90. doi: 10.22111/ieco.2019.28395.1130.
27. Qiu, Z., Duan, C., Yao, W., Zeng, P. and Jiang, L., "Adaptive lyapunov function method for power system transient stability analysis", *IEEE Transactions on Power Systems*, (2022). doi: 10.1109/TPWRS.2022.3199448.
28. Ashjaee, M. and Tavazoei, M. S., "Optimal tuning of implementable fractional order PI controllers based on ISE performance index", *Sharif Journal of Mechanical Engineering*, Vol. 35, No. 1, (2019), 133-141. doi: 10.24200/J40.2018.10795.1431.

8. APPENDIX

The proof of the property 1 is as follows:

Proof: Due to the difference equations, the coefficient of

the first side of the equation is equal to 1, therefore, in the CTDPN model, this relation always holds; $Pre(p_i, t_j) = 1$, therefore:

$$q(t_j, m) = \min_{i:p_i \in t_j} \left(\frac{M(p_i)}{Pre(p_i, t_j)} \right) = \min_{i:p_i \in t_j} (M(p_i)) \quad (25)$$

Since in the CTDPN, the maximum speed of a transition is assumed infinity; therefore, we can suppose that all of the tokens in the places before a transition t_j are discharged at time T_s and then the transitions speed is a function of enabling degree for this transition. Therefore:

$$\begin{aligned} \int_{t_1}^{t_1+T_s} v_j(t) dt &= \min_{i:p_i \in t_j} (M(p_i)) \\ \int_{t_1}^{t_1+T_s} v_j(t) dt &= v_j(t_1)(t_1 + T_s - t_1) = \\ v_j(t_1)(T_s) &\Rightarrow v_j(t_1) = \frac{M(p_i)}{T_s} \end{aligned} \quad (26)$$

The proof of the property 2 is as follows:

Proof: The fundamental equation for timed Continuous Petri Nets between times t_1 and t_2 is as follows:

$$m(t_2) = m(t_1) + \int_{t_1}^{t_2} Wv(t) dt \quad (27)$$

If $t_2 = nT_s$ and $t_1 = t_2 - dt = (n-1)T_s$ the following can be written:

$$m(nT_s) = m((n-1)T_s) + W \int_{(n-1)T_s}^{nT_s} v(t) dt \quad (28)$$

Here, T_s is sample time.

By property 1, the following holds true [26]:

$$\int_{(n-1)T_s}^{nT_s} v(t) dt = m((n-1)T_s) \quad (29)$$

Substituting Equation (29) into Equation (28) and rewriting it gives:

$$m(nT_s) = m((n-1)T_s) + Wm((n-1)T_s) \quad (30)$$

Therefore, the fundamental equation of HTDPN can be obtained as:

$$m(n) = m(n-1) + Wm(n-1) \quad (31)$$

COPYRIGHTS

©2023 The author(s). This is an open access article distributed under the terms of the Creative Commons Attribution (CC BY 4.0), which permits unrestricted use, distribution, and reproduction in any medium, as long as the original authors and source are cited. No permission is required from the authors or the publishers.

**Persian Abstract****چکیده**

هدف از این مقاله معرفی یک روش جدید برای طراحی کنترل‌کننده با استفاده از کنترل مکان در سیستم مدل شده با ابزار شبکه پتری زمان تأخیری ترکیبی است. اغلب در سیستم‌های مدل شده با شبکه پتری گسسته، از کنترل مکان برای طراحی کنترل نظارتی سیستم استفاده می‌شود. در حالیکه، رویکرد جدید معرفی شده در این مقاله از کنترل مکان برای کنترل سیستم‌های دینامیکی مدل شده با ابزار شبکه پتری زمان تأخیری ترکیبی استفاده می‌کند. این کنترل‌کننده شامل، مکان‌های کنترلی، گذرگاه‌ها، کمان‌های متصل شده به مکان‌های کنترلی است که به مدل سیستم اضافه شده و سیستم را کنترل می‌کند. در این مقاله، برای طراحی کنترل‌کننده سه گام باید انجام گیرد. در گام اول سیستم با ابزار شبکه پتری زمان تأخیری ترکیبی مدل می‌شود، و در مرحله دوم با استفاده از روش جدید ارائه شده یک کنترل‌کننده طراحی می‌شود. در نهایت، وزن کمان‌های متصل به مکان‌های کنترلی با استفاده از تئوری تابع لیاپانوف محاسبه می‌شود که پایداری حلقه بسته را تضمین می‌کند. مزیت اصلی این روش امکان استفاده همزمان از مکان‌های کنترلی پیوسته و گسسته برای کنترل سیستم‌های غیرخطی است. برخلاف اکثر رویکردهای قبلی، در روش پیشنهادی، یک طراح خبره می‌تواند یک کنترل‌کننده مطلوب را در محیط گرافیکی ایجاد کند و سپس تغییراتی را در محیط ریاضی مدل شبکه پتری مشاهده نماید. برای بررسی کارایی کنترل‌کننده پیشنهادی، این روش با استفاده از معیارهای خطا، مصرف انرژی، زمان صعود، زمان نشست و زمان شبیه‌سازی با مقایسه ارزیابی شده‌است. نتایج شبیه‌سازی نشان می‌دهد که روش پیشنهادی به ترتیب ۴۵ و ۶۰۰ درصد شرایط بهتری نسبت به روش کنترل پیش‌بین و کنترل بهینه دارد.



Microstructure and Corrosion Behavior of Al-Cu-Fe Quasi-crystalline Coated Ti-6Al-4V Alloy

M. Abaei, M. R. Rahimipour*, M. Farvizi*, M. J. Eshraghi

Department of Ceramic, Materials, and Energy Research Center, Karaj, Iran

PAPER INFO

Paper history:

Received 30 May 2023
Received in revised form 12 July 2023
Accepted 14 July 2023

Keywords:

$Al_{65}Cu_{20}Fe_{15}$ Phase
Corrosion Resistance
Quasicrystals
Thin Film
Ti-6Al-4V Alloy

ABSTRACT

Different industries, including aerospace, marine, and automotive, widely use titanium alloys such as Ti-6Al-4V. Although, this alloy has excellent properties; it is highly susceptible to corrosion and has low thermal stability and tribological characteristics, limiting its application. In this research, after preparing the $Al_{62.5}Cu_{25}Fe_{12.5}$ quasi-crystalline (QC) powder mixture and appropriate target, the magnetron sputtering method was employed to deposit the QC coating on the Ti-6Al-4V substrate. The powder mixture and AlCuFe thin films were annealed at 700°C for 2 h. The scanning electron microscope (SEM) analysis and X-ray diffraction (XRD) methods were used to investigate the microstructure and morphology of mixed powders and Al-Cu-Fe QC coatings. NaCl solution (3.5 wt.%) was utilized to conduct the electrochemical measurements. Al-Cu-Fe thin layer deposited on the Ti-6Al-4V alloy surface without any cracks. The XRD patterns related to the annealed powders and the coating after heat treatment indicated the presence of Cu_3Al , $AlFe_3$, and quasi-crystalline ternary phases of $Al_{65}Cu_{20}Fe_{15}$, Al_3Fe , $AlTi_2$, and $Al_{65}Cu_{20}Fe_{15}$ phases, respectively. Based on the polarization test results, the annealed coating at 700°C showed better electrochemical behavior than the Ti-6Al-4V substrate.

doi: 10.5829/ije.2023.36.10a.13

1. INTRODUCTION

Titanium and its alloys are extensively employed in automotive, biomedical, and aerospace industries due to their unique properties including biocompatibility, high strength-to-weight ratio, and low modulus of elasticity. In contempt of the different pleasant assets of Ti-6Al-4V alloy, the operation of this alloy is restricted, especially when it comes to tribological applications characteristics [1]. Although Ti-6Al-4V alloy has several unique characteristics, its durability in engineering is restricted because they are not hard enough and also highly sensitive to corrosion.

Quasicrystals not only show different structural features, such as the absence of translational symmetry that is representative of non-crystalline materials but also represent the feature of crystalline materials (e.g., generating sharp peaks in XRD). Quasicrystalline materials are appropriate for many practical applications

due to their unique characteristics, including significant hardness, and notable resistance to corrosion. Previous studies [2] have shown that the developing of mixed quasi-crystalline (QC) coatings can enhance the titanium alloy's wear resistance (grade five). The performance of wear resistance for the Al-Cu-5Fe coating was 2.8 times that of the substrate. Although QCs have limited applications as structural materials due to their brittle nature, their distinctive characteristics raise the possibility of applications as functional materials in several fields such as a catalytic agent to produce hydrogen [3,4].

According to the type of coating, the methods of obtaining quasicrystalline coatings are divided into two groups (including powder and film coatings). While powder coatings are made using thermal-gaseous and electrochemical procedures, film coatings are obtained through various physical procedures, including chemical vapor deposition (CVD). Plasma spray and High-

*Corresponding Authors Email: m-rahimi@merc.ac.ir (M. R. Rahimipour), mmfarvizi@yahoo.com (M. Farvizi)

Velocity Oxygen Fuel (HVOF) are widely used to make quasicrystalline coatings, but these methods are associated with problems such as porosity, unmelted particles, cracks, and oxides [5, 6].

Magnetron sputtering is a widely used method for deposition wear and corrosion-resistant coatings. This method is economic and can be applied on samples with complex shapes. The quasi-crystalline phase formation depends on the substrate temperature [7, 8]. As experimentally shown, the substrate temperature should be higher than 500°C to obtain a single-phase quasicrystalline coating. The deposition of QCs on the substrates at room temperature leads to the evolution of the semicrystalline phase after subsequent heat treatment. The advantages of this method are high spraying speed at low operating voltages (700-800 V), low working gas pressure, low degree of pollution of the resulting film, and the possibility of obtaining uniform film thickness. However, the adjustment of stoichiometry in QCs is the main challenge [9-12].

Al-Cu-Fe-based quasicrystalline thin films show exceptional surface and mechanical properties. The direct growth of quasicrystals was reported in multilayer Al-Cu-Fe thin films after subsequent heat treatment [13]. Successful application of $Al_{60}Cu_{28}Fe_{12}$ quasicrystalline and film coating obtained through three-electrode ion-plasma sputtering of assembled targets was reported, and this coating contained a quasi-crystalline *i*-phase that was stable up to 723K [14]. The formation of the $Al_{62.5}Cu_{25}Fe_{12.5}$ quasicrystalline phase was achieved by the Al-Cu system at temperatures relatively higher than 500 (T>500°C). It is important to know that there are seven various compounds (Al_2Cu , Al_4Cu_9 , $AlCu$, Al_xCu , Al_6Fe , Al_7Cu_2Fe , and $Al_{10}Cu_{10}Fe$) in the phase formation sequence before the icosahedron phase [15]. There was an increase in the amount and grain size of the *i*-phase throughout the process of annealing [16]. Phases that have a polyhedral atomic substructure in QCs, have greater nucleation rates within the system [17].

Uniaxial hot pressing was used to fabricate targets in the magnetron sputtering deposition process. The creation of cracks within the targets throughout film deposition can lead to statistical deviations in the coating composition when the AlCuFeB coating is applied in this way [7].

The Al-Cu-Fe QCs reveal high corrosion resistance and good hydrogen storage for use in catalytic reactions. These alloys, at low temperatures, have similar thermal properties to zirconia oxides, which are considered excellent insulators [18]. The investigation of corrosion resistance of AlCuFe thin film in NaCl solution approved its excellent performance [19]. The Corrosion behavior investigation of the quasicrystalline $Al_{63}Cu_{25}Fe_{12}$ alloy in a 5 % sodium chloride solution confirms the formation of a stable quasicrystalline icosahedral (ψ) phase [20]. According to corrosion experiments performed for 1, 2,

3, 4, and 8 days using 5% NaCl solution at 293 K, the Al-Cu-Fe films showed excellent corrosion resistance [21].

The limitations of titanium alloys, such as easy oxidation, and simple reaction with other materials can be overcome by adding Al and Cu to Ti. This procedure leads to the formation of significantly stable intermetallic metallurgical bonds and consequently, increases corrosion resistance. The Al-Cu-Ti combination is comparable to some icosahedrons like Al-Cu-Fe, which perform efficiently in surface engineering, as well as composite production [22, 23].

In the latest studies, icosahedral quasicrystals [24, 25], and characterization of thin films on the Ti6Al4V alloy substrate have been reported [26-29]. Als, in recent years, magnetron sputtering has received great attention for developing thin films [30].

Due to the above-mentioned problems of titanium alloys, and considering the necessity of applying an appropriate coating to improve the performance of titanium alloys, in this study, after the preparation of $Al_{62.5}Cu_{25}Fe_{12.5}$ quasi-crystalline powder mixture and appropriate target, the magnetron sputtering method was employed to deposit the QC coating on Ti-6Al-4V substrate. The microstructural aspects and electrochemical behavior of the substrate and the coated sample were studied and compared.

2. EXPERIMENTAL DETAILS

2. 1. Materials and Substrate Specifications

Aluminum, iron, and copper powders with a purity of 99.9% were weighed using a scale with the precision of 0.0001 g in appropriate proportions to reach $Al_{62.5}Cu_{25}Fe_{12.5}$ composition. The substrate of the desired alloy was cut to 1 cm × 1 cm × 1 cm dimensions. The Spark Emission Spectroscopy test was used to investigate the alloy's chemical composition, the results of which are reported in Figure 1.

2. 2. Target Preparation Method The powder mixture was milled using a planetary ball-mill. The ball-to-powder weight ratio of 5:1 and a rotation speed of 220 rpm for 3 h were considered. After drying, the powders were compressed into discs having a 70 mm diameter and a 4 mm thickness in a uniaxial hydraulic press.

2. 3. Thin Film Preparation Before the coating deposition, the surfaces of the samples were sanded, degreased, and washed. Deposition of Al-Cu-Fe thin films on Ti6Al4V alloy substrates was carried out within a magnetic sputtering chamber, which had a 10^{-4} mbar base pressure. The deposition was accomplished at a pressure of 2.5×10^{-3} mbar under Argon gas (purity 99.998%) and at room temperature. A sputtering deposition technique using an AlCuFe ternary target with

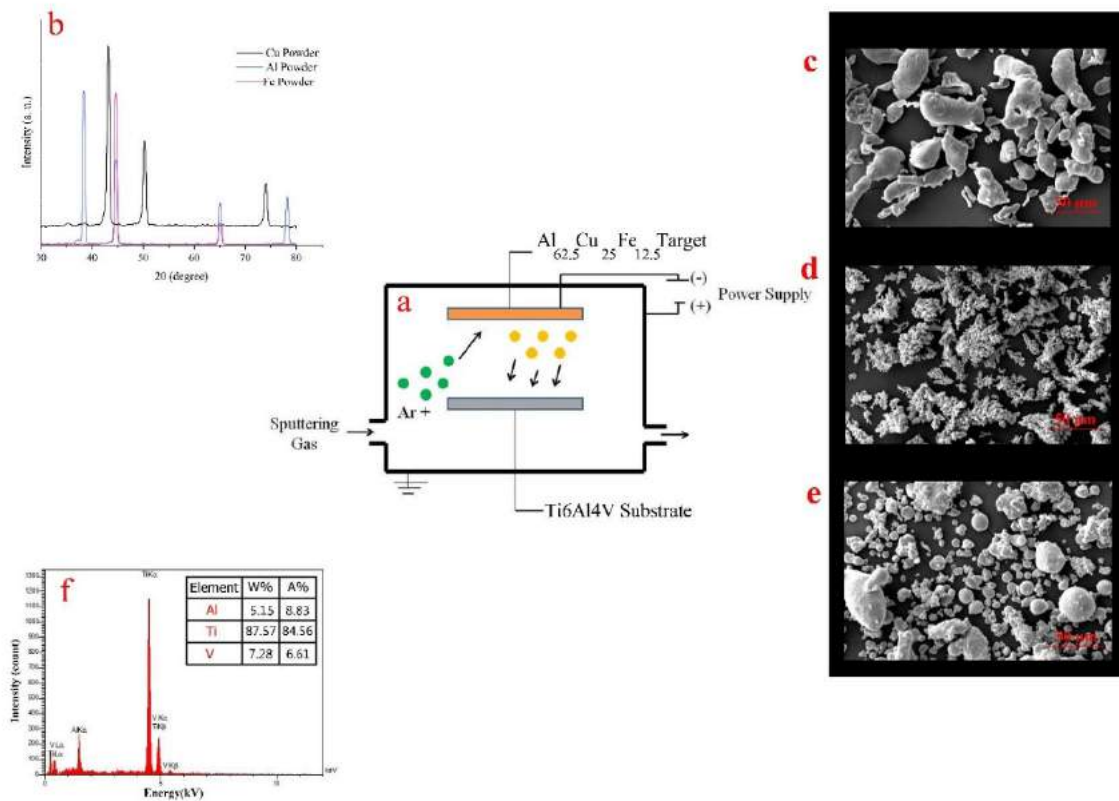


Figure 1. a) Schematic of the Magnetron Sputtering process; b) XRD results of primary powders, the morphology of the primary powders: c) Al, d) Cu, e) Fe, f) chemical composition of Ti6Al4V alloy

a composition of $\text{Al}_{62.5}\text{Cu}_{25}\text{Fe}_{12.5}$ was used to deposit the film. Figure 1 illustrates a schematic of the magnetron sputtering process. After the sputtering process, the samples were annealed with a continuous flow of 95% Argon and 5% H_2 at 700°C for 2 h [9, 10].

2. 4. Analysis Methods After annealing, the X-ray diffraction of the coated samples was performed by the Grazing-XRD method (XRD Philips PW1730 model) with the specifications of the 2.2 KW X-ray lamp. The identification of phases was done using Xpert HighScore software. The XRD method (Siemens, D500 system) with Cu K_α radiation at a 30-kV accelerating voltage was used to characterize the crystalline phases of different powders. SEM (VEGA II SCAN) and FESEM (Mira3 TESCAN model) were used to study the samples' microstructure. The EDS method was also employed to determine the chemical composition of the formed phases. A 3.5 wt% NaCl solution was considered to perform electrochemical measurements on the Ti6Al4V and AlCuFe samples (QC coated). The potentiodynamic polarization curves were examined to analyze the corrosion behavior. Model Princeton Applied Science EG&G parsta 2273 equipment was used for the

electrochemical analysis. The standard corrosion test was used STM G59- 97 conducting potentiodynamic polarization resistance measurements.

3. RESULTS AND DISCUSSION

3. 1. $\text{Al}_{62.5}\text{Cu}_{25}\text{Fe}_{12.5}$ Powder Composition Figure 2 shows the morphology of $\text{Al}_{62.5}\text{Cu}_{25}\text{Fe}_{12.5}$ powder mixture after 3 h of mixing before and after heat treatment at 700°C for 2 h. The comparison of the morphology of starting powders including aluminum, copper, and iron powders (Figure 1(c), (d) and (e)) with those after mixing (Figure 2(a)) revealed that the morphology of the primary powders transformed into laminar shapes. Also, as can be seen in Figure 2(b), heat treatment of the powder mixture changes the morphology and leads to the evolution of the polyhedral particles in the mixture.

The elemental distribution map of $\text{Al}_{62.5}\text{Cu}_{25}\text{Fe}_{12.5}$ powder composition before and after annealing were shown in Figure 3. The presence of aluminum, copper, and iron elements in the distribution of elements indicate the AlCuFe mixing composition.

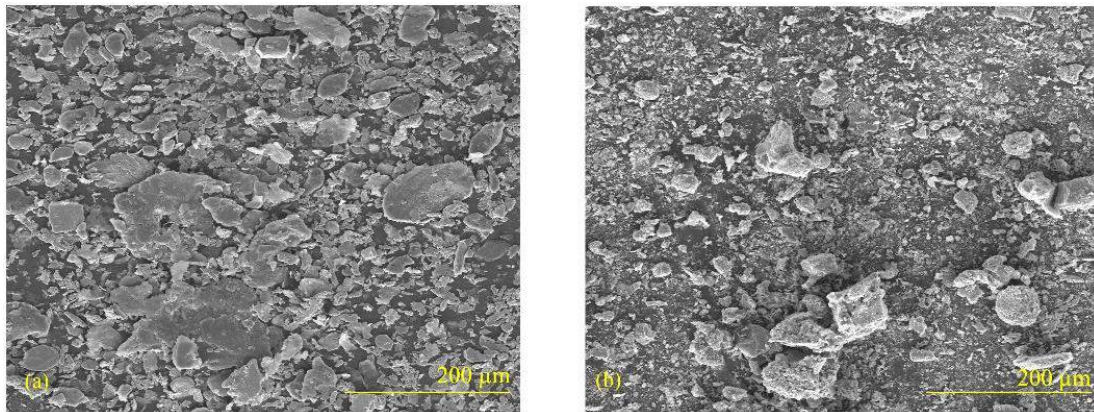
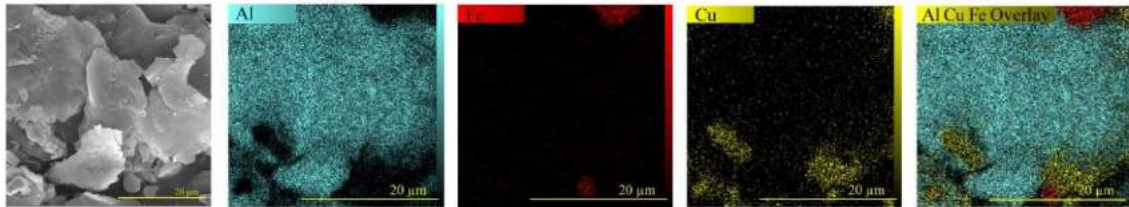


Figure 2. a) Morphology of $\text{Al}_{62.5}\text{Cu}_{25}\text{Fe}_{12.5}$ powder composition after 3 h of mixing, b) Morphology of $\text{Al}_{62.5}\text{Cu}_{25}\text{Fe}_{12.5}$ powder composition after heat treatment at 700°C for 2 h

As Sputtered



After Annealing

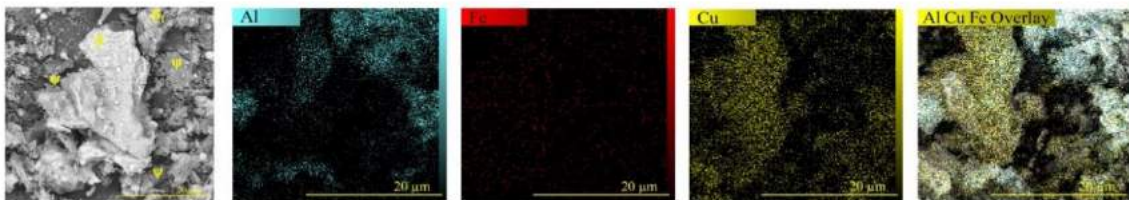


Figure 3. Elemental distribution map of $\text{Al}_{62.5}\text{Cu}_{25}\text{Fe}_{12.5}$ powder composition before and after annealing

Figure 4 shows the XRD results of the $\text{Al}_{62.5}\text{Cu}_{25}\text{Fe}_{12.5}$ powder mixture after 3 h of mixing before and after heat treatment at 700°C for 2 h.

The XRD pattern of the powder mixture before heat treatment confirmed that aluminum, copper, and iron powders were present and no new phase or solid solution appeared. The XRD pattern of the annealed powder mixture demonstrated the presence of Cu_3Al (β), and AlFe_3 (β_1) phases, as well as the quasi-crystalline ternary phase of $\text{Al}_{65}\text{Cu}_{20}\text{Fe}_{15}$ (ψ). The evolution of the post-annealing quasi-crystalline phase of $\text{Al}_{65}\text{Cu}_{20}\text{Fe}_{15}$ has also been reported in other studies [31, 32]. Crystal structures and stable phases of Al-Cu-Fe ternary mechanisms were listed in Table 1.

3. 2. AlCuFe Thin Film

Figure 5 shows the cross-section and the elemental distribution map taken

from the cross-section of AlCuFe coating. The current thickness of the AlCuFe thin film was about 800 nm. No cracks or breaks were observed in the target during 135 min of sputtering due to the appropriate preparation of the target by mixing method, eventually leading to the formation of an AlCuFe thin film. The cross-section image in Figure 5 is displayed in the backscattered electrons (BSE) mode, accordingly indicating the area related to the thin film is brighter than the substrate.

Similar studies have reported a thickness of 85-260 nm for Al-Cu-Fe and Al-Co-Cu thin films accumulated on sodium chloride or glass, and ceramic substrates with three-electrode plasma [33]. Also, Al-Cu-Fe and Al-Cu-Fe-Sc quasi-crystalline films with 200 to 260 nm thicknesses have been obtained by ion-plasma sputtering of three electrodes [34]

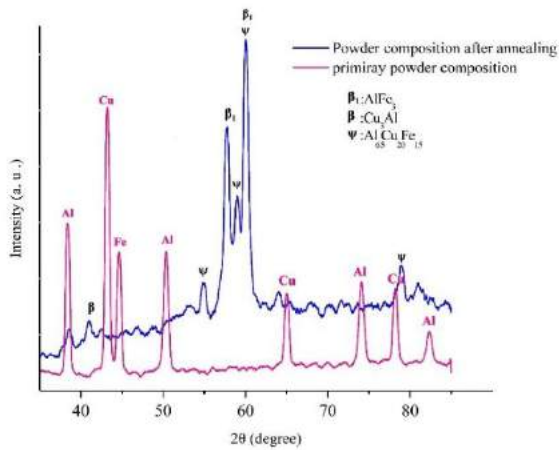


Figure 4. XRD patterns of AlCuFe powder mixture before and after heat treatment

The distribution of titanium and vanadium elements and Al, Cu, and Fe emphasized forming AlCuFe coating

on the Ti-6Al-4V alloy as the substrate. As noted, there was neither Cu nor Fe in the substrate areas, and gradients were increasing for Cu and Fe and decreasing towards the thin film areas for Ti and V. Similarly, the very high catalytic performance of this alloy for methanol steam reforming was proven using the distribution map of aluminum, copper, iron, and oxygen elements of AlCuFe quasi-crystalline coating [35].

In another research, AlCuFe coating was deposited by the electron beam method. The study reported the microstructure of the coating in the cross-section and the distribution of chemical elements of aluminum, copper, and iron compared to the thickness of the coating. The results confirmed a relatively uniform distribution of elements along the cross-section of the coating [36].

Figures 6 shows the morphology of Al_{62.5}Cu₂₅Fe_{12.5} thin film before and after heat treatment at 700°C for 2 h. The surface of the coating is completely continuous and without any visible cracks in two modes, as sputtered and after annealing. In the higher magnification, the morphological changes and multifaceted shapes are

TABLE 1. Crystal structures and stable phases of Al-Cu-Fe ternary mechanisms

Phase	Ideal formula	Present research	References Code	Structure	Other Researches
β ₁	AlFe ₃	Figure 3	00-050-0955	Body-centered cubic	[25]
β	Cu ₃ Al		00-028-0005		[24]
ψ	Al ₆₅ Cu ₂₀ Fe ₁₅		00-042-1043	Quasicrystal	[17]

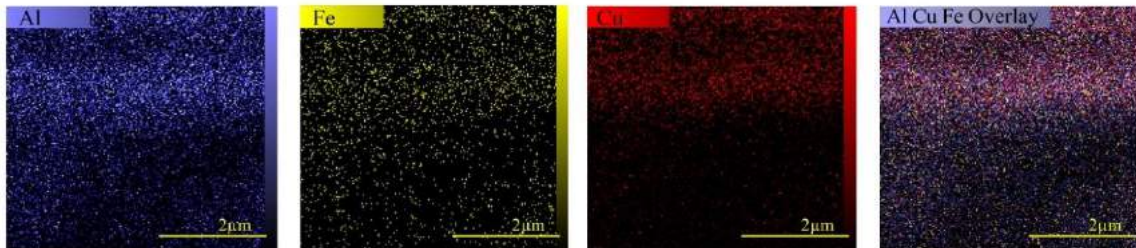
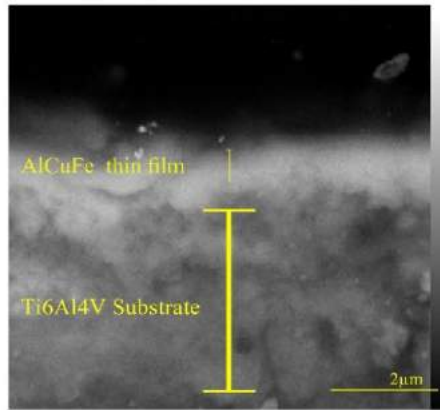
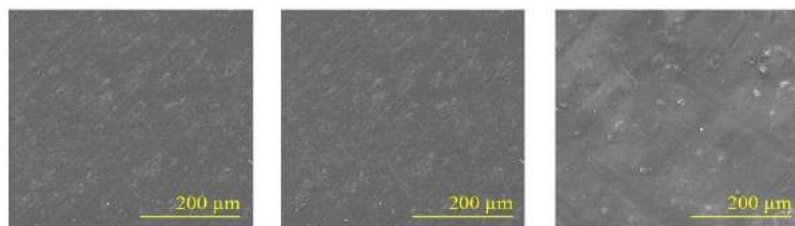


Figure 5. Cross section and distribution of cross-sectional elements of as sputtered AlCuFe coating applied on Ti-6Al-4V substrate

As Sputtered



After Annealing

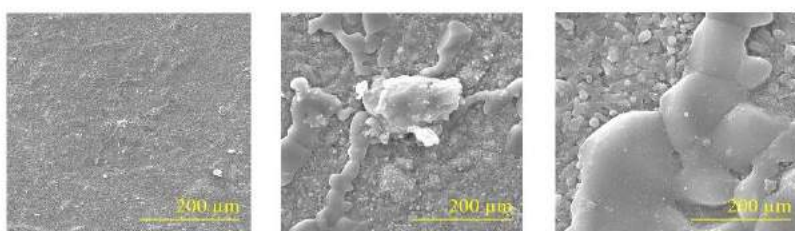


Figure 6. Morphology of AlCuFe coating applied on Ti-6Al-4V substrate before and after heat treatment at 700°C for 2 h

visible. Also, the five-facet morphology, which represents the presence of quasicrystal, is visible in the annealed thin film morphology. Figure 7 shows the distribution map of AlCuFe coating elements applied on the Ti-6Al-4V alloy substrate before and after annealing. As indicated in as sputtered thin film (before annealing), aluminum, copper, and iron elements had an even regional distribution on the coating surface. The identical distribution of aluminum, copper, and iron elements on the surface of the coating corroborates the AlCuFe coating formation. On the other hand, the distribution map of titanium element confirmed the entity of Ti-6Al-4V alloy substrate.

In the map images AlCuFe thin film after annealing, there are some areas empty of titanium, which indicates the creation of a coating on the substrate.

Figure 8 reports the XRD results of as-sputtered AlCuFe coating applied on Ti-6Al-4V after annealing. The XRD pattern of the AlCuFe coating shows the presence of Al_3Fe , and AlTi_2 phases, as well as the quasicrystalline ternary phase of $\text{Al}_{65}\text{Cu}_{20}\text{Fe}_{15}$. The quasicrystalline phase of $\text{Al}_{65}\text{Cu}_{20}\text{Fe}_{15}$ after annealing is reported in similar studies [1, 37]. According to the XRD analysis of the powders (Figure 4), the quasi-crystalline phase ψ was also visible in the AlCuFe thin film after annealing.

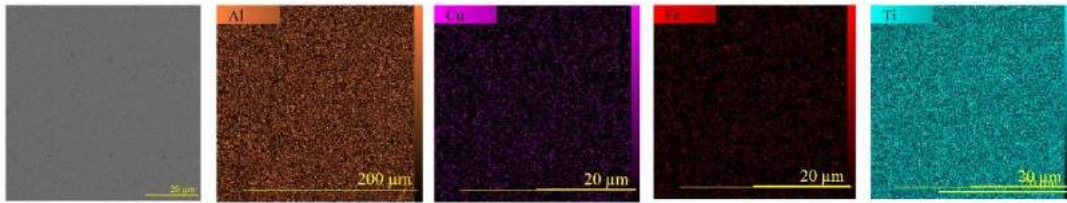
According to distribution map (Figure 7) the light areas were Cu- rich and Fe-rich, indicating ψ -phase whereas the other ones were Ti-rich revealing the AlTi_2 phase, in agreement with the phases detected by XRD (Figure 8).

The EDS results of the as-sputtered AlCuFe coating applied on the Ti-6Al-4V substrate are shown in Figure 9. The atomic percentages of aluminum, copper, and iron elements of the coating were 40.61, 9.23, and 22.71, respectively. The amount of aluminum in the coating (40.61 atomic percent) was lower than the amount of aluminum in the initial mixture (62.5 atomic percent), caused by the low deposition rate of aluminum. On the other hand, the high deposition rate led to a high amount of copper in the coating compared to the initial powder mixture.

Figure 10 shows the EDS results of the AlCuFe coating applied on the Ti-6Al-4V substrate by magnetic sputtering after heat treatment. Comparing the EDS results of the coating before annealing (Figure 9) and after annealing (Figure 10), the atomic percentage of the coating elements did not change significantly. According to Figure 10(b), the atomic percentage of aluminum, copper, and iron have been measured to be 41.15, 21.28, and 7.79, respectively, and the amount of titanium in the substrate is 29.78 atomic percent. The XRD (Figure 8) and EDS results (Figure 10(b)) confirmed the presence of the Al_3Fe and AlTi_2 phases. As can see in Figure 10(c), the EDS results related to ψ area show values of 59.25, 10.64, and 20.58 atomic percentages for aluminum, copper, and iron elements, respectively, which are very close to the EDS results of as sputtered thin film (Figure 9).

According to the EDS results from Figure 10(c) and the XRD results (Figure 8), this area indicates the presence of compounds with the stoichiometry of the initial powder ($\text{Al}_{62.5}\text{Cu}_{25}\text{Fe}_{12.5}$). It is also related to the formation of the $\text{Al}_{65}\text{Cu}_{20}\text{Fe}_{15}$ quasicrystalline phase (ψ).

As Sputtered



After Annealing

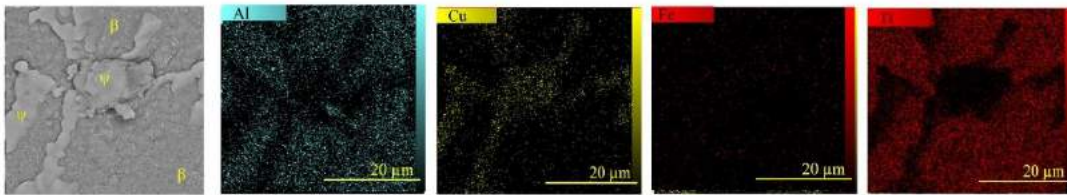


Figure 7. Elemental distribution map of AlCuFe coating applied on Ti-6Al-4V substrate before and after heat treatment

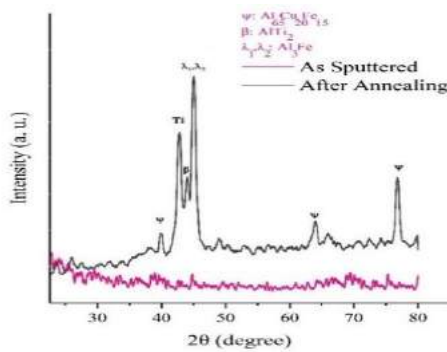


Figure 8. XRD results in AlCuFe coating applied on Ti-6Al-4V as sputtered and after annealing

3. 3. Investigating the Corrosion Properties of AlCuFe Thin Film

Figure 11 displays the Nyquist curves (Z' in terms of $-Z''$) of Ti-6Al-4V alloy (substrate) and Al-Cu-Fe thin film after annealing. In these curves, the increase in diameter demonstrates an increase in the corrosion resistance of the system. Therefore, it is clear from the shape of the Nyquist curves that the diameter of the curve in the substrate sample (Ti-6Al-4V alloy) is significantly greater than that of the Al-Cu-Fe thin film after annealing. The corresponding Bode-modulus impedance and Bode-phase angle curves of Ti-6Al-4V alloy (substrate) and Al-Cu-Fe thin film after annealing are shown in Figure 12. As indicated in Figure 12(a), the

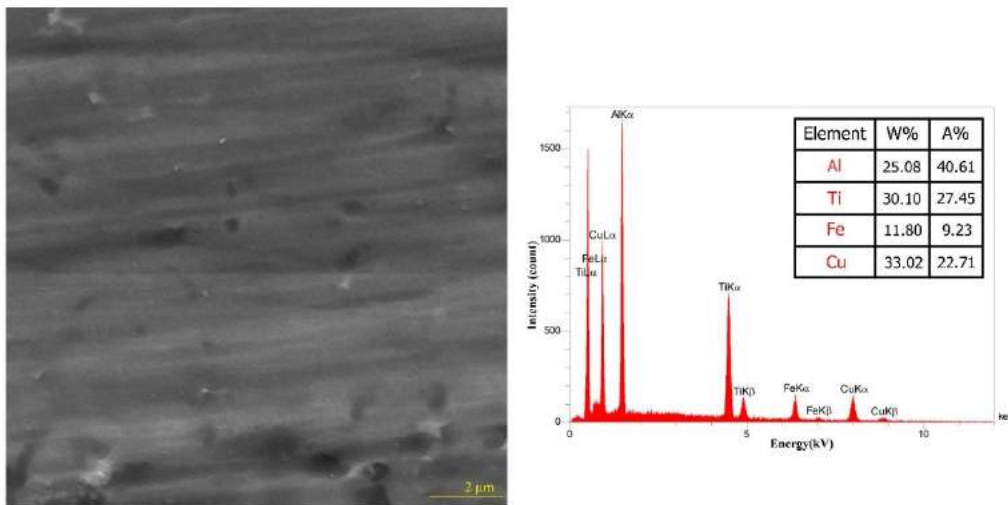


Figure 9. The EDS results of the as-sputtered AlCuFe coating applied on the Ti-6Al-4V substrate

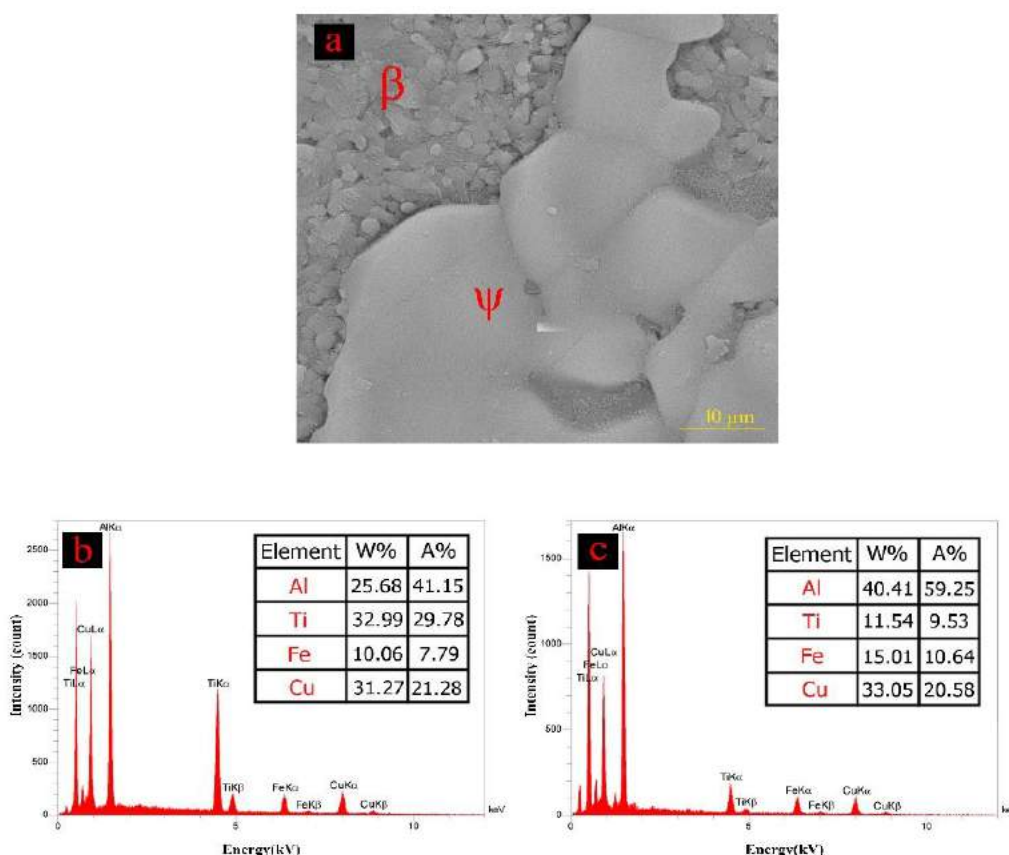


Figure 10. a) EDS results of the AlCuFe coating applied on the Ti-6Al-4V substrate after treatment, b) EDS results related to β areas, c) EDS results related to ψ area

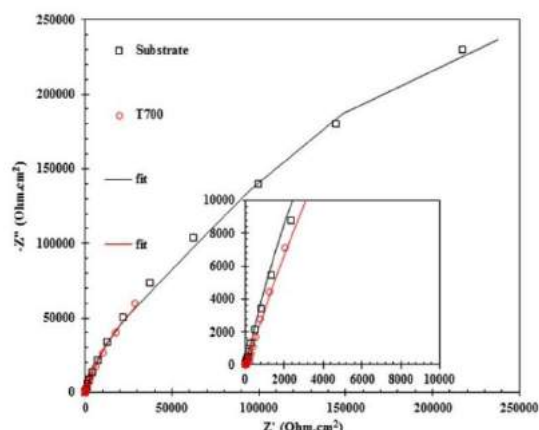


Figure 11. Nyquist diagrams in 3.5% NaCl solution at 25 °C for the selected samples in the form of Ti-6Al-4V alloy (substrate) and Al-Cu-Fe thin film after annealing (points of test results and the lines are the results of the fit)

impedance at the lowest frequency of the substrate was higher than the annealed Al-Cu-Fe thin film. Also, it is possible to obtain information about the anti-corrosion properties of the system from the Bode-phase angle

diagrams. This evidence shows that the higher the phase angle value, the greater the resistance to electrolyte penetration [38]. Accordingly, it is obvious in the graphs of Figure 12(b) that the phase angle for the Ti-6Al-4V alloy (substrate) was higher in most frequencies compared to the Al-Cu-Fe thin film after annealing.

The impedance test results were matched on the electrochemical equivalent circuit of Figure 13 to more accurately determine the electrochemical parameters. The equivalent circuit shown in Figure 13 has three resistances (from the left, solution, coating, and charge transfer resistance) and two fixed phase elements (related to coating and double layer). This equivalent circuit is used when there is a coating on the surface, but the electrolyte has passed through the coating and reached the metal surface. Therefore there are two contact points between the electrolyte and the sample, including one between the electrolyte and the coating and another between the electrolyte and the metal surface. Therefore, the equivalent circuit of two-time constants is used. Ti-6Al-4V alloy (substrate) and Al-Cu-Fe thin film after annealing show an acceptable match with this equivalent circuit.

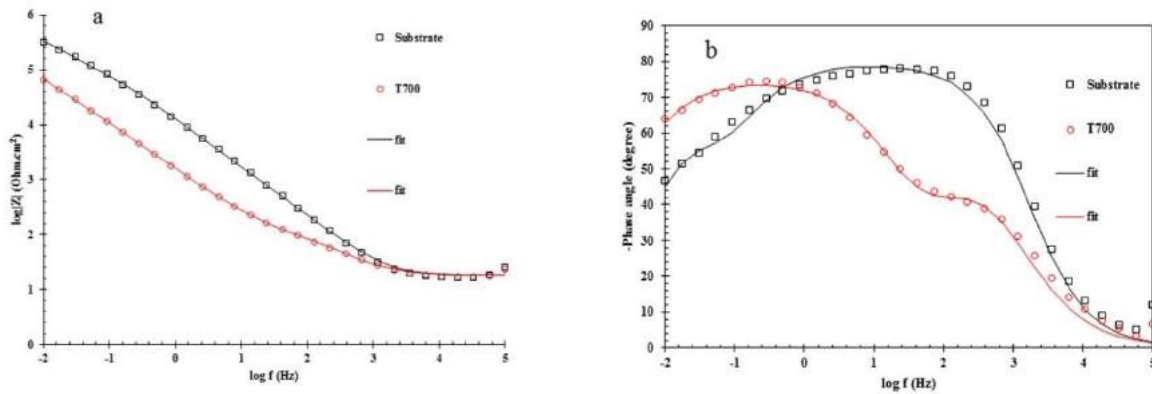


Figure 12. (a), Bode modulus diagrams (b), and Bode phase angle plots in 3.5% NaCl solution at 25 °C for the selected samples in the form of Ti-6Al-4V alloy (substrate) and Al-Cu-Fe thin film after annealing (points are test results and the lines are the results of the fit)

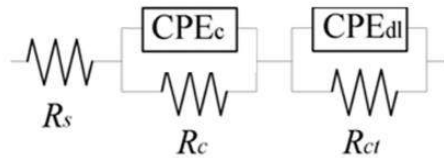


Figure 13. Electrochemical equivalent circuit of two-time constants used to model the results of the electrochemical impedance test

As can be seen, the modeling could match the Nyquist and Bud diagrams well, indicating the modeling results' reliability. The parameter values obtained from this modeling are reported in Table 2. According to Table 2, the substrate sample has a much higher total resistance than the substrate; thus, from the results of the electrochemical impedance test, it can be concluded that the substrate sample (Ti6Al4V alloy) was the optimal sample with the highest corrosion resistance value. It is

TABLE 2. Estimated values of the equivalent electric circuits of the Ti-6Al-4V alloy (substrate) and Al-Cu-Fe thin film after)

Sample	R_s (ohm.cm ²)	$Y0_c$ (S.sec ⁿ .cm ⁻²)	n_1	R_c (ohm.cm ²)	$Y0_{dl}$ (S.s ⁿ .cm ⁻²)	n_2	R_{ct} (ohm.cm ²)	R_t (ohm.cm ²)
Substrate	18.00	3.15E ⁻⁰⁵	0.89	6.01E ⁵	2.86E ⁻⁰⁵	0.88	5.43E ⁺⁰⁴	6.55E ⁺⁰⁵
T700	17.96	8.74E ⁻⁰⁵	0.78	70.3	1.36E ⁻⁰⁴	0.83	3.13E ⁺⁰⁵	3.13E ⁺⁰⁵

suggested to use higher annealing temperatures to achieve a quasi-crystalline structure with higher corrosion properties. Adding a fourth element such as chromium to the target is also suggested to attain the extraordinary corrosion properties of the quasi-crystalline coating. The polarization curves of the annealed coating and the substrate are shown in Figure 14. Data related to the current density and corrosion potential of the annealed coating and the substrate are reported in Table 3. Based on the polarization test results the annealed coating at 700°C showed a nobler behavior than the substrate (Ti-6Al-4V alloy). The data resulting from the calculations resulting from fitting the tangent to the cathodic and anodic branches are also positive (Table 3). Also, the coating annealed at 700 has become nobler by about 300 mV compared to the substrate, but its exchange current density remains almost close to the substrate. In a similar study evaluation of corrosion resistance of Bi-layered plasma-sprayed coating on

titanium implants was investigated [39].

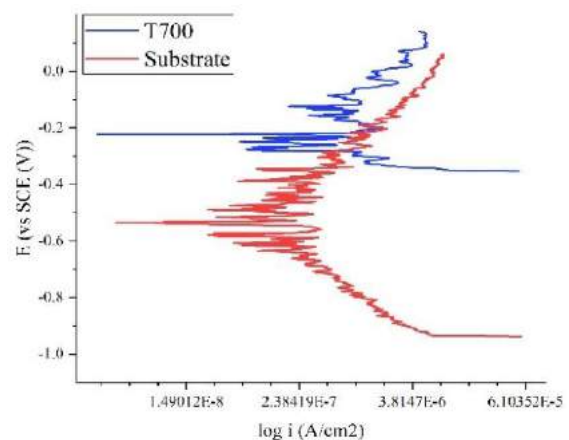


Figure 14. Polarization curves of annealed coating and substrate

TABLE 3. Current density and corrosion potential of annealed coating and substrate

Sample	E corr (mV)	i corr (A/cm ²)
Substrate	-0.54	1.31*10 ⁻⁷
T700	-.022	1.25*10 ⁻⁷

4. CONCLUSION

The following conclusions are summarized below:

- 1) After 3 h of mixing, the primary aluminum, copper, and iron powders were well mixed, and the mixed powders with Al_{62.5}Cu₂₅Fe_{12.5} composition were prepared for the target of the magnetic sputtering process.
- 2) A thin layer of AlCuFe alloy free from cracks and discontinuities was coated on the Ti-6Al-4V substrate with an approximate thickness of 800 nm.
- 3) According to the distribution map of the AlCuFe coating elements applied on the Ti-6Al-4V alloy substrate, aluminum, copper, and iron elements' uniform distribution on the coating surface indicates post-annealing coating stability. There were no cracks, separations, or heterogeneous distribution in the map of the coating elements and surface morphology distribution.
- 4) XRD patterns related to the annealed powders and coating after heat treatment indicate the presence of Cu₃Al, AlFe₃, and quasi-crystalline ternary phases of Al₆₅Cu₂₀Fe₁₅ and Al₃Fe, AlTi₂, and Al₆₅Cu₂₀Fe₁₅ phases, respectively
- 5) Based on the polarization test results, the annealed coating at 700°C showed a better electrochemical behavior than the substrate (Ti-6Al-4V alloy).

5. REFERENCES

1. Gupta, M. K., Etri, H.E., Korkmaz, M.E., Ross, N.S., Krolczyk, G.M., Gawlik, J., Yaşar, N., and Pimenov, D.Y. "Tribological and surface morphological characteristics of titanium alloys: a review", *Archives of Civil and Mechanical Engineering*, Vol. 22, No. 72, (2022), doi:10.1007/s43452-022-00392-x.
2. Fatoba, O., Akinlabi, S., Akinlabi, E. and Gharehbaghi, R., "Microstructural analysis, micro-hardness and wear resistance properties of quasicrystalline Al-Cu-Fe coatings on Ti-6Al-4V alloy", *Materials Research Express*, Vol. 5, No. 6, (2018), 066538. doi: 10.1088/2053-1591/aaca70.
3. Litynska-Dobrzyńska, L., Stan-Glowinska, K., Wójcik, A., Duraczyńska, D., and Serwicka, E.M., "Microstructure and catalytic activity of melt-spun Al-Cu-Fe ribbons", *Materials Science Forum*, Vol. 985, (2020), 109-114. 10.4028/www.scientific.net/MSF.985.109.
4. Mishra, S., Yadav, T., Singh, S., Singh, A., Shaz, M., Mukhopadhyay, N., and Srivastava, O.N., "Evolution of porous structure on Al-Cu-Fe quasicrystalline alloy surface and its catalytic activities", *Journal of Alloys and Compounds*, Vol. 834, (2020), 155-162. https://doi.org/10.1016/j.jallcom.2020.155162.
5. Parsamehr, H., Chen, T.-S., Wang, D.-S., Leu, M.-S., Han, I., Xi, Z., Tsai, A.-P., Shahani, A.J. and Lai, C.-H., "Thermal spray coating of Al-Cu-Fe quasicrystals: Dynamic observations and surface properties", *Materialia*, Vol. 8, (2019), 100432. doi: 10.1016/j.mta.2019.100432.
6. Mora, J., García, P., Muelas, R. and Agüero, A., "Hard quasicrystalline coatings deposited by HVOF thermal spray to reduce ice accretion in aero-structures components", *Coatings*, Vol. 10, No. 3, (2020), 290. doi: https://doi.org/10.3390/coatings10030290.
7. Shaïtura, D. and Enaleeva, A.J., "Fabrication of quasicrystalline coatings: A review", *Crystallography Reports*, Vol. 52, No. 6, (2007). doi: https://doi.org/10.1134/S1063774507060041.
8. Widjaja, E.J., and Marks, L.J., "In situ studies of magnetron sputtered Al-Cu-Fe-Cr quasicrystalline thin films", *Thin Solid Films*, Vol. 420, (2002), 295-299. https://doi.org/10.1016/S0040-6090(02)00809-X.
9. Parsamehr, H., Lu, Y.-J., Lin, T.-Y., Tsai, A.-P. and Lai, C.H., "In-situ observation of local atomic structure of Al-Cu-Fe quasicrystal formation", *Scientific Reports*, Vol. 9, No. 1, (2019), 1245. doi: https://doi.org/10.1038/s41598-018-37644-x.
10. Parsamehr, H., Yang, C.-L., Liu, W.-T., Chen, S.-W., Chang, S.-Y., Chen, L.-J., Tsai, A.P. and Lai, C.-H., "Direct observation of growth and stability of Al-Cu-Fe quasicrystal thin films", *Acta Materialia*, Vol. 174, (2019), 1-8. https://doi.org/10.1016/j.actamat.2019.05.024.
11. Parsamehr, H., Chang, S.Y., and Lai, C.H., "Mechanical and surface properties of aluminum-copper-iron quasicrystal thin films", *Journal of Alloys and Compounds*, Vol. 732, (2018), 952-957. https://doi.org/10.1016/j.jallcom.2017.10.229.
12. Widjaja, E.J and Marks, L.D, "Microstructural evolution in Al-Cu-Fe quasicrystalline thin films", *Thin Solid Films*, Vol. 441, No. 1-2, (2003), 63-71. https://doi.org/10.1016/S0040-6090(03)00903-9.
13. Olsson, S., Eriksson, F., Birch, J. and Hultman, L., "Formation of α -approximant and quasicrystalline Al-Cu-Fe thin films", *Thin Solid Films*, Vol. 526, (2012), 74-80. doi: https://doi.org/10.1016/j.tsf.2012.11.009.
14. Ryabtsev, S., Polonskyi, V. and Sukhova, O.V., "Structure and corrosion of quasicrystalline cast alloys and Al-Cu-Fe film coatings", *Materials Science*, Vol. 56, No. 2, (2020), 263-272. doi: 10.1007/s11003-020-00428-8.
15. Haidara, F., Duployer, B., Mangelinck, D., and Record, M.C., "In-situ investigation of the icosahedral Al-Cu-Fe phase formation in thin films", *Journal of Alloys and Compounds*, Vol. 534, (2012), 47-51. doi: https://doi.org/10.1016/j.jallcom.2012.04.036.
16. Lee, K., Chen, Y., Dai, W., Naugle, D., and Liang, H., "Design of quasicrystal alloys with favorable tribological performance given microstructure and mechanical properties", *Materials and Design*, Vol. 193, (2020), 108735. https://doi.org/10.1016/j.matdes.2020.108735.
17. Wolf, W., Kube, S.A., Sohn, S., Xie, Y., Cha, J.J., Scanley, B.E., Kiminami, C.S., Bolfarini, C., Botta, W.J. and Schroers, J., "Formation and stability of complex metallic phases including quasicrystals explored through combinatorial methods", *Scientific Reports*, Vol. 9, No. 1, (2019), 1-11. https://doi.org/10.1038/s41598-019-43666-w.
18. Jamshidi Rodbari, R. and Agostinho Jamshi, L.C.L., "Evolution of the phases of quasicrystalline alloys icosahedral/decagonal Al_{62.2}Cu_{12.5}Fe_{12.5}/Al₆₅Ni₁₅Co₂₀ and oxidative behavior", *Journal of the Chilean Chemical*

- Society*, Vol. 63, No. 2, (2018), 3928–3933. doi: 10.4067/s0717-97072018000203928.
19. Babilas, R., Bajorek, A., Spilka, M., Radoń, A., and Łoński, W., "Structure and corrosion resistance of Al–Cu–Fe alloys", *Progress in Natural Science: Materials International*, Vol. 30, No. 3, (2020), 393–401. doi: <https://doi.org/10.1016/j.pnsc.2020.06.002>.
 20. Sukhova, O., and Polonsky, V., "Peculiarities in structure formation and corrosion of cast quasicrystalline Al₆₃Cu₂₅Fe₁₂ and Al₆₃Co₂₄Cu₁₃ alloys in sodium chloride aqueous solution", *Physics and Chemistry of Solid State*, Vol. 21, No. 3, (2020), 530–536. doi: <https://doi.org/10.15330/pcss.21.3.530-536>.
 21. Ryabtsev, S.I, Sukhova, O.V, and Polonsky, V.A., "Structure and corrosion in NaCl solution of quasicrystalline Al–Cu–Fe cast alloys and thin films", *Journal of Physics and Electronics*, Vol. 27, No. 1, (2019), 27–30. doi: 10.15421/331904.
 22. Liu, S., and Shin, Y.C., "Additive manufacturing of Ti6Al4V alloy: A review", *Materials and Design*, Vol. 164, (2019), 107552. <https://doi.org/10.1016/j.matdes.2018.107552>.
 23. Fatoba, O., Lasisi, A., Ikumapayi, O., Akinlabi, S. and Akinlabi, E., "Icosahedral structure influence on the microstructural and mechanical properties of laser additive manufactured (LAM) titanium alloy grade 5", *Materials Today: Proceedings*, Vol. 44, (2021), 1263–1270. doi:10.1016/j.matpr.2020.11.263.
 24. Shukla, A.K., Ledieu, J., Gaudry, E., Wu, D.M., Lograsso, T.A., and Fournée, V., "Quantum size effects in Ag thin films grown on the fivefold surface of the icosahedral Al–Cu–Fe quasicrystal: Influence of the growth temperature", *Journal of Vacuum Science and Technology A*, Vol. 40, (2022), 013212. Doi: <https://doi.org/10.1116/6.0001450>.
 25. Singha, A., Hiroto, T., Odea, M., Takakurac, H., Tesar, K., Somekawaa, H., and Hara, T., "Precipitation of stable icosahedral quasicrystal phase in a Mg–Zn–Al alloy", *Acta Materialia*, Vol. 225, (2022), 117563. <https://doi.org/10.1016/j.actamat.2021.117563>.
 26. Gashti, M., Mehdiavaz Aghdam, R., Motallebzadeh, A., Gharibi Asl, F., Soltani, R., Ashraf, A., Balaei, H., and Razazzadeh, A., "Bio-Corrosion, Mechanical and Microstructural Properties of TiTaMoVZr High-Entropy Alloy Film on Ti–6Al–4V Substrate", *Metals and Materials International*, (2022), <https://doi.org/10.1007/s12540-023-01464-0>.
 27. Phan, N.H., Donga, P.V., Muthuramalingam, T., Thiena, N.V., Dunga, H.T., Hunga, T.Q., Duca, N.V., and Lya, N.T., "Experimental Investigation of Uncoated Electrode and PVD AlCrNi Coating on Surface Roughness in Electrical Discharge Machining of Ti-6Al-4V", *International Journal of Engineering, Transactions A: Basics*, Vol. 34, No. 04, (2021), 928–934. Doi: 10.5829/ije.2021.34.04a.19.
 28. Rahmouni, K., Besnard, A., Oulmi, K., Nouveau, C., Hidoussi, A., Aissani, L., and Zaabat, M., "In vitro corrosion response of CoCrMo and Ti-6Al-4V orthopedic implants with Zr columnar thin films", *Surface and Coatings Technology*, Vol. 436, (2022), 128310. <https://doi.org/10.1016/j.surfcoat.2022.128310>.
 29. Tsai, S.Y., Chen, Y.A., You, J.D., Chu, J.P., and You, P., "Micro-scale tribological study of a Ni–Cr–Fe–Ti–Al–V high entropy alloy thin film by magnetron co-sputtering of Inconel-718 and Ti-6Al-4V", *Surface and Coatings Technology*, Vol. 464, (2023), 129481. <https://doi.org/10.1016/j.surfcoat.2023.129481>.
 30. Nikraves, M., Akbaria, G.H., and Poladi, A., Mechanical Properties and Microstructural Evolution of Ta/TaNx Double Layer Thin Films Deposited by Magnetron Sputtering, *International Journal of Engineering, Transactions B: Applications*, Vol. 30, No. 2, (2017) 288–293. doi: 10.5829/idosi.ije.2017.30.02b.16
 31. Zhu, L., Soto-Medina, S., Cuadrado-Castillo, W., Hennig, R.G., and Manuel, M.V., "New experimental studies on the phase diagram of the Al–Cu–Fe quasicrystal-forming system", *Materials and Design*, Vol. 185, (2020), 108186. doi: <https://doi.org/10.1016/j.matdes.2019.108186>.
 32. Huttunen-Saarivirta, E.J., "Microstructure, fabrication, and properties of quasicrystalline Al–Cu–Fe alloys: A review", *Journal of Alloys and Compounds*, Vol. 363, No. 1–2, (2004), 154–178. [https://doi.org/10.1016/S0925-8388\(03\)00445-6](https://doi.org/10.1016/S0925-8388(03)00445-6).
 33. Ryabtsev, S. and Sukhova, O., "Ion-plasma deposition of thin quasicrystalline Al–Cu–Fe and Al–Cu–Co films", *Problems of Atomic Science and Technology*, Vol. 126, No. 2, (2020), 126–145. doi: 10.46813/2020-126-145.
 34. Ryabtsev, S., Polonsky, V., and Sukhova, O., "Effect of scandium on the structure and corrosion properties of vapor-deposited nanostructured quasicrystalline Al–Cu–Fe films", *Powder Metallurgy and Metal Ceramics*, Vol. 58, No. 9–10, (2020), 567–575. doi: 10.1007/s11106-020-00111-2
 35. Kameoka, S., Tanabe, T., Satoh, F., Terauchi, M., and Tsai, A.P., "Activation of Al–Cu–Fe quasicrystalline surface: Fabrication of a fine nanocomposite layer with high catalytic performance", *Science and Technology of Advanced Materials*, Vol. 15, No. 1, (2014). doi: 10.1088/1468-6996/15/1/014801.
 36. Polishchuk, S., Ustinov, A., Telychko, V., Merstallinger, A., Mozdzen, G., and Melnichenko, T., "Fabrication of thick, crack-free quasicrystalline Al–Cu–Fe coatings by electron-beam deposition", *Surface and Coatings Technology*, Vol. 291, (2016), 406–412. doi: 10.1016/j.surfcoat.2016.03.002.
 37. Wang, X., Guan, R., Misra, R., Wang, Y., Li, H., Shang, Y., "The mechanistic contribution of nanosized Al₃Fe phase on the mechanical properties of Al–Fe alloy", *Surface and Coatings Technology*, Vol. 724, (2018), 452–460. doi: 10.1016/j.msea.2018.04.002.
 38. Mahdavian, M. and Attar, M., "Another approach in the analysis of paint coatings with eis measurement: Phase angle at high frequencies", *Corrosion Science*, Vol. 48, No. 12, (2006), 4152–4157. <https://doi.org/10.1016/j.corsci.2006.03.012>.
 39. Ebrahimi, N., Sedaghat Ahangari Hosseinzadeh, A., Vaezi, M., and Mozafari, M., "Evaluation of Corrosion Resistance of Bi-layered Plasma-sprayed Coating on Titanium Implants", *International Journal of Engineering, Transactions A: Basics*, Vol. 35, No. 04, (2022) 635–643. doi: 10.5829/ije.2022.35.04A.03.

COPYRIGHTS

©2023 The author(s). This is an open access article distributed under the terms of the Creative Commons Attribution (CC BY 4.0), which permits unrestricted use, distribution, and reproduction in any medium, as long as the original authors and source are cited. No permission is required from the authors or the publishers.

**Persian Abstract****چکیده**

آلیاژ Ti-6Al-4V اغلب در صنایع هوافضا، دریایی و خودرویی کاربرد دارد. علیرغم خواص عالی آلیاژ Ti-6Al-4V، حساسیت بالا به خوردگی، پایداری حرارتی ضعیف و خواص تریبولوژیکی ضعیف کاربردهای آنها را محدود کرده است. در این تحقیق، ابتدا مخلوط پودری $Al_{62.5}Cu_{25}Fe_{12.5}$ آماده سازی گردید که این ترکیب در محدوده تشکیل فازهای شبه بلوری است. فیلم نازک Al-Cu-Fe با روش کندوپاش مگنترون بر روی زیرلایه Ti-6Al-4V با ضخامت ۸۰۰ نانومتر رسوب داده شد. لایه های نازک Al-Cu-Fe و ترکیب پودری در دمای ۷۰۰ درجه سانتیگراد به مدت ۲ ساعت آنیل شدند. تجزیه و تحلیل ریزساختار و مورفولوژی ترکیب پودری و پوشش های شبه کریستالی Al-Cu-Fe ایجاد شده بر روی آلیاژ Ti-6Al-4V با استفاده از آنالیز میکروسکوپ الکترونی روبشی (SEM) و تست XRD مورد بررسی قرار گرفت. اندازه گیری های الکتروشیمیایی در محلول ۳/۵ درصد NaCl انجام شد. نتایج نشان داد که لایه نازک آلیاژ Al-Cu-Fe بدون هیچ ترک بر روی سطح آلیاژ Ti-6Al-4V رسوب کرده است. الگوهای XRD مربوط به پودرهای آنیل شده نشان دهنده حضور فازهای $AlFe_3$ ، Cu_3Al و فاز شبه بلوری $Al_{65}Cu_{20}Fe_{15}$ است. الگوهای XRD پوشش پس از عملیات حرارتی نشان دهنده حضور فازهای $AlTi_2$ ، Al_3Fe و فاز شبه بلوری $Al_{65}Cu_{20}Fe_{15}$ است که این فاز شبه بلوری در پودرهای آنیل شده نیز مشاهده گردید. بر اساس نتایج تست پلاریزاسیون، پوشش آنیل شده در دمای ۷۰۰ درجه سانتیگراد رفتار نجیب تری نسبت به زیرلایه (آلیاژ Ti-6Al-4V) نشان داد.



A New Approach for Seismic Damage Detection Based on Results of Pushover Analysis and Modal Based Damage Index

M. Mazloom^{*a}, N. Fallah^b

^a Department of Civil Engineering, University of Guilan, Rasht, Iran

^b Faculty of Civil Engineering, Babol Noshirvani University of Technology, Babol, Iran

PAPER INFO

Paper history:

Received 15 June 2023

Received in revised form 13 July 2023

Accepted 17 July 2023

Keywords:

Damage Detection

Stiffness Variation Index

Pushover Analysis

Modal Curvature

Beam

ABSTRACT

The diagnosis of the location of structural damage and its extent after an earthquake using numerical methods is one of the ongoing research topics. After the occurrence of damage in a structure and a reduction in its stiffness, the dynamic characteristics of the structure change, and therefore, assessing the changes in its dynamic characteristics can be used as an indicator for detecting damage. In this article, an advanced technique called Direct Stiffness Calculation (DSC) and a new damage index based on flexural stiffness variations (SVI) are utilized for damage detection in structures. Initially, the proposed technique is examined on a steel beam with known specifications. Then, a reinforced concrete moment frame is modeled, and after extracting its dynamic characteristics, it is subjected to a pushover analysis to create a damage scenario without direct intervention. Based on the analysis results, the plastic hinge formation location at both ends of the beam is selected as the probable location of damage in the floor. By using the modal information of the damaged structure and calculating the SVI in the beams of the floors, it is determined that this index can accurately and significantly distinguish the location of damage only by knowing the first mode of the structure and with sufficient magnification compared to other points. Furthermore, the results demonstrate that with this method, it is possible to accurately determine the location of damage even without knowing the dynamic characteristics of the intact structure and solely with the information of the damaged structure.

doi: 10.5829/ije.2023.36.10a.14

1. INTRODUCTION

With the occurrence of an earthquake and damage to concrete structures, the members of these structures will be gradually damaged and will experience different levels of damage, including cracking, yielding and finally collapse. Therefore, information about the properties of the damage, i.e. determining the location and estimating its amount, is considered as an important issue that will be effective in the decision-making process regarding the repair and strengthening of the damaged structure. Structural damage causes changes in its physical properties, i.e. stiffness and damping of the structure, and these changes will ultimately affect the dynamic response of the structure and cause changes in its vibration characteristics [1]. A damage detection method should be able to detect damage in its early stages, determine its

location, and provide an estimate of damage severity [1]. Extensive research has been done on the development of non-destructive damage assessment methods based on changes in the vibration characteristics of the damaged structure, and among the vibration-based methods, modal damage detection methods have received more attention. The primary research that has been done on modal information is generally about damage indexes, which are based on the comparison of changes in natural frequencies [2], the modal assurance criterion (MAC) [3] and the coordinate modal assurance criterion (COMAC) [4] as well as the multiple damage location assurance criterion (MDLAC) [5] were formulated between two states of intact and damaged structures. Achenbach [6], Hongnan and Tinghua [7]. provided a comprehensive review of the history of damage detection methods in linear structures. Hearn and Testa [8]

*Corresponding Author Email: Meisam.Mazloom@yahoo.com
(M. Mazloom)

suggested that changes in frequency ratios can be indicators of different levels of damage. Although the change in frequency may be a structural damage index, it is difficult to estimate the location of damage with this method. Also, the results of the studies showed that the changes in the natural frequency, as well as the comparison of the mode shape vectors of a structure in a healthy and damaged state, were not able to significantly highlight the damage location. Compared to the modal displacement vector, its derivatives, such as the mode shape curvature, are more sensitive to the existence of damages even in small amounts. Therefore, they can be used to detect damage [9, 10]. The issue of damage detection on beam structures has been carried out with the help of the mode shape curvature method and it was concluded that this method is very successful for detecting and locating damage in beams with different support conditions [11]. Also, this method was studied on a concrete bridge model located in Switzerland in the presence of several damage scenarios. It was concluded that modal curves are very sensitive to damage to bridges .

Foti [12] conducted two investigations on the finite element model of a simple span bridge with the help of techniques for changes in mode shapes and curvature of mode shapes. The damage was introduced as a reduction in bending stiffness. The results showed that the change in modal curvature is a suitable and usable index, while the MAC and COMAC indices did not show very good results. Dutta and Talukdar [13] investigated on changes in natural frequencies, mode shape, and mode shape curvature for a bridge that included several damaged sections at different points. In their article, the authors defined the damage factor based on the curvature to detect the damage. They showed that instead of using the mode vector itself, the damage location is better estimated by using the curvature of the mode shape. It was also shown that a sufficient number of mode shapes should be considered to detect the location of damage in the case of multiple damages in several positions. A detailed study was conducted by Whalen [14], to evaluate the changes in the mode shape and its four primary derivatives to identify the damage, and it clearly showed that the changes in the higher order derivatives of the mode shape are much more sensitive to damage .

Fayyadh and Razak [15] investigated the issue of crack location in a concrete beam by studying two damage indexes, one based on the curvature of the mode shape vector and the other based on the calculation of the fourth derivative of the mode shape vector. In this article, in addition to comparing the performance of the indicators, they provided suggestions to improve the performance of the used indicators. In the work of Maeck [16] in 1999, the method of direct stiffness calculation was introduced to locate and quantify damage on a simple beam. In this method, by using the basic relationships of material resistance, by dividing the amount of modal

moment by the curvature of the beam, the amount of bending stiffness is obtained at each section, and then the location and amount of damage in the beam will be obtained with the help of this index [16]. Patel and Dewangan [17] presented a baseline-free method using roving mode shape response based, multiple damage localization in a cantilever beam. They considered the combined mass and stiffness damage, as well as only the mass change damage. From the results, it was found that the proposed method can reliably identify the damage and its position [17]. Ghasemi et al. [18] evaluated the location and severity of the damage combining two being-updated parameters of the flexibility matrix and the static strain energy of the structure using optimization technics and compared results.

A major challenge for civil engineers is to evaluate the amount of structural damage caused by moderate to severe earthquakes. Seismic damage estimation is an important task in the field of structural health monitoring and several methods to evaluate the seismic vulnerability of structures have been proposed in recent years. One method, the response-based damage index, has been critically evaluated for its applicability to seismic damage evaluation. This method uses parameters, such as stiffness, drift, rotation of an element and energy, to calculate the state of damage using mathematical functions [19]. There has been a lot of research on this method. Ozturk et al. [20] evaluated the use of dynamic analysis and fragility curves, precast industrial concrete buildings that were designed and built according to the building codes of Turkey. In another paper, based on the suggested method of damage assessment using the vulnerability index, they examined the damage in a school building. With the help of the results of this research, it is possible to provide a proper assessment of the structural damage without the need for expert observations [21]. Also, in another study, this new method was used for the seismic vulnerability assessment of two reference RC structures in Malaysia. The authors presented that the results of this damage index can be used as a guide for earthquake impact assessments in Malaysia and other countries [22]. Hait et al. [23] presented a new damage index based on a combination of different structural response criteria which provided accurate results compared to the Park&Ang damage index. Mazloom and Fallah [24] introduced a new Stiffness Based Damage Index based on the pushover analysis output. By using this index that only uses the information of the capacity curve of the structure, the amount of damage to the whole structure can be properly estimated by performing a series of simple calculations. The evaluation of the effect of ductile details in reinforced concrete structures was investigated in another study. In this research, two ductile and non-ductile frames were modeled and using the results of pushover analysis, the effect of using ductile details on the performance of the models was investigated by Chiluka

and Ogu [25].

The subject of seismic damage detection and the use of damage detection methods based on modal information in this regard, we do not have much research history. However, this issue has been pursued in some limited works. For example, in 2016, Yang et al. [26] investigated the seismic damage to reinforced concrete structures numerically and experimentally in an article using the direct stiffness calculation method. In this work, the reinforced concrete structure was subjected to earthquake records, and then based on the changes in dynamic parameters, the amount of damage in different nodes of the structure was determined. Samimifar and Massumi [27] evaluated the modal-based story damage index performance based on an analytical study on seismic responses of some RC frames subjected to a set of earthquake records. The results of the analysis were compared with Park-Ang and modal flexibility story damage indices. Also, Mazloom and Fallah [28] investigated the total damage and story-based damage of the numerical RC frame models, based on the results of the Pushover analysis, and finally developed a new story-based damage index.

Because there are few previous works regarding the use of this method in determining the location of structural damage in possible earthquake damage scenarios, in this research work, at first, a numerical model of a steel beam, which was previously investigated by other researchers, was built and with the direct stiffness calculation method, the location and amount of damage in different damage scenarios were examined. Then, a 4-story reinforced concrete frame was modeled with specific geometric details and mechanical specifications, and after performing the eigenvalue analysis and receiving the modal information of this undamaged structure, the Pushover analysis was performed on it to determine the damage scenarios based on the occurrence of yielding in the story beams. By receiving the output of the analysis, several damage scenarios were defined based on the occurrence of yielding in the beams, and the modal information of the damaged structure was extracted in these scenarios. Finally, by using the method of direct calculation of bending stiffness, the damage is located on the beam with appropriate accuracy compared to other points. The results showed that this method can identify the location of the damage properly and with appropriate accuracy in the story beams, by only having information about the first mode of the structure.

2. SVI INDEX BASED ON IMPROVED DIRECT STIFFNESS CALCULATION METHOD

For a Bernoulli-Euler beam with the shear deformation neglected, the bending stiffness EI can be expressed in the modal sense as follows [1]:

$$EI = \frac{M}{\frac{d^2\varphi}{dx^2}} = \frac{M}{k} \tag{1}$$

In this regard, M and k are respectively the modal moment and the modal curvature at the same cross-section and φ is the mode shape function. According to Yang et al. [1], Equation (1) is valid for structures for which the deformation of each mode is considered small. Another assumption is that after damage occurs, the mass of the structure will remain unchanged and only the stiffness of the structure will decrease. The free vibration equation of a structure with mass M_0 and stiffness K_0 will be written as Equation (2):

$$M_0\ddot{U} + K_0U = 0 \tag{2}$$

Assuming that the modal deformations are harmonic, the above equation can be rewritten in the form of Equation (3):

$$K_0\varphi_i = \omega_i^2 M_0\varphi_i \tag{3}$$

where ω_i and φ_i are the i th frequency and corresponding mode shape respectively. Let x_i and x_{i+1} denote two adjacent measurement sections of the beam, the bending moment M_{i+1} and shear force V_{i+1} at section x_{i+1} of the m th mode can be calculated (Figure 1):

$$M_{i+1} = \int_{x_i}^{x_{i+1}} \omega_m^2 \rho A \varphi_m(x) (x_{i+1} - x) dx + V_i (x_{i+1} - x) \tag{4}$$

$$V_{i+1} = V_i - \int_{x_i}^{x_{i+1}} \omega_m^2 \rho A \varphi_m(x) dx \tag{5}$$

Modal Curvature, k , is directly calculated from the measured Modal shapes using the central difference approximation as follows:

$$k_m = \frac{\varphi_m(i+1) - 2\varphi_m(i) + \varphi_m(i-1)}{(VI)^2} \tag{6}$$

Consequently, a damage index called the stiffness variation index (SVI) was introduced:

$$SVI = \left| \frac{EI_{damaged} - EI_{intact}}{EI_{intact}} \right| \tag{7}$$

3. RESEARCH METHODOLOGY

3. 1. Description of Study Models To evaluate the damage detection method, first, a simply supported steel

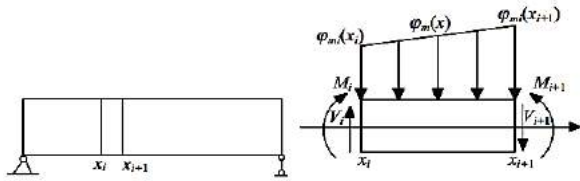


Figure 1. Sign convention of internal forces and modal displacements [1]

beam with known geometric and mechanical characteristics was modeled and then based on different damage scenarios, the value of the SVI index was calculated along the beam and compared with the literature reported data [1]. In the following, to further investigate the accuracy of the method, in an assumed damage scenario, the desired process was applied in a concrete moment frame and in another case, in seismic damage scenarios that were obtained from the results of pushover analysis, the performance of this method was investigated.

3. 2. Simply Supported Steel Beam Model The steel beam was modeled in Sap2000 software with the specifications in the literature reported data [1]. The studied beam with simple supports has a span of 2 meters and a rectangular section of 25 cm in width and 30 cm in height. The numerical model of this structure contains 20 elements (21 nodes) and it was assumed that the nodes are the places where measurement tools are installed (Figure 2). The nodes of the structure from the left support to the right support were numbered from 1 to 21 and between both nodes, a 10 cm long beam element was considered from 1 to 20, respectively. Other mechanical specifications of the desired beam model are shown in Table 1. The distribution of mass and stiffness along the beam is uniform and in all damage scenarios, the mass of the structure will not change after damage.

3. 2. 1. Damage Detection Using Svi Index First, by analyzing the eigenvalues on the intact beam, the

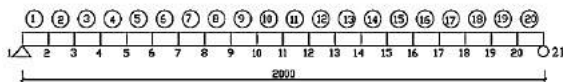


Figure 2. Geometric view of the simply supported beam [1]

TABLE 1. Material specification of the simply supported beam model

Properties	Value
Young's modulus (E)	$2 \times 10^5 \text{ MPa}$
Poisson's ratio	0.3
specific weight	7850 kg/m^3

mode shape displacements were extracted from the finite element model. Because measuring the higher modes of the structure is associated with great difficulty in practice, only the data of the first mode of vibration was used in this research. After receiving the modal shape (MS) of the healthy structure, the modal curvature (MC) was calculated using the central difference method. Also, by calculating the value of the modal moment (MM), the bending stiffness of the EI section was obtained for each element.

In the next step, by changing the modulus of elasticity of the beam, damage scenarios were created in the numerical model. According to literature [1] and Tables 2 and 4 damage scenarios were examined. In the first scenario, only one element (Element 6) was damaged. In the following scenarios, several elements were damaged at the same time. It is also necessary to remember that in all scenarios, for the entire length of the desired element, the stiffness reduction occurred equally.

According to Table 2, in the first damage scenario, only one beam element is damaged. Also, in the second and third, two elements were damaged at two different points of the beam with different severities. In the fourth scenario, damage with the same severity has occurred in three adjacent elements. In each of the damage scenarios, by receiving MS and then calculating MC, MM corresponding to it, EI was finally obtained for all beam elements. Then the SVI index was calculated and its change curve was drawn along the beam. In order to compare the results of the current research, with literature [1], the results of the fourth damage scenario, including the mode shape curve, modal curvature, modal moment and SVI index, in the first mode, were displayed in Figure 3. According to the details of damage scenario 4, only elements numbers 13, 14 and 15 were damaged by 4 different severities.

According to the literature reported data [1], around the damage zones, the value of the modal curvature is significantly increased compared to other points. This sensitivity to the occurrence of damage does not exist in the mode shape vectors. So it can be said that the value

TABLE 2. damage scenarios in the steel beam model

Damage scenarios	Damaged element	Element stiffness reduction(%)			
1	6	10	30	50	70
2	6	10	30	50	70
	13	20	40	70	80
3	13	20	40	60	80
	20	10	30	50	70
4	13	10	30	50	70
	15	10	30	50	70

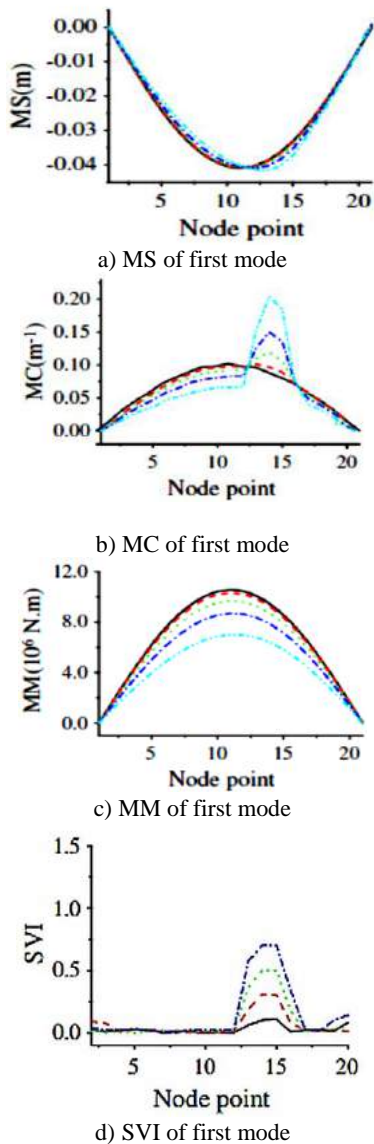


Figure 3. Damage detection results in scenario 4 [1]

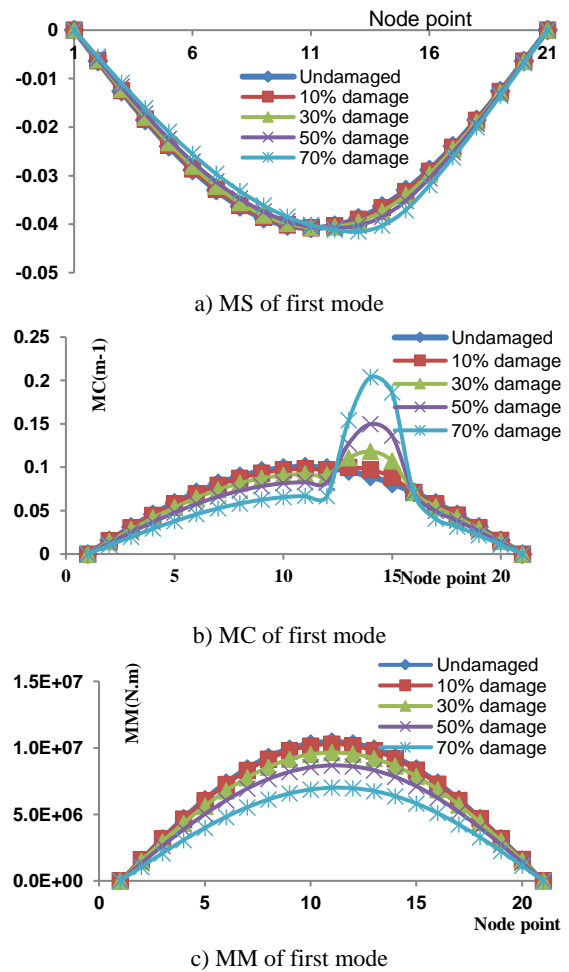
of the SVI index has a strong dependence on the value of modal curvature.

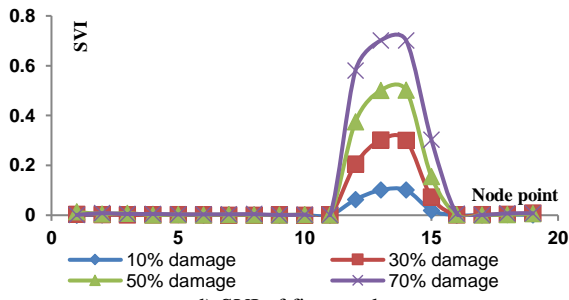
Also, the results showed that in this scenario where adjacent elements are also damaged at the same time, the SVI index was able to identify the amount of damage with high accuracy. Due to the high dependence of the value of this index on the changes of the modal curvature in the damaged position, the value of this index has gradually changed from zero on the damaged elements to the real value on the damaged elements. For example, according to the results of this scenario in Figure 4, at the damage level of 70%, the SVI index started at 0.6 in node 12 and reached 0.7 in nodes 13 to 14, which is the place where elements 12 to 14 are connected. Finally, it continued to reach the value of 0.3 at the 15th node and after that, it reached zero again. Based on the graphs, it

can be said that the SVI index has correctly determined the range of damage and its severity in elements 13 to 15.

The results also showed that in this scenario, the SVI index identifies the real damage location of the beam with a significant magnification without declaring any other point as the possible location of the damage. Other damage scenarios, i.e. scenario 1 (damage in element 6), scenario 2 (damage in elements 6 and 13) and scenario 3 (damage in elements 13 and 20) were also evaluated and the results are shown in Figures 5 to 7. As the results of the first scenario investigation showed, the value of MC as well as the value of the SVI index determined the location of the damaged element with a very appropriate magnification compared to other elements. Although there is a difference between the value of the SVI index and the exact value of the assumed damage, the accuracy of the results seems to be sufficient to identify the damaged element. In this scenario, this index was able to determine the occurrence of damage in the damaged element itself.

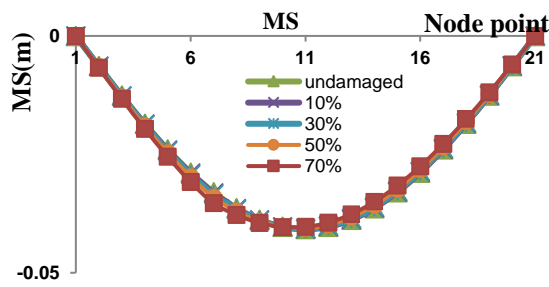
According to Table 2, element 6 is damaged in both the first and second damage scenarios. In the first scenario, this element is the only place where the damage



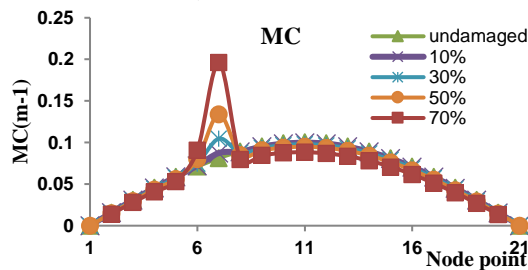


d) SVI of first mode

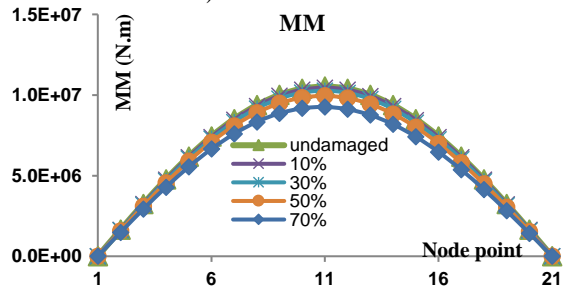
Figure 4. Simulation results of damage detection in scenario 4



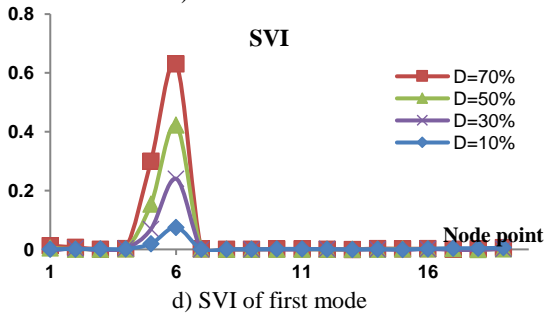
a) MS of first mode



b) MC of first mode

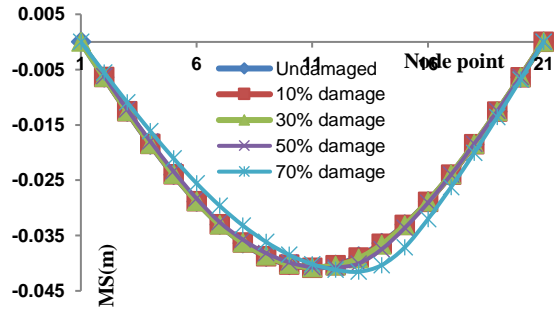


c) MM of first mode

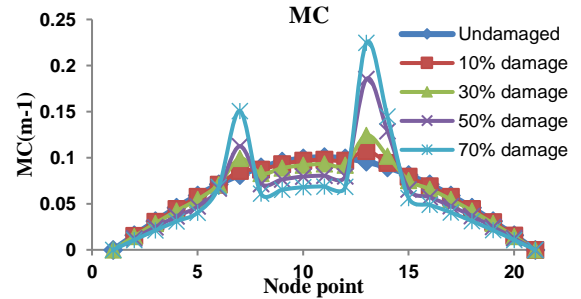


d) SVI of first mode

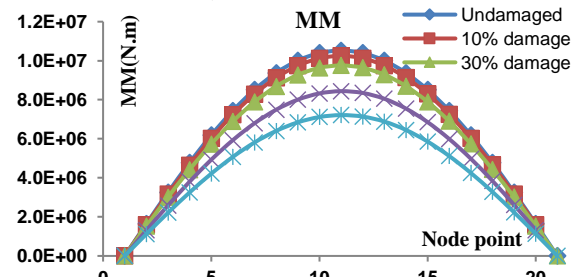
Figure 5. Simulation results of damage detection in scenario 1



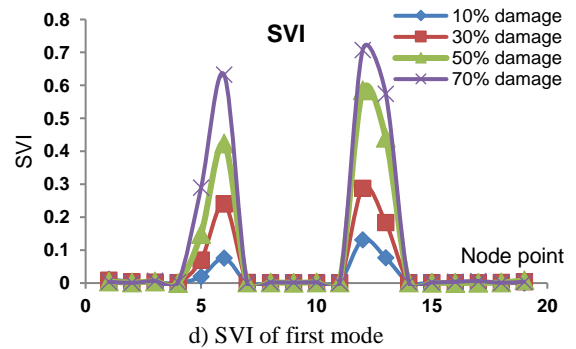
a) MS of first mode



b) MC of first mode



c) MM of first mode



d) SVI of first mode

Figure 6. Simulation results of damage detection in scenario 2

occurs in the beam, and in the second scenario, along with element 13, the damage locations in the beam are considered.

According to Figures 5 and 6, it should also be noted that in the second scenario, similar to the first, the value of the SVI index in element 6, without being affected by simultaneous damage in element 13, is still in the range of 10-70%. Also, no damage has been detected to any other element.

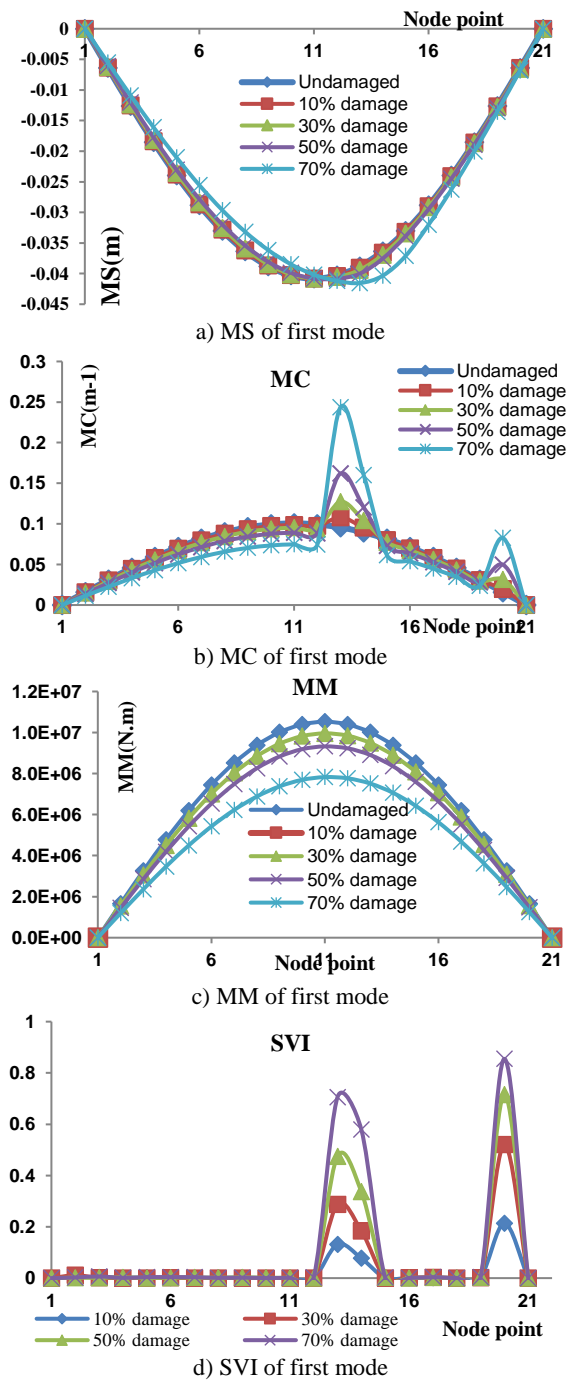


Figure 7. Simulation results of damage detection in scenario 3

Finally, it can be said that the results of the current study are absolutely accurate and reliable compared to previous research [1]. According to the results obtained in different scenarios, the SVI index was able to accurately identify the location and amount of damage in the simply supported steel beam model and distinguish it from the healthy elements with noticeable magnification.

3. 3. A 4story Reinforced Concrete Moment Frame Model

A 4-story concrete frame model was selected based on the specifications reported in the literature [29] and modeled in the SAP2000 program. The number of floors is 4 and the number of frame spans is 3 (Figure 8). The height of all floors is 3 meters, and the length of each span is 5 meters [29]. The concrete used in the model has a compressive strength of 30 MPa, and the steel used has a yield strength of 414 MPa. All columns are fixed at the base. A uniform load of 20 kN/m is placed on the beams of all floors. The geometry of the two-dimensional model along with the beam and column details is shown in Figure 8. Beams and columns were modeled with frame elements with a length of 1 meter, and after eigenvalue analysis of the frame, the mode shape displacement of the beams was measured at half-meter intervals (Figure 9).

In this research, to examine the damage detection method, the first and second modes of vibration of the undamaged structure as well as the damaged structure were considered. The deformed shape of the frame and the corresponding period in different vibration modes are shown in Figure 10. Also, to properly address the beams on all floors, the left, middle, and right beams of each floor were named BL, BM, and BR, respectively (Figure 11).

3. 3. 1. Verification of The Analysis Results

To compare the results of the first three modes of vibration obtained from the eigenvalue analysis on the modeled concrete frame, a comparison was made between the results reported by Ferracuti et al. [29] and the results of the present research (Table 3):

As is clear based on the results, the numerical modeling in the literature and the current work are in very good agreement with each other. Therefore, according to

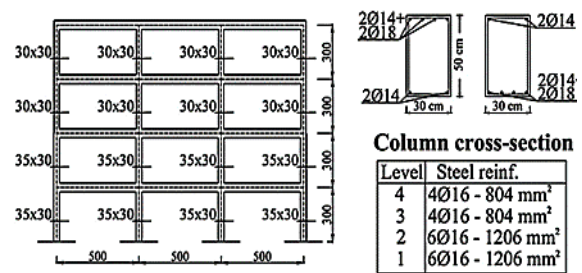


Figure 8. Specifications of the studied concrete frame model [29]

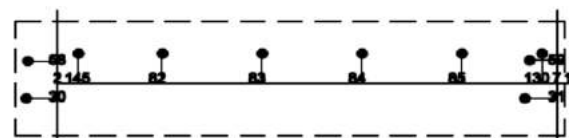


Figure 9. Placement of sensors to measure mode shape displacements

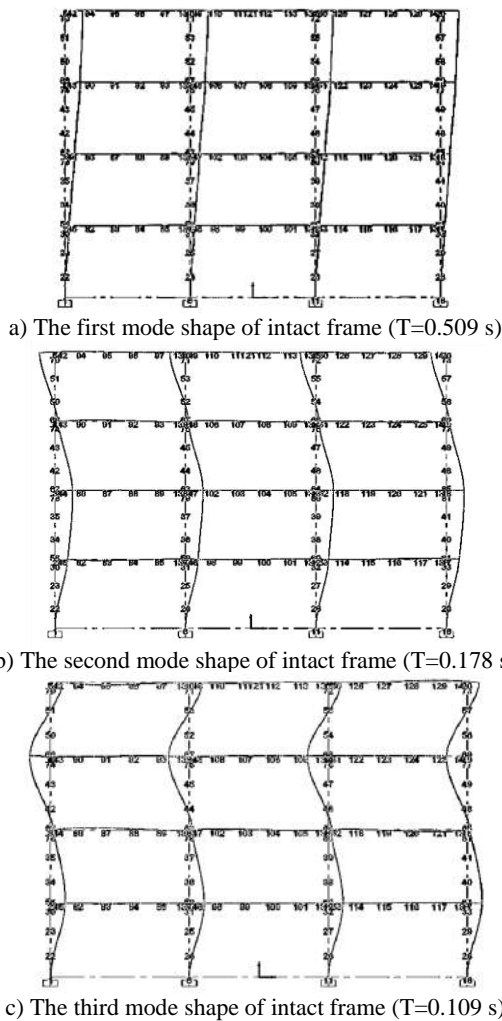


Figure 10. The first three mode shapes of the modeled frame

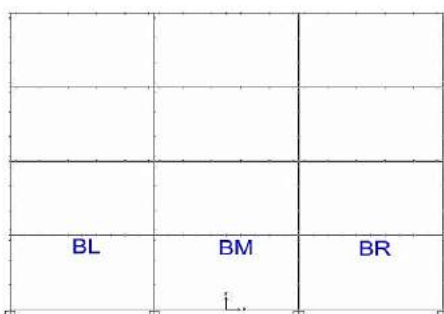


Figure 11. Naming floor beams based on their location

TABLE 3. Comparison between the results of the current study and reported data in literature [29]

Results	Model1	Mode 2	Mode 3
Ref [29]	0.50	0.17	0.11
Current Paper	0.509	0.178	0.109
Difference %	1.8	4.7	0.9

the preliminary appropriate results, damage detection will be done based on two groups of intentional damage scenarios and unintentional damage to the beams.

Damage detection based on the intentional damage scenario, which was also done in the first model of this article, is similar to most past research works. After examining the damage detection method in these scenarios, the results have been discussed. In the following, the possible damage scenarios for the frame during the earthquake will be created by performing the pushover analysis. Finally, the amount of damage and its location will be determined based on the comparison between the modal data of the damaged structure and the undamaged structure.

3.3.2. Damage Detection in Damage Scenarios

3.3.2.1. 20% Damage on The First Story Beam

The damage to the left beam of story 1 (BL) was caused by reducing the moment of inertia of the element one meter to its left by 20% (Figure 12).

The assumed location of the damage was chosen according to the possible response of the frame due to the earthquake and the potential for the formation of plastic hinges in these zones. By creating this intentional damage to the structure, the stiffness of the structure is reduced a bit, which will change the vibration characteristics of the frame. Therefore, the eigenvalue analysis was performed on the damaged frame and the mode shape information of the first two modes was extracted. By obtaining the modal information of the healthy structure and the damaged one, their comparison has been done with a coordinate system according to Figure 13. As the graphs show, the comparison of the shapes of the first and second modes alone is not able to provide clear information about the location of the damage and its amount. Using the central difference method, the modal curvature was calculated for the first two modes, and finally, the value of the bending stiffness EI of the beam was obtained in two states of the healthy and damaged structure, and its results are presented in Figure 14.

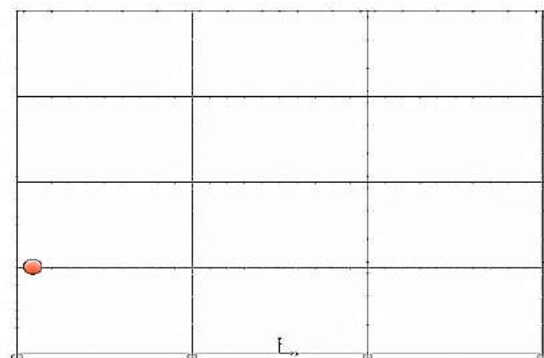


Figure 12. The location of the damaged element in the frame

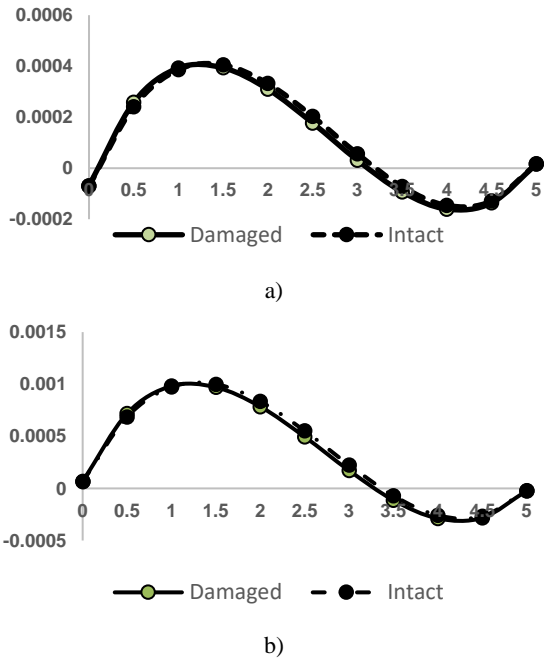


Figure 13. Comparison between the a) first mode shape and b) second mode shape of the beam BL

According to Figure 15, the SVI index was able to determine both the damage location and its amount correctly. This index has reached its highest value at the location of the one-meter element adjacent to the connection to the column, which is the real damage location.

Also, the value of this index in the adjacent node dropped from 0.20 to 0.12 and then completely zero. This issue is due to the dependence of the value of this index on the modal curvature calculated between three adjacent points along the length of the beam. On the other hand, it is clear that there is no difference between the results in the first two modes, and in other words, it can be said that damage detection with this method can only be done by receiving the displacements of the first mode of the structure.

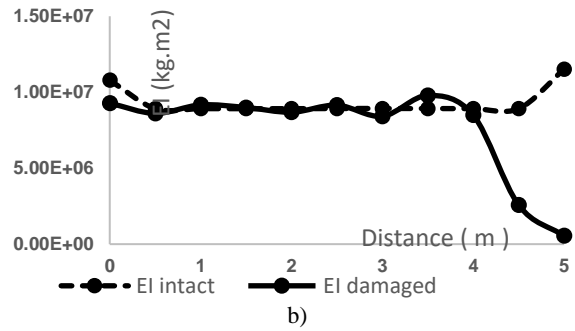
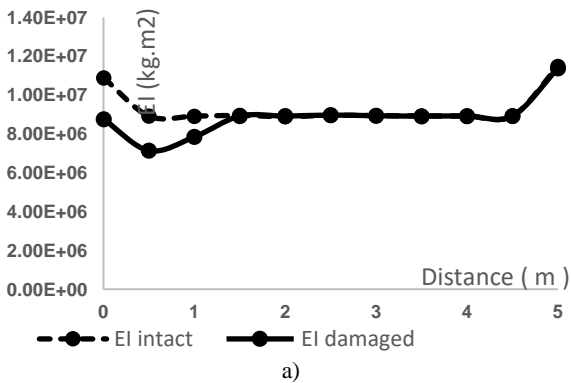


Figure 14. EI changes of beam BL in a) first mode b) second mode in two intact and damaged states

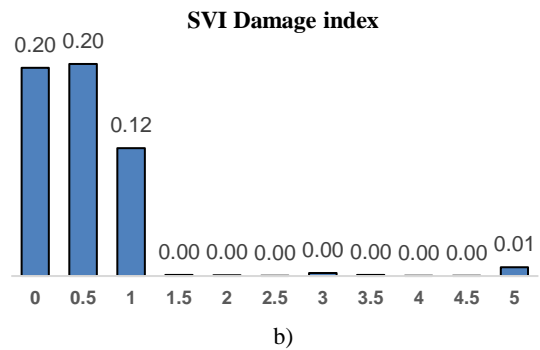
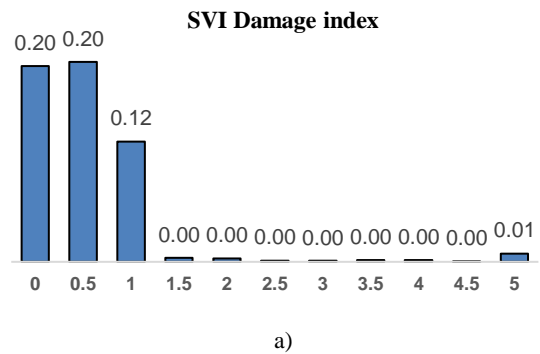


Figure 15. SVI damage index of beam BL in a) first mode b) second mode

3. 3. 2. 2. Damage Scenarios Based on The Pushover Analysis Results

After evaluating the performance of the SVI index in the considered frame based on an intentional damage scenario and obtaining a reliable response for this damage detection method, structural damage is induced using a probable realistic scenario. To create a probable damage scenario caused by an earthquake, the results of the pushover analysis are utilized. Through the pushover analysis, lateral forces are applied to the structure to gradually develop damage to its members.

Therefore, at a specific step of the analysis, the damage state in the structure is considered as a damage scenario, and the beams that experience damage earlier and to a greater extent than others are identified.

According to Figure 16, the plotted circles on the beams and columns of the frame indicate the location of plastic hinge formation and the development of failure mechanisms. In other words, the analysis results show that the beams and columns of the first-floor roof have the highest probability of damage, and therefore, the health monitoring system should be more concentrated on the members of the first floor. Based on the above descriptions, the desired reinforced concrete frame was subjected to a displacement control type pushover analysis with a uniformly distributed lateral load on the floors. The center of mass node on the last floor was considered as the control node. To determine the locations of damage mechanisms, automatic concentrated plastic hinges were used at the ends of the beams, which utilize performance levels based on measuring plastic rotation proposed by FEMA273.

The flexural automatic plastic hinge type M3 was used for the beams, and the interaction P-M3 type was used for the columns. The plastic hinge was applied at 0.05 and 0.95 of the length of these members. By performing the pushover analysis in the Sap2000 software and obtaining the structural capacity curve, in order to validate the analysis of results, the resulting curve from the analysis conducted in this study was plotted alongside the curve obtained from the literature [29] shown in Figure 17. Due to the good agreement of the two curves at different displacement levels, the necessary confidence in the modeling was achieved.

Next, in order to define the damage scenario, the occurrence of yielding in the beams at the floor levels was selected as the damage scenario using the results of the pushover analysis. According to the results and as shown in Figure 18, the onset of yielding has occurred in the vicinity of the right-side connection of beam BL in the first-floor roof.

In the second and third damage scenarios, yielding occurred in the second and third story beams of the structure, respectively. Also, in the second scenario, all the beams of the first story had already yielded and in the third scenario, the beams of the first and second stories had already yielded.

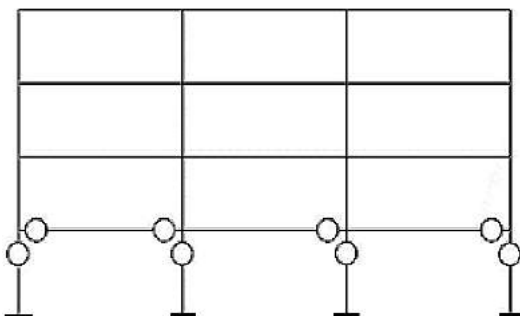


Figure 16. The location of the damage mechanism in the structure [30]

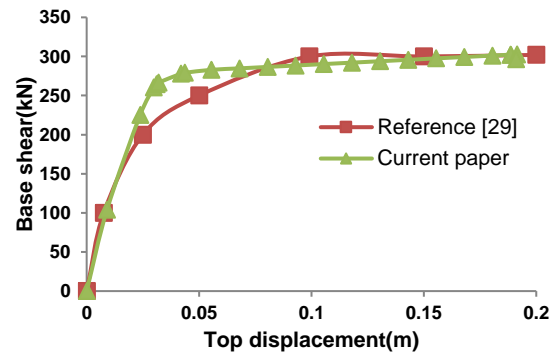
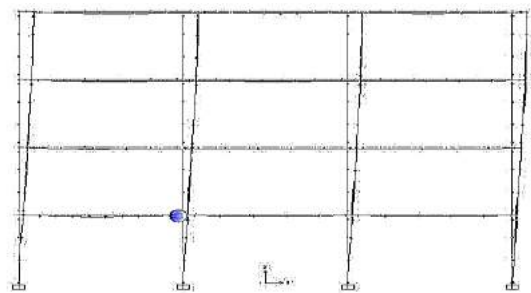
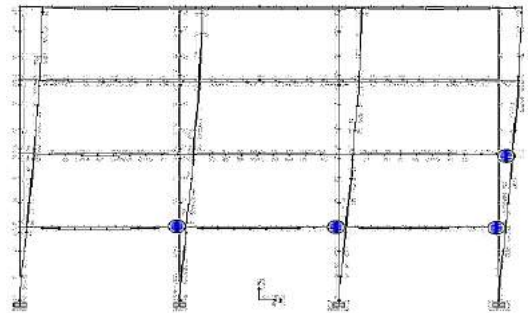


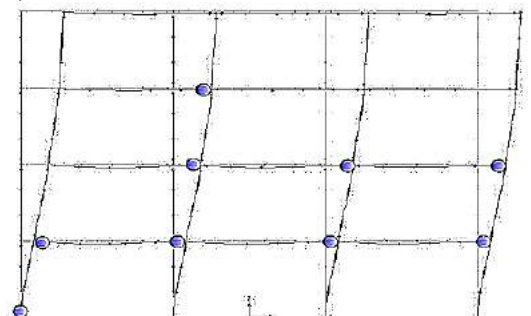
Figure 17. Comparison between the results of the current study and literature [29].



a) The first damage scenario: yielding in story1 beam (BL)



b) The second damage scenario: yielding in story2 beam (BR)



c) The third damage scenario: yielding in story3 beam (BL)
 Figure 18. Different damage scenarios based on the pushover analysis results

The vibration periods of the first three modes of the healthy structure and the damaged structure in three damage scenarios are presented in Table 4.

TABLE 4. The first three vibration periods of the intact structure and the damaged structure

Mode shape number	Vibration periods (s)			
	Intact	Damaged (Senario 1)	Damaged (Senario 2)	Damaged (Senario 3)
1	0.509	0.524	0.61	0.727
2	0.178	0.181	0.189	0.203
3	0.109	0.109	0.112	0.119

3.3.2.2.1. First Damage Scenarios Based on the results of the pushover analysis, the first yield location was in story 1 and the beam BL. Therefore, in two states of the intact and damaged structure, the modal displacement of the first and second modes of the beams of this floor was extracted. In the following, as an example, the changes in the modal displacement of the first and second modes of the beam BL are displayed in Figure 19. Using the modal displacement obtained from the previous step and the central difference method, the modal curvature of the first two modes was calculated. In the following, the changes of bending stiffness EI on the beam were obtained in two states of intact and damaged structures, and finally, the SVI was calculated.

The results are shown in Figures 20 and 21. The value of the SVI index has reached its maximum value near the right support of the beam BL. This result is completely consistent with the initial guess of the yield location in the first scenario. To see the state of damage in other beams on the first floor, the SVI index value changes in story 1 are shown in Figure 22.

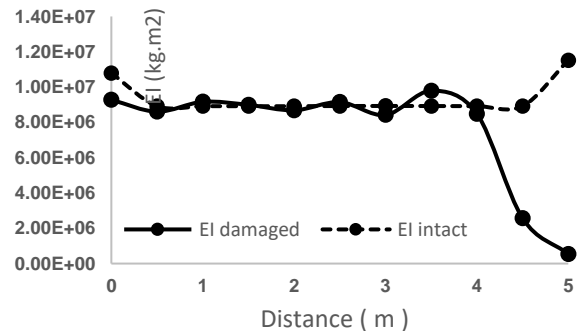
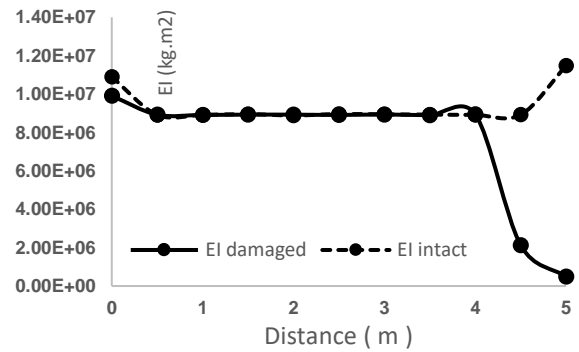


Figure 20. Comparison between calculated stiffness EI in a) first mode shape and b) second mode shape of the beam BL (story 1)

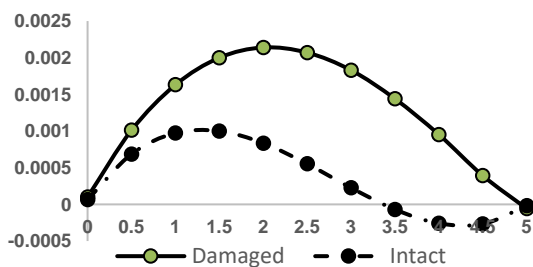
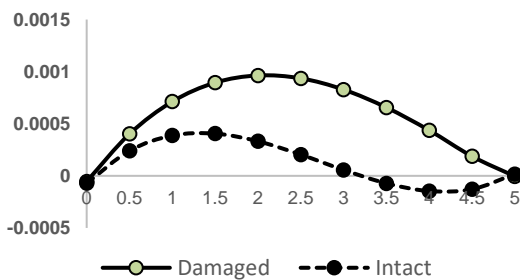
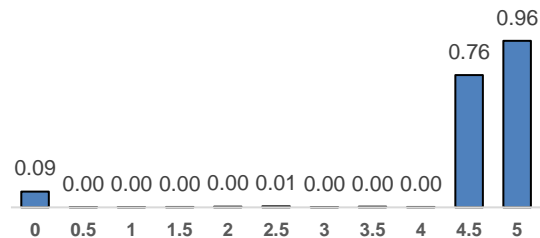


Figure 19. Comparison between the a) first mode shape and b) second mode shape of the beam BL

SVI Damage index



SVI Damage index

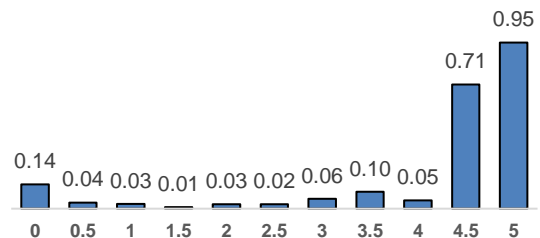


Figure 21. Comparison between Calculated SVI values in a) first mode shape and b) second mode shape of the beam BL (story 1)

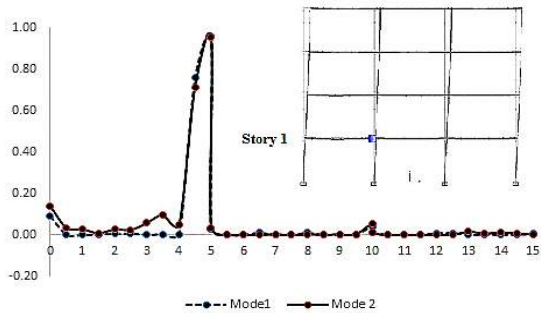


Figure 22. SVI variation in a) first mode shape and b) second mode shape of story 1 beams

3. 3. 2. 2. 2. Second Damage Scenarios In this scenario, the beam BR in the second story has yielded at one of its two end nodes. Also, in story 1, all beams have yielded at one of their two end nodes. Therefore, in this scenario, the value of the damage index has been calculated on both the first story and the second story. With a process similar to the first scenario, at half-meter intervals on the beams of story 2, the first and second modal displacements of the beams were extracted in two states of intact structure and damaged structure. In the following, the first and second modal displacements of the beam BL in story 2, as well as the changes in the bending stiffness EI of this beam, were drawn in two damage states. (Figures 23 and 24). In the following, at first, the SVI index value in the beams of the first story, all of which have yielded in this scenario, has been calculated based on the information of the first and second modes. (Figures 25 to 28). As it is clear, based on the results of this index, the yielding in the right node of the beams is known, and it is completely consistent with the results of pushover analysis.

Based on Figure 29, changes in the SVI index in the beams of the second story show that the beam BR has yielded at its right node, which is proven based on the value of the index in the first two modes. Also, at the two end nodes of the beam BM on the same floor, the value of the index has grown a lot. It indicates that this beam is ready to yield and will reach yielding with increasing lateral displacement of the structure, similar to the beam BR.

3. 3. 2. 2. 3. Third Damage Scenarios In scenario 2, in story 3, beam BL has yielded. Also, in the first and second stories, all the beams have yielded, and on the first floor, the column in the left corner of the frame has yielded. Similar to the process of evaluating the first and second damage scenarios, in damage scenario 3, the first and second mode shape displacements of the third story beams were compared with each other in the two states of the intact structure and the damaged structure (Figure 30).

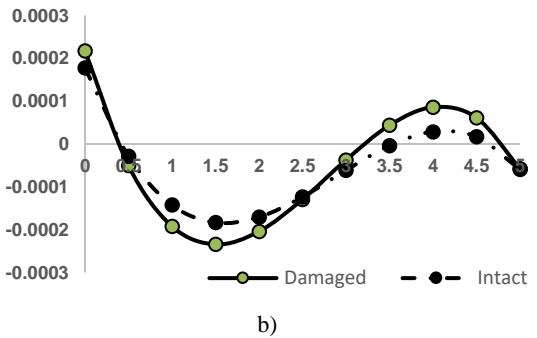
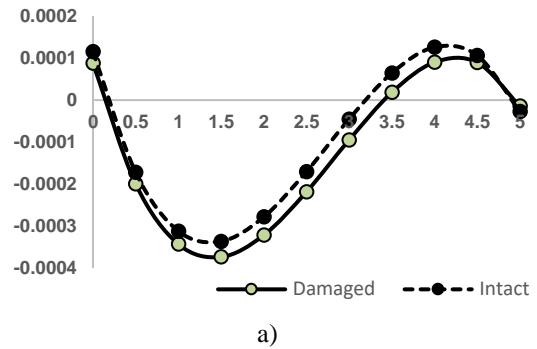


Figure 23. Comparison between mode shapes of the beam BL (story 2) in a) mode1 b) mode2

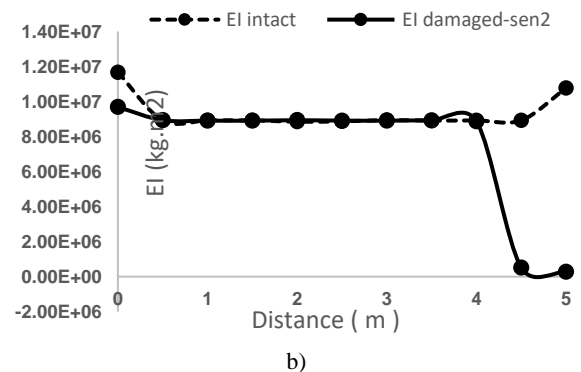
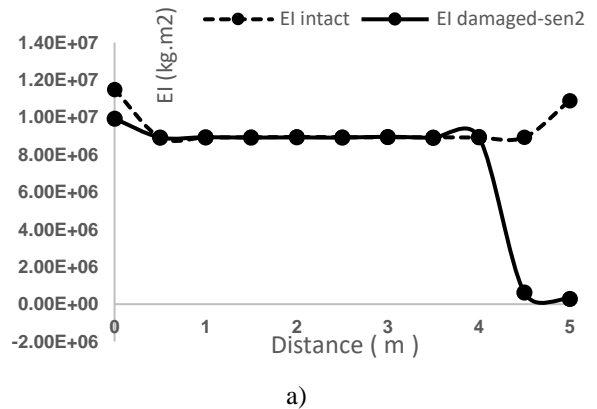
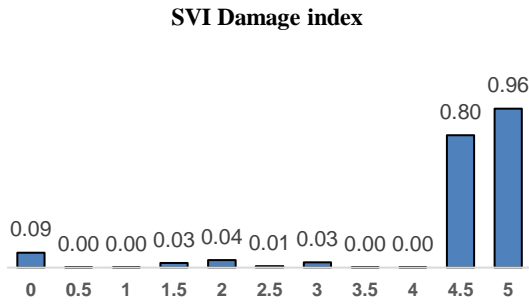
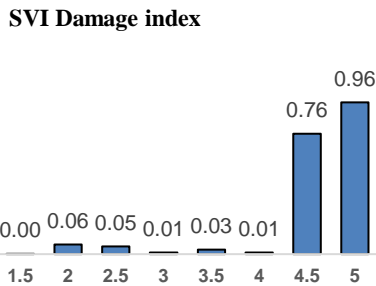


Figure 24. Comparison between calculated stiffness EI in a) first mode shape and b) second mode shape of the beam BL (story 2)

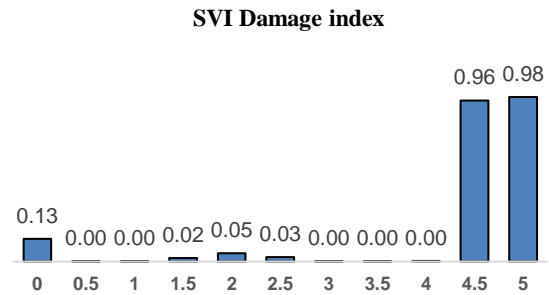


a)

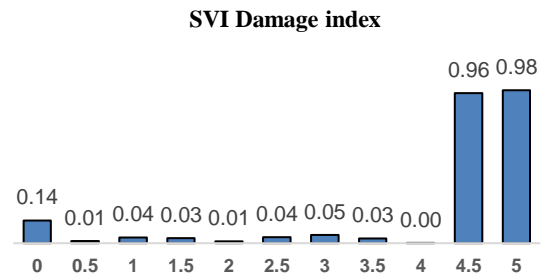


b)

Figure 25. Comparison between Calculated SVI values in a) first mode shape and b) second mode shape of the beam BL (story 1)

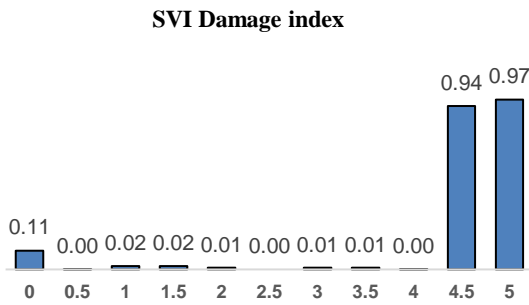


a)

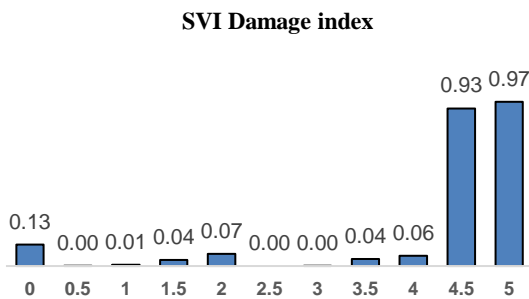


b)

Figure 27. Comparison between Calculated SVI values in a) first mode shape and b) second mode shape of the beam BR (story 1)



a)



b)

Figure 26. Comparison between Calculated SVI values in a) first mode shape and b) second mode shape of the beam BM (story 1)

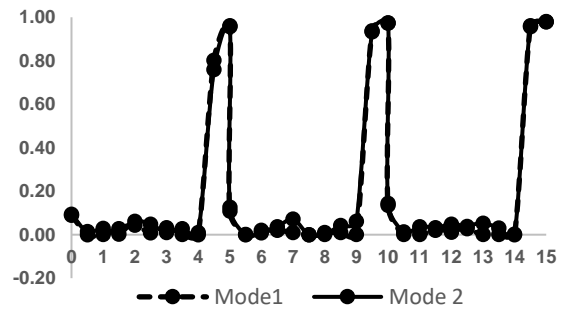


Figure 28. SVI variation in story 1 beams (senario 2)

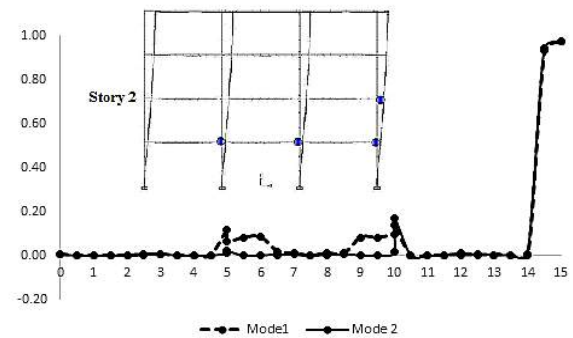


Figure 29. SVI variation in a) first mode shape and b) second mode shape of story 2 beams

The damage to the first and second story beams is shown in Figures 31 and 32. Also, changes in the SVI index on the beams of the third floor (Figure 33), in the first two modes of the structure, showed that the BL beam yielded at its right node.

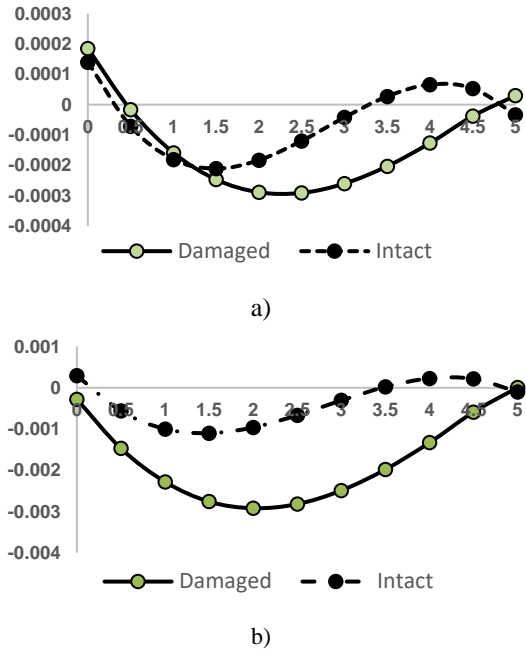


Figure 30. Comparison between mode shapes of the beam BL (story 3) in a) mode 1 and b) mode 2

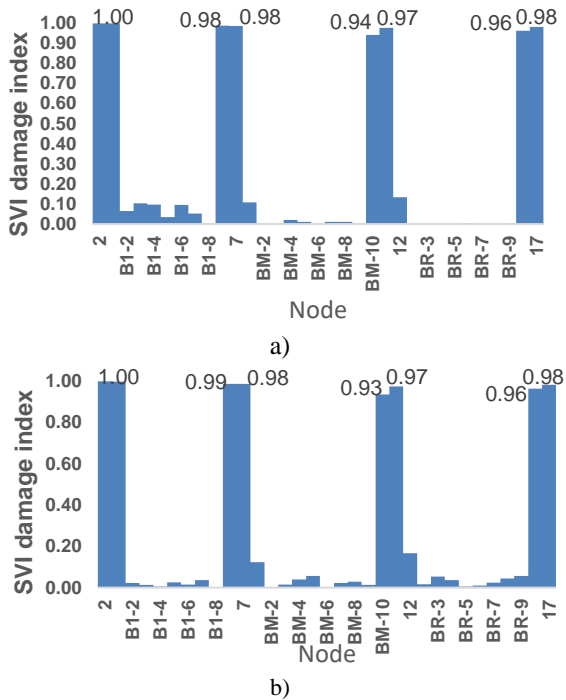


Figure 31. Comparison between Calculated SVI values in a) first mode shape and b) second mode shape of story 1 beams

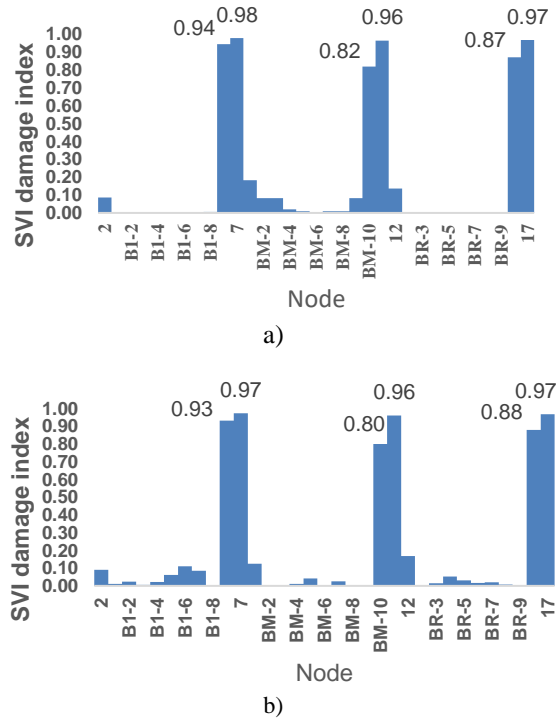


Figure 32. Comparison between Calculated SVI values in a) first mode shape and b) second mode shape of story 2 beams

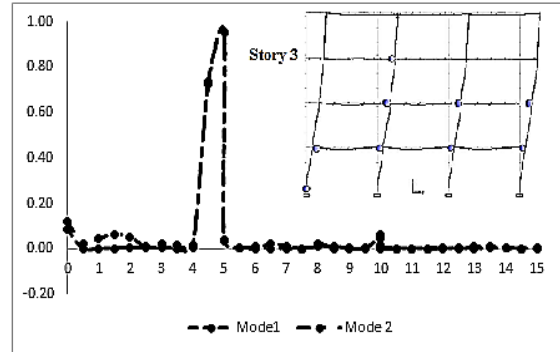


Figure 33. SVI variation in a) first mode shape and b) second mode shape of story 3 beams

4. CONCLUSIONS

1. In this article, the SVI index was used to investigate the location and magnitude of damage in beams. Initially, a simple steel beam that had been previously studied by others was modeled and examined in several intentional damage scenarios. The results showed that this index was able to predict the location and magnitude of damage along the beam with appropriate magnification and acceptable accuracy. Additionally, the results demonstrated that in scenarios involving simultaneous damage occurrence in multiple elements along the beam, the SVI index was able to correctly identify the damaged

locations and provide an accurate estimation of their magnitude. This investigation continued with the analysis of a reinforced concrete frame.

After validating the results of the frame model, an intentional and logical scenario was created in one of the beams of the concrete frame, and its location and magnitude were monitored. Then, based on the seismic scenarios according to the results of the pushover analysis, these evaluations were continued. Using this analysis method, an initial prediction of the vulnerable floor(s) was obtained, and as a result, the placement of the sensors in the field would be feasible based on the priority of the analysis results. In all of these analyses, the reading location of modal data was embedded at half-meter intervals along the beams, and the effects of environmental noise were not considered. In the first mode of the structure, the dominant displacement of the frame was in the transverse direction, and therefore, the greatest deformation occurred in the columns while the beams had less deformation. In this case, comparing the mode shape displacements of the intact and damaged structures alone did not provide tangible information regarding the location of damage in the beams.

2. The SVI index was able to accurately amplify the location of damage by utilizing the second derivative of the mode shape vector, which is highly sensitive to mode shape variations. The results also demonstrated that the use of the second mode in structural damage assessment did not significantly change the results, indicating that it is sufficient to have the first mode of the structure to identify the location of damage in the beams.

3. One common error among many modal-based damage detection methods is reporting damage in locations other than the actual damaged area on the member. This error was not observed in the performance of the studied index in this research. The SVI index was able to perform well in seismic damage scenarios where damage occurred simultaneously in multiple beams.

4. In order to better understand the changes in the flexural stiffness of the beam after damage, beam BL in the first story of the concrete frame, which had sustained damage in all scenarios, was selected, and the variations in its stiffness along its length were presented in different scenarios. As shown in the provided figure, the EI value of the beam in the damaged locations is clearly lower than in the undamaged locations. Therefore, even without access to information about the intact structure, the location of damage can be determined by comparing the EI values at different sections

5. According to the results obtained from the analysis, the SVI index was able to accurately determine both the location and magnitude of damage in a scenario where intentional damage was created at a specific location on the beam. This is in contrast to the reported damage magnitude based on the received modal data after the seismic damage, which was a very large numerical value close to 100%, indicating significant amplification of

damage in comparison to seismic damage indices. Considering the level of damage that occurred at the beam level due to yielding, the magnitude of the damage index shows significant amplification in determining the extent of damage.

5. REFERENCES

1. Yang, Y., Liu, H., Mosalam, K.M. and Huang, S., "An improved direct stiffness calculation method for damage detection of beam structures", *Structural Control and Health Monitoring*, Vol. 20, No. 5, (2013), 835-851. <https://doi.org/10.1002/stc.1503>
2. Cawley, P. and Adams, R.D., "The location of defects in structures from measurements of natural frequencies", *The Journal of Strain Analysis for Engineering Design*, Vol. 14, No. 2, (1979), 49-57. <https://doi.org/10.1243/03093247V142049>
3. West, W.M., "Illustration of the use of modal assurance criterion to detect structural changes in an orbiter test specimen", (1986).
4. Lieven, N. and Ewins, D., "Spatial correlation of mode shapes, the coordinate modal assurance criterion (comac)", in Proceedings of the 6th international modal analysis conference, Kissimmee Florida, USA. Vol. 1, (1988), 690-695.
5. Lu, Q., Ren, G. and Zhao, Y., "Multiple damage location with flexibility curvature and relative frequency change for beam structures", *Journal of Sound and Vibration*, Vol. 253, No. 5, (2002), 1101-1114. <https://doi.org/10.1006/jsvi.2001.4092>
6. Achenbach, J.D., "Structural health monitoring—what is the prescription?", *Mechanics Research Communications*, Vol. 36, No. 2, (2009), 137-142. <https://doi.org/10.1016/j.mechrescom.2008.08.011>
7. Li, H., Gao, D. and Yi, T., "Advances in structural health monitoring systems in civil engineering", *Advances in Mechanics*, Vol. 38, No. 2, (2008), 151-166.
8. Hearn, G. and Testa, R.B., "Modal analysis for damage detection in structures", *Journal of Structural Engineering*, Vol. 117, No. 10, (1991), 3042-3063. [https://doi.org/10.1061/\(ASCE\)0733-9445\(1991\)117:10\(3042\)](https://doi.org/10.1061/(ASCE)0733-9445(1991)117:10(3042))
9. Pandey, A. and Biswas, M., "Damage detection in structures using changes in flexibility", *Journal of Sound and Vibration*, Vol. 169, No. 1, (1994), 3-17. <https://doi.org/10.1006/jsvi.1994.1002>
10. Ndambi, J.-M., Vantomme, J. and Harri, K., "Damage assessment in reinforced concrete beams using eigenfrequencies and mode shape derivatives", *Engineering structures*, Vol. 24, No. 4, (2002), 501-515. doi: [https://doi.org/10.1016/S0141-0296\(01\)00117-1](https://doi.org/10.1016/S0141-0296(01)00117-1)
11. Dawari, V. and Vesmawala, G., "Structural damage identification using modal curvature differences", *IOSR Journal of Mechanical and Civil Engineering*, Vol. 4, (2013), 33-38.
12. Foti, D., "Dynamic identification techniques to numerically detect the structural damage", *The Open Construction & Building Technology Journal*, Vol. 7, No. 1, (2013). doi: [10.2174/1874836801307010043](https://doi.org/10.2174/1874836801307010043).
13. Dutta, A. and Talukdar, S., "Damage detection in bridges using accurate modal parameters", *Finite Elements in Analysis and Design*, Vol. 40, No. 3, (2004), 287-304. [https://doi.org/10.1016/S0168-874X\(02\)00227-5](https://doi.org/10.1016/S0168-874X(02)00227-5)
14. Whalen, T.M., "The behavior of higher order mode shape derivatives in damaged, beam-like structures", *Journal of Sound and Vibration*, Vol. 309, No. 3-5, (2008), 426-464. <https://doi.org/10.1016/j.jsv.2007.07.054>
15. Fayyadh, M.M. and Razak2a, H.A., "Experimental validation of dynamic based damage locating indices in rc structures",

- Structural Engineering and Mechanics, An Int'l Journal*, Vol. 84, No. 2, (2022), 181-206. doi: 10.12989/sem.2022.84.2.181.
16. Maeck, J., "Damage assessment of civil engineering structure by vibration monitoring, Phd dissertation. Department of civil engineering, Katholieke Universiteit Leuven, Belgium, (2003).
 17. Patel, B. and Dewangan, U., "A baseline free method for multiple damage identification and localization using the roving mode shape response", *International Journal of Engineering, Transactions B: Applications*, Vol. 36, No. 5, (2023), 946-954. doi: 10.5829/ije.2023.36.05b.11.
 18. Ghasemi, S., Ghodrati Amiri, G. and Mohamadi Dehcheshmeh, M., "Structural damage assessment via model updating using augmented grey wolf optimization algorithm", *International Journal of Engineering, Transactions A: Basics*, Vol. 33, No. 7, (2020), 1173-1182. doi: 10.5829/IJE.2020.33.07A.02.
 19. Aghagholizadeh, M. and Massumi, A., "A new method to assess damage to rcmrfs from period elongation and park-ang damage index using ida", *International Journal of Advanced Structural Engineering*, Vol. 8, (2016), 243-252. doi: 10.1007/s40091-016-0127-8.
 20. Ozturk, B., Sahin, H.E. and Yildiz, C., "Seismic performance assessment of industrial structures in turkey using the fragility curves", in 15th World Conference on Earthquake Engineering, Lisbon, Portugal. (2012), 1-7.
 21. Kassem, M.M., Nazri, F.M., Farsangi, E.N. and Ozturk, B., "Improved vulnerability index methodology to quantify seismic risk and loss assessment in reinforced concrete buildings", *Journal of Earthquake Engineering*, Vol. 26, No. 12, (2022), 6172-6207. <https://doi.org/10.1080/13632469.2021.1911888>
 22. Kassem, M.M., Nazri, F.M., Farsangi, E.N. and Ozturk, B., "Development of a uniform seismic vulnerability index framework for reinforced concrete building typology", *Journal of Building Engineering*, Vol. 47, (2022), 103838. <https://doi.org/10.1016/j.jobte.2021.103838>
 23. Hait, P., Sil, A. and Choudhury, S., "Damage assessment of reinforced concrete buildings considering irregularities (research note)", *International Journal of Engineering, Transactions A: Basics*, Vol. 32, No. 10, (2019), 1388-1394. doi: 10.5829/ije.2019.32.10a.08.
 24. Mazloom, M. and Fallah, N., "Seismic vulnerability assessment of existing rc moment frames using a new stiffness based damage index", *International Journal of Engineering, Transactions B: Applications*, Vol. 36, No. 5, (2023), 1000-1011. doi: 10.5829/IJE.2023.36.05B.16.
 25. Chiluka, S. and Oggu, P., "Performance assessment of ductile detailing code-based reinforced concrete special moment resisting frames", *International Journal of Engineering, Transactions C: Aspects*, Vol. 36, No. 3, (2023), 457-464. doi: 10.5829/ije.2023.36.03c.04.
 26. Yang, Y., Yang, Y. and Chen, Z., "Seismic damage assessment of rc structures under shaking table tests using the modified direct stiffness calculation method", *Engineering Structures*, Vol. 131, (2017), 574-586. <https://doi.org/10.1016/j.engstruct.2016.10.030>
 27. Samimifar, M. and Massumi, A., "Simplification and assessment of modal-based story damage index for reinforced concrete frames subjected to seismic excitations", *Journal of Earthquake Engineering*, Vol. 22, No. 3, (2018), 333-355. <https://doi.org/10.1080/13632469.2016.1217803>
 28. Mazloom, M. and Fallah, N., "Evaluation of seismic damage indexes in concrete frames and introducing a new damage index for detection of damaged stories", *Journal of Structural and Construction Engineering*, Vol. 8, No. 7, (2021), 31-55. doi: 10.22065/JSCE.2020.216248.2053.
 29. Ferracuti, B., Pinho, R., Savoia, M. and Francia, R., "Verification of displacement-based adaptive pushover through multi-ground motion incremental dynamic analyses", *Engineering structures*, Vol. 31, No. 8, (2009), 1789-1799. <https://doi.org/10.1016/j.engstruct.2009.02.035>
 30. Horiuchi, K.K.P., "Structural health monitoring with the modal strain energy method during seismic loading", Submitted in partial satisfaction of the requirements for the degree of master of science in Civil Engineering, California State University, Sacramento, (2014).

COPYRIGHTS

©2023 The author(s). This is an open access article distributed under the terms of the Creative Commons Attribution (CC BY 4.0), which permits unrestricted use, distribution, and reproduction in any medium, as long as the original authors and source are cited. No permission is required from the authors or the publishers.

**Persian Abstract****چکیده**

تشخیص محل و مقدار آسیب سازه‌ها پس از زلزله با روش‌های عددی، یکی از موضوعاتی است که همچنان مورد توجه محققین این حوزه می‌باشد. پس از وقوع آسیب در سازه و کاهش سختی آن، مشخصات ارتعاشی سازه تغییر کرده و لذا ارزیابی تغییرات مشخصات ارتعاشی آن می‌تواند به عنوان شاخصی برای تشخیص آسیب مورد استفاده قرار بگیرد. در این مقاله، به منظور تشخیص آسیب در سازه‌ها، از تکنیک ارتقاء یافته محاسبه مستقیم سختی (DSC) و نیز یک شاخص جدید آسیب بر اساس تغییرات سختی خمشی (SVI) استفاده شده است. تکنیک مورد نظر در ابتدا بر روی یک تیر فولادی با مشخصات موجود بررسی شده و در سناریوهای آسیب مختلف، مورد مطالعه قرار گرفت. سپس، مدلی عددی از قاب خمشی بتن‌آرمه ساخته شد و پس از استخراج مشخصات ارتعاشی آن، به منظور ایجاد سناریوی خرابی بدون دخالت مستقیم، تحت تحلیل بارافزون قرار گرفت. با توجه به نتایج تحلیل سه سناریوی آسیب بر اساس وقوع تسلیم در تیرهای طبقات در نظر گرفته شد و محل تشکیل مفصل پلاستیک در دو سر تیر به عنوان محل احتمالی وقوع آسیب در طبقه انتخاب شد. با استفاده از اطلاعات مودال سازه معیوب و محاسبه شاخص تغییرات سختی SVI در تیرهای طبقات، مشخص شد که این شاخص توانست محل وقوع آسیب را تنها با اطلاع از مود اول سازه به درستی و با بزرگنمایی کافی نسبت به سایر نقاط مشخص نماید. همچنین نتایج نشان داد که با این روش می‌توان حتی بدون اطلاع از مشخصات ارتعاشی سازه سالم و تنها با داشتن اطلاعات مودال سازه معیوب، محل آسیب را به درستی مشخص کرد.



NiO-Ni-Al₂O₃(γ) Nanocatalyst by Pulse Electrocodeposition Over Ni Open-cell Foam for Methane Reforming

M. Zafardoagoo^{*a}, S. K. Sadrnezhad^b, J. Mostaghimi^c

^a Department of Materials Science and Nanotechnology, School of Science and Engineering, Sharif University of Technology, International Campus-Kish Island, Iran

^b Department of Materials Science and Engineering, Sharif University of Technology, Azadi Ave., Tehran, Iran

^c Centre for Advanced Coating Technologies, Faculty of Applied Science & Engineering, University of Toronto, 5 King's College Road, Toronto, Ontario, M5S 3G8, Canada

PAPER INFO

Paper history:

Received 16 June 2023

Received in revised form 24 July 2023

Accepted 26 July 2023

Keywords:

Nickel Foam

γ -alumina

Methane Reforming

Nanocatalyst

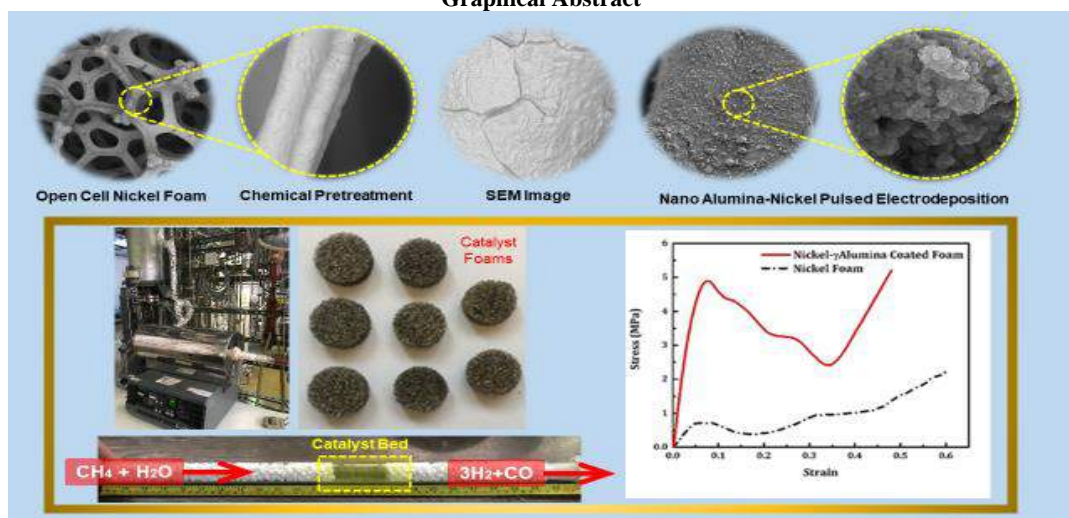
Pulse Electrocodeposition

ABSTRACT

Global warming persuades researchers to improve the effectiveness of renewable energy technologies, such as H₂ production by methane steam reforming (MSR) an endothermic process. Herein, a nanocatalyst based on open-cell nickel foam 40 (pore per inch) with high thermal conductivity was prepared. The nanocatalyst was synthesized with a chemical stepwise synthesis approach, chemical pretreatment, pulsed electrocodeposition of Ni-Al₂O₃(γ) nanoparticles, and calcination. Measurements of thermal diffusivity(α) with flash xenon technique gained $4.41 \times 10^{-6} \text{ m}^2 \text{ s}^{-1}$ and values of specific heat capacity, Cp, by differential scanning calorimetry (DSC) and thermal conductivity(λ) enhanced by 65% in temperature range of 150 to 550°C in Ni-alumina(γ) foam nanocatalyst. Furthermore, characterization and tests for comparing nickel foam and Ni-alumina(γ) foam indicated that the hardness improved from 145 Vickers hardness (HV) to 547 HV and compression strength increased from 1.1 MPa to 5MPa and specific surface area (S_{BET}) from $1.48 \text{ m}^2 \text{ g}^{-1}$ to $48 \text{ m}^2 \text{ g}^{-1}$. XRD (x-ray diffraction) analysis showed NiO and NiAl₂O₄ in the structure. The interface between the catalytic component (NiAl₂O₄), and nickel affected the catalytic ability for MSR, and the efficiency gained at low temperature 500 °C was the same as reported at 720°C by other investigations.

doi: 10.5829/ije.2023.36.10a.15

Graphical Abstract



*Corresponding Author Email: m.zafardoago@gmail.com (M. Zafardoagoo)

Please cite this article as: M. Zafardoagoo, S. K. Sadrnezhad, J. Mostaghimi, NiO-Ni-Al₂O₃(γ) Nanocatalyst by Pulse Electrocodeposition Over Ni Open-cell Foam for Methane Reforming, *International Journal of Engineering, Transactions A: Basics*, Vol. 36, No. 10, (2023), 1908-1918

NOMENCLATURE

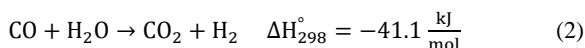
		Greek Symbols	
C_p	Specific thermal capacity($Jg^{-1}^{\circ}C^{-1}$)	ρ	Density (kg/m^3)
HV	Vickers hardness	α	Thermal diffusivity(m^2S^{-1})
MPa	Mega Pascal	λ	Thermal conductivity ($Wm^{-1}^{\circ}C^{-1}$)
MSR	Methane Steam Reforming	θ	Duty cycle (%)
PPI	Pore per Inch		
f	Frequency (Hertz)		

1. INTRODUCTION

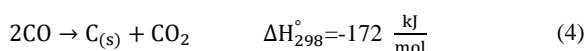
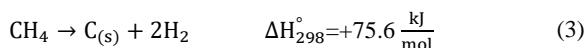
Environmental concerns of fossil fuels have motivated scientists to develop sustainable energies like wind, solar and hydrogen. Hydrogen is a clean energy with no exhaust contaminants during combustion [1]. The availability of immense natural gas reservoirs in the globe justifies reforming natural gas methane, to produce hydrogen by steam, carbon dioxide, and oxygen. The endothermic methane steam reforming, MSR, reaction Equation (1) required extensive energy at a temperature range of 700-720 °C on the catalytic bed.



Mostly water gas shift reaction (WGS) Equation (2) goes along MSR.



Moreover, during MSR some side reactions occur at high temperatures ($T > 750$ °C) via Equation (3), and Boudouard reaction at low temperatures (300–450 °C) as Equation (4) [2].



Usually, combining transition and/or noble metals catalysts on stabilized supports (alumina, ceria, ceria promoted alumina, zeolite, etc. in catalysts have been frequently used [3-5]. However, nickel was the most common catalyst for being cheap, active, and selective in MSR [6, 7]. Nevertheless, considering some drawbacks like Ni-sintering and carbon deposition maybe by hotspots and poor uniform temperature profile of pelletized catalysts bed, persuade researchers to modify catalysts structure [8-12]. Therefore, any attempt to fabricate novel catalysts for lowering carbon deposition, good heat transfer, decrease energy consumption, high thermal stability, high mechanical strength and increase lifetime are valuable [13-15]. Open-cell metal foams have a special set of materials properties such as low density, high thermal conductivity, ductility, resilience to thermal shock resistance, fluid permeability, and high surface area [16, 17]. Recently, application of nickel foams in MSR have been investigated for good heat distribution which increased [18] the CH_4 conversion inside the reformers by high interface area between the

gaseous reactants and the microporous catalysts [19-21]. In fact, higher thermal conductivity limits the thermal gradient among reactants to gain higher catalytic performance in methane reforming [9, 10, 15, 22-24]. Moreover, metal foams are attractive for compression loading applications such as in catalysts bed for their progressive crushing whilst tensile loading caused a fast, brittle fracture [16]. In the compression stress-strain curve of metallic foams three deformation stages seen as 1. Linear short elastic, 2. Long plastic plateau and 3. Densification [25-30]. Thus, this study place a focus on developing nickel foam structured catalyst reinforced by alumina (γ) nanoparticles to increase the plastic plateau region for mechanical strengthening and prevent catalyst brittle crushing [23, 31].

Furthermore, recently it is studied to find that catalytic performance of the Ni foam based catalyst is highly dependent on the pre-treatment and reaction temperature [18, 32, 33]. Pegios et al. [34] reported a Ni-foam catalyst aluminium oxide precursors by dip coating method over Ni-foams with MgO and SiO₂ as promoters for methane reforming. Results indicated that chemical pretreatment conditions increase the active metal surface and active sites probably at the nickel-alumina interface.

Chai et al.[33] indicated among Ni/MO_x(M=Al, Zr or Y) binary catalysts, Ni foam/ Al₂O₃ possesses the largest specific surface area and the highest amount of NiO species (Ni active site), and as a result, exhibits the best catalytic performance. Lajevardi et al. [35] indicated that Ni-nano Al₂O₃ with applied pulse electrodeposition had higher hardness than direct current. Applied nanoparticles locked dislocation at the grain boundaries movements and recrystallization at elevated temperatures. Therefore, microhardness and thermal stability increased [36-38]. In the pulse current state, less nano particles agglomerated, and caused more uniform dispersion of nano particles [39]. The metal foam structure does not in itself have a high surface area; thus, in catalyst applications, deposition of a high surface area coat e.g., Al₂O₃(γ), SiO₂, or zeolite by wash-coating, sol-gel, electrochemical deposition, electrophoretic, chemical vapor deposition (CVD) or physical vapor deposition (PVD) is necessary [9, 40, 41].

The utilization of appropriate ceramic nanoparticles with high specific surface area such as Al₂O₃(γ) reinforcement in a porous metal matrix in catalysis would be interesting candidate for enhancing thermal conductivity, hardness and compression strength [17, 42-

44]. Cimino et al. [18] applied Re/Ce via electroprecipitation and pulse deposition methods on nickel foam catalyst in methane reforming to increase heat transfer by support metal foam structure. To date, only a limited number of studies have been examined the effect of alumina(γ) nanoparticles in Ni-foam as nanocatalyst by pulse codeposition for compression strengthening, more thermal conductivity and MSR operating at low temperature as a way of energy saving. By applying this concept, we aim at increased thermal conductivity, a lower thermal gradient through the reaction chamber for more heat transfer and better interaction between the gas-solid reactants' active Ni phase and alumina(γ) nanoparticles. The MSR pilot test of this nanocatalyst indicated the same efficiency at 500 °C compared to MSR efficiency of common catalysts at 720 °C that reported by other works [9, 22, 23].

2. MATERIALS METHOD

2. 1. Experimental The procedure consists of several steps for nanocatalyst fabrication of nickel-alumina(γ) foam, briefly, such as (a) open-cell nickel foam fabrication over polyurethane (PU) as substrate, (b) chemical pre-treatment or etching, and (c) Ni-alumina(γ) nanoparticles pulse electro co-deposition. Firstly, the 40 pores per inch (ppi) open cell PU with the density of 0.021 gcm⁻³ became conductive by nickel electroless deposition. We used the electroless bath containing nickel sulfate and sodium hypo-phosphide (NaPO₂H₂) at 82-85°C with a pH of 4. Afterward, the foam was nickel electrodeposited by complex nickel salt solution (including nickel(II) sulfate hexahydrate (NiSO₄.6H₂O), Merck 180 gL⁻¹, ammonium chloride (NH₄Cl), Merck 25 gL⁻¹ and boric acid (H₃BO₃), Merck, 30gL⁻¹) at 55 °C, pH 5.5, and direct surface current density 20 Adm⁻² for 60 min. All the chemicals used with the grade for analysis. Then foam was put into a tube furnace flowing 99.99% purity argon gas to eliminate the PU substrate by pyrolysis as per the procedure explained in another work [16]. In continue, chemical pre-treatments were applied to increase the roughness of the surface of the foam's strands in 6 Molar (M) hydrochloric acid (HCl) at three different temperatures (i.e., 60, 70, and 80 °C) for 10 and 15 minutes. Then the foam was rinsed thoroughly with deionized water, dipped into acetone and dried. Each specimen with dimensions 10×40×40 mm³ was pulse electro codeposited by two solutions to gain nickel- γ -alumina nanocomposite over the etched nickel foam. Analytical reagents and deionized water were used to prepare the plating solutions. Firstly, a suspension of nano Al₂O₃(γ) powder (99.99%, particle size 20-50 nm, BET surface area >150 m²g⁻¹) (5 gL⁻¹) and sodium dodecyl sulfate (SDS) (1.5 gL⁻¹) as surfactant dispersed, stirred for 21 hours with 200 rpm and agitated by

ultrasonic waves for 20 min to break the weak-bonded agglomerations. Secondly, the nickel watt bath type (including nickel(II) sulfate hexahydrate (NiSO₄.6H₂O), Merck, 250 gL⁻¹, Nickel(II) chloride - hexahydrate (NiCl₂.6H₂O) 40 gL⁻¹, boric acid (H₃BO₃), 35 gL⁻¹) was prepared. Then the nano-suspension was added to it and well stirred. Afterwards, pulsed electro co-deposition was performed with frequency 5 Hz, duty cycle 50%, current density 27.5 Adm⁻², stirring rate 200 rpm, the electrolyte pH 4.2, temperature 50±2°C exposed time 90 minutes for nickel foam as the cathode. Finally, the pulse electrodeposited nickel-nano alumina foam was rinsed with deionized water, dried, and calcined at 720 °C.

2. 2. Characterization and Tests We performed the thermogravimetric analysis (TG, TA Instrument Bahr STA 503) to determine the thermal stability of the PU foam before plating. In this study, X-ray diffraction (XRD) patterns for identifying crystalline phases of the specimens were collected with a PANalytical X-ray diffractometer using Cu K α radiation ($\lambda=0.15406$ nm, 40 kV, 40 mA). Scanning electron microscopy (SEM) and field emission electron microscopy (FESEM) were used to investigate the specimen morphology and elemental analysis. The compression strength test of the specimens with dimensions 10×20×20 mm³ was conducted at room temperature by HOUNSFIELD (H10KS-UK) test machine. The surface hardness (on the Vickers scale) of nanocomposite coatings was measured by a micro-hardness measurement device that applied a 50 g load for 15 seconds. The nickel foam specimens were etched for 15 s with a mixture of 3 mL HF and 80 mL HNO₃, and the thickness of struts was determined by an optical microscope. Specific heat capacity Cp was measured by the Mettler Toledo thermal analysis with N₂ gas flow and thermal diffusivity α by Xenon Flash model XFA 500 was quantified. The H₂-TPR (temperature-programmed reduction) experiments were carried out in the NanoSord instrument (Sens Iran Co.), under a mixture of 5% H₂-95% argon gas with 10 sccm flow rate to determine the reducibility of nickel-alumina catalyst. Ni-alumina(γ) foam specimen was heated with a rate of 10 °Cmin⁻¹ up to 950 °C.

2. 3. Experimental Set-Up for Catalytic Reaction

The performance of the foam catalysts was studied in a pilot system under atmospheric pressure, as shown in Figure 1. A quartz tube reactor with a 28 mm inner diameter was loaded with a 7.64 g synthesized foam catalyst, 50 mL, and the remained volume was filled with inactive alumina(α). First, the Ni-alumina(γ) foam was reduced in situ before injecting methane/steam mixture by pure hydrogen at 430 °C for 120 min with a 5 °Cmin⁻¹ heating rate. The methane-water mixture (Steam/CH₄; v/v:3) was injected into the quartz tube through a dosing

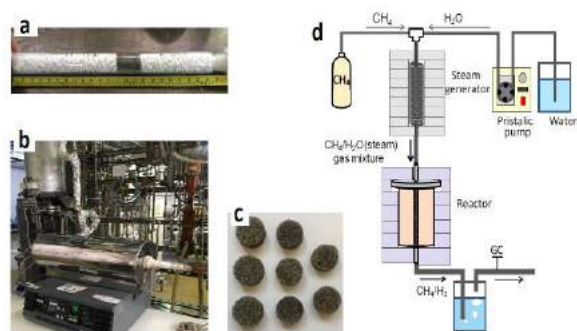


Figure 1. (a) Quartz tube filled with Ni-alumina foam catalysts, (b) catalysts of test pilot, (a) Ni- alumina (γ) foams, and (d) schematic picture for catalyst test setup

pump (LATEK- P700), which controlled the feed rate with gas hourly space velocity (GHSV) of 2000 h^{-1} . The tube reactor temperature was set at $500 \text{ }^\circ\text{C}$. The product gasstream passed through a condenser at the outlet of the reactor, and the unreacted water was stored in a tank. The dry gas outlet (H_2 , CH_4) was analyzed by the online gas chromatography (GC) (model Agilent Technologies 6890N) equipped with a thermal conductive detector (TCD) and flame ionization detector (FID). The catalytic performances of the Ni-alumina(γ) coated layer on nickel foam prepared in situ were measured.

3. RESULTS AND DISCUSSION

Thermogravimetric analysis was performed to determine the thermal stability of polyurethane foam by using a TA Instrument BAHN STA 503. Samples of 0.22 g were heated up to $650 \text{ }^\circ\text{C}$ at a heating rate of $10 \text{ }^\circ\text{Cmin}^{-1}$ in a nitrogen atmosphere. As shown in graph Figure 2, a very slight rate change seen at $100\text{-}120 \text{ }^\circ\text{C}$ may be for water evaporation while PU foam was decomposing with a rapid rate at $290\text{-}400 \text{ }^\circ\text{C}$ that was associated with the polyol main chain and urethane bond breaking as reported by other researches [45, 46]. As mentioned pyrolysis was done to remove PU substrate with the least probable crack formation by a controlled procedure [16]. Moreover, the alumina must penetrate uniformly inside the tortuous nickel foam without blocking the foam pores. In continue chemical pre-treatment by 6 M HCl was applied to the pure nickel foam to increment the adhesion of the strands' surface for pulsed electrodeposition of Ni- γ alumina [34]. As per SEM images, in Figure 3(a), pure nickel foam showed sound struts with no cracks. Moreover, in Figure 3(b), (c) and (d) grain boundaries of nickel foams pre-treated in HCl at 70 and $80 \text{ }^\circ\text{C}$ for 10 and 15 minutes were obviously seen. Here, the foam at $70 \text{ }^\circ\text{C}$ in HCl was observed more stable than that of the specimen heated at $80 \text{ }^\circ\text{C}$, however, etching the foam at severe conditions, heated at $80 \text{ }^\circ\text{C}$ for

15 min , caused the foam losing integrity. Therefore, the optimized condition for chemical pretreatment by 6 M HCl at $80 \text{ }^\circ\text{C}$ for 10 min by firm struts in foam structure.

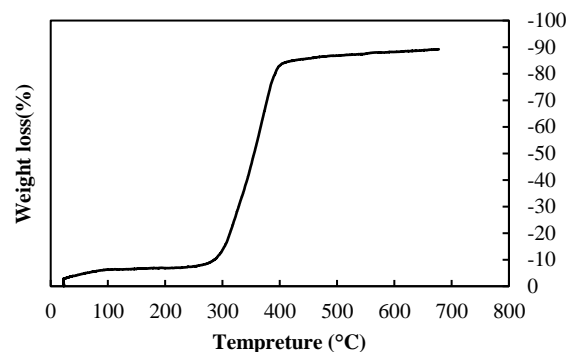


Figure 2. Thermal stability analysis of PU foam

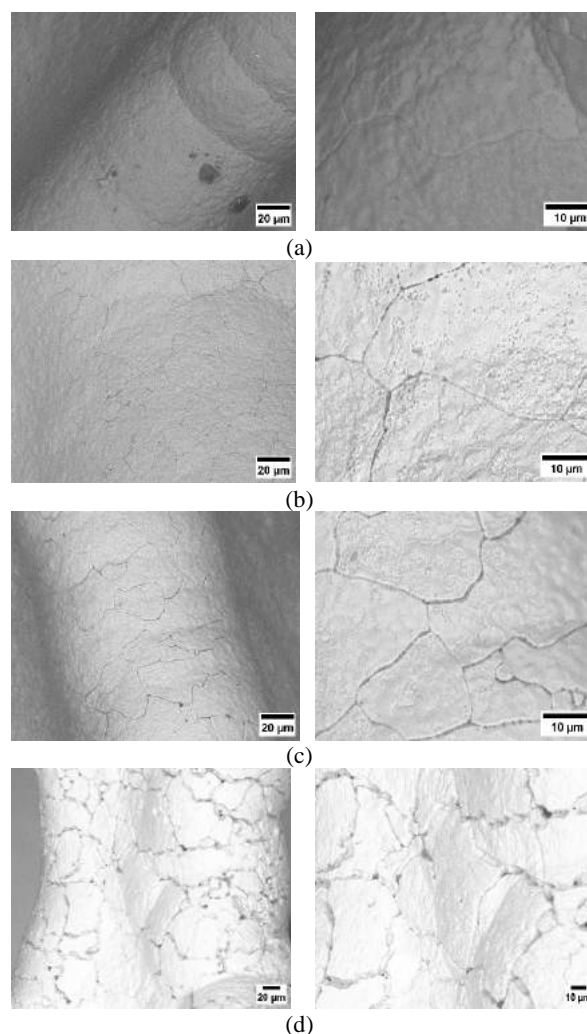


Figure 3. SEM images of surface of struts of (a) pure nickel foam, (b) pretreated nickel foam at $70 \text{ }^\circ\text{C}$ for 10 min , (c) pretreated nickel foam at $80 \text{ }^\circ\text{C}$ for 10 min , and (d) pretreated nickel foam at $80 \text{ }^\circ\text{C}$ for 15 min

According to XRD patterns illustrated in Figure 4, three primary reflections at 2θ of 44.64° , 51.92° , and 76.46° designated to the (111), (200), and (220) planes of the face-centered-cubic (FCC) nickel, confirmed that Ni was the dominant constituent of the obtained foam (JCPDS no. 04-0850). Meanwhile, there were small peaks of Ni-P in the XRD pattern, due to the sodium hypophosphite reducing agent in the plating solution. However, by reducing the concentration of the reducing agents and plating solution with a higher pH, the amount of phosphorus and sodium to form the Ni-P layer can be minimized [16]. For nickel foam coated by Ni- γ -alumina in this study displayed spinel NiAl_2O_4 at $2\theta=31.4^\circ$, 45° , 68.9° , 80° (JCPDS no. 10-0339). However, some other detected peaks $2\theta=25.1^\circ$, 37.7° , 57.5° , 68° , and 70° corresponding to deposited alumina (JCPDS no. 46-1212) and rhombohedral phase NiO at $2\theta=43^\circ$, 62.8° (JCPDS no. 22-118) was observed and via the following reaction and calcination at temperatures above 700°C , the NiAl_2O_4 formed as Equation (5). Calcination causes formation of NiAl_2O_4 spinel phase, especially in the case of Al_2O_3 (γ) presence [47].



Here, surface area of Ni-alumina(γ) foam measured by BET method and reported in Table 1 for comparison. Figure 5 indicated cross-sectional micrographs of nickel- γ -alumina nanocomposite foams. In fact, the wall thickness of $2\text{-}5\ \mu\text{m}$ gained after electroless then increased to $50\text{-}80\ \mu\text{m}$ by electrodeposition. In continue, by pulse electro- codeposition coating of nickel- γ -alumina nanocomposite over the former foam gave a three-dimensional structure with $230\ \mu\text{m}$ thick and hollow struts. The white sections indicated foam cell struts and the grey section for the empty space between

TABLE 1. Specific surface area (BET) of investigated nickel foam catalysts

Sample	S.S.A (m^2g^{-1})	PPI
Nickel foam	1.48	45
Ni- alumina(γ) foam	48	45
Ru/Ce/Ni foam (Ni foam via CeO_2 electroprecipitation and impregnation with Ru [18])	39	75
AlSB/Ni foam aluminium tri-sec butylate (AlSB) [34]	5.6	-
Allp/Ni foam ,aluminium isopropoxide (AllP) [34]	6.9	-
Pre-treated Ni foam in catalytic methane decomposition (CMD) [32]	5.4	110
Pre-treated Ni foam with grown carbon nanofibers in catalytic methane decomposition(CMD) [32]	8.7	110

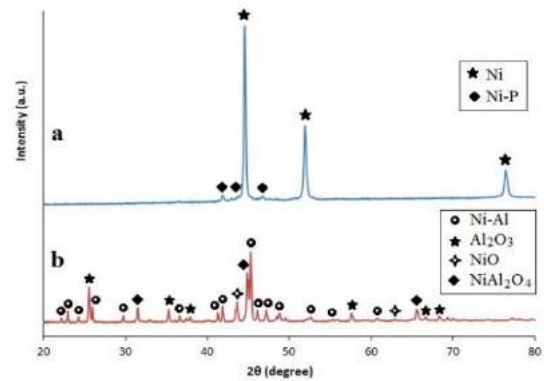


Figure 1. XRD patterns for (a) pure nickel foam and (b) nickel foam coated with nickel- γ -alumina

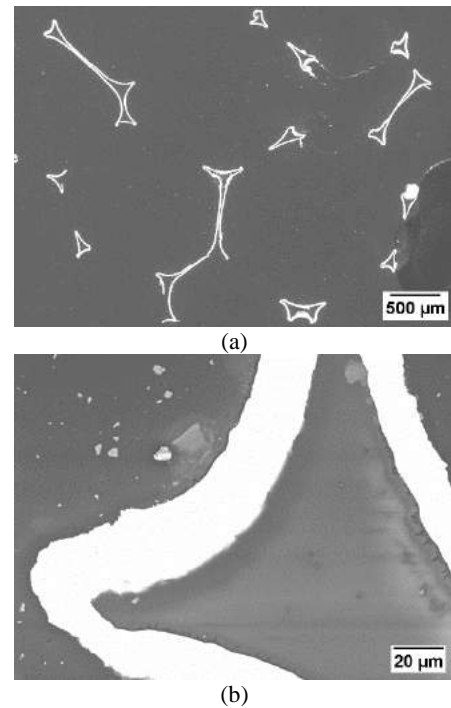
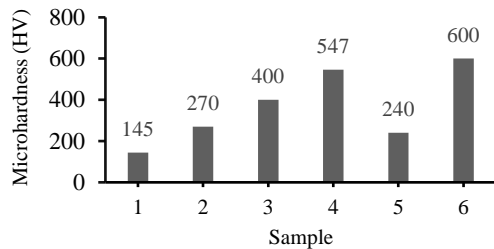


Figure 2. Optic microscopic images of electrodeposited Ni-alumina (γ) nanocomposite open cell foam specimen mounted in epoxy resin and polished, a) $\times 40$, b) $\times 1k$

the cells and the separate islands seen because of three-dimensional porous skeleton of foam appear in the surface by polishing. In the current work, using pulse codeposition of Ni/alumina(γ) reinforced nanoparticles on nickel foam increased hardness from 145 to 547 (HV). The average of five different measurements determined the final hardness shown in Figure 6.

The compressive stress-strain curves of nickel foams and Ni-alumina(γ) coated foam indicated in Figure 7. In these curves, three distinct regions seen as: (i) the linear elastic deformation (cell edges yield in bending area), (ii) collapse plateau (sudden decrease in stress after the first



- 1 Nickel foam (electrodeposited Ni foam)
- 2 Ni coating over steel substrate [37]
- 3 Nickel foam (electrolyt jet electrodeposited Ni foam) [25]
- 4 Ni-nano γ alumina codeposition over Ni foam
- 5 Open cell Ni-35Cr-22Fe foam(gas-phase codeposition of Cr and Fe over Ni foam) [48]
- 6 Ni-8.5% nano Al_2O_3 coating over steel substrate [37]

Figure 6. Results of the micro-hardness tests conducted at room temperature

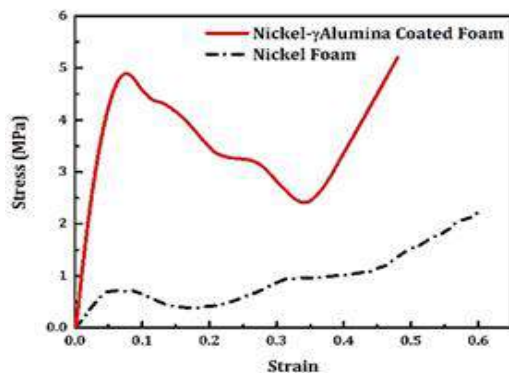


Figure 7. Compressive stress-strain curves of nickel foams and Ni-alumina(γ) coated foam

peak of stress and plateau area), and (iii) densification region (slight increase in strain, rapid growth of stress, and more significant line slope). The mechanism of linear elasticity depends on whether the cells are open or closed. At low relative densities, open-cell foams deform primarily by cell-wall bending [49, 50]. Therefore, in this study we tried to increase the strength by struts thickness growth from $50 \mu\text{m}$ to $230 \mu\text{m}$. As shown in Figure 7, nickel foam does not oscillate from beginning to end in stage II with good compressive stability; in contrast, in the Ni-alumina(γ) nanocomposite, noticeable oscillation and a sudden decrease in stress were seen in stage II. Compressive strength (stress peak after linear elastic phase) of foams for nickel foam obtained 1.1 MPa. However, compression strength of Ni-alumina(γ) nanocomposite foam increased to 5MPa by adding reinforcement alumina nanoparticles. Ni- Al_2O_3 (γ) foam compression strength increased drastically by pulse

electro codeposition of the Ni-alumina and its elastic modulus improved. Reasons for increasing the strength and elastic modulus of nickel foam with the electrochemical coating are alumina nano particles. Higher compression strength could mean high mechanical stability of bottom-bed catalysts against upper-bed catalysts in the reformer where a suitable gas permeability is required. Thermal conductivity of Ni- Al_2O_3 (γ) foam with density (ρ) of 0.20 gcm^{-3} calculated by measurements of thermal diffusivity (α) and specific heat capacity C_p . Thermal diffusivity (α) gained $4.41 \times 10^{-6} \text{ m}^2\text{s}^{-1}$ with flash xenon technique and values of specific heat capacity, C_p , measured by differential scanning calorimetry (DSC). Moreover, the changes of α by temperature rise was negligible.

The thermal conductivity calculated by Equation (6) [51, 52].

$$\lambda = \alpha \times \rho \times C_p \quad (6)$$

As stated in Table 2 by temperature rise, both C_p and thermal conductivity (λ) of nanocomposite Ni-alumina(γ) foam increased as well. Besides, the distribution of alumina coat over nickel foam and all of the other elements dispersed uniformly as seen in Figure 8. Pure nickel crystalline coatings have a truncated pyramidal structure, i.e., a typical morphology for pure nickel electrodeposits with (111) preferred texture [53, 54]. The modifications in the surface morphologies are attributed to the change from a preferred orientation to a random-oriented electrodeposit, and the addition of Al_2O_3 particulates deteriorates the pyramidal structure [54]. Considering FESEM images in Figure 9, a large number of irregularly indicated spherical nanoparticles with sizes 45 to 89 nm of Al_2O_3 and NiO. Al_2O_3 . In fact, the layer of nanocomposite coating was less uniform and rougher with cauliflower morphology and the surface morphology could be attributed to the change from a preferred orientation to a random-oriented electrodeposition, and the embedded alumina nano particles in nickel matrix deteriorates the pyramidal structure [54, 55]. As known the reduced metal present on the surface of the catalyst was considered active in the partial oxidation of methane. The temperature-programmed reduction (TPR) can suggest the number of species and a relative classification of energy bonds between the reducing element and its environment. Ni-alumina foam specimen with a rate of $10 \text{ }^\circ\text{C}\cdot\text{min}^{-1}$ heated up to $950 \text{ }^\circ\text{C}$. The result, the H_2 -TPR graph in Figure 10, exhibited two reduction peaks a sharp one at $400 \text{ }^\circ\text{C}$ and a broader peak at $700\text{-}720 \text{ }^\circ\text{C}$. Ni was reduced at a relatively low temperature (lower than $450 \text{ }^\circ\text{C}$). The sharp peak at $400 \text{ }^\circ\text{C}$ was related to nickel oxide reduction having weak interaction with alumina support and this reduction leads to the deposition of nickel metal on γ - Al_2O_3 . In contrast, the second broader peak at $700\text{-}720 \text{ }^\circ\text{C}$

relates to the reduction of the spinel NiAl_2O_4 occurred at high temperature in a large range of temperatures [56, 57].

As depicted in Figure 11, the conversion of methane to products was calculated via the difference between

TABLE 1. Specific heat capacity (Cp) measurement by temperature

T (°C)	Cp (Jg ⁻¹ °C ⁻¹)	Thermal Conductivity (Wm ⁻¹ °C ⁻¹)
150	0.92	0.81
250	1.00	0.88
300	1.08	0.95
350	1.17	1.03
400	1.21	1.06
450	1.31	1.15
500	1.43	1.26
550	1.53	1.35

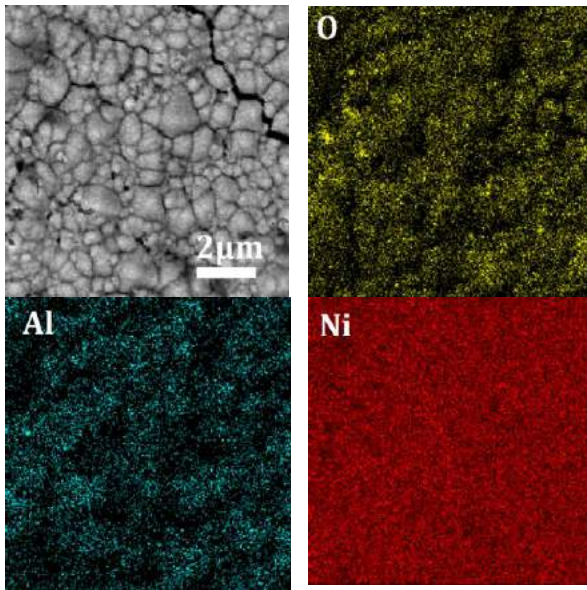


Figure 3. Map of the uniform dispersion of alumina on the Ni foam

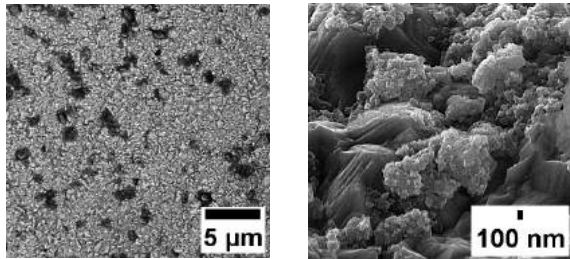


Figure 9. FESEM images of synthesized nickel foam with pulsed deposition of $\text{Ni-Al}_2\text{O}_3$ (γ) at $f=5$ Hz, $\theta=50\%$, time=60 min

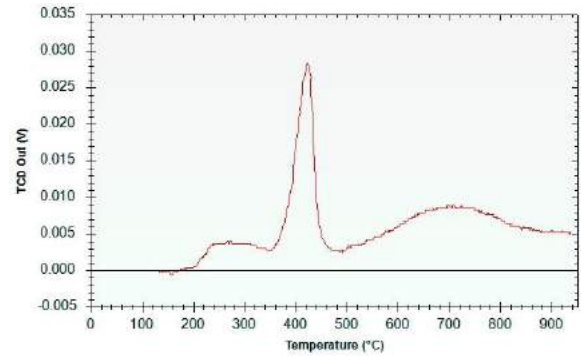


Figure 4. H₂-TPR graph of calcined nickel-alumina foam

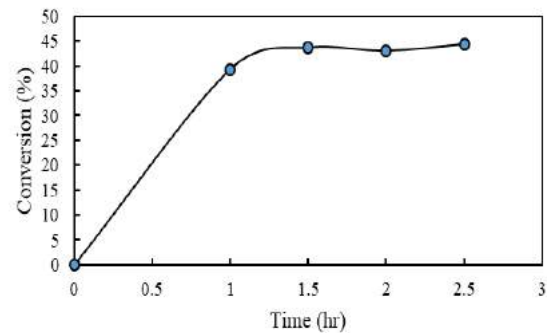


Figure 5. Methane conversion(%) -time of MSR

inlet and outlet flowrates ($F_{CH_4.in}$, $F_{CH_4.out}$) measured by online GC. After about two hours, the conversion of CH_4 reached 44% at 500 °C. The conversion of MSR reaction calculated by Equation (5). However, with the Boudouard reaction as Equation (4) occurrence at low temperatures (300–450 °C) carbon deposited on catalyst’s surface during MSR and caused it to deactivate some parts of the nickel foam catalyst and declined its efficiency.

For the selectivity, the below equation was used. The selectivity toward the hydrogen production calculated by Equation (6) that $F_{H_2.out}$ was outlet H_2 flowrate in online GC, then, the selectivity H_2 gained 2.4 upon reaching steady state phase as shown in Figure 12. Figure 13 depicted compositions of methane and hydrogen in the outlet at different time intervals for nickel foam coated with nickel-alumina(γ). Hydrogen synchronized with methane conversion and did not change significantly after 60 min. Methane exhibited a slight decreasing behavior with time. After 90 min stream time at 500 °C, H_2 and CH_4 reached 64.2% and 18%, respectively. The flowrate of hydrogen in the outlet did not match with stoichiometry of the reaction and there is an approximately 10 – 20 % error. This difference could be attributed to the purge of hydrogen at the beginning of the process and reduction of free NiO at lower temperature gave small metallic nickel particles.

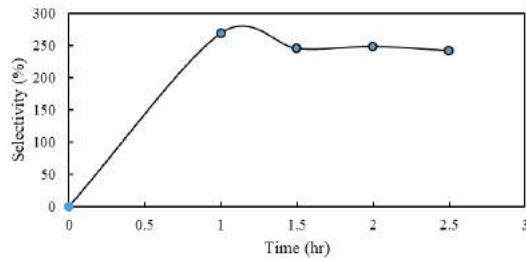


Figure 6. H₂ selectivity-time produced in MSR

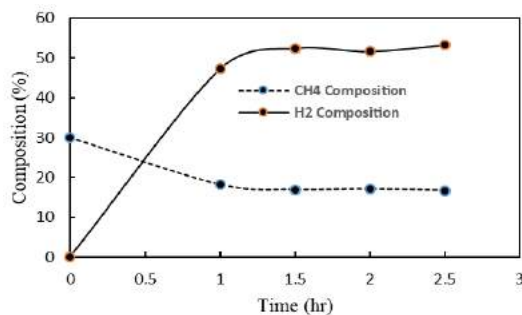


Figure 7. Composition of hydrogen and methane in the outlet of a MSR reactor

The free nickel foam without deposited alumina (metal oxide) showed no catalytic activity because the interface between nickel and alumina assumed as active sites necessary for catalytic reactions and the nickel-alumina interface by the presence of NiAl₂O₄ nanoparticles spinel improved catalytic properties. In nickel-alumina foam catalysts, coating Al₂O₃(γ) nanoparticles with high specific surface area over metal foam with high thermal conductivity improve heat transfer in MSR reformers. Then, at lower temperatures, the required heat flux provided with the appropriate efficiency in MSR [9, 22]. Furthermore, the use of metal foam increases CH₄ conversion due to improved heat distribution inside the reformer with better contact between the gas mixture and the open-cell foam catalyst.

$$\text{Conversion } CH_4(\%) = \frac{(F_{CH_4, in} - F_{CH_4, out})}{F_{CH_4, in}} \times 100 \quad (7)$$

$$SH_2 = \frac{(F_{H_2, out})}{F_{CH_4, out} - F_{CH_4, in}} \times 0.5 \quad (8)$$

To produce hydrogen, H₂O reacts with nickel surface atoms to absorb oxygen and produce gaseous hydrogen. Methane was also adsorbed on nickel surface atoms. The adsorbed methane either reacts with the adsorbed oxygen or decomposes to form chemical radicals [58].

Considering the catalytic test in this study, it resulted that the favorable temperature for the MSR decreased to 500 °C compared to the common MSR reaction

temperature at 700 °C to 720 °C. It could be concluded that here open-cell nickel foam coated with Ni-alumina utilization as nanocatalyst caused better heat transfer through reaction chambers and furthermore somehow the purged H₂ into the reactor for the catalysts reduction, the unreacted hydrogen can be burned to supply heat.

4. CONCLUSIONS

In this work, coating Ni-Al₂O₃(γ) nanocatalyst by pulse electrocodeposition over nickel foam is a way to enhance the thermal properties of it for MSR. Results indicated that the catalysts prepared by the nickel foam yielded higher thermal conductivity and compression strength compared to the nickel based pellet catalyst. By measuring thermal diffusivity(α) gained $4.41 \times 10^{-6} \text{ m}^2\text{s}^{-1}$ and values of specific heat capacity, C_p , and thermal conductivity (λ) increased by 65% with temperature increment between 150 to 550°C in Ni-alumina(γ) foam nanocatalyst. XRD analysis indicated NiO, NiAl₂O₄ in the synthesized nickel-alumina(γ) foam. The nickel-alumina(γ) nanocomposite plus NiAl₂O₄ and alumina(γ) nanoparticles increased the hardness to 547 (HV) and the compressive strength of the fabricated nanocatalyst from 1.1 MPa to 5 MPa with a progressive crushing instead of a brittle failure. In addition, S_{BET} of the pure nickel foam was $1.48 \text{ m}^2\text{g}^{-1}$, which increased to $48 \text{ m}^2\text{g}^{-1}$ by adding alumina(γ) nanoparticles. The Ni-alumina(γ) nanocomposite had active sites at the nickel-alumina interface and the deposited NiAl₂O₄ spinel, which increased the catalytic activity of the product. The reason for the low-temperature MSR in this study could be stated as the metallic nickel foam with high thermal conductivity made it a potential attraction for the novel design in this study by decreasing the favorable temperature for the MSR to 500 °C due to highly heat transfer compared to the traditional steam reforming reaction temperature at 700 °C.

Despite the above advances, further improvement should be focused on effective parameters such as micro and mesopores supports and utilization of different promoters like rare earth elements such as lanthanum and cerium or their oxides in synthesizing new alloyed foam nanocatalysts for hydrogen production. However, few investigations have been done to the challenges of Ni-Alumina foam nanocatalysts regeneration, as well as the kinetics study of the catalytically active sites in methane reforming reactions.

5. ACKNOWLEDGEMENT

The authors are grateful Sharif University of technology, University of Toronto for general support and Research Institute of Petroleum Industry (RIPI) of assistance catalytic pilot tests.

6. DATA AVAILABILITY

The raw/processed data required to reproduce these findings cannot be shared at this time due to technical or time limitations.

7. REFERENCES

- Acar, C. and Dincer, I., "Review and evaluation of hydrogen production options for better environment", *Journal of Cleaner Production*, Vol. 218, (2019), 835-849. <https://doi.org/10.1016/j.jclepro.2019.02.046>
- Etmnan, A. and Sadrnezhaad, S., "A two step microwave-assisted coke resistant mesoporous ni-co catalyst for methane steam reforming", *Fuel*, Vol. 317, (2022), 122411. <https://doi.org/10.1016/j.fuel.2021.122411>
- Hosseini, Z., Mollazadeh Beidokhti, S., Vahdati khaki, J. and Pourabdoli, M., "Preparation of porous alumina/nano-nickel composite by gel casting and carbothermic reduction", *International Journal of Engineering, Transactions A: Basics*, Vol. 35, No. 1, (2022), 220-227. DOI:10.5829/IJE.2022.35.01A.21
- Tribalis, A., Panagiotou, G.D., Bourikas, K., Sygellou, L., Kennou, S., Ladas, S., Lycourghiotis, A. and Kordulis, C., "Ni catalysts supported on modified alumina for diesel steam reforming", *Catalysts*, Vol. 6, No. 1, (2016), 11. <https://doi.org/10.3390/catal6010011>
- Silva, C.K.S., Baston, E.P., Melgar, L.Z. and Bellido, J.D.A., "Ni/al₂O₃-la₂O₃ catalysts synthesized by a one-step polymerization method applied to the dry reforming of methane: Effect of precursor structures of nickel, perovskite and spinel", *Reaction Kinetics Mechanisms and Catalysis*, Vol. 128, No. 1, (2019), 251-269. DOI:10.1007/s11144-019-01644-3
- Naeem, M.A., Al-Fatesh, A.S., Fakeeha, A.H. and Abasaeed, A.E., "Hydrogen production from methane dry reforming over nickel-based nanocatalysts using surfactant-assisted or polyol method", *International Journal of Hydrogen Energy*, Vol. 39, No. 30, (2014), 17009-17023. <https://doi.org/10.1016/j.ijhydene.2014.08.090>
- Pashchenko, D., "Experimental investigation of reforming and flow characteristics of a steam methane reformer filled with nickel catalyst of various shapes", *Energy Conversion and Management*, Vol. 185, (2019), 465-472. <https://doi.org/10.1016/j.enconman.2019.01.103>
- Rohani, A., Allahkaram, L. and Omidvar, A., "Effect of nickel-alumina nanoparticle catalyst on the performance of methane steam reforming process", *American Journal of Nanoscience and Nanotechnology*, Vol. 1, No. 3, (2013), 74-78. DOI:10.11648/j.nano.20130103.13
- Meloni, E., Martino, M. and Palma, V., "A short review on ni based catalysts and related engineering issues for methane steam reforming", *Catalysts*, Vol. 10, No. 3, (2020), 352. <https://doi.org/10.3390/catal10030352>
- Baharudin, L. and Watson, M.J., "Monolithic substrate support catalyst design considerations for steam methane reforming operation", *Reviews in Chemical Engineering*, Vol. 34, No. 4, (2018), 481-501. <https://doi.org/10.1515/revce-2016-0048>
- Maleki, B., Natheghi, H., Tayebee, R., Alinezhad, H., Amiri, A., Hossieni, S.A. and Nouri, S.M.M., "Synthesis and characterization of nanorod magnetic co-fe mixed oxides and its catalytic behavior towards one-pot synthesis of polysubstituted pyridine derivatives", *Polycyclic Aromatic Compounds*, Vol. 40, No. 3, (2020), 633-643. <https://doi.org/10.1080/10406638.2018.1469519>
- Tsiotsias, A.I., Charisiou, N.D., Yentekakis, I.V. and Goula, M.A., "Bimetallic ni-based catalysts for CO₂ methanation: A review", *Nanomaterials*, Vol. 11, No. 1, (2020), 28. <https://doi.org/10.3390/nano11010028>
- Aramouni, N.A.K., Touma, J.G., Tarboush, B.A., Zeaiter, J. and Ahmad, M.N., "Catalyst design for dry reforming of methane: Analysis review", *Renewable and Sustainable Energy Reviews*, Vol. 82, (2018), 2570-2585. <https://doi.org/10.1016/j.rser.2017.09.076>
- Barzegari, F., Kazemeini, M., Farhadi, F., Rezaei, M. and Keshavarz, A., "Preparation of mesoporous nanostructure nio-mgo-sio₂ catalysts for syngas production via propane steam reforming", *International Journal of Hydrogen Energy*, Vol. 45, No. 11, (2020), 6604-6620. <https://doi.org/10.1016/j.ijhydene.2020.01.007>
- Bianchi, E., Heidig, T., Visconti, C.G., Groppi, G., Freund, H. and Tronconi, E., "Heat transfer properties of metal foam supports for structured catalysts: Wall heat transfer coefficient", *Catalysis Today*, Vol. 216, (2013), 121-134. <https://doi.org/10.1016/j.cattod.2013.06.019>
- Zafardoagoo, M. and Sadrnezhaad, S.K., "Synthesis of porous nickel foam based on electroless plating on polymeric substrate and electrodeposition", *Journal of Advanced Materials and Technologies*, Vol. 11, No. 1, (2022), 69-79. <https://doi.org/10.30501/jamt.2022.325426.1210>
- Kulshreshtha, A. and Dhakad, S.K., "Preparation of metal foam by different methods: A review", *Materials Today: Proceedings*, Vol. 26, (2020), 1784-1790. <https://doi.org/10.1016/j.matpr.2020.02.375>
- Cimino, S., Cepollaro, E.M., Lisi, L., Fasolin, S., Musiani, M. and Vázquez-Gómez, L., "Ru/ce/ni metal foams as structured catalysts for the methanation of CO₂", *Catalysts*, Vol. 11, No. 1, (2021), 13. <https://doi.org/10.3390/catal11010013>
- Settar, A., Abboudi, S. and Lebaal, N., "Effect of inert metal foam matrices on hydrogen production intensification of methane steam reforming process in wall-coated reformer", *International Journal of Hydrogen Energy*, Vol. 43, No. 27, (2018), 12386-12397. <https://doi.org/10.1016/j.ijhydene.2018.04.215>
- Ashraf, M.A., Sanz, O., Montes, M. and Specchia, S., "Insights into the effect of catalyst loading on methane steam reforming and controlling regime for metallic catalytic monoliths", *International Journal of Hydrogen Energy*, Vol. 43, No. 26, (2018), 11778-11792. <https://doi.org/10.1016/j.ijhydene.2018.04.126>
- Gokon, N., Nakamura, S., Matsubara, K. and Kodama, T., "Carbonate molten-salt absorber/reformer: Heating and steam reforming performance of reactor tubes", *Energy Procedia*, Vol. 49, (2014), 1940-1949. <https://doi.org/10.1016/j.egypro.2014.03.206>
- Palma, V., Ricca, A., Martino, M. and Meloni, E., "Innovative structured catalytic systems for methane steam reforming intensification", *Chemical Engineering and Processing-Process Intensification*, Vol. 120, (2017), 207-215. <https://doi.org/10.1016/j.cep.2017.07.012>
- Basile, F., Benito, P., Del Gallo, P., Fornasari, G., Gary, D., Rosetti, V., Scavetta, E., Tonelli, D. and Vaccari, A., "Highly conductive ni steam reforming catalysts prepared by electrodeposition", *Chemical Communications*, No. 25, (2008), 2917-2919. <https://doi.org/10.1039/B801645C>
- Cheri, A. and Nebbali, R., "Numerical analysis on autothermal steam methane reforming: Effects of catalysts arrangement and metal foam insertion", *International Journal of Hydrogen Energy*, Vol. 44, No. 39, (2019), 22455-22466. DOI:10.1016/j.ijhydene.2018.12.203

25. Chen, J., "Mechanical properties of electrolyte jet electrodeposited nickel foam", *Journal of Engineering Science and Technology Review*, Vol. 6, No. 2, (2013), 53-56. DOI:10.25103/jestr.062.12
26. Li, Y.-g., Wei, Y.-h., Hou, L.-f., Guo, C.-l. and Yang, S.-q., "Fabrication and compressive behaviour of an aluminium foam composite", *Journal of Alloys and Compounds*, Vol. 649, (2015), 76-81. <https://doi.org/10.1016/j.jallcom.2015.07.049>
27. Wang, X., Zhou, Y., Li, J. and Li, H., "Uniaxial compression mechanical properties of foam nickel/iron-epoxy interpenetrating phase composites", *Materials*, Vol. 14, No. 13, (2021), 3523. <https://doi.org/10.3390/ma14133523>
28. Parveez, B., Jamal, N.A., Anuar, H., Ahmad, Y., Aabid, A. and Baig, M., "Microstructure and mechanical properties of metal foams fabricated via melt foaming and powder metallurgy technique: A review", *Materials*, Vol. 15, No. 15, (2022). <https://doi.org/10.3390/ma15155302>
29. Liu, J., Zhang, L., Liu, S., Han, Z. and Dong, Z., "Effect of si content on microstructure and compressive properties of open-cell mg composite foams reinforced by in-situ mg2si compounds", *Materials Characterization*, Vol. 159, (2020), 110045. <https://doi.org/10.1016/j.matchar.2019.110045>
30. Chen, J., Zhang, P., Cheng, Y. and Liu, J., "On the crushing response of the functionally graded metallic foams based on 3d voronoi model", *Thin-Walled Structures*, Vol. 157, (2020), 107085. <https://doi.org/10.1016/j.tws.2020.107085>
31. Somwanshi, S.B., Somvanshi, S.B. and Kharat, P.B., "Nanocatalyst: A brief review on synthesis to applications", in *Journal of Physics: Conference Series*, IOP Publishing. Vol. 1644, No. 1, (2020), 012046. DOI:10.1088/1742-6596/1644/1/012046
32. Ren, Z., Zhang, J., Bai, Y., Wang, J., Chen, H., Hao, Q. and Ma, X., "Unsupported nickel catalyst prepared from nickel foam for methane decomposition and recycling the carbon deposited spent catalyst", *International Journal of Hydrogen Energy*, Vol. 46, No. 42, (2021), 21853-21865. <https://doi.org/10.1016/j.ijhydene.2021.04.026>
33. Chai, R., Li, Y., Zhang, Q., Zhao, G., Liu, Y. and Lu, Y., "Monolithic ni-mox/ni-foam (m= al, zr or y) catalysts with enhanced heat/mass transfer for energy-efficient catalytic oxy-methane reforming", *Catalysis Communications*, Vol. 70, (2015), 1-5. <https://doi.org/10.1016/j.catcom.2015.07.007>
34. Pegios, N., Schroer, G., Rahimi, K., Palkovits, R. and Simeonov, K., "Design of modular ni-foam based catalysts for dry reforming of methane", *Catalysis Science & Technology*, Vol. 6, No. 16, (2016), 6372-6380. <http://dx.doi.org/10.1039/C6CY00282J>
35. Lajevardi, S.A., Shahrabadi, T. and Szpunar, J.A., "Synthesis of functionally graded nano Al₂O₃-Ni composite coating by pulse electrodeposition", *Applied Surface Science*, Vol. 279, (2013), 180-188. <https://doi.org/10.1016/j.apsusc.2013.04.067>
36. Jegan, A. and Venkatesan, R., "Characterization and optimization of pulse electrodeposition of Ni/nano- Al₂O₃ composite coatings", *International Journal of Minerals, Metallurgy, and Materials*, Vol. 20, No. 5, (2013), 479-485. <https://doi.org/10.1007/s12613-013-0754-z>
37. Gül, H., Kılıç, F., Aslan, S., Alp, A. and Akbulut, H., "Characteristics of electro-co-deposited Ni- Al₂O₃ nano-particle reinforced metal matrix composite (mmc) coatings", *Wear*, Vol. 267, No. 5-8, (2009), 976-990. <https://doi.org/10.1016/j.wear.2008.12.022>
38. Mirzamohammadi, S., Khorsand, H., Aliofkhaezai, M. and Shtansky, D., "Effect of carbamide concentration on electrodeposition and tribological properties of Al₂O₃ nanoparticle reinforced nickel nanocomposite coatings", *Tribology International*, Vol. 117, (2018), 68-77. <https://doi.org/10.1016/j.triboint.2017.08.003>
39. Karimi, E.Z., Barzegar, F., Moloodi, A. and Zolfaghari, R., "Hardness and compressive properties of open-cell nickel foam reinforced by nano-sic particles", *Metallurgical and Materials Transactions B-Process Metallurgy and Materials Processing Science*, Vol. 52, No. 5, (2021), 3439-3446. DOI:10.1007/s11663-021-02273-9
40. Kolaczowski, S.T., Awdry, S., Smith, T., Thomas, D., Torkuhl, L. and Kolvenbach, R., "Potential for metal foams to act as structured catalyst supports in fixed-bed reactors", *Catalysis Today*, Vol. 273, (2016), 221-233. <https://doi.org/10.1016/j.cattod.2016.03.047>
41. Syamsuir, S., Soegijono, B., Yudanto, S.D., Basori, B., Ajiriyanto, M.K., Nanto, D. and Susetyo, F.B., "Electrolyte temperature dependency of electrodeposited nickel in sulfate solution on the hardness and corrosion behaviors", *International Journal of Engineering, Transactions C: Aspects*, Vol. 36, No. 6, (2023), 1193-1200. DOI:10.5829/ije.2023.36.06c.18
42. Oveisi, H. and Geramipour, T., "High mechanical performance alumina-reinforced aluminum nanocomposite metal foam produced by powder metallurgy: Fabrication, microstructure characterization, and mechanical properties", *Materials Research Express*, Vol. 6, No. 12, (2020), 1250c1252. DOI:10.1088/2053-1591/ab608b
43. Kim, S., Tserengombo, B., Choi, S.H., Noh, J., Huh, S., Choi, B., Chung, H., Kim, J. and Jeong, H., "Experimental investigation of heat transfer coefficient with Al₂O₃ nanofluid chock in small diameter tubes", *Applied Thermal Engineering*, Vol. 146, No., (2019), 346-355. DOI:10.1016/j.applthermaleng.2018.10.001
44. Sharifi, Z., Asgari, G. and Seid-Mohammadi, A., "Sonocatalytic degradation of p-chlorophenol by nanoscale zero-valent copper activated persulfate under ultrasonic irradiation in aqueous solutions", *International Journal of Engineering, Transactions C: Aspects*, Vol. 33, No. 6, (2020), 1061-1069. DOI:10.5829/IJE.2020.33.06C.03
45. Kirgizov, A.Y., Il'yasov, I.R., Laskin, A.I. and Lamberov, A.A., "An investigation of surface transformations of nickel highly porous cellular material with an applied alumina layer during its synthesis", *Protection of Metals and Physical Chemistry of Surfaces*, Vol. 54, No. 5, (2018), 788-794. DOI:10.1134/s2070205118040068
46. Jiao, L., Xiao, H., Wang, Q. and Sun, J., "Thermal degradation characteristics of rigid polyurethane foam and the volatile products analysis with tg-ftir-ms", *Polymer Degradation and Stability*, Vol. 98, No. 12, (2013), 2687-2696. <https://doi.org/10.1016/j.polymdgradstab.2013.09.032>
47. Nikolić, V., Kamberović, Ž., Korać, M., Anđić, Z., Mihajlović, A. and Uljarević, J.B., "Nickel-based catalysts: Dependence of properties on nickel loading and modification with palladium", *Hemijaska industrija*, Vol. 70, No. 2, (2016), 137-142. DOI:10.2298/HEMIND140928090N
48. Qiu, P., WU, G.-h., SUN, D.-l., XIU, Z.-y., ZHANG, Q. and HU, Z.-l., "Compressive property and energy absorption characteristic of 3d open-cell Ni-Cr-Fe alloy foams under quasi-static conditions", *Transactions of Nonferrous Metals Society of China*, Vol. 22, (2012), 566-572. [https://doi.org/10.1016/S1003-6326\(12\)61762-2](https://doi.org/10.1016/S1003-6326(12)61762-2)
49. Luo, G., Xue, P. and Li, Y.L., "Experimental investigation on the yield behavior of metal foam under shear-compression combined loading", *Science China-Technological Sciences*, Vol. 64, No. 7, (2021), 1412-1422. DOI:10.1007/s11431-020-1786-6
50. Wan, T., Liu, Y., Zhou, C., Chen, X. and Li, Y., "Fabrication, properties, and applications of open-cell aluminum foams: A review", *Journal of Materials Science & Technology*, Vol. 62, (2021), 11-24. <https://doi.org/10.1016/j.jmst.2020.05.039>
51. Mishra, R., Militky, J. and Venkataraman, M., 7 - nanoporous materials, in *Nanotechnology in textiles*, R. Mishra and J. Militky,

- Editors, 2019, Woodhead Publishing, 311-353. <https://doi.org/10.1016/B978-0-08-102609-0.00007-9>
52. Speight, J.G., 3 - unconventional gas, in Natural gas (second edition), J.G. Speight, Editor. 2019, Gulf Professional Publishing: Boston. 59-98. <https://doi.org/10.1016/B978-0-12-809570-6.00003-5>
53. Feng, L., Ren, Y.-Y., Zhang, Y.-H., Wang, S. and Li, L., "Direct correlations among the grain size, texture, and indentation behavior of nanocrystalline nickel coatings", *Metals*, Vol. 9, No. 2, (2019), 188. <https://doi.org/10.3390/met9020188>
54. Sajjadnejad, M., Omidvar, H. and Javanbakht, M., "Influence of pulse operational parameters on electrodeposition, morphology and microstructure of ni/nanodiamond composite coatings", *International Journal of Electrochemical Science*, Vol. 12, No. 5, (2017), 3635-3651. <https://doi.org/10.20964/2017.05.5>
55. Shafiee, Z., Bahrololoom, M.E. and Hashemi, B., "Electrodeposition of nanocrystalline Ni/Ni- Al₂O₃ nanocomposite modulated multilayer coatings", *Materials & Design*, Vol. 108, (2016), 19-26. <https://doi.org/10.1016/j.matdes.2016.06.018>
56. Tanksale, A., Beltramini, J., Dumesic, J. and Lu, G.Q., "Effect of pt and pd promoter on ni supported catalysts—a tpr/tpo/tpd and microcalorimetry study", *Journal of Catalysis*, Vol. 258, No. 2, (2008), 366-377. <https://doi.org/10.1016/j.jcat.2008.06.024>
57. Daroughegi, R., Meshkani, F. and Rezaei, M., "Enhanced low-temperature activity of CO₂ methanation over ceria-promoted ni-Al₂O₃ nanocatalyst", *Chemical Engineering Science*, Vol. 230, (2021). DOI:10.1016/j.ces.2020.116194
58. Navarro, M.V., Plou, J., Lopez, J.M., Grasa, G. and Murillo, R., "Effect of oxidation-reduction cycles on steam-methane reforming kinetics over a nickel-based catalyst", *International Journal of Hydrogen Energy*, Vol. 44, No. 25, (2019), 12617-12627. DOI:10.1016/j.ijhydene.2018.12.056

COPYRIGHTS

©2023 The author(s). This is an open access article distributed under the terms of the Creative Commons Attribution (CC BY 4.0), which permits unrestricted use, distribution, and reproduction in any medium, as long as the original authors and source are cited. No permission is required from the authors or the publishers.

**Persian Abstract****چکیده**

گرمایش بی رویه کره زمین محققین را برای ارتقاء تکنولوژی تولید انرژیهای پایدار اعم از تولید هیدروژن توسط ریفرمینگ متان-بخار آب، فرایندی اندوترم واداشته است. در این تحقیق نانوکاتالیستی بر پایه فوم سلول باز نیکل ۴۰ (حفره در اینج) با هدایت حرارتی بالا ساخته شد. این نانوکاتالیست با یک فرایند شیمیایی چندمرحله ای، عملیات پیش آماده سازی، تجزیه حرارتی، رسوب همنشینی الکتروشیمیایی پالسی نیکل-نانوذرات آلومینا (گاما) و کلسینه سنتز شد. ضریب دیفیوژن حرارتی (α) با تکنیک فلش زنون ۴۱/۴ مترمربع بر ثانیه و ظرفیت حرارتی ویژه (Cp) توسط گرماسنجی پوششی تفاضلی (DSC) اندازه گیری شدند و محاسبه هدایت حرارتی (λ) نشان می دهد این خواص با افزایش دما از ۱۵۰ به ۵۵۰ درجه سلسیوس حدود ۶۵٪ فزونی می یابند. بعلاوه توسط روشهای شناسایی و آزمایشات مواد، با مقایسه فوم نیکل با فوم نیکل-آلومینا افزایش سختی از ۱۴۵ به ۵۴۷ ویکرز و استحکام فشاری از ۱/۸ به ۵ مگاپاسکال و سطح ویژه (S_{BET}) از ۱/۴۸ به ۴۸ مترمربع بر گرم بدست می آید. آنالیز پراش اشعه ایکس نشاندهنده اکسید نیکل و NiAl₂O₄ در ساختار می باشد. فصل مشترک بین جزء کاتالیستی NiAl₂O₄ و نیکل روی قابلیت کاتالیتی اثر گذاشته و کارایی این نانوکاتالیست در تست پایلوت در دمای پایین ۵۰۰ درجه سلسیوس نسبت به نتایج گزارش شده توسط تحقیقات دیگر در ۷۲۰ درجه سلسیوس یکسان بدست آمد.



Use of Waste Materials for Sustainable Development of Rigid Pavement

L. A. A. Al-Hindawi, A. M. Al-Dahawi, A. Sh. J. Al-Zuheriy*

Civil Engineering Department, University of Technology – Iraq, Baghdad, Iraq

PAPER INFO

Paper history:

Received 12 June 2023
Received in revised form 11 July 2023
Accepted 16 July 2023

Keywords:

Sustainable Concrete
Ground-granulated Blast-furnace Slag
Waste Concrete
Rigid Pavement
Concrete Strength

ABSTRACT

Earth's natural resources belong to everyone and must be maintained for future generations. Thus, waste management and consumption are researchers' main concerns. Using waste resources to build sustainably. It's growing increasingly popular due to its environmental and economic advantages. This paper uses waste materials to increase the sustainability in construction work with cement-based such as waste concrete as a normal aggregate replacement and ground-granulated blast-furnace slag (GGBFS) as supplementary cementitious materials (SCMs) to improve the sustainability in rigid pavements production, to decrease the use of raw materials, and to reduce the CO₂ production in Portland cement (PC) factories. Cubic, cylindrical, and prismatic specimens were prepared in the laboratory with (0%, 10%, 20%, 30%, and 40%) by weight of aggregates waste concrete (WC) as replacements from the natural aggregates. The strength activity index (SAI) of the concrete specimens was in the acceptance strength zone with a slight reduction when compared with the conventional concrete strength. On the other hand, the hybridized effect of using the GGBFS as SCMs with various proportions of GGBFS/PC (0.8, 1.2, 1.6, 2), and WC at (40%, 30%, 20%, and 10%) respectively appeared that SAI was enhanced. Three manufactured specimens in each type of mixture were tested after 7 and 28 days of age curing. The findings from compressive strength, splitting, and flexural tests conducted on mixtures containing recycled aggregate indicate their suitability for use in rigid pavements for secondary roads. It was observed that as the proportion of recycled aggregate in the mixture increased, the strength of the concrete decreased. when ground granulated blast furnace slag (GGBFS) was added to the concrete mixtures, the results varied depending on the ratio of GGBFS present in the mixture. Among the different mixes tested, the mix designated as R30S1.2 was the highest strength load and it can be used for main roads. The results indicate that the use of recycled aggregates at a ratio of 30% and 55% GGBFS gave the best strength results and at the same time reduces the amount of cement and natural aggregates used, and this has an impact on the environment by reducing the presence of waste.

doi: 10.5829/ije.2023.36.10a.16

1. INTRODUCTION

The positive side of sustainable concrete includes preserving the environment by reducing harmful effects such as the accumulation of concrete waste resulting from the demolition of buildings, as well as reducing the use of natural aggregates. This is driven not just by environmental concerns, but also by the preservation of natural aggregate resources, a scarcity of trash disposal sites, and the rising expense of waste treatment before disposal. Several research investigations have been carried out on the utilization of RA in concrete to comprehend the properties of RA cement; however, the majority of these studies are focused on the mechanical

characteristics of the results concrete. An effort is made to comprehend durability. Aspects of construction materials derived from them and a comparison to concrete produced with natural aggregates [1, 2]. It is estimated that annually around 15.5 million tons of building debris are created in China [3], the bulk of which is concrete and bricks. Waste concrete aggregate is achieved by using the demolished concrete into small pieces with a specific process called grinding or crushing process to produce the waste aggregate in different sizes. This process is done by fixed crusher or mobility, as this process results in recycled aggregate and its use in various concrete mixtures. Several works used recycled materials to achieve the sustainability concept by using

*Corresponding author email: ahmed.sh.jeber@uotechnology.edu.iq (A. Sh. J. Al-Zuheriy)

recycled concrete aggregate (RCA) and studied the behavior of concrete including the physical and chemical properties of fresh and hardened concrete [4-7].

The consumption of raw aggregates (fine and coarse), accounting for up to 70-80% of the overall volume of the concrete mixture design, is accelerating in tandem with the expansion of concrete production and use. The use of reused stones derived from demolition and building waste is introducing new construction trends, substituting for basic (natural) aggregates. It conserves natural resources and reduces the amount of landfill space required [8-10]. RCA concrete typically has a lower compressive strength than concrete with pristine aggregate. Depending on the grade of RCA, Manimaran et al. [11] suggested that the compressive strength of RCA concrete might reduce by up to 25%. According to Tam et al. [12], an increase in the proportion of coarse RCA used as a replacement for virgin aggregate decreased compressive strength. The reduction in strength was attributed to the weak residual mortar in RCA. Dawood et al. [13] confirmed this trend, attributing it to RCA's low specific gravity and high absorption or porosity. In addition, they stated that the strength of RCA concrete was determined by the weakened interface between the residual mortar and the original stone and between the residual mortar and the new mortar. Olivier et al. [14] stated that the compressive strength is affected by several variables, such as the water-to-cement ratio, the percentage of coarse aggregate substituted with RCA, and the quantity of residual mortar in the RCA.

To modify bitumen and porous asphalt mixtures, it was used the ground granulated blast-furnace slag (GGBS) as a substitution material for styrene-butadiene-styrene (SBS) [10]. An effort was made in investigating the viability of utilizing industrial waste Ground Granulated Blast Furnace Slag (GGBS) and agricultural waste Groundnut Shell Ash (GSA) as stabilizing agents in the soil stabilization technique [11].

The use of ground granulated blast furnace slag (GGBFS) as an alternate material to cement leads to reduce the production of carbon dioxide (CO₂) resulting from the cement industry. Nowadays, global cement production contributed to increased CO₂ pollution of around 8% with subtracted 1 ton of CO₂ pollution per ton of cement production and decreased raw materials (limestone, clay, etc.) that are used in the production process of Portland cement. The GGBFS is one of the products of the molten iron industry [12-14]. The American Concrete Institute, ACI 318 code, section 5.1.1, indicates that concrete should have a compressive strength of more than 17.3 MPa after 28 days of casting to refer to it as structural concrete [9]. So, this indicates that this type of concrete has good strength properties and can be used in building facilities at various members. On the other hand, the usage of waste materials to

achieve sustainability at this time become necessary and urgent to reduce the negative impacts on the environment, keep the raw materials for future generations and reduce landfilled materials.

The (GGBS) should be activated by combining it with Portland cement before it can be utilized in concrete. A typical mixture consists of 50% GGBS and 50% Portland cement, but amounts of GGBS [4] ranging from 20% to 80% are frequently employed. The greater the amount of GGBS, the greater impact on the properties of concrete.

The importance of this research came from the need for test results and their practical effects on the construction industry. The research includes an evaluation of the properties and behaviour of high-strength concrete mixtures. This evaluation includes factors such as compressive strength, toughness, workability, and other mechanical properties. By understanding how these admixtures perform, the study provides valuable insights to improve concrete design and construction practices and is important to identify accessible data on the properties and behavior of high-strength formwork with recycled aggregates and/or with GGBFS. To do this, recycled concrete aggregate (RCA) is produced and partially replaced by virgin aggregate to manufacture concrete mixes. Furthermore, the hybrid use of RCA as a pre-preparation of virgin aggregates and GGBFS as a partial substitute for Portland cement is also being investigated. In summary, this research is important because it explores the use of recycled concrete aggregates and GGBFS in high-strength concrete, contributing to sustainable construction practices, resource efficiency, performance assessment, potential industry impact, and filling the knowledge gap in this field.

2. EXPERIMENTAL TEST DETAILS

2.1. Materials The following raw materials were employed in the work:

2.1.1. Portland Cement The Portland cement used is sulfate resistant, Type VCEM I 42.5SR according to Iraqi Standard No. 5/1984, which is a production of the Karbala cement factory [15]. The chemical and physical properties confirm to ASTM C150 (Table 1) [16]. The sulfate-resistant 3 cement (SRC) is the result of crushing a dry mix of SRC clinker and gypsum and it is a hydraulic bonding grey fine powder. The applications of this type of cement are in concrete foundations and structures like rigid pavement, which is in contact with the soil that contains sulfates. The Chemical and physical requirements of sulfate-resistant Portland cement summarized in Table 1.

TABLE 1. Chemical and physical requirements of sulfate- resistant Portland cement [15]. (Data processing was done by a material processor)

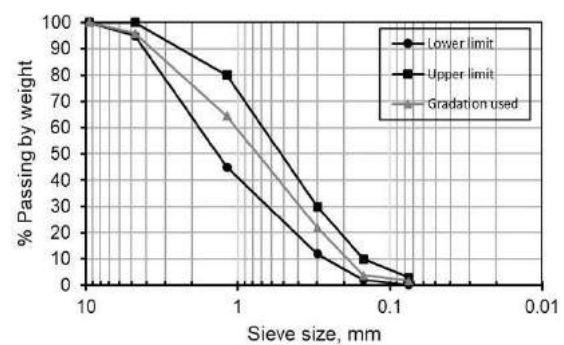
Chemical requirements			
Test Type	Test Method	Limitation	Test result
“Loss on ignition (as LOI), %		< 4.0	3.56
Non-Soluble Substances, %		≤ 1.5	0.50
SO ₃ Content, %	IQS 472/1993	2.5 if C ₃ A ≤ 3.5 2.5 if C ₃ A ≥ 3.5	2.37
C ₃ A, %		≤ 3.5	2.49
MgO, %		≤ 5.0	1.75
Chloride content, %	BS EN 196-2/2013	≤ 0.1	0.03
Physical and mechanical requirements			
Finesse (Blaine), m ² /kg	IQS 198/1990	≥ 300	344
Initial setting time, minute		≥ 45	150
Final setting time, hour	BS EN 196-3/2016	≤ 10	3.18
Soundness (expansion)-LeChatle, mm		≤ 10	0.29
Compressive strength, notless than (mN/m ²): 2 days	BS EN 196-3/2016	≥ 20.0	23.9
28 days		≥ 42.5	48.2

2. 1. 2. Sand The sand used in this work was washed and screened red sand, and it was quarried from the Al-Ukhaidir area in Karbala. Water-washed sand is used to get rid of salts and impurities, as well as clay particles because their presence affects concrete and reduces the cohesion of the mixture. The other benefit of this process is to obtain clean, saturated and saturated surface dry (S.S.D) sand. It was sieved to meet the gradation requirements of Iraqi SCRB Standards/R10-2003 [15]. The gradation test was carried out using 1 kg of fine aggregates by using a sieve shaker and the results are shown in Table 2 and figuratively presented in Figure 1.

2. 1. 3. Coarse Aggregate The crushed coarse aggregate used in the research is from the Al-Nibai quarry, which is located north of Baghdad. It is washed with water to clean the impurities that affect concrete and reduce cohesion. Crushed aggregates with multiple

TABLE 2. Gradation of the sand used according to Iraqi specifications R10 [15]

Sieve size (mm)	% Passing by weight	
	Gradation limit	Gradation used
9.5	100	100
4.75	95-100	95.87
1.18	45-80	64.37
0.30	12-30	21.96
0.15	2-10	3.95
0.075	0-3	1.71

**Figure 1.** Gradation limits and the selected gradation of the fine aggregates used [15]

angles were used to increase bonding and reduce voids in concrete. Specific particle sizes were used that meet the grading requirements according to Iraqi SCRB Standards/R10-2003 [16]. The gradation test was carried out using 5 Kg of coarse aggregates by using a sieve shaker as given in Table 3 and presented in Figure 2.

TABLE 3. Gradation of the crushed gravel used according to Iraqi specifications R10 [15]

Sieve size (mm)	% Passing by weight	
	Gradation limit	Gradation used
50.0	100	100
37.5	90-100	99
19.0	35-70	70
9.5	10-30	30
4.75	0-5	1

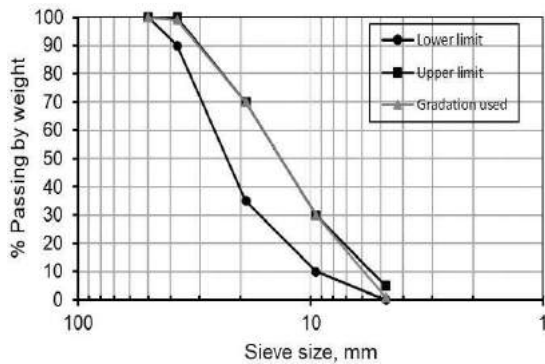


Figure 2. Gradation limits and the selected gradation of the coarse aggregates used [15]

2. 1. 4. Ground-granulated Blast-furnace Slag (GGBFS)

It is considered as a supplementary cementitious material with hydraulic bonding properties used in construction materials that contain cement based. This material is produced from the process of making iron molten by placing iron ore, limestone, and coke in a blast furnace. Various chemical reactions occur at a high temperature of up to 1500°C, resulting in molten iron and molten slag, which is considered a waste material. The molten slag is quickly cooled with water or steam, and it produces calcium silicate hydrate (granular slag), which is a fine, glassy powder then milling well, produces GGBFS, which is then mixed with cement to obtain a concrete mix with perfect cementitious properties. It is greenish and symbolized particles.

2. 1. 5. Water and Superplasticizers

For the mixing and curing stage of the samples, clean water that was free of contaminants was employed. A water-reducing admixture was also used as a chemical additive to reduce the amount of water, as well as increase the workability. The physical properties and test results of GGBFS are summarized in Tables 4 and 5. Its characteristics are shown in Table 6.

2. 2. Testing Setup

The ELE for compressive strength test setup is shown in Figure 3.

➤ ELE International compressive test machine – 3000 kN:

1. Cube:- To check the compressive strength of concrete, cubic models of 100 were used, which are sufficient to obtain results of concrete resistance to failure, and at the same time have a benefit in sustainability by reducing the use of concrete materials, as well as in terms of

disposal of these models after testing, and determining this measurement depending on the type of examination as well as the highest size of coarse aggregate. The user, where three concrete models were used and the average test results were relied upon, which are sufficient to meet the routine test for compressive strength and achieve approved results for the projects. The test is carried out by placing the concrete cube inside a compressive strength device between two steel surfaces, where pressure is applied to the surface area of the cube. The models were tested at the rate of loading 6 KN/s until failure.

Calculate the compressive strength of the specimen as follows: $C = A/P$ Where: A= area of square mm² and P= maximum applied load, N

According to ASTM C39 [17]

2. Cylinder: Possibility to perform a splitting test for cylindrical samples with a length of 200 mm and a diameter of 100 mm, since the test results are based on 28 days of water curing. When the sample is placed in the device, uniaxial loading causes a relatively high stress along the length of the sample, and 25 mm thick wood strips are placed between the surface of the sample and the upper and lower bearing steel blocks to distribute the stress on the axis. Calculate the splitting tensile strength

TABLE 4. Physical properties of GGBFS (Data processing was done by a material processor)

Model Number	Slag	Color	Type	Fineness	Standard
S95	Hot	Near White Color	Powder	490-510 M2/Kg	GB/T 18046 BS6699

TABLE 5. Test results of GGBFS (Data processing was done by a material processor)

No.	Items of testing	Limits	Results	Decision
1	Specific surface area, m ² /kg	≥400	418	Passed
2	Relative water, %	≥95	106	Passed
3	Density, g/cm ³	≥2.8	2.9	Passed
4	Moisture Content, %	≤1.0	0.1	Passed
5	Sulfur trioxide, %	≤4.0	0.3	Passed
6	Chlorine ion, %	≤0.06	0.02	Passed
7	Loss on ignition, %	≤3.0	0.2	Passed
8	Vitreous content, %	≥85	93	Passed

TABLE 6. Technical information on the superplasticizer used is provided by the manufacturer (Data processing was done by a material processor)

Base	Appearance/ colour	Specific gravity	Chloride content	Air environment	Compatibility
Polycarboxylate polymer technology	Brownish liquid	1.085 ± (0.01) g/cm ³	Nil	Nil	All types of Portland cement



Figure 3. (a) ELE for compressive strength test (b) ELE splitting tensile strength test, (c) Prism of flexural test concrete

of the specimen as follows:

$$T = 2P/\pi ld \quad (1)$$

where: T = splitting tensile strength, MPa ,
 P = maximum applied load indicated by the testing machine, N
 l = length, mm , and d = diameter, mm.
 tested at the rate of loading 0.95 kN/sec until failed, and according to ASTM C496/C496M [18].

➤ ELE International Flexural strength_ 1000 KN:
 used four points for prism sample 100×100×400 mm, four-point load, and span length 300 mm between support blocks, All sample surfaces must be smooth to obtain accurate results and keep the samples moist in the period between removal from water curing to the time of examination because drying of the sample surface results in a measure of bending strength. The examination is carried out by shedding the pregnancy continuously and without shock. the rate of loading 0.2 KN/s until failure. Calculate the splitting tensile strength of the specimen as follows:

$R = PL/bd^2$ according to ASTM C78/C78M [19] where:

R = modulus of rupture, MPa,

P = maximum applied load indicated by the testing machine, N,

L = span length, mm,

b = average width of specimen, mm, at the fracture, and

d = average depth of specimen, mm

2. 3. Methods of Working and Samples Processing

The trial program is first stage was to study the effect of using recycled aggregates to produce concrete materials from the recycled aggregate. Slump according to ASTM, C143 [20], was used to analyze the properties of fresh concrete from recycled aggregates. The compressive, tensile, and flexural strengths of hardened concrete are determined after 7, and 28 days of age. These tests are performed to obtain the properties of the hardened concrete.

The proportions of Portland cement, sand, and gravel used in this work by weight are (1:2.32:3.26) respectively. The properties of mixes of part 1 are

explained in Table 7. It demonstrates the use of recycled aggregates obtained from crushing concrete, with replacement ratios of (0%, 10%, 20%, 30%, and 40%) by natural aggregates.

The second part of the research is shown in Table 8, which explains the same proportions of RCA, with the addition of GGBFS as a replacement ratio for cement with four different proportions of GGBFS/PC (0.8, 1.2, 1.6 and 2.0)

The specimens produced in this work within the first and second stages are cubes with dimensions of 10×10×10 cm, cylinders with a diameter × height of 10×20 cm, and prisms with 10×10×40 cm (height × width × length). The cubic specimens were monotonically tested under compression loads. Indirect tension test was carried out specimens were tested under four-point flexural loads.

The primary reason for utilizing three geometric shapes, namely the cube, cylinder, and prism, is to represent the strength characteristics of concrete under different loading conditions. Each shape represents the specific testing method used in concrete strength testing. The cube shape is commonly employed to determine the compressive strength of concrete. Cubes are cast and subjected to a compressive load until failure occurs. The dimensions of the cube faces are equal, providing a uniform distribution of stress during the test. The cylinder shape is typically used to evaluate the tensile strength of concrete. Cylinders are subjected to a point load until they fracture. This test helps determine the resistance of concrete to cracking or splitting. The prism shape, specifically a rectangular prism, is utilized to represent the flexural strength of concrete. The prism specimens have longer dimensions in one direction, simulate a beam or a structural element. The load applied to the prism determines the amount of bending that occurs before fracture. This test is significant for evaluating the capacity of concrete to bear vehicle loads or other types of loads without failure. These three geometric shapes provide different insights into the strength properties of concrete under varying loading conditions, allowing engineers and researchers to represent its performance in real-world applications. Figure 4 presents the manufactured specimens.

The process of preparing the models was done by preparing the weights of the materials and lubricating the molds, and the materials were mixed in two stages, the dry mixing, where the materials were mixed well until they were evenly distributed inside the mixer, and the second stage was the wet mixing, by adding water and plasticizer gradually to the mixture until the appropriate consistency was obtained. When the concrete was put into the molds it was then placed on the vibration table. The goal of concrete consolidation, referred to as compaction, is to produce the densest concrete. In low-slump concrete, air voids may make up to 20% of the

TABLE 7. Concrete mix proportions – part 1

Mix	Code of mixes	Waste concrete (R)%	Cement, %	Fine aggregate	Coarse aggregate	Water/ cement ratio	SP, %	Slump(mm)
Mix1	R0 Plain mix	0%	100	100	100	0.35	0.3	50
Mix2	R10	10%	100	100	90	0.35	0.3	48
Mix3	R20	20%	100	100	80	0.35	0.3	45
Mix4	R30	30%	100	100	70	0.35	0.3	42
Mix5	R40	40%	100	100	60	0.35	0.3	39

TABLE 8. Concrete mix proportions – part 2

Mix	Code of mixes	GGBFS/ Cement	GGBFS, %	Cement, %	Waste concrete%	Natural coarse	Fine aggregate	W/C	SP, %	Slump (mm)
Mix6	R10S2	2	67	33	10	90	100	0.40	0.3	41
Mix7	R20S1.6	1.6	62	38	20	80	100	0.40	0.3	38
Mix8	R30S1.2	1.2	55	44	30	70	100	0.40	0.3	36
Mix9	R40S0.8	0.8	45	55	40	60	100	0.40	0.3	33



Figure 4. Samples of the produced specimens

total volume of freshly cured concrete. The movement of the particles has the effect of dispersing the liquid in the mixture, thus reducing the internal friction and filling the coarse aggregate. in respectof obtaining a composition similar to coarse aggregate particles. The vibration continues to expel the majority of the trapped air to increase the strength of the concrete [15]. Tables 7 and 8 summarized concrete mix proportions.

3. RESULTS

3. 1. Effects of the Composition of Mixtures

3. 1. 1. Using of Recycled Aggregate

The study's goal is to determine the impact of employing recycled materials such as waste coarse aggregates produced from crushing concrete and mixing in proportion with natural aggregates and creating new concrete suitable for rigid pavement, high traffic loads, and the lowest possible cost.

The effect of replacing coarse aggregate for waste

was explored by 10%, 20%, 30%, and 40% on fresh concrete, where the stagnation values of sustainable concrete is shown in Table 8. Data were recorded, as the results showed a decrease in slump values with an increased in thereplacement percentage.

The compressive strength of mixes that included recycled aggregates was found to be lower compared to thebase mix containing natural aggregates, as given in Table

9. Similar findings were reported in other studies as well [21-23]. The reduction in compressive strength exhibited arange of approximately 0.73-12.25%. The underlying cause of the strength reduction can be ascribed to the heterogeneous composition of the recycled aggregate, which is due to the existence of bound of the old mix on the outside surface of the recycled aggregates. Concrete production was adversely affected due to the high porosity of the material, as reported by Tam et al. [24].

As can be seen in Table 9, all the mixtures showed a decrease in tensile strength compared to the plane mix, andit seems that the strength was affected by the amount of recycled aggregate replacement and this is due to the quality of the crushed concrete [6].

Cylindrical specimens of crushed sustainableconcrete were tested to evaluate the failure condition. Figure 7, shows the values obtained from examining mixtures that contain returned aggregate. It was found that increasing the percentage of recycled aggregates in concrete leads to a decrease in the amount of tensile resistance by a rate ranging between 0.33%-40% comparedwith the natural mix.

According to the results of flexural strength, all concrete mixtures made of recycled aggregates achieved less strength than the results of the base mixture (Table 9) after comparing the results of concrete mixtures with recycled aggregates with the reference mix. The results exhibit that the higher the amount of reconstituted aggregate, the lower the load resistance to fracture [25].

Age curing has several effects on sustainable concrete content, Ground Granulated Blast Furnace Slag (GGBFS), and recycled concrete aggregate (RCA) in concrete.

Age curing positively influences the performance of GGBFS in concrete. As the concrete cures and ages, the GGBFS particles continue to react with the calcium hydroxide produced during cement hydration. This reaction leads to the formation of additional hydration products, such as calcium silicate hydrate (C-S-H) gel, which contributes to increased strength and improved durability of the concrete. As for the recycled aggregate Age curing can have a positive impact on the properties of concrete incorporating RCA. With time, the RCA particles continue to bond and interact with the cementitious matrix, resulting in improved interfacial transition zones and enhanced mechanical properties. Age curing allows for the further development of strength and durability, making the concrete with RCA more sustainable.

3. 1. 2. The Effect of Using Recycled Concrete Aggregate and GGBFS

Table 9 shows that the use of recycled aggregates contributed to reducing the compressive, splitting and flexural strengths of concrete compared to the concrete made with natural aggregates. This deficiency was tried to compensate by adding GGBFS, and thus sufficient strength was reached. As stated in [26-28], the strength of concrete is affected by the exact properties of the surface area between the RCA and the cement paste. Thus slag is believed to strengthen concrete by strengthening the bond between the cement

paste and the recycled aggregate. It has been shown that the microstructure and microhardness in this transition zone of sustainable concrete can be improved with increasing slag content in the concrete mixture [29]. This can help explain the advances made concretely.

The inclusion of more than 50% GGBFS in the concrete gave activity at 7 and 28 days after curing the specimens in clean water. Among the four mixtures studied, mixture 8 gave the highest compressive strength by 16.7%, thus obtaining a stronger and better mixture than the base mixture, and reducing the use of cement and natural aggregate by 55% and 30%, respectively. The use of GGBFS with high percentages of more than 60% in mix R20S1.6 led to an 11.59% reduction in compressive strength compared to the concrete containing recycled aggregates.

Table 9 gives the results obtained from examining the cylindrical specimens that manufactured by adding GGBFS to concrete with recycled aggregate under indirect tensile load. The strength gained by mixtures containing GGBFS with RCA compared to mixtures containing RCA only can be seen clearly. Moreover, a slight improvement of mix 8 compared with the plane mixture has been achieved.

The concrete increased the rate of strength gain progressively with an increase in the percentage of GGBFS in the mixture, where the mix R30S1.2 which contains 55% slag achieved the highest results, The substitution of cement reaches 45%.

The flexural strength performance of the recycled aggregates with GGBS is shown in Table 9. The results showed an increase in the flexural strength in all mixtures containing GGBFS and RCA compared with mixtures that were manufactured with RCA only or those made with virgin aggregates and a full amount of Portland cement. As a reminder, these mixtures contain GGBFS with different dosages of 45%, 55%, 62, and 67% that represent the ratios of GGBFS/PC of 0.8, 1.2, 1.6 and 2.0 respectively. The superiority of mixtures containing

TABLE 9. The test results of mechanical properties of concrete samples

Mix ID	Mix code R (recycle coarse aggregate) S (slag), Sh (steel shaving)	Compressive Strength (MPa)		Splitting Strength (MPa)		Flexural Strength (MPa)	
		7 days	28 days	7 days	28 days	7 days	28 days
Mix1	R0	22.18	31.13	2.12	2.99	2.28	2.97
Mix2	R10	22.07	31.09	1.85	2.71	2.24	2.92
Mix3	R20	21.93	30.74	1.80	2.54	1.96	2.55
Mix4	R30	20.87	30.04	1.44	1.97	1.53	2.01
Mix5	R40	19.76	27.92	0.88	1.20	1.38	1.78
Mix6	R10S2	20.33	27.86	1.77	2.36	2.57	3.23
Mix7	R20S1.6	21.19	28.73	1.75	2.43	3.15	4.20
Mix8	R30S1.2	28.01	35.07	2.24	3.03	4.72	6.13
Mix9	R40S0.8	25.41	31.65	2.08	2.93	2.43	3.20

GGBFS and RCA over those made with RCA only are with percentages of 10.62, 64.71, 67.21 and 79.77 at 28 days age for the mixtures that have RCA of 10, 20, 30 and 40% respectively.

3. 2. Interpretation of Results and Discussion

3. 2. 1. Workability

The workability of all compounds was evaluated using the slump test for the base mixture and mixtures containing reconstituted materials. Figure 5 exhibits the values of the slump in each mixture. It was noted that the slump values differ from one mixture to another based on the proportions of additives such as recycled aggregates and GGBFS. The workability is lower in the sustainable mixtures (R10, R20, R30 and R40) compared to the reference mixture, as presented in Figure 4. The decrease in the slump values when the RCA is increased in the mix is because of the negative effect of incorporating crushed concrete into the new concrete, as this decrease can be attributed to the coarse surface of the recycled aggregate containing the old concrete, which is mainly due to the higher absorption capacity of the restored aggregate, and the lower water level in the fresh mix that leads to a decrease in the workability and a decrease in the amount of slump of the concrete relative to the concrete containing only virgin aggregates [30-32].

In the presence of recycled concrete aggregates, the addition of GGBFS had a detrimental effect on the workability and slump. The value of slump decreased with the increase in the proportion of GGBFS in the mixes (R10S2 and R20S1.6). This negative effect has been attributed to the fact that the surface area of GGBFS particles is larger than that of cement particles [19, 33].

Mostly, the compressive strength of the mixtures that contain natural aggregates is higher than the compressive strength of the concrete containing RCA because it is a weaker material. The amount of decrease in the compressive strength depends on the percentage of recycled aggregates in the mixture and on the quality of the concrete waste.

3. 2. 2. Strength Activity Index

In Figure 6, it can be observed that the compressive strength in the mixtures from R10 through R40 decrease gradually for both curing ages (7 and 28 days) if it is compared with

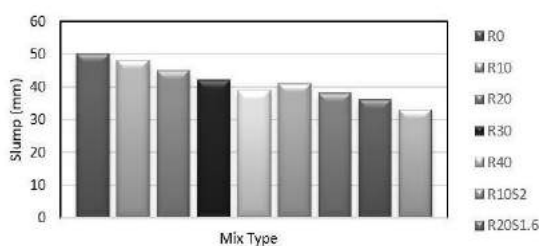


Figure 5. Slump test results

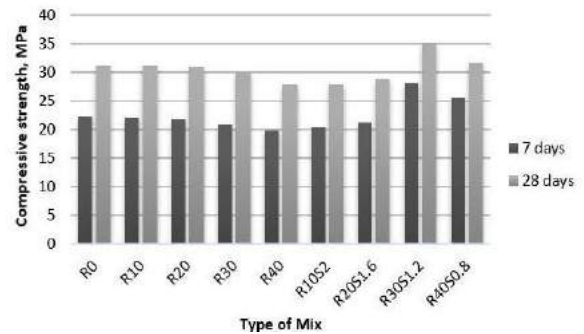


Figure 6. Compressive strength test results

the reference mixture (R0) and in close proportions. According to ASTM C39 [17] and previous studies, many factors may affect the mechanical properties of concrete such as:

- The water absorption of recycled coarse aggregate is more than that of natural aggregate, and the higher the water absorption percentage, the lower the concrete compressive strength [30, 34, 35].

- The source of crushed concrete also may affect the compressive strength of the sustainable concrete. If the demolished concrete has high load-bearing strength, this leads to the production of concrete with high strength compared with the concrete produced from normal recycled concrete. Moreover, the workability of fresh concrete can also be attributed to a decrease by a small amount compared to the base concrete [36-38].

- The phenomenon under observation pertained to the compression of concrete cubes on a vibration table. Poon et al. [39] stated that recycled aggregate particles have the potential to migrate toward the cement during vibration. Design a region characterized by a progressive increase in the water-to-cement ratio, resulting in an elevated level of porosity. The aforementioned process has the potential to diminish the cohesion between the repurposed aggregates and the matrix of cement [40].

Previous works suggested that the utilization of recycled aggregates in concrete, when exposed to saturated water, may lead to an ineffective interfacial transition zone (ITZ), thereby significantly impacting the concrete's properties. The effects have been observed to be the potential weak link in the chain, in comparison to cement paste and the accumulation of particles. It should be noted that the use of recycled aggregates in concrete production has both advantages and disadvantages in different regions. A new bond can be formed between recycled aggregates, including gravel and old mortar, as well as between these recycled aggregates and newly created cement putty. A specific condition can create a non-uniform region that has the potential to diminish the strength of concrete [6, 37].

The compressive strength changes by adding GGBFS as a relative alternative material to cement. It

was noted that the suitable replacement ratio in the compressive strength examination was in the mixture R30S1.2 with 30% recycled aggregate and GGBFS 55%. The strength increased by 26.3 and 12.6% compared to the base mixture for the curing periods 7 and 28 days respectively, which may be due to the increased effectiveness of the pozzolanic reaction [41]. When the percentage of GGBFS decreases for the R40S0.8 mixture to be 45% of cementitious materials, the compressive strength begins to decrease compared with the previous mixture but is still a little higher than the reference mixture.

With the addition of higher amounts of GGBFS in the cases of mixtures R10S2 and R20S1.6 (more than 55% of total cementitious materials), the compressive strength registered lower values than that of the original mixture, which is due to the acute shortage of Portland cement

Figure 7 presents the results of the tensile strength. By comparing the splitting tensile results of concrete containing both ground granulated blast furnace slag (GGBFS) and recycled aggregates with those of concrete containing only recycled aggregates, an increased splitting tensile strength was observed.

The use of GGBFS as a partial replacement for cement in concrete improved the mechanical properties of the material. GGBFS is a by-product of the iron and steel industry with pozzolanic properties, which means that it can react with calcium hydroxide to produce additional cementitious compounds. This reaction improves the strength and tensile properties of concrete.

Recycled aggregate is crushed concrete or construction waste that is replaced with natural aggregate in concrete production. Although the use of recycled aggregates alone may reduce the overall strength of the concrete due to the presence of weak interfacial transition zones between the old and new cementitious materials, it can still provide satisfactory performance depending on the application.

However, when combined with recycled aggregates, GGBFS can help mitigate a potential decrease in strength that would result from using recycled aggregates alone. GGBFS contributes to the formation of additional hydration products and a denser

microstructure in concrete, thus improving tensile strength. By combining GGBFS and recycled aggregates in concrete, the tensile strength to fracture was increased compared to concrete containing only recycled aggregates. The exact extent of improvement depends on variables such as the proportions and properties of the materials used, the curing conditions, and the mix design of the concrete. According to ASTM C496 [18].

Figure 8 demonstrates the results of the flexural test. It is also called the modulus of rupture test. This test was conducted by applying a gradual four points flexural load on concrete prisms according to ASTM C78 [19], which simulates traffic loads on rigid pavement. The addition of GGBFS and recycled aggregate to concrete can improve flexural performance in comparison to using recycled aggregate alone. GGBFS is a cementitious material that can be used to supplant a portion of the cement in concrete. It increases the workability and durability of concrete while decreasing hydration heat. GGBFS can enhance flexural strength by enhancing the chemical and physical properties of the concrete matrix as a whole. Recycled aggregate: When using recycled aggregate in concrete, the pulverized concrete residue is substituted for a portion of the natural coarse aggregate. Typically, recycled aggregate has weaker tensile properties than natural aggregate. Therefore, recycled aggregate alone results in lower flexural strength than concrete with natural aggregate. However, when GGBFS and recycled aggregate are combined in concrete, the GGBFS can help improve the recycled aggregate's properties, mitigating the recycled aggregate's potentially negative impacts on strength. The pozzolanic activity of GGBFS can enhance the adhesion between the cementitious matrix and recycled aggregate particles, resulting in enhanced flexural strength.

By combining GGBFS and recycled aggregate, it is possible to create a concrete mixture that takes advantage of the strength-enhancing properties of GGBFS while still making use of recyclable materials. This combination can result in greater flexural strength than using recycled aggregate concrete alone table, the precise increase in flexural strength will depend on many variables, including the exact proportions of GGBFS and

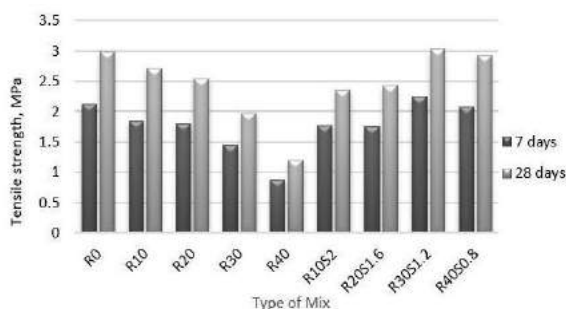


Figure 7. Indirect tensile strength of different mixtures

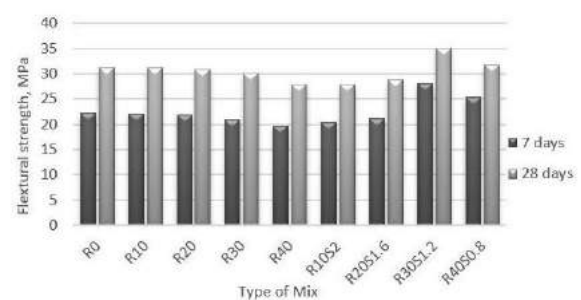


Figure 8. Results of flexural strength test

recycled aggregate, the grade of the materials, curing conditions, and the overall mix design. According to ASTM C78 [19].

It is common knowledge that GGBFS endures a pozzolanic reaction when combined with water and cement. In addition to improving the durability, the addition of GGBFS may have a positive influence on its mechanical properties [20, 39, 42]. The pozzolanic response, which results in an increase in calcium silicate hydrate (C-S-H) and contributes to the improvement of cement paste strength and, by extension, the general strength of concrete [43, 44], is the primary cause of the strength and durability enhancements.

The reason is due to the increase in concrete strength after adding GGBFS to the fresh mortar, as the cement reacted with water to produce C-S-H gel (concrete bond strength), which represents the strength of concrete but it is fixed at 60-70% by volume of concrete with 20-25% calcium hydroxide. The use of supplementary cementitious materials is to make a chemical reaction between these materials and calcium hydroxide to produce a new concrete bond (C-S-H) that has the same strength when compared to conventional concrete.

Instead of natural to reach sustainability and at the same time the strength required to bear the loads placed on the pavement, on the other hand, the mechanical behaviour of these materials acts as filling for the voids that exist due to the mechanical interaction and this is another reason for increasing the strength (the optimal water content of the concrete to complete the reaction is 0.23 but the excess amount helps to make the concrete easier to operate and weakens the concrete). So, the surplus water undergoes evaporation until the void ratio of the reactant attains approximately 5-6%. The reactant materials assume a role in the void ratio by functioning as fillers. The fillers like GGBFS present in the material are composed of particles that are smaller in size than cement, which consequently enhance the mechanical characteristics and the overall structure of the material [13].

Adding GGBFS into concrete reduces the heat of hydration by substantially lowering the amount of heat produced during the hydration process. This is particularly important in large concrete structures, such as dams or foundations, where excessive heat accumulation can lead to thermal fracture. Using GGBFS assists in preventing hyperthermia and heat-related complications [40].

In contrast, adding GGBFS to concrete reduces its carbon footprint because the production of GGBFS involves fewer carbon emissions than conventional cement. Since GGBFS is a byproduct, its incorporation into concrete reduces the quantity of cement required, thereby reducing the greenhouse gas emissions associated with cement production. This makes GGBFS an environmentally preferable option for the production of concrete [41].

It can be noted from the above results that the presence of the reconstituted aggregate in the mixture gave good results, but less than the results of the main mixture, indicating that the reconstituted aggregate is less strong than the natural aggregate and that the old concrete surrounded by the aggregate constitutes a weak point, and at the same time this concrete absorbed a quantity of water from the mixture, and this in turn led to Reduction in workability and slump, and this conclusion has an inverse relationship with the proportion of recycled aggregate added to concrete.

Moreover, the presence of the reconstituted aggregate in the mixture gave good results, but less than the results of the main mixture, indicating that the reconstituted aggregate is less strong than the natural aggregate and that the old concrete surrounded by the aggregate constitutes a weak point, and at the same time this concrete absorbed a quantity of water from the mixture, and this in turn led to Reduction in workability and precipitation, and this conclusion has an inverse relationship with the proportion of recycled aggregate added to concrete. However, adding GGBFS at a ratio of (62, 67%) leads to a decrease in resistance. The reason for this is due to a lack of chemical bonding because granular furnace slag contains a high percentage of silicates and alumina, which are materials that act as pollutants with the cement components. When using a high percentage of GGBFS, competition may occur between cement components and slag for water and calcium available for chemical bonding, which reduces the speed of formation of calcium hydroxide compounds, silicates and alumina required for concrete strength, and the other reason is the increase in empty parts because granular slag has high porosity properties and when using a high percentage of it, it increases the empty parts in the concrete. The presence of empty parts leads to weak concrete strength and a lack of strength to external influences such as freezing, thawing and corrosion.

However, when using GGBFS at a ratio of (44, 55%) the led to an increase in strength, especially in the mixture (R30S1.2) which contains the ideal ratio of GGBFS and recycled aggregates, where the highest results of stress resistance were obtained compared to other mixtures in this research.

4. CONCLUSION

The above study shows the following conclusions:

1. The research findings demonstrate the potential of wastematerials, specifically waste concrete and ground-granulated blast-furnace slag (GGBFS), in enhancing sustainability in construction practices.
2. The workability of the sustainable mixtures was observed to decrease compared to the reference mixture due to the rough surface of recycled aggregate and the

adverse impact of GGBFS on workability and slump.

3. The compressive strength of mixtures containing recycled concrete aggregates (RCA) gradually decreased compared to the reference mixture, primarily influenced by factors such as higher water absorption of recycled coarse aggregate and variations in the load-bearing strength of the original concrete.

4. Incorporating GGBFS as a substitute for cement positively influenced the compressive strength, with the optimal replacement ratio identified as 30% recycled aggregate and 55% GGBFS.

5. The combination of GGBFS and recycled aggregates resulted in improved splitting tensile strength compared to concrete containing only recycled aggregates, attributed to the pozzolanic activity of GGBFS. GGBFS and other pozzolanic materials react with calcium hydroxide (CH) generated during cement hydration to form additional cementitious compounds. These compounds occupy the voids and strengthen the bond between the cement matrix and aggregates, thereby increasing the tensile strength, attributed to the pozzolanic activity of GGBFS.

6. The flexural strength of concrete improved when GGBFS and recycled aggregates were combined. GGBFS contributes to this improvement by strengthening the bond between the cement matrix and the recycled aggregate particles. The finer particles of GGBFS occupy the cavities between the larger recycled aggregates, resulting in more efficient load transmission across the matrix-aggregate interface. This enhanced bonding increases flexural rigidity.

7. Integrating refuse materials into construction can contribute to sustainable practices by decreasing the demand for virgin materials and waste disposal. However, it is essential to optimize the proportions and properties of the materials to assure their suitability for particular applications and conditions. During the material selection and design process, factors such as the type and quality of the waste materials, the intended performance requirements, and environmental considerations must be taken into account.

8. Further research is warranted to determine optimal combinations of waste materials and explore additional factors influencing mechanical properties and the overall performance of the concrete.

9. The study highlights the potential of refuse materials, such as waste concrete and GGBFS, to increase sustainability and improve the mechanical properties of building materials. The construction industry can reduce its environmental impact and contribute to a circular economy by reusing refuse materials. This strategy is consistent with the principles of sustainable development and offers opportunities to create more enduring and resilient structures while simultaneously reducing resource consumption and refuse production.

5. REFERENCES

- Olorunsogo, F. and Padayachee, N., "Performance of recycled aggregate concrete monitored by durability indexes", *Cement and Concrete Research*, Vol. 32, No. 2, (2002), 179-185. doi: 10.1016/s0008-8846(01)00653-6.
- Olorunsogo, F., "Properties of concrete made with recycled concrete aggregate", *Concrete/Beton*, Vol. 92, (1999), 3-7. doi.
- Kisku, N., Joshi, H., Ansari, M., Panda, S., Nayak, S. and Dutta, S.C., "A critical review and assessment for usage of recycled aggregate as sustainable construction material", *Construction and Building Materials*, Vol. 131, (2017), 721-740. doi: 10.1016/j.conbuildmat.2016.11.029.
- Dhir, R., Limbachiya, M., Leelawat, T., BS and 882, B., "Suitability of recycled concrete aggregate for use in bs 5328 designated mixes", *Proceedings of the Institution of Civil Engineers-Structures and Buildings*, Vol. 134, No. 3, (1999), 257-274. doi: 10.1680/istbu.1999.31568.
- Hariato, T., "Performance of subbase layer with geogrid reinforcement and zeolite-waterglass stabilization", *Civil Engineering Journal*, Vol. 8, No. 20, (2022), 251-262. doi: 10.28991/CEJ-2022-08-02-05.
- Balamuralikrishnan, R. and Saravanan, J., "Effect of addition of alccofine on the compressive strength of cement mortar cubes", *Emerging Science Journal*, Vol. 5, No. 2, (2021), 155-170. doi: 10.28991/esj-2021-01265.
- Junaid, M., Shah, M.Z.A., Yaseen, G., Awan, H.H., Khan, D. and Jawad, M., "Investigating the effect of gradation, temperature and loading duration on the resilient modulus of asphalt concrete", *Civil Engineering Journal*, Vol. 8, No. 02, (2022). doi: 10.28991/CEJ-2022-08-02-07.
- Aguilar, J.R., Mendoza, D.N., Fuertes, R.H., González, B.B., Gilmore, A.T. and Ramírez, R.P., "Caracterización del hormigón elaborado con áridos reciclados producto de la demolición de estructuras de hormigón", *Materiales de Construcción*, Vol. 57, No. 288, (2007), 5-15. doi.
- Committee, A., "Building code requirements for structural concrete (aci 318-08) and commentary, American Concrete Institute. (2008).
- Marandi, S.M., Ghasemi, M. and Shahiri, J., "Effects of partial substitution of styrene-butadiene-styrene with granulated blast-furnace slag on the strength properties of porous asphalt", *International Journal of Engineering, Transactions A: Basics*, Vol. 30, No. 1, (2017), 40-47. doi: 10.5829/idosi.ije.2017.30.01a.06.
- Manimaran, A., Seenu, S. and Ravichandran, P., "Stimulation behaviour study on clay treated with ground granulated blast slag and groundnut shell ash", *International Journal of Engineering, Transactions B: Applications*, Vol. 32, No. 5, (2019), 673-678. doi: 10.5829/ije.2019.32.05b.08.
- Tam, V.W., Wang, K. and Tam, C.M., "Assessing relationships among properties of demolished concrete, recycled aggregate and recycled aggregate concrete using regression analysis", *Journal of Hazardous Materials*, Vol. 152, No. 2, (2008), 703-714. doi: 10.1016/j.jhazmat.2007.07.061.
- Dawood, E.T., Al-Attar, A.a.A. and Zinad, O.S., "The influence of wood ash on different cement mortar mixes", in AIP Conference Proceedings, AIP Publishing. Vol. 2213, (2020).
- Olivier, J.G., Peters, J.A. and Janssens-Maenhout, G., "Trends in global CO₂ emissions. 2012 report", (2012). doi: 10.2788/33777.
- Officials, T., "Standard specifications for highway bridges, AASHTO, (2002).
- Karthiga, S., Devi, C.R., Ramasamy, N., Pavithra, C., Sudarsan, J. and Nithiyantham, S., "Analysis on strength properties by replacement of cement with calcium carbide remains and ground

- granulated blast furnace slag", *Chemistry Africa*, Vol. 3, (2020), 1133-1139. doi: 10.1007/s42250-020-00169-w.
17. ASTM, C., "Astm c39: Standard test method for compressive strength of cylindrical concrete specimens", ASTM International West Conshohocken, PA, USA, (2001).
 18. ASTM, A., "Astm c496/c496m-04e1 standard test method for splitting tensile strength of cylindrical concrete specimens", Annual Book of ASTM Standards, Vol. 4, (2008).
 19. Astm, A., "C78/c78m-18: Standard test method for flexural strength of concrete (using simple beam with third-point loading) astm international", USA, Vol. 4, (2002), 1-3.
 20. Standard, A., "Standard test method for slump of hydraulic-cement concrete", ASTM Annual Book of ASTM Standards, (2015).
 21. Aparicio, S., Hernández, M. and Anaya, J., "Influence of environmental conditions on concrete manufactured with recycled and steel slag aggregates at early ages and long term", *Construction and Building Materials*, Vol. 249, (2020), 118739. doi: 10.1016/j.conbuildmat.2020.118739.
 22. Younis, K.H., Amin, A.A., Ahmed, H.G. and Maruf, S.M., "Recycled aggregate concrete including various contents of metakaolin: Mechanical behavior", *Advances in Materials Science and Engineering*, Vol. 2020, (2020), 1-17. doi: 10.1155/2020/8829713.
 23. El-Hassan, H., Kianmehr, P. and Zouaoui, S., "Properties of pervious concrete incorporating recycled concrete aggregates and slag", *Construction and Building Materials*, Vol. 212, (2019), 164-175. doi: 10.1016/j.conbuildmat.2019.03.325.
 24. Tam, V.W., Soomro, M. and Evangelista, A.C.J., "A review of recycled aggregate in concrete applications (2000–2017)", *Construction and Building Materials*, Vol. 172, (2018), 272-292. doi: 10.1016/j.conbuildmat.2018.03.240.
 25. Otsuki, N., Miyazato, S.-i. and Yodsudjai, W., "Influence of recycled aggregate on interfacial transition zone, strength, chloride penetration and carbonation of concrete", *Journal of Materials in Civil Engineering*, Vol. 15, No. 5, (2003), 443-451. doi: 10.1061/(ASCE)0899-1561(2003)15:5(443).
 26. Yang, J., Du, Q. and Bao, Y., "Concrete with recycled concrete aggregate and crushed clay bricks", *Construction and Building Materials*, Vol. 25, No. 4, (2011), 1935-1945. doi: 10.1016/j.conbuildmat.2010.11.063.
 27. McCarthy, M. and Dhir, R., "Development of high volume fly ash cements for use in concrete construction", *Fuel*, Vol. 84, No. 11, (2005), 1423-1432. doi: 10.1016/s0140-6701(06)80743-5.
 28. Gao, J., Qian, C., Liu, H., Wang, B. and Li, L., "Itz microstructure of concrete containing ggbs", *Cement and Concrete Research*, Vol. 35, No. 7, (2005), 1299-1304. doi: 10.1016/j.cemconres.2004.06.042.
 29. Younis, K.H. and Mustafa, S.M., "Feasibility of using nanoparticles of SiO₂ to improve the performance of recycled aggregate concrete", *Advances in Materials Science and Engineering*, Vol. 2018, (2018). doi: 10.1155/2018/1512830.
 30. Ahmed, H.G., Younis, K.H. and Maruf, S.M., "Mechanical performance of sustainable concrete including recycled fine and coarse aggregate improved by silica fume", *International Journal of Scientific & Technology Research*, Vol. 9, No. 2020, (2020), 576-580.
 31. Mukharjee, B.B. and Barai, S.V., "Influence of incorporation of nano-silica and recycled aggregates on compressive strength and microstructure of concrete", *Construction and Building Materials*, Vol. 71, (2014), 570-578. doi: 10.1016/j.conbuildmat.2014.08.040.
 32. Younis, K.H., Pilakoutas, K., Guadagnini, M. and Angelakopoulos, H., "Feasibility of using recycled steel fibres to enhance the behaviour of recycled aggregate concrete", in FRC 2014 Joint ACI-Fib International Workshop-Fibre Reinforced Concrete: From Design to Structural Applications. (2014), 598-608.
 33. Kou, S.-c., Poon, C.-s. and Agrela, F., "Comparisons of natural and recycled aggregate concretes prepared with the addition of different mineral admixtures", *Cement and Concrete Composites*, Vol. 33, No. 8, (2011), 788-795. doi: 10.1016/j.cemconcomp.2011.05.009.
 34. Sajedi, F. and Razak, H.A., "Comparison of different methods for activation of ordinary portland cement-slag mortars", *Construction and Building Materials*, Vol. 25, No. 1, (2011), 30-38. doi: 10.1016/j.conbuildmat.2010.06.060.
 35. Mefteh, H., Kebaili, O., Oucief, H., Berredjem, L. and Arabi, N., "Influence of moisture conditioning of recycled aggregates on the properties of fresh and hardened concrete", *Journal of Cleaner Production*, Vol. 54, (2013), 282-288. doi: 10.1016/j.jclepro.2013.05.009.
 36. González Corominas, A., "Evaluation of the effects of recycled aggregates on the properties of high performance concrete", Vol., No., (2016). doi: 10.1016/s0008-8846(03)00186-8.
 37. Hawileh, R.A., Abdalla, J.A., Fardmanesh, F., Shahsana, P. and Khalili, A., "Performance of reinforced concrete beams cast with different percentages of ggbs replacement to cement", *Archives of Civil and Mechanical Engineering*, Vol. 17, (2017), 511-519. doi: 10.1016/j.acme.2016.11.006.
 38. Jalal Khoshnaw, G. and Haidar Ali, B., "Experimental study on performance of recycled aggregate concrete: Effect of reactive mineral admixtures", *Ijciet International Journal of Civil Engineering and Technology (IJCIET)*, Vol. 10, No. 1, (2019), 2566-2576.
 39. Poon, C.-S., Lam, L., Kou, S., Wong, Y.-L. and Wong, R., "Rate of pozzolanic reaction of metakaolin in high-performance cement pastes", *Cement and Concrete Research*, Vol. 31, No. 9, (2001), 1301-1306. doi: 10.1016/s0008-8846(01)00581-6.
 40. Dinakar, P., Sahoo, P.K. and Sriram, G., "Effect of metakaolin content on the properties of high strength concrete", *International Journal of Concrete Structures and Materials*, Vol. 7, No. 3, (2013), 215-223. doi: 10.1007/s40069-013-0045-0.
 41. Abbas, R., Abo-El-Enin, S.A. and Ezzat, E.-S., "Properties and durability of metakaolin blended cements: Mortar and concrete", *Materiales de Construcción*, Vol. 60, No. 300, (2010), 33-49. doi: 10.1016/j.conbuildmat.2009.02.011.
 42. Berndt, M.L., "Properties of sustainable concrete containing fly ash, slag and recycled concrete aggregate", *Construction and Building Materials*, Vol. 23, No. 7, (2009), 2606-2613. doi: 10.1016/j.conbuildmat.2009.02.011.
 43. Çakır, Ö., "Experimental analysis of properties of recycled coarse aggregate (rca) concrete with mineral additives", *Construction and Building Materials*, Vol. 68, (2014), 17-25. doi: 10.1016/j.conbuildmat.2014.06.032.
 44. H Younis, K., "Nano-silica modified recycled aggregate concrete: Mechanical properties and microstructure", *Eurasian Journal of Science & Engineering*, Vol. 3, No. 3, (2018), 167-176.

COPYRIGHTS

©2023 The author(s). This is an open access article distributed under the terms of the Creative Commons Attribution (CC BY 4.0), which permits unrestricted use, distribution, and reproduction in any medium, as long as the original authors and source are cited. No permission is required from the authors or the publishers.

**Persian Abstract**

چکیده

منابع طبیعی زمین متعلق به همه است و باید برای نسل های آینده حفظ شود. بنابراین مدیریت و مصرف زیاده دغدغه اصلی محققین است. استفاده از منابع ضایعاتی برای ساخت و ساز پایدار این به دلیل مزایای زیست محیطی و اقتصادی آن به طور فزاینده ای محبوب شده است. این مقاله از مواد زاید برای افزایش پایداری در کارهای ساختمانی با پایه سیمانی مانند بتن ضایعاتی به عنوان جایگزین سنگدانه معمولی و سرباره کوره بلند دانه بندی شده زمینی (GGBFS) به عنوان مواد سیمانی مکمل (SCMs) برای بهبود پایداری در تولید روسازی های صلب، کاهش استفاده از مواد خام CO₂ و کاهش تولید سیمان بندری استفاده می کند. نمونه های مکعبی، استوانه ای و منشوری در آزمایشگاه با (۰، ۱۰، ۲۰، ۳۰، ۴۰ درصد) وزن دانه های بتن زیاله (WC) به عنوان جایگزین از سنگدانه های طبیعی تهیه شدند. شاخص فعالیت مقاومتی (SAI) نمونه های بتن در ناحیه مقاومت پذیرش با کاهش جزئی در مقایسه با مقاومت بتن معمولی بود. از سوی دیگر، اثر ترکیبی استفاده از GGBFS به عنوان SCM با نسبت های مختلف GGBFS/PC (0.8، 1.2، 1.6، 2)، و WC به ترتیب (۴۰٪، ۳۰٪، ۲۰٪ و ۱۰٪) به نظر می رسد که SAI افزایش یافته است. سه نمونه تولید شده در هر نوع مخلوط پس از ۷ و ۲۸ روز از سن پخت مورد آزمایش قرار گرفتند. یافته های حاصل از آزمون های مقاومت فشاری، شکافتن و خمشی انجام شده بر روی مخلوط های حاوی سنگدانه بازیافتی، مناسب بودن آن ها برای استفاده در روسازی های صلب برای جاده های فرعی را نشان می دهد. مشاهده شد که با افزایش نسبت سنگدانه های بازیافتی در مخلوط، مقاومت بتن کاهش می یابد. هنگامی که سرباره کوره بلند دانه بندی شده آسیاب شده (GGBFS) به مخلوط های بتن اضافه شد، نتایج بسته به نسبت GGBFS موجود در مخلوط متفاوت بود. در میان مخلوط های مختلف آزمایش شده، مخلوطی که به عنوان R30S1.2 تعیین شده است، بالاترین بار مقاومتی را داشت و می توان از آن برای جاده های اصلی استفاده کرد. نتایج حاکی از آن است که استفاده از سنگدانه های بازیافتی به نسبت ۳۰٪ و ۵۵٪ GGBFS بهترین نتایج استحکام را به همراه داشته و در عین حال میزان مصرف سیمان و سنگدانه های طبیعی را کاهش می دهد و این امر با کاهش حضور ضایعات بر محیط زیست تأثیر می گذارد.



Prediction of Hardness of Copper-based Nanocomposites Fabricated by Ball-milling using Artificial Neural Network

R. M. Babaheydari^a, S. O. Mirabotalebi^{*a,b}, G. H. Akbari^a, H. Salehifar^c

^a Department of Materials & Metallurgy, Faculty of Engineering, Shahid Bahonar University of Kerman, Kerman, Iran

^b College of Science and Engineering, James Cook University, Townsville, Queensland, Australia

^c Department of Computer Science and Automation, Technical University of Ilmenau, Germany

PAPER INFO

Paper history:

Received 16 June 2023

Received in revised form 21 July 2023

Accepted 23 July 2023

Keywords:

Copper Nanocomposites

Copper Alloys

Mechanical Alloying

Artificial Neural Network

Prediction Micro-hardness

Mechanical Properties

ABSTRACT

Copper-based alloys are one of the most popular materials in the power distribution, welding industry, hydraulic equipment, industrial machinery, etc. Among different methods for the fabrication of Cu alloys, mechanical alloying (MA) is the major approach due to the fact that this approach is simple, inexpensive, suitable for mass production, and has a high capacity for homogeneous distribution of the second phase. However, the prediction of the hardness of products is very difficult in MA because of a lot of effective parameters. In this work, we designed a feed-forward back propagation neural network (FFBPNN) to predict the hardness of copper-based nanocomposites. First, some of the most common nanocomposites of copper including Cu-Al, Cu-Al₂O₃, Cu-Cr, and Cu-Ti were synthesized by mechanical alloying of copper at varying weight percentages (1, 3, and 6). Next, the alloyed powders were compacted by a cold press (12 tons) and subjected to heat treatment at 650°C. Then, the strength of the alloys was measured by the Vickers microscopy test. Finally, to anticipate the micro-hardness of Cu nanocomposites, the significant variables in the ball milling process including hardness, size, and volume of the reinforcement material, vial speed, the ball-to-powder-weight-ratio (BPR), and milling time; were determined as the inputs, and hardness of nanocomposite was assumed as an output of the artificial neural network (ANN). For training the ANN, many different ANN architectures have been employed and the optimal structure of the model was obtained by regression of 0.9914. The network was designed with two hidden layers. The first and second hidden layer includes 12 and 8 neurons, respectively. The comparison between the predicted results of the network and the experimental values showed that the proposed model with a root mean square error (RMSE) of 3.7 % can predict the micro-hardness of the nanocomposites.

doi: 10.5829/ije.2023.36.10a.17

1. INTRODUCTION

Nanocomposites and advanced materials have a widespread application in various fields, and based on the production methods, there are different generation strategies [1-3]. Adding alloying elements to the copper lattice is a common way to increase the mechanical properties alongside the electrical properties of copper-based composites. In other words, copper alloys are able to strengthen without a major decrease in their electrical properties [4, 5]. The creation of a saturated solid solution and the nano-sized precipitations in the copper lattice is

a desirable method to increase the toughness, tensile strength, creep resistance, and thermal stability of Cu with negligible reduction in the electrical conductivity [6, 7]. Except for Cu-Be, different copper-based alloys are being developed. Cu-Ti alloy is a striking example, which is a favorable alternative for Cu-Be. In general, Cu composites have proper strength, excellent electrical conductivity, high corrosion resistance, and suitable thermal stability [8, 9]. Likewise, each of the Cu-based composites has various applications. For instance, Cu-Al in solar powers and memory alloys [10], Cu-Al₂O₃ in

*Corresponding Author Email: oveis@eng.uk.ac.ir
(S. O. Mirabotalebi)

electrodes [11], Cu-Cr in fuel cells [12], and Cu-Ti in solar cells [13]; are being used.

The common methods for fabrication copper composites including in-situ reduction [14], melting and casting [15, 16], electrolysis [17], hydrothermal [18], severe plastic deformation (SPD) [19], sol-gel [20, 21], accumulative roll-bonding (ARB) [22], and high-energy ball milling [5, 23]. Among these approaches, mechanical alloying is a simple, inexpensive, and environmental-friendly process with the uniform dispersion of the alloying elements and has been widely used for the fabrication of advanced materials and nanocomposites [24, 25].

The effective parameters during the milling process influence various properties of Cu nanocomposites, especially the micro-hardness. The wrong combination of the MA parameters leads to an undesirable product and disrupts the balance between the electrical and mechanical properties of Cu-based nanocomposites. The exact determination of the micro-hardness of Cu-based composites results in the optimal usage of the process for the widespread synthesizing of copper nanocomposites.

There are several numerical analyses for the prediction of desirable output and optimization of the process, such as ANN [26], Genetic Algorithm [5], and Taguchi [27, 28]. ANN owing to its high capacity for the classification of big data, reaching a trusted solution, and approaching various variables, is a powerful machine learning approach for the prediction of outputs [29-31]. This method could be used as a parallel process with non-linear handling and adaptability which has a high capability to analyze various factors (noisy data) to predict the outputs. As a result, the artificial neural network is widely used in mechanical alloying owing to various major factors and the stochastic nature of the MA. The mechanism of ANN is also relatively simple and is based on training and then the anticipation of output. Nevertheless, no previous study has investigated a comprehensive model for the anticipation of the hardness of the main copper composites.

In this study, Cu-Al, Cu-Al₂O₃, Cu-Cr, and Cu-Ti with different percentages of the reinforcement elements were produced by MA. Then, the generated Cu composites were analyzed by X-ray powder diffraction (XRD) and scanning electron microscopy (SEM). Afterward, the sintering process was carried out and the micro-hardness of the Cu solid solutions was investigated via a Vickers hardness tester. Lastly, the obtained hardness data were used to design an ANN for predicting the micro-hardness of Cu-nanocomposites.

2. ANN MODELING

ANN is based on the intelligent creatures learning procedure containing interrelated cells called nodes or

neurons. They are the basic computational units that are linked together through the signals. The signals aggregate into layers and signal transmission between input and output is performed several times [32]. ANN is constructed of the input, hidden, and output layers. The learning process of a neural network includes regulating the neuron's bias, altering the weights, and output normalization via the transfer functions. The process of the training process will be extended till the ANN network reach near the favorable output and attain a reasonable percentage error.

The mathematical equation of an artificial neural network is able to be extracted from the mentioned component including biases, weights, transfer functions, and neurons. The connection between neurons is defined by Equation (1):

$$x = \sum_{i=1}^p w_i x + b \quad (1)$$

where x is the output and p is the number of components in the layer. $w_i x$ and b are the weight and bias, respectively.

3. EXPERIMENTAL

High-purity flakes of copper, chromium, aluminum, alumina, and titanium were chosen as the precursors. Specimens with different weight percentages of the second phase (1, 3, and 6) were mechanically alloyed in a planetary ball mill under the Argon. Two sizes of balls (15 and 10 mm in diameter) were used and BPR was kept at 15:1. The primary raw material was copper powders (15 g). Cu-Al and Cu-Al₂O₃ were milled for 40 h and the activation time for Cu-Ti and Cu-Cr was 90 h at a vial speed of 350 rpm. The selection of milling times was based on the experience of similar studies for the creation of the solid solution of Cu alloys.

A Philips X'PERT MPD (Cu-K α) was used to analyze the crystallographic structures of samples. Morphology and size of Cu particles were studied by SEM (Cam Scan mv2300). For the annealing of the specimens, the alloying powders were molded to a thickness of 1 mm and a diameter of 1 cm. 1.4 g of samples were have been pressed by an automatic powder cold press machine (12 tons). The annealing process was applied in a simple heat treatment oven for 30 minutes at 650°C under Argon atmosphere. The Vickers hardness testing was carried out as stated in the ASTM International Standards (E-348-89) and hardness was monitored by an impression of a load (98.7 mN) which is applied smoothly for 5 s at high magnification.

4. RESULTS AND DISCUSSION

The XRD patterns of Cu-based solid solutions after the mechanical alloying are shown in Figure 1. It is very

significant to confirm the creation of XRD patterns of Cu-based solid solutions. In the MA process, all of the particles are rigorously distorted through the collision of the balls which causes a rise in the atomic diffusion and regional temperature [33]. The solubility of alloying elements in Cu is increased by raising the temperature. Simultaneously, the concentration of crystallographic defects (dislocations, stacking faults, and vacancies) was significantly developed throughout the MA. Consequently, the flakes become work-hardened after a while, and the width of peaks was also enhanced by the rise in the work-hardening of the micro-strain [9]. Growth in weight percentage of the second phase brings on the height reduction and width broadening of the XRD profiles, as well as, peaks shifting to lower angles (except Cu-Al₂O₃). Chromium, titanium, and aluminum have a larger atomic size than Cu. Thus, the disintegration of the reinforced materials and increasing concentration in the copper lattice rise the lattice constant of copper and move the X-ray diffraction patterns to the left. The non-movement of the major peaks of Cu in the XRD patterns of Al₂O₃ illustrates that the particles of alumina were not dissolved within the copper lattice.

The morphology of the samples is depicted in Figures 2-5. The particle size of Cu-Al alloys is declined by proportion enhancement in Al₂O₃. Generally, particles are soft at the start of the MA, although, they were welded together and tend to agglomeration during the mechanical alloying [34]. The reduction of powder particle size of Al₂O₃ follows two distinct mechanisms.

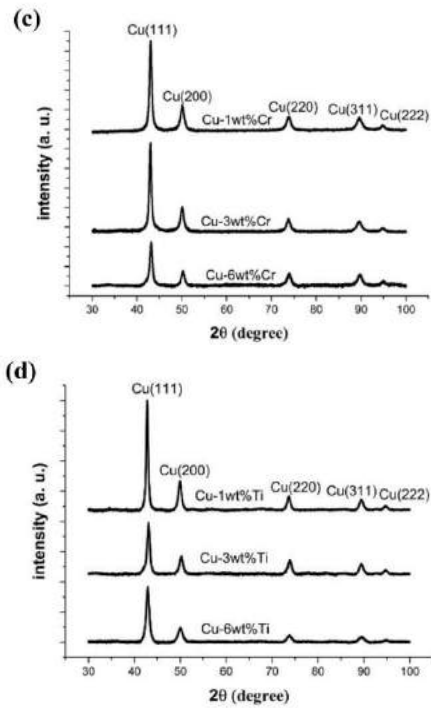
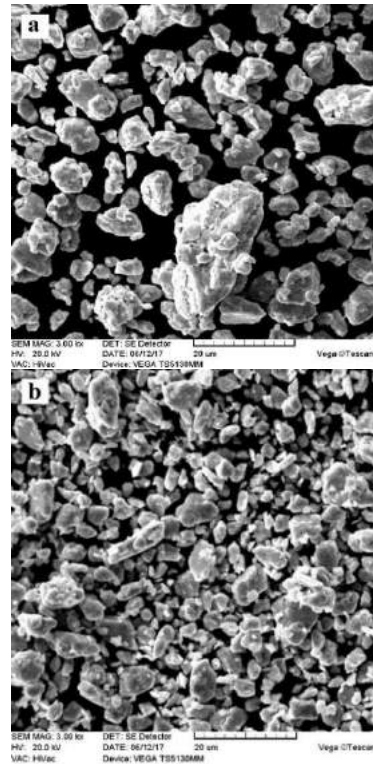
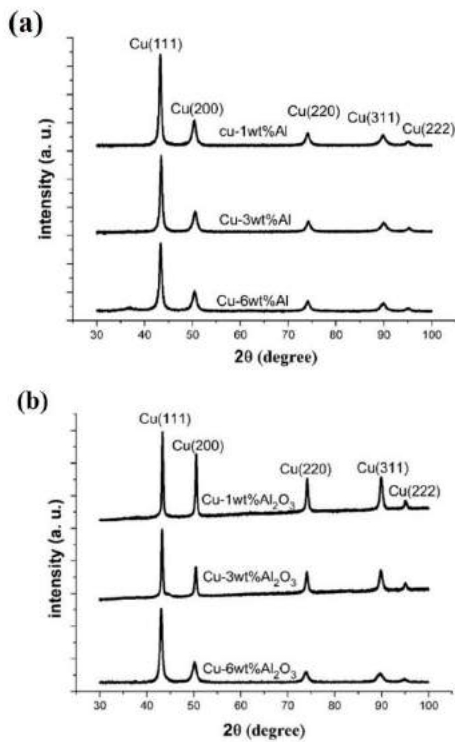


Figure 1. XRD of Cu-Al (a), Cu- Al₂O₃, Cu-Cr, and Cu-Ti nanocomposites prepared by MA

First, through incorporating the Cu particles. Second, by increasing the strain of the lattice via fracturing the



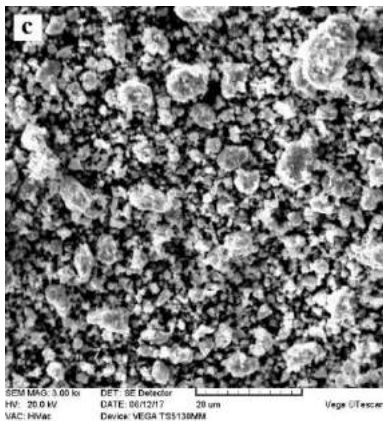


Figure 2. SEM images of Cu-Al alloys with 1, 3, and 6 weight percentages

alumina particles during the milling process. Therefore, the crisp particles of Al_2O_3 are broken and become smaller by rising the work hardening [35].

The long milling time due to high cold working (90 h) results in the dissolution of chromium in the copper matrix. Moreover, the dissolution of Cr in the structure was increased at high chromium proportions, thereby fracturing and crisping of Cu parties were performed. In addition, intense work-hardening leads to the formation of micro-cracks and motion-less dislocations, because of the BCC crystallographic structure of Cr. The other micro-cracks will be created at the margin of the particles. Cr powders will be spread in the matrix and induce these micro-cracks to develop and open [36]. So,

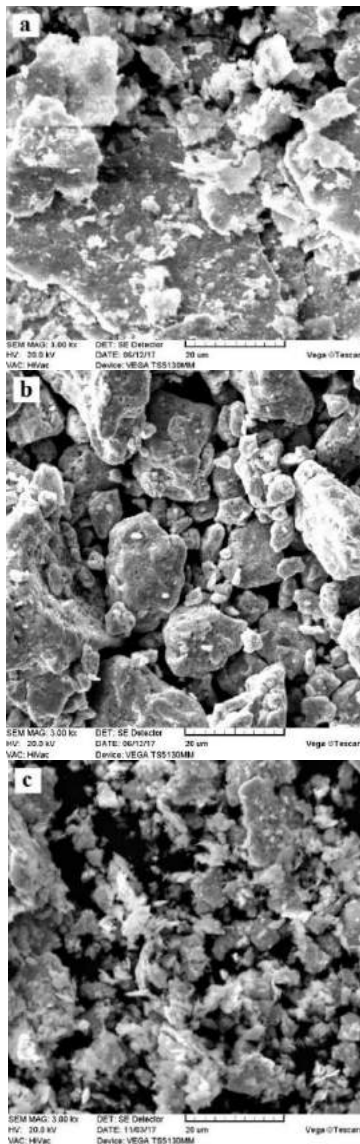


Figure 3. SEM images of Cu- Al_2O_3 samples with 1, 3, and 6 weight percentages

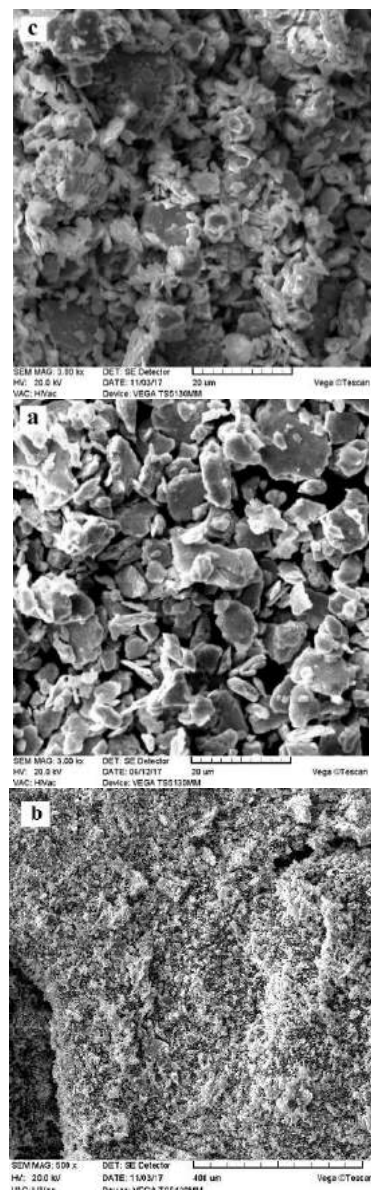


Figure 4. SEM images of Cu-Cr alloys with 1, 3, and 6 weight percentages

it can be assumed that the higher percentage of chromium results in the smaller Cr composite particles at the same activation time. Finally, fine and uniform morphology is acquired by repeated fractures.

Likewise, the particle size distribution of copper-titanium alloys is reduced and they also became agglomerated because of the long activating time (90 h) and creation of a balance between fracture and cold welding. The hexagonal close-packed (HCP) crystal structures of Ti particles are trapped between Cu powders with the face-centered cubic (FCC) structures, which have a more quick work-hardening than Cu [37]. At the current step, the higher fragile Ti powders are spread into the smoother Cu powders and they generate small cracks in their margins which significantly decreases the mechanical properties of the composites [36].

Figure 3 shows SEM images of Cu-Al₂O₃ samples with 1, 3, and 6 weight percentages. SEM images of Cu-Cr alloys with 1, 3, and 6 weight percentages is shown in Figure 4. Also, Figure 5 depicts SEM images of Cu-Ti alloys with 1, 3, and 6 weight percentages.

The micro-hardness of the products after the heat treatment is represented in Figure 6. Cu-1wt%Al₂O₃ and Cu-6wt%Ti had the lowest and highest micro-hardness, respectively. It is worth noting that the inserted forces during the pressing stage did not cause a major change in the hardness of specimens. This is because of an extensive cold hardening of the particle during the process [36].

The number of vacancies and dislocations declined significantly after the annealing procedure. This process is similar to solid solutions, which decomposed after the heat treatment step [38]. Hence, porosity, grain boundaries, and particles of alloying elements are the main reasons for residual resistivity.

By enhancement in the percentage of the second phase, the hardness of all Cu-based composites was raised. As mentioned previously, the enhancement volume of alloying elements causes a boost in the lattice constant and strength of nanocomposites. A higher proportion in reinforcement materials, richer solid solution, and a higher density of dislocations result in Cu cold working and as a result, micro-hardness of the composites was improved. On the one hand, a high amount of coherent precipitates will be created because of the high content of a solid solution in aging. On the other, defects create favored areas to precipitate. Therefore, generated precipitates inhibit the recrystallization and recovery.

Ti has low solvability in Cu at ambient temperature (less than 0.1% of atomic weight) [39]. During the MA process, the density of Ti in the Cu lattice is raised and attained a balance status. The created Ti super-saturation in the copper matrix via mechanical alloying and sintering presents an appropriate condition for the fabrication of Ti with a nano-scale structure.

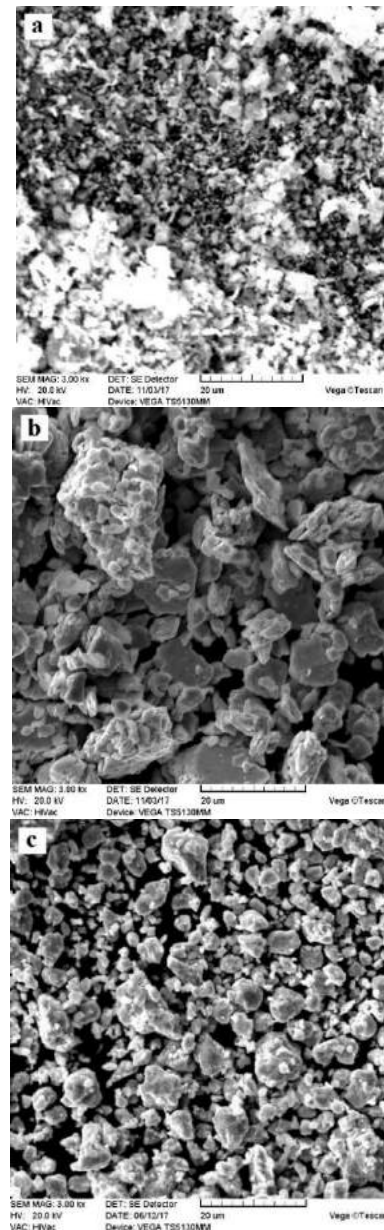


Figure 5. SEM images of Cu-Ti alloys with 1, 3, and 6 weight percentages

Subsequently, the creation of the rich titanium particles in the Cu lattice at the annealing stage coincides with the recovery and recrystallization. This phenomenon frequently ceased the softening procedure. Formed Cu₄Ti at the beginning steps of heat treatment is in the shape of uniform nanostructures [40]. The mentioned precipitates are produced inside the grain boundaries [41] and they act as obstacles to dislocation movements. As a result, they will delay recovery and recrystallization, and the micro-hardness of nanocomposites will be increased.

Similar to Cu-Ti, the mentioned hardening mechanism is valid for Cu-Cr and Cu-Al alloys and so

the second phase rises the heat of recrystallization and postpones the recrystallization and recovery. Uniform precipitation of copper-chromium and copper-aluminum that was created at the aging step, causes the halt of recrystallization and rises the strength. The maximum hardness in copper-based composites is achievable if all of the effective variables in the milling and annealing steps are performed accurately. Figure 7 indicates the schematic diagram of the ideal Cu-based nanocomposites with homogenous dispersion of nano-sized particles in the grains.

4. 1. ANN Architecture There is no general rule to determine the minimum or the maximum number of required datasets in an ANN network [42]. However, it seems the model needs a reasonable number of data to avoid under-training or over-training. Here, 12 and 85 data were used for verification and training of the model, respectively.

FFBPNN was used for the learning module. Feed-forward back propagation neural network is a specific type of ANN with many capabilities to attain favorable outcomes and is extensively applied in the MA to participate in major variables in previous works [43-45]. There are two steps per turn of the process in FFBPNN.

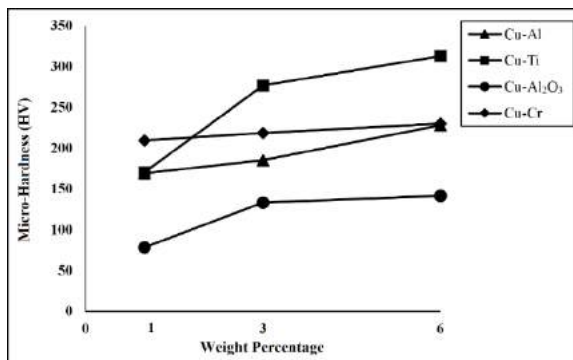


Figure 6. The micro-hardness of the Cu-based composites at different weight percentages of alloying element

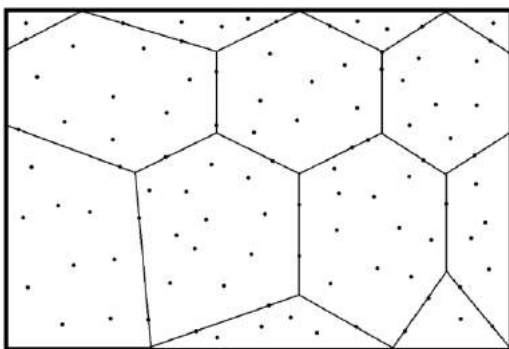


Figure 7. Schematic illustration of an ideal nano-dispersed of the second phase particles to achieve the maximum strength in the Cu-based nanocomposites

First is the specification of a random number for all weight factors which is the feed-forward. Next, altering the weights to reach the outcome with lower error and closer to the actual quantity which is the back-propagation. The cycle is done frequently till the outcome of the model reaches the closest actual value for all of the training data [46, 47].

Basically, there is no straightforward way to optimize the structure of an ANN model [29]. For the effective function of the network, various learning architectures have been applied to assess the structure of the network during the learning step. The created model includes two hidden layers with input and output layers. The hidden layers include 12 and 8 neurons in the first and second layers, respectively. Input parameters were the hardness, volume, and size of reinforcements, BPR, speed and time of ball-milling, and the initial size. As well as, the hardness of the nanocomposite was the output. Figure 8 shows the graphical abstract of the designed ANN.

In order to compute the regression, the finite element method and the trained model were applied. The regression is illustrated in Table 1. Regarding the regression, “Tansig”, “Purelin”, and “Logsig” are the finest functions for the hidden layers (1st and 2nd) and output layer, respectively (number 10). Obviously, trial and error do not follow a general pattern. As a result, it needs to train the network several times to reach an acceptable error without any specific approach. The trial and error strategy is used vastly in other similar studies in order to find a more suitable network structure and decrease the regression [48, 49].

To design the network, MATLAB (2014) owing to its user-friendly was used. Moreover, the Levenberg–Marquardt algorithm due to rapid training ability was employed for training the model. In addition, the log-sigmoid activation function was utilized as the transfer function. This is a non-linear and S-shaped function which is defined according to Equation (2):

$$f(x) = \frac{1}{1+e^{-x}} \quad (2)$$

The collected data had been normalized and homogenized (0.1-0.9) according to Equation (3):

$$N = 0.8 \left(\frac{x-x_{min}}{x_{max}-x_{min}} \right) + 0.1 \quad (3)$$

RMSE is defined as the standard deviation of the differences between the actual and predicted values. Here, the RMSE of the model was calculated using Equation (4):

$$RMSE = \frac{1}{N} \sum_{i=1}^N \left(\frac{|\text{True value} - \text{Predicted value}|}{\text{True value}} \times 100 \right) \quad (4)$$

4. 2. ANN Results

Regression analysis was performed for testing the precision of the designed network. Figure 9 illustrates the result of the regression analysis. Based on Figure 9, the general regression is

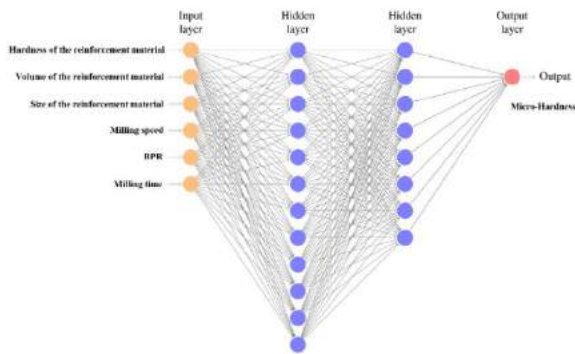


Figure 8. Architecture of the designed ANN

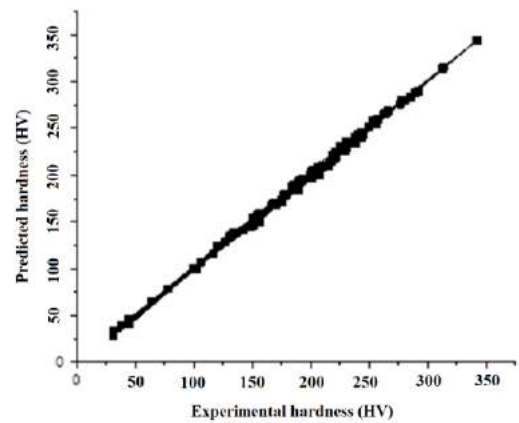


Figure 9. The regression of the ANN model

TABLE 1. The values of regressions for different ANN structures

No.	Transfer function		Output layer	Nodes in hidden layers		Regression (R ²)
	Hidden layers			Layer two	Layer one	
	Layer two	Layer one				
1	Tansig	Tansig	Tansig	16	12	0.8843
2	Tansig	Logsig	Purelin	12	7	0.7634
3	Logsig	Logsig	Tansig	3	5	0.6674
4	Logsig	Logsig	Logsig	7	5	0.4219
5	Logsig	Logsig	Purelin	9	6	0.7396
6	Logsig	Tansig	Logsig	3	7	0.5732
7	Tansig	Tansig	Tansig	16	12	0.9318
8	Tansig	Logsig	Purelin	12	7	0.8843
9	Logsig	Logsig	Tansig	3	5	0.7634
10*	Tansig	Purelin	Logsig	12	8	0.9914

*Best ANN structure

0.9914. The result of the regression graph shows that there is a good fit between experimental hardness and predicted hardness. Therefore, the network model is prepared to anticipate the micro-hardness of copper composites with a reasonable percentage of error.

For verification of the generated model, a comparison between experimental and predicted data was performed. The error of the network was calculated by 3.7% regarding Equation (4). Table 2 indicates the actual and anticipated values for the micro-hardness of the different Cu nanocomposites. The validation results confirm that created network is reliable and with high accuracy anticipates the experimental values of the micro-hardness. As a consequence, it can be assumed that the designed ANN could predict another similar study with such high reliability and approximation. Additionally, the created model results in a more proximate evaluation of lab-based works, due to several major variables in

TABLE 2. Comparison of the actual and predicted values for different Cu-based nanocomposites

Experimental Micro-Hardness (HV)	Anticipated Micro-Hardness (HV)	Samples
169	171	Cu-1wt%Al
185	183	Cu-3wt%Al
228	232	Cu-6wt%Al
78	89	Cu-1wt%Al ₂ O ₃
133	143	Cu-3wt%Al ₂ O ₃
141	153	Cu-6wt%Al ₂ O ₃
209	210	Cu-1wt%Cr
218	219	Cu-3wt%Cr
229	228	Cu-6wt%Cr
170	175	Cu-1wt%Ti
276	276	Cu-3wt%Ti
312	293	Cu-6wt%Ti

mechanical alloying and the complexity of coordinating and launching them.

5. CONCLUSION

1. The morphology of Cu-based alloys was fundamentally different from each other and tends to be smaller particles via the rising volume of the reinforcement materials. Adding Al₂O₃ to the Cu matrix forms a sheet-like morphology; while adding aluminum, chromium, and titanium leads to homogeneous morphology in Cu-based composites.
2. The hardness of the alloys was raised via the enhancement in the percentage of the second phase. Al₂O₃ and Ti had the lowest and highest impact on the micro-hardness, respectively.

3. The FFBPNN with 12 and 8 neurons in the first and second hidden layers, respectively, is an efficient approach for the anticipation of the microhardness of Cu nanocomposites produced via mechanical alloying.
4. To design a reliable ANN architecture, “Tansig”, “Purelin”, and “Logsig” are the favourable activation functions for the hidden layers (1st and 2nd), and output layer, respectively.
5. RMSE of the proposed network for prediction of the micro-hardness of Cu nanocomposites was 3.7%.

6. REFERENCES

1. Saindane, U., Soni, S. and Menghani, J., "Dry sliding behavior of carbon-based brake pad materials", *International Journal of Engineering*, Vol. 34, No. 11, (2021), 2517-2524. doi: 10.5829/IJE.2021.34.11B.14.
2. Saindane, U., Soni, S. and Menghani, J., "Performance evaluation of brake pads developed using two different manufacturing methods", *Materialwissenschaft und Werkstofftechnik*, Vol. 54, No. 2, (2023), 186-195. <https://doi.org/10.1002/mawe.202100407>
3. Asgharian Marzabad, M., Jafari, B. and Norouzi, P., "Determination of riboflavin by nanocomposite modified carbon paste electrode in biological fluids using fast fourier transform square wave voltammetry", *International Journal of Engineering, Transactions C: Aspects*, Vol. 33, No. 9, (2020), 1696-1702. doi: 10.5829/IJE.2020.33.09C.01.
4. Pellizzari, M. and Cipolloni, G., "Tribological behaviour of cu based materials produced by mechanical milling/alloying and spark plasma sintering", *Wear*, Vol. 376, (2017), 958-967. <https://doi.org/10.1016/j.wear.2016.11.050>
5. Torabi, A., Babaheydari, R., Akbari, G. and Mirabootelebi, S., "Optimizing of micro-hardness of nanostructured cu–cr solid solution produced by mechanical alloying using ann and genetic algorithm", *SN Applied Sciences*, Vol. 2, No. 11, (2020), 1-9. <https://doi.org/10.1007/s42452-020-03722-x>
6. Fathy, A., Wagih, A. and Abu-Oqail, A., "Effect of zro2 content on properties of cu-zro2 nanocomposites synthesized by optimized high energy ball milling", *Ceramics International*, Vol. 45, No. 2, (2019), 2319-2329. <https://doi.org/10.1016/j.ceramint.2018.10.147>
7. Abu-Oqail, A., Samir, A., Essa, A., Wagih, A. and Fathy, A., "Effect of gnps coated ag on microstructure and mechanical properties of cu-fe dual-matrix nanocomposite", *Journal of Alloys and Compounds*, Vol. 781, (2019), 64-74. <https://doi.org/10.1016/j.jallcom.2018.12.042>
8. Eze, A.A., Jamiru, T., Sadiku, E.R., Durwoju, M.O., Kupolati, W.K., Ibrahim, I.D., Obadele, B.A., Olubambi, P.A. and Diouf, S., "Effect of titanium addition on the microstructure, electrical conductivity and mechanical properties of copper by using sps for the preparation of cu-ti alloys", *Journal of Alloys and Compounds*, Vol. 736, (2018), 163-171. <https://doi.org/10.1016/j.jallcom.2017.11.129>
9. Babaheydari, R., Mirabootelebi, S. and Akbari, G., "Investigation on mechanical and electrical properties of cu-ti nanocomposite produced by mechanical alloying", *International Journal of Engineering, Transactions C: Aspects*, Vol. 33, No. 9, (2020), 1759-1765. doi: 10.5829/IJE.2020.33.09C.09.
10. Alex, S., Chattopadhyay, K., Barshilia, H.C. and Basu, B., "Thermally evaporated cu–al thin film coated flexible glass mirror for concentrated solar power applications", *Materials Chemistry and Physics*, Vol. 232, (2019), 221-228. <https://doi.org/10.1016/j.matchemphys.2019.04.078>
11. Hussain, M., Khan, U., Jangid, R. and Khan, S., "Hardness and wear analysis of cu/Al₂O₃ composite for application in edm electrode", in IOP Conference Series: Materials Science and Engineering, IOP Publishing. Vol. 310, (2018), 012044.
12. De Marco, V., Grazioli, A. and Sglavo, V.M., "Production of planar copper-based anode supported intermediate temperature solid oxide fuel cells cosintered at 950 c", *Journal of Power Sources*, Vol. 328, (2016), 235-240. <https://doi.org/10.1016/j.jpowsour.2016.08.025>
13. Saha, S., Abd Hamid, S.B. and Ali, T.H., "Catalytic evaluation on liquid phase oxidation of vanillyl alcohol using air and H₂O₂ over mesoporous cu-ti composite oxide", *Applied Surface Science*, Vol. 394, (2017), 205-218. <https://doi.org/10.1016/j.apsusc.2016.10.070>
14. Shen, D., Zhu, Y., Yang, X. and Tong, W., "Investigation on the microstructure and properties of cu-cr alloy prepared by in-situ synthesis method", *Vacuum*, Vol. 149, (2018), 207-213. <https://doi.org/10.1016/j.vacuum.2017.12.035>
15. Gustmann, T., Dos Santos, J., Gargarella, P., Kühn, U., Van Humbeeck, J. and Pauly, S., "Properties of cu-based shape-memory alloys prepared by selective laser melting", *Shape Memory and Superelasticity*, Vol. 3, No. 1, (2017), 24-36. <https://doi.org/10.1007/s40830-016-0088-6>
16. Li, J., Chang, L., Li, S., Zhu, X. and An, Z., "Microstructure and properties of as-cast cu-cr-zr alloys with lanthanum addition", *Journal of Rare Earths*, Vol. 36, No. 4, (2018), 424-429. <https://doi.org/10.1016/j.jre.2017.11.006>
17. Vorotilo, S., Loginov, P.A., Churyumov, A.Y., Prosviryakov, A.S., Bychkova, M.Y., Rupasov, S.I., Orekhov, A.S., Kiryukhantsev-Korneev, P.V. and Levashov, E.A., "Manufacturing of conductive, wear-resistant nanoreinforced cu-ti alloys using partially oxidized electrolytic copper powder", *Nanomaterials*, Vol. 10, No. 7, (2020), 1261. <https://doi.org/10.3390/nano10071261>
18. Agboola, P.O., Shakir, I., Almutairi, Z.A. and Shar, S.S., "Hydrothermal synthesis of cu-doped cos₂@ nf as high performance binder free electrode material for supercapacitors applications", *Ceramics International*, Vol. 48, No. 6, (2022), 8509-8516. <https://doi.org/10.1016/j.ceramint.2021.12.061>
19. Rodak, K., "Cu-cr and cu-fe alloys processed by new severe plastic deformation: Microstructure and properties", *Severe Plastic Deformation Techniques*, (2017), 115. doi: 10.5772/intechopen.68954.
20. Awadallah, O. and Cheng, Z., "Formation of sol-gel based cu₂znsns₄ thin films using ppm-level hydrogen sulfide", *Thin Solid Films*, Vol. 625, (2017), 122-130. <https://doi.org/10.1016/j.tsf.2017.01.054>
21. Liao, L.C.-K. and Huang, J.-S., "Energy-level variations of cu-doped zno fabricated through sol-gel processing", *Journal of Alloys and Compounds*, Vol. 702, (2017), 153-160. <https://doi.org/10.1016/j.jallcom.2017.01.174>
22. Hosseini, M., Pardis, N., Manesh, H.D., Abbasi, M. and Kim, D.-I., "Structural characteristics of cu/ti bimetal composite produced by accumulative roll-bonding (ARB)", *Materials & Design*, Vol. 113, (2017), 128-136. <https://doi.org/10.1016/j.matdes.2016.09.094>
23. Cheng, J., Cai, Q., Zhao, B., Yang, S., Chen, F. and Li, B., "Microstructure and mechanical properties of nanocrystalline al-zn-mg-cu alloy prepared by mechanical alloying and spark plasma sintering", *Materials*, Vol. 12, No. 8, (2019), 1255. <https://doi.org/10.3390/ma12081255>
24. Mirabootelebi, S. and Akbari, G., "Phase transformation in carbon during mechanical alloying of graphite: Experimental and

- molecular dynamic study", *Journal of Materials Engineering and Performance*, (2022), 1-11. <https://doi.org/10.1007/s11665-022-07706-3>
25. Mirabootalebi, S.O., "Experimental and molecular dynamic studies of phase transformation and amorphization in silicon during high-energy ball milling", *Materials Today: Proceedings*, Vol. 76, (2023), 607-615. <https://doi.org/10.1016/j.matpr.2022.12.098>.
 26. Mirabootalebi, S. and Babaheydari, R., "Prediction length of carbon nanotubes in cvd method by artificial neural network", *Iran JOC*, Vol. 11, No. 4, (2019), 2731.
 27. Majumder, H. and Maity, K., "Multi-response optimization of weld process parameters using taguchi based desirability function analysis", in IOP Conference Series: Materials Science and Engineering. IOP Publishing. (2018).
 28. Saindane, U., Soni, S. and Menghani, J., "Friction and wear performance of brake pad and optimization of manufacturing parameters using grey relational analysis", *International Journal of Engineering, Transactions C: Aspects*, Vol. 35, No. 3, (2022), 552-559. doi: 10.5829/IJE.2022.35.03C.07.
 29. Shaikh, R., Shirazian, S. and Walker, G.M., "Application of artificial neural network for prediction of particle size in pharmaceutical cocrystallization using mechanochemical synthesis", *Neural Computing and Applications*, Vol. 33, No. 19, (2021), 12621-12640. <https://doi.org/10.1007/s00521-021-05912-z>
 30. Babaheydari, R. and Mirabootalebi, S., "Prediction micro-hardness of al-based composites by using artificial neural network in mechanical alloying", *Journal of Environmental Friendly Materials*, Vol. 4, No. 1, (2020), 31-35.
 31. Petrucci, A.M. and Rahmani, M., "Validation and optimization of thermophysical properties for thermal conductivity and viscosity of nanofluid engine oil using neural network", *Journal of Modeling and Simulation of Materials*, Vol. 3, No. 1, (2020), 53-60. <https://doi.org/10.21467/jmsm.3.1.53-60>
 32. Da Silva, I.N., Spatti, D.H., Flauzino, R.A., Liboni, L.H.B. and dos Reis Alves, S.F., Artificial neural network architectures and training processes, in Artificial neural networks. 2017, Springer.21-28.
 33. Mirahmadi Babaheydari, R., Mirabootalebi, S.O. and Akbari Fakhrabadi, G.H., "Effect of alloying elements on hardness and electrical conductivity of cu nanocomposites prepared by mechanical alloying", *Iranian Journal of Materials Science and Engineering*, Vol. 18, No. 1, (2021), 1-11. doi: 10.22068/ijmse.18.1.1.
 34. Mirabootalebi, S., "A new method for preparing buckypaper by pressing a mixture of multi-walled carbon nanotubes and amorphous carbon", *Advanced Composites and Hybrid Materials*, Vol. 3, (2020), 336-343. <https://doi.org/10.1007/s42114-020-00167-z>
 35. Safi, S. and Akbari, G., "Evaluation of synthesizing al₂o₃ nano particles in copper matrix by mechanical alloying of cu-1% al and copper oxide", *Journal of Advanced Materials in Engineering (Esteghlal)*, Vol. 36, No. 1, (2017), 71-85. doi: 10.18869/ACADPUB.JAME.36.1.71.
 36. Suryanarayana, C., "Mechanical alloying and milling", *Progress in Materials Science*, Vol. 46, No. 1-2, (2001), 1-184. [https://doi.org/10.1016/S0079-6425\(99\)00010-9](https://doi.org/10.1016/S0079-6425(99)00010-9)
 37. Pourfereidouni, A. and Akbari, G.H., "Development of nano-structure cu-ti alloys by mechanical alloying process", in Advanced Materials Research. Vol. 829, (2013), 168-172.
 38. Wang, Y., Bossé, G., Nair, H., Schreiber, N., Ruf, J., Cheng, B., Adamo, C., Shai, D., Lubashevsky, Y. and Schlom, D., "Subterahertz momentum drag and violation of matthiessen's rule in an ultraclean ferromagnetic sruo 3 metallic thin film", *Physical Review Letters*, Vol. 125, No. 21, (2020), 217401. <https://doi.org/10.1103/PhysRevLett.125.217401>
 39. Murray, J., "The cu-ti (copper-titanium) system", *Bulletin of Alloy Phase Diagrams*, Vol. 4, No. 1, (1983), 81-95. <https://doi.org/10.1007/BF02880329>
 40. Datta, A. and Soffa, W., "The structure and properties of age hardened cu-ti alloys", *Acta Metallurgica*, Vol. 24, No. 11, (1976), 987-1001. [https://doi.org/10.1016/0001-6160\(76\)90129-2](https://doi.org/10.1016/0001-6160(76)90129-2)
 41. Lopez-Hirata, V.M., Hernandez-Santiago, F., Saucedo-Muñoz, M.L., Avila-Davila, E.O. and Villegas-Cardenas, J.D., Analysis of β'(cu 4 ti) precipitation during isothermal aging of a cu-4 wt% ti alloy, in Characterization of minerals, metals, and materials 2020. 2020, Springer.403-412.
 42. Akinwekomi, A.D. and Lawal, A.I., "Neural network-based model for predicting particle size of az61 powder during high-energy mechanical milling", *Neural Computing and Applications*, Vol. 33, No. 24, (2021), 17611-17619. <https://doi.org/10.1007/s00521-021-06345-4>
 43. Varol, T. and Ozsahin, S., "Artificial neural network analysis of the effect of matrix size and milling time on the properties of flake al-cu-mg alloy particles synthesized by ball milling", *Particulate Science and Technology*, Vol. 37, No. 3, (2019), 381-390. <https://doi.org/10.1080/02726351.2017.1381658>.
 44. Varol, T., Canakci, A. and Ozsahin, S., "Prediction of effect of reinforcement content, flake size and flake time on the density and hardness of flake aa2024-sic nanocomposites using neural networks", *Journal of Alloys and Compounds*, Vol. 739, (2018), 1005-1014. <https://doi.org/10.1016/j.jallcom.2017.12.256>
 45. Devadiga, U., Poojary, R.K.R. and Fernandes, P., "Artificial neural network technique to predict the properties of multiwall carbon nanotube-fly ash reinforced aluminium composite", *Journal of Materials Research and Technology*, Vol. 8, No. 5, (2019), 3970-3977. <https://doi.org/10.1016/j.jmrt.2019.07.005>
 46. Panda, S. and Panda, G., "Performance evaluation of a new bp algorithm for a modified artificial neural network", *Neural Processing Letters*, (2020), 1-21. <https://doi.org/10.1007/s11063-019-10172-z>.
 47. Mirabootalebi, S.O., Fakhrabadi, G.H.A. and Mirahmadi, R., "Carbon via ball milling of graphite and prediction of its crystallite size through ann", *Organomet. Chem.* Vol. 1, No. 2, (2021), 76-85. <http://dx.doi.org/10.22034/jaoc.2021.288020.1021>
 48. Zhou, G., Moayedi, H., Bahiraei, M. and Lyu, Z., "Employing artificial bee colony and particle swarm techniques for optimizing a neural network in prediction of heating and cooling loads of residential buildings", *Journal of Cleaner Production*, Vol. 254, (2020), 120082. <https://doi.org/10.1016/j.jclepro.2020.120082>
 49. Moayedi, H., Tien Bui, D., Gör, M., Pradhan, B. and Jaafari, A., "The feasibility of three prediction techniques of the artificial neural network, adaptive neuro-fuzzy inference system, and hybrid particle swarm optimization for assessing the safety factor of cohesive slopes", *ISPRS International Journal of Geo-Information*, Vol. 8, No. 9, (2019), 391. <https://doi.org/10.3390/ijgi8090391>

COPYRIGHTS

©2023 The author(s). This is an open access article distributed under the terms of the Creative Commons Attribution (CC BY 4.0), which permits unrestricted use, distribution, and reproduction in any medium, as long as the original authors and source are cited. No permission is required from the authors or the publishers.

**Persian Abstract****چکیده**

نانوکامپوزیت‌های بر پایه مس یکی از پرطرفدارترین مواد در توزیع برق، صنعت جوش، تجهیزات هیدرولیک، ماشین‌آلات صنعتی و غیره می‌باشند. در میان روش‌های مختلف برای ساخت آلیاژهای مس، آلیاژ مکانیکی (MA) رویکرد اصلی است. که این روش ساده، ارزان، مناسب برای تولید انبوه است و ظرفیت بالایی برای توزیع همگن فاز دوم دارد. با این حال، پیش‌بینی سختی محصولات در MA به دلیل وجود پارامترهای مؤثر بسیار دشوار است. در این کار، ما یک شبکه عصبی انتشار برگشتی پیش‌خور (FFBPNN) برای پیش‌بینی سختی نانو کامپوزیت‌های مبتنی بر مس طراحی کردیم. ابتدا، برخی از رایج‌ترین نانو کامپوزیت‌های مس از جمله Cu-Ti، Cu-Cr، Cu-Al₂O₃، Cu-Al با آلیاژ مکانیکی مس در درصدهای وزنی متفاوت (۱، ۳ و ۶) سنتز شدند. سپس پودرهای آلیاژی توسط پرس سرد (۱۲ تن) متراکم شده و تحت عملیات حرارتی در دمای ۶۵۰ درجه سانتیگراد قرار گرفتند. سپس استحکام آلیاژها با تست میکروسکوپ ویکرز اندازه‌گیری شد. در نهایت، برای پیش‌بینی ریزسختی نانو کامپوزیت‌های مس، متغیرهای مهم در فرآیند آسیاب گلوله‌ای شامل سختی، اندازه و حجم مواد تقویت‌کننده، سرعت و بال، نسبت وزنی توپ به پودر (BPR) و زمان آسیاب؛ به عنوان ورودی تعیین شد و سختی نانو کامپوزیت به عنوان خروجی شبکه عصبی مصنوعی (ANN) در نظر گرفته شد. برای آموزش شبکه عصبی مصنوعی، بسیاری از معماری‌های شبکه عصبی مصنوعی مختلف به کار گرفته شده است و ساختار بهینه مدل با رگرسیون ۰/۹۹۱۴ به دست آمد. این شبکه با دو لایه مخفی طراحی شده است. لایه پنهان اول و دوم به ترتیب شامل ۱۲ و ۸ نرون است. مقایسه بین نتایج پیش‌بینی شده شبکه و مقادیر تجربی نشان داد که مدل پیشنهادی با ریشه میانگین مربعات خطا (RMSE) 3.7 درصد می‌تواند ریزسختی نانو کامپوزیت‌ها را پیش‌بینی کند.

AIMS AND SCOPE

The objective of the International Journal of Engineering is to provide a forum for communication of information among the world's scientific and technological community and Iranian scientists and engineers. This journal intends to be of interest and utility to researchers and practitioners in the academic, industrial and governmental sectors. All original research contributions of significant value focused on basics, applications and aspects areas of engineering discipline are welcome.

This journal is published in three quarterly transactions: Transactions A (Basics) deal with the engineering fundamentals, Transactions B (Applications) are concerned with the application of the engineering knowledge in the daily life of the human being and Transactions C (Aspects) - starting from January 2012 - emphasize on the main engineering aspects whose elaboration can yield knowledge and expertise that can equally serve all branches of engineering discipline.

This journal will publish authoritative papers on theoretical and experimental researches and advanced applications embodying the results of extensive field, plant, laboratory or theoretical investigation or new interpretations of existing problems. It may also feature - when appropriate - research notes, technical notes, state-of-the-art survey type papers, short communications, letters to the editor, meeting schedules and conference announcements. The language of publication is English. Each paper should contain an abstract both in English and in Persian. However, for the authors who are not familiar with Persian, the publisher will prepare the latter. The abstracts should not exceed 250 words.

All manuscripts will be peer-reviewed by qualified reviewers. The material should be presented clearly and concisely:

- *Full papers* must be based on completed original works of significant novelty. The papers are not strictly limited in length. However, lengthy contributions may be delayed due to limited space. It is advised to keep papers limited to 7500 words.
- *Research notes* are considered as short items that include theoretical or experimental results of immediate current interest.
- *Technical notes* are also considered as short items of enough technical acceptability with more rapid publication appeal. The length of a research or technical note is recommended not to exceed 2500 words or 4 journal pages (including figures and tables).

Review papers are only considered from highly qualified well-known authors generally assigned by the editorial board or editor in chief. Short communications and letters to the editor should contain a text of about 1000 words and whatever figures and tables that may be required to support the text. They include discussion of full papers and short items and should contribute to the original article by providing confirmation or additional interpretation. Discussion of papers will be referred to author(s) for reply and will concurrently be published with reply of author(s).

INSTRUCTIONS FOR AUTHORS

Submission of a manuscript represents that it has neither been published nor submitted for publication elsewhere and is result of research carried out by author(s). Presentation in a conference and appearance in a symposium proceeding is not considered prior publication.

Authors are required to include a list describing all the symbols and abbreviations in the paper. Use of the international system of measurement units is mandatory.

- On-line submission of manuscripts results in faster publication process and is recommended. Instructions are given in the IJE web sites: www.ije.ir-www.ijeir.info
- Hardcopy submissions must include MS Word and jpg files.
- Manuscripts should be typewritten on one side of A4 paper, double-spaced, with adequate margins.
- References should be numbered in brackets and appear in sequence through the text. List of references should be given at the end of the paper.
- Figure captions are to be indicated under the illustrations. They should sufficiently explain the figures.
- Illustrations should appear in their appropriate places in the text.
- Tables and diagrams should be submitted in a form suitable for reproduction.
- Photographs should be of high quality saved as jpg files.
- Tables, Illustrations, Figures and Diagrams will be normally printed in single column width (8cm). Exceptionally large ones may be printed across two columns (17cm).

PAGE CHARGES AND REPRINTS

The papers are strictly limited in length, maximum 8 journal pages (including figures and tables). For the additional to 8 journal pages, there will be page charges. It is advised to keep papers limited to 3500 words.

Page Charges for Papers More Than 8 Pages (Including Abstract)

For International Author ***	\$55 / per page
For Local Author	100,000 Toman / per page

AUTHOR CHECKLIST

- Author(s), bio-data including affiliation(s) and mail and e-mail addresses).
- Manuscript including abstracts, key words, illustrations, tables, figures with figure captions and list of references.
- MS Word files of the paper.



THOMSON REUTERS

WEB OF SCIENCE



Scopus®



CAS®

A DIVISION OF THE
AMERICAN CHEMICAL SOCIETY



Scientific Indexing Services

Google
Scholar